ANALYTIC
IN-15

27th Aerospace Mechanisms Symposium

```
(NASA-CP-3205)   THE 27TH AEROSPACE          N94-29627
MECHANISMS SYMPOSIUM  (NASA. Ames            --THRU--
Research Center)   384 p                     N94-29651
                                             Unclas


                                    H1/15   0002905
```

Proceedings of a symposium sponsored by the National Aeronautics and Space Administration, Washington, D.C., the California Institute of Technology, Pasadena, California, and the Lockheed Missiles and Space Company, Inc., Sunnyvale, California, and held at NASA Ames Research Center, Moffett Field, California
May 12–14, 1993

NASA

27th Aerospace Mechanisms Symposium

Compiled by
Ron Mancini
Ames Research Center
Moffett Field, California

*Proceedings of a symposium sponsored by the National Aeronautics
and Space Administration, Washington, D.C., the California Institute
of Technology, Pasadena, California, and the Lockheed Missiles
and Space Company, Inc., Sunnyvale, California, and held at
NASA Ames Research Center, Moffett Field, California
May 12–14, 1993*

PREFACE

The proceedings of the 27th Aerospace Mechanisms Symposium, which was hosted by Ames Research Center, Moffett Field, California, on May 12, 13, and 14, 1993, are reported in this NASA Conference Publication. The symposium was sponsored by the National Aeronautics and Space Administration, the California Institute of Technology, and Lockheed Missiles and Space Company, Inc.

The purpose of the symposium was to provide a forum for the interchange of information among those active in the field of mechanisms technology. To that end, 24 papers were presented on aeronautics and space flight, with special emphasis on actuators, aerospace mechanism applications for ground-support equipment, lubricants, latches, connectors, robotics, and other mechanisms for large space structures. The papers were prepared by authors from a broad aerospace background, including the U.S. aerospace industry, NASA, and European and Asian participants.

The efforts of the review committee, session chairmen, and speakers contributing to the technical excellence and professional character of the conference are especially appreciated.

The use of trade names or names of manufacturers in this publication does not constitute an official endorsement of such products or manufacturers, either expressed or implied, by the National Aeronautics and Space Administration.

CONTENTS

SESSION I

SESSION II

SESSION III

SESSION VII

SESSION VIII

SYMPOSIUM SCHEDULE

Registration will take place at the symposium hotel (Holiday Inn, Palo Alto) on Tuesday evening and on each day of the symposium at the Auditorium, Bldg N201, NASA Ames.

TUESDAY, 11 MAY 1993

6:00-8:00 pm   EARLY REGISTRATION AND SOCIAL
(Holiday Inn, Palo Alto)

WEDNESDAY, 12 MAY 1993

8:30   Wednesday Authors' Breakfast
(Cafeteria, Bldg N235, NASA Ames)

9:30   REGISTRATION AND COFFEE
(Main Auditorium, Bldg N201, NASA Ames)

10:30   INTRODUCTORY REMARKS
Mr. Ronald E. Mancini, Host Chairman
  NASA Ames Research Center
Dr. Charles W. Coale, General Chairman
  Lockheed Missiles & Space Co., Sunnyvale, CA

CENTER WELCOME
Dr. Dale L. Compton, Center Director
  NASA Ames Research Center

11:00   SESSION I
Dr. Hans E. Hintermann, Session Chairman
CSEM, Neuchatel, Switzerland
- *Collecting Cometary Soil Samples? Development of the Rosetta Sample Acquisition System*
    P. A. Coste and M. Eiden, European Space Agency, Noordwijk, The Netherlands
    M. Fenzi, TECNOSPAZIO, Milan, Italy
- *A Compact Roller-Gear Pitch-Yaw Joint Module: Design and Control Issues*
    Mark E. Dohring and Wyatt S. Newman
    Case Western Reserve University, Cleveland, OH
    William J. Anderson, NASTEC, Inc., Brookpark, OH
    Douglas A. Rohn, NASA Lewis Research Center, Cleveland, OH
- *Mars Rover Mechanisms Designed for Rocky IV*
    Tommaso P. Rivellini, Jet Propulsion Laboratory, Pasadena, CA

12:30   LUNCH

1:30   SESSION II
        Mr. Steven Burdette, Session Chairman
        Hughes Aircraft Co., El Segundo, CA
        − A Module Concept for a Cable-Mesh Deployable Antenna
            Akira Meguro
            Nippon Telegraph and Telephone Corporation,
            Kanagawa. Japan
        − Waves in Space Plasma Dipole Antenna Subsystem
            Mark Thompson
            Astro Aerospace Corp., Carpinteria, CA
        − Design and Testing of the LITE Variable Field Stop Mechanism
            Robert A. Dillman
            NASA Langley Research Center, Hampton, VA

3:00   BREAK

3:25   SESSION III
        Mr. John W. Redmon, Sr., Session Chairman
        NASA Marshall Space Flight Center, Huntsville, AL
        − Integration of Pyrotechnics into Aerospace Systems
            Laurence J. Bement
            NASA Langley Research Center, Hampton, VA
            Morry L. Schimmel
            Schimmel Co., St. Louis, MO
        − Retention Latch Mechanism for the Wake Shield Facility
            Timothy G. Vendrely
            Space Industries, Inc., League City, TX
        − Development and Testing of the Automated Fluid Interface
            System (AFIS)
            Martha E. Milton and Tony R. Tyler
            NASA Marshall Space Flight Center, Huntsville, AL

6:00-8:00   WELCOMING RECEPTION
                (Justines and Piazza Rooms, Holiday Inn, Palo Alto)

THURSDAY, 13 MAY 1993

7:30   Thursday Authors' Breakfast
        (Cafeteria, Bldg N235, NASA Ames)

8:30   SESSION IV
        Mr. Carl A. Marchetto, Session Chairman
        Astro Space, General Electric Co., Princeton, NJ

- *Lockup Failure of a Four-Bar Linkage Deployment Mechanism*
    Michael Zinn
    Lockheed Missiles & Space Co., Sunnyvale, CA

2:50   BREAK

3:15   SPECIAL PRESENTATION
        12 ft Wind Tunnel Restoration Project Overview
          Michael J. Ospring
          NASA Ames Research Center

7:00   DINNER AND SOCIAL EVENING
        5:30   Buses depart from Holiday Inn, Palo Alto
        7:00   Board yacht *Monto Carlo* for Bay Cruise and Dinner
        10:00   Return to dock
        10:15   Buses depart for return to Holiday Inn

FRIDAY, 14 MAY 1993

7:30   Friday Authors' Breakfast
        (Cafeteria, Bldg N235, NASA Ames)

8:30   SESSION VII
        Mr. Obie H. Bradley, Session Chairman
        NASA Langley Research Center, Hampton, VA
        - *Miniature Linear-to-Rotary Motion Actuator*
            Michael R. Sorokach
            NASA Langley Research Center, Hampton, VA
        - *Portable Linear Sled (PLS) for Biomedical Research*
            Wilbur Vallotton and John Temple
            Sverdrup Technology Inc., Moffett Field, CA
            Dennis Matsuhiro and Tom Wynn
            NASA Ames Research Center, Moffett Field, CA
        - *Laminar Flow Supersonic Wind Tunnel Primary Air Injector*
            Brook E. Smith
            NASA Ames Research Center, Moffett Field, CA

10:00   BREAK

10:25   SESSION VIII
        Mr. Angelo Giovannetti, Session Chairman
        NASA Ames Research Center (Ret), Moffett Field, CA
        - *Design and Test of Electromechanical Actuators for Thrust Vector Control*
            J.R. Cowan and Rae Ann Weir
            NASA Marshall Space Flight Center, Huntsville, AL

— *SP-100 Control Drive Assembly Development*
Thomas E. Gleason, A. Richard Gilchrist and Gary Schuster
General Electric Co., San Jose, CA

11:25   NASA AMES RESEARCH CENTER OVERVIEW
James P. Murphy
Director, Office of Engineering and Technical Services
NASA Ames Research Center

12:00   PRESENTATION OF THE HERZL AWARD
Mr. Otto H. Fedor
NASA Kennedy Space Center (Ret.), FL

12:10   CLOSING REMARKS
Mr. Stuart H. Loewenthal
Lockheed Missiles & Space Co., Sunnyvale, CA

12:30   LUNCH

1:30-3:30   FACILITY TOUR
Mr. Salvador A. Rositano, Tour Chairman
NASA Ames Research Center

ORGANIZING AND REVIEWING COMMITTEE

The papers presented at the symposium were selected and reviewed by the Organizing Committee. Each author is responsible for the content and the technical accuracy of their respective paper. The committee was composed of the following members:

Ronald E. Mancini	Host Chairman	NASA ARC
David F. Engelbert	Co-Host Chairman	NASA ARC
Charles W. Coale	General Chairman	LMSC
Stuart J. Loewenthal	Operations Chairman	LMSC

Edward A. Boesiger	LMSC
Obie H. Bradley	NASA LaRC
Homer S. Brown	NASA KSC
Charles L. Cornelius	NASA MSFC
Michael Eiden	ESTeC
Harvey H. Horiuchi	JPL
Jerry E. McCullough	NASA JSC
Stewart C. Meyers	NASA GSFC
John W. Redmon, Sr.	NASA MSFC
John F. Rogers	NASA LaRC
Douglas A. Rohn	NASA LeRC
William C. Schneider	NASA JSC
Donald R. Sevilla	JPL
Sterling W. Walker	NASA KSC
Bowden W. Ward, Jr.	NASA GSFC

ADVISORY COMMITTEE

Paul W. Bomke	JPL
Aleck C. Bond	NASA JSC (Ret.)
Thomas F. Bonner	Space Industries
H. Mervyn Briscoe	ESTeC (Ret.)
Kenneth C. Curry	JPL (Ret.)
Otto H. Fedor	LSOC (Ret.)
Angelo Giovannetti	NASA ARC (Ret.)
Frank T. Martin	NASA GSFC (Ret.)
James D. Phillips	NASA KSC (Ret.)
James H. Parks	NASA LaRC (Ret.)
Alfred L. Rinaldo	LMSC (Ret.)
Nathan D. Watson	NASA LaRC (Ret.)

SYMPOSIUM SUPPORT STAFF

Fred G. Martwick	Logistics Coordinator	NASA ARC
Merle Simbe	Registration/Security Coordinator	NASA ARC
Salvador A. Rositano	Facility Tour Coordinator	NASA ARC
Edward A. Wegner	Publications Coordinator	LMSC (Ret.)

COLLECTING COMETARY SOIL SAMPLES ? DEVELOPMENT OF THE ROSETTA SAMPLE ACQUISITION SYSTEM

P. A. Coste *, M. Fenzi **, M. Eiden*

ABSTRACT

In the reference scenario of the ROSETTA CNRS mission, the Sample Acquisition System is mounted on the Comet Lander. Its tasks are to acquire three kinds of cometary samples and to transfer them to the Earth Return Capsule. Operations are to be performed in vacuum and microgravity, on a probably rough and dusty surface, in a largely unknown material, at temperatures in the order of 100 K.

The concept and operation of the Sample Acquisition System are presented. The design of the prototype corer and surface sampling tool, and of the equipment for testing them at cryogenic temperatures in ambient conditions and in vacuum in various materials representing cometary soil, are described. Results of recent preliminary tests performed in low temperature thermal vacuum in a cometary analogue ice-dust mixture are provided.

INTRODUCTION

The goal of the ROSETTA Comet-Nucleus Sample-Return (CNSR) Mission, is to send an unmanned spacecraft to a comet, to collect and bring back to the Earth samples of cometary material for further laboratory investigations. The analysis of this material will constitute a fundamental step towards understanding the early evolutionary stages of the Solar System.

The **Sample Acquisition System (SAS)** is to be mounted on the lower part of the **Comet Lander,** together with the Anchoring Subsystem. SAS's tasks are first to anchor the Lander to the Comet, then to acquire **three kinds of cometary samples** and transfer them to the **Earth Return Capsule (ERC)** attached to the Return Carrier (the anchored Lander will eventually be abandoned on the Comet). The SAS is primarily made up of : a **coring tool,** a **shovelling tool,** an **external cutting device,** a **manipulator arm,** the associated three **anchoring systems** and the control electronics. Fig. 1 shows the anchored spacecraft with an earlier SAS concept (inset, from ref. 7), and sketches the present design concept.

---

*   ESA-ESTEC, Noordwijk (The Netherlands)
** TECNOSPAZIO, Milan (Italy)

This development is the result of a technology study performed by TECNOSPAZIO and their sub-contractors, under European Space Agency (ESA) contract.

GENERAL ROSETTA REQUIREMENTS

Based on the results of Halley and other comet missions, there is a general agreement that cometary matter consists of volatile and non-volatile components and that the bulk composition and the physical properties of cometary material change spatially throughout the comet and its nucleus. For these reasons, three different types of sample are considered essential in order to obtain the optimum information about the comet nucleus :

1. A **core sample** : this to be a continuous sample taken from the surface of the nucleus down to a depth of at least 1 m (goal 3 m); it should provide the interrelation between volatile and refractory compounds in the comet. This sample should be subdivided and stored in separate segments, preserving also its coarse stratigraphy.

2. A **volatile sample** : this is to be taken from a location where the most volatile components can be expected, i.e. from the bottom of the core sample hole (it may be the lower part of the core sample). To retain these components, the sample should be stored in a totally sealed container.

3. A **surface sample** : this is to be collected from one or more locations at the surface of the nucleus. This sample is intended for studies of the refractory carbonaceous and inorganic compounds.

The Sample Acquisition System is designed for the minimum scientific coring depth requirement of 1 m, whilst operating under the following constraints :

- **Environmental (comet surface at 5 AU)** : milligravity, vacuum, surface temperature from 100 to 150 K; soil compressive strength ranging from 10^{-4} to 100 MPa ; soil density from 0.05 to 2 g/cm^3 (dust mantle) and from 0.1 to 1.5 g/cm^3 below. Composition: ca. 80 % H_2O (ice), remainder inorganic and organic (volatile) materials (ref. 3).

- **Scientific** : acquire nominally 1 m core, diameter 100 mm; mass 15 kg of core/volatile sample, 5 kg of surface sample, including loose hard pieces, max. size 5 cm; minimize perturbation and contamination : limit sample temperature increase to 10 K; seal volatile sample; sample compression allowed.

- **System and engineering** : one core hole minimum; acquire sample on a rough surface, 0.5 m above or under the level of the landing pads; max. storage length for 100 mm dia. core segments and surface sample containers : 0.6 m, dia. ca. 140 mm; max. electrical power 100 W, torque 100 Nm, vertical thrust 100 N. (ref. 4). Mass and size budget goal: 100 kg, 1 m^3.

- **Anchoring** : react with margins in maximum sampling thrust and forces (i.e. typically 300 N per anchor).

One of the greatest difficulties is that the physical properties of the cometary soil are not well-known, and therefore a very wide range of possible values must be considered : the hardness ranges over 6 orders of magnitude from that of soft snow's to that of a medium-hard rock (tuff). This extreme hardness, scientifically foreseen for loose pieces only, has been taken as a development goal : the spacecraft has to be anchored and a single corer needs to operate in the hardest soil. As the spacecraft can only provide limited power and thrust (unusually low for rock-like material), this combination of hard soil, relatively large core and limited resources presents the most challenging design constraint.

SAMPLING ACQUISITION SYSTEM CONCEPT AND OPERATIONS

The Sampling Acquisition System (SAS) has to provide the following functions :

* anchoring of the spacecraft to the comet soil;
* collecting of core, volatile and surface samples;
* handling of samples in order to store them in the Earth re-entry capsule.

To ensure maximum simplicity and reliability, the essential functions have been assigned to dedicated mechanisms, in particular that for coring, which is the most demanding sampling function.

Core Sampling Subsystems, Description and Operations

The initial configuration from which all subsystems are deployed is their upper position, required at comet landing, to avoid collision of lowest parts such as the drill bit with the highest foreseen surface irregularities at the landing site. This may also represent a launch mounting position, which can be maintained until after landing.

The functions and operations of the subsystems necessary to acquire a core sample are best described with reference to the schematic of Fig. 1. : it shows an intermediate position where several components have already been disconnected

The **corer rod** is composed of the **drill bit (1)** fixed to the **torque tube (2)**, whose **helical augers** ensure chip removal. The corer rod is connected to the **main rotary joint (10)** and encloses the **core canister (8)** whose bottom **shutter valves (4)** are open. At the start, the **support table (5)** is lowered by the **secondary linear joint (3)**, and stopped when the drill bit reaches the surface, after a maximum descent of 1 m. The main rotary joint provides torque and rotates the corer rod only : the core canister does not turn with the torque tube (to minimize mechanical or thermal disturbances on the core sample which penetrates and fills it, e.g. twisting or temperature increase due to friction). The **main linear joint (12)** provides downwards thrust and controls the advance of the corer ; its stroke allows a maximum coring depth of 1 m.

When this lower coring position is reached, rotation is still maintained, and the inner systems are operated sequentially. First, the spherical sectors of the shutter valves (4) are closed to perform the core bottom sectioning (a detailed description of the bottom shutter subsystem follows). The shutter valves eventually close the core canister. Rotation is then stopped, and the **separable link (9)** disconnects the torque tube (2) from its actuator (10). The closed core canister is lifted alone, the drill rod being left in the soil (possibly spring-latched on the support table). Fig. 1 illustrates the end of this stage, where the sample-filled core canister is completely extracted.

Core segmentation and handling operations then proceed as follows : the **ancillary rotary joint (11)** positions the core canister sideways in the **gripper (6)** which closes its claws. **Sawing disks** of the **external cutting device (7)** are rotated; facing the **middle position to be cut(14)**, they translate towards the canister and cut it with its core sample. The joint (11) rotates the separated assembly to place the upper canister segment above a **first cap (16)**, into which it is lowered and engaged by action of the joint (12) − (care is required at this stage, as both canister ends remain open momentarily, while containing loosely restrained core samples; this sequence, with a short critical path, is acceptable in microgravity).

The **manipulator arm** (similar to the one shown in Fig.1) grasps a **second cap (15)**; after retraction of the saw disks, it closes the upper end of the lowest canister segment, grasps the whole lower sample and, with gripper released, it transports and stores it into the ERC − (the core sample containing volatile compounds is then stored first in the capsule).

Similar operations are performed on the upper sample segment: displacement by actions of joints (12) and (10) with its **upper section to be cut (13)** facing disks (7), capture by (6), cutting, top closing by a **third cap (17)**, and finally

storage in the ERC - (this second sample contains core with some crust at the top).

Surface Sampling

The surface tool (similar to the one of Fig. 3) is driven by the manipulator arm. It is composed of a fixed **outer tube** and an inner **helical screw** with a cutting blade at the bottom, which rotates until the tube is filled with chips and loose pebbles. It is foreseen to cap it and disconnect its drive before storage in the ERC.

The use of brushless DC or stepper motors is generally foreseen for all relevant subsystems, most linear and rotary joints being provided with a brake and a position encoder.

It can be noted that tasks in the core sample acquisition sequence are performed by a succession of well separated operations of dedicated mechanisms. The only exception is the manipulator arm : this complex subsystem is used for handling and manipulation, but is also essential for surface sampling. It requires 7 degrees of freedom, and complex joints. As it has the additional benefit of being available for assisting in eventual recovery strategies, this dexterous item could not be easily replaced by a set of simpler mechanisms.

Mass and Power System Budgets

The provisional mass budget for a SAS coring to 1 m depth is 159 kg, without margins, composed essentially of 110 kg for the sampling systems (structure and actuators, including 19 kg of tools (corer : 12 kg; surface tool : 7 kg) and 40 kg for the manipulator arm. 30 kg for the anchoring subsystem (i.e. 3 anchors, each with their deployment and lateral actuation devices) are also included in this budget.

The maximum power budget is 202 W, bearing in mind that operations are non-simultaneous : coring (109 - 202 W), external cutting (20 W), surface tool (125 - 155 W) and handling (105 W).

The testing program will allow refinement of these figures, which represent approximately twice the mass and power budget goals (100 kg, 100 W) for a nominal core diameter of 100 mm. If necessary to achieve compatibility with mission budgets, the present 100 mm core diameter can be scaled down to approximately 70 mm.

PROTOTYPE CORER AND SURFACE TOOLS

A prototyping activity has been started in order to verify the design feasibility of critical subsystems by testing, and to demonstrate the ability to collect different types of

materials, ranging from snow to tuff, under severe environmental conditions, i.e. vacuum and −180 C (ca. 90 K, or boiling temperature of liquid nitrogen (LN2)).

Currently under development are :

* the coring tool;
* the surface tool;
* the external cutting device;
* the anchors.

The core canister extraction and other further operations are not yet modelled. No special motor development is included in the programme at this stage. The manufactured prototype tools are only representative of the samples and other main outer tool dimensions. In accordance with the test objectives, they are not otherwise mass and material representative, as they are mostly manufactured from stainless steel AISI 304, instead of aluminium alloy 7075. Tubes are thicker than required, to allow testing for a wider range of forces and torques with these development models.

Corer Tool Prototype Description

The corer tool prototype (Fig. 2) is mainly composed of :
- the torque tube;
- the drill bit (Fig. 2 d);
- the core canister;
- the shutter valves (Figs. 2 b,c and e);
- the shutter mechanism (Fig. 2 a).

The **torque tube** transmits the torque and the thrust from the actuators to the drill bit, and torque to the shutter valves. Its outer surface and augers are covered with a thick PTFE coating (EMRALON 333).

The "multistep" **drill bit** (Fig. 2 d) cuts the soil in an area of ca. 100 cm^2 (OD 150, ID 100 mm) by means of twelve **polycrystalline diamond (PCD) cutters**. The cutters are positioned at three different levels or "steps" to allow a gradual cutting action. There are two pairs of cutters at each step with a slight overlap between their cutting envelopes. They are brazed onto their stainless steel support by a silver/copper alloy that is suitable for use at low temperature. Each cutter has a negative (apparent) rake angle of 10 deg. and a relief angle of 15 deg., and a cutting edge of either 3.5 or 4.5 mm.

The **core canister** is the thin inner tube that contains the sample during the sample extraction and handling phase, and which is later sectioned and returned with the samples. The shutter valves are attached to its lower end.

The **shutter valves** (cf. figs. 2 b, c and e) sever the core sample when the desired depth is reached. They are two pivoting spherical sectors which may rotate through 60 deg. from open to closed position around a pivot radial to the corer axis. Four PCD cutters are brazed onto the closing edges, as for the drill bit. The **valve pivots** are part of an intermediate **mobile collar**, itself linked by a rotary joint to the bottom of the canister around which it turns freely. **Keys** on the collar engage opposite slots inside the torque tube, which drives the open valves, and transmits torque to them when they start closing. Closure is commanded by the shutter mechanism linked to the shutter valves.

The **shutter mechanism** is located in the upper part of the corer tool. In the concept illustrated by Fig 2 a, two **long rods** of ca. 1 m are connected to a **linkage** of the shutter valves and at the top to a **threaded sliding nut** with keys, which can slide inside the torque tube. A **driving screw** inside this nut is the rotor of a **motor**, normally not powered and turning freely. When the motor is activated, a differential rotational speed between the torque tube and the driving screw occurs, which lifts the sliding nut, pulling the rods and consequently closing the shutter valves. It can be noted that the rods will later be sectioned with the sample canister.

For a cutting thrust of 20 N on each shutter edge (worst-soil case), the maximum rod closing force is 120 N (at start of closure); the power required to pull the rods is only 12 W, which adds to the cutting power provided by the main rotary actuator (comparatively lower for bottom cutting than the one required for drilling).

Surface Tool

The aim of the prototype surface tool (Fig. 3) is to demonstrate the collection of soft and medium hard materials, with superficial layer of dust and harder grains, under various environmental condition. It is sized for the collection of grains with diameters of up to 5 cm. The surface tool consists primarily of :

* a fixed outer tube;
* a rotating inner screw, with double helix;
* a double cutting edge;
* a fill sensor;
* a motor and gear box drive unit.

The collection function is performed with the combined action of the rotating **helical screw**, which allows lifting of the cut material, and of the static **outer tube** (OD 140 mm), which provides storage for the sample.

The helical screw is made by welding an helicoidal structure onto a shaft. It transmits the torque and the thrust to the cutting edge. To avoid jamming while the material is transported, the screw pitch of ca. 130 mm is slightly increased upwards. The **cutting edge** is composed of a conical support structure with a series of ceramic (WIDIA) cutters, brazed onto the support. A spike made of the same ceramic provides centring action at soil contact. The **fill sensor** stops the motor when the outer tube is full. It is positioned in the upper part of the outer tube and is composed of two springs connected with an electrical contact and a plate. When the material reaches the plate, the closure of the electrical contact signals the motor to stop. The **motor and gear box** system comprizes a 750 W DC motor, deliberately oversized for testing purposes. It is a customized item derived from a standard model with some modifications in order to work in the hostile test conditions (i.e. vacuum at -180 C). The gearbox has a 1:4 ratio. The motor axis is parallel to that of the helix for compactness.

Selection of Materials and Lubricants

All the materials used for the prototypes are either space qualified or able to withstand space environments, including very low working temperatures. On-ground cryogenic applications have been taken into account during the material selection process. Major attention has been paid to tribology during the prototype design phase due to the environmental testing conditions (vacuum and -180 C/ 90 K). Since the lowest temperature limit of any liquid lubricant is about -70 C, dry lubrication is required. Duty cycle and components considerations led to the choice of MoS_2 for ball bearings and of PTFE films or VESPEL for sliding parts. A thick PTFE coating coats the corer augers and surface-tool helix, to provide both efficient tool penetration and chip transport, and to resist abrasion.

PRELIMINARY TESTS ON CRITICAL CORER COMPONENTS

To assess the corer tool's performance for the anticipated range of comet soil properties and the environmental conditions expected (vacuum and very low temperature, 100-150 K), series of gradually more complex preliminary tests were performed, to determine the behaviour of some critical components.

Model materials were, from softer to harder, porous ice, Cometary Analogue Material(s) (CAMs, essentially LN_2-sprayed ice/Olivine dust mixtures), compact ice and natural Ettringer tuff (medium-hard rock with harder inclusions).

Corer bits and shutter mechanisms were manufactured and tested to assess first the adequacy of the cutting technology and then select the most suitable design, providing low cutting

power and proper "dry chip removal", i.e. without the assistance of any cutting and chip transportation fluid.

Ambient and Low Temperature Rig and Corer Tests

An **early test rig** using an industrial power drill on a sliding carriage was first used (Fig.4); a constant thrust was imposed by imbalanced counterweight. The rig was instrumented to measure drilling torque and advance.

Up to nine **"single step" drill bits** with different types and geometries of cutters (various tungsten carbide, impregnated and polycristalline diamond) were subjected to screening tests on tuff under ambient conditions before selecting a **multistep drill bit** with polycristalline diamond cutters and specifying its final design (Fig. 3 a).

Tests were performed at ambient temperature on tuff and at -25 C on tuff, ice and ice-sand mixture. A number of problems and difficulties were encountered, mainly related to dry chip removal. Test on ice showed some problems due to increased temperature, which changes the water phase from solid to liquid, and vice versa, resulting in ice production on the auger, inducing rapid chip clogging and stopping drill penetration.

Despite these initial problems, it was decided to pursue tests in conditions more representative of the cometary one's, at **-180 C** (LN2), but still at **ambient nitrogen pressure**. Tests on ice, tuff and CAMs (shown in Fig. 4) demonstrated **successful coring performance** of the multistep drill bit (cf. Table 1) under these otherwise more demanding conditions : the average hardness of the tuff rock had noticeably increased above the maximum specified value. Temperature elevation of the drill bit was in the order of 30 C max. for this harder material.

The **shutter valves** were tested at component level in association with the drill bit and corer with a **simplified shutter mechanism**, dead-weight loaded, (Fig. 5), to verify their cutting action. Their design (Fig. 3 e) is derived from that of the drill bit, reaping thereby the benefit of its good performance. Tests were conducted on graphite and on a specially prepared porous concrete ("Gasbeton") in order to define the correct valve geometry and the most efficient position for the PCD cutters. After final definition of the valves, tests were successfully performed on tuff at ambient temperature, then at -180 C on ice and on the same concrete.

Low Thermal-Vacuum Rig and Corer Tests

An **"external" test rig** (cf. Figs. 6 to 8) has been built to allow testing with full **control of rotation and drill advance** parameters under ambient pressure and, with **external actuation**, under **thermal vacuum (TV)** conditions : it features

the main rotational and translational joints of the SAS (items 10 and 12 of Fig.2).

TV tests are performed on this external test rig with the additional implementation of a long feed-through between the external actuation and the corer tool inside the TV chamber : as no emphasis on motors is given at this stage of the development programme, the external actuation of the tools was acceptable. The feed-through is made of two concentric tubes of ca. 3 m long.: the outer tube transmits the torque to the corer rod alone, and the inner tube translates the core canister. This concentric feed-through slides on a fixed support mounted on the upper flange of the TV chamber, some 3 m from the sample upper surface, which imposes such a tube length.

At full stroke, some 4 m of tube and corer extend inside the chamber : the lateral stiffness must still be high enough to rotate the corer up to 150 rpm below the first critical speed; it imposes a rigid guidance on the flange. Consequently, a very careful alignment of the whole driving shaft is necessary, to limit the additional friction on the flange bearings, despite the implementation of an external compliance joint. Tubes are initially subject to a large temperature gradient from outer ambient to that of the cold shroud, and then encounter rapid temperature variations during their downwards displacement while coring.

The concentric joints and the flange bearings present a design challenge, as they need to be vacuum-tight but also to allow rotation and translation of 1 m with a minimum friction, in order not to overload the external actuators, and to limit force-torque variations which pose a control problem.

A hydraulic piston assists the linear actuation during the TV tests, compensating for the additional forces due to the feed-through weight and to the vacuum.

All of these various mechanical, structural and thermal development problems were eventually overcome. For a leak rate allowing to maintain a vacuum of 10^{-3} Pa, the resulting friction torque of the outer seal did not exceed 100 Nm, and was less than 60 Nm for most of the 1 m stroke. Future improvement should reduce this friction still further.

Preliminary coring tests have been repeated with this equipment under low thermal vacuum conditions, in a LN2 cooled CAM sample (Fig.10) and in porous ice, with equal success as at ambient pressure. Controlling the speed of advance, two 1 m cores were drilled at the lower speed of 30 rpm within 15 min. The observed chips were fine, and there was no clogging problem : no qualitative difference due to the vacuum could be noted compared with previous tests.

Measurements, derived externally from motor current, and thus subject to uncertainties on the additional feed-through friction, indicated that the coring torque did not exceed 10 Nm, well in the order of magnitude of previous values of 4 to 5 Nm. For the next TV tests, adequate force and torque sensors will be placed in the chamber, mounted at the tip of the feed-through outer tube close to the corer rod, in order to measure and control these parameters more directly and more accurately.

Test results achieved so far are promising with respect to the next tests in this programme : in a near future, a prototype **integrated corer** including its **shutter valves** and **shutter mechanism** will also be operated in thermal vacuum.

To our knowledge, this was the first time such a corer's capabilities had been demonstrated in a hard material under extremely cold conditions, using such a low specific thrust and power, and moreover in vacuum.

CONCLUSION

The Sample Acquisition System has been developed to meet the particular and highly unusual requirements of the ROSETTA CNSR mission. A functional design via which well-defined actions are performed sequentially by specific tools has been selected to provide reliability of operation.

A step-by-step test programme has demonstrated so far that a corer and shutter valves with synthetic diamond cutters provide adequate performance under low specific thrust and power at low temperature and in vacuum even for a rocky material with hardness superior to that anticipated in the cometary soil. It is concluded that, subject to there being a successful anchorage, coring is an effective means of cometary soil sampling.

Testing of the prototype corer with bottom shutter and of the surface tool under thermal vacuum will be the next step in the development of the Sample Acquisition System.

The design of the tool described here is expected to find application in the context of other planetary missions in which large soil samples have to be acquired either for in-situ analysis or for return to Earth.

ACKNOWLEDGEMENTS

REFERENCES

1. Magnani PG. et al 1992, Sample Acquisition System for ROSETTA/CNSR, TECNOSPAZIO Phase 1 and CCN2 Final Report of **ESA contract** No. 9005/90.
2. Atzei A. et al. 1992, ROSETTA Comet-Nucleus Sample Return Mission, Ann. Geophysicae 10, 121-122
3. Stoeffler D. 1989, Petrographic working model of the ROSETTA sampling and modelling subgroup for a comet nucleus, Proc. Workshop on Physics and Mechanics of Cometary Material, Muenster, FRG, **ESA SP-302**, 23-29
4. Schwehm G. et al. 1991, ROSETTA, Mission and system definition document ESA/NASA, **ESA SP-1125**
5. Eiden M. et al. 1991, The Challenge of Sample Acquisition in a Cometary Environment, **ESA Journal** 1991, Vol. 15, 199-211
6. Elfving A. 1992, Automation Technology for Remote Sample Acquisition, **Int. Symposium on Missions, Technologies and design of planetary mobile vehicles,** 1992, Sept. 28-30, Toulouse (F)
7. MATRA 1991, Final Report of the System Definition Study, ESA contract 8228/89/NL/SK, Jan. 1991

Table 1: Main drill bit test results achieved at -180 C (multistep drill bit, OD 150 / ID 100 mm)

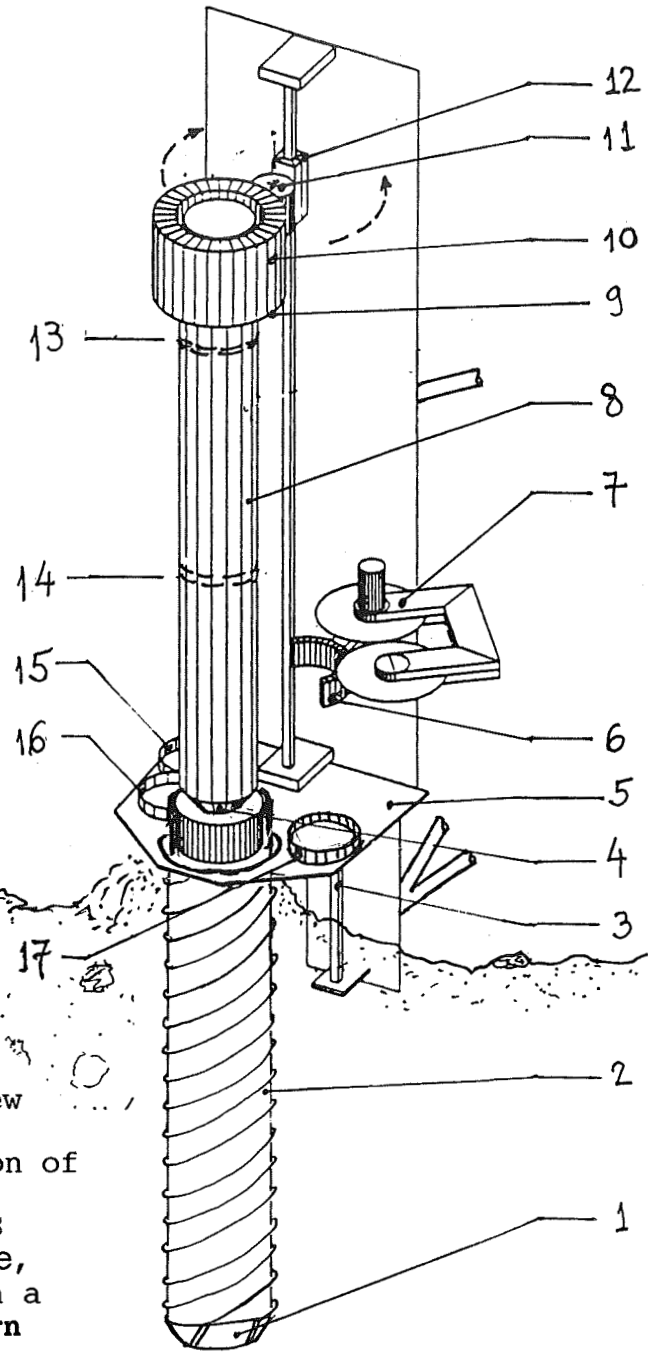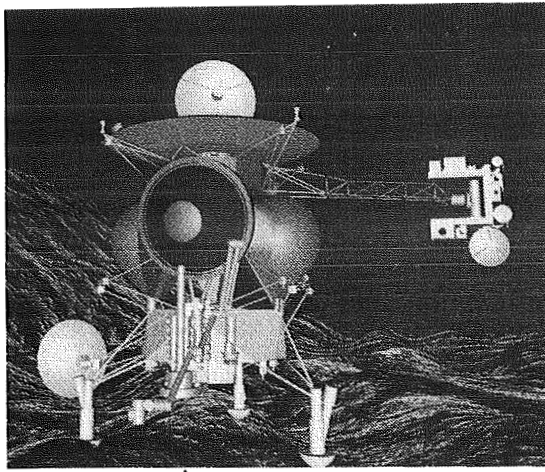| Sample Material		CAM	CAM	CAM	Ice	Tuff
Sample Temperature	C	-190	-190	-190	-170	-180
Depth	mm	380	417	420	501	490
Tool Average Penetration Rate	mm/min	380	296	134	30	1.6
Tool Thrust	N	50	50	20	60-100	60-350
Tool Torque	N.m	4	5	1.5	5-10	3-26
Tool Speed	rpm	150	100	100	150	130-150
Tool Average Power	W	63	52	17	80	100-400
Average Specific Energy	MPa	1	1	1	40	1250

Fig. 1. Sample Acquisition
         Systems (SAS) overview

top left : artist's conception of
the anchored ROSETTA CNSR
spacecraft (ref. 7), with **SAS**
(early concept) at bottom centre,
manipulator arm sampling with a
surface tool, and **earth return
capsule** at the centre.

right : present SAS design, sketched after extraction of the
1 m core sample.   **Main elements** : 1 : drill bit; 2 : torque
tube; 3 : secondary linear joint; 4 : shutter valves; 5 :
support table; 6 : gripper; 7 : external cutting device; 8:
core canister; 9 : separable link; 10 : main rotary joint; 11 :
ancillary rotary joint; 12 : main linear joint; 13, 14 : resp.
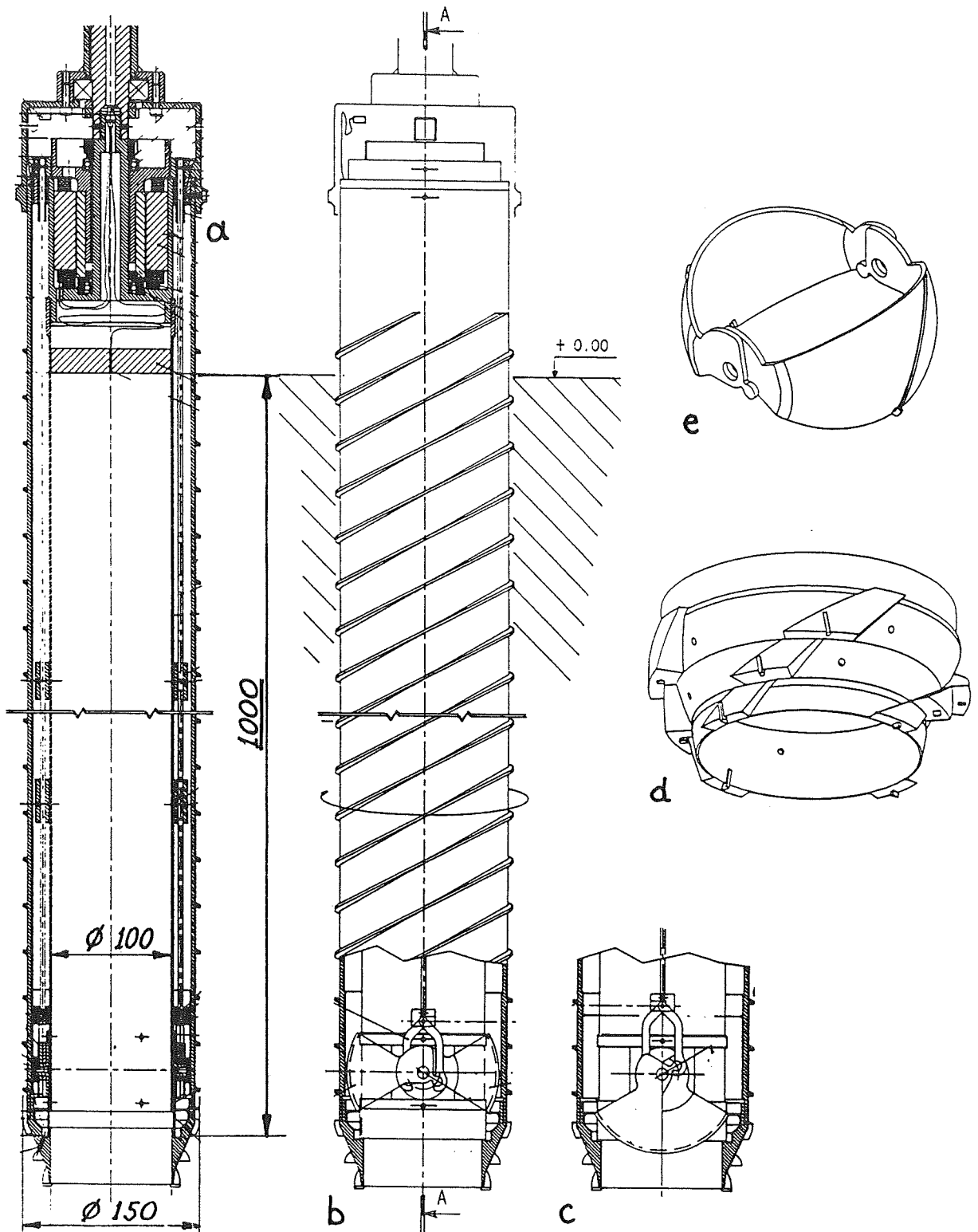upper and middle positions to be cut; 15-17 : caps.

Fig. 2. Integrated corer tool prototype.
a : shutter mechanism; b, c : shutter linkage;
d : multistep drill bit; e : shutter valves.
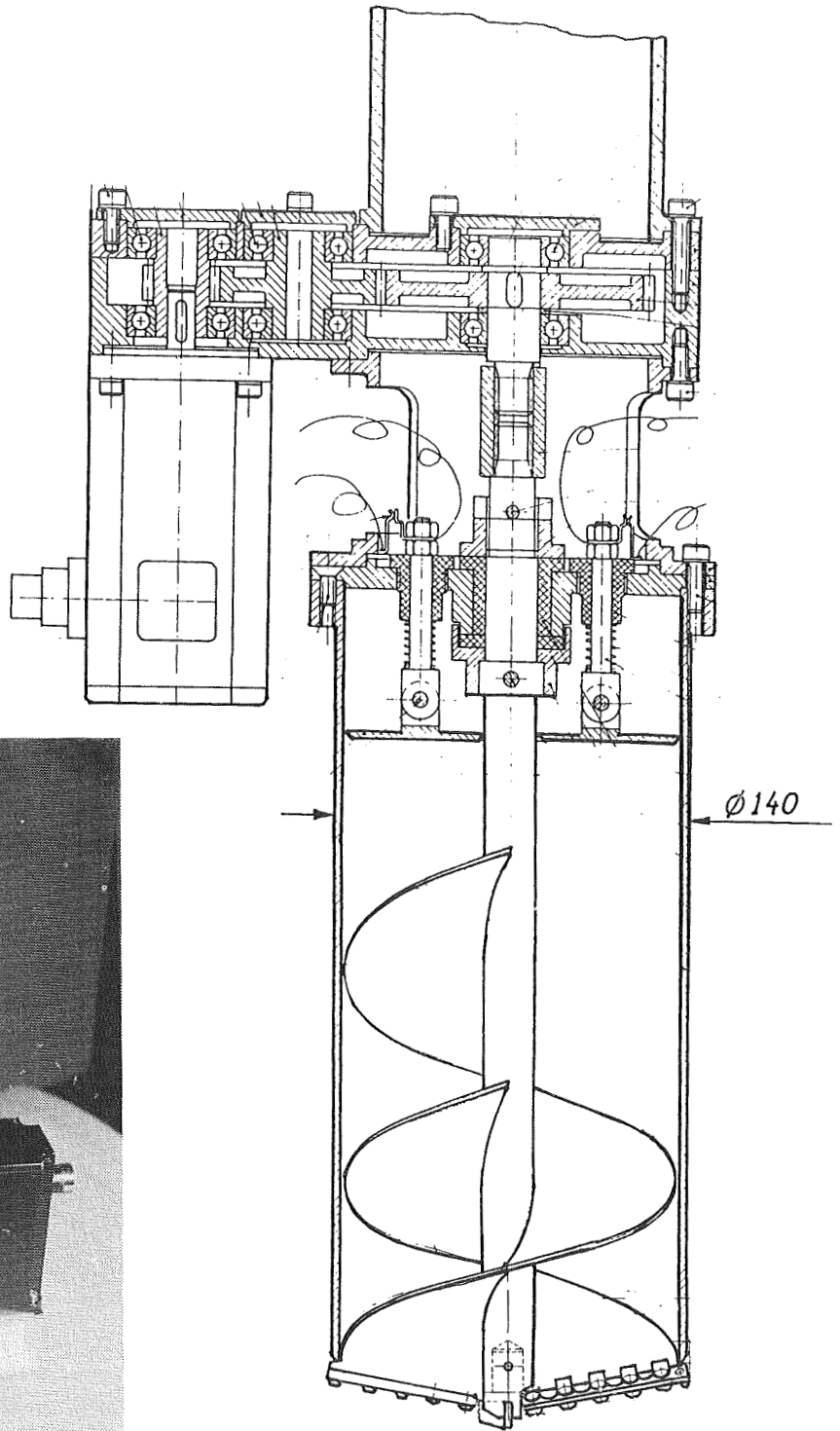
Fig. 3. Surface tool prototype

Ø140

15

Fig. 5. Shutter valves development model

Fig. 4. Early test rig during low temperature coring under nitrogen atmosphere
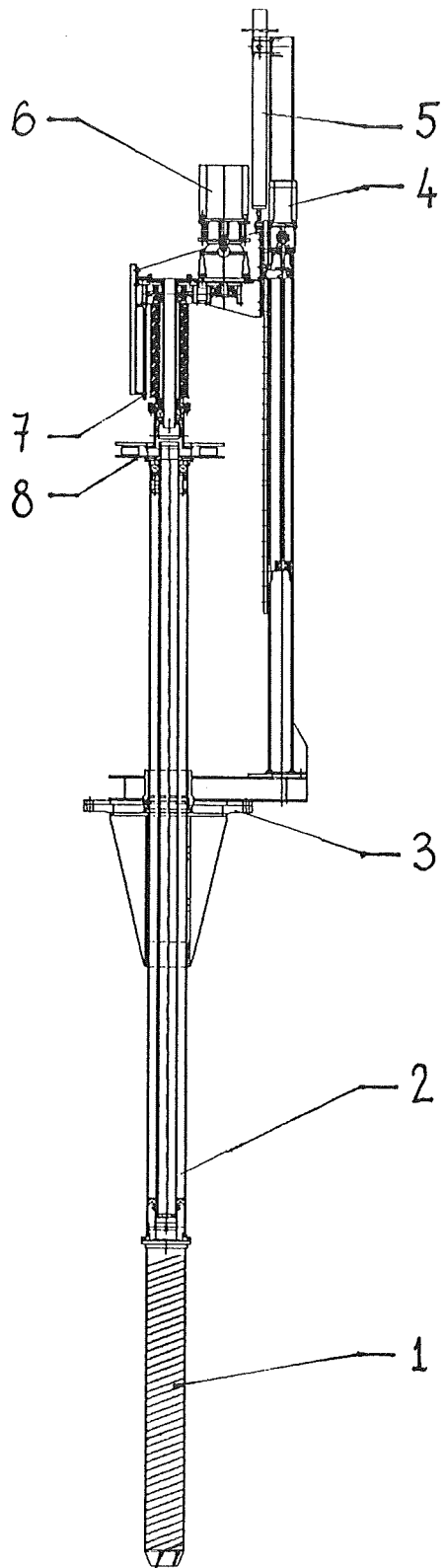
1 : corer tool
2 : feed-through
3 : interface with TV chamber
4 : linear actuation
5 : hydraulic piston
6 : rotary actuation
7 : sliding contacts
8 : compliance joint

Fig. 6. External test rig, main
components for Low TV tests

Fig. 8. External test rig and controls

Fig. 7. External test rig on TV chamber

18

Fig. 10. Corer with cometary analogue sample

Fig. 9. Corer tool prior to TV tests

A Compact Roller-Gear Pitch-Yaw Joint Module: Design and Control Issues

Mark E. Dohring * William J. Anderson †
Wyatt S. Newman ‡ Douglas A Rohn §

Abstract

Robotic systems have been proposed as a means of accomplishing assembly and maintenance tasks in space. Desirable charac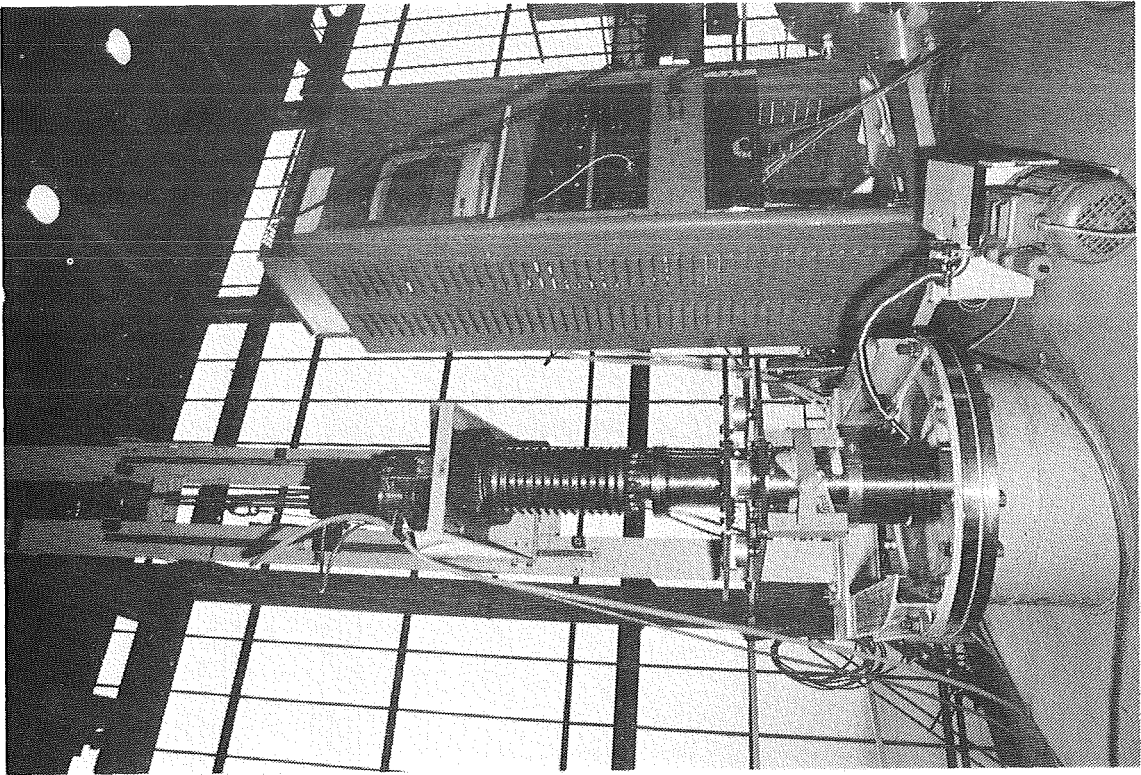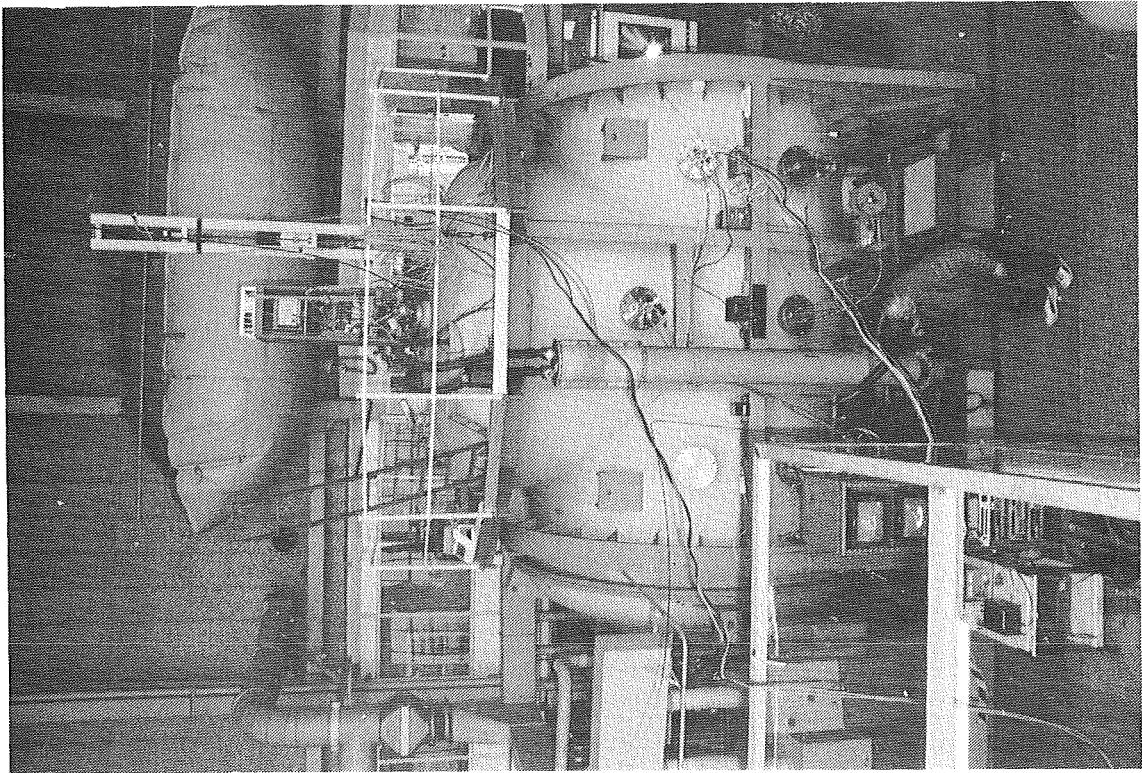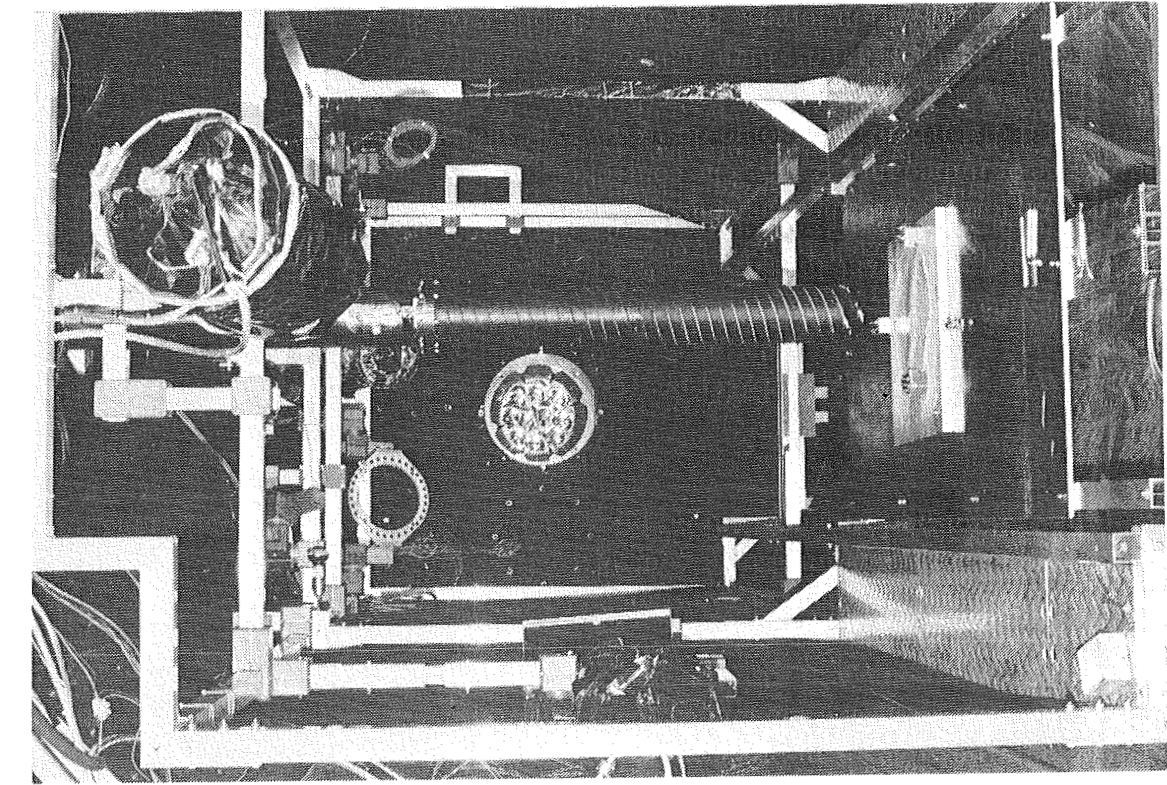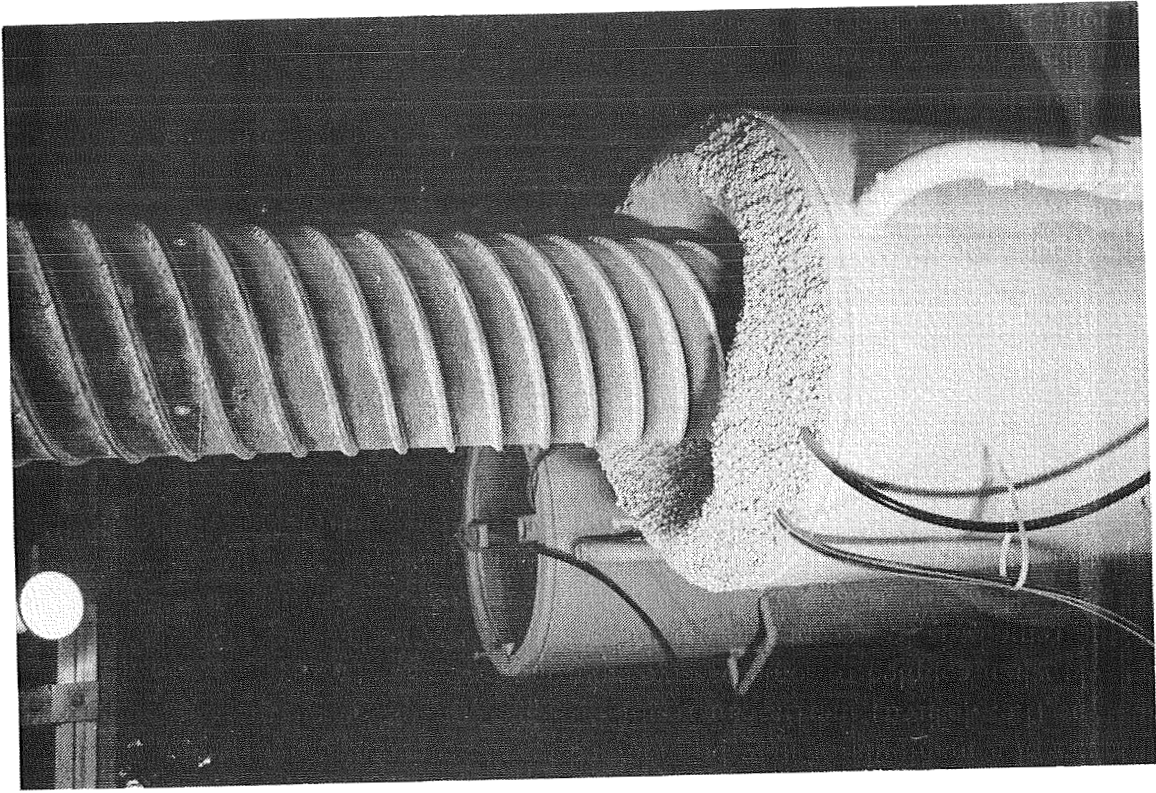teristics of these systems include compact size, low mass, high load capacity, and programmable compliance to improve assembly performance. In addition, the mechanical system must transmit power in such a way as to allow high performance control of the system. Efficiency, linearity, low backlash, low torque ripple and low friction are all desirable characteristics. This work presents a pitch-yaw joint module designed and built to address these issues. Its effectiveness as a two degree-of-freedom manipulator using natural admittance control, a method of force control, is demonstrated.

1 Introduction

The use of robotic manipulators is attractive in space operations, whether as autonomous systems, or as tele-operated devices. Possible uses include assembly, repair and servicing, inspection, retrieval and exploration. Much effort has been devoted to the development of controls to accomplish suitable tasks. Somewhat less has been expended for improving the mechanical components in robotic systems. The interaction of the controls and the mechanical components' characteristics (i.e.: stiffness, backlash, friction) is often a serious issue.

The major task in any control scheme is enforcing the desired behavior of the controlled system in the presence of disturbances: gravity, end effector forces, and collisions with obstacles; and internal dynamics: friction, mechanical stiffness, transmission dynamics, actuator dynamics, sensor noise, and time delay. Position control attempts to force a specific end-effector trajectory. Force control tries to enforce a specified end-effector contact force. However, classical approaches to force control have had severe limitations and problems with instabilities [1].

---

*Case Western Reserve University, Cleveland, OH
†NASTEC, Cleveland, OH
‡Case Western Reserve University, Cleveland, OH
§NASA Lewis Research Center, Cleveland, OH

21

An alternate approach to direct or explicit force control is to control not a vector of positions or forces, but the relationship between those variables using a programmable compliance or impedance [2, 3]. The controller specifies the manipulator's response to environmental disturbances in some desired way, usually emulating programmable springs and dampers. In impedance control, the stiffness and damping parameters can be adjusted to the task at hand: high stiffness for precise positioning, and low stiffness to accommodate interaction forces. However, stability of the system when interacting with its environment is still a problem [4, 5, 6, 7, 8] If the controlled system is to remain stable when coupled to an arbitrary passive environment (one that can be modeled using only passive elements), it must itself present a passive mechanical admittance to the environment at the end effector [7]. This imposes restrictions on how the intrinsic endpoint dynamics of a manipulator may be modified by the control. In particular, reducing the apparent (i.e. desired) inertia can result in a system that is not passive which will be unstable when coupled to some passive environment.

One remedy is to accept the natural manipulator inertia and make no attempt to change it. However, this is often disappointing on machines which have large amounts of friction and other non-linearities such as gearing backlash. Friction limits sensitivity to small end effector forces and backlash makes stable control more difficult. Robots can be designed with lower friction and direct drive actuators to reduce transmission dynamics, but payload capacities are reduced, and the motors become larger and heavier. This raises several questions. Is it possible to compensate for friction and other effects without violating passivity? If systems must contain high friction components to meet payload, weight, and size requirements, can they be designed to make the compensation task easier? What approach can be used to get the maximum possible performance, given a particular manipulator system?

Natural admittance control (NAC) [9, 10] addresses these issues. Using this approach, it is not only possible to improve performance while maintaining stability, but also to identify mechanical design guidelines that improve ultimate performance. Also, it suggests that the endpoint admittance is a good performance measure.

In this paper, we review the design of a 2-degree-of-freedom (2-DOF) pitch-yaw roller-gear joint module which has been developed to exhibit low friction and no backlash. The application of natural admittance control to the transmission will also be examined. Resulting system performance will be presented, along with recommendations for other designs.

2   Two Degree of Freedom Arm

The pitch-yaw module is part of a 2-DOF manipulator and was designed and built by NASTEC under contract to NASA Lewis Research Center [11]. It is similar in specifications to the large joint of the Micro-Gravity Manipulator and the Laboratory Telerobotic Manipulator built by Oak Ridge National Laboratories for NASA-Lewis and NASA-Langley, respectively [12, 13], but uses roller-gears for torque transmission. Transmissions of this type have been shown to have some of the smoothness of pure traction drive

transmissions with higher torque capacity at a given roller loading due to the gear teeth [14]. The module input is driven by a pair of gear motor drives having a 90:1 ratio in the gear heads. A link is mounted to the pitch- yaw module output, creating a 2-DOF manipulator arm, capable of moving payloads through a spherical-surface workspace. Over all, the joint is capable of lifting 220 Newtons (50lbs) at a moment arm of 0.84m (33in), the length of the link.

2.1 Pitch-Yaw Module Design

The pitch-yaw module provides two degrees of freedom in a compact space. Figure 1 shows a cross-section of the components in the module. In this drawing, the roller and
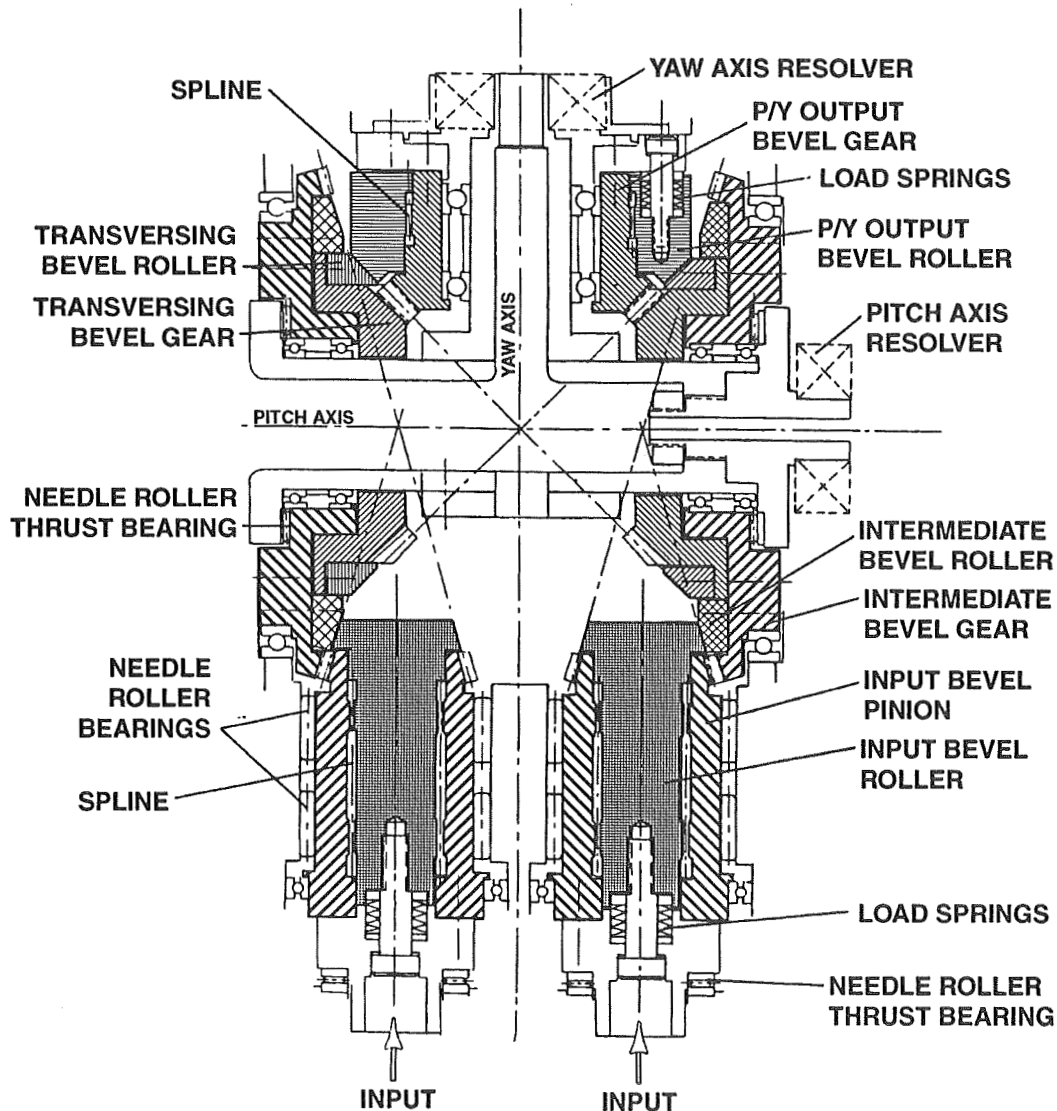

Figure 1: Drawing of pitch yaw module

gear elements are cross-hatched, and much of the housing detail is omitted for simplicity. The module is a differential, having two parallel bidirectional inputs and a crossed-axis output which moves in pitch and yaw. Referring to the figure, the input bevel pinion gears drive the intermediate bevel gears. The input bevel rollers are splined to the pinion gears, and are spring-loaded axially against the intermediate bevel rollers. On each side of the module, the intermediate gear and roller are fixed to each other as well as to the transversing bevel gears and rollers. These intermediate/transversing assemblies are not, however, fixed to each other, but rotate individually about the pitch axis. Both transversing bevel gears drive the pitch-yaw output gear. The output roller is spring-loaded against the transversing bevel rollers and moves axially on the bevel gear via a spline. Rotation of the two inputs in the same direction at the same speed results in a pure yaw output; rotation in opposite directions at the same speed results in a pure pitch motion. All other combinations of input speed and rotation result in motions about both the pitch and yaw axes. The speed ratio across the module to either a pure pitch or pure yaw output is 3.4283.

Figure 2 shows a photo of the module partially assembled. In this orientation, the two
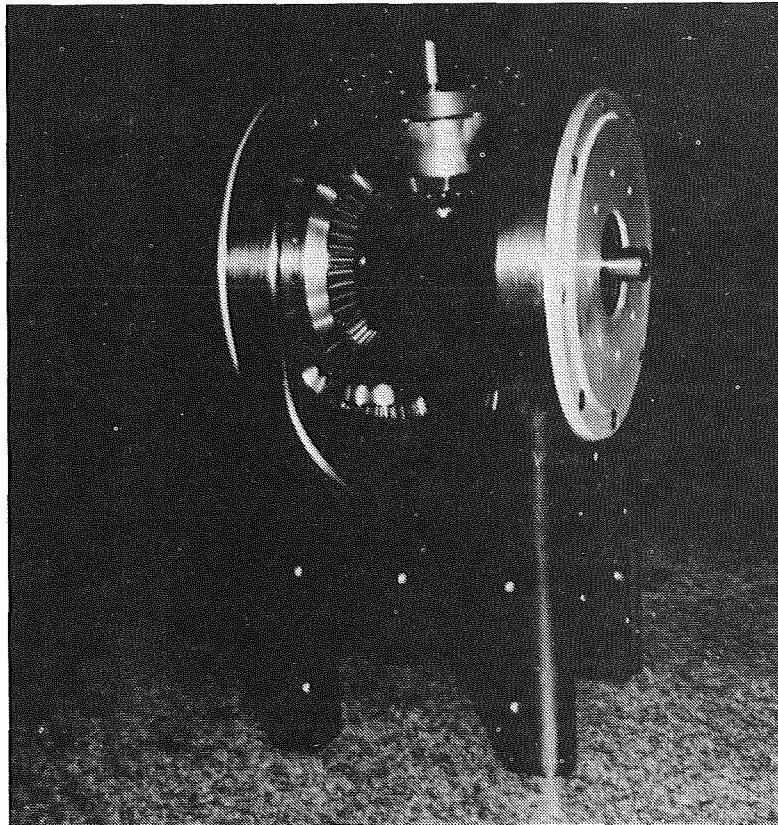

Figure 2: Photo of pitch yaw module

input members are hidden at the bottom with axes vertical. The pitch-yaw output bevel-roller is on top, with the yaw axis vertical and the pitch axis horizontal. A bracket (not shown) is bolted to the output member, to which the link is attached. When integrated in the manipulator arm, the module's pitch axis, yaw axis, and the centerline of the

24

output link are mutually perpendicular. The input members are each driven by a 90:1 ratio gearbox at a maximum input speed of 2.3radians/sec (22rpm). Maximum input torques are 27.1 N-m (240 in-lbf). Maximum output torque is 186 N-m (1650 in-lbf) on each axis.

All gears are 20° pressure angle Zerol bevel gears of case carburized AISI 9310 steel. Gear data are as follows:

	Number of teeth	Diametrical pitch	Pitch dia., in.
Input Bevel Pinion (2)	28	16	1.750
Intermediate Bevel Gear (2)	96	16	6.000
Transversing Bevel Gear (2)	39	12	3.250
P/Y Output Bevel Gear	39	12	3.250

Rollers are also made of case carburized AISI 9310 steel with slightly crowned cones to produce elliptical contact areas. Rollers are loaded so that they can transmit 20 percent of rated torque at a traction coefficient of 0.06 with traction grease. This requires a normal force of 4900N (1100 lbf) at each input bevel roller/intermediate bevel roller contact (axial spring force of 1370N (308 lbf)), and a normal force of 6620N (1490 lbf) at each transversing bevel roller/output bevel roller contact (axial spring force per contact of 9360N (2100 lbf)). Other critical features of the roller-gear design include the following: precision setup of each bevel gear pair with fitted spacers for minimum backlash; precision control of roller-gear pair axis concentricity; and high capacity needle thrust and radial bearings for reacting input roller forces. Complete details are given in [11].

The value of having rollers in the drive train is twofold. First, they remove backlash from the system. At startup, when the gear teeth are not fully engaged, rollers transmit torque. Although the theoretical speed ratio of each roller pair is identical to that of its paralleled gear pair, rollers undergo a small loss in motion known as "creep" when transmitting torque. This allows the gear pair to "catch up", and begin transmitting torque shortly after motion ensues. Second, they attenuate gear cogging and ripple in the output motion. Rollers accomplish this by reacting the radial component of gear tooth contact forces so that the teeth transmit purely tangential forces.

An alternative design which uses only rollers and transmits all torque through traction contacts will produce smoother motion that is completely free of gear induced ripple. A pure roller design, however, requires much higher magnitudes of normal forces at the roller contacts. This necessitates incorporation of a cam-actuated variable load system to maintain reasonable part load efficiencies, and larger bearings and heavier housings to minimize deflections. Also, high preloads result in high inherent friction. In comparison, the large, all-roller pitch-yaw joint, with a dry-lubed traction coefficient of 0.1 [12] had roller normal loads 2.5 to 3 times greater than those in the present roller-gear drive module. If the roller drive had been designed with a coefficient of 0.06, as was the roller-gear drive, the loads would have been even higher. Further, the present spring-loaded, constant roller-preload design represents a simplification over the variable preload mechanism.

2.2 Drive System and Instrumentation

The system is well-instrumented, making it useful for analyzing its characteristics and developing sophisticated control strategies. Each gear motor has a tachometer (as well as a brake) coupled directly to the motor shaft. The roller-gear inputs are driven through a torque meter, and a brushless resolver for measurement of input angle is built into each input drive train. As shown on figure 1, brushless resolvers are incorporated in both the pitch and yaw axes for measurement of output angle. For measurement of end-effector force, a load cell was mounted at the end of the link, although this signal was not used for control.

The module is controlled from a PC with custom made electronics for either preprogrammed tasks or operation with a joystick. A data processing system stores values from all system variables at 5 millisecond intervals for either digital printout or direct plotting of motor speeds, input angular positions, input torques, output pitch and yaw positions, output pitch and yaw velocities, and endpoint force parallel to the yaw axis.

2.3 Pitch-Yaw Module Tests

Static stiffness tests were conducted by fixing the inputs and measuring deflections of the output link in the pitch direction only under various dead-weight loads. The input pinion couplings were locked, and a .0001 in/div dial indicator was used to measure output deflections at a distance from the axis centerline of 0.84 m (33 in). The link and loading system represented a tare torque of 28.7 N-m (254 in-lbf) at the initially "zero" deflection point. Load torques of 9.29, 18.8, 37.2, and 58.4 N-m (82.2, 166, 329, and 517 in-lbf) were applied. The resulting deflection data were fairly linear, producing a least-squares fit for the slope (i.e.: stiffness) of 15,100 N-m/rad (134,000 in-lbf/rad).

By comparison, at full rated input torque, the theoretical stiffness of the gears was calculated to be 565,000 N-m/rad (5,000,000 in-lbf/rad). Since the rollers act in parallel with the gears, and are expected to have approximately the same order of magnitude stiffness as the gears [15], the stiffness of the roller-gear train should be higher than the gears alone. Note that this is for the rollers and gears alone. The large discrepancy between measured and theoretical is due to the fact that the theoretical value does not include the compliance of shafting, bearings, structure, and connections. It has been shown that the soft elements in similar systems are the structure and bearings [16]. The complex interaction of these components is beyond the scope of this paper. Backlash was also evaluated with the stiffness setup. No backlash was measured at the output pitch-yaw member with the inputs locked.

Efficiency of the pitch-yaw module was measured by summing the input torques from each input while lifting weights through a 30° angle with the link near horizontal. The loading system made it impossible to apply a torque about the yaw axis without also loading the pitch axis. Therefore for simplicity, tests were limited to pitch moves. The module was operated at four load levels: 0, 24.4, 81.9, and 137 N-m (0, 216, 725, 1210 in-lbf). Measurements were averaged during the constant speed portions of open-loop lifts, consisting of an acceleration, constant speed, and deceleration to stop. The total

26

lift move required less than one second; the duration of the constant speed portion was about 0.35 sec.

The total frictional loss at zero output load was determined to be .89 N-m (7.9 in-lbf). Efficiency data are plotted as a function of percent design load in figure 3. As
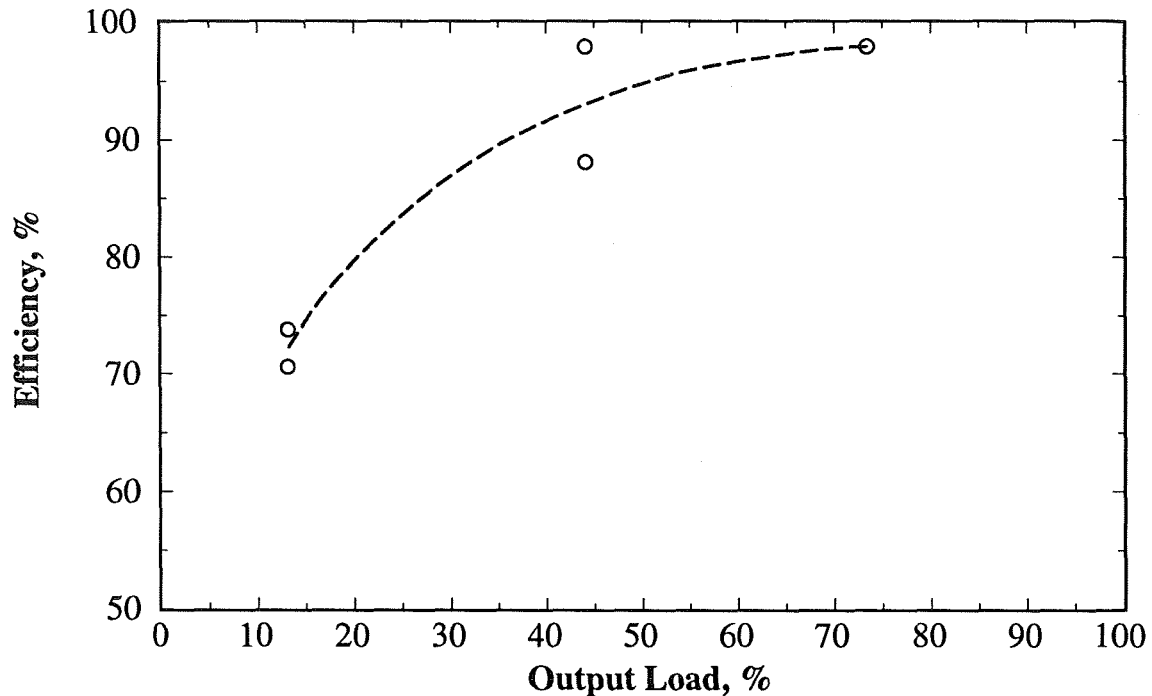

Figure 3: Pitch-Yaw Module Efficiency: Pitch Axis

would be expected for roller or gear systems, efficiency increases with increasing load. At approximately 50% load, measured values ranged from 88 to over 97% efficiency. The results indicate that pitch axis efficiencies of 98% or greater can be expected when the module is loaded at 80% or greater of full load rating.

2.4   Implications for Natural Admittance Control

This system is well-suited to NAC. Perhaps the most important feature is the location of the torque transducers between the gear-motors and the pitch-yaw module. Other experimenters have shown that closing torque or force loops around transmissions, not around links or whole manipulators, produces more robust force control [17, 18, 19]. In this configuration the pitch-yaw module and its link mass act as a filter for the environment, in effect becoming part of it. The filtering effect of the combination of link mass and transmission compliance makes the control more robust by limiting the apparent environmental stiffness. Further, endpoint dynamics are bandwidth limited by the physical dynamics between the sensor and the endpoint.

27

The pitch-yaw module's design qualities: smoothness, low-backlash, and moderate friction, provide a fairly linear, distortion-free filter. This is important since the location of the torque transducers makes it impossible to perform feedback compensation of any friction or other dynamics in the pitch-yaw module itself (or the link). Fortunately, most of the friction and backlash in the system resides in the gear-motor. This friction, located between the actuators and the torque transducers, *can* be compensated by the control using torque-feedback compensation.

An obvious question immediately comes to mind: why not put a sensor at the endpoint and compensate for all of the friction? The answer is fundamental to the nature of force control and the guiding principle behind NAC. Simply put, one can, but the limit on how far the dynamics at the end effector can be improved (i.e. friction reduced) is more restrictive. It is far more difficult to passively compensate for friction located beyond a major compliance in a mechanical chain. This has been analyzed elsewhere (see [20]), however to get a feel for why this might be so, consider the task of pulling a cinder block slowly along a floor using a bungee cord. As one begins to pull, the cord stretches, building up a force until it exceeds the maximum static friction between the block and the floor. The block then breaks free and begins to slide, possibly too fast requiring the actuator (person pulling the cord) to back off. The block then stops and the cycle repeats. The resulting motion is jerky instead of smooth.

Placing a force sensor at the distal end of the block and using it in a force feedback scheme is an exaggerated analogy to the task of force feedback around an entire manipulator. However, if one mounts the actuator firmly to the block, places the sensor, as before, on the other side, and connects the cord to the sensor and to a second, polished block, the task of making this second block move smoothly is much easier and much of the friction in the cinder block can also be masked. This is similar to the situation in the present mechanism. Most of the friction is close to the actuator. The torque sensor is next, and the output, the pitch-yaw module, is relatively low friction.

Another beneficial feature of this system for NAC is the selection of feedback sensors, which is larger than that in more standard manipulator designs. These sensors allow for the identification of important dynamic quantities used in the control, and also provide more flexibility for feedback. The tachometers, mounted directly on the motor shafts, are particularly important because the velocity loops closed around the motors include a minimum of unmodeled dynamics.

3 The controller

3.1 A simple model

In designing any controller, several goals must be met; a crucial one is stability. For systems that interact with the environment, stability must be assured not only for isolated operation, but also when the system is coupled to the environment. Guaranteeing coupled stability for an arbitrary environment is not possible; however, the class of environments presenting a passive impedance (i.e. one that could be constructed entirely

from passive elements) represents a useful class of target environments. By designing a controller that presents a passive endpoint admittance, coupled stability with any passive environment is assured. Passivity places limits on what is achievable in masking manipulator dynamics [6]. In particular, attempting to reduce the apparent mass of the manipulator is problematical at best and easily violates the passivity criterion, resulting in coupled instability for some passive environment.

Consider the simple, linear, 1 degree of freedom model of figure 4. This model represents a single mechanical link with one resonance. M_m is the actuator inertia reflected
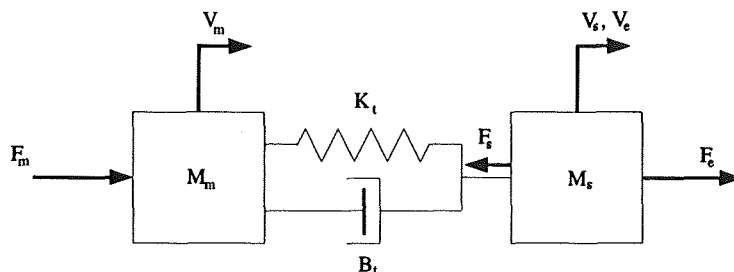

Figure 4: Simple two mass model

through the transmission, and M_s is the link inertia. F_m and v_m are the actuator effort and velocity, while F_e and v_e are the force and velocity at the end of the link. K_t and B_t represent transmission stiffness and damping. F_s represents the force in the spring-damper combination. This model can be used for one joint on any manipulator with rigid links and one dominant compliance in the transmission.

Feedback from an end-mounted effort sensor is often used to implement force control on an existing manipulator. This is the approach used in [10] where an implementation of NAC on a General Electric P-50 manipulator is presented in detail. The two-port admittance matrix was used to develop an appropriate control law using feedback from v_m and F_e. As shown in [10], the high frequency closed loop endpoint admittance approaches

$$Y_s = \frac{v_e}{F_e} = \frac{1}{M_s s} \qquad (1)$$

This represent the maximum possible performance at low frequency as well since, increasing the low frequency admittance above this asymptote will violate passivity conditions.

Nevertheless, NAC can be successfully implemented on this type of architecture if this limit is accepted. However, if the sensor is moved closer to the motor, as in the manipulator in this work, measuring F_s instead, the control problem is not only simplified, but stability is easier to achieve, since the distal mass, M_s, and transmission compliance form a mechanical filter which effectively limits the environmental stiffness the control will encounter. Thus, passivity with respect to $\frac{v_s}{F_s}$ need only be maintained over a certain band of frequencies to achieve passivity with respect to $\frac{v_e}{F_e}$.

The following is a description of the natural admittance controller implemented on the pitch-yaw module manipulator. For convenience, all measurements were reflected

29

to the input pinions of the pitch-yaw module and converted to SI units, providing a consistent frame of reference for all dynamic quantities and eliminating the need for explicitly including the transmission ratios in the design.

3.2 Natural Admittance controller

A natural admittance controller operates by enforcing the manipulator's behavior to track a frictionless dynamic model of the manipulator, thus maximizing the end-point mechanical admittance. NAC also recognizes that there is a theoretical limit to what that maximum is. The limit (at low frequency, arguably the most important region for interaction tasks) is set by the intrinsic inertia of the manipulator as seen at the endpoint. In our case, most of the inertia in the system is the inertia of the gear-motors seen through the 90:1 transmission.

An inner proportional+integral velocity loop is given commands based on what the acceleration of the drive axis would be if there were no friction. The torque transducer signals are combined with gravity and friction estimates, as well as a virtual torque command derived from the desired endpoint stiffness and damping, to generate a net torque. The net torque is divided by the control's design inertia (normally the best estimate of the actual inertia) to generate a desired acceleration. This acceleration is integrated once for the velocity command, and a second time for the position (integral velocity) command.

If the velocity loop was perfect, then the manipulator would indeed appear frictionless from the torque transducer to the motor. Again, since the friction in the pitch-yaw module itself is outside the feedback loop, it is not compensated for in any way. However, making the velocity loop as good as possible motivated two key components of the control strategy: an observer to reduce tachometer signal noise, and a feed-forward friction model containing a dependence on the load applied. The friction model was used not only to reduce the burden on the velocity loop, but to improve the filtering capabilities of the observer. A more detailed presentation of the control design appears in [21], while a simple mechanical model offers an explanation of the load dependence of the friction appears in [22].

It is, in principle, possible to choose a control design inertia different from the actual inertia. Decreasing it would increase the low frequency admittance and help reduce impact transients. However, this will exceed the restrictions imposed by passivity requirements and lead to instability in contact with some stiff but passive environments. It is possible to increase the design inertia higher than the actual, but this will reduce the endpoint admittance at low frequency.

The endpoint's desired stiffness and damping can be controlled, however. This is done using a virtual reference frame (i.e. desired endpoint position and velocity) which is connected (mathematically) to the actual endpoint position and velocity through virtual, and programmable, springs and dampers. A correcting force is calculated based on the deviation of the desired and actual endpoint states and the desired stiffness and damping characteristics. This force is projected mathematically to the individual drive axes as torque commands and added to the other torques (sensed, gravity, and friction)

in the NAC algorithm. Thus, dragging the virtual frame around the workspace causes the manipulator to follow, but, when obstacles (or work surfaces) are encountered, the endpoint force is regulated by the desired stiffness and damping characteristics chosen by the operator.

3.3 Friction Measurements under Natural Admittance Control

With the virtual end-point stiffness and damping set to zero, the manipulator would ideally behave like a pure inertia. In reality, it comes quite close. The friction in the gear-motor drives is nearly completely masked, leaving only the much lower friction in the pitch-yaw roller-gear module.

Measurements were taken to determine the extent of the natural admittance controller's effect on the gearbox friction. A force was applied through the load cell to impart a slow, constant-velocity pure pitch motion. With NAC off, a force of 67N at the endpoint was required to overcome the friction of the drive trains and establish motion. Turning NAC on reduced the force required to about 2.5N. These figures translate into expected pinion torques (assuming lossless transmission through the differential) of 8.3N-m (NAC off) and 0.31N-m, (NAC on). The torque transducer signals were 6.5N-m and 0.07N-m for the two cases, implying frictional torques in the pitch-yaw differential of 1.8N-m and 0.24N-m.

The reduction in the required effort at the endpoint (and similarly the reduced torque measured at the pinion roller-gears) indicates that the apparent friction in the gear-motor drives was attenuated by more than an order of magnitude. Therefore the minimum force the manipulator can present to the environment under NAC is now limited mainly by the friction in the pitch-yaw differential itself. Since this friction is inherently low, the end-point force deadband is also low, and the system using NAC exhibits good sensitivity to end-point forces.

This result illustrates the advantage of placing the majority of the mechanical friction in a manipulator close to the actuator, between the actuator and the torque sensor. Friction beyond the torque sensor is not compensated for in the present implementation. One may well ask why not? Why not use the endpoint sensor in the natural admittance controller? One could, but doing so forfeits the robustness enhancing effects of a mechanical filter between the sensor and the environment.

3.4 Stiff Environment Contact Tests

To test the ability of our control to exhibit stable behavior when interacting with stiff environments, the endpoint was programmed for moderate stiffness and damping and commanded to collide with a rigidly mounted aluminum angle bracket at moderate speed. The load cell mounted on the end of the link measured the contact force. As shown in figure 5, the contact force reached a stable final value.

To explore the effects of incorrectly estimating the inertia, we repeated the experiment
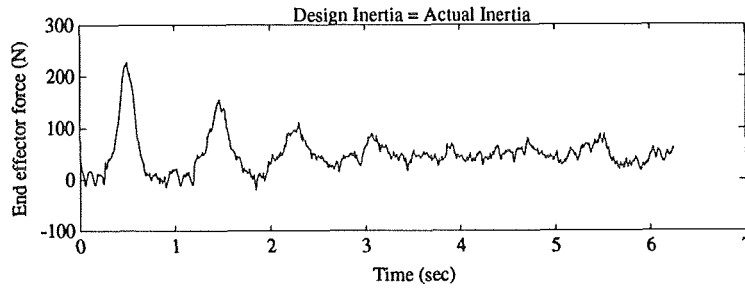
Figure 5: Impact with best estimate of inertia

using different inertias to compute the desired acceleration in the natural admittance controller. (The observer still used the best estimate of the inertia.) Values of one-half, one-quarter, twice, and four times the measured inertia were tried. Values for the endpoint stiffness and damping were also scaled to maintain a similar response. As expected, lower inertia values resulted in contact instability (figure 6). Contact using high inertia values was stable and tended to settle sooner (figure 7).
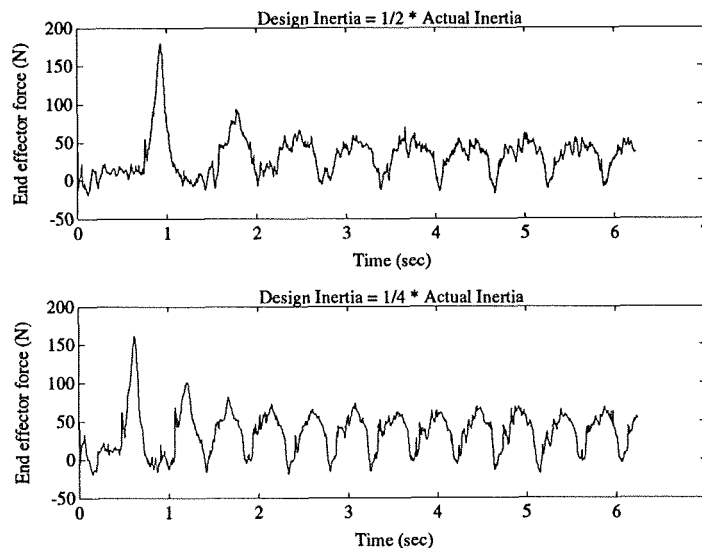

Figure 6: Impact with underestimated inertia

4 Discussion

Natural admittance control provides a mechanism for implementing force control in systems containing high levels of friction and transmission non-linearities in a manner that maintains passivity, provided that those undesirable characteristics are placed carefully in the mechanical design. Performance can approach the theoretical limit.

Our experiments indicate the beneficial effects of a final transmission stage that is low in inherent friction. It can be shown that there are fundamental restrictions on the
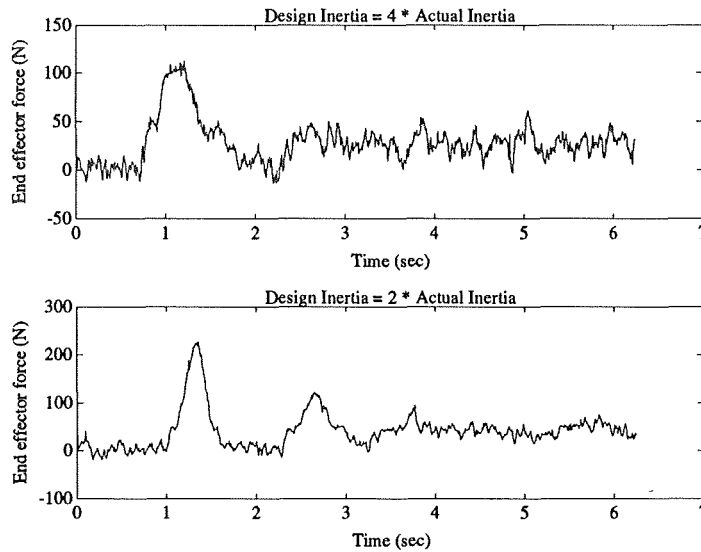
Figure 7: Impact with overestimated inertia

ability of a control algorithm to reject friction in a mechanical system. A particular problem occurs if the friction to be rejected is located far from the actuator coupled to it through a compliance, even a linear one. Trying to reject this "distal" friction can lead to an unstable system, showing the importance of designing mechanical systems with low inherent friction near the output, instead concentrating mechanical compliance (linear and non-linear), backlash, and non-linear friction such as Coulomb friction close to the actuator so that they can be successfully mitigated.

Also, as shown by this investigation, a crucial factor in the design of a controller is simply the availability of sensor signals. These are important for control model development, as well as for actual use by the control algorithms. Additionally, it is important to have at least one signal directly from the motor, either position or velocity.

5 Summary and Conclusions

A pitch-yaw joint was developed making use of a unique cone roller and Zerol bevel gear differential module. The use of rollers and gears in parallel combines the backlash-free operation of pure roller drives with the high torque capacity and lower bearing loads of gears. Reaction loads on the bearings of the roller-gear module were at least 2.5 times smaller than a similarly designed pure roller module. The variable preload devices required on pure roller drives were also replaced with a simpler spring-load system. The pitch-yaw module was driven by two gear motors via inline torque transducers. Rated load in either pitch or yaw was 186 N-m (1650 in-lbf). Mechanical efficiency of 97.5% was measured at 73% of rated output load, and zero backlash was found.

A force-control scheme modeled on natural admittance control was implemented on the drive system. The system exhibited good force control performance maintaining

stable interaction with a stiff environment. The natural inertia of the system was accepted and used as the desired inertia and friction was compensated through the natural admittance controller which made the manipulator track an ideal, frictionless manipulator. An observer greatly improved the performance of the velocity controller, allowing a four-fold increase in the loop gain. Interestingly, using the integrated velocity estimate for the position (integral velocity) feedback was also beneficial. The observer, in turn, was improved through the use of a friction estimator which included a load-dependent friction component and was fit to experimental data. As implemented, we successfully compensated for a large measure of the friction in the gear-motors in the presence of severe backlash.

The configuration of the joint module helped make the control more robust. The placement of the pitch-yaw module between the torque transducers and the environment limits the apparent environmental stiffness presented to the control by acting as a mechanical filter. However, any friction, backlash, or other undesirable mechanical effects located past the torque sensors could *not* be compensated for. Therefore the properties of the pitch-yaw module, with its low friction, smoothness, and low backlash, were crucial to the ultimate performance of the system.

Two mechanism design principles may be drawn from this for force-controlled manipulator systems. First, it is beneficial to have some form of mechanical filtering between the force or torque sensor and the environment. Second, since it is not possible to use the torque sensor to compensate for down-stream dynamics, it is important to make them as "friendly" as possible, i.e. put the most "ideal" (e.g.: low friction) components down stream of the sensor and put the components with undesirable dynamics (e.g.: high friction) up stream, closer to the actuator than the sensor is.

6   Acknowledgments

References

[1] S. D. Eppinger and W. P. Seering, "Understanding bandwidth limitations in robot force control," in *Proceedings of International Conference on Robotics and Automation*, pp. 904–909, IEEE, April 1987.

[2] J. K. Salisbury, "Active stiffness control of a manipulator in cartesian coordinates," in *IEEE Conference on Decision and Control*, pp. 95–100, 1980.

[3] N. Hogan, "Impedance control: an approach to manipulation: parts i, ii, and iii-theory," *Journal of Dynamic Systems Measurement, and Control*, vol. 107, pp. 1–24, March 1985.

[4] J. E. Colgate, *The Control of Dynamically Interacting Systems*. PhD thesis, Department of Mechanical Engineering, MIT, August 1988.

[5] J. E. Colgate and N. Hogan, "On the stability of a manipulator interacting with its environment," in *Proceedings of the Twenty Fifth Annual Allerton Conference on Communication, Control, and Computing*, pp. 821–828, March 1988.

[6] J. E. Colgate and N. Hogan, "Robust control of dynamically interacting systems," *International Journal of Control*, vol. 48, no. 1, pp. 65–88, 1988.

[7] J. E. Colgate, "Strictly positive real admittances for coupled stability," *Journal of the Franklin Institute*, vol. 329, no. 3, pp. 429–444, 1992.

[8] R. J. Anderson and M. W. Spong, "Asymptotic stability for force reflecting teleoperators with time delay," *The International Journal of Robotics Research*, vol. 11, pp. 135–149, April 1992.

[9] W. S. Newman and Y. Zhang, "Stable interaction control and coulomb friction compensation using natural admittance control," Printed TR-91-151, Center for Automation and Intelligent Systems Research, Case Western Reserve University, Cleveland, Ohio, Sept 1991.

[10] G. D. Glosser, *The Implementation of a Natural Admittance Controller on a Robotic Manipulator*. Master's thesis, Case Western Reserve University, Department of Systems Engineering, January 1993.

[11] W. J. Anderson and W. Shipitalo, "Roller-gear drives for robotic manipulators: design, fabrication, and test," Printed, Final Report for NASA Lewis Research Center, Contract NAS-25803,, September 1991.

[12] J. N. Herndon, R. L. Glassell, P. L. Butler, D. M. Williams, D. A. Rohn, and J. H. Miller, "Manipulation hardware for microgravity research," Proceedings, 38th conference on remote systems technology, vol 2, pp161-168, American Nuclear Society, Nov 1990.

[13] D. P. Kuban and D. M. Williams, "Traction-driven seven-degree-of-freedom telerobot arm: a concept for manipulation in space," in *NASA CP-2470: 21st Aerospace Mechanisms Symposium*, pp. 111–130, NASA, April 1987.

[14] W. S. Newman, W. J. Anderson, W. Shipitalo, and D. Rohn, "A 23.2:1 ratio, 300 watt, 26 n-m output torque, planetary roller-gear robotic transmission: design and evaluation," in *Proceedings of the 26th Aerospace Mechanisms Symposium*, (Greenbelt, MD), p. , NASA, May, 1992.

[15] D. A. Rohn and S. H. Loewnthal, "An analysis of traction drive torsional stiffness," *ASME Journal of Mechanisms, Transmissions, and Automation in Design*, vol. 107, pp. 573–581, December 1985.

[16] B. M. Steinetz, D. A. Rohn, and W. J. Anderson, "Evaluation of a high torque backlash-free roller actuator," in *NASA CP-2423 (Revised): 20th Aerospace Mechanisms Symposium*, pp. 205–230, NASA, May 1986.

[17] C. H. Wu and R. P. C. Paul, "Manipulator compliance based on joint torque control," in *IEEE Conference on Decision and Control*, (Albuquerque, New Mexico), pp. 88–94, December 1980.

[18] W. S. Newman, M. E. Dohring, J. D. Farrell, P. H. Eismann, and H. I. Vold, "Preliminary work in impedance control on a kinematically redundant manipulator," in *Proceedings of the ASME Winter Annual Meeting*, (San Francisco), ASME, December 11-15, 1989.

[19] M. E. Dohring, *Impedance Control of Redundant Manipulators: Theory and Experiments*. Master's thesis, Case Western Reserve University, Cleveland, Ohio, May 1990.

[20] W. S. Newman, G. D. Glosser, J. H. Miller, and D. Rohn, "The detrimental effect of friction on space microgravity robotics," in *Proceedings of International Conference on Robotics and Automation*, (Nice, France), pp. 1436–1462, IEEE, May 1992.

[21] M. E. Dohring, W. J. Anderson, W. S. Newman, and D. A. Rohn, "Natural admittance control of a compact roller-gear pitch-yaw joint module," printed 92-155, Center for Automation and Intelligent Systems Research, Case Western Reserve University, Cleveland, OH, December 1992.

[22] M. E. Dohring, E. Lee, and W. S. Newman, "A load-dependent transmission friction model: theory and experiments," printed 92-140, Center for Automation and Intelligent Systems Research, Case Western Reserve University, Cleveland, OH, October 1992.

Mars Rover Mechanisms
Designed for Rocky IV

Tommaso P. Rivellini*

ABSTRACT

A Mars rover prototype vehicle named Rocky IV was designed
and built at the Jet Propulsion Laboratory during the fall of 1991 and
spring 1992. This vehicle is the fourth in a series of rovers designed
to test vehicle mobility and navigation software. Rocky IV was the
first attempt to design a vehicle with "flight like" mass and
functionality. It was consequently necessary to develop highly
efficient mechanisms and structures to meet the vehicles very tight
mass limit of 3 Kg for the entire mobility system (7 Kg for the full
system). This paper will discuss the key mechanisms developed for
the rover's innovative drive and suspension system. These are the
wheel drive and strut assembly, the rocker-bogie suspension
mechanism and the differential pivot. The end-to-end design,
analysis, fabrication and testing of these components will also be
discussed as will their performance during field testing. The lessons
learned from Rocky IV are already proving invaluable for the design
of Rocky VI. Rocky VI is currently being designed to fly on NASA's
MESUR mission to Mars scheduled to launch in 1996.

INTRODUCTION

Research on planetary rovers began in the early sixties for the
Surveyor lunar rover (which never flew) by M.G. Bekker [1].
Bekker's work culminated in a six wheeled rover with a flexible
body. Planetary rover work lapsed for many years until the Mars
Rover Sample Return mission was conceived. At that time the Jet
Propulsion Laboratory (JPL) began investigating new rover
configurations to offer even higher mobility. The design evolution
began with the invention of six wheeled configurations utilizing links
to articulate the body so that equal weight distribution was
maintained on all wheels at all times. This rover was

_____

* Jet Propulsion Laboratory, California Institute of Technology
4800 Oak grove Dr, Pasadena, CA 91109

named the Pantograph. A Rocker-Bogie configuration was then developed to overcome some of the limitations of the link articulated rovers. Rocky and Rocky III were built to prove their rock climbing capability. Rocky III, a rover weighing 25 kg and 60 cm long showed enough potential as an integrated rover system that Rocky IV was funded by NASA's code-R to demonstrate a full end-to-end behavior controlled high mobility planetary rover system. The project was managed in a fast paced "skunk works" fashion to show that such a vehicle could not only be built, but that it could be done quickly and inexpensively. In addition to the functional requirements of the rover system it was required that the rover be built to "flight-like" mass of only 7 kg. Some of the key components of the rover mobility system will be discussed in more detail.

SUSPENSION

The term Rocker-Bogie refers to the two link suspension system comprised of a trailing rocker arm with one wheel, and a bogie with two wheels pivoted at one end of the rocker arm. This configuration gives the vehicle excellent terrain following abilities which is crucial for a high mobility vehicle. The suspension geometry, which includes wheel diameter and spacing, pivot locations and center of gravity location, was optimized in 2-D for the minimum coefficient of friction required to climb axle high vertical bumps when the vehicle was going both forward and backward. The 3-D performance on rocky terrain was then analyzed using an elastodynamic analysis software package called Adams [2].

Figure 1 shows the geometry of the Rocky IV suspension system. The front and rear wheels are steerable whereas the center wheels are not. This allows Rocky IV to turn in place by steering about its center point. The behavior control navigation scheme relies on sensor information on the rover suspension to tell it what the rover is doing and what position it is in. This allows the computer to decide if the rover is getting into a hazardous situation or not. To provide this information potentiometers are used to give the angular position of the bogie with respect to the rocker arm. Physical stops limit the maximum rotation but the sensors allow the rover to stop and back away before these limits are reached. A potentiometer is also located in the differential link, which will be discussed later, to provide the rest of the information required to define the state of the

rover. The two physical stops are called the bump stop and the cable stop. The bump stop consists of two rubber pads attached to a steel pin through the back of the bogie, which makes contact with the back side of the rocker arm's forks This limits foreword rotation of the bogie. The cable stop is a cable attached to the aft end of the bogie going up the the rocker arm through a small hole. Impact shock is mitigated by compressing a foam pad between the rocker arm and the cable end as the cable reaches maximum extension.

The maximum rotation of the bogies with respect to the rocker was chosen by considering the rover's ability to traverse a trench. Figure 2 shows the rover configuration analyzed. If the front wheel is allowed to fall too far, the moment created when contacting the far side of the trench would have a tendency to overturn the vehicle. If the front wheel was not allowed to rotate enough the vehicle's terrain following ability would have been reduced. The angle was chosen which required the front wheel to have the same minimum coefficient of friction to climb the far wall as the largest minimum coefficient of friction required for any one of the wheels to climb a step directly in front of it. This angle is 30 degrees.

A static test model of the main rocker arm structure was fabricated early on to verify the structural analysis done on it. A series of dead weight static tests were conducted where the maximum deflection was recorded. The tests were performed by incrementally adding and then removing weights suspended from the rocker arm. No more weight was added when there was 2% yield on the structure. The results verified the analysis to within 10 percent of the predicted performance. The results of the tests were that the servo mounting structure was thinned down and some thickness was added to the top of the arm just above the main pivot.

WHEEL DRIVE ASSEMBLY

The wheel drive assembly is comprised of two major parts, the wheel strut and the motor-gearbox. The wheel strut is the structure which holds the wheel to the suspension. Steering is done on four of the six struts at the top of the strut. Due to the fact that there were six wheel drive assemblies, it was crucial that as much mass as possible be removed from the structure without compromising its integrity. The first attempt at the strut design involved machining a channel down the length of the strut and then closing the cross

section by welding on a cover. A complete test strut was fabricated in this manor early on. The machine time and the added wall thickness' required to counter the effect of annealing caused by welding, proved to be costly and heavy. With the knowledge gained from having fabricated the first test model we were able to invent a lighter and cheaper strut. This approach involved designing a tool to allow under cutting in the strut cross section. The process utilized an end mill with a neck whose diameter was half that of the cutting diameter. The tool first penetrated all the way through the strut, it was then raised so that the cutting length of the tool was in the middle of the strut cross section, thus leaving a predetermined wall thickness above and below the tool. The part was then moved around under the tool (N/C machine) so that a region larger than the through hole was milled out, in effect hollowing out the strut. Figure 3 shows the resultant wavy pattern in the strut walls. The machining for the strut was done on a numerical control end mill in order to save both time and money.

A NASTRAN analysis was done on the strut using the worst case loading conditions. The worst case loading was assumed to be an accidental drop of one wheel diameter. Figure 4 shows the NASTRAN model of the strut. The maximum stress was found to be on the inner portion (of the arc) of the 3rd and 5th through holes (from the top) as well as the outside portion of the 4th through hole. There was not enough time in the project to optimize the strut design so the NASTRAN analysis was used only to verify that the structure was not stressed beyond its limits. The analysis did give a considerable amount of insight as to where mass could be removed and were mass should be added. This information is already proving useful in planing the follow-on rover strut design.

Steering is performed on four of the six wheels. A single thin-line X-type bearing is used to allow rotation. The bearing is protected from dust by two O-rings, one above and one below it. In an effort to save time and money, commercial radio controlled model sailboat servo motors are used to perform the steering. One servo per steerable wheel is used. The servos are hard wired into the computer which controls their rotation. Ackerman steering is employed for Rocky for efficient turning. Rather than compute all the angles required for all wheels for any given turn angle, six discrete turn angles were preprogramed and the ackerman angles were "looked up" to make a turn.

The drive mechanism contains a single 12 volt DC permanent magnet electric motor coupled to a four stage planetary gearbox. The motors were purchased from Escap but the gearbox was purchased from a surplus store and modified to reduce the mass of the casing. The gearing ratio is 400:1 and provides a maximum of 0.20 N cm of torque. This torque level ensures that Rocky 4 is not torque limited under the worst predicted loading conditions. The motor rotations are counted for the computer via an optical encoder mounted just before the pinion on the motor drive shaft. An encoder wheel, painted half black and half white alternately reflects light back to the encoder once per revolution. Four hundred revolutions indicated one wheel revolution. The last stage of the gearbox couples directly to the wheel hub through four steel pins, one per planet gear. The wheel hub was also machined with a numerical controlled milling machine. Figure 5 shows a photograph of a complete bogie assembly with all the parts of one wheel drive assembly displayed. The wires are for the optical encoder, no motor wires are shown.

DIFFERENTIAL PIVOT

Rocky 4 is a single body design with independent left and right suspension. The main structural support to the body is via a single aluminum tube connecting the left and right side. This alone however leaves one degree of freedom unconstrained, pitch rotation. This degree of freedom is taken out by a differential pivot which mounts at the rear of the rover body and connects the left and right suspension. The pivot has the effect of averaging the motion of the left and the right, thus providing a relatively smooth and stable ride for onboard electronics. The pivot mechanism is made up of a main mast with a pivot at the top. The angle of the pivot axis of rotation is parallel to the line connecting the rocker arm main pivot and the link attach point. A cross arm pivots about this axis and extends from the left to the right suspension. The cross bar is connected to the suspension via two links with ball joint ends. The ball joint ends allow the links to rotate and follow the rocker arm and the cross bar freely. The height of the mast was determined by the maximum angle the ball links could rotate laterally. To save time and money model airplane ball links purchased from a local hobby shop were used, and performed very well.

As was previously mentioned the differential link was encoded using a potentiometer to provide the computer with "attitude"

information. The potentiometer was designed into the pivot design from the beginning to allow easy access for calibration and removal.

VEHICLE SYSTEM DESIGN

The total vehicle mass came out to 7.1 kg which was distributed as follows:

Control Electronics	1212 g
Rock Chipper	150 g
Video transmitter	500 g
Electrical systems	1717 g
Mobility System (structure)	3521 g

Rocky IV was designed and sponsored for a demonstration which occurred in early may at JPL in a dry riverbed behind the lab.. The Rocky IV complete system included the rover, a "lander" which provided a radio link to the rover, stereo imaging, an optical homing beacon and a radio link to the control crew. The purpose of the demonstration was to show an end-to-end operation of the high mobility behavior controlled rover system. To this end the demo required the rover to first exit the lander and deploy a functional micro seismometer one meter from the lander. A soil sample was then taken by Rocky with an onboard scooping mechanism. A rock to be inspected was then selected by the ground crew via the lander imaging system. The rover drove to the rock, avoiding hazardous obstacles on the way, took a spectrum of the weathered rock, chipped the weathering rind off the rock and took another spectrum of the virgin rock. The rover then returned to the lander on its own and deposited the previously acquired sample. A considerable amount of time was spent debugging and refining the software responsible for controlling the vehicle. The final result was a highly successful demonstration of the fully functioning system. Figure 6 shows the computer drawings used to fabricate piece parts as well as to configure the rover. Figure 7 is a photograph taken of Rocky IV just after final assembly.

CONCLUSIONS

The experiences gained from the end-to-end design and fabrication of Rocky 4 are already proving to be of great value. We are currently designing Rocky 6 which is scheduled to be launch aboard NASA's MESUR Pathfinder Mars lander in 1996. Many of the issues the design team must address have already been dealt with on a first order basis therefore allowing us to design a much better system. Some of the lessons learned are given here.

The field test verification of the quasi static computer modeling and optimization was tremendously valuable. It gives the rover design team a very high level of confidence in the design tools which have been developed over years. This level of confidence is very important for making accurate predictions for highly constrained missions such as MESUR which can not afford to carry large rovers to Mars. The field testing also revealed aspects of the design which are not feasible for modeling on a computer. Vehicle-ground interaction over rough and rocky terrain is the most important aspect. Field testing has shown when and where the rover would "hang up" on obstacles. It showed us that almost every time the rover became caught on a rock, it was able to successfully back out of the situation. It was also found that the wheel struts would occasionally catch on rocks and hold the rover back. Such testing is not only valuable for design purposes but will also prove valuable to operations planning.

Integration of the potentiometers into the vehicle structure was not as simple a matter as thought. Simplicity was a design goal in order to increase reliability. Unfortunately the simplest ideas were not always the lightest. Often the most mass efficient ideas were impossible to assemble. The final designs for the potentiometer integration was both simple and light, but was somewhat delicate at first. The potentiometers slipped during the first week of field testing. Fortunately only a simple modification was required to fix the problem.

Finally, the fast paced, low cost approach to the design was very successful. So successful that the JPL micro-rover project was singled out in the latest NASA report card as a successful example of cheaper, faster, better, and a paradigm for future projects.

43

ACKNOWLEDGEMENTS

REFERENCES

1. Bekker, M.G., *Introduction to Terrain-Vehicle Systems*, University of Michigan Press, Ann Arbor, Michigan, 1969.

2. Lindemann, R.A., "Dynamic Modeling and Simulation of Planetary Rovers," AIAA 92-1269, presented at the AIAA Aerospace Design Conference, February 3-6 1992, Irvine Ca.
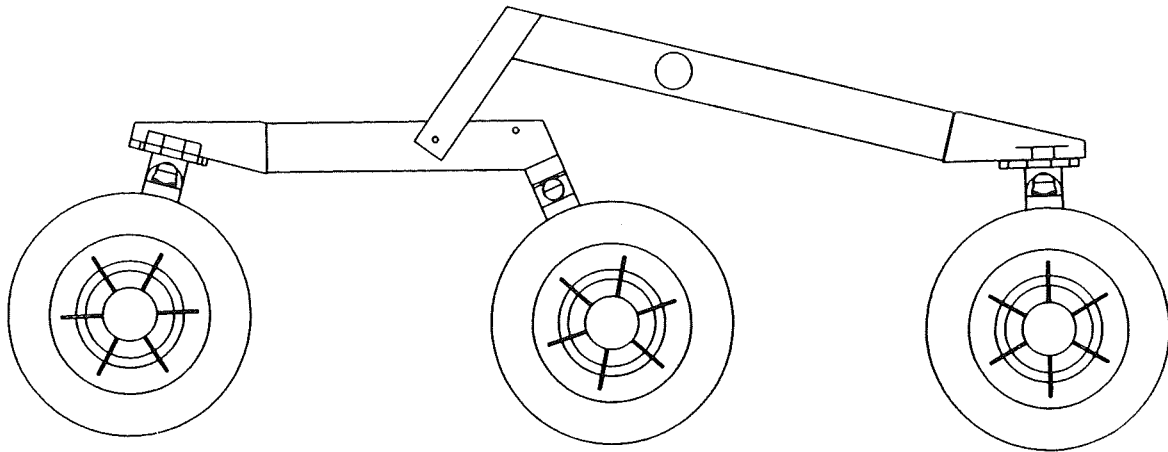
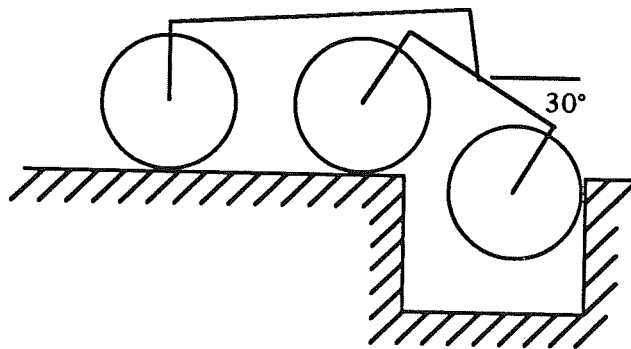Figure 1.   Rocky IV Rocker-Bogie suspension geometry.

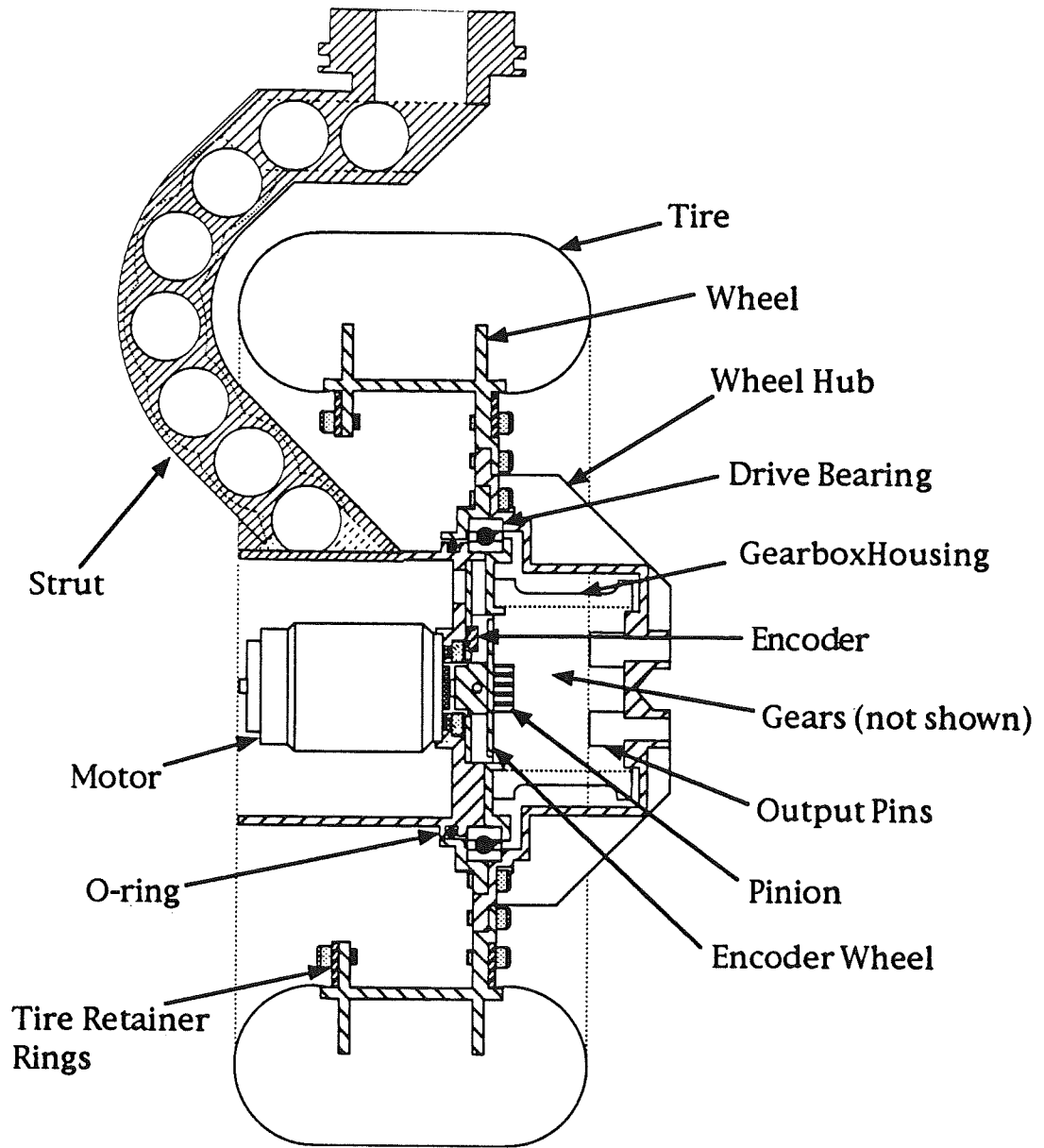Figure 2.   Geometry analyzed for the rover crossing a trench.
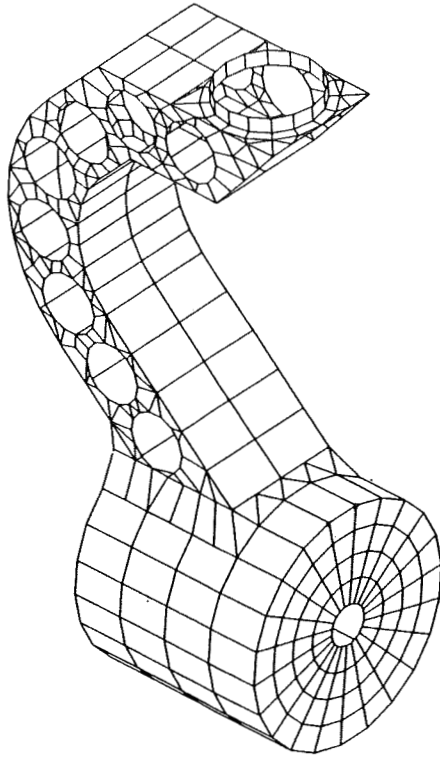
Figure 3.　Wheel strut and drive assembly.

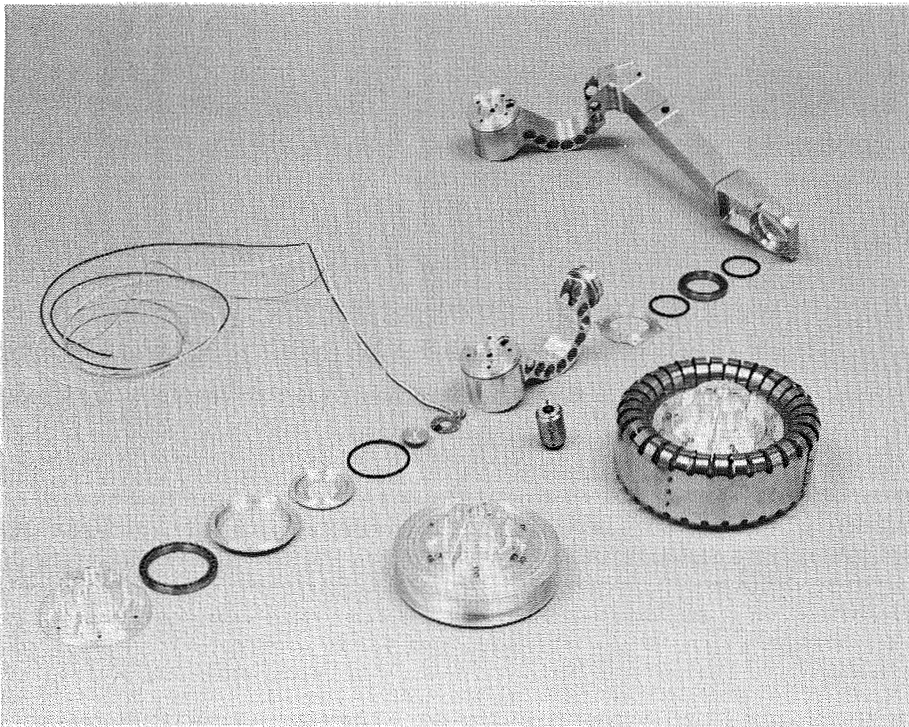Figure 4. NASTRAN model of the wheel strut.

Figure 5. Photograph of the bogie assembly showing all of the parts for one wheel drive mechanism.
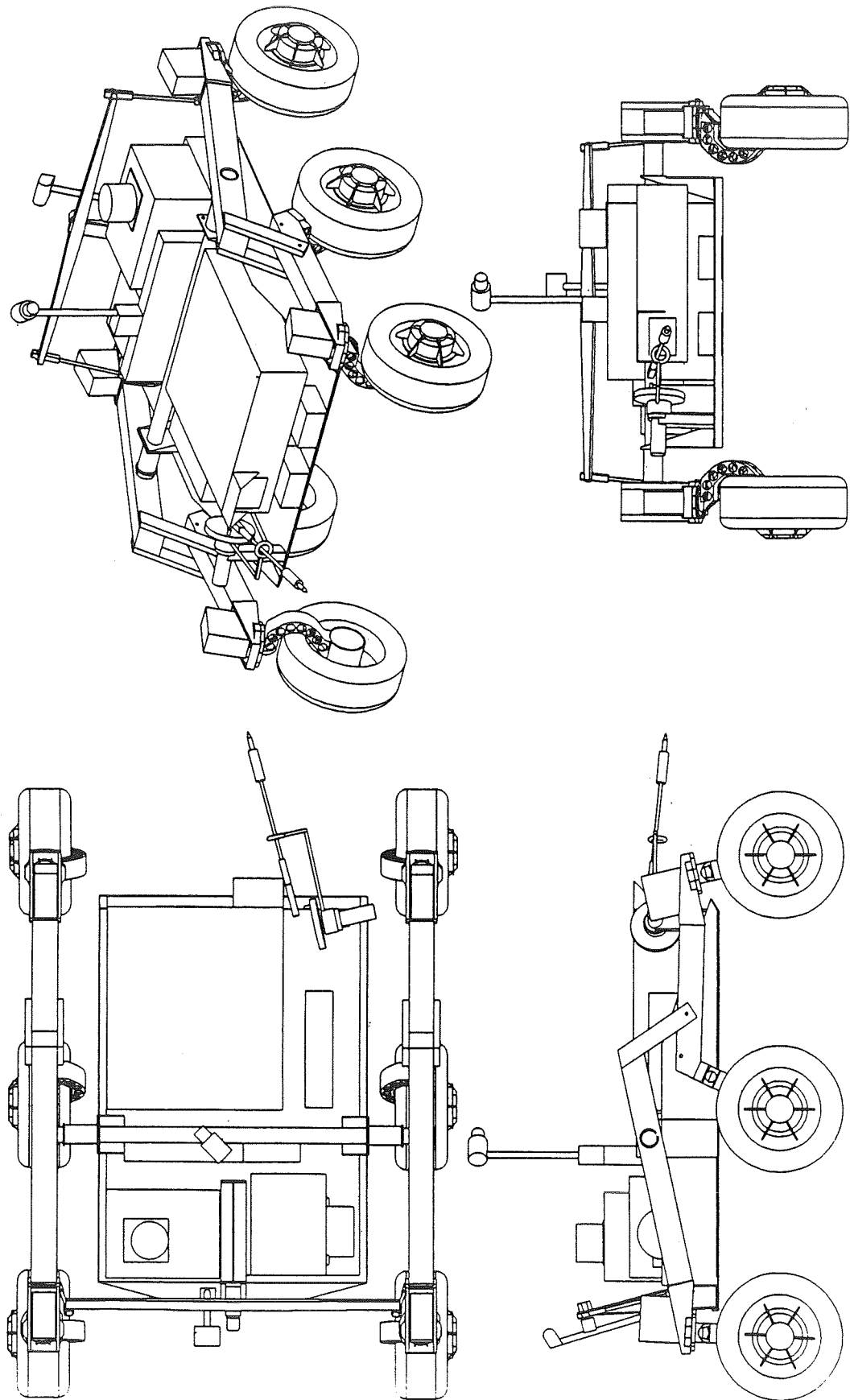
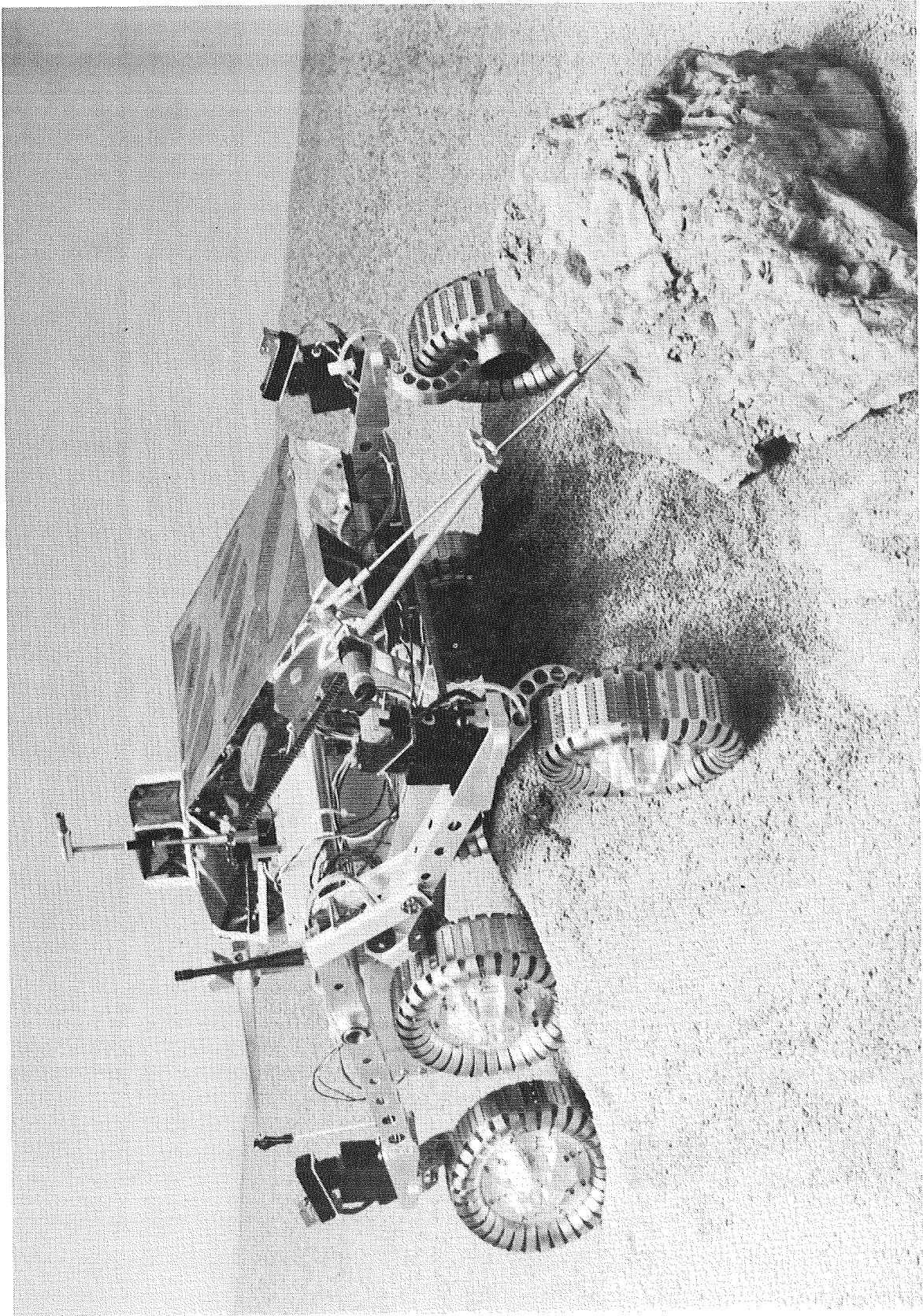Figure 6.   Rocky IV configuration drawings.

Figure 7. Rocky IV in the sandbox.

A Module Concept for a Cable-Mesh Deployable Antenna   434636

Akira Meguro[*]

Abstract

This paper describes the design, manufacture, and deployment tests of a modular mesh deployable antenna. Reaction forces and moments created by a mesh and cable network are estimated using CASA. Deployment analysis is carried out using DADS. Three types of deployable antenna modules are developed and fabricated. Their design approach and deployment characteristics are also presented. Ground deployment tests are performed to verify design criteria.

INTRODUCTION

In recent years, the role of satellite communication has changed from being a supplemental system to being the main element of an advanced mobile communication system. An advance satellite communication experiment is being conducted using the engineering test satellite VI (ETS-VI) which is equipped with two deployable antennas 2.5 m and 3.5 m in diameter. While ETS-VI is expected to achieve its primary goal of advanced satellite communication, it may be insufficient for personal and anytime-anywhere satellite communication due to it's limited mission capabilities and relatively high cost. The future advanced satellite communication system, represented by the super compact hand-held telephone, will not be accomplished without carrying out further innovative research.

Large scale on-board antennas from 10 m to 100 m in diameter are desirable for future advanced mobile satellite communication systems. The current trend of recent reseach into large deployable space structures is the metamorphosis of a solid into a plane, a plane into a line and a line into a point. The weight per unit volume decreases rapidly with each of these metamorphoses. However, the ratio of deployment mechanism weight to the entire structure weight rapidly increases. Moreover, difficulties in ground testing would also increase. Figure 1 plots the estimated difficulty of deployment tests (DDT) in dimensionless units.[1] It indicates that antennas whose apertures exceed 10 m would be difficult to test on the ground. There is some influence from the diameter of the antenna's stowed configuration. Therefore, large antennas whose aperture is over 10 m would be best realized with a modular structure.

A 10-15 m diameter deployable mesh antenna is under development at NTT. The antenna reflector consists of a gold plated mesh surface, a spatially determined cable network, and deployable truss modules as the supporting structure. Seven standoffs connect each cable network to its truss structure. The cable network consists of surface, tie and back cables. Adjustment of tie cable length controls the

---

[*] Senior research engineer, NTT Radio Communication Systems Laboratories, 1-2356 Take, Yokosuka-shi, Kanagawa, 238-03 Japan

displacement of the surface cable nodes. Seven deployable truss modules will be used to construct the 10 m diameter antenna reflector. The modules are independent of each other, so a larger reflector can be easily achieved by adding more modules. In addition, the modules can be independently fabricated and tested, and they are easy to handle and adjust.

MODULAR MESH DEPLOYABLE ANTENNA

System configuration

Figure 2 shows a system configuration candidate for the future advanced mobile communication satellite. Several deployable antenna modules will be used to construct antenna reflectors ranging from 10 m to 15 m in diameter. Each module is hexagonal and is from 2 m to 4 m in equivalent diameter. They are arranged annularly.

Structure of the basic module for large deployable antenna

Figure 3 shows the general composition of the basic deployable antenna module. Each module consists of a gold plated mesh surface, a spatially determined cable network, and a deployable truss module as the supporting structure. The cable network and deployable truss are connected to stand-offs. The cable network consists of three kinds of cables: surface, tie, and back cables. Surface cables link surface nodes that are distributed uniformly on the parabolic surface. Adjustment of tie cable length displaces the surface cable nodes. Nylon 6 was used for the surface cables and polyester coated Kevlar was used for the tie and back cables. They exhibit good mechanical performance in the cable network. However, they have not been proven suitable for long term space usage. Nylon 6 may not be suitable for the space environment.

Deployable truss structure

Figure 4 shows the basic deployment truss structure. The structure consists of longitudinal members, radial members, circumference members, folding members, diagonal members, revolving hinges, folding hinges, sliding hinges, and one driving motor. The basic concept of the deployable truss modules is a statically determined truss structure with a synchronized deployment motion. Truss joints are capable of either revolving or translating, and each truss module has only one degree of freedom. Thus only one driving motor is necessary for full deployment. Figure 5 shows the BBM (bread board model) of the central module of the 10m antenna that was fabricated to confirm the basic concept of the synchronized deployment truss structure.[2] It is 4m in equivalent diameter. Seven deployable antenna modules will be used to construct the 10 m diameter antenna reflector. A surface control experiment was performed, and after a few surface adjustments, surface accuracy of less than 1 mm RMS, was obtained.

As shown in figure 5, the synchronized deployment motion was confirmed by ground deployment tests. Moreover, the deployment characteristics were analyzed using the Dynamic Analysis and Design System (DADS). The synchronized deployment motion was also analytically evaluated. However, some problems due

to hinge mechanisms were found. Successful results have been obtained by a model that consists of rigid elements and tight hinges. In practice, the BBM suffered from joint slop, joint elasticity, and structural elasticity, so that the BBM actually had many degrees of freedom. This seriously degraded the deployment characteristics. For example, the peripheral sliding hinge did not reach its final position even though the driving motor hinge reached its final position. The points at issue can be summarized as (1) insufficient latch torque at folding hinges against cable network reaction forces, (2) insufficient transmission efficiency of the driving forces due to hinge slop or hinge elasticity.

Design of integrated antenna modules

Although the previously described 4 m diameter BBM is symmetrical, the antenna reflector curvature required that peripheral modules should be slightly skewed. The reason for this is that standoff length would be excessive if the modules were symmetrical. In addition, considering the connectivity of each module, at least three types of deployable truss modules are necessary to assemble a structure of seven or more modules. The lacing pattern of the truss must be designed such that truss members can be synchronized to the adjacent modules. Because the design of the peripheral truss modules is complex, the hinge mechanisms of the 4 m diameter BBM were modified. Moreover, the driving mechanism and the latch mechanisms were also modified to improve deployment performance.

Figure 6 shows the upper view of the 4 m diameter BBM; the radial members and peripheral members are drawn as grid lines. As shown in this figure, grid lines of the 4 m diameter BBM cross at a 60 degree angle. In contrast to the 4 m diameter BBM, the integrated truss modules were designed to have square grids (90 degree crossing angle). The deployment truss modules with orthogonal grid lines have simple and superior deployment characteristics. The basic concept of the deployment and stowing motion of the deployment truss module is represented by the two dimensional shearing transformation of square links in the cross section of the deployment truss module. The initial shearing transformation of square links is accomplished by sliding one end of a diagonal member of the square links. Final shearing transformation, i.e., transformation from plane form to parabolic form, is accomplished by elongating or shortening the diagonal members of the square links. In this square grid concept, all deployment truss modules share common design criteria. The amount of elongation or shortening of the diagonal members and the length of folding members determines the final shape of the deployable truss module. In order to improve the deployment characteristics of the folding hinge mechanism, the square link hinge was employed. In addition, to offset the loss of transmission efficiency, two additional motors were set on each module.

BREAD BOARD MODELS OF INTEGRATED DEPLOYABLE ANTENNA MODULES

Figure 7 shows a photograph of the three integrated antenna modules. The modules were designed to have the same F/D (Focus divided by Diameter) value as the 4 m diameter BBM. They are 1m in equivalent diameter.

Structural basis

The deployable truss structure consists of longitudinal members, radial members, circumference members, diagonal member, folding members, revolving hinges, sliding hinges, folding hinges, and driving motors. Longitudinal, radial and circumference members are made of CFRP (Carbon Fiber Reinforced Plastic). Diagonal members consist of an aluminum tube, a steel stem, a coil spring, and a lock/release mechanism. Figure 8 shows the cross section of both a collapsing and a extending diagonal member. The folding hinge mechanism consists of a revolving hinge axis, two linkage arms and a spiral spring set on a linkage node. Sliding hinges move along the motor axes and are driven by motors.

Three functionally independent antenna modules were fabricated and integrated. They were named type 1, type 2, and type 3. Their locations on the parabolic surface are shown in figure 9. Figure 10 explains the deployment direction of the truss nodes. In this figure, filled triangles denote in-plane motions, double circles denote upward motions and crosses denote downward motions. In order to synchronize a module to the two adjacent modules, one of the three modules must be designed to turn the truss topology upside down. The type 3 module was designed to achieve this. Structural features of each antenna module are described as follows.
(1) The type 1 antenna module is placed on the center of the parabolic surface, so it is symmetrical.
(2) Diagonal members of each antenna module have different combinations of collapsing and extending elements.
(3) The final shape of each antenna module is determined by the length of the folding and diagonal members.

Design and analysis of deployment mechanism

The sliding hinge mechanisms and the latch mechanisms of the folding members must driven with sufficient force and moment to overcome the resistant forces of the cable network and surface mesh. These resistant forces were estimated by calculating the reaction forces against the cable network at each standoff point using CAble Structure Analyzer (CASA)[3]. Figure 11 shows the transition in standoff force during deployment as a function of the rotation angle of the truss member. These forces rapidly increase as the fully deployed position is approached.

Excessive torque of folding members results in anomalous deployment. Figure 12 shows the motor reaction force transition during deployment motion. The instant that the truss module is released, rapid deployment motion is induced independently of the three driving motors. The reason for this is that elastic deformations arise at hinge mechanisms due to folding members. Soon, these deployed members rebound to their original position. When this happens,

unexpected reaction forces arise at the driving motors which then failed to hold their predetermined positions.

GROUND DEPLOYMENT TEST

The object of ground deployment tests is to confirm design criteria for the integrated antenna modules under the 1G environment and to get meaningful data for the estimation of deployment characteristics. These data will be compared to the actual deployment characteristics under micro-gravity environment to improve the accuracy of analytical models.

Test equipment

Ground deployment tests must be carried out to verify the deployability of the antenna modules and improve the analytical model. However, the antenna module has insufficient structural strength to overcome gravity, especially the integrated modules. In addition, deployment characteristics are seriously altered by gravity. Therefore, a gravity compensation technique was developed around a simple suspension method. Figure 13 shows the ground deployment apparatus for both the unit module and the integrated modules. The suspension equipment consists of nine movements set on nine linear bearings, pulleys, suspending wires and counter weights. The linear bearings are aligned along the projected motion tracks of the deployment truss nodes. Suspension wires are fixed to truss nodes and the wires are tensioned by counter weights through pulleys. The nine bearings are not driven by any actuators, but follow the truss nodes passively. The antenna module is fixed to the ground plate at lower end of the central motor axis for single deployment while the antenna modules are fixed at lower end of the central motor axis of the central modules for integrated deployment.

Measurement and Data handling method

Deployment characteristics were quantitatively measured by several strain gauges and qualitatively observed by a video recording system. Several LEDs were set on truss nodes to indicate instantaneous position in the video records. The video tracking system will be used to deal with these data. The operations of the diagonal members and latch mechanisms were confirmed by this visual observation. Figure 14 indicates the locations selected for the strain gauges. These locations were selected considering the following evaluation items.
(1) Reaction force transitions due to the cable network during deployment.
(2) The influence of diagonal members on the deployment motion.
(3) Twisting mode shapes due to excessive torque of folding members or inadequate gravity compensation.
(4) The influence of module integration on the deployment motion.
A pair of strain gages was fastened to the center of each member to be tested. Strain data were amplified by a strain amplifier and quantized by a micro computer. These data were then converted into axial forces and bending moments using the following equations,

$$F = EA\frac{(\varepsilon_1 + \varepsilon_2)}{2} \text{ (N)}$$

$$.....(1)$$

$$M = EI\frac{(\varepsilon_1 - \varepsilon_2)}{d} \text{ (Nm)},$$

$$.....(2)$$

where ε_1 and ε_2 are the pair of strain data, E is Young's ratio (N/m²), A is the cross-sectional area of the member (m²), d is the diameter of the member (m), I is the moment of inertia (m⁴), F is the axial force, and M is the bending moment.

Experimental results

Figure 15 shows the deployment motion of the integrated antenna modules. The deployment of each antenna module and the integrated antenna modules were successfully completed and latch up was achieved. However, unexpected stresses arose at hinge mechanisms during deployment. Figure 16 shows bending moment transition in a radial upper member of the type 1 module. This figure indicates that bending moments arise when the diagonal members are released but disappear at full deployment. The reason for this is the unexpected deformations that arose at the hinge mechanisms. Figure 17 shows bending moment transition in a standoff during deployment. The reaction forces against the cable network(the bending moment divided by standoff length) increase gently as compared to analytical results(figure 11). The most undesirable result was that the cable network frequently clung to the hinge mechanisms. To prevent cable entanglement, the cable network must be arranged carefully before deployment.

DEPLOYMENT ANALYSIS FOR SQUARE GRID DEPLOYABLE TRUSS

As described previously, transformation from a plane form to a parabolic form, is accomplished by elongating or shortening the diagonal members of the square links. The transformation must be smoothly accomplished without any elastic deformation. According to experimental results, however, some elastic deformations were created when the diagonal members were released. These elastic deformations vanished at full deployment. The reason for this is that the antenna modules were not designed for transient deployment but only for stowed and deployed configurations. In order to clarify the transient deployment motions, a simple geometric model and a actual dynamic model were considered. Elastic deformations at hinge mechanisms in a dynamic model were calculated using DADS (Dynamic Analysis and Design System).

Deployment to a plane form

Figure 18 shows a simple geometric model of the integrated antenna modules. In this figure, P_{ij} denotes a grid point located at the i-th coordinate in the x direction and the j-th coordinate in the y direction. α_{ij} and β_{ij} denote inclination angles of members which are connected to P_{ij} from x direction and y direction, respectively. α_{ij} and β_{ij} are defined as ,

$$\alpha_{ij} = \beta_{ij} = (-1)^{i+j-1} \theta$$

56

$$\dots\dots(3)$$

where θ is the stowing angle from full deployment position. The coordinates of grid point P_{ij} are expressed as follows.

$$x_{ij} = \sum_{m=1}^{i} (l\cos\alpha_{mj}) = l\cos\theta \cdot i$$

$$\dots\dots(4)$$

$$y_{ij} = \sum_{m=1}^{j} (l\cos\beta_{im}) = l\cos\theta \cdot j$$

$$\dots\dots(5)$$

$$z_{ij} = \sum_{m=1}^{i} (l\sin\alpha_{m0}) + \sum_{m=1}^{j} (l\sin\beta_{im}) = \frac{l\sin\theta\{1 - (-1)^{i+j}\}}{2}$$

$$\dots\dots(6)$$

These equations indicate that x_{ij} and y_{ij} are independent of j and i, respectively. Thus grid lines that consist of truss members cross at an orthogonal angle during deployment to a plane.

Shearing deformation from a plane form

In this analytical case, the shearing deformation to a parabolic surface is assumed to begin at the fully deployed plane form. Assuming the surface to be the central part of a parabolic surface, the coordinates on the surface are related through focal length f where $z_{ij} = \dfrac{x_{ij}^2 + y_{ij}^2}{4f}$. Thus shearing angles in the line parallel to the x axis or y axis, have the same value. α_{ij} and β_{ij} are defined as

$$\alpha_{ij} = \varphi_i^x$$

$$\dots\dots(7)$$

$$\beta_{ij} = \varphi_j^y,$$

$$\dots\dots(8)$$

where φ_i^x, φ_j^y are the shearing angles in x direction, and y direction respectively. φ_i^x, φ_j^y are arbitrary values during deployment . The final values are determined as

$$\cos^2\varphi_1 = \frac{8f^2}{l^2}\left[\sqrt{\left(1 + \frac{l^2}{4f^2}\right)} - 1\right]$$

$$\dots\dots(9)$$

$$\tan\varphi_{m+1} = \frac{1}{4f}\left(2\sum_{k=1}^{m}\cos\varphi_k + \cos\varphi_{m+1}\right)$$

$$\dots\dots(10)$$

Considering $\varphi_m^x = \varphi_m^y = \varphi_m$, the coordinates of grid points are expressed as

$$x_{ij} = \sum_{m=1}^{i} (l\cos\varphi_m) = x_{ij}(i)$$

$$\dots\dots(11)$$

$$y_{ij} = \sum_{m=1}^{j} (l\cos \varphi_m) = y_{ij}(j)$$

.....(12)

These equations also indicate that x_{ij} and y_{ij} are independent of j and i, respectively. Thus grid lines that consist of truss members cross orthogonally during shearing deformation.

Composite deployment motion

During composite deployment motion, inclination angles of truss members and coordinates of grid points can be written as follows.

$$\alpha_{ij} = \varphi_i + (-1)^{i+j-1}\theta$$

.....(13)

$$\beta_{ij} = \varphi_j + (-1)^{i+j-1}\theta$$

.....(14)

$$x_{ij} = \sum_{m=1}^{i} l\cos \alpha_{mj} = \sum_{m=1}^{i} \cos \varphi_m\cos \theta - \sum_{m=1}^{i} (-1)^{m+j-1}\sin \varphi_m\sin \theta$$

.....(15)

$$y_{ij} = x_{ij}$$

.....(16)

$$z_{ij} = \sum_{m=1}^{i} \sin \alpha_{mj} + \sum_{m=1}^{j} \sin \beta_{im}$$

$$= \left(\sum_{m=1}^{i} \cos \varphi_m + \sum_{m=1}^{j} \cos \varphi_m \right)\cos \theta$$

$$+ \left(\sum_{m=1}^{i} (-1)^{m+j-1}\cos \varphi_m + \sum_{m=1}^{j} (-1)^{m+i-1}\cos \varphi_m \right)\sin \theta$$

.....(17)

Above equations indicate that x_{ij} and y_{ij} are functions of i and j. This means that the grid points x_{in} (n=1,2,3,...) or x_{nj} (n=1,2,3,...) are not in line, and the crossing angles of grid lines vary with their position. Thus some elastic deformation arises when the diagonal members are released.

Dynamic deployment analysis using DADS

According to the above simple model, hinge stress is inevitable. However, elasticity and hinge mechanism slop would ease geometric distortion in actual deployment modules. Forces and moments at a hinge mechanism can be calculated using DADS. Truss members are assumed to be rigid bodies. Their degrees of freedom are connected to each other by elastic elements (except for the rotation around the hinge axes). Deployment motion is divided into three portions: deployment to a plane form, composite deployment, and deployment to a parabolic form. Extending or shortening of diagonal members can be modeled by three discontinuous constraint conditions. These conditions are fixed initial length, a constant elongation or shortening rate and fixed final length. Joint slop is not

58

considered in this case. Figure 19 shows schematic deployment motions of a portion of the deployment antenna module. In this figure, a gap between two portions of a diagonal member indicates elongation of the diagonal member. Figure 20 shows axial force transition at a hinge mechanism during deployment. Elastic deformation arises when the diagonal members are released, and vanishes at full deployment.

CONCLUSION

The modular concept for the construction of cable-mesh deployable antennas was proposed. In order to extend the unit antenna module to the integrated antenna modules, square grid deployable trusses were designed, fabricated, and tested. The integrated antenna modules were successfully deployed and latched up in both 1 G and micro gravity environment. However, unexpected loads arose in the hinge mechanisms. These loads could be analytically estimated by a simple model and DADS. More consideration has to be paid to the difference in the deployment characteristics between the 1 G and micro gravity environments.

REFERENCE

1. Jin Mitsugi and Tetsuo Yasaka, A Modular Approach to Build a Large Space Antenna, Proceedings of 42nd Congress of the International Astronautical Federation, IAF-91-315, October 5-11, 1991/Montreal, Canada.
2. Jin Mitsugi and Tetsuo Yasaka and Koryo Miura, Shape Control of the Tension Truss Antenna, AIAA Journal, Vol. 28, No.2, Feb., 1990, pp. 316-322.
3. Jin Mitsugi and Tetsuo Yasaka, Nonlinear Static and Dynamic Analysis Method of Cable Structures, AIAA Journal, Technical Note, vol. 29, No., 1991, pp. 150-152.

BIBLIOGRAPHY

A. Meguro : Design and Analysis of a Deployable Truss for the Large Modular Mesh Antenna, Proceedings of the 18th International Symposium on Space and Science, Kagoshima, vol. 2, pp. 485-490, 1992.
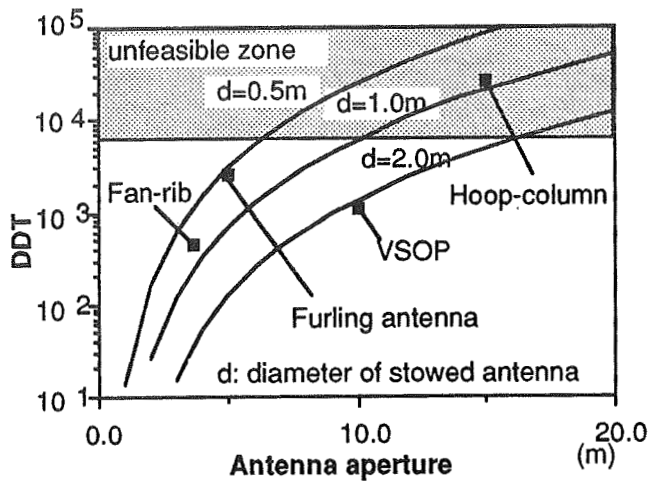
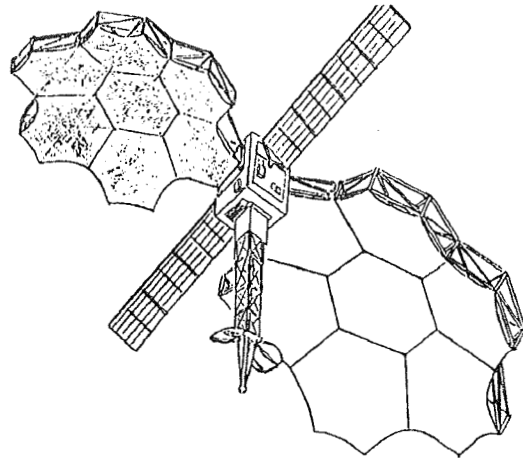**Figure 1 Ground test feasibility**

unfeasible zone

d=0.5m

d=1.0m

d=2.0m

Fan-rib

Hoop-column

VSOP

Furling antenna

d: diameter of stowed antenna

DDT

Antenna aperture (m)

Figure 2 The future advanced mobile communication satellite.

Surface Cable

Surface Mesh

Tie Cable

Back Cable

Stand Off
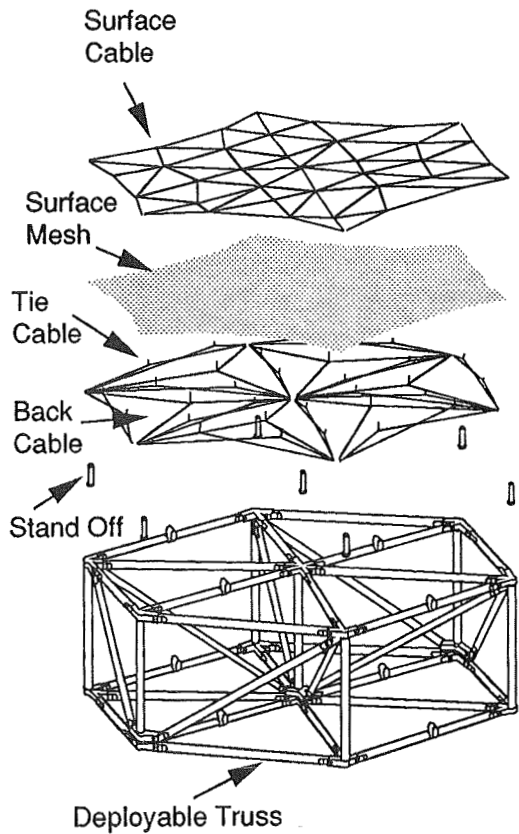
Deployable Truss

Figure 3 Basic Module Structure

Revolving hinge

Radial member

Folding member

Folding hinge

Revolving hinge

Diagonal member

Radial member

Longitudinal member

Diagonal member

Revolving hinge

motor

Circumference member

Folding member

Longitudinal member

Sliding hinge

Revolving hinge
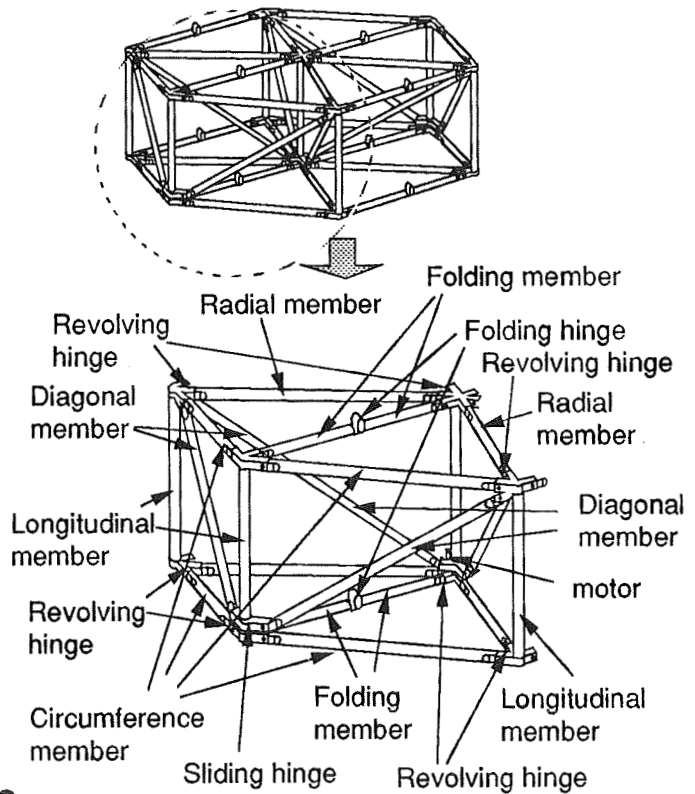
Figure 4 Deployable Truss Structure
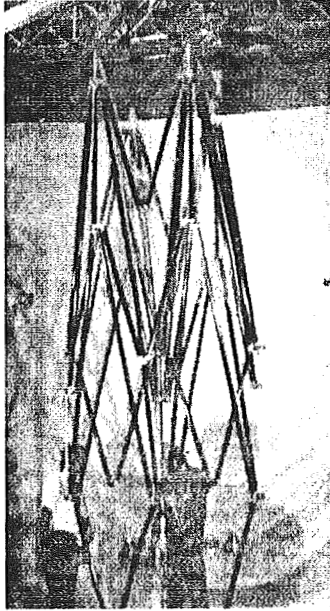
Stowed
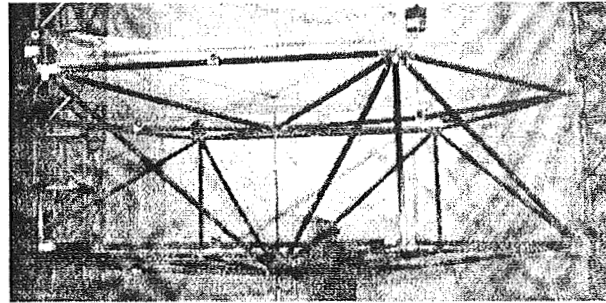
Deployed

Figure 5 The BBM of the central module of the 10 m antenna

60 deg
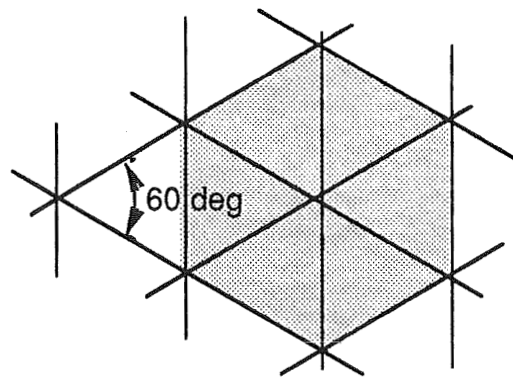
Figure 6 The upper view of the 4 m diameter BBM
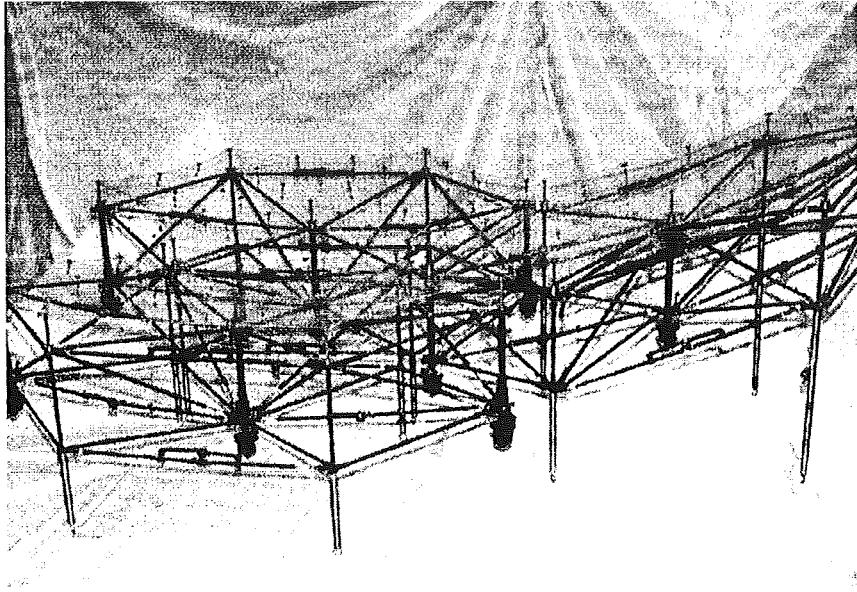
Figure 7 The integrated antenna modules

Spring   Elongation member
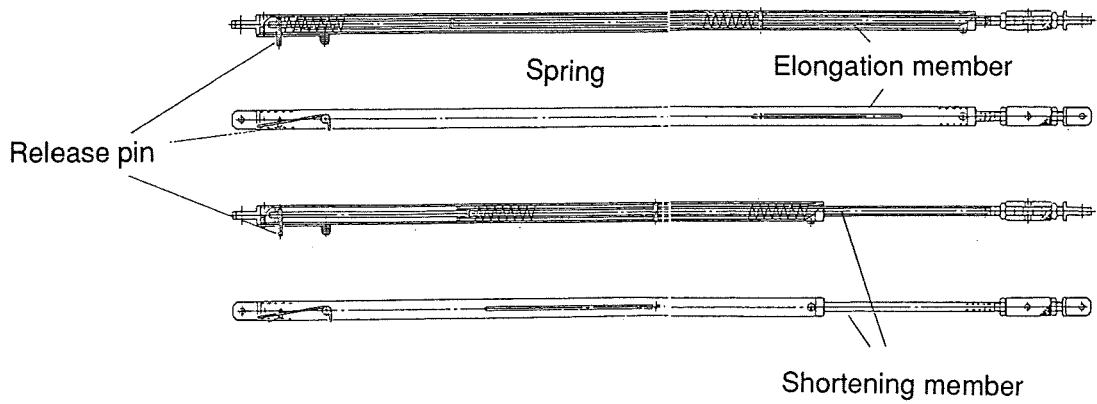
Release pin

Shortening member

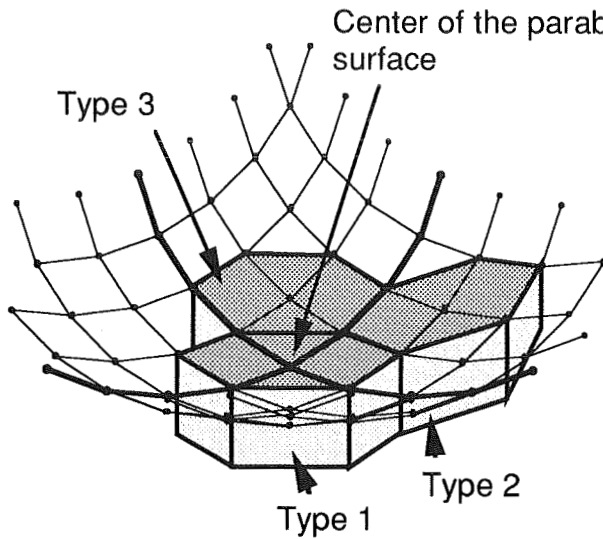**Figure 8 Shortening and elongation diagonal members**

Figure 9 Locations of antenna modules on the parabolic surface

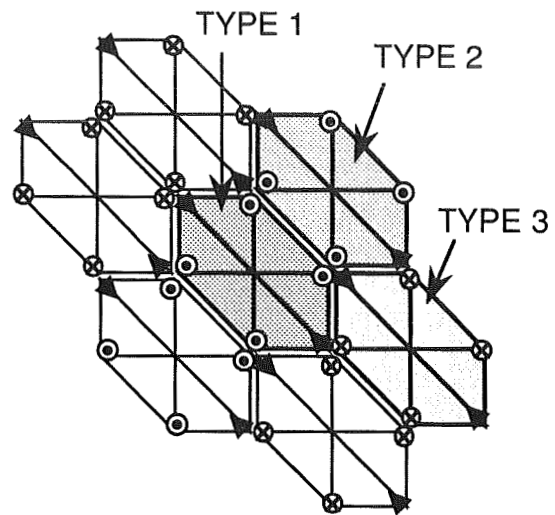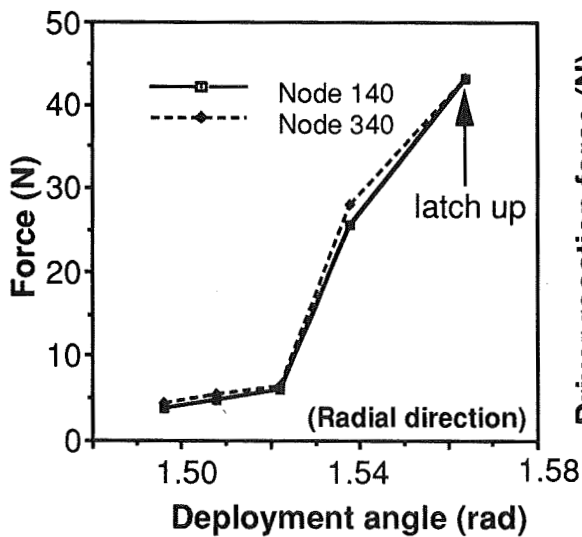**Figure 10 Deployment direction of truss nodes.**

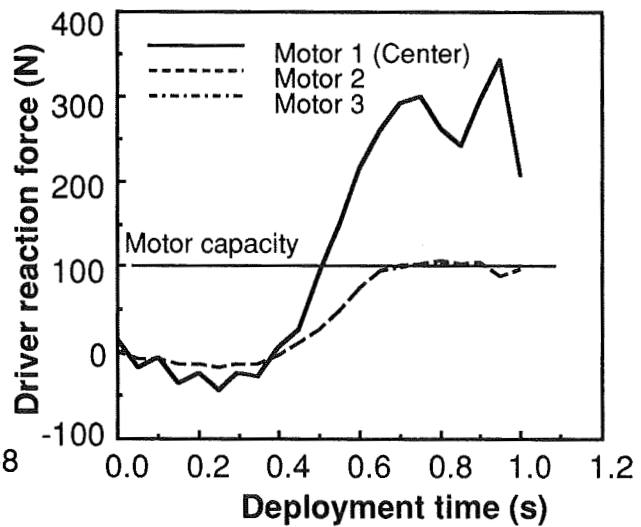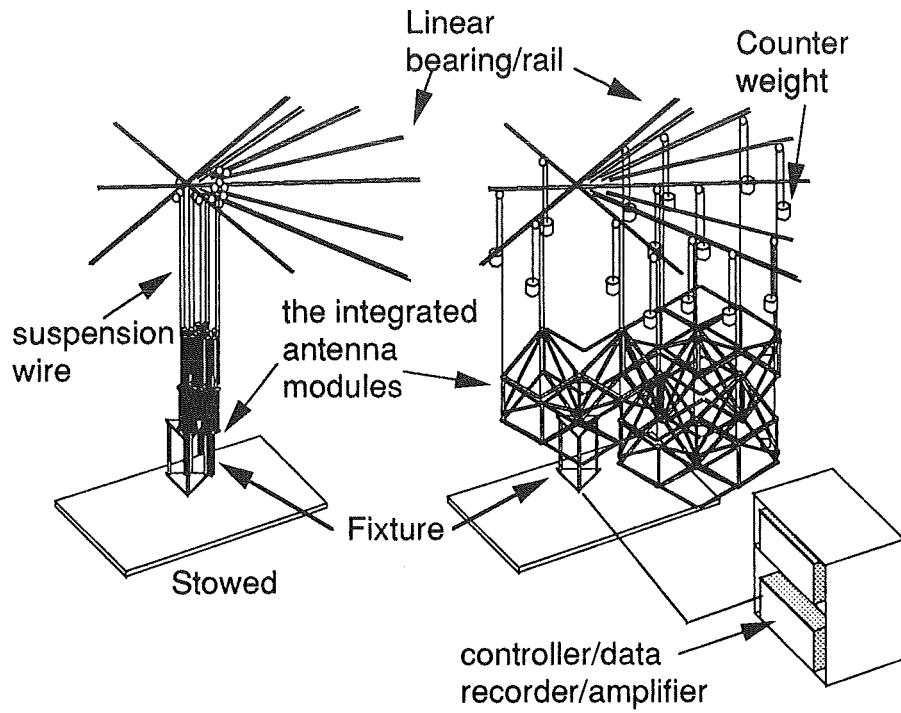**Figure 11 Stand-off force during deployment**

Figure 12 Motor reaction force during deployment
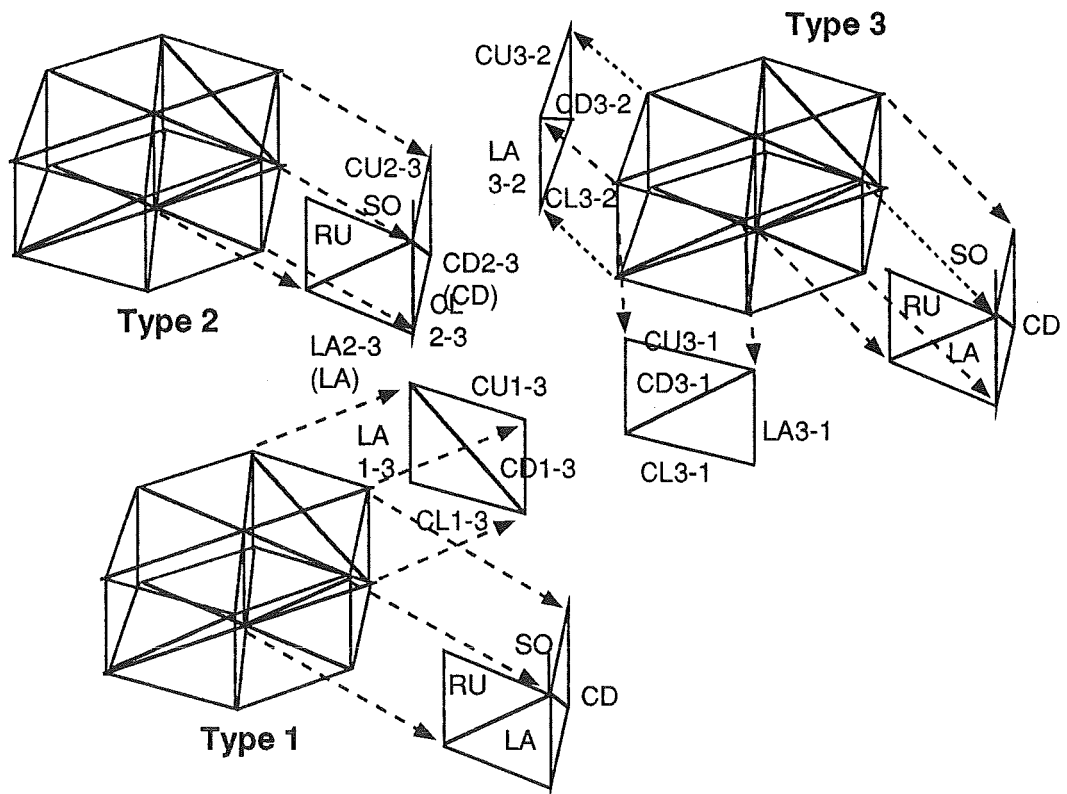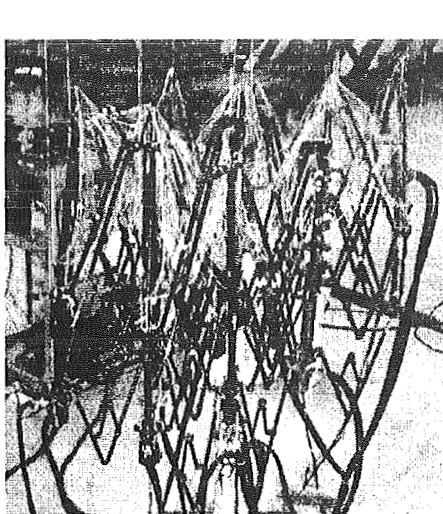
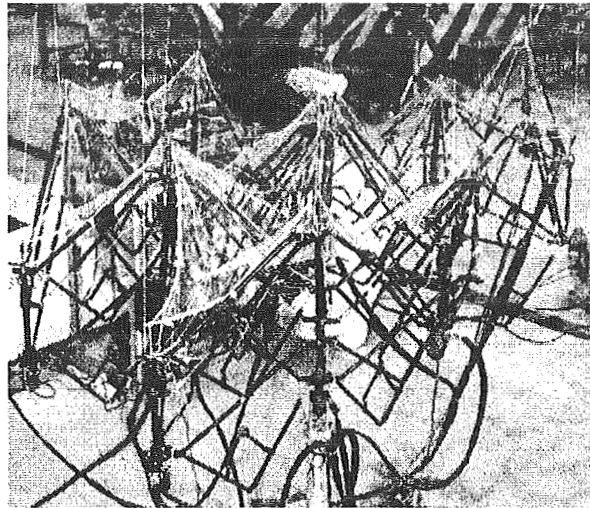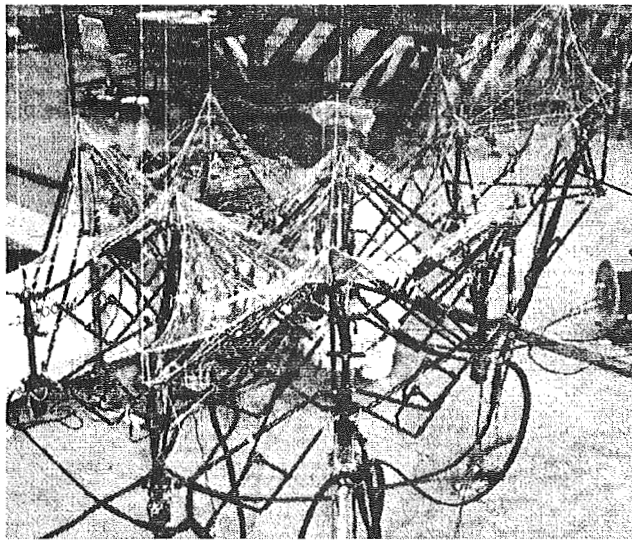63

Figure 13 Ground test apparatus

Figure 14 Selected locations of strain gages

Stowed

Deployment to a plane surface

Deployment to a parabolic surface

Elongation of the diagonal member

Figure 15 Deployment motion of the integrated modules
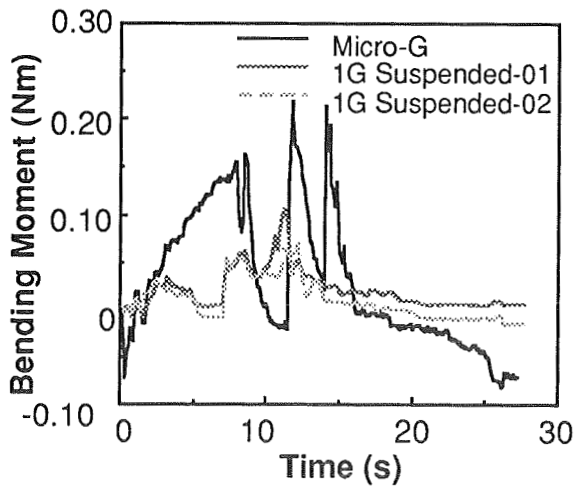
Figure 16 Bending moment in a radial upper member

Figure 17 Standoff bending moment transition

Figure 18 A simple geometric model of the integrated antenna modules

Stowed

Deployment to a plane surface

Elongation

Deployment to a parabolic surface
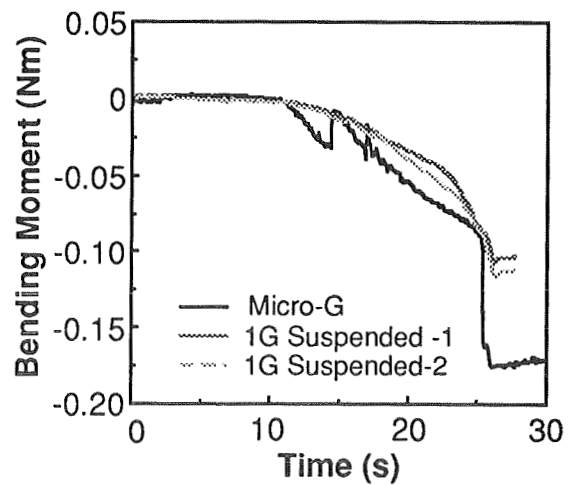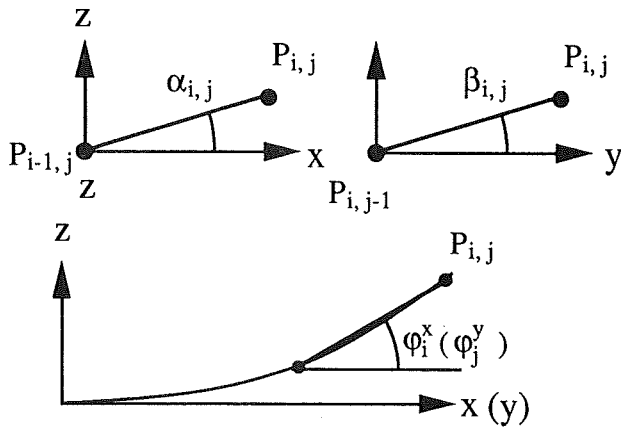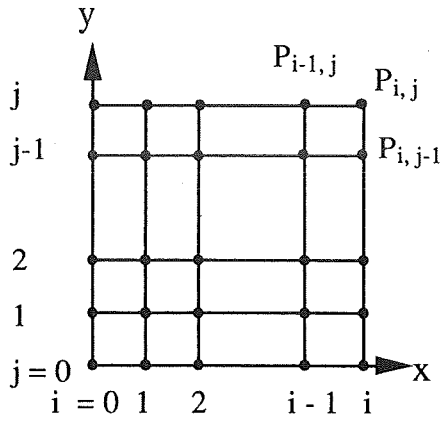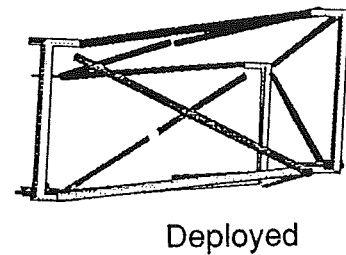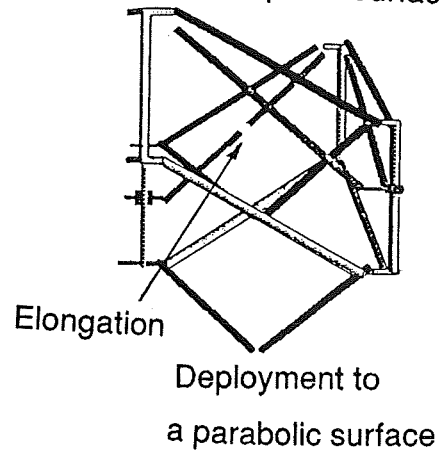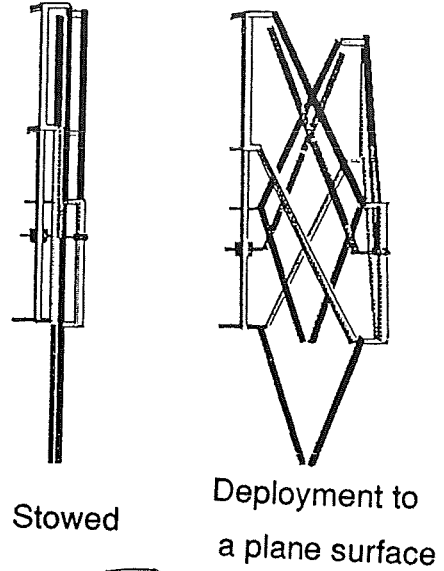
Deployed

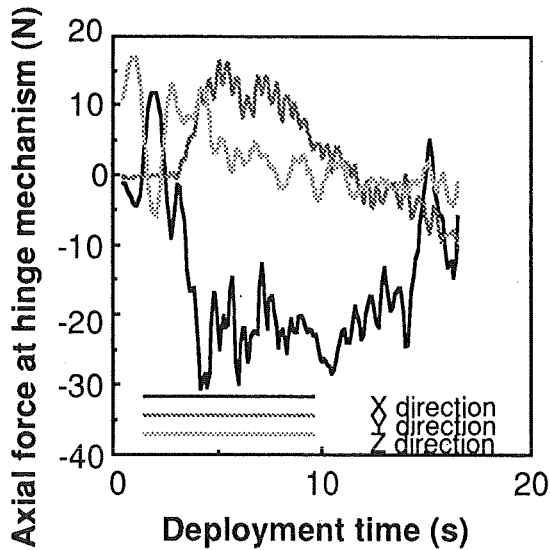Figure 19 Deployment motion of a portion of the deployment antenna module

Figure 20 Axial force transition at a hinge mechanism

X direction
Y direction
Z direction

66

WAVES IN SPACE PLASMA DIPOLE ANTENNA SUBSYSTEM /3 4640

Mark Thomson*

ABSTRACT

The Waves In Space Plasma (WISP) flight experiment requires a 50-meter-long deployable dipole antenna subsystem (DASS) to radiate radio frequencies from the STS Orbiter cargo bay. The transmissions are to excite outer ionospheric plasma between the dipole and a free-flying receiver (Spartan) for scientific purposes. This report describes the singular DASS design requirements and how the resulting design satisfies them. A jettison latch is described in some detail. The latch releases the antenna in case of any problems which might prevent the bay doors from closing for re-entry and landing of the Orbiter.

INTRODUCTION

The DASS is composed of 25-meter-long monopoles mounted back to back in the aft end of the cargo bay as shown in Figure 1. They are deployed from the 1.2-meter-long antenna element assemblies (AEAs) shown in Figure 2. The antenna elements are storable tubular extendible members (STEMs™) which are each deployed 23.6 meters from an aperture in the deployer mechanism housing. During the experiment the Orbiter executes a number of complex maneuvers with the DASS at various deployed extensions during as many as 50 deployment cycles.

A veteran of many space flights, a STEM™ mechanism is the basic component of the DASS. It is formed into a tubular configuration from a single strip of thin metal, then spread and flattened so it can be rolled onto a spool for launch. Its simplicity is appropriate for the high degree of reliability and straightness that are demanded of the DASS antenna elements.

All functions of the AEA must have redundant backup. Furthermore, for re-entry and landing it must be possible to safe the cargo bay from failure of the monopoles despite two electrical and/or mechanical faults. If there is a failure to retract and cage the STEM, the element must be jettisoned cleanly away from the Orbiter. A unique and single-fault-tolerant jettison latch is the result of this need.

The powerful jettison latch is subject to a common problem: Just at the point of release, contact stresses go up exponentially, thus yielding or fracturing the latch. Although the mechanism was designed to be tolerant of this tendency, an anomaly was observed during initial testing. The latch and results of the anomaly are highlighted in the discussion.

---

*Astro Aerospace Corporation, Carpinteria, CA

The WISP experiment transmitter has a peak power of 500 watts at frequencies up to 30 MHz. This range of propagation is outside that to which the Orbiter was designed and qualified. Understandably, there is significant concern about any effects the strong radiated emissions might have on electrical equipment in the AEA and the Orbiter. Mechanisms that will be at RF potential are therefore isolated from the components that are susceptible to EMI. The requirement for a reliable jettison capability and for electrical isolation have influenced the design of the AEA to the greatest extent.

REQUIREMENTS

The AEA configuration evolved from the most influential of the electrical and mechanical DASS performance requirements.

Electrical design drivers include the following:

- Dipole lengths of 5.0, 6.0, 7.0 ±0.01 m to 50 ±0.05 meters

- Total shunt capacitance of 20 picofarads or less at the RF interface

- Low sensitivity to EMI

- Magnetic permeability ±0.190 of that of free space

- Antenna element DC surface resistivity of 1,000 ohms/cm^2 or less

- Electrical control of safety critical functions two-fault-tolerant

Mechanical design drivers include:

- Antenna element linearity:

  - ±1 percent tip deflection due to Orbiter induced loads based on monopole length

  - ±4 percent tip deflection due to the worst combination of:
    - As-manufactured straightness
    - Repeatability upon multiple deployments
    - Alignment errors relative to the Orbiter
    - Thermal distortions

- Safety Critical: safe the cargo bay with a tolerance to two faults

  - Single-fault-tolerant capability to jettison the element without debris in the event of buckling or a failure to retract

  - Single-fault-tolerant capability to cage the elements during launch and landing

- 5 cm/sec (2 in/sec) minimum deployment rate

- Peak random vibration spectral density of 0.14 G^2 Hz, 150 to 250 Hz

- 182 kg (400 lb) maximum DASS total weight

DESIGN APPROACH

Electrical Isolation

The STEM deployer and its contiguous mechanisms are at RF potential by necessity. They are thus mounted on top of a NEMA G-11 dielectric tower structure to electrically isolate them. As shown in Figure 3 and amplified by the cutaway view in Figure 4, the electromechanical components are underneath the tower. An assembly of two electronic controllers, potentiometers, seventeen switches, wiring harnesses and 4 DC motors are mounted on grounded base plate. Actuation of the deployer and the related mechanical status indicators are attained by the rotation of hollow shafts that are also of NEMA G-11.

To meet the capacitance requirement the amount of dielectric separation between the deployer housing and the grounded base was controlled. On the basis of the surface area presented between the two large assemblies it was necessary to provide an average separation of 0.2 meters (8.0 inches) to achieve an overall DASS shunt capacitance below 20 picofarads.

Mechanical Drives

Four electromechanical actuators are powered by 28 V DC brushed gear motors that protrude from the underside of the base plate. The motors drive 25 mm (1 inch) inside diameter G-11 tubes that are visible in Figure 4. Crowned-spline couplings are used at the ends of the tubes. The pivoting splines prevent thermal distortions and misalignment between the upper and lower structures from being a concern, and carry out an important function of the jettison latch.

The motors are modular in design. Three different groupings of the modules are needed to power antenna deployment, jettison, and caging functions. A tandem motor with a redundant power-off-brake drives the STEM deployer. Redundant potentiometers track the length of the deployed STEM via a gear reduction at the output spline of this actuator. Another tandem motor drives the caging shutter mechanism, but without a brake. Two single armature motors drive the redundant jettison latches. The jettison and STEM drive motors protrude from underneath the base assembly at the near (inboard) end of the AEA in Figure 4.

Retraction stores a significant amount of potential energy in the STEM and is therefore the sizing case for the motor. Motor power is based on a deployment speed of 5 cm/sec (2 in/sec) under the worst conditions. The output speed of the gear motor was set at 9 RPM so that the jettison latch and caging mechanisms could operate slowly without further gear reductions.

All switches are actuated through smaller hollow G-11 tubes. The deployed position of the STEM is indicated accurately by rollers that fall into pre-punched slots in the STEM. Rockers attached to the rollers cause the tubes to rotate, which actuates the redundant switch assemblies attached below. A number of other status indications are available by way of switches that are actuated in the same manner. Because the indicator tubes can only rotate, the switches will not be abused during vibration testing and launch. A simple flexure fitting allows the indicator shafts to rotate without angular play while behaving like a gimbal of limited range to mitigate the need for careful alignment of the deployer and base assemblies.

Design for Cost

The chosen design approach results in an increase in size and complexity compared to what is typical for a STEM unit. It was possible to keep the cost of the AEA and related engineering relatively low, however, by taking advantage of the specified 182-kg (400-lb) maximum weight limit. A finite element model of the unit was generated to yield the loads on subassemblies. The ample weight ceiling allows individual structures and mechanisms to be of sturdy proportions. Because it is not necessary to relieve weight at every opportunity, the effort required for the detail design and machining of the parts is greatly reduced. With worst-case strength margins of 400 to 1,000 percent in most cases, the detailed stress analysis of piece parts could be carried out in a somewhat abbreviated manner. The analytical scope for the fracture critical components is significantly reduced as well.

Most space flight mechanisms require some kind of adjustment or inspection before flight. Every effort was therefore made to ensure that more complex components would not be buried within the AEA. Assembly and disassembly of the unit were streamlined by making each G-11 panel in the tower individually removable. Access to every component inside the AEA is available from several directions with a minimum of effort. The indicator shafts are easily removed for access to multiple-switch assemblies which are calibrated in a separate fixture. The motors and electronic controllers can be unbolted directly from the external surface of the base assembly. The larger G-11 tubes for the actuator drives have female splines in each end and are thus easily removed.

The STEM and Guidance Mechanism

To satisfy the overall antenna element linearity requirements, the STEM material must be formed into uncommonly straight and long lengths. The resulting elements display a basic straightness of less than ±1.0 cm (±0.4 inch) RMS over the 23.6-m deployed length. Straightness was measured by supporting the element on floats in a water table, which closely approximates zero-g in a plane, as shown in Figure 5.

The antenna element itself is made of beryllium copper to conform to the requirement for magnetic permeability. Its thickness is 0.18 mm (0.007 inch), and it is formed into a 34-mm (1.34-inch) diameter tubular shape from 15.2-cm (6-inches) wide flat strip, as shown in Figure 6. The resulting circumferential overlap of 153

degrees places the mechanical shear center of the element in coincidence with the geometric center of the tube.

The element is plated with silver to maintain the lowest possible surface resistivity and operating temperatures. Metallic plating is the only type of conductive coating that is compatible with the deployable STEM element, and silver has a lower α/ε ratio than any metal that is appropriate for plating STEMs. The maximum solar thermal gradient across the STEM is about 3°C. This results in a deflection of 0.44 m (17 in) at the tip of the element.

A special guidance mechanism supports the STEM, as shown in the figure, while adding a minimum amount of friction during retraction. Shown schematically in Figure 6, the guidance mechanism keeps pointing hysteresis upon multiple deployments within ±0.1 degree. The combined straightness, including hysteresis, became ±2 cm (±0.8 inch) RMS. The stiffness of support provided by the guidance rollers and edge guides is 97 percent of the ideal value, which is based on a potted element.

Thermal Control

The original plan was to coat the antenna element deployer housing with a conductive, optically benign coating such as indium tin. A white, inorganic and electrically conductive paint developed by Marshall Space Flight Center for the tethered satellite program also came to our attention. The principle investigator ultimately decided, however, that the surface conductivitymust be constant along the length of the monopole. A mismatch might not result in a consistent path for DC current to flow into the plasma when it is attached to the dipole. It thus became necessary to plate the deployer housing with silver as well as the STEM.

Silver-plating the housing results in temperatures of 180°C (356°F) when re-radiation and reflectivities of the cargo bay are accounted for. This temperature is compatible with the exclusively mechanical deployer, but not with the electronic components. It is fortunate, then, that the NEMA G-11 tower also serves as an effective thermal isolator for the base assembly. The actuators and electronics have a maximum temperature of about 70°C (158°F) during long transients, which is acceptable.

Jettison Mechanism

The height of the deployer on the pallet in the cargo bay is just sufficient to ensure that a jettisoned port-side unit will clear the remote manipulator system (RMS) arm when stowed on the sill. The monopole must be jettisoned without generating debris and with a highly predictable trajectory. The track and roller ejection scheme shown in Figure 7 were therefore selected.

During launch and normal operation, the deployer is supported by a rigid four-point support system that is integral with the aluminum jettison tracks. The outboard supports, visible in Figure 4, are Vespel™ bushings that are located on crowned pins facing outboard from the base assembly. The inboard two supports are cups

71

centered on cones. The cones are backed by large stacks of disc springs that are compressed in series. The jettison latch preloads the springs flat to establish a precisely repeatable deployer position. When the latch is released, the kickoff springs provide a total initial impulse of 365 kg (800 lb). This accelerates the 30-kg (65-lb) deployer to 1 m/sec over the 1-cm distance that the springs act.

Mechanical interfaces with the actuators and indicators in the base assembly are separable. The STEM deployment and caging drive mechanisms have pairs of spur gears meshed at the points of separation. The teeth simply disjoin laterally along a line connecting the pitch axes. The indicator mechanisms, which normally exchange rotary motion through levers with pins in forks, disengage similarly. If any one of these interfaces become jammed, the high kickoff force ensures that the parts will separate.

Redundant negator motors then accelerate the deployer at 0.3 g up to 2.3 m/sec until only a few rollers remain engaged with the track to guide a straight trajectory away from the Orbiter. Each negator motor pulls one end of a shared cable that is wrapped around pulleys on the deployer. The course of the cable through the mechanism is well-shielded, and all features near the pulleys are controlled to defeat jamming. The cable is attached to each reel with less than 1 inch of excess length when the latch is armed. If one of the negator motors fails to operate, the other reel simply pulls in all the cable. The 23-kg (50-lb) accelerating force normally exerted by both negators on the deployer is reduced by only a few percent when one negator is operating. The losses are due to cable friction around what becomes a 2:1 purchase.

An initial concern was that the deployer might spin when jettisoned because the jettison tracks and spring forces do not act through the deployer center of gravity. A vertical, off-loaded jettison test was therefore conducted which verified the function of the latch and proved that a significant rotation is not induced by the mechanism.

Jettison Latch and Preload Assembly

The safety-critical jettison latch is shown in Figure 8. The two cups that seat the deployer on the inboard ejection cones are machined from blocks of Custom 455™ stainless steel. The cup blocks have teeth that face inward to engage the toothed faces of the latches. The teeth make contact at an angle of 30 degrees. The latches are also made of Custom 455™. They are held in engagement with the cup block by the presence of two square-headed Nitronic 60™ release shafts and a cylindrical Custom 455™ shuttle rod in between. The latches swivel inward on pivots in the jettison track assembly to release the deployer. All the latch components are dry-film lubricated with Vitrolube™ to provide durable lubrication and inhibit metal-to-metal contact.

Finally, disc springs on each pivoting latch arm is tightened against the jettison track assembly to pull the deployer cups onto the cones with a controlled preload of 1,400 kg (3,100 lb). This load is 25 percent greater than the maximum load resulting from the specified launch limit load environment per a detailed finite

element analysis. The 30-degree inclination of the latch faces cam the latches inward to squeeze the release shafts and shuttle rod with up to 700 kg (1,550 lb). If either release shaft is pulled out of engagement, the resulting gap is wide enough for both latches to swivel inwards while the shuttle rod finds a more neutral position.

Jettison Latch Release Shaft

The release shafts have acme lead screws on their lower ends as shown in Figure 9. The force needed to overcome friction between the dry lubricated surfaces of the latch and the shuttle rod was estimated between 35 and 70 kg using a friction coefficient of 0.05 to 0.1. The acme nut and gear motor are capable of exceeding this force by more than an order of magnitude.

When rotated, the nut ascends the lead screw within an operating gap as the dielectric shaft slides on the crowned spline. At the full extent of its travel in the gap, the nut flattens a thin disk spring and bears firmly on a thrust bearing that is backed by the track assembly. The spring normally preloads the bearing and thrust-washer combination to prevent them and the release shaft from rattling during vibration. It is sized by the launch limit load environment with 11 kg of force when flat. It also is intended to help ram the shaft assembly downward and out of the way upon release of the latch. The gap ensures that the assembly has room to move downward as the radiused edge of the release shaft is powerfully cammed by the force of the opposing latch, via the shuttle rod. The dielectric drive shaft slides on the crowned splines at the motor shaft to accommodate its axial motion.

The clamped tip of the square release shaft cannot turn. When the acme nut seats firmly on the thrust bearing, the lead screw begins to retract. Once it is clear of the shuttle rod the latch adjacent to it swivels to the right to release the deployer, which pushes the shaft assembly to the right as shown in Figure 9. This lateral motion is accommodated by the oblong retainer and a slotted penetration in the track assembly while the shaft rocks about 2 degrees on the crowned spline.

The shuttle rod or the release shaft will obviously yield or fail in some manner as contact stresses approach infinity at the bitter end of engagement. It was decided that such yielding could be made acceptable. The release shaft was therefore made of Nitronic 60™, which has an extremely high galling threshold of about 50 ksi, versus 2 or 3 ksi for other stainless alloys. Its strength and hardness are half or less that of the Custom 455™ shuttle rod. The shuttle rod should thus cut a clean groove in the edge of the release shaft tip during release.

The shaft tips have four sides and can be rotated to present fresh material. Nonetheless, it was hoped that once formed the grooves would have a better geometry for the intended purpose and that they would be work-hardened. If this were to be the case, the grooves could be re-used. The initial jettison test would simply be the final step in machining and subsequent operation would not produce a "failure."

73

The Latch Anomaly

The first jettison tests verified that the latch functioned, but the tip of the release shaft was grooved well into its center, as shown on the left in inset A, Figure 9. The deep curved groove traced the path of shuttle rod. This was not immediately understood. Subsequent tests on the fresh surfaces produced the same results. Then a faint peak of motor current with indiscernible duration was noticed on the strip chart. The peak was nearly coincident with a sharp reduction of current that immediately follows release. The release shaft was obviously jammed into contact with the accelerating shuttle rod and instantaneously stalling the motor as the kickoff springs did their job.

On a hunch, the thin disc spring that preloads the thrust bearing and the shaft assembly was removed, see Figure 9. This time a clean groove was produced that was on the edge of the release shaft tip only, as originally expected. The anomaly was caused by the fact that the force exerted by the thin disc spring exceeds the static friction force between the release shaft, latch and shuttle rod. The acme nut never climbed the lead screw into the gap to compress the spring. When the shuttle rod cammed across the radius on the tip of the shaft, the shaft had nowhere to go since it was still in contact with the flanged retainer below. The effectivecoefficient of sliding friction displayed by the surfaces lubricated with Vitrolube™ is estimated to be in the vicinity of 0.01, which is far below the anticipated value.

The fix for the problem was to use a very light spring for the operating gap in the release shaft assembly, its purpose being only to prevent the thrust bearing and washer from rattling in vibration. While working with the engineering model it became clear that the consequences of a release shaft shifting position during vibration are insignificant.

The latches were tested further by repeatedly releasing the latch over the same groove in the release shaft tip. It was confirmed that their geometry remains essentially unchanged after the first cycle of release.

CONCLUSIONS

The WISP DASS configuration evolved from the synthesis of electrical, radio frequency and mechanical design requirements with emphasis on Shuttle safety-critical functions. The requirements to safe the elements, provide high surface conductivity, low shunt capacitance, and electrically isolate the radiating elements were the most influential.

The combination of antenna element length, basic straightness and positional repeatability required by the plasma investigations is unprecedented for a STEM or BI-STEM. A straightness of ±2 cm (±0.8 inch) RMS, including hysteresis from multiple deployments, was achieved over the 23.6-m (930-in) length of each monopole by refining the forming process used at Astro Aerospace Corporation. This allowed a very comfortable margin to the overall straightness requirement.

The generous weight allocated to the DASS allows for a very robust design with minimal analysis. Consequently, a very fast detail design and fabrication process took place during months 7 through 11 of the program to produce an engineering model that is very close to the flight design.

The latch anomaly that was described was not serious, yet it reminds us that friction is not a very reliable phenomenon on which to base our designs. The tendency is to be conservative about the value of whatever coefficient we use, but this does not necessarily ensure success. The results also verified that controlled and well understood material yielding is acceptable for single event designs.
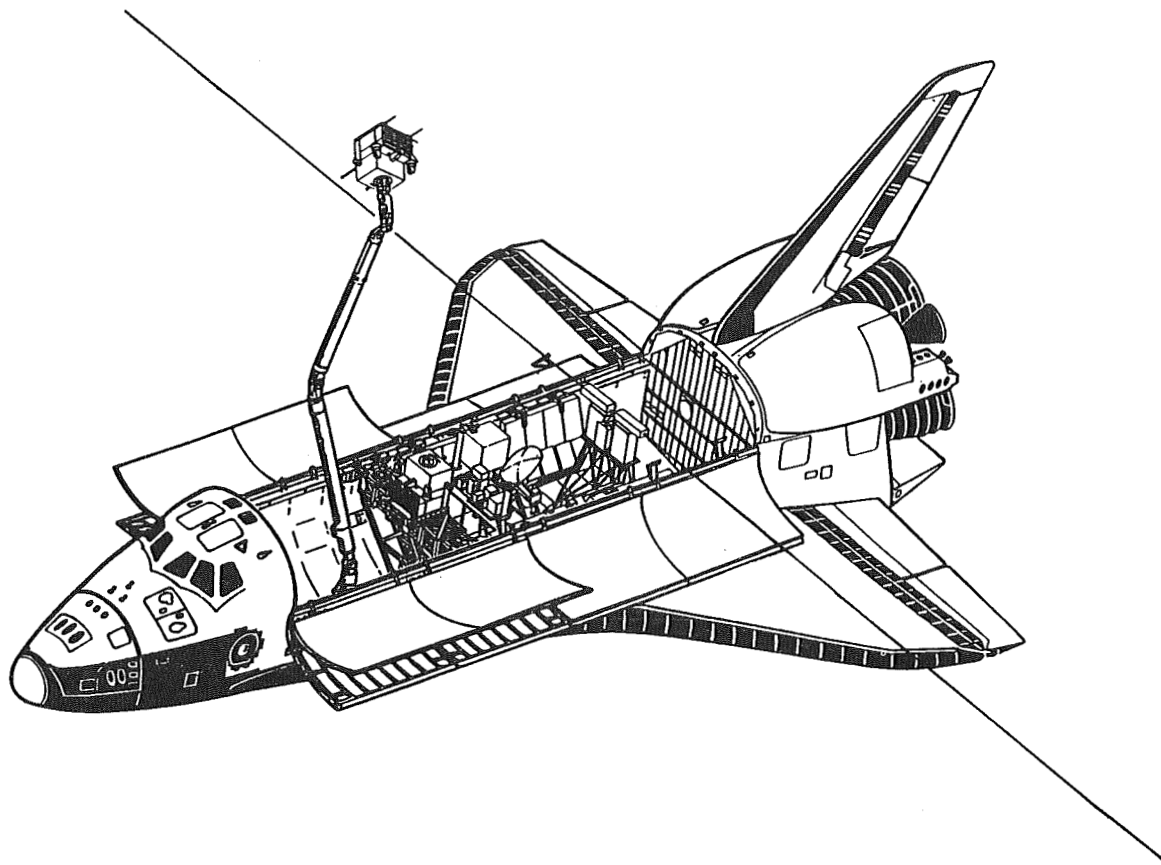
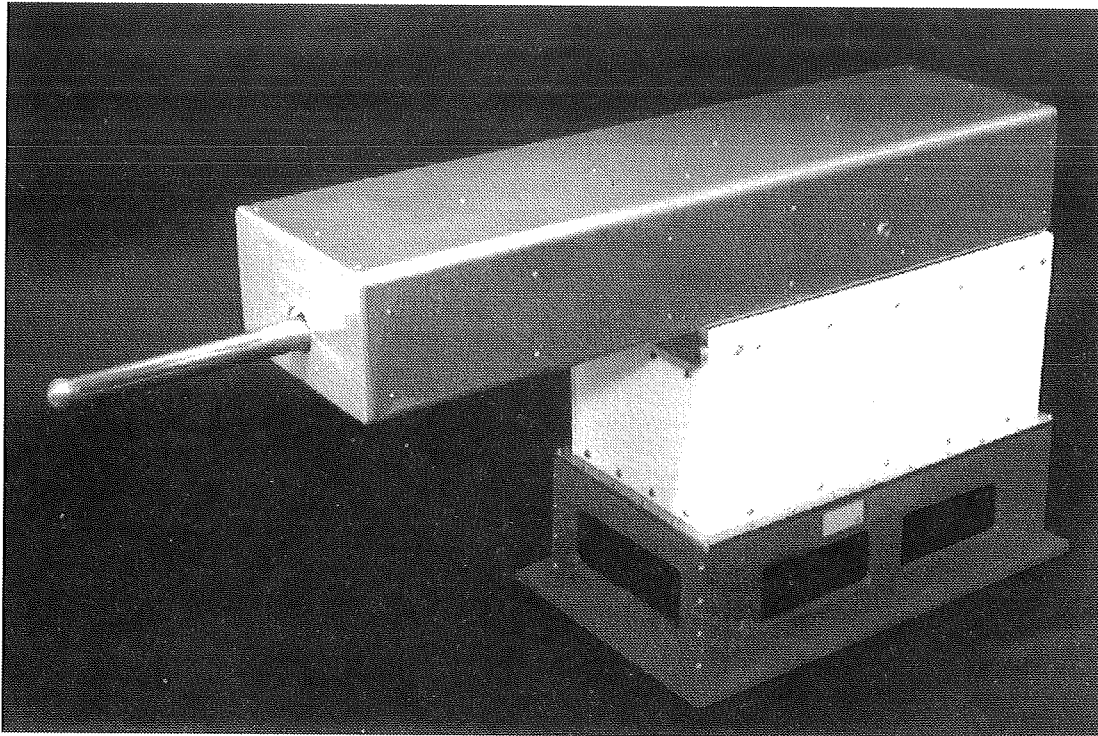**Figure 1. DASS Deployed on the Space Shuttle Orbiter.**

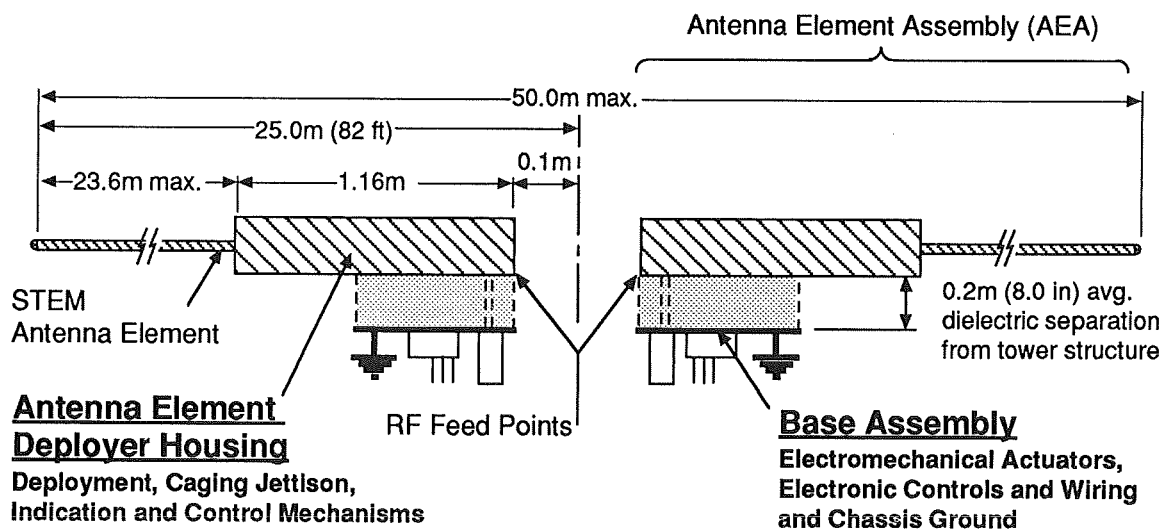Figure 2. Antenna Element Assembly Partially Deployed.

5072

Antenna Element Assembly (AEA)

STEM
Antenna Element

**Antenna Element
Deployer Housing**
Deployment, Caging Jettison,
Indication and Control Mechanisms

RF Feed Points

Base Assembly
Electromechanical Actuators,
Electronic Controls and Wiring
and Chassis Ground

0.2m (8.0 in) avg.
dielectric separation
from tower structure

Figure 3. DASS Design Concept.

77

4973

STEM caging
shutter and
snubber

STEM element

AEA deployer and housing

RF terminal (2)

Jettison
latch/preload
assembly (2)

STEM drive
mechanism

Potentiometer (2)

Jettison release
drive mechanism (2)

Caging mechanism
Outboard supports
Jettison rail (2)
Negator cable
and pulleys
Negator motor (2)

AEA base assembly
STEM position indicators (7)
Junction box and wiring

Electronic controllers

STEM and jettison drive motors

Figure 4. Cutaway View of the AEA.

78

Figure 5. Deployed Engineering Model Antenna Element.

Spool

15.2 cm (6.0 in)

Guidance rollers
and edge control
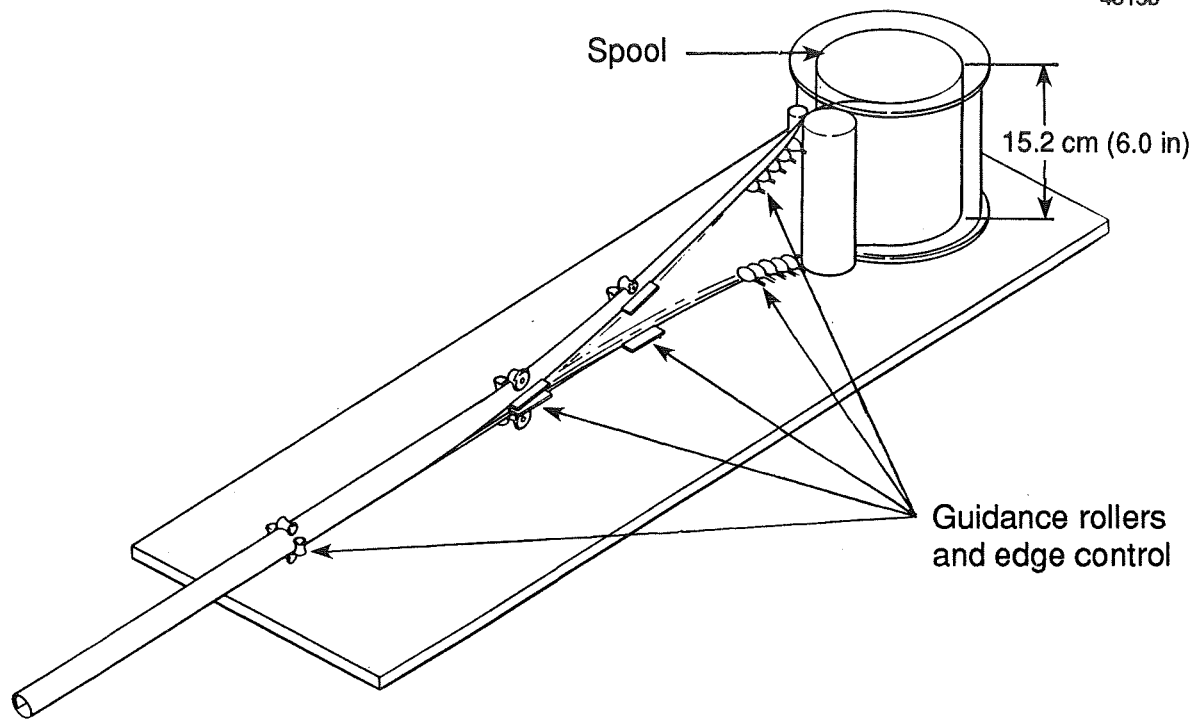
Figure 6. The STEM Mechanism.

Base
assembly

Tracks

Deployer

Rollers
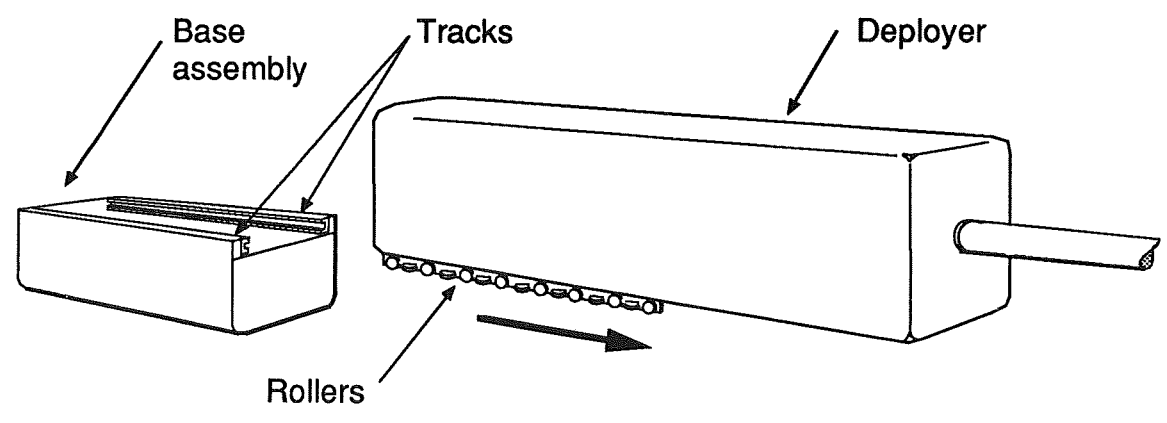
Figure 7. Deployer Mechanism Jettison Scheme.

Outboard direction

DEPLOYER

Jettison cable   4201a

Release shaft
engaged (2)

Jettison latch
secured (2)

Shuttle rod

To negator   Pulleys
motors

Jettison track
rollers (48)

Precision
cone (2)

Preload disc
spring (2)

Kickoff disc
springs (2)

Dielectric shafts (2)

Crowned spline (2)

Jettison indicator
switches (4)

Motor (2)
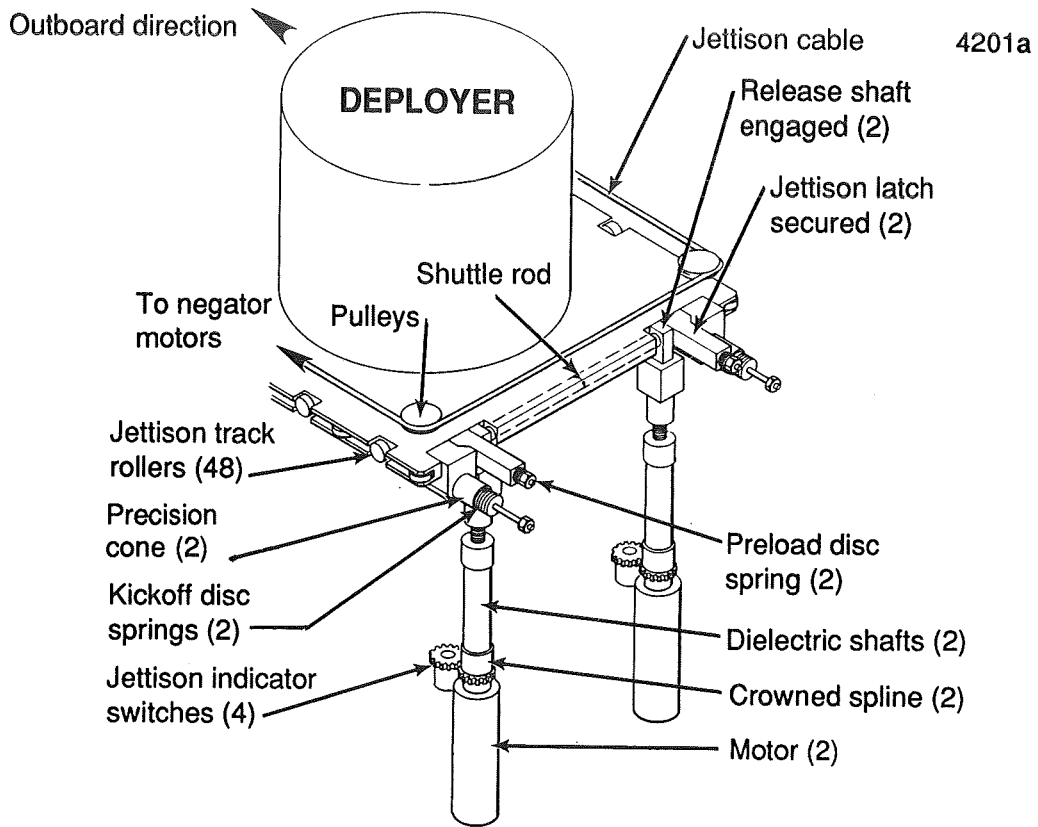
a) Jettison latch engaged

Cup block

Jettison latch
released

Disengaged release
shafts (2)
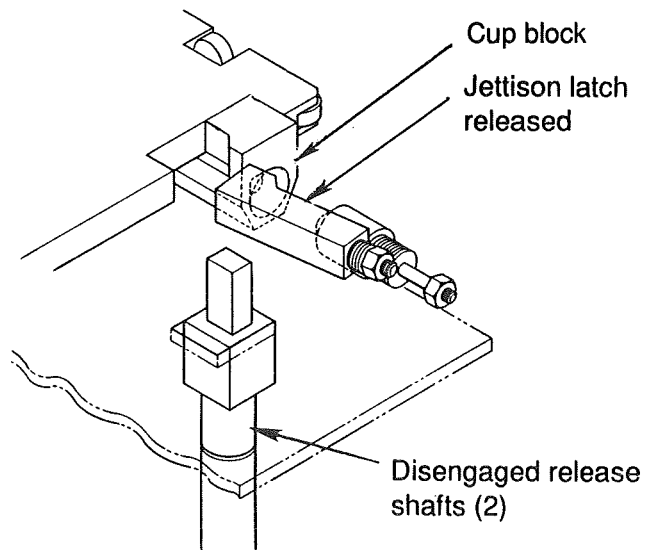
b) Jettison latch released

Figure 8.   Jettison Latch.

81
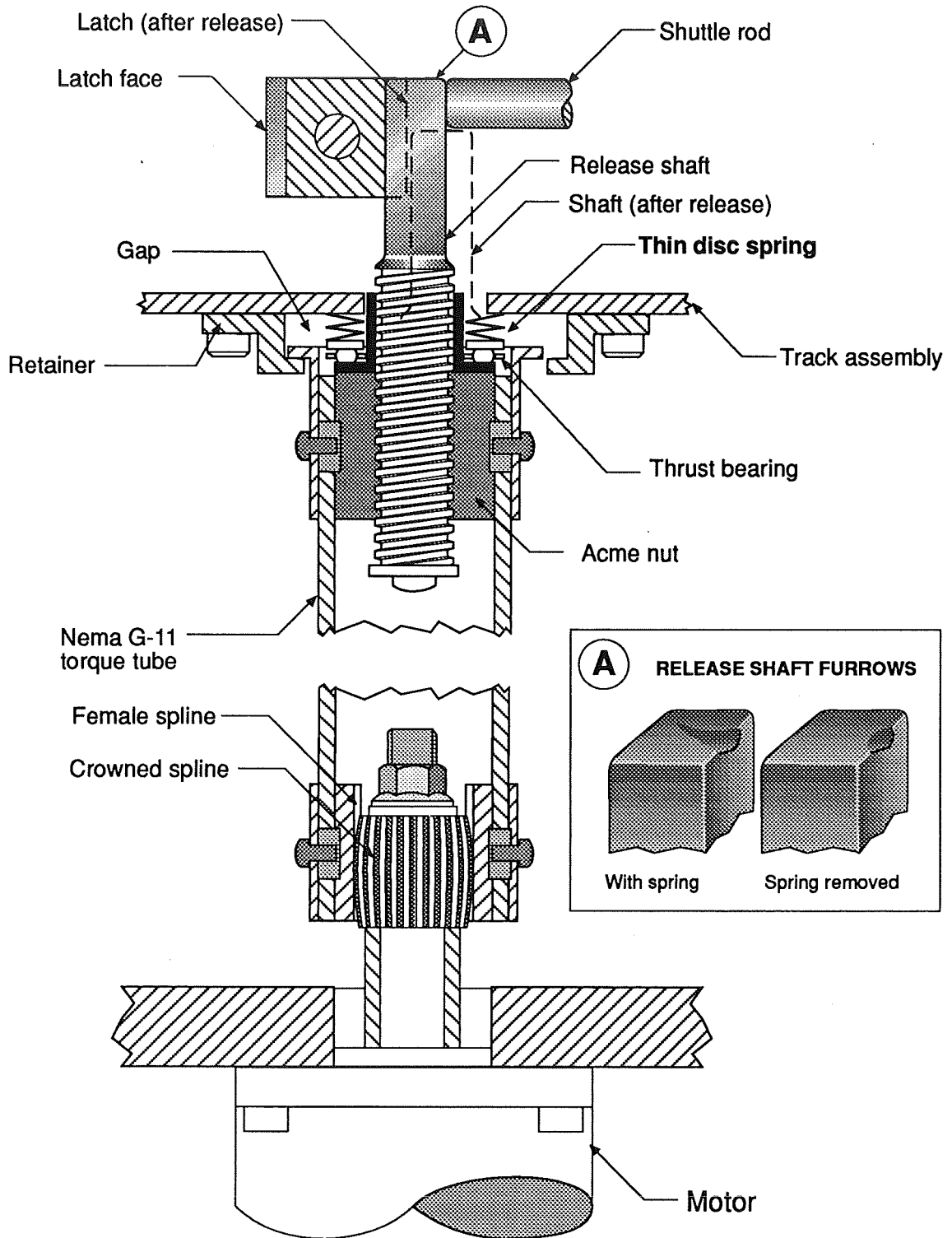
Figure 9. Jettison Latch Release Shaft Assembly.

The figure is labeled with the following callouts:

- Latch (after release)
- Latch face
- Shuttle rod
- A
- Release shaft
- Shaft (after release)
- **Thin disc spring**
- Gap
- Track assembly
- Retainer
- Thrust bearing
- Acme nut
- Nema G-11 torque tube
- Female spline
- Crowned spline
- **A RELEASE SHAFT FURROWS**
  - With spring
  - Spring removed
- Motor

C-2

DESIGN AND TESTING OF THE
LITE VARIABLE FIELD STOP MECHANISM

Robert A. Dillman*

ABSTRACT

The Variable Field Stop (VFS) is a rotary mechanism that reliably positions any of four aperture plates in the optical path of a space-flight experiment, limiting the amount of light reaching the detectors. This paper discusses the design, operation, and testing of the VFS.

INTRODUCTION

The Lidar In-Space Technology Experiment (LITE) is the primary payload of a Shuttle mission scheduled to be flown in March of 1994. LITE will generate a three-wavelength, pulsed laser beam and direct it down toward the Earth, then catch the return signal from atmospheric scattering in a 1-meter Cassegrain telescope. The return signal intensities will be measured by detectors in the Aft Optics subsystem, mounted behind the primary telescope mirror; later analysis will yield data on the composition of the upper atmosphere as a function of altitude.

The VFS is one of the first elements in the Aft Optics encountered by the beam of light coming in from the telescope. It is designed to limit the amount of light reaching the sensitive photomultiplier tubes that are the main sensors in the Aft Optics. On command from ground controllers, the VFS positions one of three apertures in the beam; a fourth option is a solid mirrored plate intended for use during any Shuttle maneuvers that involve pointing the telescope near the Sun.

One of the challenges that this design meets is to allow fine adjustment of the aperture positions while using a motor with a fixed step size. The VFS achieves this through use of a flex pivot between the drive motor and the cam and ratchet that determine aperture positions. Other requirements on the design include stability and repeatability of the aperture positions, reliability, fitting in limited

---

* NASA Langley Research Center

83

space in the Aft Optics, survival of shuttle launch and landing conditions, and operation on-orbit.

VFS HARDWARE

The VFS mechanism is shown in Figure 1, along with an arrow that represents the light coming from the telescope. The VFS is 22 centimeters (8.5 inches) long, 14 centimeters (5.6 inches) high, and 16 centimeters (6.2 inches) wide, with a total mass of 1.4 kilograms (3.1 pounds). Most visible surfaces are coated with a non-reflective black paint (see photo in Figure 2.)

The three apertures of the VFS are machined into interchangeable 0.25 centimeter (0.10 inch) thick aluminum plates. Two of the apertures are circular; the larger is 1.7 centimeters (0.67 inches) in diameter, and the smaller is 0.53 centimeters (0.21 inches) in diameter. The third aperture shares both these dimensions, having a large circular opening with a small obscuration disk supported in the center. The solid mirrored plate in the fourth position is thicker than the other three; its thickness was increased to 0.64 centimeters (0.25 inches) to provide more margin for the high thermal load that occurs while blocking sunlight from the rest of the Aft Optics. The apertures and the mirrored plate are shown in Figure 3.

These four plates attach to the Aperture Base, which holds them at 45 degrees to the VFS axis of rotation. The active plate is perpendicular to the incoming light, with the aperture centered on the beam. The spaces between the plates are blocked by a light baffle, to prevent stray light from entering the system during aperture changes.

To change apertures, the VFS rotates 90 degrees about its main shaft, which attaches to the back of the Aperture Base (see Figure 4). This shaft turns on two bearing rings, which fit inside the shaft housing. Stop positions are set by a four-position cam, which attaches to the shaft on the far side of the housing. A ratchet arm rides against the outside of the cam, held in place by a torsion spring; the rubbing surfaces of the ratchet and cam are coated with a type III anodize to reduce wear. The four stop points on the cam each have a protruding set screw, which is what actually contacts the tip of the ratchet. These set screws allow adjustment of the cam stop points.

Power to rotate the VFS comes from a DC stepper motor, which moves in 1.5 degree increments. It is connected to the main shaft through a bellows coupling to prevent axial misalignment from causing the motor to bind. The motor rotates the cam past each desired stop point, then backs up to place the ratchet tip in contact with the set screw from the cam. Since the screw positions are adjustable and the motor steps are fixed, a flex pivot was also included between the motor shaft and the main shaft which turns the cam. The stepper motor backs the cam into contact with the ratchet, and then continues backing several more steps; the flex pivot takes up the rotation, and its spring force holds the cam against the tip of the ratchet. This allows the aperture positions to be controlled by the set screws in the cam, despite the relatively large step size of the motor. Once the new aperture is in place, the motor power is turned off; the motor brake locks it in position until power is applied again.

However, the flex pivot is fairly delicate, and winding it up more than ten degrees can cause damage. To prevent excessive winding, a hard stop was added. The hard stop consists of a pair of protrusions from the coupling that connect the flex pivot to the main VFS shaft. These protrusions span the joint of the flex pivot and fit into notches in the end of the bellows coupling, as shown in Figures 5 and 6. When the flex pivot has wound up six degrees, the protrusions come into solid contact with the bellows, and prevent further motion of the flex pivot. An exploded view of the shaft coupling, flex pivot, bellows coupling, and the pins that attach them is shown in Figure 7.

The VFS attaches to the Aft Optics Bench at three points, using fasteners which fit through oversized clearance holes in the VFS Base. Spacer rings between the Bench and the VFS Base adjust the height of the apertures above the Bench, to roughly center them on the beam of light; the system is designed to require the spacers even if all parts are machined perfectly, so it can be lowered as well as raised in height. Once the VFS Base is positioned properly, epoxy is injected through small holes around the three fasteners to lock them in place. Coarse adjustment of the aperture positions is made by turning the cam set screws so that the apertures are perpendicular to the incoming beam of light, and the set screws are then staked in place. Final centering of each aperture is made by sliding the aperture plates relative to the Aperture Base, using the clearance on the mounting holes. Once this is completed, the aperture plate fasteners are also staked in place.

TESTING

After assembly, the VFS was functionally tested. Some initial problems with the stepper motor mis-stepping were fixed by adjusting the cam set screws so that the coupling hard stop points coincided with whole steps of the motor. This caused the apertures to tilt slightly relative to the incoming light and forced them off-center. The apertures were recentered by opening up the aperture plate fastener holes to form slots. The aperture tilt could have been corrected by shimming the aperture plates at the three points where they attach to the Aperture Base, but calculations showed the tilt to have negligible effect.

The mechanism was then subjected to random and sine vibration tests as described in Figures 8 and 9; optical alignment checks were included to measure the stability of the apertures. The vibration tests were passed successfully, and the optical tests showed the aperture alignment to be stable and repeatable to within a few arc-minutes. While not equal to the stability of a fixed optical mount, this was deemed acceptable.

Thermal/vacuum testing followed the vibration tests. The VFS was mounted inside a bell jar (see photo in Figure 10) and put through four cycles of the profile shown in Figure 11, while under vacuum. The test included operation of the mechanism at room temperature, after the one-hour cold soak, and after the one-hour hot soak. The mechanism operated properly in all cases, and the optical alignment tests were again acceptable.

After cycling concluded, a strip heater was attached to the mirrored shield plate; once vacuum was reestablished in the bell jar, this heater was energized, simulating use of the shield plate to reflect focused sunlight. Data from the shield test were used to verify the computer thermal model.

The VFS mechanism was then attached to the Aft Optics Bench and aligned with the installed optical elements. It operated successfully for several months, until problems developed with the ratchet spring. Examination of the spring showed that it had deformed and was no longer holding the ratchet in contact with the cam. The spring was replaced and the mounting hardware was modified slightly, giving the spring a bit more room to expand. Testing of several spare springs

indicated no change in spring tension or behavior out to 10,000 cycles, many times the expected lifetime.

CONCLUSIONS

The VFS achieves its design goal of accurately and reliably positioning three apertures and one mirrored plate. The mechanism also allows adjustment of these positions through set screws and three-point mounting systems. Thorough functional and environmental testing has qualified the VFS for space flight; the test results indicate that it will perform as intended in the expected environment.

OBSCURED APERTURE
PLATE

CAM

LIGHT BAFFLE

LARGE APERTURE
PLATE

STEPPER
MOTOR

RATCHET

MIRROR

SMALL APERTURE
PLATE

RATCHET SPRING
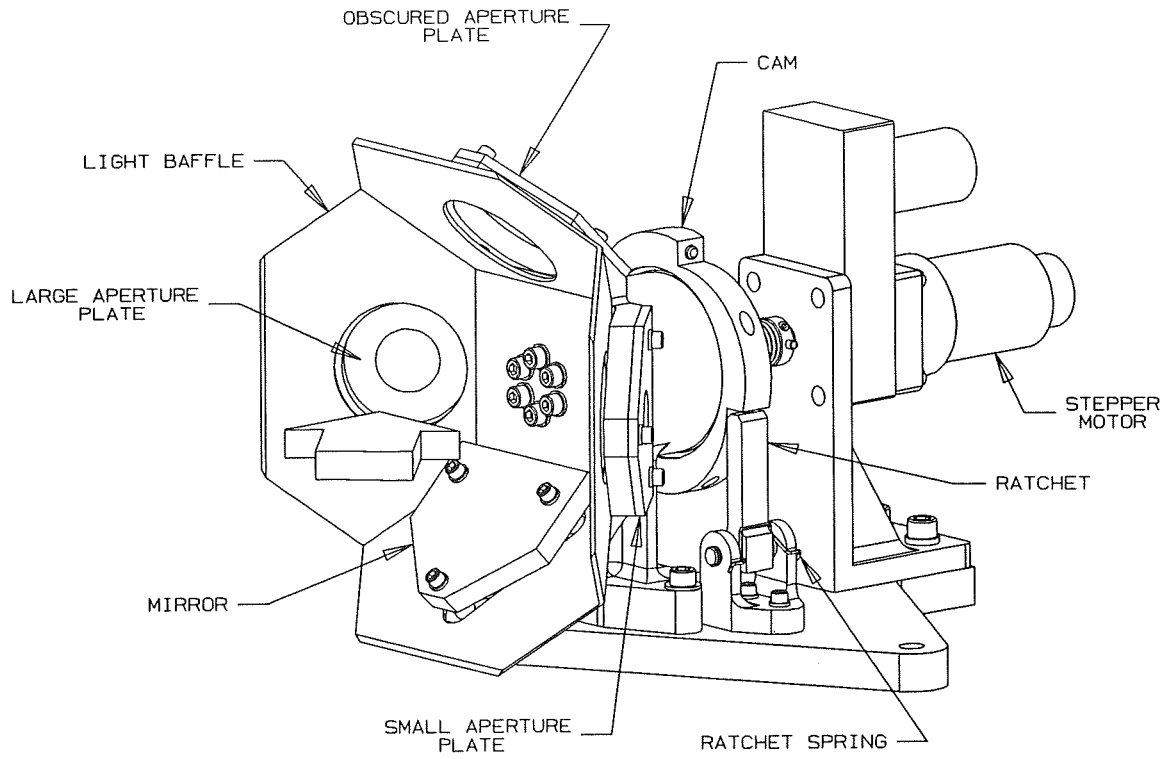
Figure 1. VFS Mechanism

Figure 2. VFS Photograph

88

LARGE APERTURE
PLATE

SMALL APERTURE
PLATE

OBSCURED APERTURE
PLATE
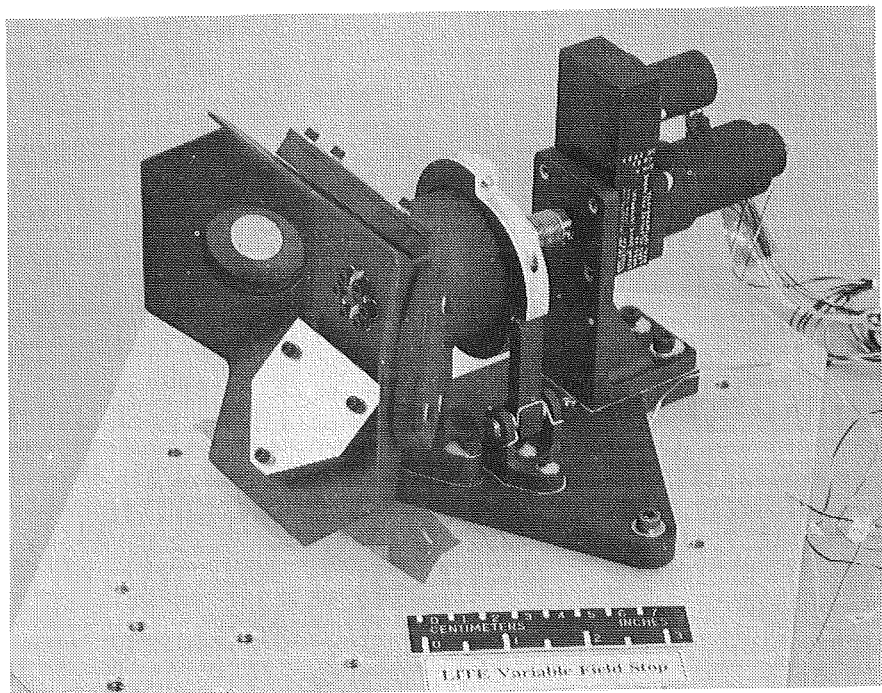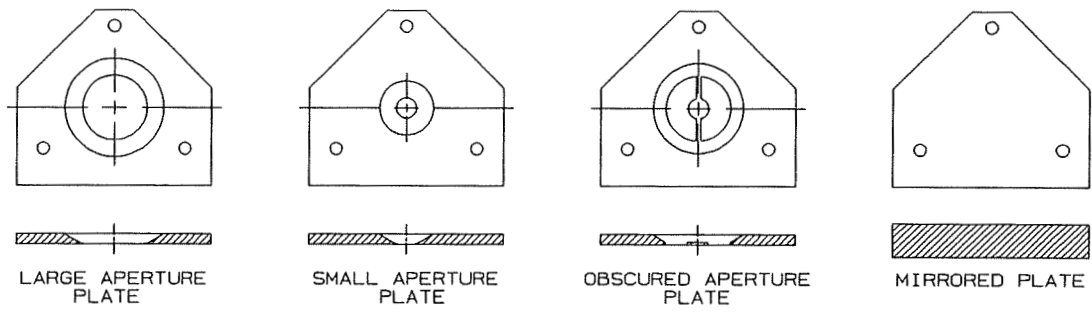
MIRRORED PLATE

Figure 3.   Aperture Plates and Mirrored Plate

APERTURE BASE
SHAFT
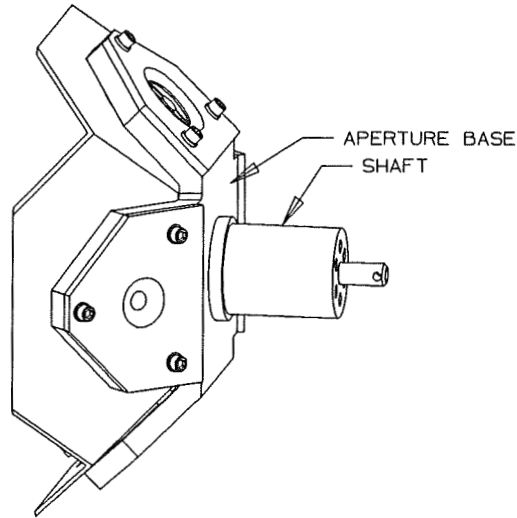
Figure 4.   Aperture Base and Shaft

SOLID COUPLING
CAM
BELLOWS
BASE

Figure 5.   VFS   Mechanism

SIX DEGREE GAP

HARD STOP
PROTRUSION

Figure 6. Shaft Coupling

SET SCREWS (4)
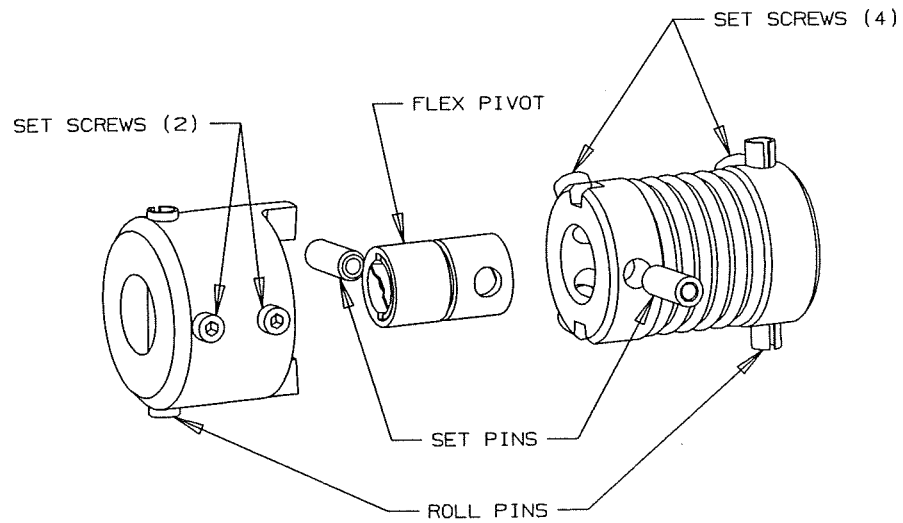
SET SCREWS (2)

FLEX PIVOT

SET PINS

ROLL PINS
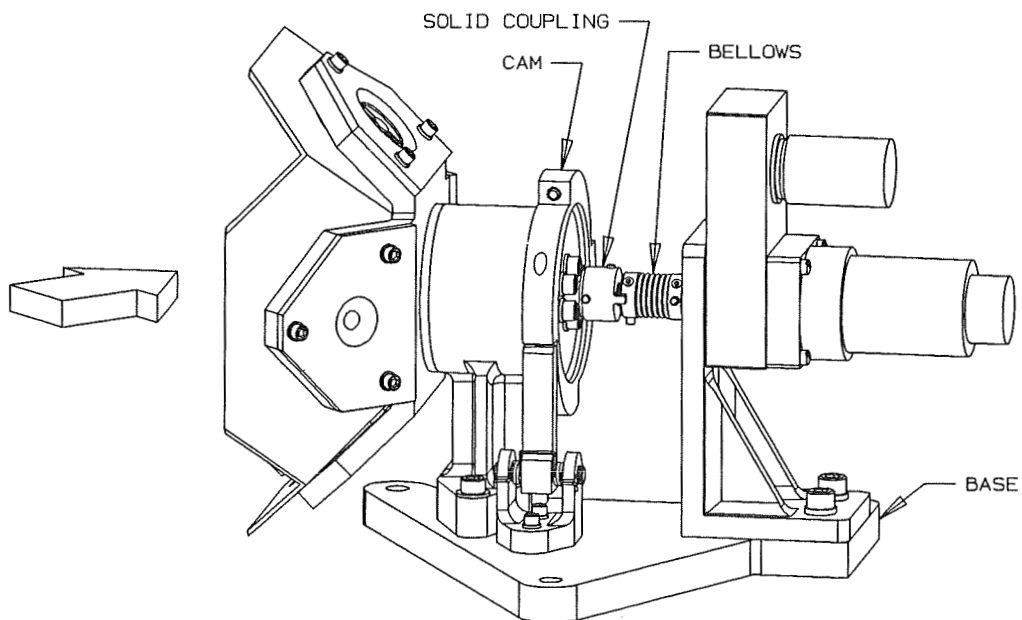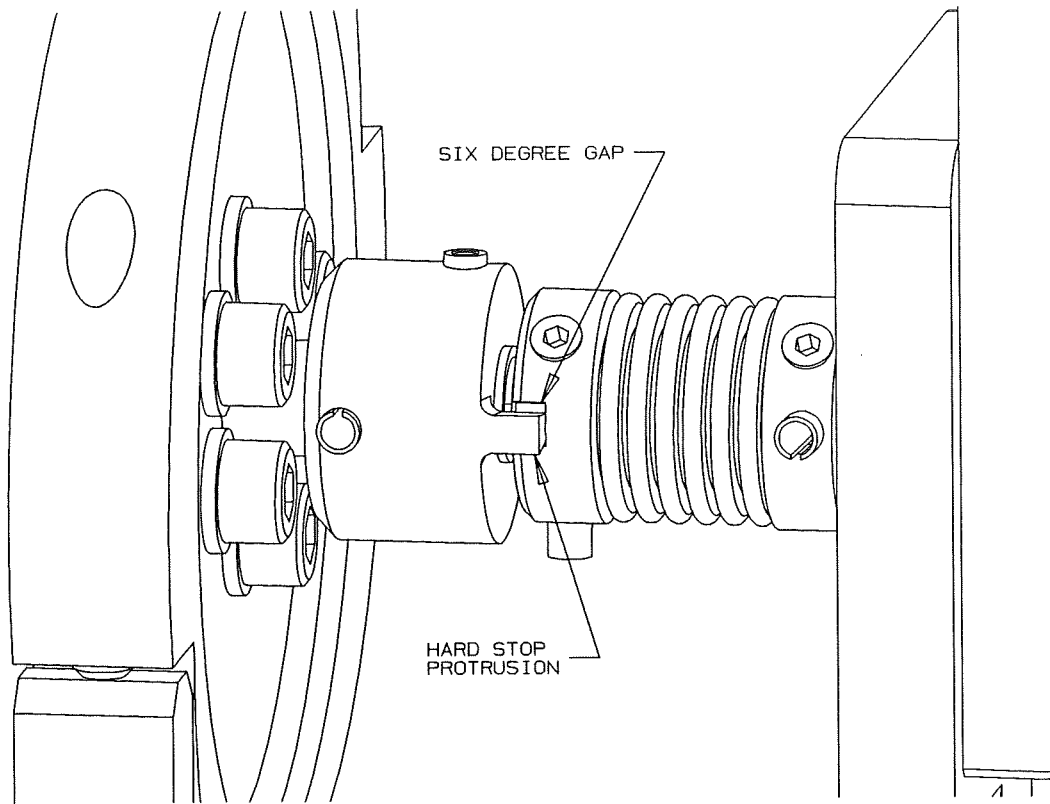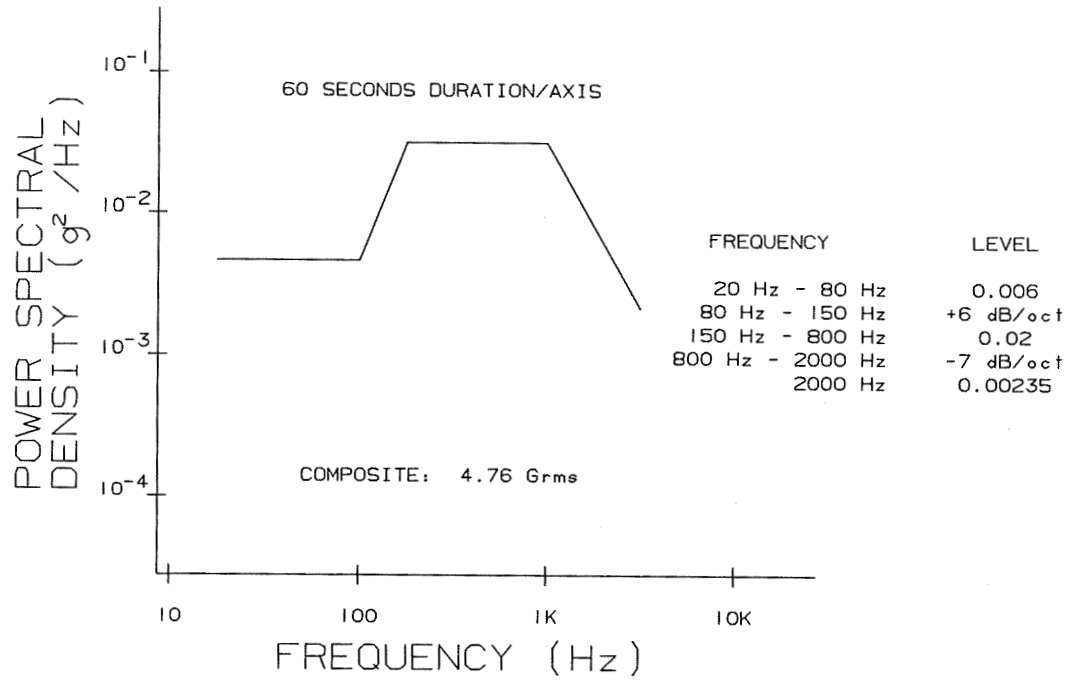
Figure 7. Exploded View

90

Figure 8. Random Vibration Spectrum
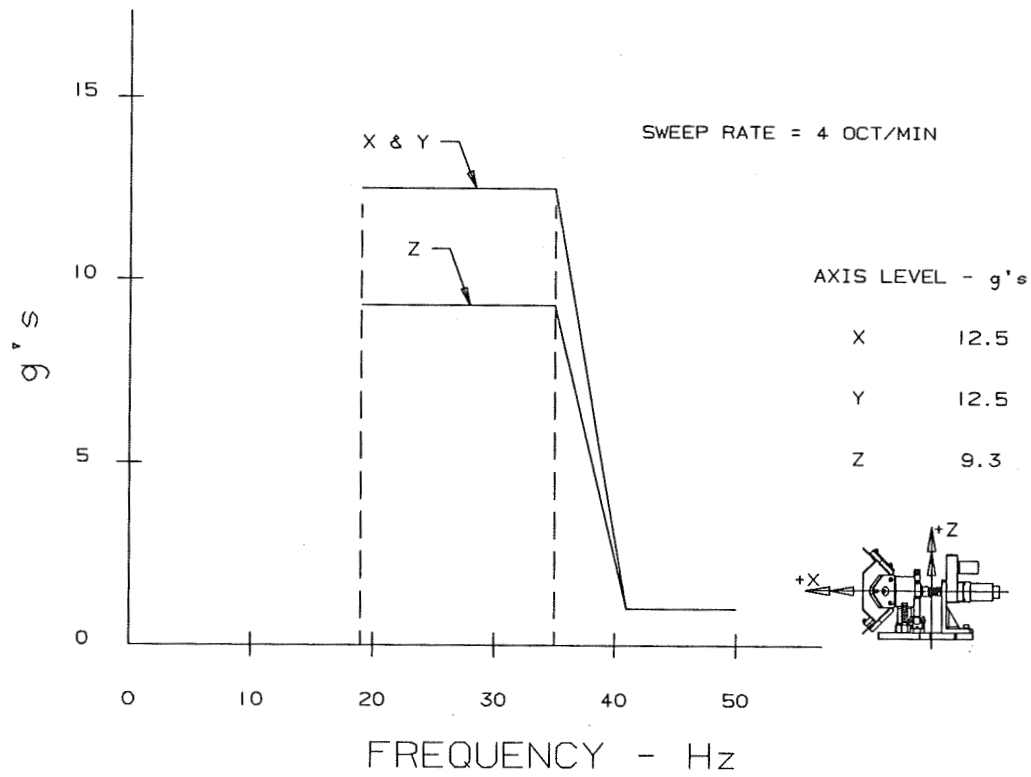
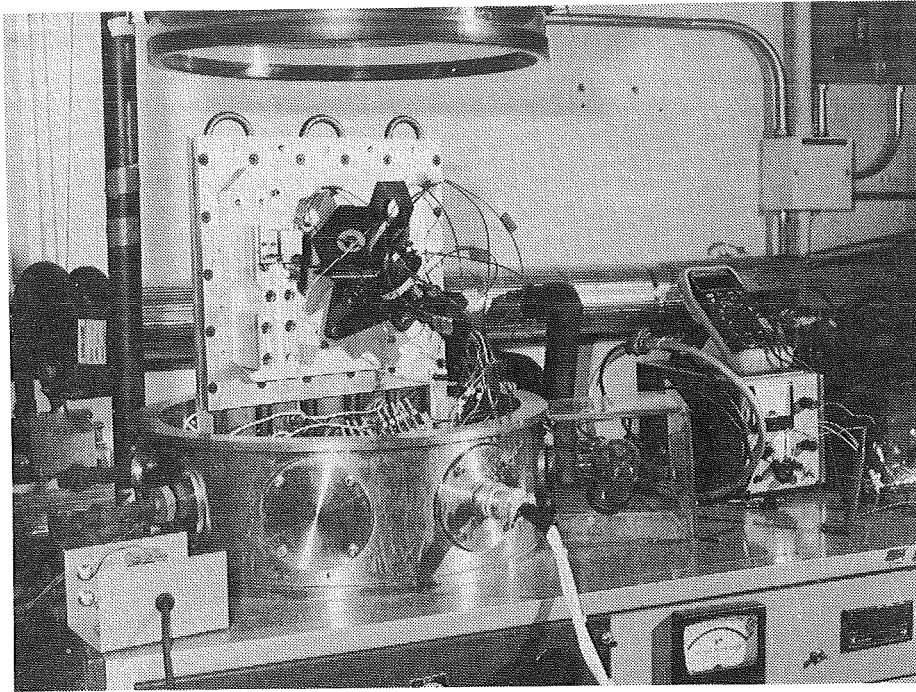
Figure 9. Sine Vibration Spectra

91

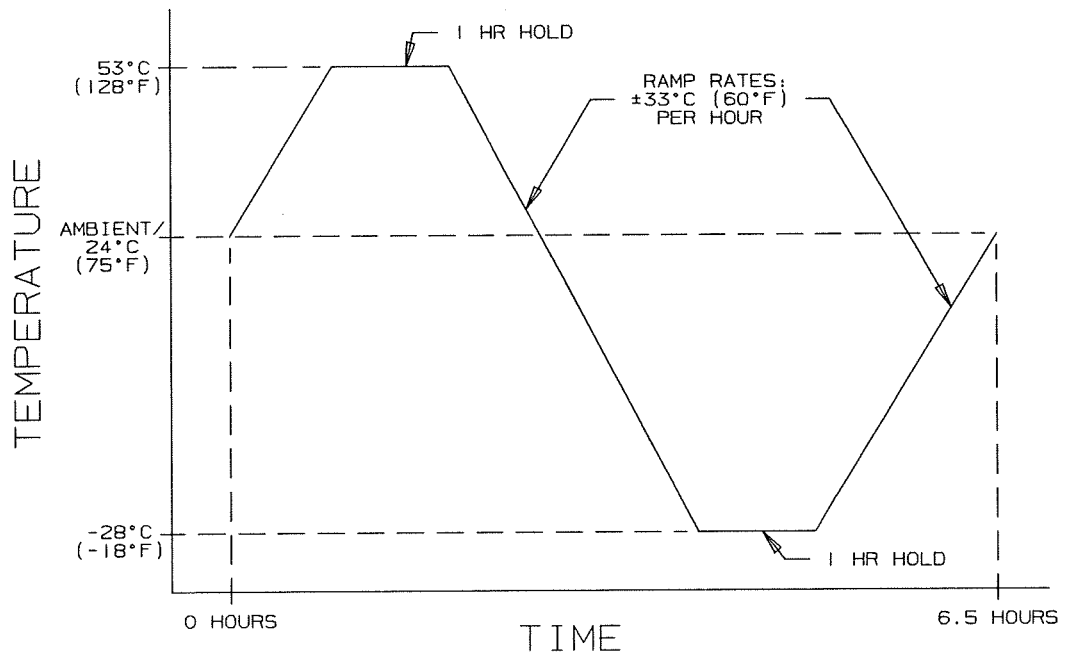Figure 10.   Thermal Test Photograph

Figure 11.   Thermal Test Profile

92

/9 9 4 0 2 5 1 3 ⬦

4 3 4 6 4 8

INTEGRATION OF PYROTECHNICS INTO AEROSPACE SYSTEMS

by

Laurence J. Bement
NASA Langley Research Center
Hampton, Virginia

Morry L. Schimmel
Schimmel Company
St. Louis, Missouri

ABSTRACT

The application of pyrotechnics to aerospace systems has been resisted because normal engineering methods cannot be used in design and evaluation. Commonly used approaches for energy sources, such as electrical, hydraulic and pneumatic, do not apply to explosive and pyrotechnic devices. This paper introduces the unique characteristics of pyrotechnic devices, describes how functional evaluations can be conducted, and demonstrates an engineering approach for pyrotechnic integration. Logic is presented that allows evaluation of two basic types of pyrotechnic systems to demonstrate functional margin.

INTRODUCTION

The reluctance to use pyrotechnic devices (explosive and propellant-actuated mechanisms) is based on their unique functional characteristics and limited engineering approaches to pyrotechnic system integration. Although pyrotechnic devices have been successfully applied to a wide variety of mission-critical functions for aerospace systems, failures (references 1, 2 and 3) continue to occur. During the early development of the Space Shuttle, there was substantial resistance to the use of pyrotechnic devices. This resistance was based on one-shot devices being inappropriate for a reusable vehicle. Yet now more than 400 such devices fly on each Orbiter. Pyrotechnic devices: are single-shot, cannot be functioned prior to flight (such as repeatedly cycling an electrical switch), provide short-duration, impulsive outputs (microseconds to milliseconds), and contain explosive materials, requiring special safety considerations. For these reasons, the search for alternate mechanisms is understandable.

Adding to the resistance was the inability to apply approaches for design, test and evaluation that are used on conventional energy sources (electrical, hydraulic and pneumatic). Well-defined test methods and a logic to demonstrate system functional margins were not always available to support new pyrotechnic applications. For example, devices are sometimes qualified with a limited number of "go/no-go" tests. Consequently, systems could be marginal or overpowered. If marginal, unexpected failures could occur with changes in system variables. And if

overpowered, other problems could occur, such as inadvertently actuating valves on the Apollo mission, reference 2, and inducing possible damage through structural deformation, fragmentation and pyrotechnic shock (references 4 and 5).

The objectives of this paper are to provide:

1. An introduction to pyrotechnic functional principles and test methods.
2. An engineering approach (with examples) for pyrotechnic integration, including demonstration of functional margin.

PYROTECHNIC FUNCTIONAL PRINCIPLES AND TEST METHODS

Pyrotechnics have been extensively applied, because of high efficiency in terms of long-term storable energy per unit volume and weight.

Some functions accomplished by pyrotechnic systems are:

* initiation   * release   * severance/fracture
* jettison   * valving   * switching
* time delay   * actuation

The majority of pyrotechnically actuated mechanical functions are accomplished through piston/cylinder devices. Others are accomplished through the use of linear explosives.

Piston/cylinder functional mechanisms - Typical actuators, a thruster and a pin puller, are shown in figure 1 (reference 6). Firing the propellant-loaded, gas-generating cartridges pressurizes the volume behind the pistons to drive each pin from left to right. These actuators can be used to accomplish work by: thrusting or pulling against a force, jettisoning a mass, or working against a mechanism.

To measure the energy delivered in working against a constant force, the energy sensor apparatus, shown in figure 2 and described in references 7, 8 and 9, can be used. The actuator can be simulated by using the piston/cylinder configuration in the initiator firing block, or the actual device could be used. On firing the cartridge, the piston is driven against calibrated aluminum honeycomb cubes, which crush at a constant force. Multiplying the crush distance by the crush strength provides a measurement of energy delivered in inch-pounds. This apparatus, as shown, has been used to measure and compare the outputs of a variety of cartridges.

To measure the energy delivered in jettisoning a mass, the dynamic test device apparatus, shown in figure 3 and described in references 8 and 9, can be used. The piston in

this case is a 1-pound, 1-inch diameter mass with an o-ring set to vent after a 1-inch stroke. Energy is obtained by measuring the velocity and calculating the kinetic energy, $1/2 \, mv^2$. The pressure vs time history of the cartridge is also obtained in this apparatus for further comparison. Again, this apparatus provides a comparative test method to evaluate a variety of cartridges. Simulating or using the exact mass and piston/cylinder interface is critical for determining the energy deliverable in the actual production item.

Linear explosive functional mechanisms - Figure 4 (reference 6) shows the application of round cross-section explosive cord, called mild detonating cord (MDC), to sever or fracture structure. MDC is composed of a high-explosive core, encased in metal sheaths, such as lead, silver or aluminum. On initiation, the explosive combustion (detonation) proceeds along its length at a rate of about 25,000 feet/second. The detonation pressure (several million psi) is directed against the skin structure, as shown in the sketch on the left, to accomplish severance. Explosive products can be fully contained through the use of a flattened steel tube, as shown in the sketch on the right. Considerable energy is attenuated by the work required to expand the tube, so a notch is machined in the structure to focus the fracture point. Figure 5 (reference 6) shows flexible linear shaped charge (FLSC), which is also used to sever structure. Rather than a round cross section, the metal sheath has been shaped into a chevron. The explosive pressure wave leaves the source perpendicularly from the surface. The two legs of the chevron focus the pressure waves into a high-velocity jet of metal sheathing particles and gases, which penetrate the target structure. This penetration, in conjunction with the pressure wave, can sever structure without FLSC confinement.

The apparatus, shown in figure 6 (reference 8), was developed to measure the capability of linear explosives to accomplish severance as well as detonation and energy-delivery characteristics. The linear explosive is placed in a machined groove, which represents the backup structure shown in figure 4. A tapered plate of the same material to be severed for a particular application is placed on the linear explosive and is followed by the external backup structure (hold-down plate), which further enhances it's severance ability. The energy sensor, described in figure 2, is placed over a length of the explosive to measure the energy delivered. Timing circuit wires are placed across the explosive to measure the velocity of detonation propagation (typically 40 microseconds/foot) through supporting electronic timing circuits. The tapered plate provides a method of obtaining the maximum severance capability of the linear explosive in each firing. The thickest dimension of the plate is selected to assure that full severance is not achievable. Again, emphasis must be placed on simulating or

using the flight structure to relate test results with expected system performance.

APPROACHES FOR PYROTECHNIC SYSTEM INTEGRATION

Following are two examples of the engineering evaluation of pyrotechnic devices. These efforts were prompted by failures (fortunately in non-flight evaluations) of two devices that had been fully qualified 20 years earlier.

The approach for these investigations was either: 1) measure and compare the energy required to accomplish the desired mechanical function with the energy deliverable from the pyrotechnic or explosive source; or 2) quantify functional performance. To obtain a reliable functional margin: 1) the energy deliverable must substantially exceed the energy required; or 2) the performance of key functional parameters must substantially exceed conditions allowed in flight hardware. In the following examples, functional margin based on an energy comparison was applied to the Viking pin puller; margin based on functional performance was applied to the Super*Zip separation joint.

Viking Pin Puller

The Viking pin puller released an antenna on the mission's Mars Lander. It's design and system variables are shown in figure 7, and the investigation is described in reference 3. Firing either cartridge first failed the shear pin and drove the piston from left to right to withdraw the pin. The shock absorber, a thin-walled steel crush cup, expanded on impact to lock the piston, remove the excess energy from the piston and reduce the pyrotechnic shock impulse.

Following failures in subsequent attempts to apply this same device to current spacecraft, an investigation was initiated.

Energy required - The energy required to stroke the piston/pin was determined by dropping small weights on the vertically oriented pin. The drop height, multiplied by the weight, produced a direct measurement of energy in inch-pounds. Furthermore, dropping these weights at heights of several feet, simulated the dynamics of an actual firing (3 ms for the drop tests versus 0.5 ms for the actual pyrotechnic function). Increasing the energy in subsequent drop tests provided a calibration of the shock absorbing crush cup.

The largest energy consumer was friction, particularly without lubrication of the o-rings. Without lubrication, the o-ring rolled on its axis and had material torn from its body, yielding an energy required to stroke of over 100 inch-pounds. For the properly lubricated flight hardware, the

energy required to stroke was less than 20 inch-pounds. The total energy required to fail the shear pin, stroke the piston/pin and lock the energy absorbing cup was 25 inch-pounds.

Energy deliverable - The energy deliverable (measured by the crush of the steel shock absorber cup) by the cartridge was influenced by the housing material, the coatings on the pin and the interior housing and the o-ring seals.

Early firings at Langley Research Center of residual Viking hardware in three system-level tests indicated no excess energy. That is, the piston had not traveled its total possible stroke, or the shock absorber cup had just contacted the pin puller cap with no indication of crush.

Three different cartridge lots, manufactured to similar specifications in 1972 (the original Viking unit), 1985 and 1988, were functionally evaluated, using the honeycomb energy sensor placed against the stroking piston in a steel-bodied pin puller. Five to ten units tested in each group produced 99 inch-pounds with a standard deviation of 21; 127 with a standard deviation of 20; and 53 with a standard deviation of 49; respectively. These variations were caused by combustion inefficiencies, possibly by different particle sizes of the cartridge propellant materials. The 1985 lot was selected for flight.

As examples of design and manufacturing variables influencing energy deliveries, the first laboratory firing at Langley Research Center produced considerable melting and deformation of the bottom of the cartridge port. Also, blowby occurred around each set of o-rings. The blowby problem was caused by the coatings. Some of the molybdenum disulfide coating on the pin wiped off and was deposited on the pressurized side of the o-ring, preventing contact with the pin. This was corrected by using an electrodeposited nickel/Teflon coating. The soft chemical chromate coating on the piston bore wiped off on the o-rings, again preventing a seal. This was corrected by using a steel housing for the flight units. This problem was also corrected in later tests, using hard anodized aluminum housings.

The energy deliverable by the flight cartridges in system-level tests (functioned in a spacecraft interface with a maximum side load on the pin), as determined by the amount of shock absorber cup crush, averaged 165 inch-pounds.

Functional margin - The functional margin for the redesigned pin puller was determined as follows:

$$\text{Functional Margin} = \frac{\text{energy deliverable} - \text{energy required}}{\text{energy required}}$$

$$= \underline{165 - 25} = 5.6$$
$$25$$

Lockheed Super*Zip Separation Joint

The Super*Zip separation joint has been used on a wide variety of rocket staging systems, including the release of the Inertial Upper Stage (IUS) from the Shuttle cargo bay. It's design and functional variables are shown in figure 8, and the investigation is described in reference 10. Initiating either explosive cord produces an explosive pressure wave that is transferred through the silicone rubber extrusion and steel tube to the 7075 aluminum doublers. Expansion of the steel tube fractures the doubler ligaments.

Functional Parameters - Since this design did not permit an energy comparison, functional parameters were quantified and compared. The key parameters were explosive load and doubler severability. A standard tapered witness plate, was used to quantify severance (reference 10).

Explosive load - The influence of the explosive on joint severance was established by determining the functional limits of the system. The minimum explosive load that could fracture the worst-case joint conditions (maximum thickness) was determined to be 7.5 grains/foot. Since the tube ruptured at 11 grains/foot, the maximum allowable explosive load was set at 10 grains/foot. The flight load was controlled at a maximum of 10 grains/foot and a minimum of 9.5 grains/foot.

Doubler severability - Of the total of 18 variables evaluated, the primary functional parameters proved to be the mechanical properties of the doublers, the web thickness (thickness of the doubler at the edge of the fasteners), and the ligament thickness. The aluminum doubler was heat treated (annealed) from 7075-T6, a fracture-sensitive condition to 7075-T73, a fracture-resistant condition to avoid stress-corrosion. The web thickness was critical, because the plates had to bend to induce the tensile failure at the ligament. Failures occurred in ground tests of a complete separation joint at doubler thicknesses of 0.083 to 0.086 inch. Tapered plate tests, using a nominal explosive load for the redesigned joint, demonstrated that the maximum thickness of the doubler to allow ligament fracture was 0.098 inch; the maximum allowable thickness of the doubler for flight was 0.082 inch.

Functional margin - The functional margin for this system was analyzed based both on explosive load and on web thickness.

For explosive load, functional margin is:

$$\frac{\text{minimum flight load} - \text{min. load to break thickest doubler}}{\text{min. load to break thickest doubler}}$$

$$= \frac{9.5 - 7.5}{7.5} = 0.27$$

For web thickness, recognizing that the bending moment to deflect beams is proportional to the thickness of the beam, cubed, and assuming that the web behaves in that manner through failure, Functional Margin is:

$$\frac{(\text{minimum thickness severed})^3 - (\text{max. allowable thickness})^3}{(\text{Maximum allowable thickness})^3}$$

$$= \frac{(0.098)^3 - (0.082)^3}{(0.082)^3} = 0.71$$

These margin equations indicate: 1) the minimum flight explosive load is 27% greater than that required to sever the thickest flight doubler, and 2) the severing capability of the doublers in this joint is 71% greater than the flight doublers.

CONCLUSIONS AND RECOMMENDATIONS

Engineering test methods and logic have been demonstrated to integrate pyrotechnics into aerospace systems by providing quantitative assessments of performance and functional margin. The unique characteristics of pyrotechnics (single shot, inability to evaluate flight units functionally, and short-duration, dynamic delivery of output) require a quantitative approach for evaluation and analysis. Principles of pyrotechnic performance, test methods and functional analysis have been explained and justified in this paper by providing examples of investigations of two pyrotechnic designs that had failed to function 20 years after their initial qualification. The cause of these failures was demonstrated to be that adequate functional margins had not been achieved in the original designs. In the case of the pin puller, the initial design could not accommodate lot-to-lot variations in cartridges, combined with improper o-ring seals. In the case of the separation joint, the design had inadequate functional margin to accommodate changes in the properties and thicknesses of the material to be fractured.

To avoid such failures, it is recommended that variables of a pyrotechnic system be evaluated and functional margins established. Tests should be conducted with flight-representative hardware and functional dynamics to either: 1) measure and compare the energy delivery capability of the explosive or pyrotechnic power source to the energy required by the mechanical function, or 2) quantify and compare key functional performance parameters.

99

REFERENCES

1. Bement, Laurence J.: "Pyrotechnic System Failures: Causes and Prevention." NASA TM 100633, June 1988.

2. "Flight Separation Mechanisms." NASA Space Vehicle Design Criteria. NASA SP-8056, October 1970.

3. Bement, Laurence J. and Schimmel, Morry L.: "Determination of Pyrotechnic Functional Margin." Presented at the 1991 SAFE Symposium, Las Vegas, NV November 11-14, 1991.

4. Bement, Laurence J. and Neubert, Dr. Vernon H. (Pennsylvania State University): "Development of Low-Shock Pyrotechnic Separation Nuts." Presented at the Eighth Aerospace Mechanisms Symposium, NASA LaRC, Hampton, VA; October 18 and 19, 1973.

5. Evans, Maria J.; Neubert, Vernon H.; Bement, Laurence J.: "Measurement, Data Analysis, and Prediction of Pyrotechnic Shock from Pin Pullers and Separation Joints." Presented at the 57th Shock and Vibration Symposium, New Orleans, LA, October 14-16, 1986.

6. Lake, E. R, Thompson, S. J., and Drexelius, V. W.: "A Study of the Role of Pyrotechnic Systems on the Space Shuttle Program." NASA CR-2292.

7. Schimmel, M. L. and Drexelius, V. W.: "Measurement of Explosive Output." Proceedings of the Fifth Symposium on Explosive Devices, June, 1967.

8. Bement, Laurence J.: "Monitoring of Explosive/Pyrotechnic Performance." Presented at the Seventh Symposium on Explosive and Pyrotechnics, Philadelphia, PA, September 8-9, 1971.

9. Bement, Laurence J. and Schimmel, Morry L.: "Cartridge Output Testing: Methods to Overcome Closed-Bomb Shortcomings." Presented at the 1990 SAFE Symposium, San Antonio, TX, December 11-13, 1990.

10. Bement, Laurence J. and Schimmel, Morry L.: "Investigation of Super*Zip Separation Joint." NASA TM 4031, May, 1988.
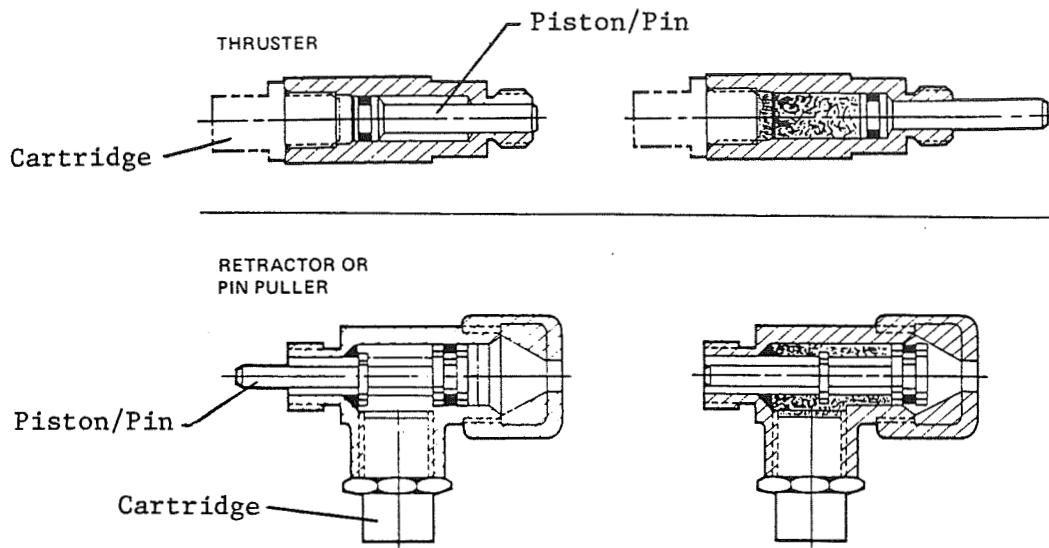
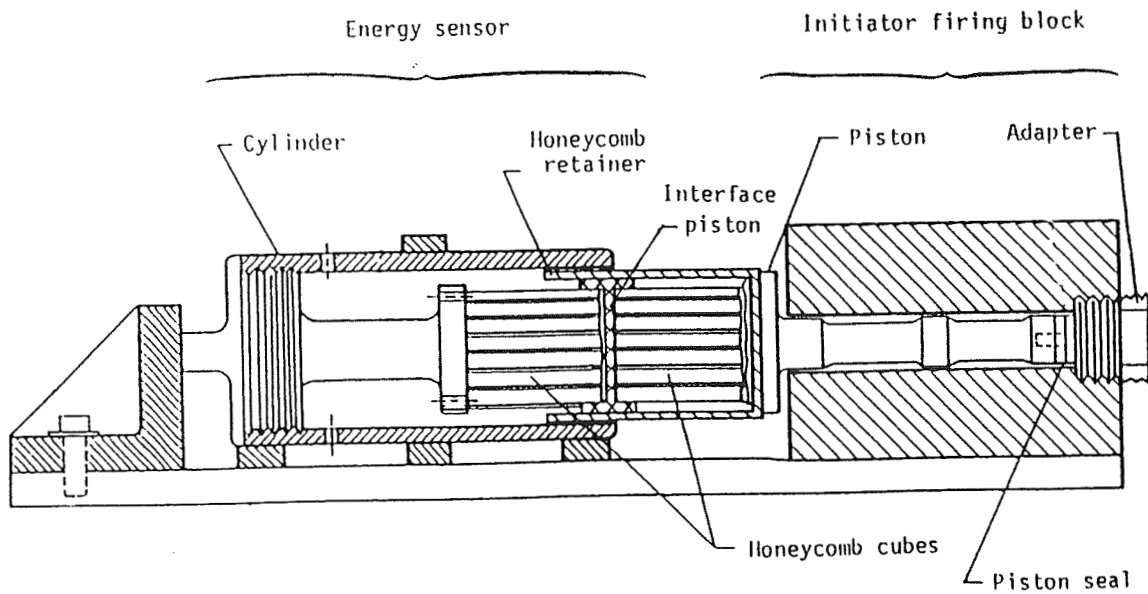Figure 1.- Typical propellant-powered actuators.
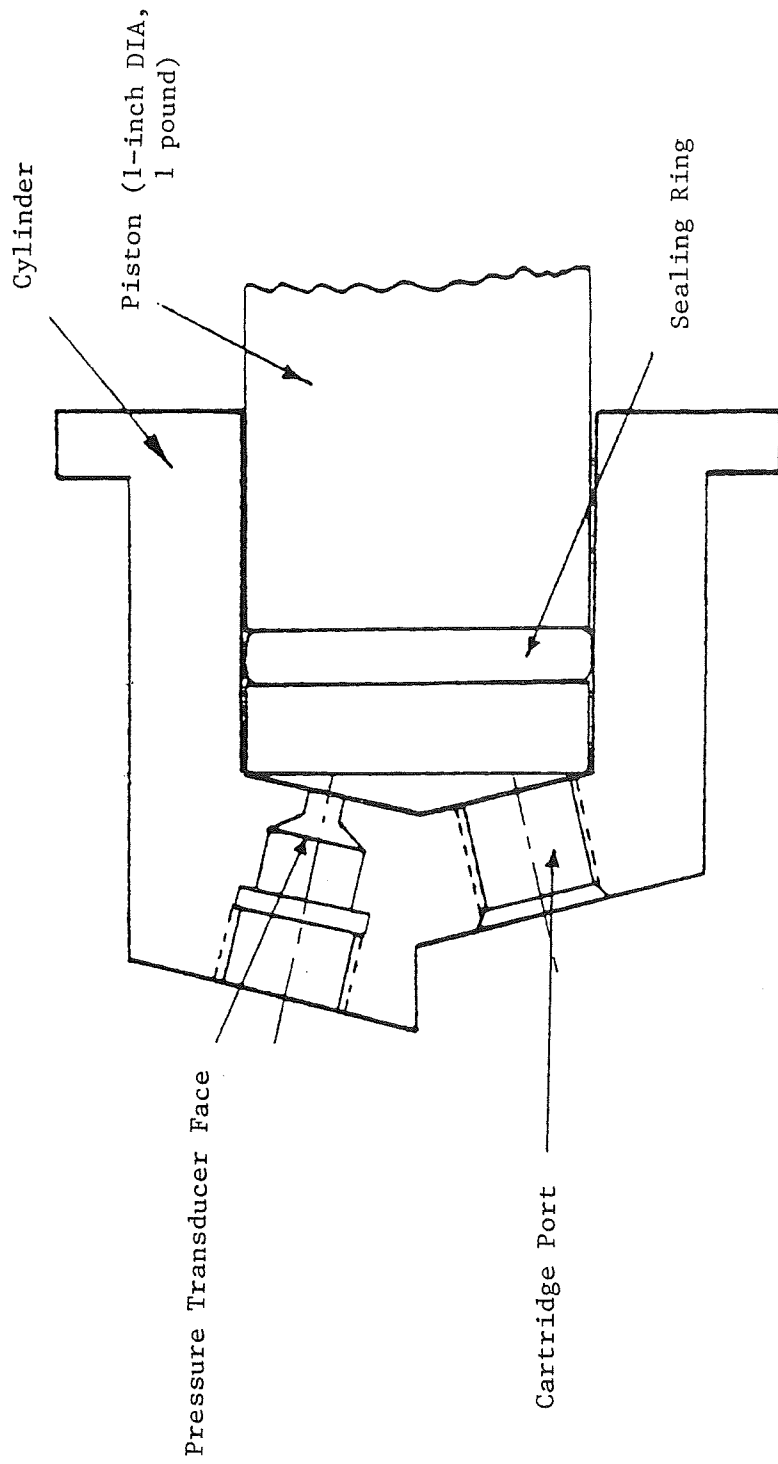

Figure 2.- McDonnell energy output test fixture.
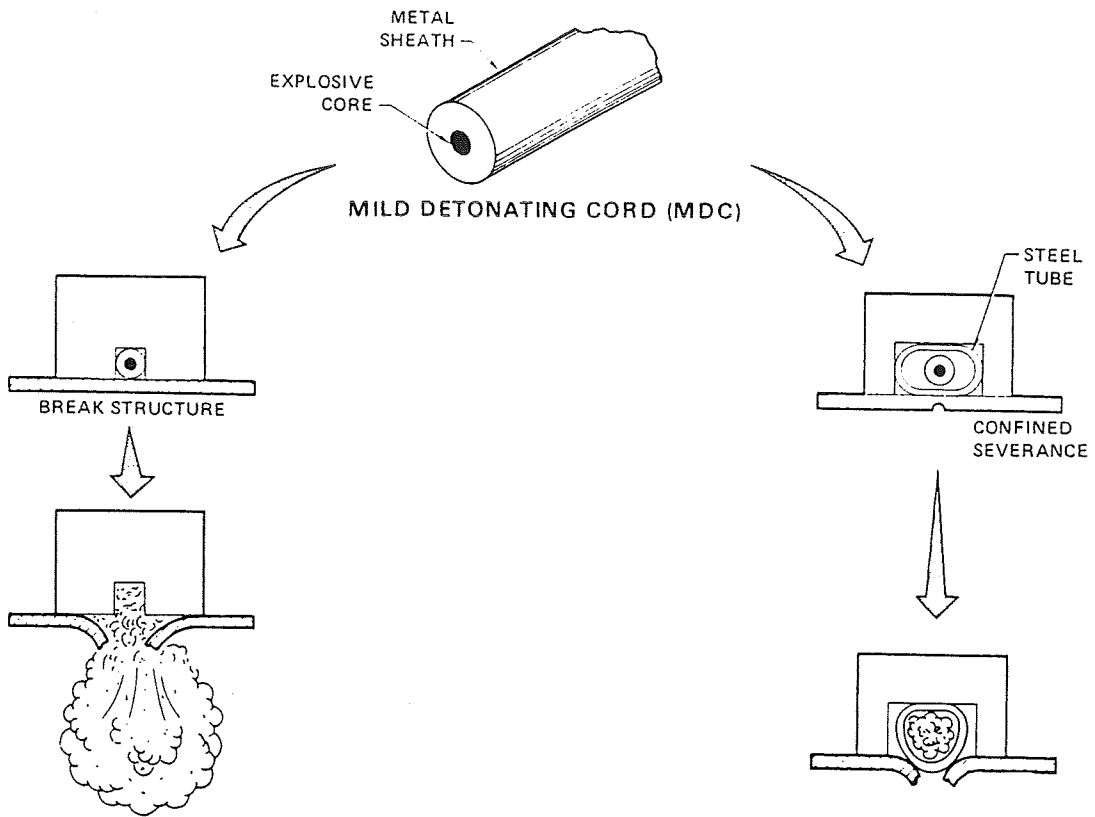
Figure 3.- NASA LaRC dynamic test device.

METAL
SHEATH
EXPLOSIVE
CORE

MILD DETONATING CORD (MDC)

BREAK STRUCTURE

STEEL
TUBE

CONFINED
SEVERANCE

Figure 4.- Linear explosive (MDC) applications.

EXPLOSIVE
CORE

METAL
SHEATH

FLEXIBLE LINEAR SHAPED CHARGE (FLSC)

FLSC HAS GREATER DIRECTIONAL
SEVERANCE ABILITY THAN MDC
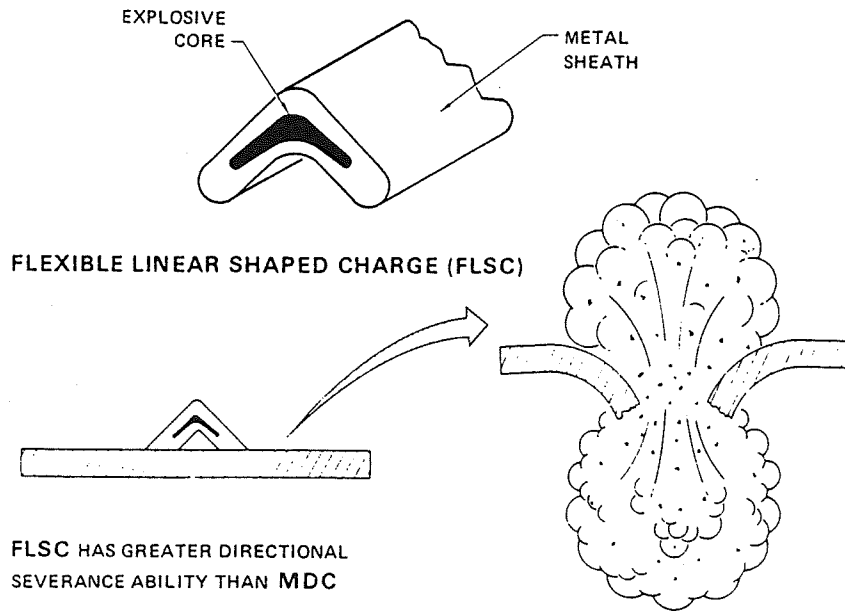
Figure 5.- Linear explosive (FLSC) application.

103

Hold-down Plate

Screw Assembly

Test Stand

Energy Sensor

Two-Inch Plate

Zinc Chromate Putty

Detonator

Tapered Plate

Test Specimen

Specimen Holder

Timing Circuit Wires
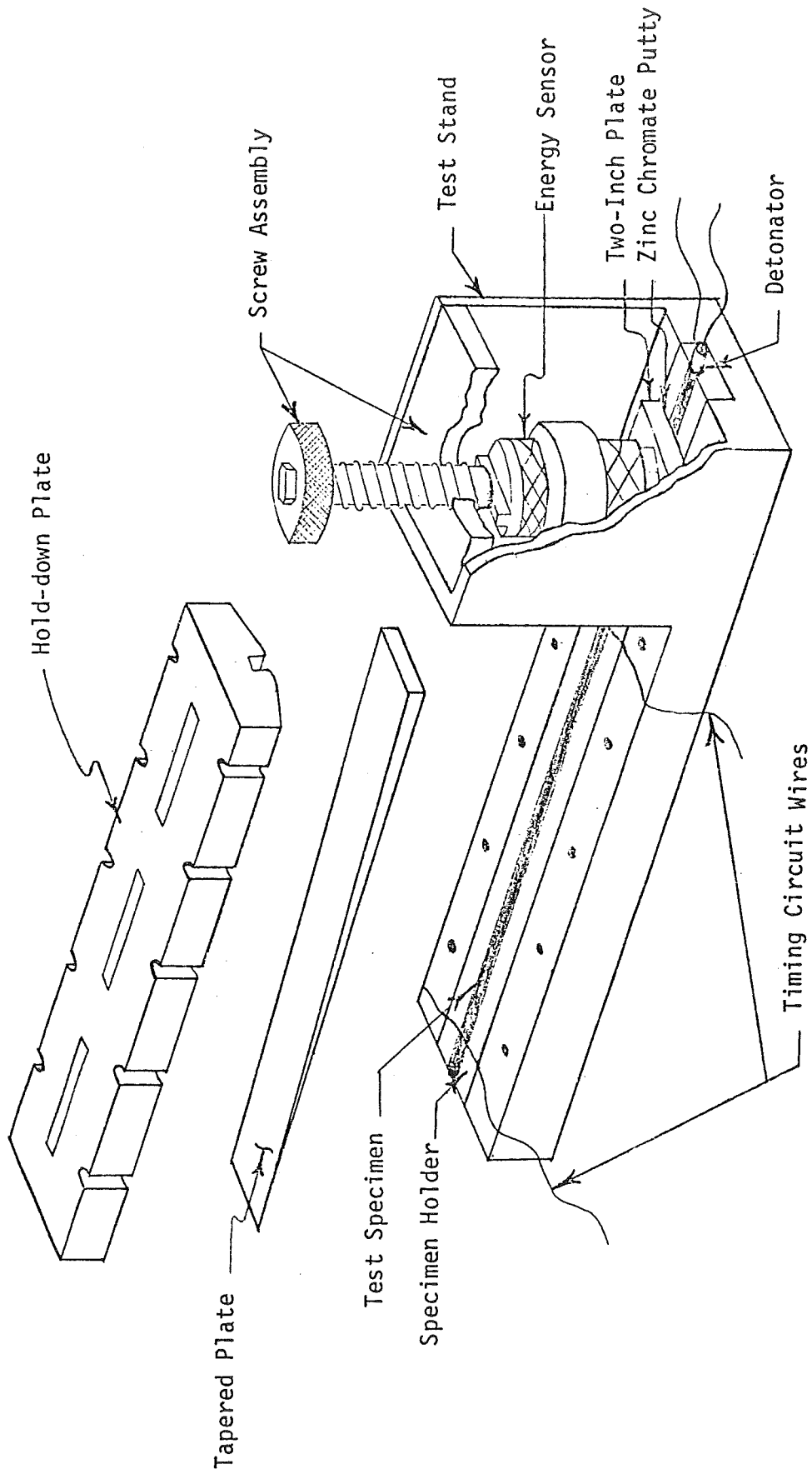
Figure 6.- Linear explosive test fixture.

104

Viking PYRO OPERATED PIN PULLER — 1/4"

O-rings (with lubrication)

Cap

Shock Absorber
(Crush Cup)

Cartridge Port (2)

Housing (material and
interior coating)

Shear Pin

O-rings (with lubrication)

Pin (with dry lubricant)

Cartridge
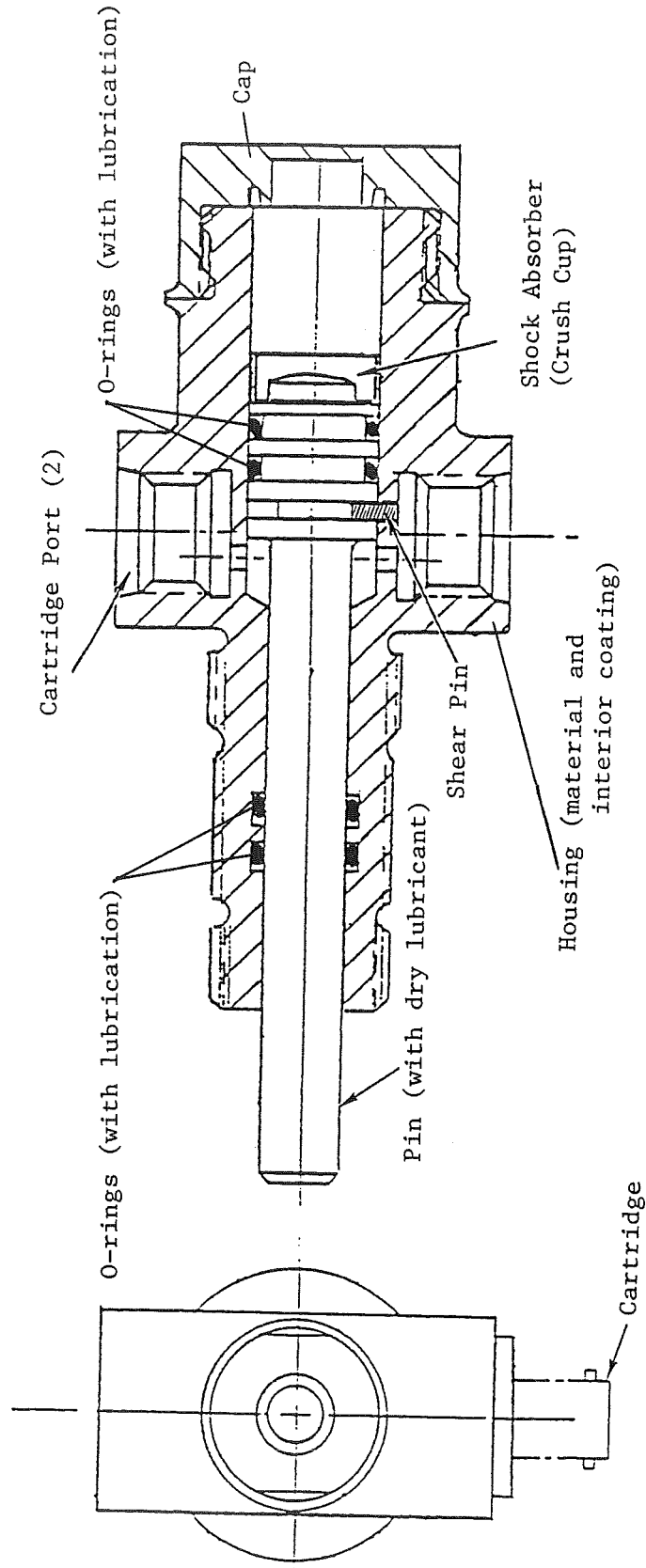
Figure 7.- Viking pin puller design and functional variables.
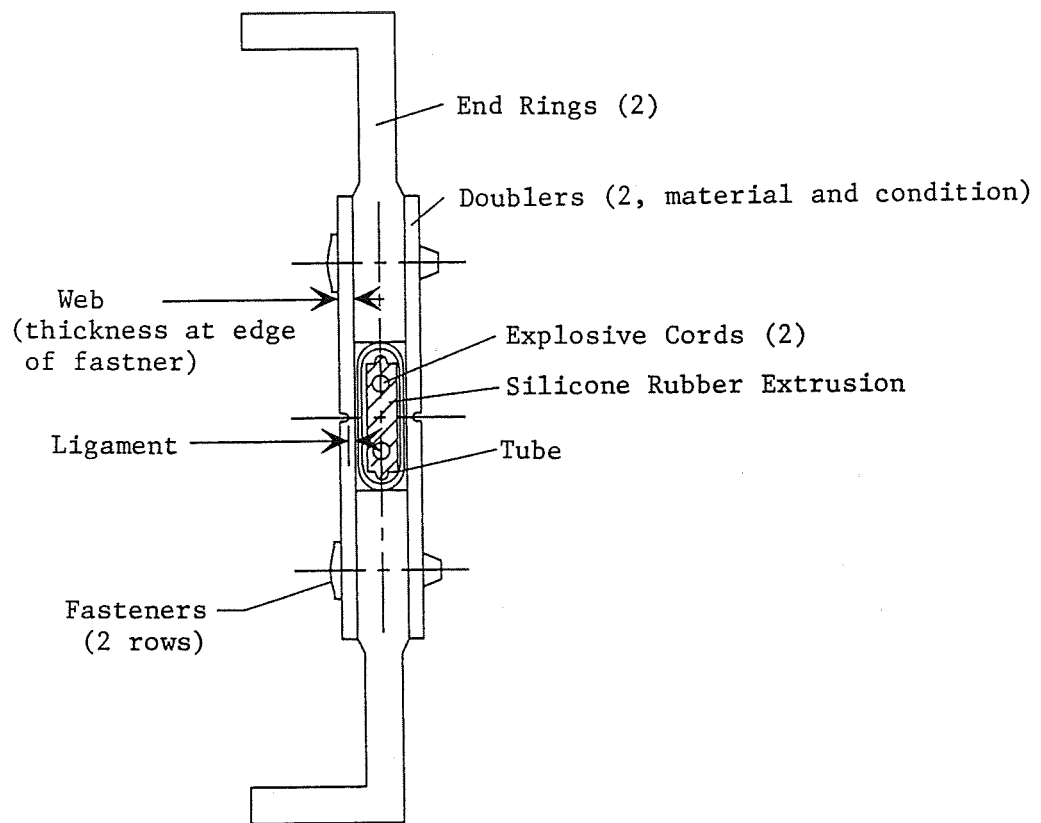
Figure 8.- Super*Zip separation joint design and functional variables.

199?0 25132

434649

Retention Latch Mechanism for the Wake Shield Facility

Timothy G. Vendrely*

ABSTRACT

The Wake Shield Facility (WSF) is a space transportation system (STS) payload that is scheduled for launch on STS-60 in November, 1993. It is being designed, tested and integrated into the STS by Space Industries Inc. for the University of Houston's Space Vacuum Epitaxy Center, a NASA Center for the Commercial Development of Space. The WSF is composed of two main components: a cross-bay carrier and a free-flying experimental platform. The WSF's primary objective is the epitaxial growth of thin films by controlled beam techniques in the ultra-high vacuum that exists in the wake of the free-flyer. The Retention Latch Mechanism (RLM) has been developed to act as the structural interface between the free-flyer and the carrier.

INTRODUCTION

Functionality, redundancy, reliability and cost were the driving factors in the design of the RLM. The RLM has three main functions: to connect the free-flyer to the carrier during ascent; to release the free-flyer for the experimentation portion of the mission; and then to re-attach the free-flyer to the carrier for the return to Earth. The WSF in its payload bay configuration is shown in Figure 1 and the free-flyer is shown in Figure 2. During all portions of the flight when the free-flyer is attached to the carrier, the RLM must be able to effectively transmit any loads encountered during flight from the free-flyer to the carrier. As a secondary function of the RLM is to ensure that the sensitive materials processed on the WSF are protected during ascent and during re-entry. This is accomplished by the RLM also providing a clamping force to an o-ring seal between the free-flyer and a sealed container in the carrier. The RLM must allow for unrestricted un-berthing and berthing procedures. Additionallly it must be able to capture the free-flyer, given the operational tolerances of the Remote Manipulator System (RMS). The system must be reliable enough and redundant enough that the operation of the RLM can be accomplished without any Extra-Vehicular Activity (EVA). The RLM should be

---

* Space Industries, Inc., League City, TX

simple, using "off-the-shelf-technology" and proven materials to drive total costs down and to reduce the amount of testing required.

DESCRIPTION OF RETENTION LATCH MECHANISM

Developed to satisfy the design requirements of the WSF program, the RLM consists of two sets of four (4) over center latches that are mechanically connected through a linkage system to two dual drive electromechanical rotary actuators. Each set of latches has four (4) hooks that are driven in cam-slots near the interface ring between the free-flyer and the carrier. The primary latch hooks are spaced at 90 degrees from each other, while the second set of hooks is slightly offset from the first set. The RLM and associated hardware are shown in Figure 3. One set of four (4) latches and hooks is adequate to perform all of the requirements of the RLM; the other set is used in the event of a mechanical failure, providing a redundant feature. Once on orbit, the RLM is activated which causes the electromechanical actuators to unlock the latch mechanism and move the hooks out of the way so that the free-flyer can be deployed. When material processing is completed, the RMS positions the free-flyer within the capture envelope of RLM. As the RLM is activated, the actuators cause the hooks to move in their cam-slots which first center the free-flyer over the carrier then move the free-flyer into mating position. The RLM continues its motion until the latches lock the free-flyer in place. The position of the RLM is monitored by microswitch assemblies on the carrier and is controlled by crew members in the Orbiter.

The heart of the RLM are two dual drive electromechanical rotary actuators. Each actuator has two 3-phase, 110 volt motors that are driven differentially through a 5:1 reduction gear box. This allows for no loss in torque due to the loss of a motor; only the time for actuation is increased. The primary latch system's actuation time for both motors running is 1.17 minutes. For the secondary system, the actuation time is 1.02 minutes. If a motor were to not operate in either of the actuators, the actuation time would double for that actuator. These actuators, made by Honeywell, are flight proven having the same design been flown on SPARTAN. The rotary actuators translate their rotary motion into linear motion via two industrial precision ballscrew assemblies. The structure of the RLM has been designed so that the motors can be stalled with no adverse effects. A stalled actuator event would only happen if there were a failure of one of the RLM position sensing microswitch assemblies. The rotary actuators and ballscrew assemblies of the lower latch mechanism are shown in Figure 4.

As the actuators rotate and drive the ballscrew assemblies, their linear motion drives two unique aspects of the RLM. These

unique features are the over center pivot mechanisms, and the
hooks and cam-slots. The ballscrews are mechanically connected
through linkages to the over center pivot mechanisms and then
also to the hooks in their cam-slots at the interface ring
between the free-flyer and the carrier. These linkages, pivots,
and hooks are the main load carrying members of the RLM. They
are fabricated from 15-5PH stainless steel in the 1025 heat
treat condition. The container in the carrier that serves as
the support structure for the RLM is a welded structure
fabricated from 304L stainless steel. A detail of the RLM
linkages, pivot assembly and hooks is shown in Figure 5. When
the free-flyer is attached to the carrier and the pivots are
locked over center, any loads impacted to the hooks tend to
drive the pivot farther over center. The loads are then
dispersed into the support structure and will not travel down
the linkages to the ballscrew assemblies and actuators. A close
up of the pivot mechanism is shown in Figure 6. The hooks and
cam-slots allow for sizable misalignment during berthing
operations between the free-flyer and the carrier. The reach-
then-grab action of the hooks results in a large capture
envelope that is well within the positional tolerances of the
RMS. The operational reach limits of the latch hooks are shown
in Figure 7. Microswitch assemblies around the interface ring
between the free-flyer and the carrier notify the crew if the
free-flyer is within the latching envelope. The crew then
activates the RLM and the hooks begin their motion in which they
center the free-flyer then move it into position for mating.
The hooks, linkages and pivots also are the mechanism by which
an o-ring seal is compressed at the interface ring to provide a
controlled environment for sensitive components on the free-
flyer. A total force of 56.5 kN (12700 lb) is needed to
compress the o-ring and provide an adequate seal. This
translates to a preload in each hook-linkage-pivot system of
14.12 kN (3175 lb). The actual preload used during flight is
28.9 kN (6500 lb) per hook-linkage-pivot system, which prevents
any gap occurring between the free-flyer and container during
any flight loading condition due to deflections of the
structure.

To ensure that the RLM meets all of the safety criteria for
a safety critical system, all moving parts must have a redundant
feature. To facilitate this, all rotating parts of the
mechanism have two sliding surfaces so that the chances of a
failure due to any one of the surfaces galling and siezing is
reduced. Friction between sliding surfaces is reduced by
coating all sliding and rotating surfaces with molybdenum
disulfate solid film lubrication.

To minimize costs but still ensure safety, all of the
fasteners used are commercially available, high strength
military specification hardware. In highly loaded areas, the
fasteners are high strength alloy steel, and in support areas,

the fasteners are 300 series stainless steel. All of the
fasteners have full traceability and are subjected to the
requirements stated in the JSC Fastener Testing Integrity
Program.

Since the RLM is located in the environmentally harsh area
of the Orbiter payload bay, environmental effects have played a
key role in its design. However due to the mechanical nature of
the RLM, the thermal/vacuum environment is the key design
driver. All of the load carrying, rotating components and
support structures of the RLM are fabricated from stainless
steels. These steels minimize problems encountered due to
thermal expansion or contraction because of their similar
thermal expansion coefficients. The sealed container in the
carrier, the attachment bell, is fabricated from stainless steel
and provides a great thermal inertia which minimizes temperature
gradients across the structure. Problems that may arise due to
the vacuum, cold welding specifically, are eliminated by the
rotating redundancy and friction reduction methods described
above.

Another key component of the RLM are the microswitch
assemblies that relay the position of the RLM to the crew in the
Orbiter. These assemblies have to be effective, reliable,
simple, and redundant. There are three different microswitch
assemblies associated with the RLM: the ready-to-latch
indicators, the latched indicators and the unlatched indicators.
The first of these assemblies, the ready-to-latch indicators,
are located around the interface ring between the free-flyer and
the carrier. Each of the four locations have two microswitches
in one assembly, offering dual redundancy. The assembly
actuates the switches when the free-flyer is 25.4 mm (1.0 in)
from the carrier in the four (4) locations of the assemblies. A
close up of the ready-to-latch assembly is shown in Figure 8.
The second microswitch assemblies are the latched indicators.
These switches are located at the pivot assembly of the RLM.
Each latch system has two microswitch assemblies and each
assembly contains one microswitch for a total of four latched
microswitches. The assembly activates the microswitch only when
the pivot is in its over center position and locked in place.
When the microswitch is activated, the circuit that carries
power the drive motors in each actuator is broken. A detailed
view of the latched microswitch indicator assembly is shown in
Figure 9. The final microswitch assemblies are the unlatched
indicators. These assemblies are located adjacent to the
ballscrew assemblies. The switches are activated only when the
latch hooks are at the end of their stroke and fully open. When
the microswitches are activated by the assemblies, again the
circuit that carries power to the motors is broken. Like the
latched indicators, there are two microswitches per latch
system, for a total of four (4) microswitches in the unlatched

indicator assemblies. A detailed view of the unlatched indicators is shown in Figure 10.

The design of the RLM was completed in accordance with the WSF program requirements for structural design. These requirements state that all load carrying elements will have a factor of safety of at least two on flight limit loads. Structural testing must then be completed at 140 percent of flight limit loads. Testing is then completed on the flight hardware to qualify the structure for flight loads. The RLM has successfully met the above requirements.

CONCLUSION

The RLM has been designed and developed expeditiously. The conceptual design was finalized in the fall of 1990 and detail design, fabrication, and assembly was completed just eight months later. To date, the entire structure of the WSF, including the RLM, has been through modal, acoustic and static structural testing at NASA's Johnson Space Center. The RLM has met or exceeded all of its planned objectives, and at the time of this writing, the WSF is undergoing final integration. Through proven mechanical design techniques and proper attention to the design criteria, an effective, reliable, redundant, safe and cost effective system has been developed in a short amount of time.
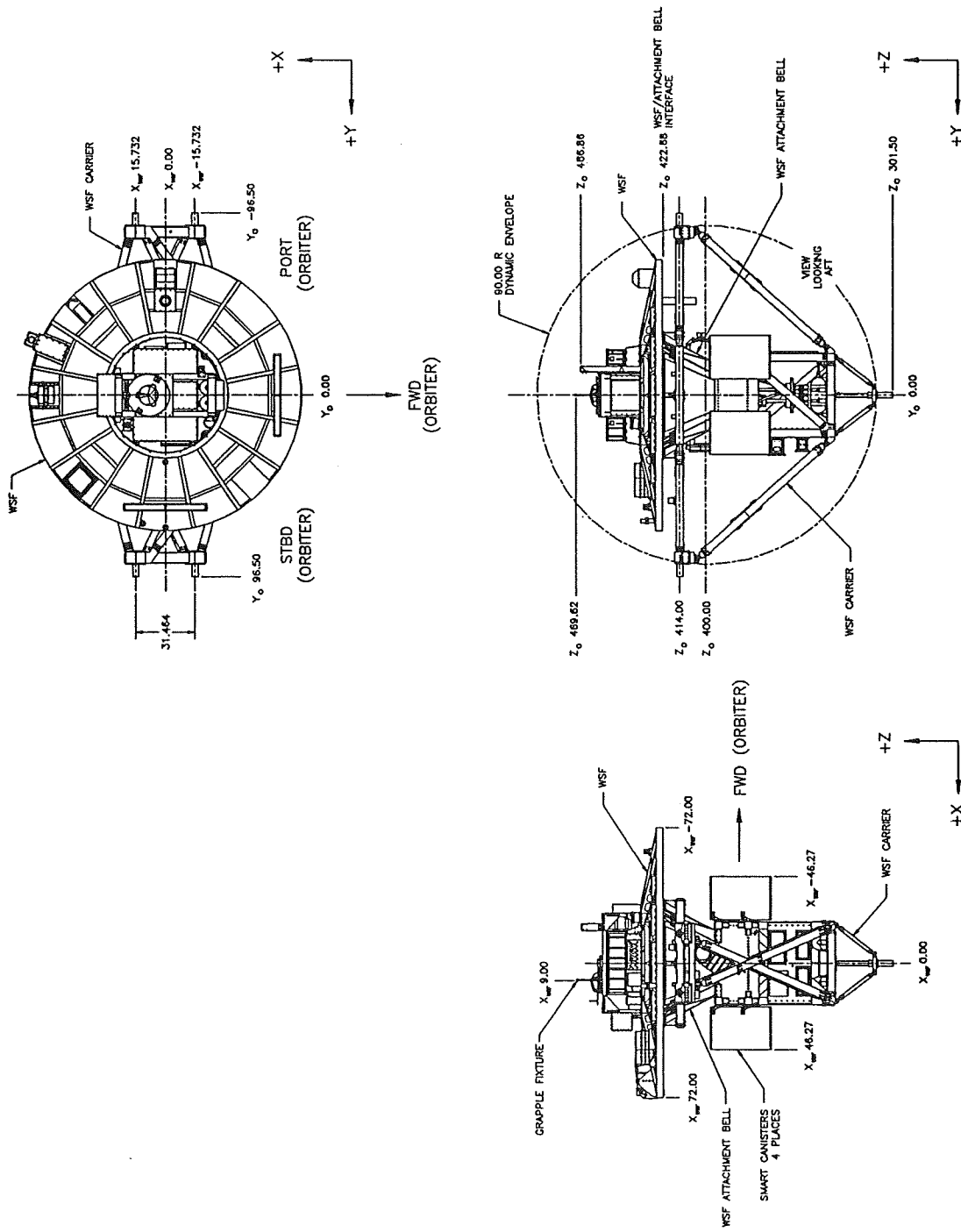
ACKNOWLEDGEMENTS

Figure 1. WSF Payload Bay Configuration 3-View
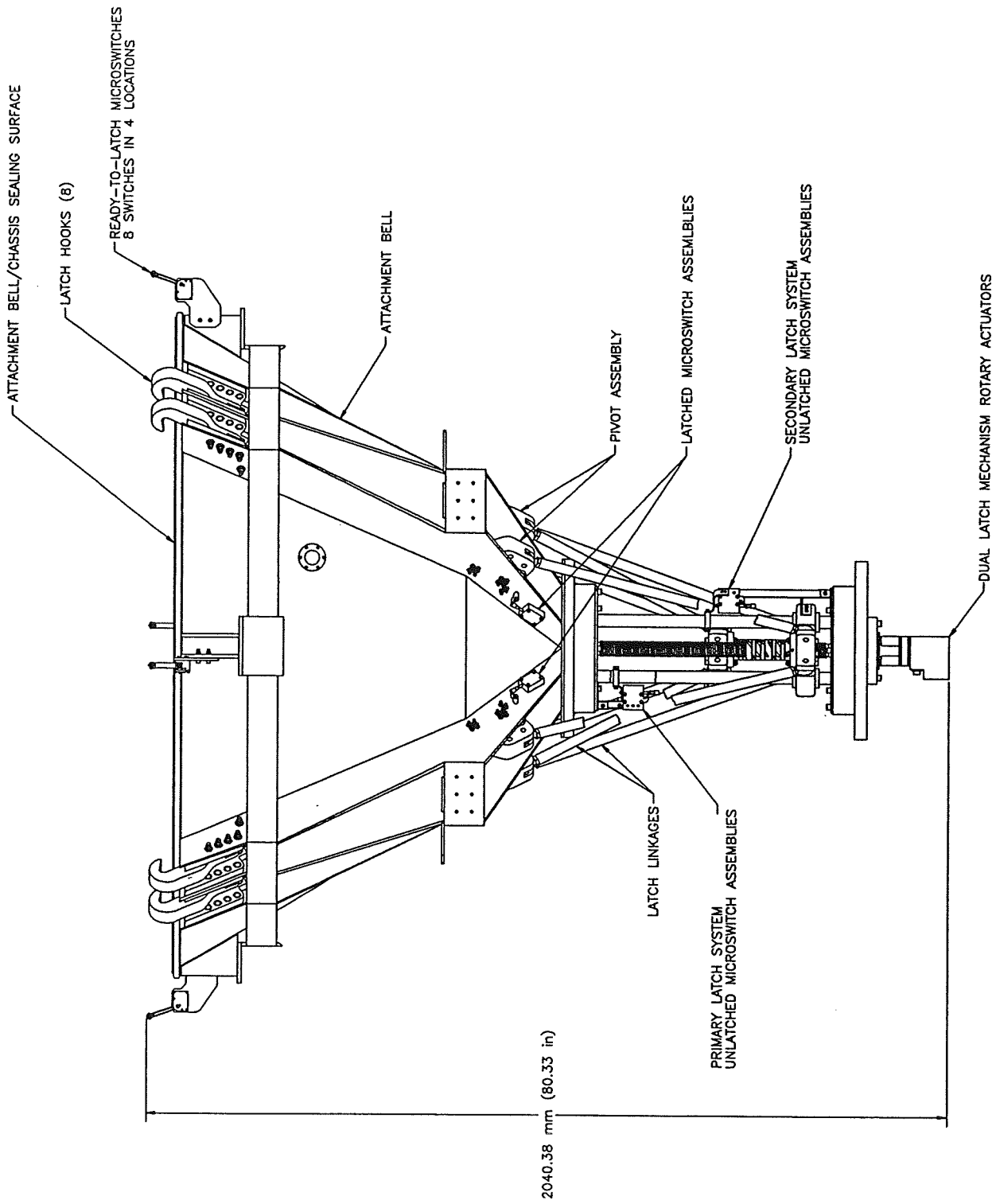
112
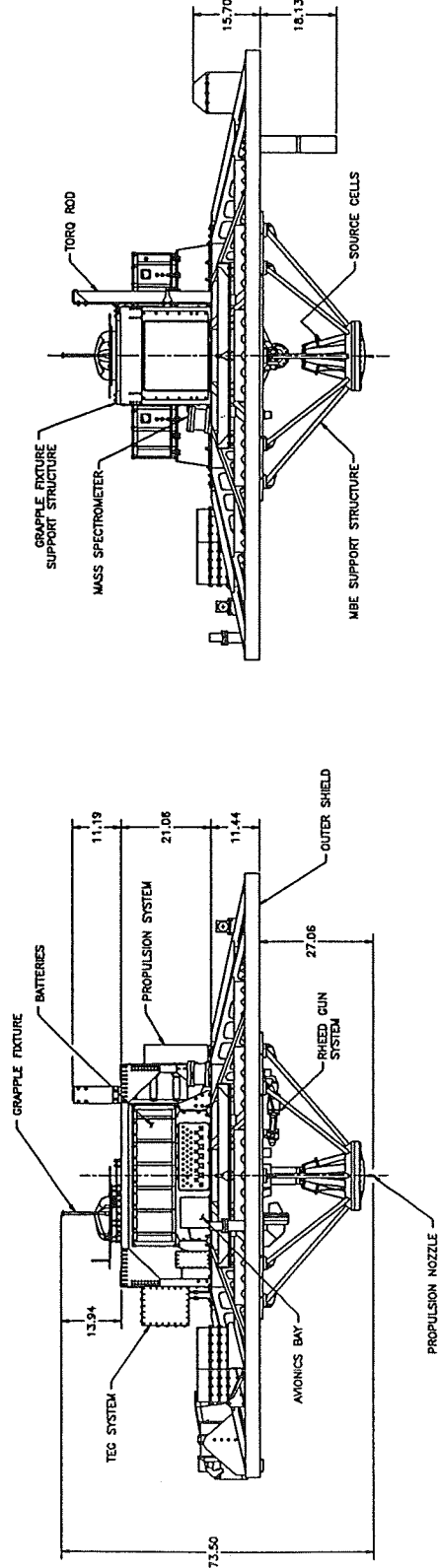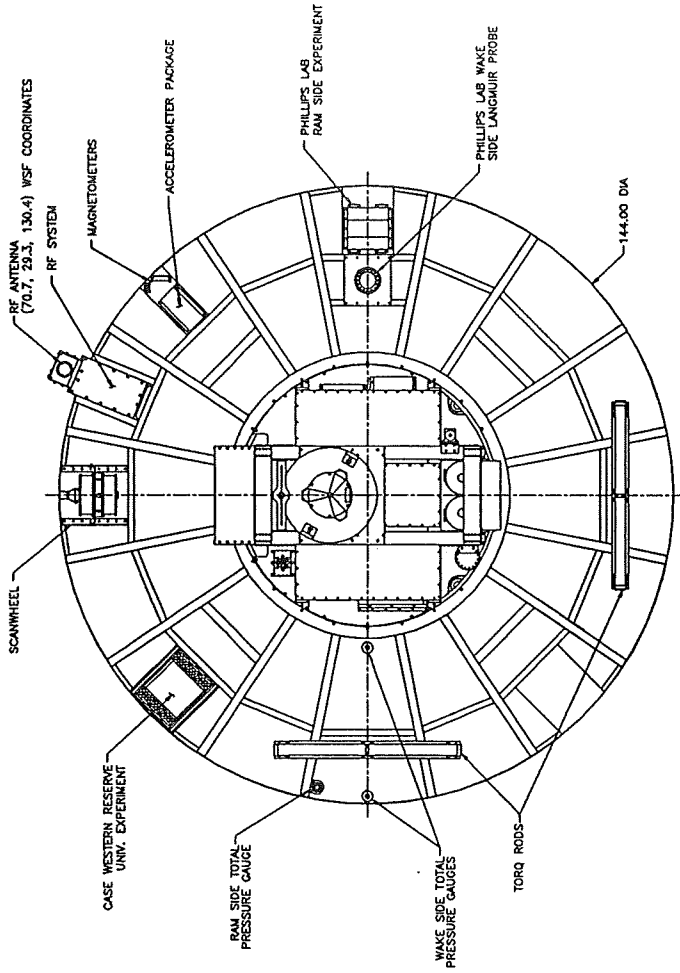
Figure 2. WSF Free-Flyer 3-View

113

ATTACHMENT BELL/CHASSIS SEALING SURFACE

LATCH HOOKS (8)

READY-TO-LATCH MICROSWITCHES
8 SWITCHES IN 4 LOCATIONS

ATTACHMENT BELL

PIVOT ASSEMBLY

LATCHED MICROSWITCH ASSEMLBIES

SECONDARY LATCH SYSTEM
UNLATCHED MICROSWITCH ASSEMBLIES

DUAL LATCH MECHANISM ROTARY ACTUATORS

LATCH LINKAGES

PRIMARY LATCH SYSTEM
UNLATCHED MICROSWITCH ASSEMBLIES

2040.38 mm (80.33 in)

Figure 3. RLM System Components

114
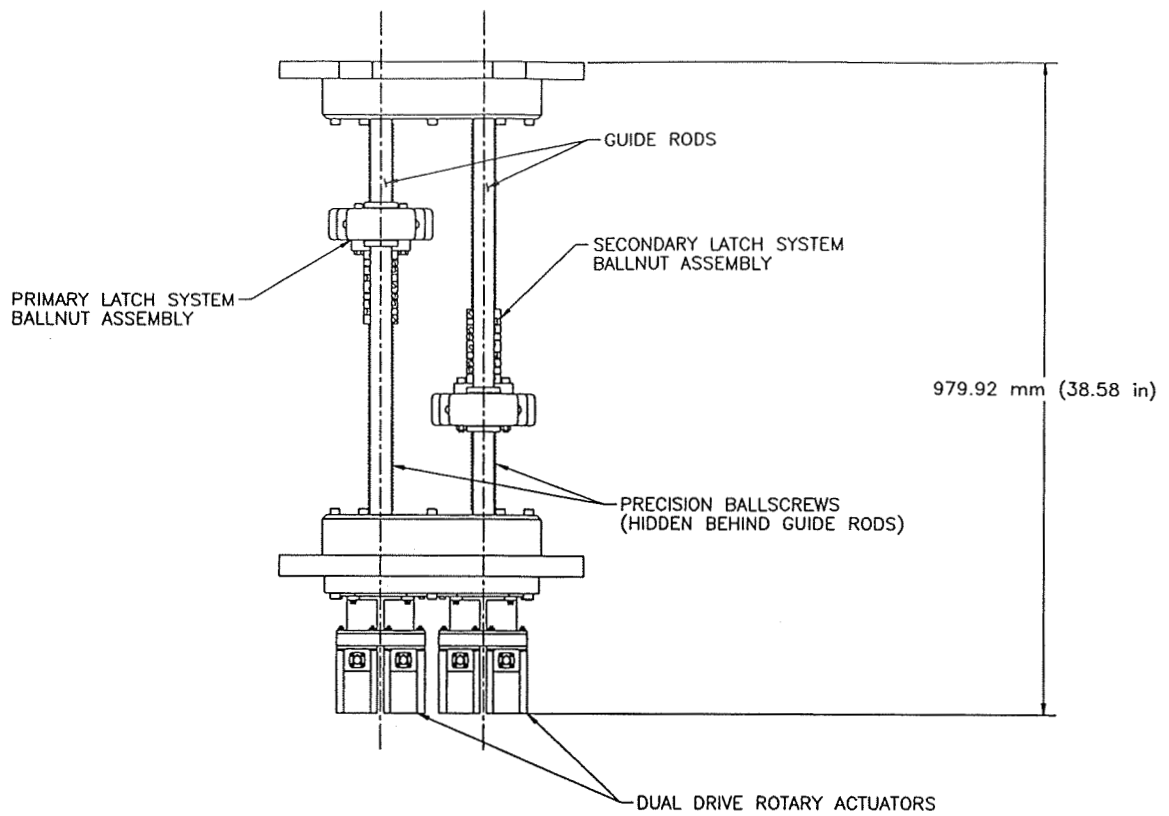
Figure 4. Lower RLM System Details
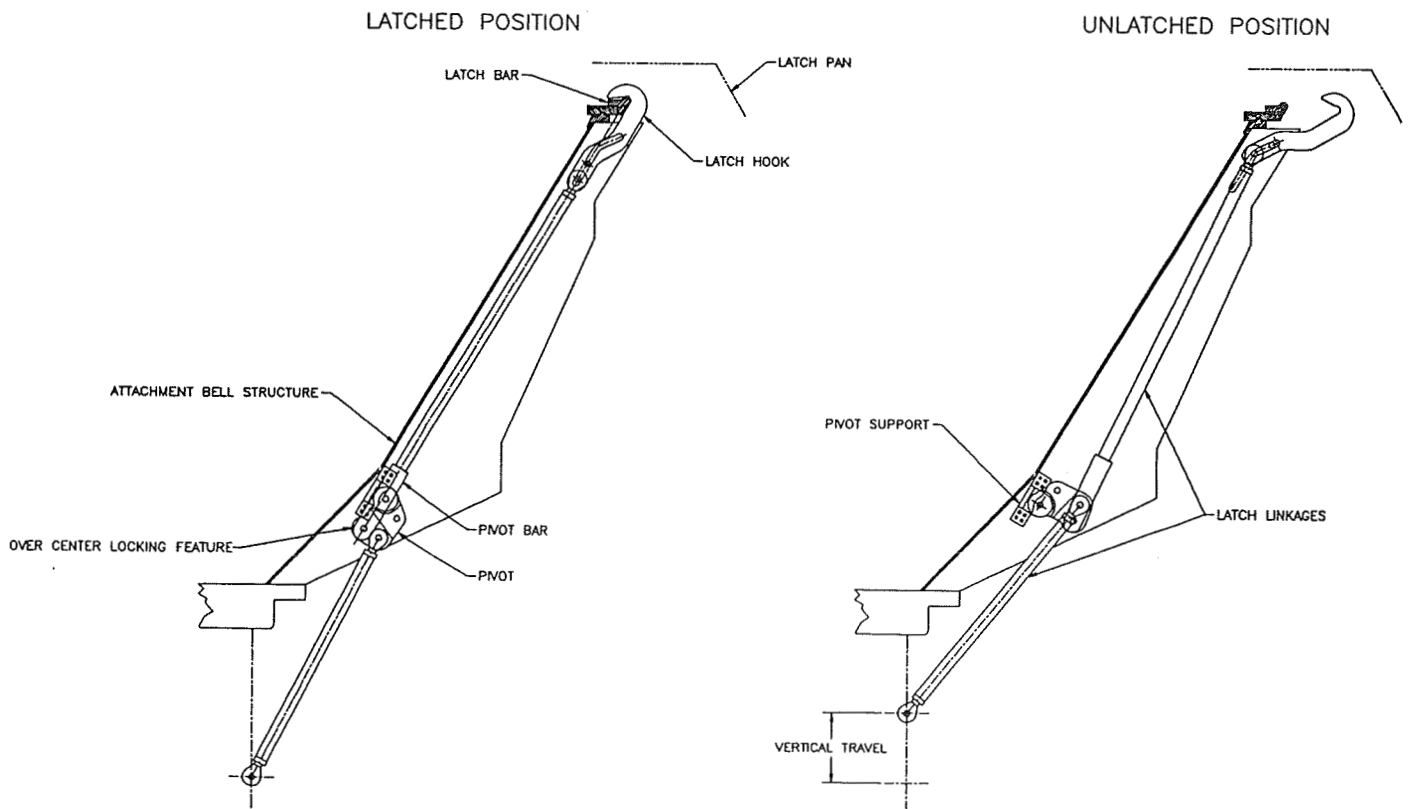
Figure 5. RLM Linkage, Pivot, and Hook Details

115

LINE OF ACTION TO HOOKS

PIVOT BAR

PIVOT POINT

OVER CENTER FEATURE

PIVOT

LINKAGE TO BALLSCREWS

PIVOT SUPPORT

PIVOT STOP
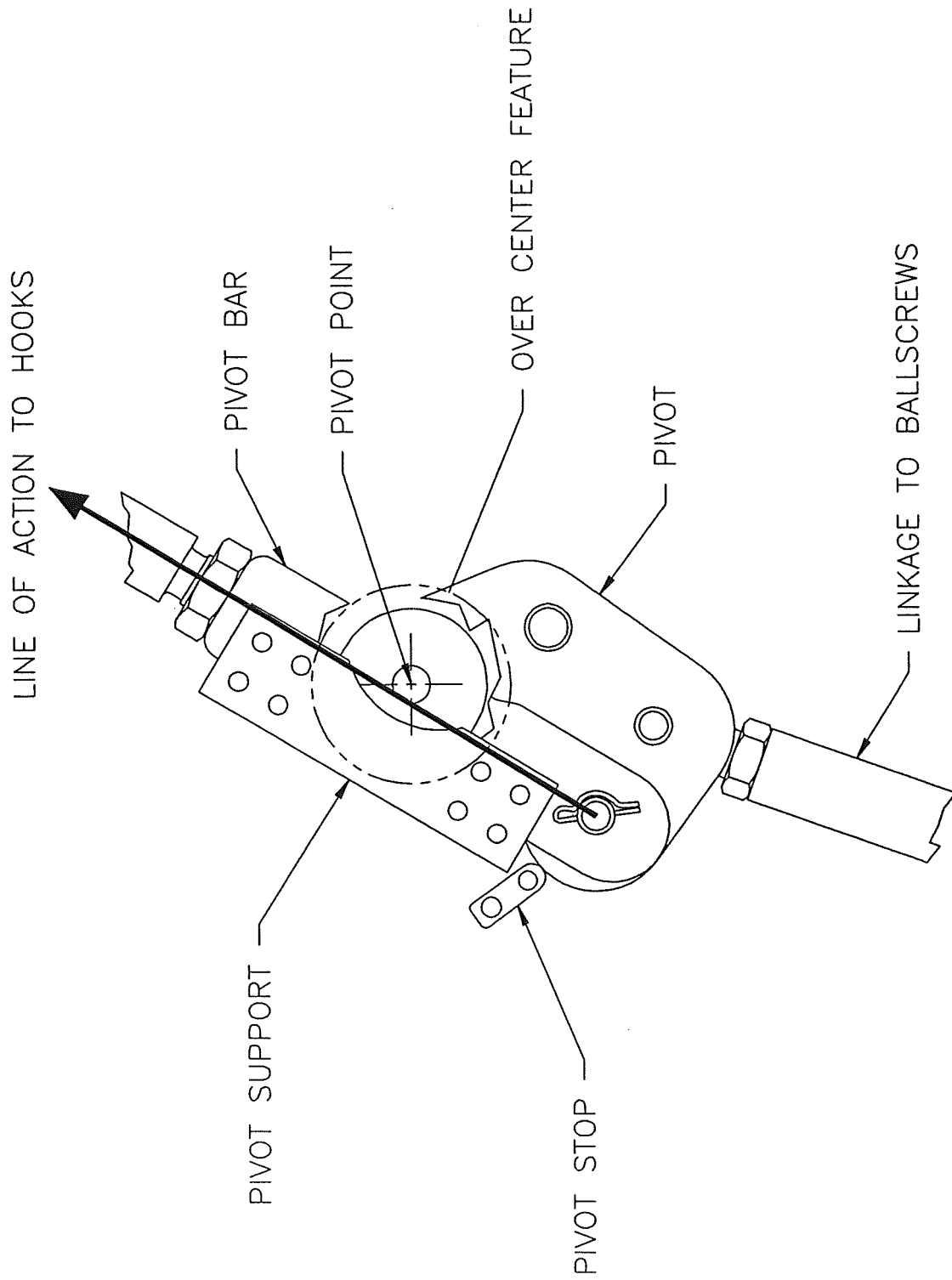
Figure 6. RLM Pivot Mechanism

LATCH PAN OUTLINE

71.12 mm (2.80 in) HORIZONTAL REACH

27.94 mm (1.10 in) VERTICAL REACH

LATCH BAR

CHASSIS SEALING SURFACE

ATTACHMENT BELL

HOOK IN RELEASED POSITION

HOOK IN LATCHED POSITION
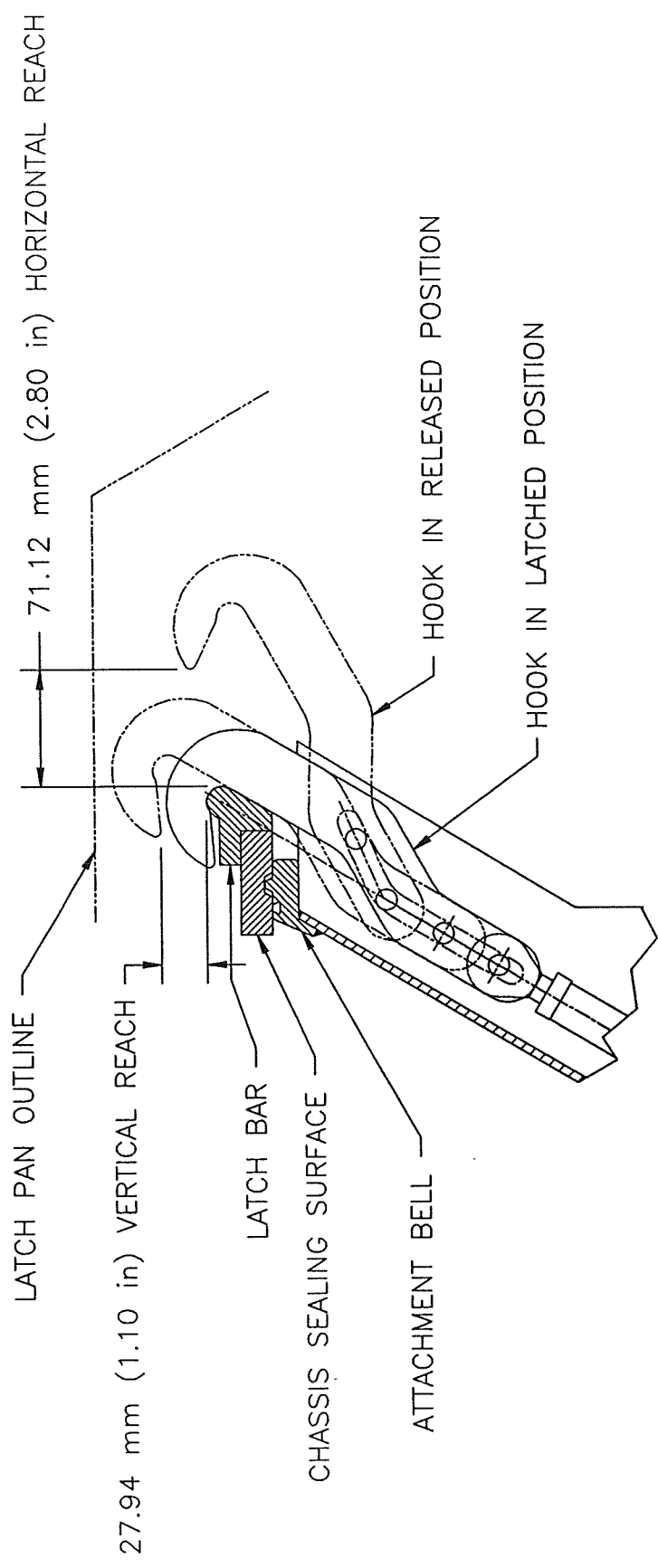
Figure 7. RLM Hook Reach Limits

117

CHASSIS SEALING SURFACE

OUTER SHIELD

ROTATING ARM

MICROSWITCH ASSY
2 HAYDON MICROSWITCHES
P/N 6302

MOUNTING BRACKET

ATTACHMENT BELL

CHASSIS

ATTACHMENT
BELL
SEALING
SURFACE
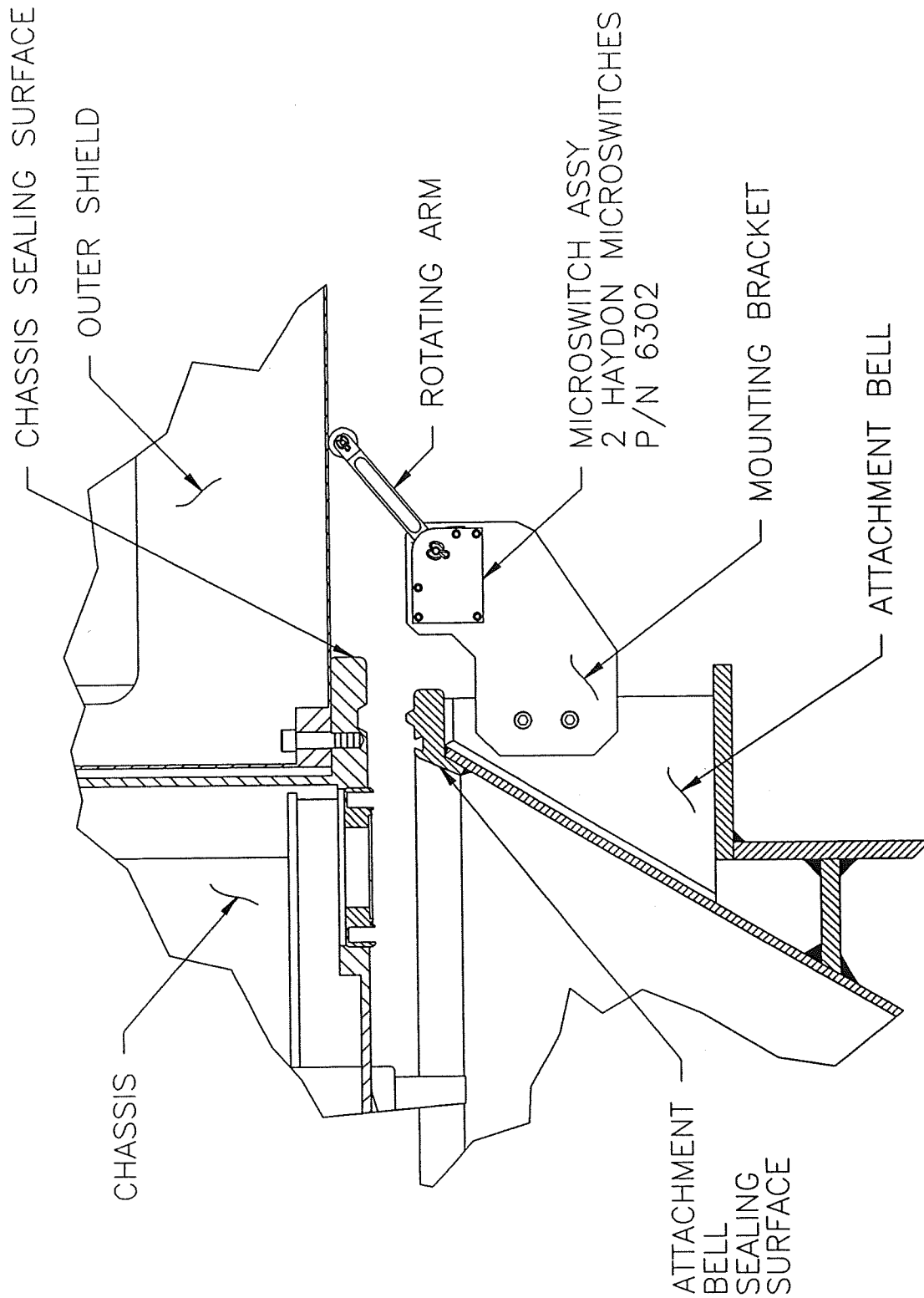
Figure 8. Ready-To-Latch Microswitch Installation

ATTACHMENT BELL

PIVOT IN LATCHED POSITION

LATCH LINKAGE

PIVOT STOP

FLAP ARMS

ADJUSTABLE PLUNGER
MECHANISM

MOUNTING HARDWARE

HAYDON MICROSWITCH
P/N 6301
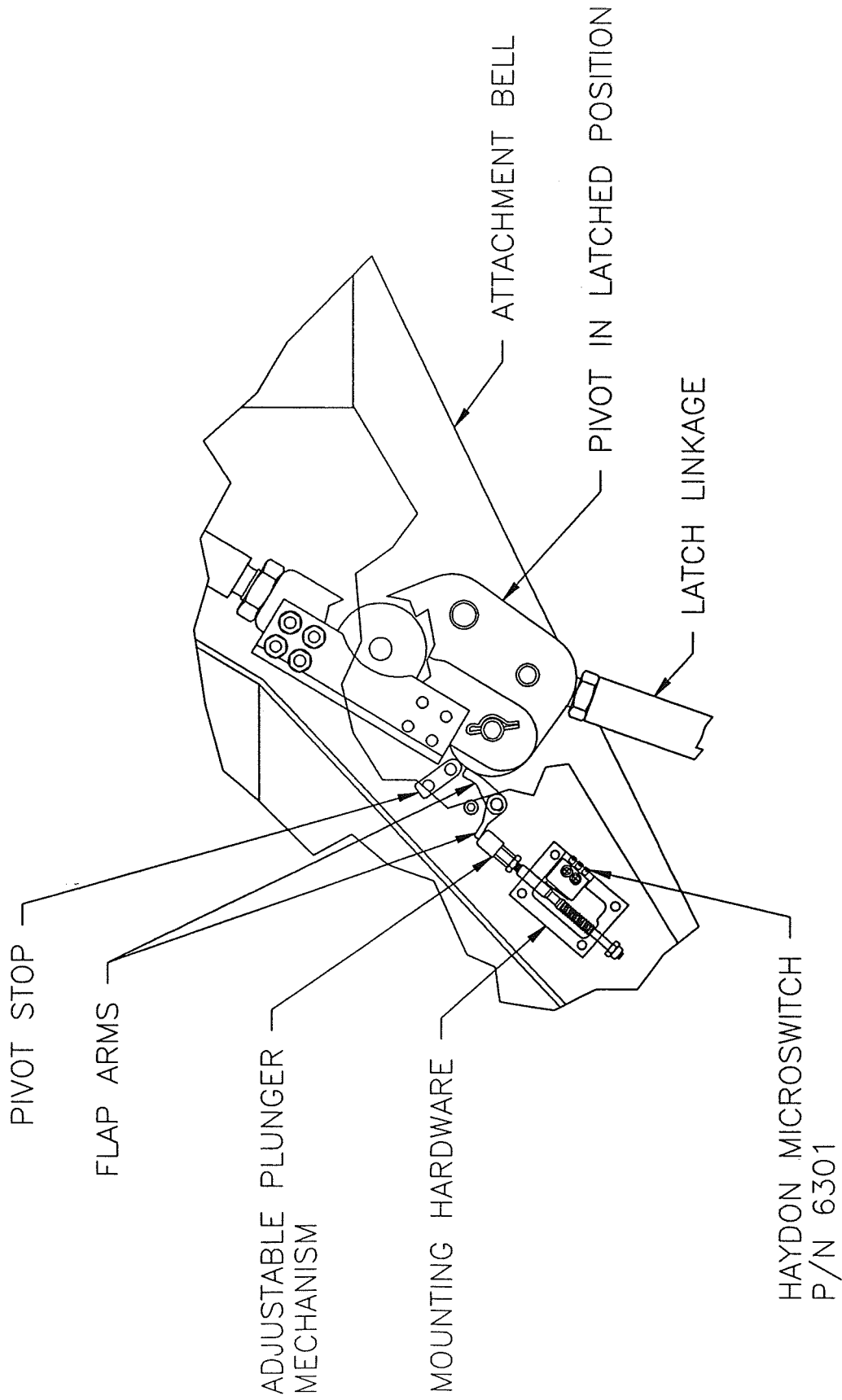
Figure 9. Latched Microswitch Installation

119

MOUNTING BRACKETS AND HARDWARE

MICROSWITCH ASSY (2)

ADJUSTABLE PLUNGER MECHANISM

LATCH SYSTEM IN UNLATCHED POSITION

POSITION STRIKER PLATE

LATCH SYSTEM IN LATCHED POSITION

GUIDE ROD

BALLSCREW ACTUATOR

BALLNUT PLATE

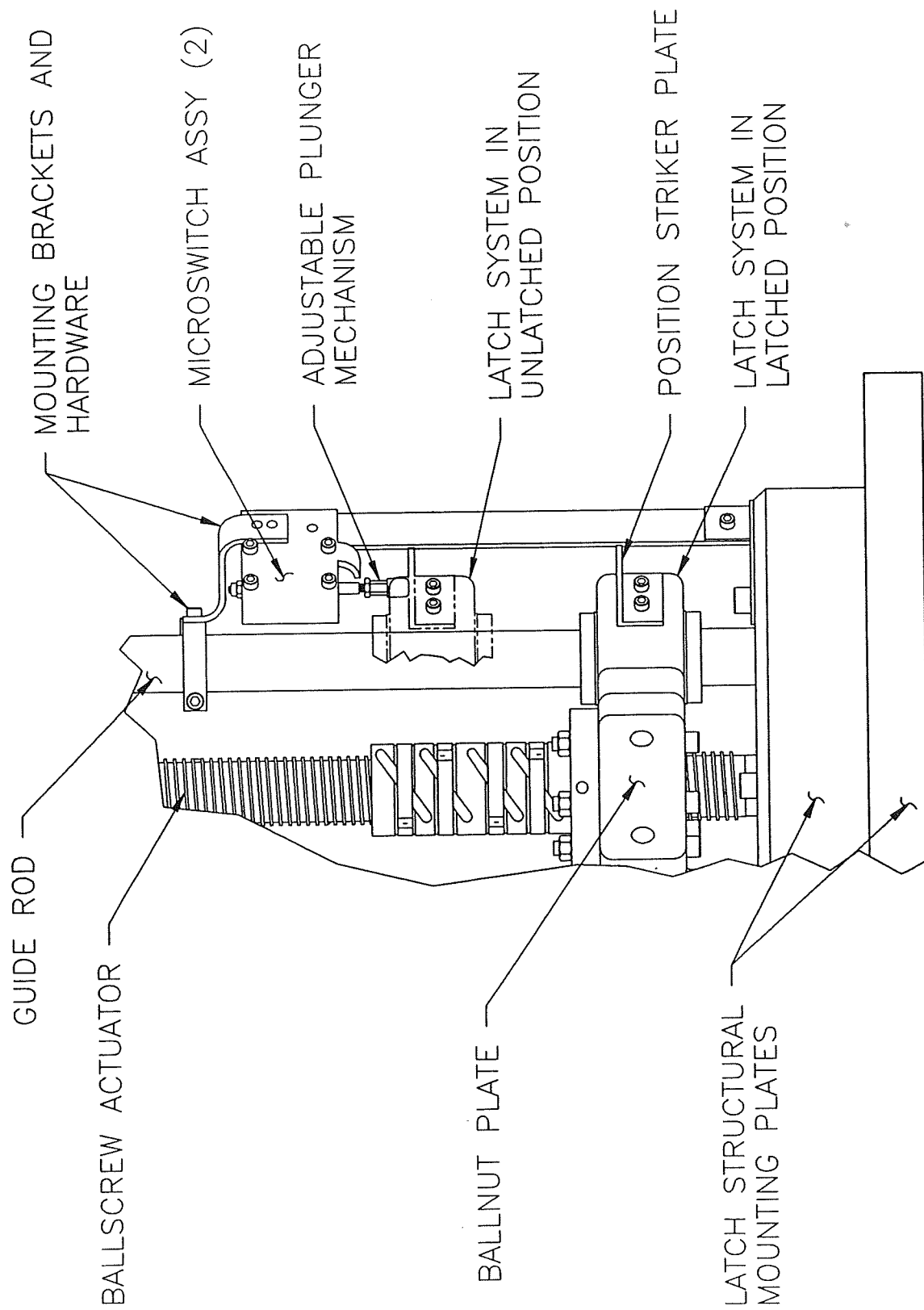LATCH STRUCTURAL MOUNTING PLATES

Figure 10. Unlatched Microswitch Installation

120

DEVELOPMENT AND TESTING OF THE
AUTOMATED FLUID INTERFACE SYSTEM

Martha E. Milton*, Tony R. Tyler*

ABSTRACT

The Automated Fluid Interface System (AFIS) is an advanced development program aimed at becoming the standard interface for satellite servicing for years to come. The AFIS will be capable of transferring propellants, fluids, gasses, power and cryogens from a tanker to an orbiting satellite. The AFIS program currently under consideration is a joint venture between the NASA/Marshall Space Flight Center and Moog, Inc. An engineering model has been built and is undergoing development testing to investigate the mechanism's abilities.

INTRODUCTION AND BACKGROUND

The overall goal of the AFIS program is to develop and demonstrate a system capable of making multiple fluid and electrical connections between two docked spacecraft. This system would become the standard interface for satellite servicing and other similar applications. The end goal of the program is to build a flight qualified AFIS and demonstrate its capability on-orbit.

The primary mission of the AFIS is to resupply consumables to on-orbit satellites. This technology could greatly increase the life and flexibility of future satellites. Other possible applications could include space station systems, space based engines, and on-orbit integration of space systems too large to launch as a single unit.

The AFIS was initially developed to be a flight experiment as part of the Satellite Servicer System (SSS). The AFIS has been delivered to MSFC and technically evaluated. As a result of this evaluation, follow-on testing is being conducted at the MSFC and is the subject of this paper. The SSS program was canceled but the AFIS development is continuing.

DESIGN REQUIREMENTS

In order to meet the objectives of providing a flexible system for satellite servicing, the following requirements were imposed:

---

* NASA/Marshall Space Flight Center, Huntsville, AL

- Compatible with both the Orbital Maneuvering Vehicle (OMV) and the Orbital Spacecraft Consumables Resupply System (OSCRS) tanker.
- Compatible with both existing docking mechanisms; the Three Point Docking Mechanism (TPDM), and the Remote Grapple Docking Mechanism (RGDM). (Spacecraft would be docked before transfer would take place).
- Accommodate final engagement compliance.
- Reusable for launched servicing activities to all orbits.
- Life of forty missions.
- Minimize life cycle costs and maximize safety and reliability.
- Carry loads resulting from fluid transfer (2000 pounds total).
- Provide coupling contamination protection as well as separation between oxidizer and fuel couplings.
- Minimize hardware and moving parts on spacecraft side.
- Allow for a standard footprint for all spacecraft.
- Reconfigurable for monopropellant, bipropellant or cryogenic supply.

DESCRIPTION

The AFIS utilizes technology previously developed for a system called the Automated Umbilical Connector (AUC). The AUC was used by NASA/Johnson Space Center to demonstrate cryogenic resupply.

The AFIS is comprised of an active and passive side. The active side is on the tanker and the passive side is on the spacecraft. Both sides are octagon shaped and measure 26 inches across the flats. The active side weighs approximately 36 pounds and the passive side weighs 17 pounds without couplings. Figure 1 shows both sides of the AFIS positioned and ready for engagement. This initial alignment is done by the docking mechanism.

Figure 2 depicts an exploded view of the active side of the AFIS. This side contains all components requiring electrical power and/or control and is comprised of a chassis and a carriage assembly. The chassis is hard mounted to the spacecraft structure, provides a structure for the carriage assembly to ride on, and contains a rotating cover which protects the couplings.

The main component of the carriage assembly is an electromechanical actuator that powers and controls all AFIS functions. This actuator is responsible for the following tasks:

- Rotates covers on both the spacecraft and tanker side.
- Locks/unlocks the two sides together.
- Engages/disengages couplings and connectors.
- Aligns the tanker and spacecraft sides of AFIS.
- Carries the loads from fluid transfer.

The carriage assembly also contains the couplings and connectors. This assembly is stiffened by a truss assembly and is compliantly mounted to the chassis assembly. The compliant mounting allows the AFIS to adjust for misalignments resulting from the docking mechanism.

The passive side of the AFIS is shown in Figure 3. It was designed to be as simple and lightweight as possible and to require no power or control. Moving parts are limited to a rotating cover which is rotated by the active side.

The operation of the AFIS is controlled by three signals: "Enable", "Engage", and "Disengage". The AFIS has redundant electronics and motors which are selected by choosing different channels. When the AFIS is disengaged, as shown in Figure 4a, the carriage assembly is preloaded against the back of the rotating covers. This allows the floating carriage to withstand the necessary vibration loads. When the "engage" command is received by the actuator, a square shaft is extended across the interface as shown in Figure 4b. Once this actuator is fully extended, it has protruded into the center hub of the passive side. The actuator then rotates 45 degrees which rotates both covers and locks the two sides together. The two halves are locked together by having the square end of the actuator rod rotated 45 degrees from the square center hub hole. The actuator then begins retracting. Because the end of the actuator is now fixed, the carriage assembly of the active side (with couplings) begins to move across the interface towards the passive side. The engagement is complete when all couplings are engaged as is shown in Figure 4c. Disengagement is the reverse of engagement.

DEVELOPMENT TESTING

In order to fully understand the characteristics of the AFIS and determine the acceptability of the design, a full series of development tests are being conducted at the MSFC. These include:

Functional Checkout

Upon receipt of the AFIS engineering model, it was functionally checked out to assure the design requirements were fully satisfied. The AFIS performed well and adequately satisfied all requirements. Figure 5 shows the AFIS in the disengaged and engaged configurations while mounted in a

structure which simulated a docked spacecraft. This structure
also provided the means to introduce misalignments. The AFIS
easily performed with all required misalignments.

A major mishap did occur during this phase of the
testing. The square end of the actuator rod did not disengage
from the center hub of the passive half during disengagement
operations. As a result, the AFIS was damaged. The AFIS was
repaired and this problem has not reoccurred.

Demonstration Docking and Fluid Transfer

In order to evaluate the compatibility of AFIS with the
three point docking system and the ability of the AFIS to
transfer fluids, a demonstration docking and engagement was
accomplished in the flight robotics facility of the MSFC. The
active side was integrated into the Orbital Maneuvering
Vehicle (OMV) mock-up. This mock-up was stationary and
contained a working Three Point Docking Mechanism (TPDM).
This mounting arrangement is shown in Figure 5. A truss
structure and tubular frame were used to attach the AFIS.

The passive side of the AFIS was mounted on a mobile cart
which contained a trunnion arrangement compatible with the
TPDM. The mobile cart floated on air bearings and was
propelled by air thrusters. The test apparatus is shown in
Figure 6. The mobile cart was flown in and docked to the OMV
mock-up using a Automatic Rendezvous and Docking system
developed at the MSFC. Once docked, the AFIS was engaged and
power and air were successfully transferred across the
interface.

This demonstration placed the AFIS in the horizontal
orientation. Because the AFIS was designed for microgravity,
several changes were required for this test. Even with these
changes, the actuator sag prevented any misalignment studies
during this demonstration.

This test successfully demonstrated that the AFIS can be
integrated with the TPDM. It also demonstrated gas and power
transfer across the interface. The AFIS performed well even
in the horizontal orientation and with the excessive
tolerances inherent with the experimental hardware.

Load Test

A primary concern with the AFIS is the amount of force
transmitted back to the spacecraft. A load test is planned
which will evaluate this. The passive side of the AFIS is
mounted to a load frame and is integrated into the spacecraft
simulator used for the functional checkout. The loads

transferred back to the spacecraft and tanker are expected to be small. The loads measured will be those caused by the mechanisms engagement. Fluid transfer loads are carried internally by the AFIS. This test will also provide additional information on the effects of misalignment on the AFIS.

Thermal Vacuum Test

The objective of the thermal vacuum test is to examine the AFIS in an on-orbit configuration. Both the active and passive sides will be thermally isolated from the space environment except for the front mounting plates and rotating covers. Before docking, both sides will be independently subjected to the extreme temperature variations of space. This will result in the active and passive sides being at different temperatures. In order to assimilate these conditions a special test fixture was required.

This test fixture includes four basic components: the test support structure, a translational system, solar lamps, and the AFIS support structure including the mechanical stops (Figure 8). The test support structure is a tubular frame approximately eight feet long. It encompasses all testing hardware and provides an interface with the vacuum chamber.

The translation system provides a means of separating the active and passive sides for independent thermal conditioning (Figure 9). The system is made up of several components including: a single axis linear translation table, stepper motor, and the computer hardware necessary for operations. This system is operated remotely by compumotor and personal computer.

The AFIS support structure simulates the tanker and the spacecraft in that they provide a mounting structure and thermal protection for the AFIS (Figure 10). The upper/passive side attaches to the test support structure. The lower/active side is connected to the translation table and has a bank of eleven solar lamps cantilevered to one side to heat the upper/passive half during testing. These solar lamps simulate on-orbit solar heating. They have a lighted length of ten inches giving a maximum temperature on a target surface of 375 degrees F. The lower/active half is heated by a second bank of eleven solar lamps located on the test support structure. Both AFIS support structures contain two lamps to maintain ambient temperature within the enclosures. Also included in the AFIS support structure are the mechanical stops which keep the lower/active support structure from being pulled upward during the AFIS engagement.

This hardware provides the means to simulate an on-orbit AFIS engagement. In addition to this engagement test the transfer of power, cryogens and gas will be demonstrated. Alignment studies will also be a part of this thermal vacuum testing.

Vibration Test

When launched into orbit, the AFIS will be subjected to a severe vibration environment. In order to evaluate the effect of launch and landing on AFIS, a vibration test will be done. A shaker table at the MSFC will be used to conduct the test. Each half of the AFIS will be tested independently.

The test will consist of a sine sweep and random vibration test. The sine sweep will determine the natural frequencies and modes for the mechanism. The random vibration test will determine the mechanisms response to the launch environment. These tests will also provide information on the internal stresses of the AFIS. Initial analysis has already shown that the mounting plate for the Type I half may require stiffening and will be verified.

SUMMARY

A design for an Automated Fluid Interface System (AFIS) which can meet the challenge of satellite servicing has been successfully developed. The AFIS is very flexible in that it lends itself very easily to a variety of spacecraft, tankers, launch vehicles and fluids. The AFIS is capable of monopropellant, bipropellant or cryogenic supply. Up to twenty couplings can be used and can be sized up to 6 inches in diameter. The couplings can easily be reconfigured on the AFIS for various missions. The AFIS design is redundant, reliable, and simple. The passive side of the AFIS is very simple and light weight making it very attractive for satellites requiring fluid or cryogen resupply.

At least two improvements are necessary with the current design. The issue of emergency separation was not addressed. If the actuator fails or the actuator rod does not unlock from the spacecraft side, the two spacecraft will be stuck together, possibly causing the loss of both vehicles. It would not be very difficult to include a means of emergency separation with the current design. Another weakness of the current AFIS is in the locating mechanism of the rotating covers. In one instance, the cover did not lock in the proper position and a coupling snagged the cover during engagement. Only operator awareness prevented any damage from being done. Another possible improvement would be the

availability of additional feedback during operation. This is very important in the robotics operation of spacecraft where visual feedback is limited.

Additional Testing of the AFIS will provide the required experience and knowledge for the development of specifications for flight unit procurement.
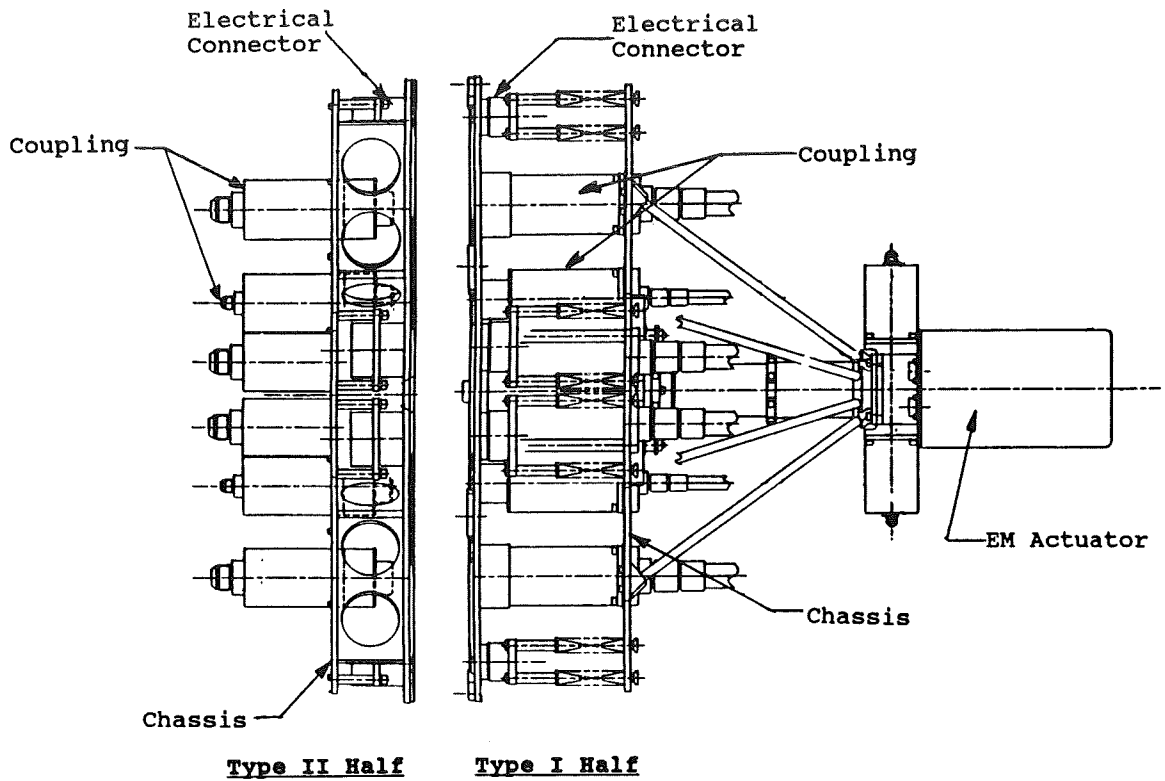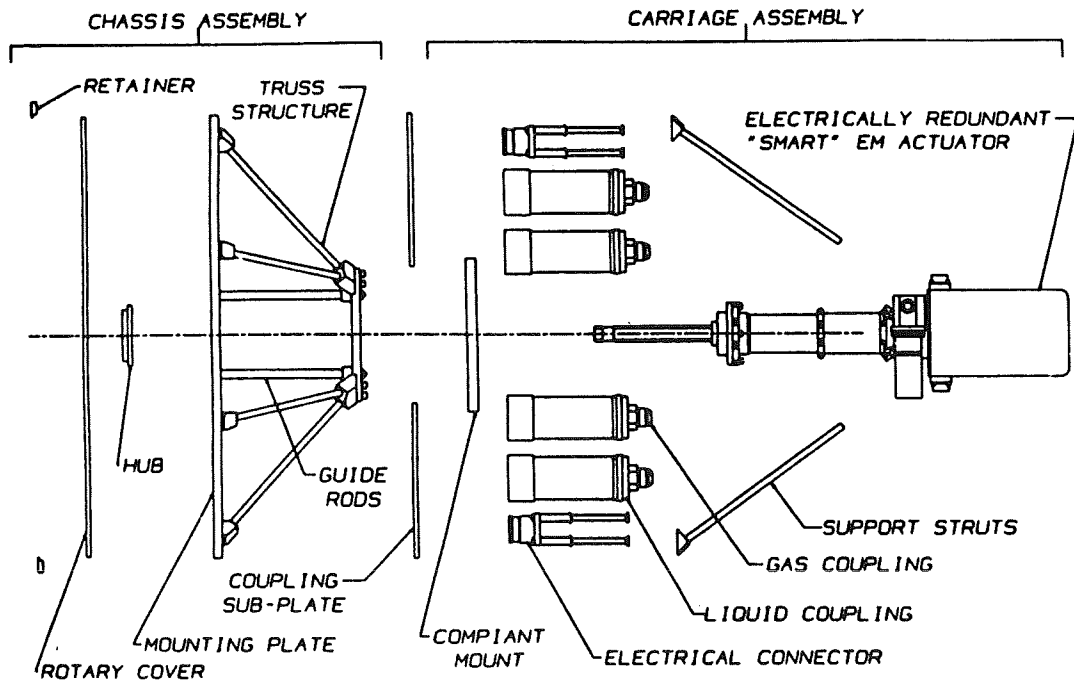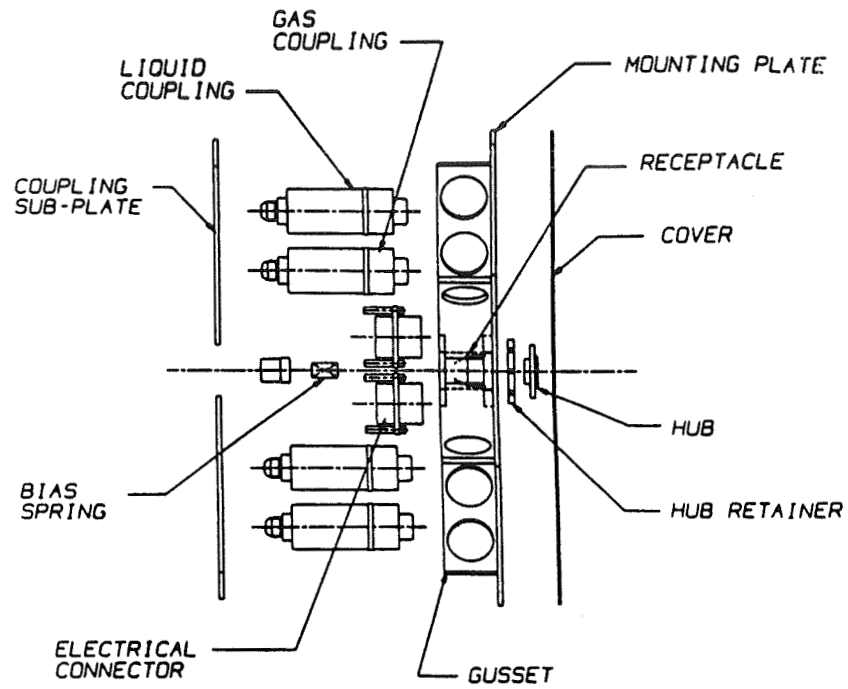
Figure 1: Moog AFIS

Type II Half   Type I Half

Figure 2: Type I Half of AFIS.

Figure 3: Type II Half of AFIS.
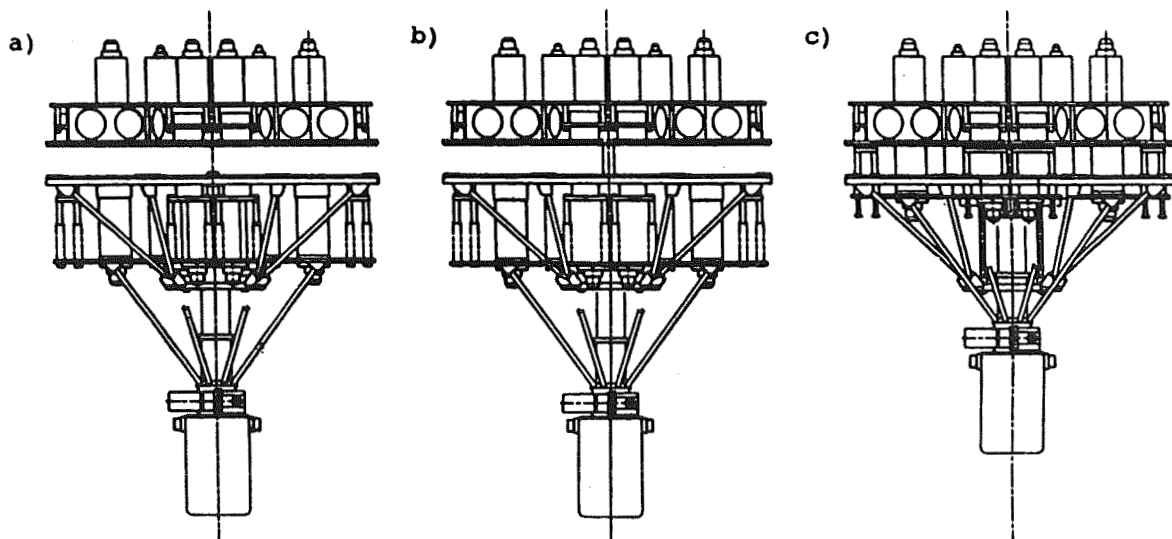
Figure 4: a) Disengaged, b) Actuator Extended, c) Engaged.

129

a)
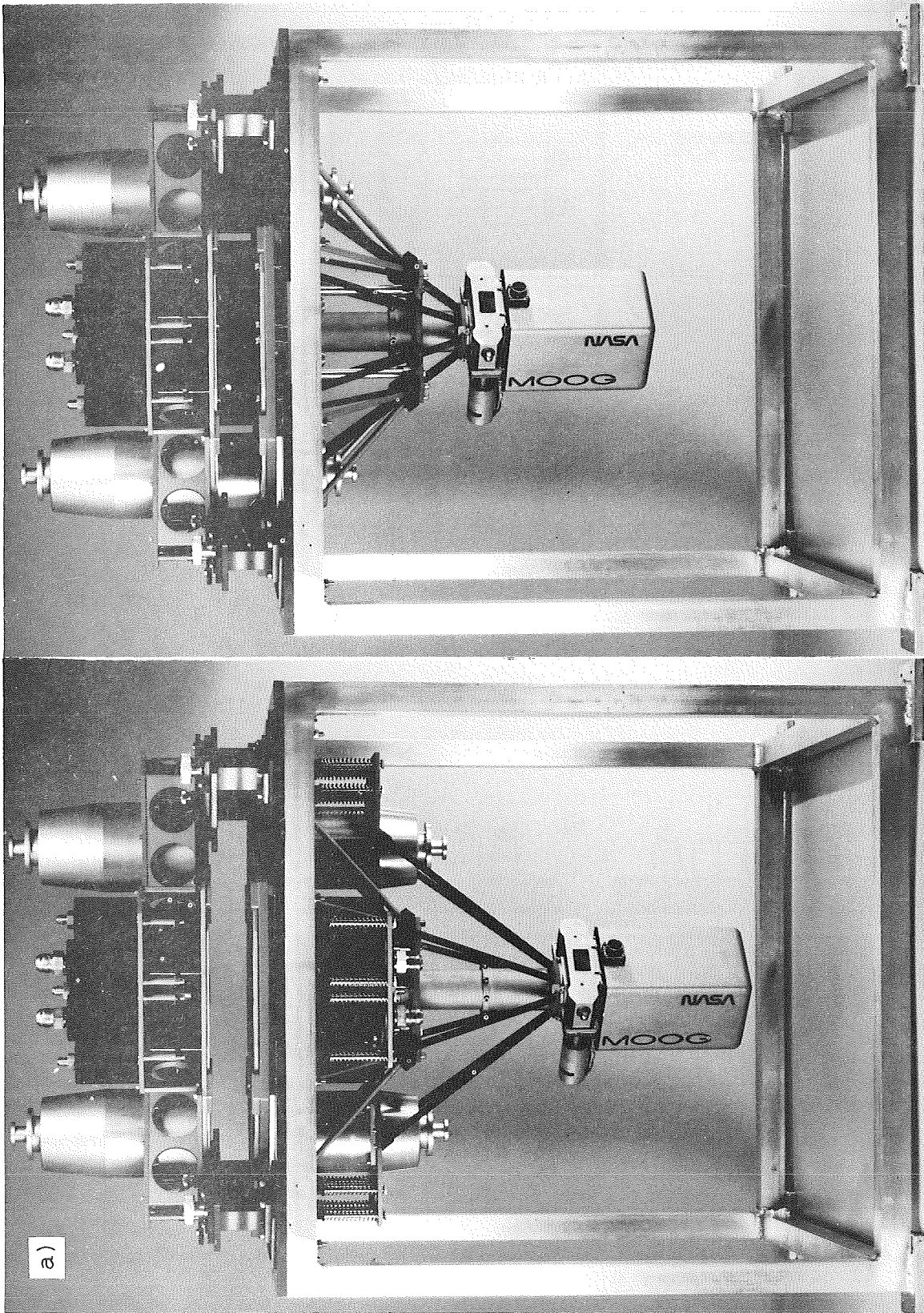
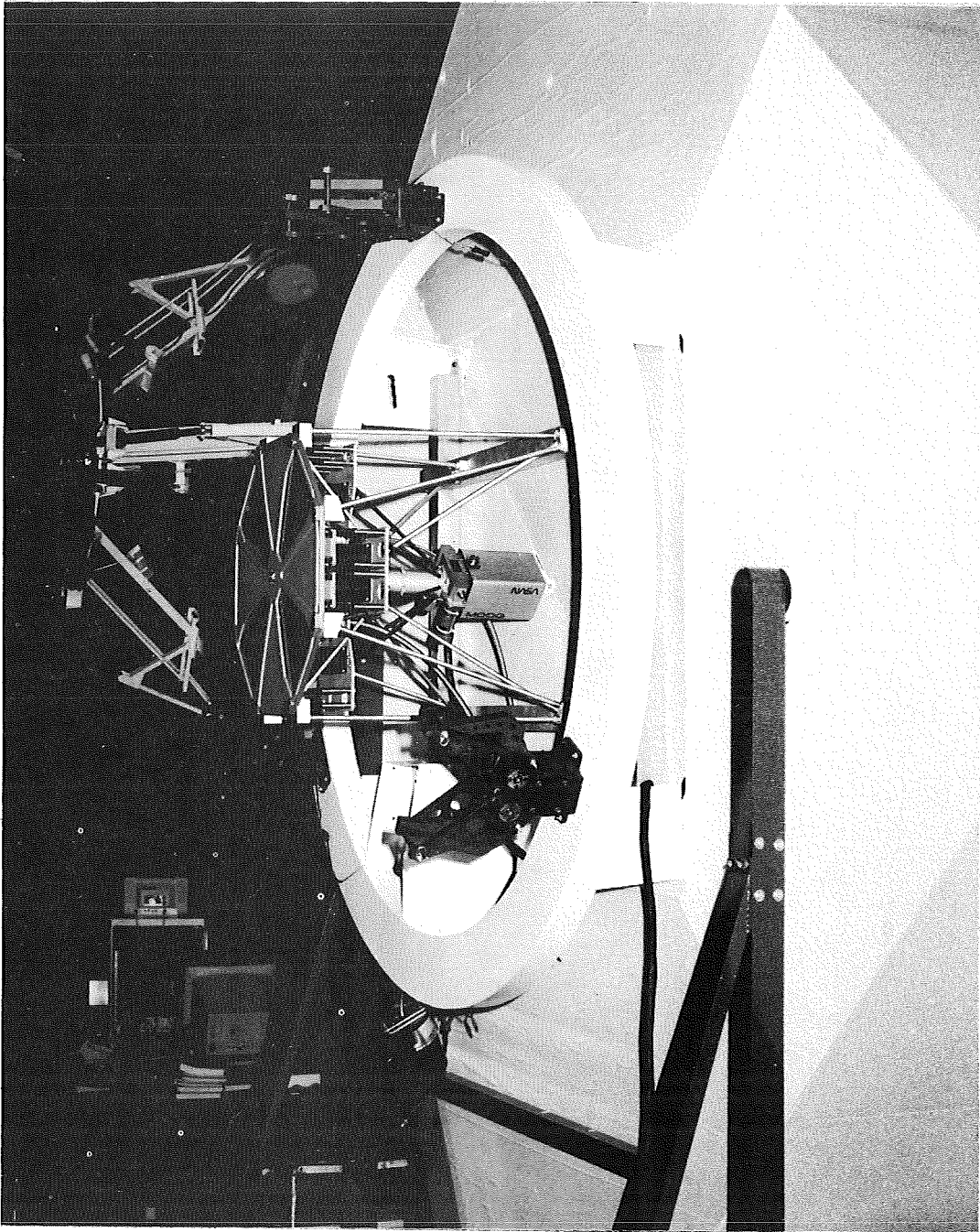Figure 5: AFIS and Spacecraft Simulator a) Disengaged and b) Engaged.

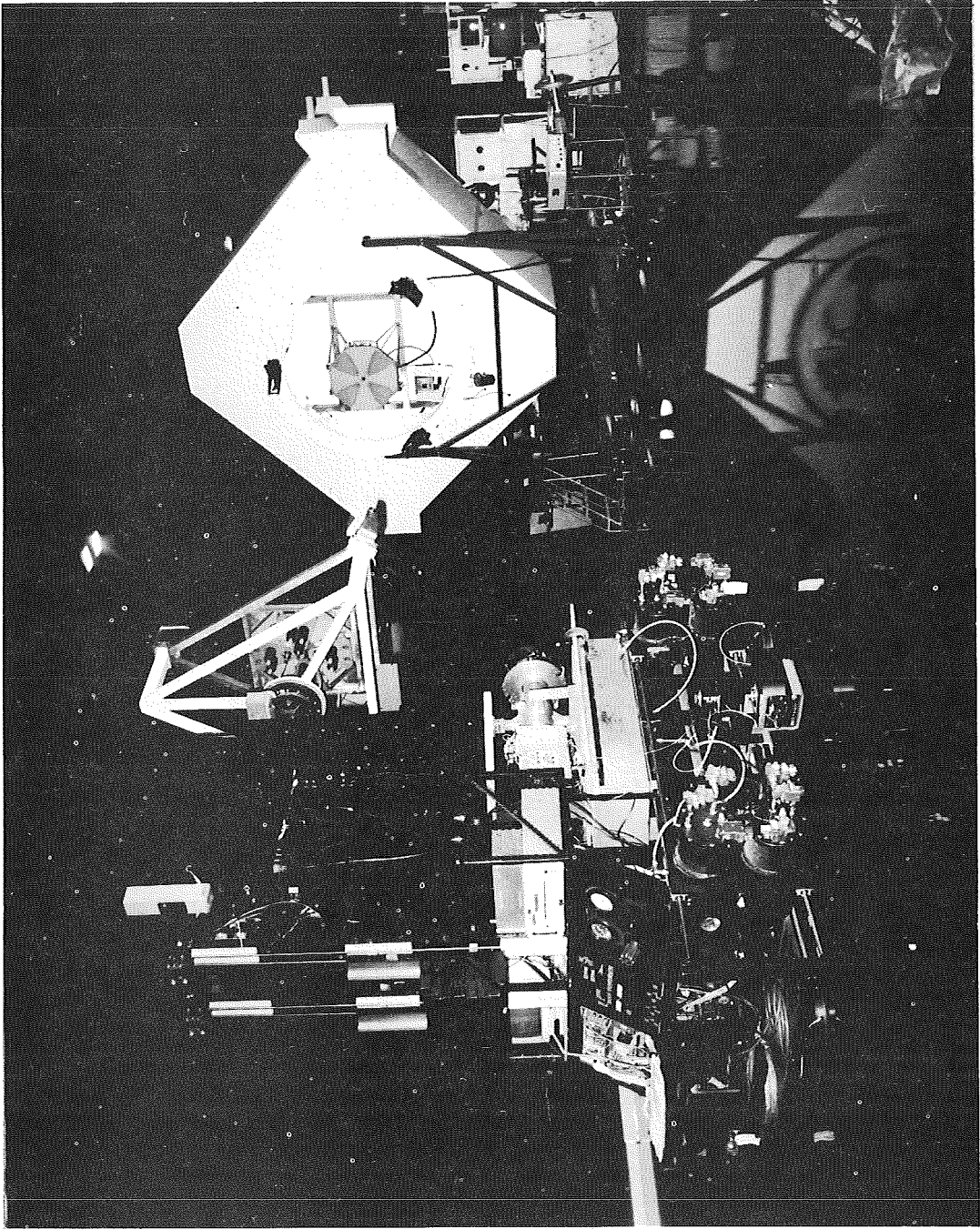Figure 6: AFIS Ingtegrated with TPDM on OMV Mock-up.

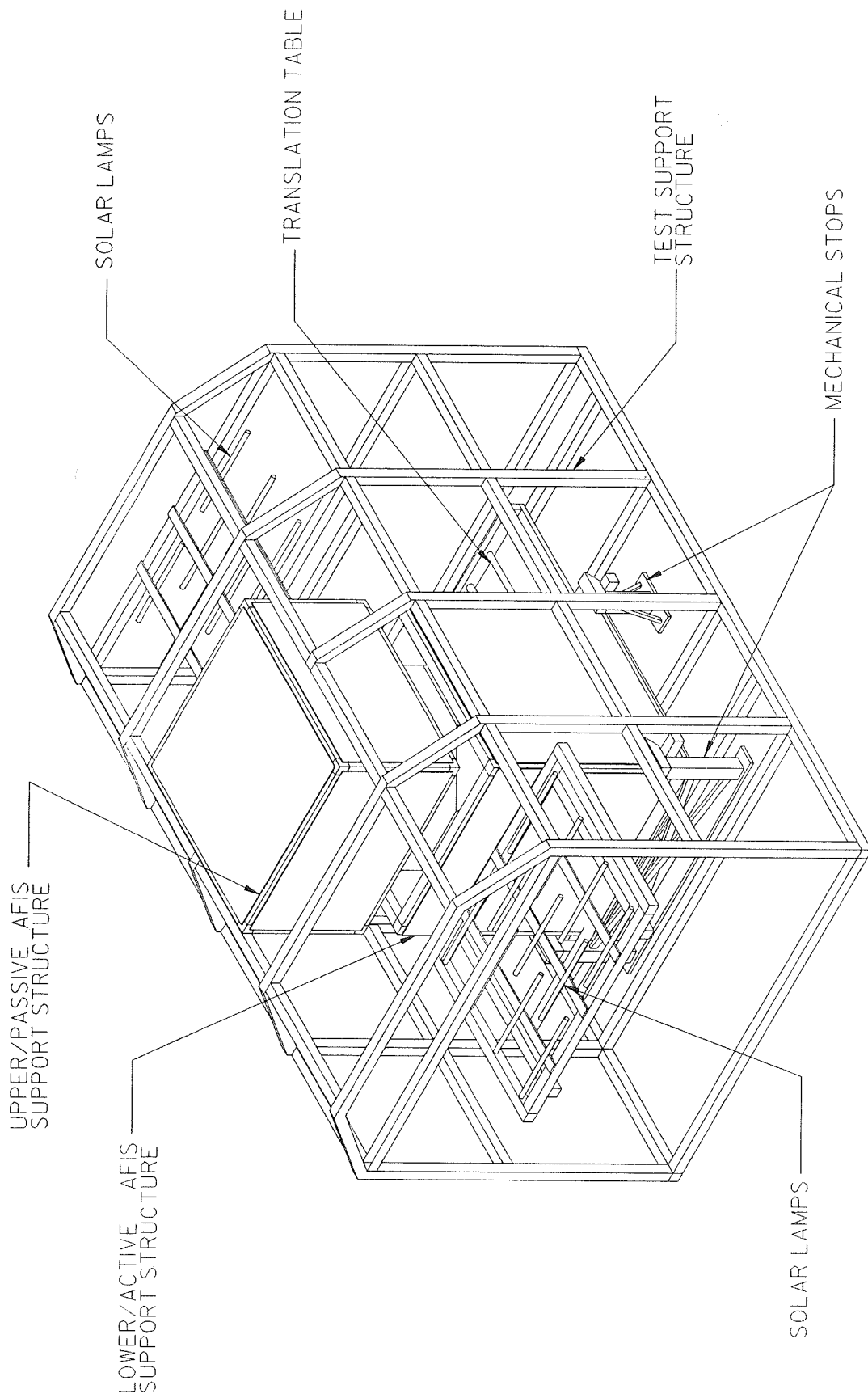Figure 7: Demonstration Docking and Fluid Transfer in Robotics Facility.

SOLAR LAMPS

TRANSLATION TABLE

TEST SUPPORT STRUCTURE

MECHANICAL STOPS

UPPER/PASSIVE AFIS SUPPORT STRUCTURE

LOWER/ACTIVE AFIS SUPPORT STRUCTURE

SOLAR LAMPS

Figure 8:   AFIS Thermal Vacuum Test Hardware with AFIS ready for Engagement.

133

TEST SUPPORT STRUCTURE
SOLAR HEATING LAMPS

TEST SUPPORT
STRUCTURE

LOWER/ACTIVE AFIS
SUPPORT STRUCTURE

TRANSLATIONAL TABLE

UPPER/PASSIVE AFIS
SUPPORT STRUCTURE

MECHANICAL STOPS
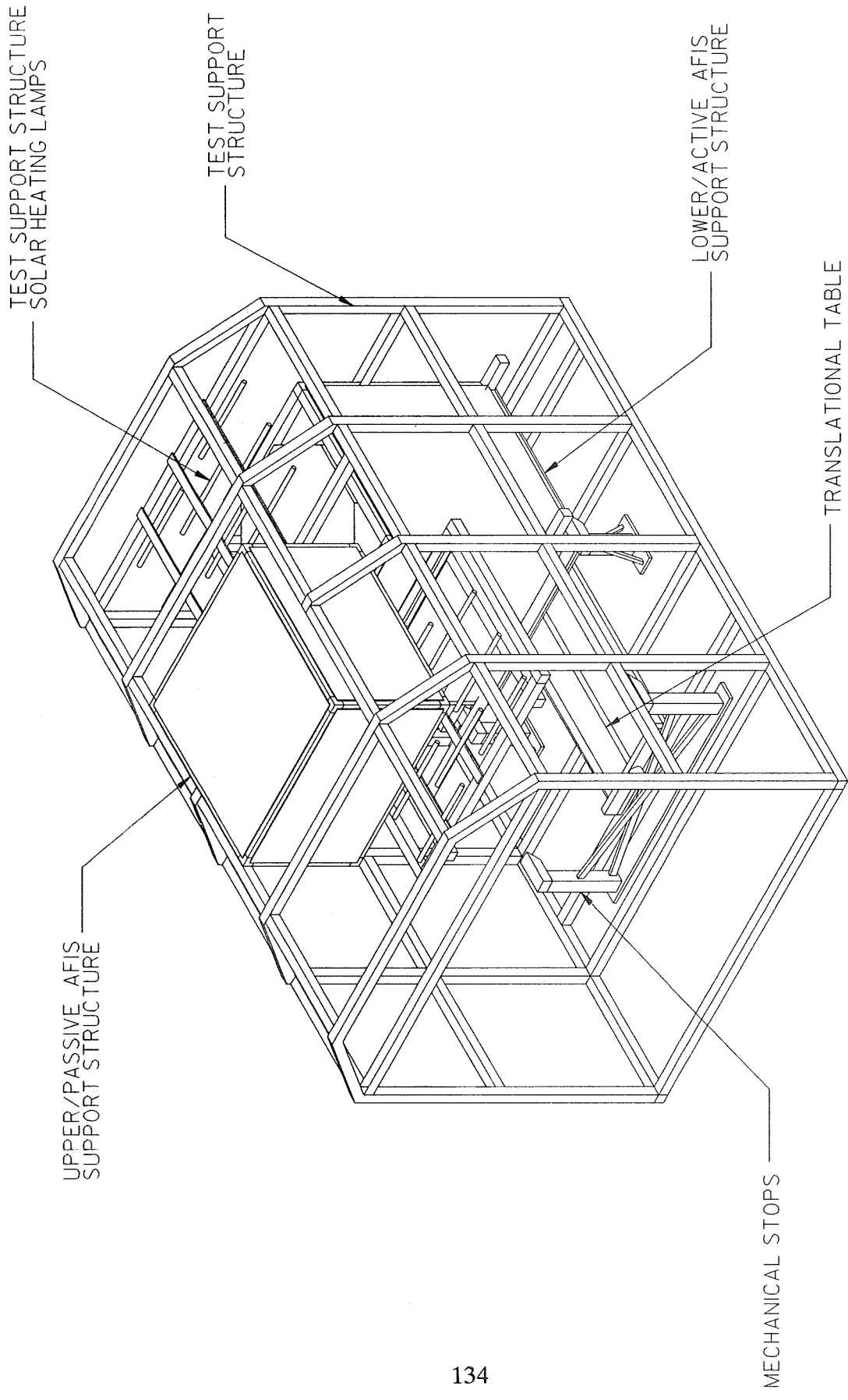
Figure 9: AFIS Thermal Vacuum Test Hardware with AFIS in Heating/Cooling Position.

UPPER/PASSIVE AFIS
SUPPORT STRUCTURE

LOWER/ACTIVE AFIS
SUPPORT STRUCTURE

MECHANICAL STOPS

SOLAR HEATING LAMPS
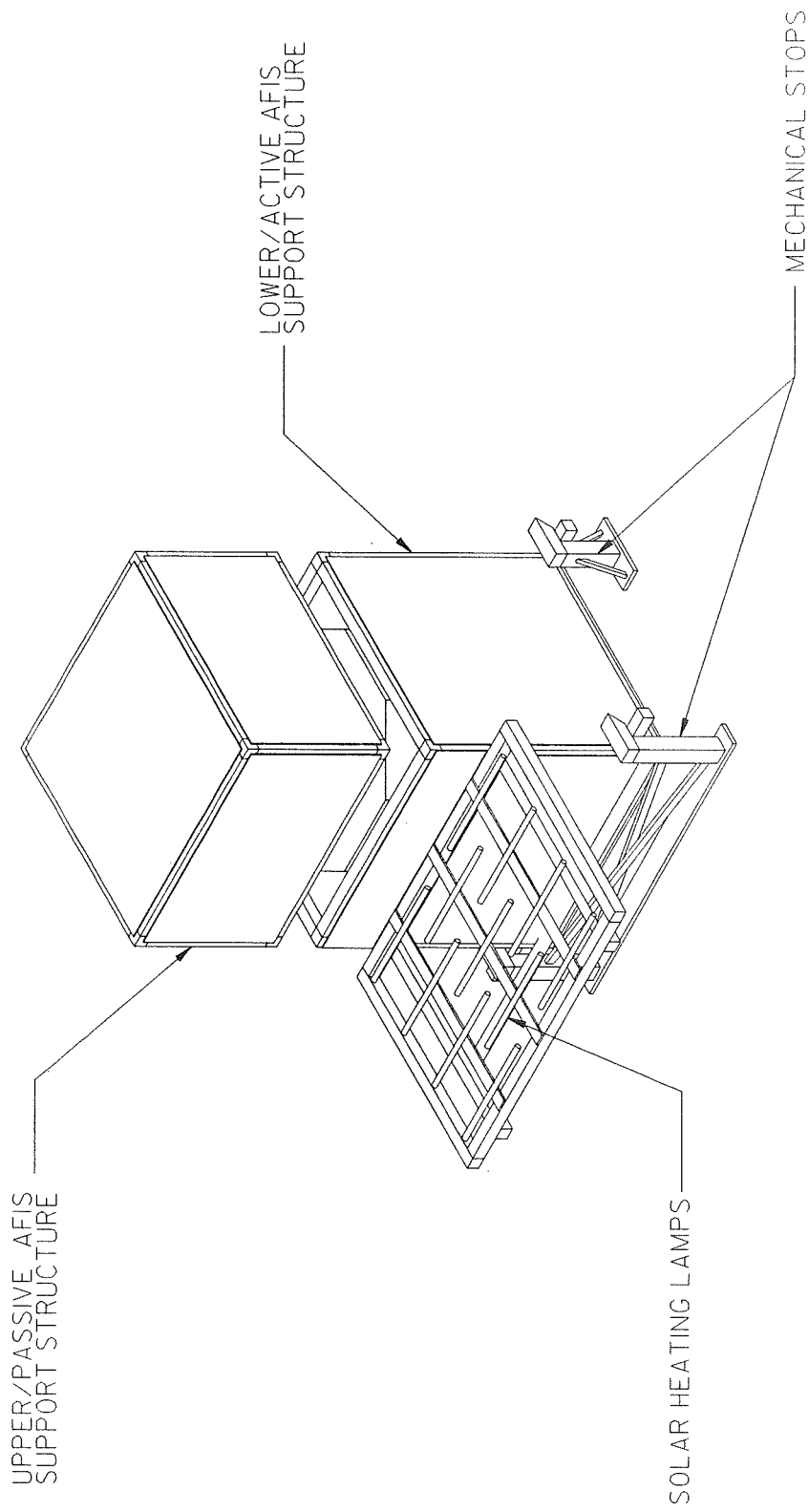
Figure 10: AFIS Support Structure.

135

METAL BAND DRIVES IN SPACECRAFT MECHANISMS

Daryl Maus*

ABSTRACT

Transmitting and changing the characteristics of force and stroke is a requirement in nearly all mechanisms. Examples include changing linear to rotary motion, providing a 90° change in direction, and amplifying stroke or force. Requirements for size, weight, efficiency and reliability create unique problems in spacecraft mechanisms. Flexible metal band and cam drive systems provide powerful solutions to these problems.

Band drives, rack and pinion gears, and bell cranks are compared for effectiveness. Band drive issues are discussed including materials, bend radius, fabrication, attachment and reliability. Numerous mechanisms are shown which illustrate practical applications of band drives.

1.0 PERSPECTIVE

1.1 Approaches to changing force and stroke

Various mechanical methods can be used to change force and stroke including gears, linkages and belt drives. Appended to this paper, are scale drawings (figures 1.1.1, 1.1.2, 1.1.3) illustrating the typical layout and part sizing for transmitting a linear input of 444 N (100 lbs) over 1.9 cm (.75") into a rotary output.

1.2 Summary of effectiveness

Each of these three approaches was evaluated for its effectiveness in small compact mechanisms transmitting relatively high loads in contamination sensitive environments. They are ranked in descending order of effectiveness for each issue.

1.2.1 Size and Weight
Band- Smallest size and weight for a given load
Rack- Gear teeth strength requirements increase size
Crank- High loads require large rollers which interfere with short lever arms

1.2.2 Efficiency
Band- 96%, from loss at axle bearing
Rack- 94%, additional loss at gear teeth interface
Crank- 88%, angular input requires more sliding surfaces creating more friction

---

* Starsys Research Corporation, Boulder, Colorado

1.2.3 Contamination
Band- Band produces no contamination
Crank- Limited to rolling surfaces
Rack- Gear teeth wear and produce particles

1.2.4 Life/wear
Band- Nearly infinite fatigue life
Crank- Higher number of sliding surfaces
Rack- Lubrication determines gear teeth life

1.2.5 Tolerance requirements
Band- Minimal
Crank- Minimal
Rack- Precision alignment of gear teeth required

1.2.6 Capability for linear to rotary transmission
Rack- Infinite angular capability
Band- 270° maximum rotation limit
Crank- 90° maximum rotation limit

1.2.7 Other limitations, advantages
Rack- Fixed output ratio, Bi-directional
Band- One direction (only pulls), variable output ratio
Crank- One direction (only pushes), variable output

2.0 DESIGNING WITH METAL BANDS

Metal band drives are easy to use. However they do have some unique design and production issues that require careful attention.

2.1 Material

The ideal metal drive band would have very high strength and a high modulus of elasticity. A thorough review of available materials and their properties led to a material with the trade name of Elgiloy. It was developed in the 1940's for watch springs. Elgiloy is a cobalt chromium nickel alloy with the following composition:

CO 39/41%
CR 19/21%
NI 14/16%
MO 6/8%
MN 1.5/2.5%
C 0.15%max
BE 0.10%max
FE balance

Elgiloy is available as strip, ribbon wire, rod and cable. Its mechanical properties are derived from a combination of cold work and subsequent heat treatment. This material processing produces thin bands with very high strength.

Ultimate tensile strength - 1,724 to 2,414 MPa (350 Kpsi)
Hardness (HRC) - 45 to 60
Elastic modulus - up to 206,910 MPa (30,000,000 psi)
Fatigue life - excellent (see fatigue, S-N curve)
Corrosion resistance - Excellent (MSFC-SPEC-250)
Stress corrosion cracking - (A rating MSFC-SPEC-522)
Compatibility - GOX,LOX,N_2O_4,HDZE,H_2
Magnetic permeability - 1.00004 at 25°C
Coefficient of thermal expansion - 15.17 x 10^6 per °C
Temperature range for normal performance - -150°C to 450°C

For comparison titanium has a tensile strength of only 827 MPa (120,000 psi) and a modulus of 114,000 MPa (16,500,000 psi).

2.2   Bend radius

Spacecraft mechanisms frequently have severe envelope restrictions. A band drive provides a good solution to these restrictions. Minimizing the overall size of a band drive can require using the smallest possible cam diameter and band bend radius. The graph shown in figure 2.2 illustrates the relationship between bend radius and yield strength for bands typically used in Starsys Research mechanisms.

We typically allocate 50% of the band yield strength to load transmission and use the remaining strength for bending stress. Final selection of bend radius, band thickness and band width can be made after assigning their relative priority in the design and band strength margin requirements. It should be noted that by simply cold forming the bands to 2x the bend radius bending stress can be reduced by 50%.

2.3   Fatigue

Elgiloy bands have excellent fatigue resistance. The S-N curve shown in figure 2.3 illustrates this.

2.4   Attachment

Mechanical methods of attachment are superior to other methods in fatigue and strength. Spot welding, soldering and brazing can be used but they weaken the material. A simple, reliable method of mechanical fastening was developed and is used in the mechanisms illustrated. The drawing shown in figure 2.4.1 is from a telescope launch lock. It illustrates both flat and radial attachments.

139

The geometry for attachment is shown in figure 2.4.2. The following formulas relate to the figure. Band stress at the thinnest point in the attachment is equal to the load carried divided by the sum of the width minus the hole diameter times the thickness, $S=F/(W-D)xT$.

The length of the band end from the end of the band to the attachment hole center is ideally a minimum of 2 times the diameter. Shorter lengths have been used but they significantly reduce the load carrying capability of the attachment (see Testing).

Band bearing stress is equal to the load divided by the hole diameter times the thickness, $S=F/(DxT)$. Because band attachment is typically sized to carry 50% of the yield stress of the band, the hole diameter should be from 1/2 to 1/3 the band width. This is consistent with allowing 50% of the absolute stress for bending.

Bearing stress of the pin on which the band bears are high. The band clamp design used induces tri-axial stress which increases the effective strength of the material. Only minor deformation has been seen with 303 stainless steel pins.

2.5 Fabrication

Because the band shape is so simple, the first band components were fabricated by conventional machining technology. The band material was clamped between two pieces of aluminum and shaped with carbide tooling. While good quality bands were produced, this method was difficult and tooling wore out quickly. Practical tolerances were limited to ± 50 microns (.002").

Because of these difficulties subsequent band components were fabricated by Wire Electrical Discharge Machining or WEDM. Starsys Research regularly uses WEDM for cutting complex shapes in electrically conductive materials. This fabrication process uses the electrical arc from a wire held at both ends and submerged in a water solution to remove material. It easily produces parts with tolerances of ±5 microns (.0002").

Developing a process to fixture the thin band material was straight forward. After machining, minimal deburring of the edges is required. The parts produced by WEDM are of very high quality and accuracy.

2.6 Design and assembly

Metal band drives function well with easily obtained tolerances, typically ±.127 mm (.005") for most mechanism parts. Attachment holes and through pins are held to ± 13 microns (.0005"). Be careful to control fillet radii of integral clamp and pin assemblies so they do not interfere with clamping.

Since the bands tend to adjust themselves to proper alignment, only normal visual alignment is required during assembly. Care must be taken to properly align and

secure attachment clamps. 2-56 and 4-40 screws were used to secure band clamps.

Metal band deformation or stretch from loads is minimal. A band loaded to 25% of its yield strength would stretch .2%.

3. FAILURE MODES AND TESTING

3.1   Attachment testing

Testing was performed to verify the performance of the band drive designs. The majority of the testing focused on band attachment. Bands were fabricated and tested to failure. The following observations summarize the testing.

1) When the band clamps were tight, .56 to .06 N-m (5 to 0.5 in-lb) torque, failures occurred at 91 - 83% of the design yield strength of the attachment.
2) When the band clamps were loose, .08 cm (.030") gap, failure occurred at 66% of the design yield strength of the attachment. Failures began with buckling of the band in the bearing area. Buckling of the band concentrated stress in adjacent areas and allowed the attachment pin to tear out of the band.

These bands had a band end length to attachment diameter ratio of 1.5 to 1.0. A longer attachment length would perform better. Testing to verify band attachment strength is highly recommended.

3.2 Corrosion

The corrosion resistance of Elgiloy is excellent, as good or better than other metals typically used on spacecraft. Its galvanic potential is cathodic or protected, similar to passivated chromium stainless steel.

3.3   Reliability/Redundancy

The reliability of single bands should be established by component testing. Redundant bands have been successfully utilized on two mechanisms. In one design, the bands were slotted on one end and therefore not constrained in motion. In the other, the bands move through two reverse radii which equalize band length.

Because of band elasticity and stretch, parallel bands will accommodate normal variations in tolerance and still distribute loads. Burnishing molydisulfide onto the band surfaces that contact each other eliminates visible abrasion and wear.

4. CONCLUSION

Metal band drives offer several advantages including; small size, high efficiency, low contamination and long life. They provide unique solutions to difficult problems for example, providing variable output from a constant input. They are straightforward to design and easy to fabricate.

Because of its high tensile strength and other properties Elgiloy is an excellent choice of material for the drive band in these mechanisms. Bands should be analyzed for bending stress and attachment design should be tested.
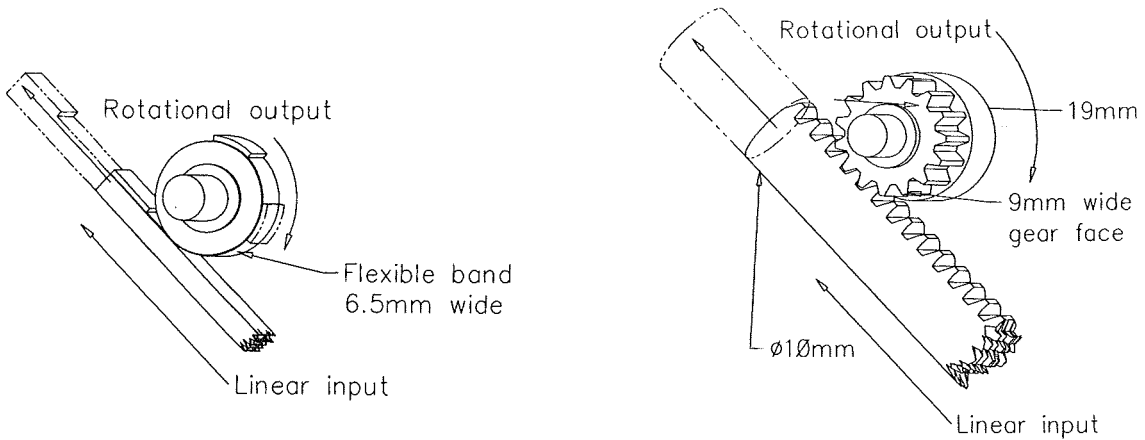
Figure 1.1.1
Belt drive - Metal band drive
Output: 3.39 Nt-m (30 in-lbs) over 137°
Efficiency: 96%

Figure 1.1.3
Gears - Rack and pinion
Output: 3.28 Nt-m (29 in-lb) over 137°
Efficiency: 93%
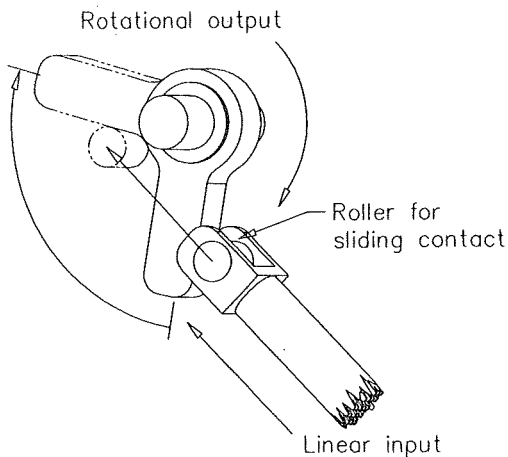
Figure 1.1.2
Linkage - Bell crank
Output: 3.73 Nt-m (33 in-lb) over 90°
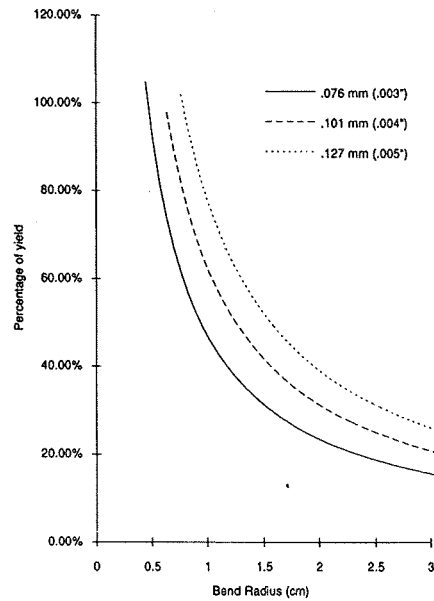(maximum efficient rotation)
Efficiency: 88%

Figure 2.2
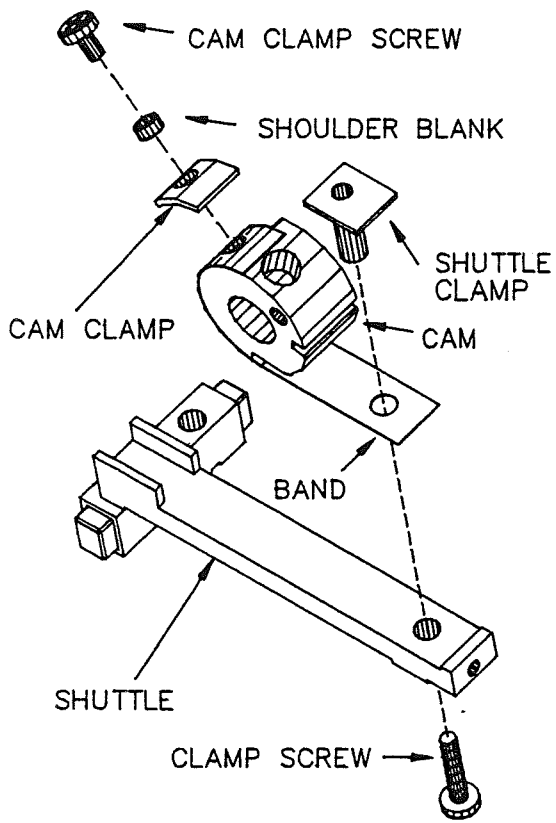Yield strength vs. Bend radius in Elgiloy bands

142

CAM CLAMP SCREW

SHOULDER BLANK

SHUTTLE CLAMP

CAM CLAMP

CAM

BAND

SHUTTLE

CLAMP SCREW

Figure 2.4.1
Flat and radial band attachment

MPa	KPSI
1793	260
1655	240
1517	220
1379	200
1241	180
1103	160
965	140
827	120
689	100
551	80
414	60
276	40

Stress

10^4 10^5 10^6 10^7
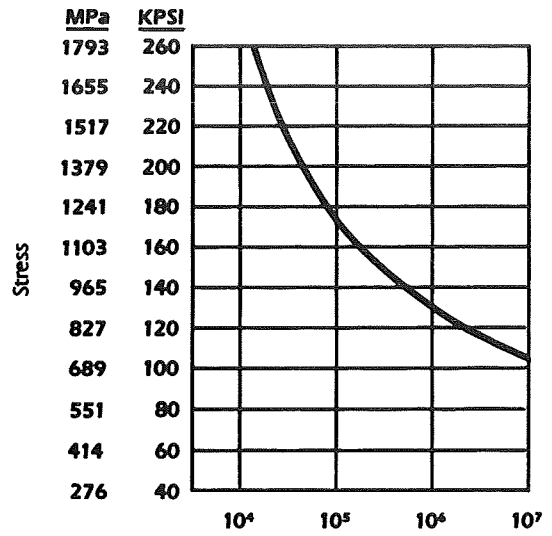
Figure 2.3
Number of cycles to failure from reverse bending

Width "W"

Load "F"

Length of band end "L"

Attachment hole "D"

Thickness "T"
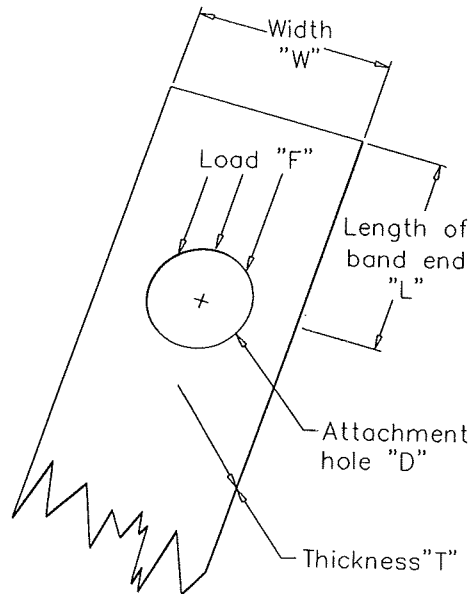
Figure 2.4.2
Band attachment geometry
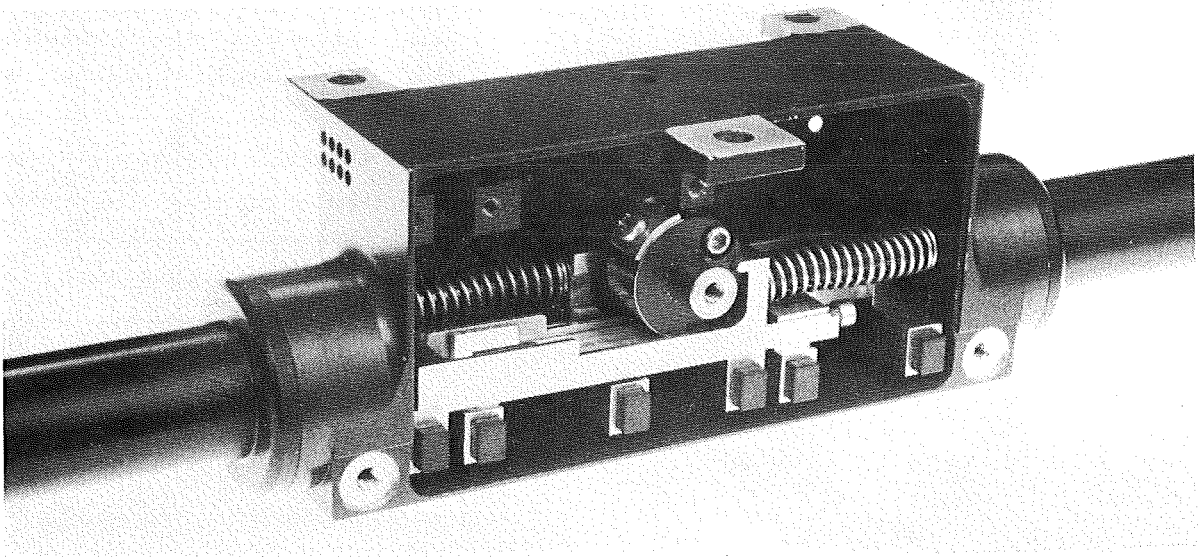
143

4. MECHANISMS

Figure 4.1 - Telescope launch lock for UVCS on SOHO-MAMA - Translates linear input to rotary output
Input: 2x 444 Nt (100 lbs) over 14 mm (.55") extension
Output: 2x 1.7 Nt-m (15 in-lb) over 90° plus latching
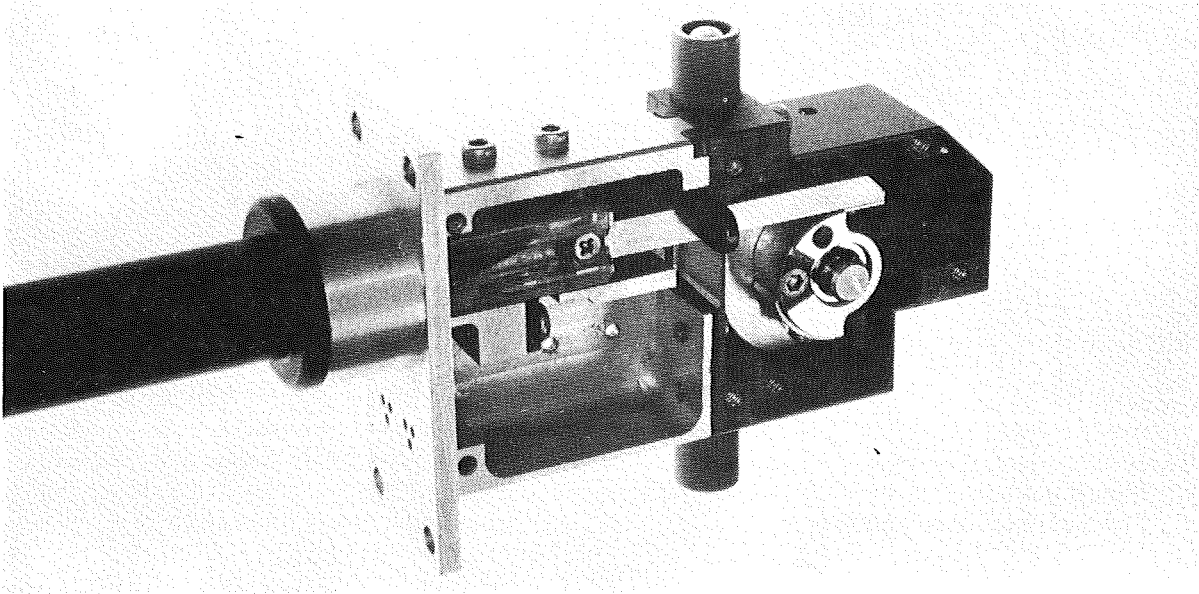Bands: Two .076 mm (.003") by 6.7 mm (.265") wide

Figure 4.2 - Cover operator for UVI on POLAR - Amplifies stroke
Input: 444 Nt (100 lbs) over 14 mm (.55") extension
Output: 222 Nt (50 lbs) over 19 mm (.75") extension plus latching and spring retraction
Bands: Input .076 mm (.003") thick by 7.6mm (.300") wide, output .076 mm (.003") thick by 5.8 mm (.230") wide
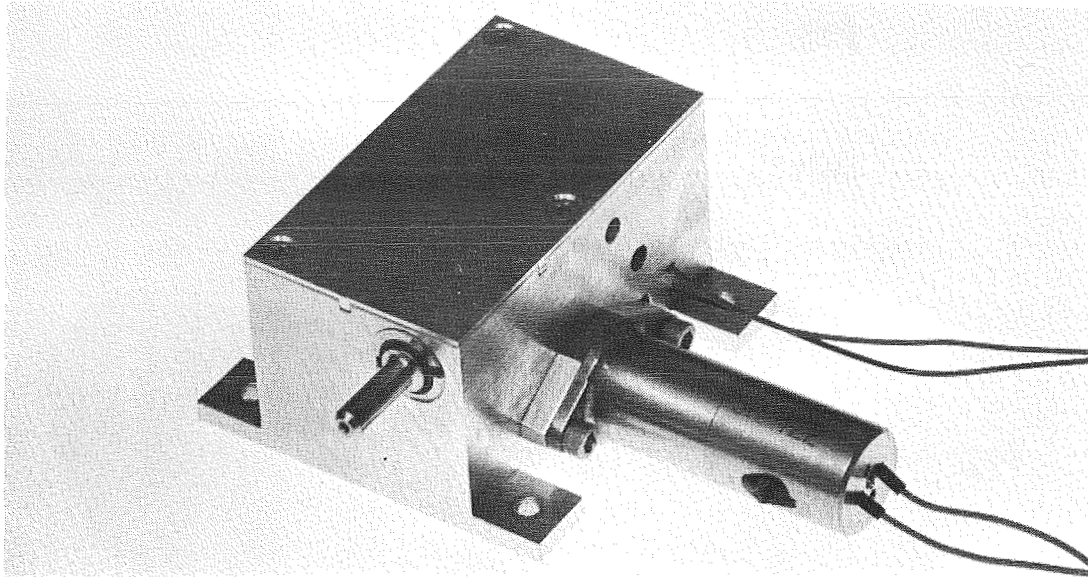
144

Figure 4.3 - Scan mirror lock for TIR on ASTER and launch lock for SWAN on SOHO-MAMA - Pin puller
Input: 311 Nt (70 lbs) over 6.4 mm (.25") extension
Output: 222 Nt (50 lbs) over 8.1 mm (.32") retraction
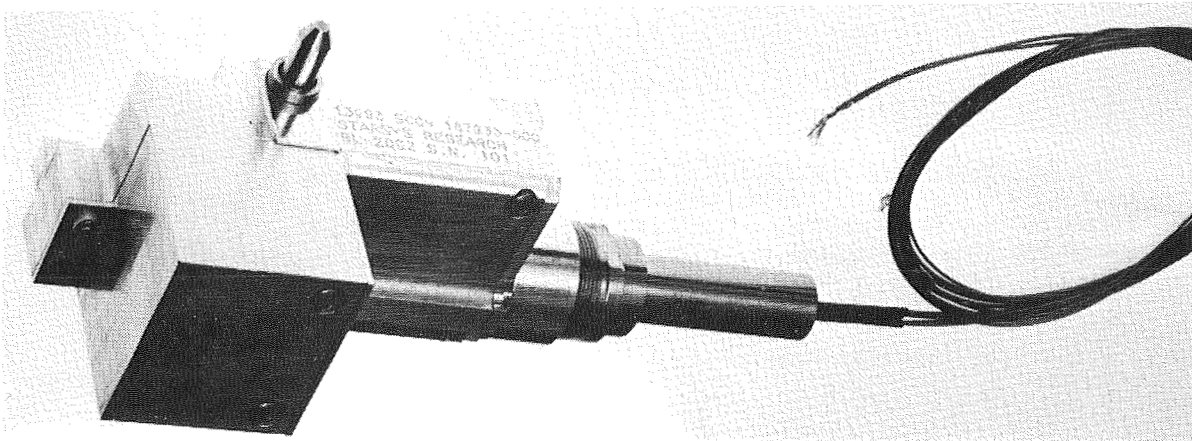Bands: Two .076 mm (.003") thick by 5.7 mm (.225") wide

Figure 4.4 - Mirror and occulter lock for UVCS on SOHO-MAMA - Turns push into pull
Input: 444 Nt (100 lbs) over 14 mm (.55") extension
Output: 222 Nt (50 lbs) retraction over 11 mm (.45") plus latching and spring extension
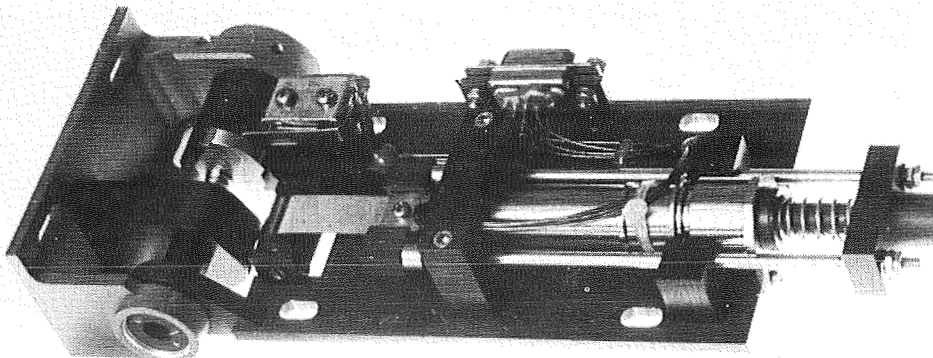Bands: Redundant .076 mm (.003") thick by 7.6 mm (.300") wide

Figure 4.5- Powered hinge for APEX - Variable torque output
Input: 533 Nt (120 lbs) over 19 mm (.75") extension
Output: 3.4 to 6.8 Nt-m (30 to 60 in-lb) over 90°
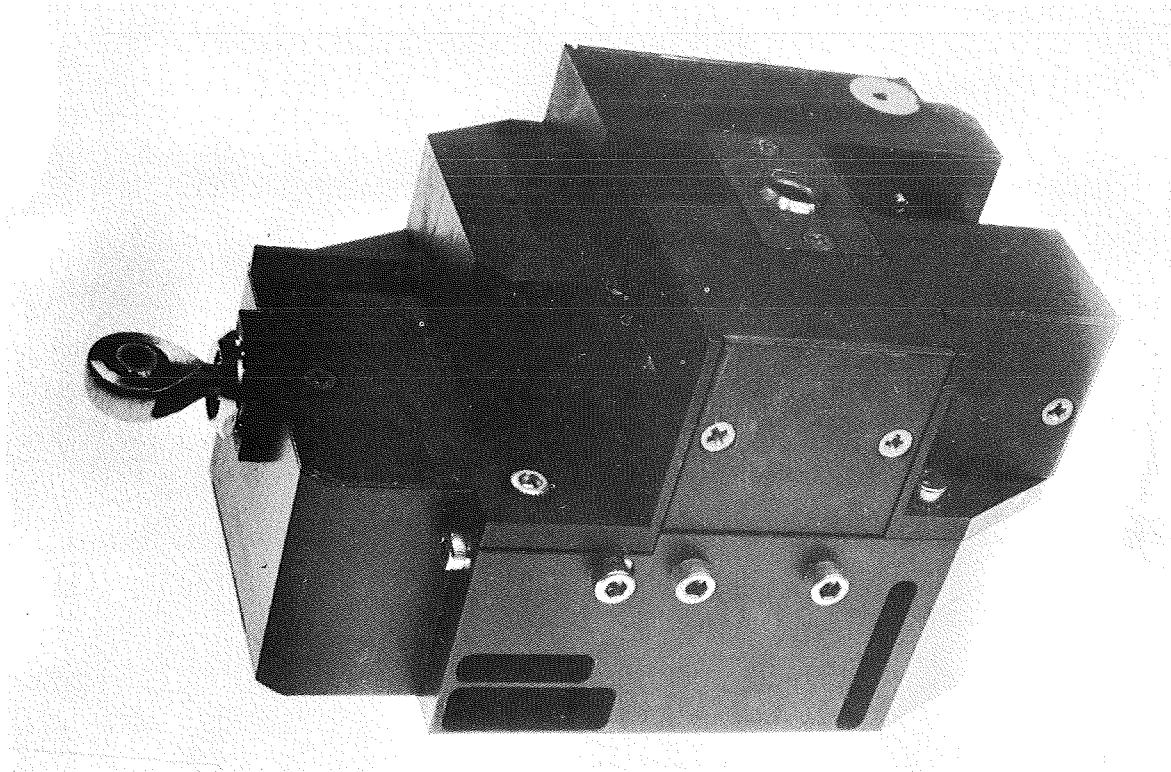Bands: Redundant .076 mm (.003") thick by 10 mm (.400") wide

145

Figure 4.6- Detector cover operator for UVCS & SOHO-MAMA - Stroke doubler
Input: 2,224 Nt (500 lbs) over 16 mm (.65") extension
Output: 667 Nt (150 lbs) over 32 mm (1.25") plus latching and spring extension
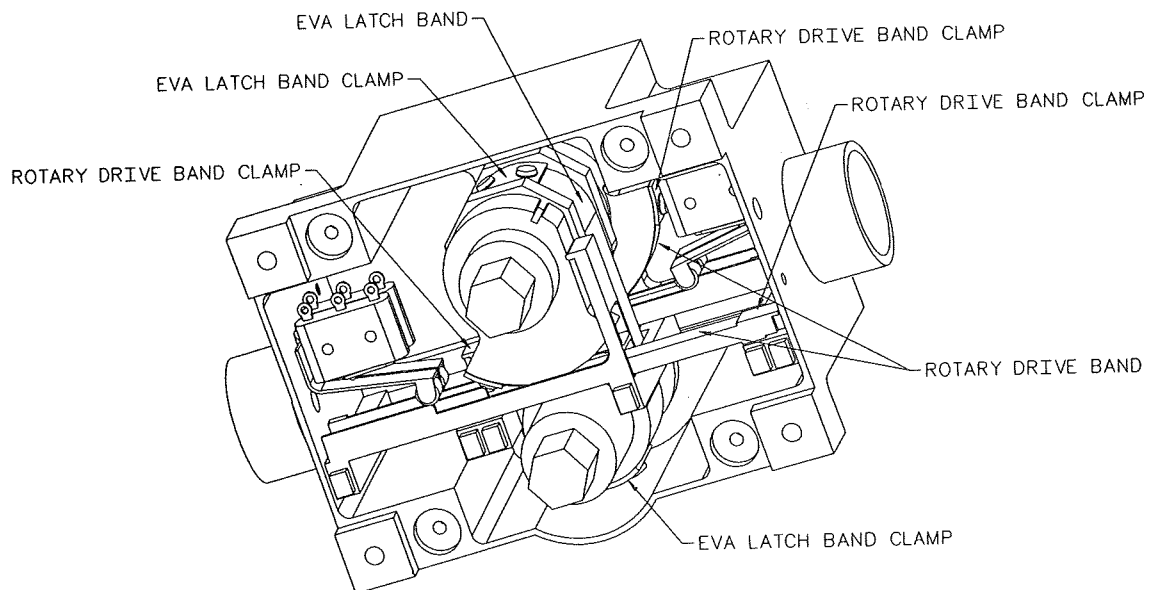Bands: Two .127 mm (.005") thick by 7.62 mm (.300") wide

Figure 4.7 - Launch lock with EVA override for for Space Station Freedom - Rotary to rotary
Input: 2x 444 Nt (100 lbs) over 19 mm (.75") extension
Output: 2x 333 Nt (75 lbs) over 45° with EVA override
Bands: Two .127 mm (.005") thick by 6.7 mm (.265") wide and two .127 mm (.005") thick by 15 mm (.580") wide

146

N94- 29638

/ 9 9 4 0 2 5 7 3 5

POINTING MECHANISMS FOR THE SHUTTLE RADAR LABORATORY

Gerald W. Lilienthal, Argelio M. Olivera, Lori R. Shiraishi* 4 3 4 6 6 7

ABSTRACT

The Shuttle Radar Laboratory (SRL) is scheduled for launch in December of 1993 on the first of its two missions. The SRL has three major radar instruments: two distributed phased-array antennas, which make up the Spaceborne Imaging Radar-C System (SIR-C) and are capable of being electronically steered, and one X-Band Synthetic Aperture Radar (X-SAR), which is pointed mechanically by a suite of mechanisms. This paper will describe these mechanisms and summarize the development difficulties that were encountered in bringing them from the design stage through prototype development and protoflight testing.

INTRODUCTION

The Shuttle Radar Laboratory (SRL) is a Space Transportation System (STS or Space Shuttle) borne imaging radar laboratory that will be used in global scientific studies in geology, hydrology, ecology, oceanography and meteorology. The radar laboratory is the most massive flight instrument system ever designed, fabricated and assembled at the Jet Propulsion Laboratory (JPL). The SRL's mass is 10,400 kg, including electronics, and it measures 12 meters by 3.5 meters (Figure 1). It is made up of three integrated radar instruments:

o Two U.S. radars, designated the Spaceborne Imaging Radar (SIR-C), which are fixed to the main Antenna Core Structure (ACS). These phased array antennas are fixed relative to the Space Shuttle coordinate system and are electronically steered.

o The X-Band Synthetic Aperture Radar (X-SAR), which was developed jointly by the German Space Agency and the Italian Space Agency. This antenna is steered mechanically.

Early Mechanisms and the SRL Systems Design

The SRL has its roots in two prior STS instrument laboratories called SIR-A and SIR-B which were launched in 1982 and 1984, respectively (Figure 2). These instruments were smaller than the SRL and and the last, SIR-B, was constructed so that the panels could be folded up onto a pallet, thus saving space in the STS bay for additional

---

*Jet Propulsion Laboratory, California Institute of Technology, Pasadena, California.
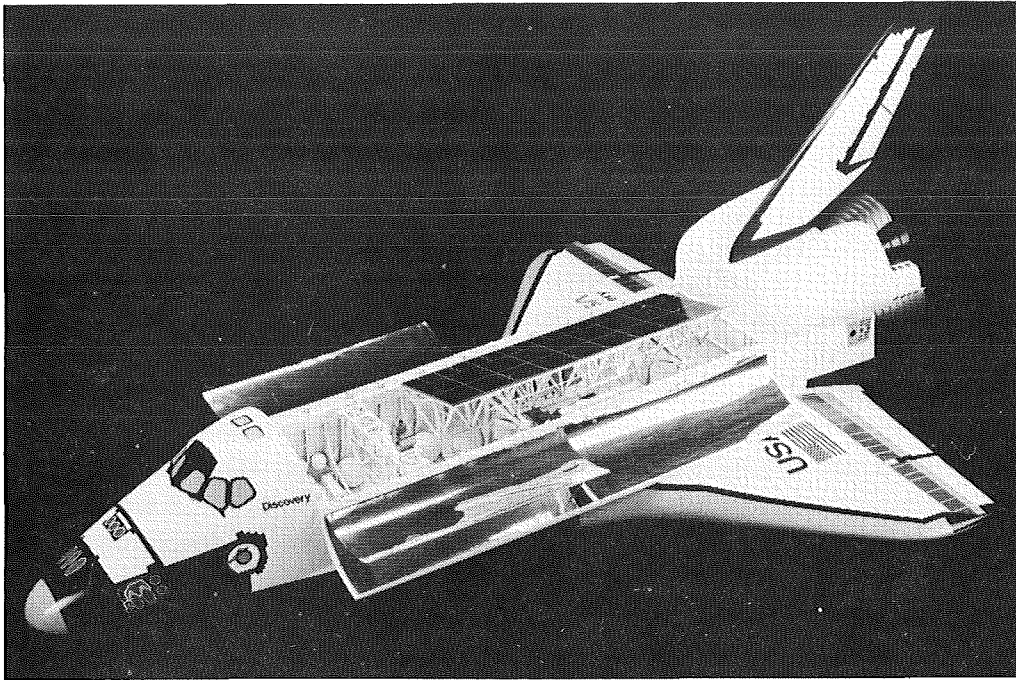
Figure 1. Model of the Shuttle Radar Laboratory Integrated Into the STS Bay

payloads. The forward and aft leaves deployed 180 degrees from their stow position and then the tilt actuator would point the antenna to the desired angle. It was decided that a similar design approach would be followed for the SRL. Significant difficulties were encountered, however, because of several differences between it and the earlier laboratories and because of new, post-Challenger STS constraints.

The SRL is considerably larger than the earlier Laboratories. The total area of its radar panels is 42 sq. meters in comparison to SIR-B's 14.9 sq. meters, and the total masses are 10,400 kg and approximately 3,500 kg, respectively. Simply scaling the hardware would not be sufficient since the stiffness and strength did not increase as quickly as the mass.

As the work progressed, it quickly became apparent that the structure holding the SIR-C radar panels was not sufficiently stiff to prevent contact between the folded, inner leaf panels and the fixed and outer leaves under launch and landing loads. Since the inner leaves were sandwiched between the fixed and
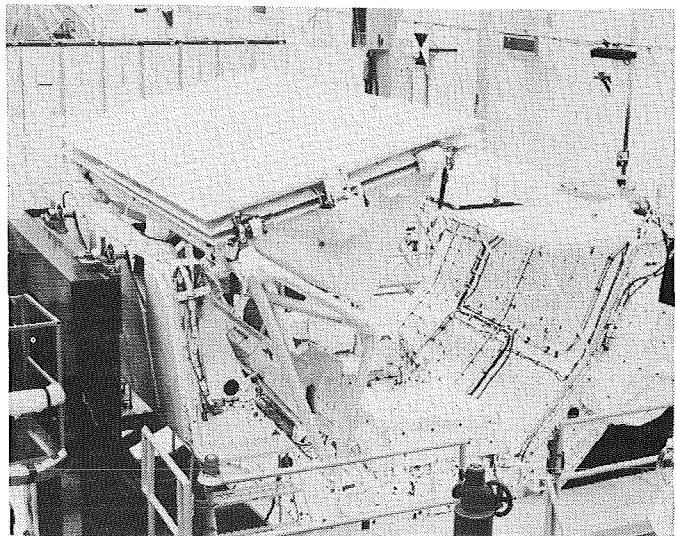

Figure 2. The SIR-B Antenna Assembly

148

outer leaves, there was little room to increase the stiffness of the supporting structure. It was decided that the least costly change would be to introduce springs with hardstops between the panels in an effort to control the deflections. Many sizes and placements of the springs were tried until the dynamic model confirmed that a configuration had been found that would control the deflections adequately. As these springs became progressively stiffer, the latching mechanisms required to preload them became larger. In addition, the original hinges were found to have inadequate stress margins and the tilt actuators too low a torque margin.

Estimated completion costs were escalating rapidly. The total number of mechanisms and their relative positions can be seen in Figure 3. Finally, it was determined that the number and position of the springs that were necessary to prevent contact between the radar panels were very sensitive to minor changes in the structure; changes that would probably be necessary as the design work progressed. Thus, not only were the present costs high, but we would be chasing the design downstream with potentially large schedule and cost risks. The folded design was considered too risky, and we began a parallel investigation to determine the feasibility of an unfolded design that would allow us to add considerable structural supporting members to the panels and eliminate some of the mechanisms. The initial results looked promising, and with that assessment, we traveled to NASA headquarters with the proposal. It was accepted and we were given permission to start over and develop an unfolded design that would take up nearly the entire STS bay for the mission. (A small volume was still available in which the ASTROS Instrument would fly.)

This change in the system configuration reduced the required number of mechanisms from a total of 29 (9 different types) to a total of 12 (7 different types). They were, however, going to be massive in order to tilt such a large antenna and latch it securely in place for launch and landing.

It was then determined that the SIR-C antennas could be rigidly fixed within the shuttle bay at a 14° inclination. They could be electronically steered in this

Figure 3. Baseline Mechanism Schematic for the Folded Design

orientation without significant loss of science, and only the long, narrow X-Band antenna would need to be tilted.

The X-Band antenna would still violate the dynamic envelope of the shuttle bay doors when operated through the data collection range of tilt angles. It thus would still need to be pointed by a suite of mechanisms that would have to carry the designation of "STS
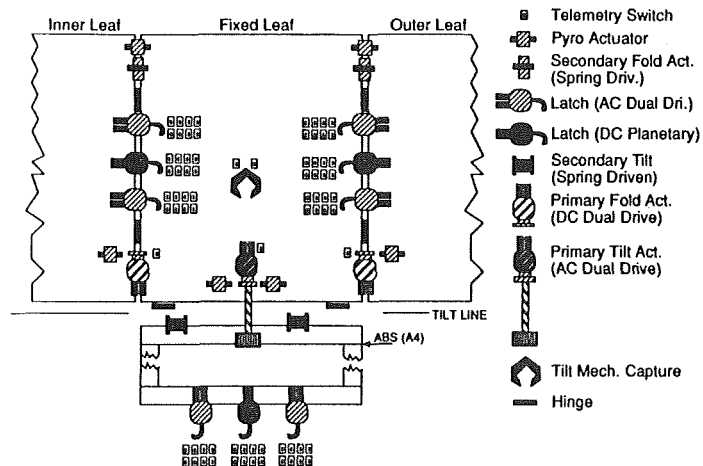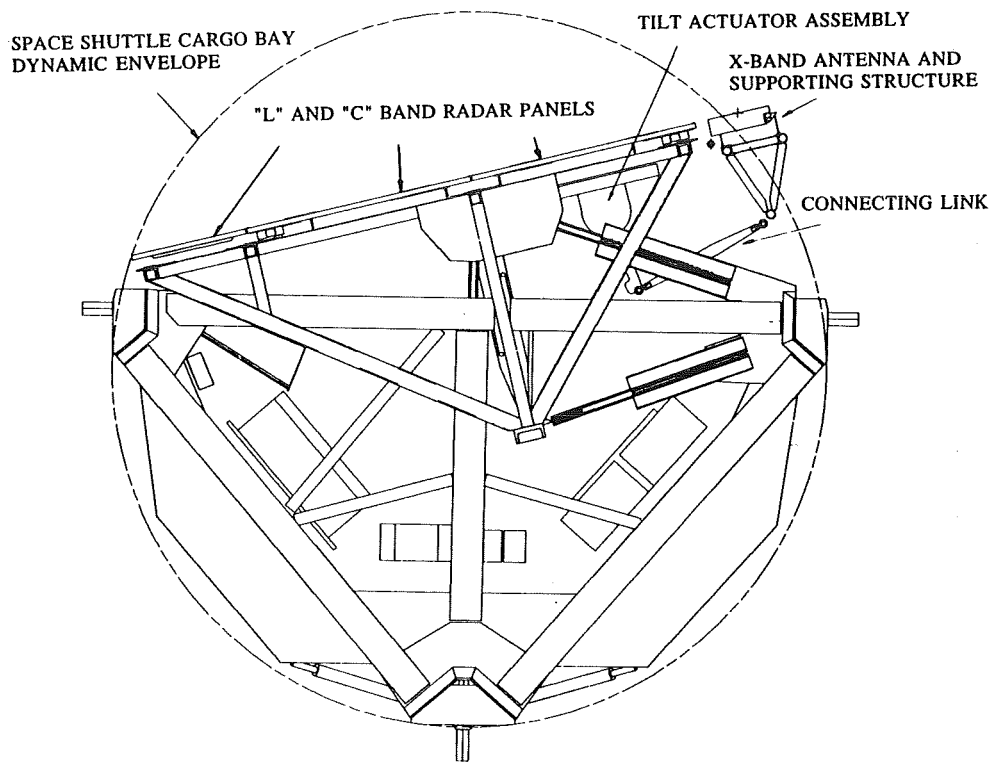
Figure 4. SRL Intrusion Into the Shuttle Door Radiator Dynamic Envelope

Safety Critical" (Figure 4). Now, however, they were fewer in number and could be smaller.

The antenna needed to be capable of being successfully stowed away even if two independent failures were to occur. Douglas Packard, who developed the JPL Dual Drive Actuator, proposed using the same technology in a larger, triple redundant drive that he called the Tri-Drive. This actuator would have three independent and redundant drives instead of two. A single actuator assembly could now be used, eliminating all of the devices that were required to switch from one stowing mechanism to another.

DEVELOPMENT OF THE FLIGHT MECHANISMS

The mass of the X-Band antenna and its supporting structure is about 318 kg, with a center of gravity offset of 26 cm (10 in.), producing an 805 N-m (7210 in.-lb) maximum torque in a 1 G field. The maximum pull-out torque is about 90 N-m (800 in.-lb) during launch and landing. The maximum hinge-line torque was estimated to be about 34 N-m. We had the choice of designing and building separate latching and pointing mechanisms or designing a tilt actuator that could fulfill both functions. We decided to take the latter approach and implemented it by combining the Tri-Drive dual fault-tolerant actuator with a four-bar linkage arrangement that would put the crank in a bottom dead-center position at stow (Figure 5). This protects the gear train of the actuator from significant launch or

landing loads and reduces the possibility of accidental deployment. Ground support equipment costs and complexity were reduced further by designing an actuator that could articulate the antenna in 1 G to support ground testing of the radar and easily verify that the safety-critical mechanisms functioned properly immediately before launch.
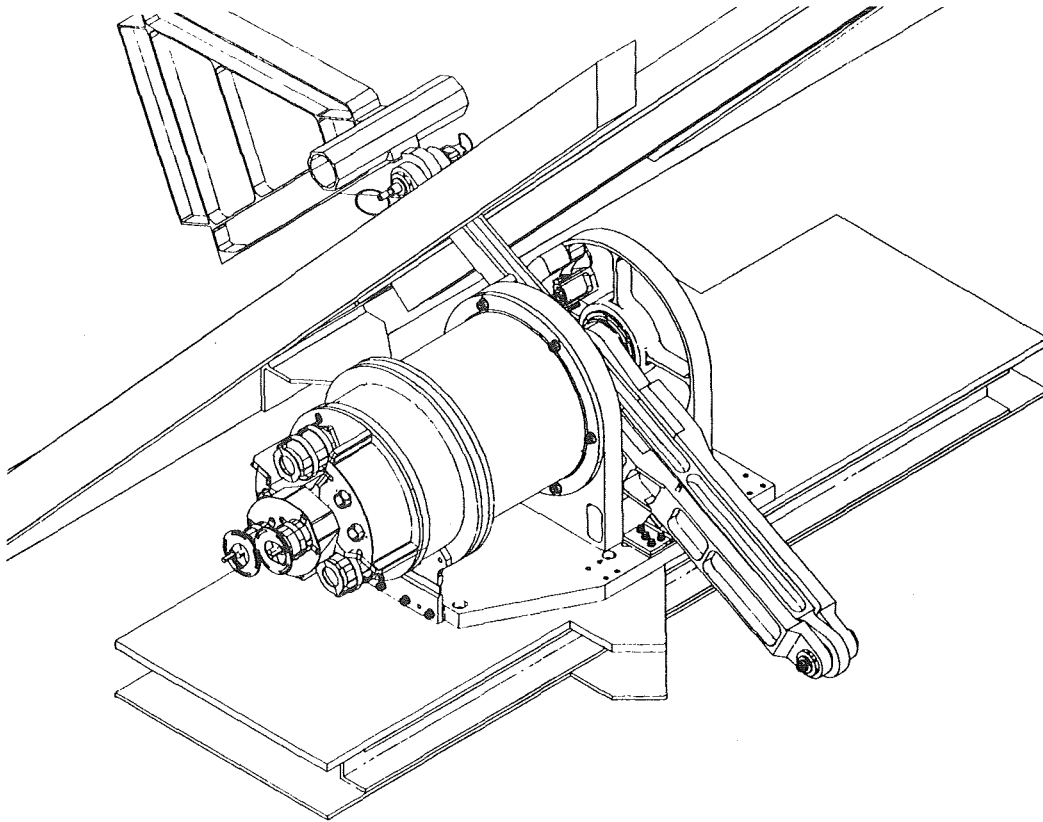

Figure 5. Tilt Actuator in Stow Position

The only other mechanisms needed once this decision had been made were the hinges and a backlash eliminator that would eliminate linkage play (lost motion). Figure 6 shows the positions of the final suite of mechanisms that were developed for the SRL. Table 1 lists some of the other requirements imposed on the mechanisms subsystem.

Table 1. Requirements Summary

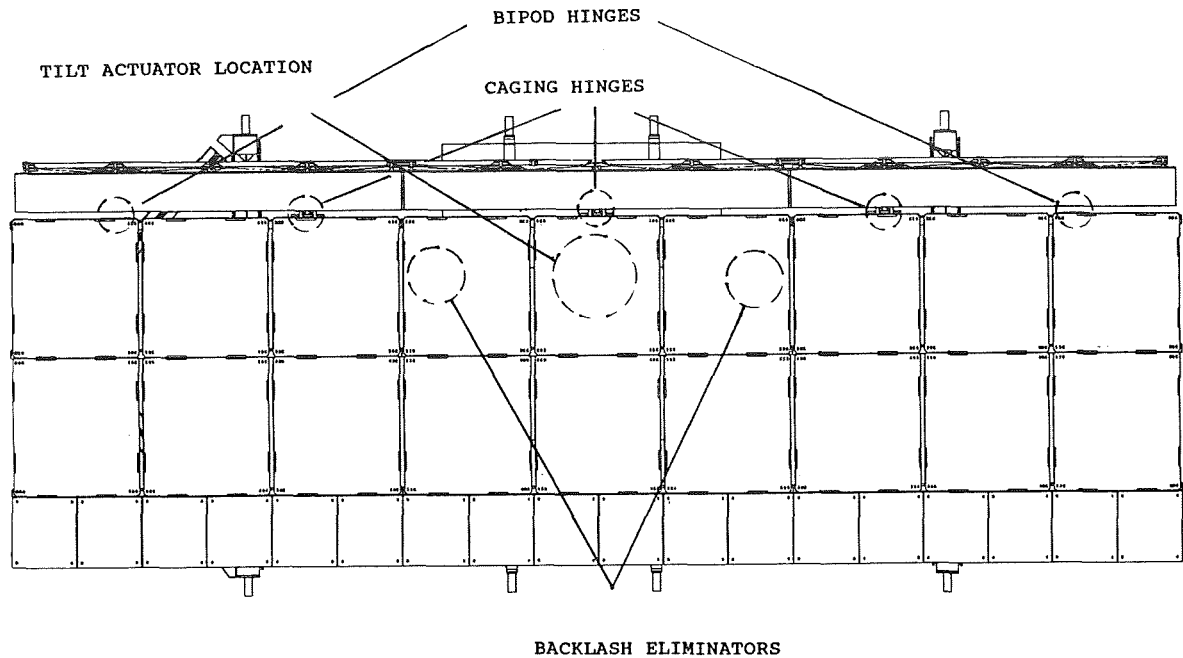|	
Maximum Tilt Control Error	0.5°
Tilt Angle Knowledge	0.1°
Minimum Angular Velocity Between Data Takes	0.9°/s
Fault Tolerance of Safety Critical Mechanisms	Dual
Fault Tolerance of Mission Critical Mechanisms	Single
Tilt Actuator Flight Allowable Temperature Range . . .	-45°/35° C.
Hinge Subsystem Flight Allowable Temperature Range	-75°/45° C.

Figure 6. Locations of Mechanisms on the SRL Structure

The X-Band antenna can tilt between 20° and -68° relative to the SIR-C panels. Except for the Backlash Eliminator, all of the mechanisms are classified as STS safety critical. As such, the mechanisms must be dual fault-tolerant to credible mechanical or electrical failures. Other designs for STS safety critical mechanisms are described in references 1, 3 and 4.

Tilt Actuator Assembly

The 156 kg (343 lb) Tilt Actuator Assembly is comprised of two major subsystems: (1) the "Tri-Drive," and (2) the Crank and Linkage Assembly.

Tri-Drive

The following major subassemblies comprise the Tri-Drive (Figure 7):

1. 319.5:1 Size 50 harmonic drive stack.
2. Spur gear box assembly.
3. Three clutch assemblies.
4. Dual-Drive Assembly (DDA) (motor 'C').
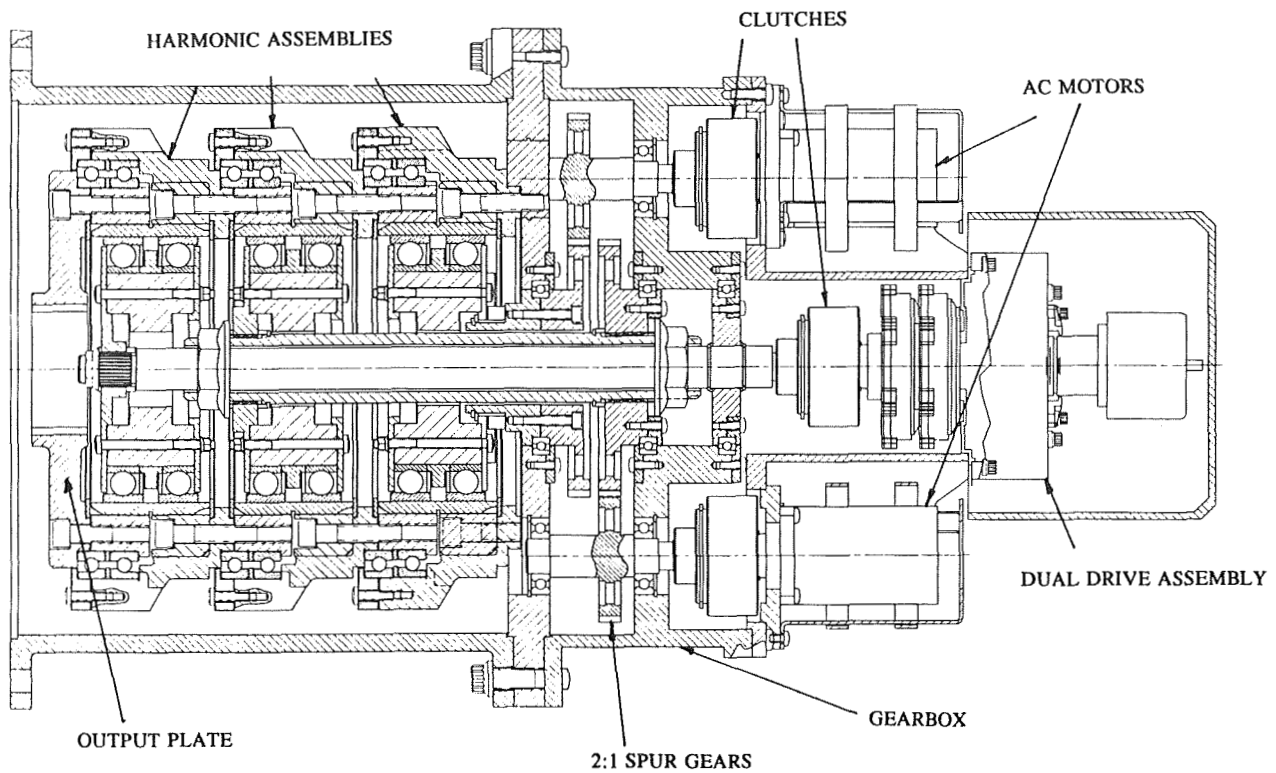5. Two AC motor assemblies (motors 'A' and 'B').

Figure 7. Tri-Drive Assembly Cross-Section

The Tri-Drive is a triple redundant, two-fault-tolerant actuator that can tolerate any two separate mechanism failures in which a gear or bearing interface is jammed or motors fail. Redundancy is also maintained electrically by the use of three independent drives: two AC motors and one DC driven actuator, a Dual-Drive Assembly. Each drive is supplied through three independent STS power supplies via separately routed cables and connectors. Those load paths in the Tri-Drive which are not two-fault-tolerant are designed to satisfy shuttle safety-critical-structure design criteria. Table 2 lists some of the Tri-Drive's principal operating characteristics.

Table 2. Tri-Drive Specifications

Output Torque Capability	782 N-m (7,000 in.-lb)
Angular Velocity (data collection range)	0.9°/s
Mass	97 kg (214 lb)
Stall Power (DC)	30 W
Stall Power (AC)	130 W
Nominal Stop and Hold Torque	339 N-m (3,000 in.-lb)

Figure 8 is a block diagram of the actuator transfer function, neglecting the electrical dynamics of the system and focusing on the gear ratio amplifications and driving sources. As can be seen, each motor independently drives one of the actuator's stages. The angular excursions and angular velocities sum together if all inputs rotate in the same direction. The principle of operation is similar to the Dual-Drive Actuator mechanism described in reference 2.
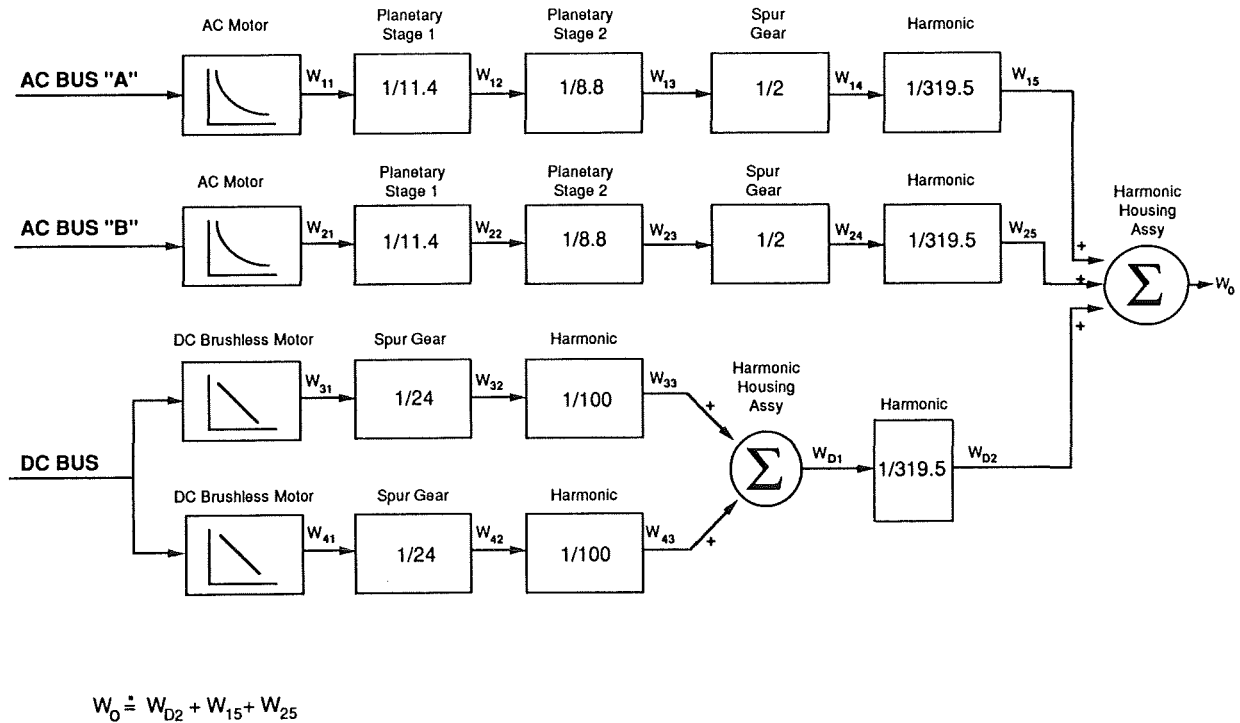

$$W_o \doteq W_{D2} + W_{15} + W_{25}$$

Figure 8. Tri-Drive Actuator Block Diagram

The motors may be operated concurrently by switching any two or three of them on together at the STS SP-1 panel, which is operated by the astronauts. In normal operation, ground control will issue a command to slew the X-Band antenna to a desired tilt angle. The Tri-Drive will rotate the antenna until telemetry received from the hingeline encoder indicates that the angle has been reached. Coast-down of the antenna system is less than 1 degree.

The core of the Tri-Drive is made up of dual-ratio, single-output harmonic drive assemblies (Figure 9) that have a gear ratio of 319.5:1. Each of the three harmonic gear sets is independently driven by an AC or DC actuator.

Our prior experience with Dual-Drive actuators that we built and tested for other
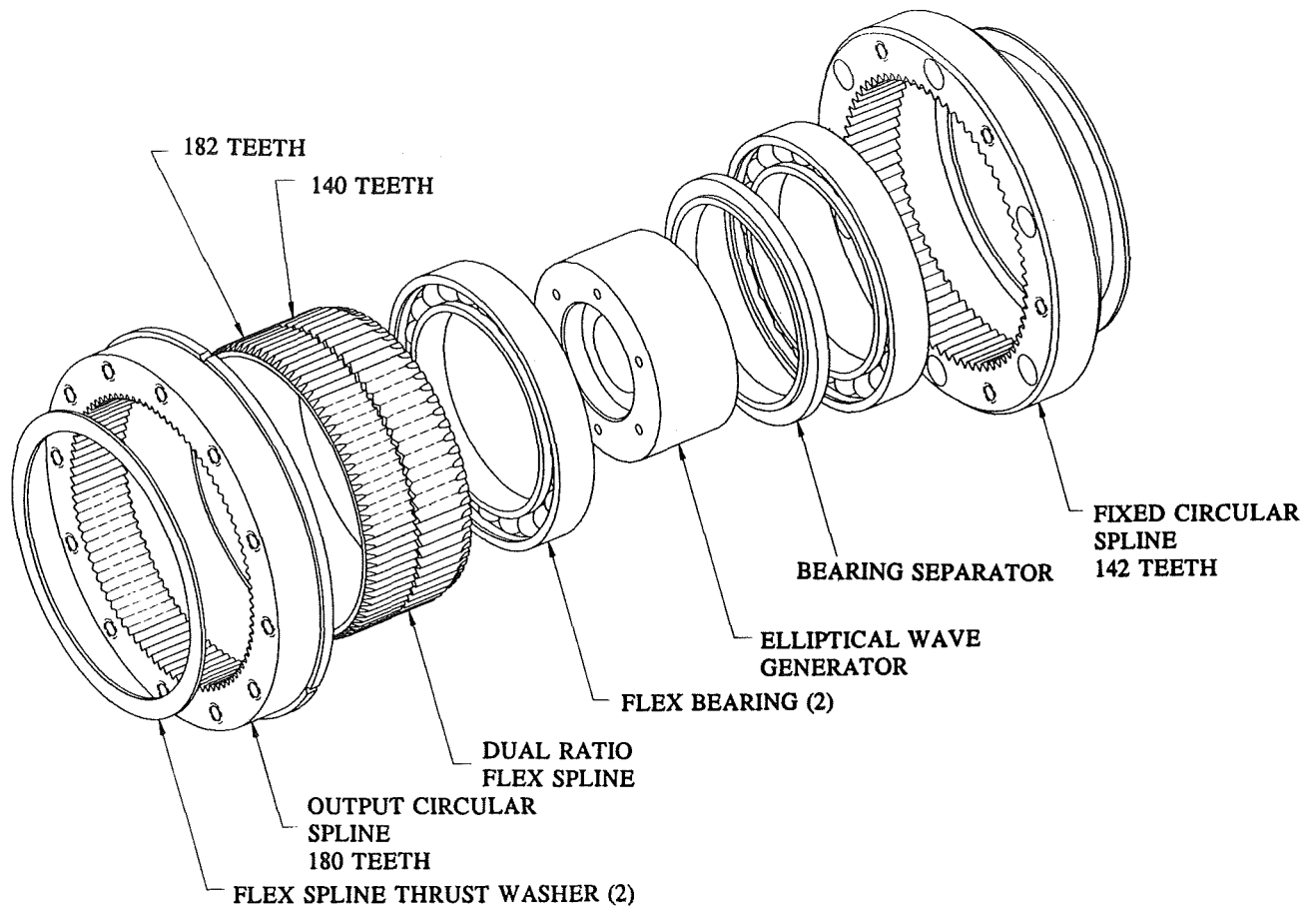
Figure 9. Harmonic Drive Exploded View

programs has shown us that Size 14 1110:1 ratio and Size 20 605:1 ratio units would not backdrive but that Size 14 110:1 ratio units would. We did not know at what gear ratios the backdriving would occur in the Size 50 units. It was necessary to prevent the non-driven harmonic gears in a dual or triply redundant harmonic drive actuator from rotating backwards and thus lowering the actuator output torque or angular velocity.

A development unit was built and tested extensively. It was discovered that the Size 50 319.5:1 ratio harmonic gears would, in fact, backdrive. Backdriving was most pronounced at higher temperatures, as expected. As a consequence, the stop and hold torque of the actuator was low and we could not rely upon the actuator to keep the crank arm preloaded against the hard stop during launch or landing. Thus it was necessary to develop a method of maintaining that preload in some other way. We developed the Detent Device, to be described later, to accomplish this.

The backdrive threshold is dependent on drivetrain friction (which decreases slightly with wear-in) and temperature. We determined that the units are non-backdriveable to a limit of about 782 N-m (7,000 in.-lb) for the AC motors and only 223 N-m (2,000 in.-lb) for the DC Dual Drive Actuator, which runs at 10% of the speed of the AC motors. However, at the high end of the torque range, backdriving will reduce the output velocity

155

of the Tri-Drive. Since the maximum expected resistive torque under mission operations will be about 27.9 N-m (250 in.-lb), no reduction in output velocity during mission operations should be seen. In some ground testing orientations, the Tri-Drive will not be able to hold the antenna in place after it is turned off, but this is acceptable.

The AC motor output is geared down by a factor of 2:1 in the gearbox. The DDA output is passed unchanged through the gearbox. Even without a need for gear reduction, the gearbox would be necessary in order to offset the drive centers to allow mounting of the three motors on the unit. The gearbox and its cover are a precision match drilled assembly.

Tri-Drive AC Actuators

Considerable budget and schedule costs could have been incurred by procuring a space-qualified AC motor/gearbox actuator for the Tri-Drive. For the limited duty cycle required, it seemed reasonable that a high quality aircraft motor/gearbox might suit our purposes well. Therefore we procured some development units from the Astro Instrument Corporation in Deerfield, Florida. The assembly includes a high-performance, four-pole AC motor attached to a 100:1 two-stage planetary gearbox (Figure 10).
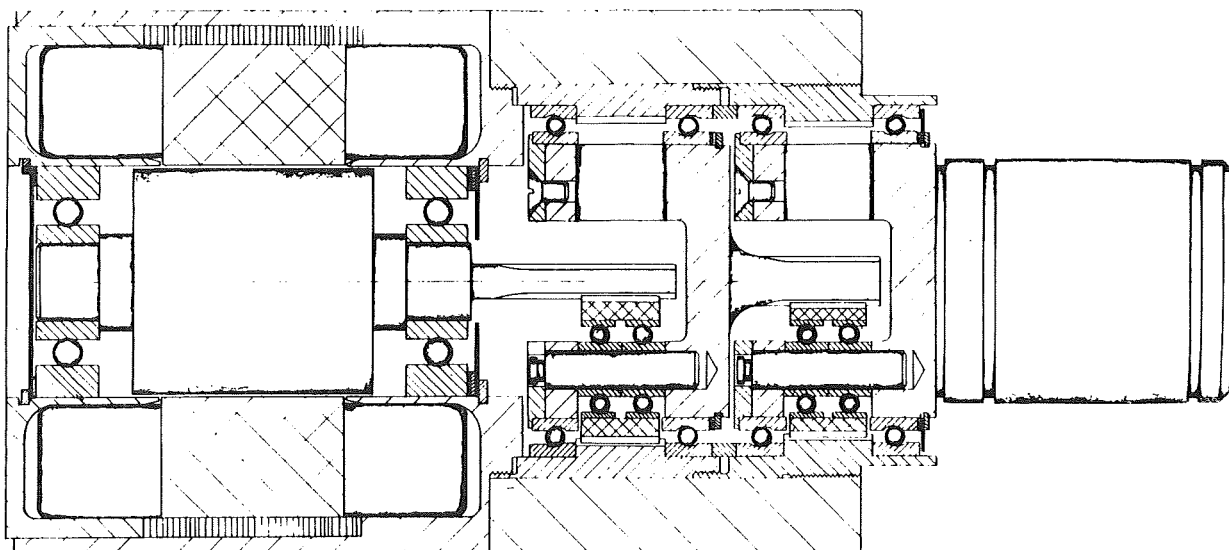

Figure 10. AC Motor Actuator Cross-Section

Table 3 lists some of the actuator's important specifications.

Table 3. AC Actuator Specification

Actuator Stall Torque	6.70 N-m (60in.-lb) at 60°C
Motor Stall Torque	>0.095 N-m (8.5 in-oz)
Stall Current	<0.85 A/Winding
Stall Power	130 W
Backdrive Torque	<0.279 N-m (40 in-oz)
No Load Output Speed	110 RPM

We disassembled one of the early development unit actuators that we procured. A thorough examination, including the generation of an engineering layout of the assembly and reverse engineering the gearbox planetary design, taught us much about the product. The gearbox is a precision-fabricated, well-designed mechanism. We also conducted life tests in air on the gearbox assembly, running it continuously at a medium load for about 72,000,000 input cycles without incident. A post-test examination revealed no unusual wear.

Astro Instrument considered the grease to be a vendor proprietary product. They did, however, reveal to us what the lubricant was. After obtaining a sample, talking with the manufacturer, and running a vacuum condensibles and outgassing test, we became convinced that the lubricant was adequate to meet our needs.

Rigorous thermal vacuum tests on the motor revealed that high torque conditions coupled with high motor ambient temperatures would cause the rotor to expand enough to contact the inner surface of the stator and seize. The first seizure took place after the motor had run for over 1.5 hours in a vacuum against a 5.0 N-m (45 in-lb) load and with a motor mounting interface temperature of 60°C. The peak recorded motor housing temperature was 109°C. Upon cool-down, the motor ran normally.

We proposed to the vendor that the problem could be reduced or alleviated by increasing the air gap in the motor. However, after some motor efficiency calculations, it was determined that more harm than good might come of such a change. Although the efficiency degradation from the increased air gap was minor, the rotor would tend to run even hotter, which would somewhat offset the gap improvement under nominal conditions. Worse yet, the motor might be permanently disabled by an eventual seizure. This is because it would have to grow more and thus have a higher temperature before the actuator shut down. Of course, no motor seizure was acceptable, but it was better to have a robust design.

Thermal tests were conducted on a disassembled prototype to determine the interface heat transfer coefficients for a computer model. Evaluation of this model showed that altering the emissivity and absorptance of the stator bore and rotor diameter would not appreciably lower the rotor temperature until the rotor temperature was too high in a stall condition.

Now that we had determined the limits of the motor's operation, we reduced the severity of the tests to levels that could be used in qualifying the motors. No further seizures occurred when the motors were limited to running a duty cycle of 5 minutes on and 45 minutes off against a 5.0 N-m resistance (45 in-lb).

Two short-duration flights with the SIR-C instrument are planned. Each flight will subject the actuator to intermittent operation of no more than 3 minutes on for every 45-minute operating window, for a total accumulation 1.5 hours of operation over the seven-day period. We experienced no further degradation in performance in the actuator motor or gearbox during the remainder of our development or qualification tests.

Tri-Drive Clutches

We are wary of operating an AC motor for any significant time in a stalled condition in a vacuum, believing that the rotor could be damaged by high temperatures. Therefore, we have included a breakaway roller clutch (Figure 11) in the design which will prevent the motor from stalling should the Tri-Drive output shaft be prevented from rotating for some reason.

The two AC motor clutches are set to ratchet at about 3.91 N-m (35 in.-lb), whereas the DDA clutch ratcheting level is about 7.26 N-m (65 in.-lb). These units have undergone significant development testing that has demonstrated their durability and consistency in ratchet level (+/- 10%).

Figure 11. Tri-drive Clutch Assembly Cross-Section

Tri-Drive Dual Drive

The tertiary drive system must use the STS DC power supply. Instead of procuring a costly new DC drive unit, we incorporated the SIR-B Dual Drive Actuator, originally used to fold the leaves, into the design. The development and flight units were rebuilt using new spur gears. The harmonic gears were changed from 1110:1 to 100:1 to increase the velocity, and the output plate was changed to provide an interface with the clutch. Both output motors run simultaneously, drawing power from a single DC bus, because no redundancy is required at this level.

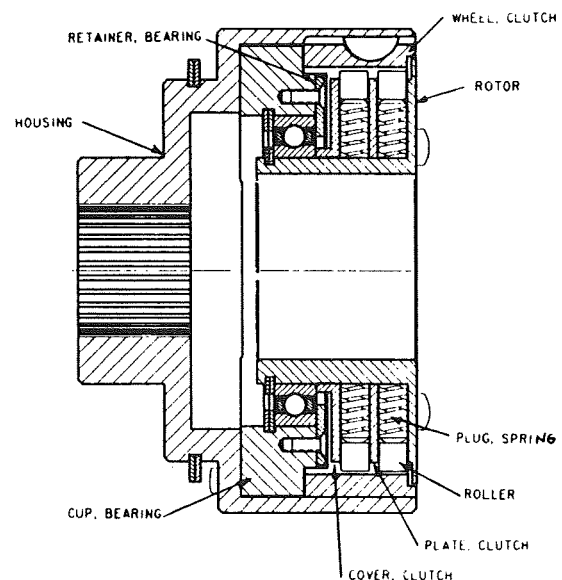For details concerning the Dual Drive, see reference 2.

158

Crank and Linkage Assembly

The Tri-Drive is mounted to the Crank and Linkage Assembly (Figure 12). Crank torques produced by launch and landing translational vibrations are minimized by a counterweight that balances out the mass moment of the crank and connecting link. Mallory 2000 tungsten alloy was used to increase the mass with a minimum of volume within the counterweight. Torques that might otherwise act on the crank due to pushing or pulling of the X-Band Antenna Assembly are eliminated by stowing the antenna in a bottom dead-center position. This leaves only the rotational accelerations acting to produce a "back-out" torque during launch. We had hoped that the stop and hold torque of the harmonic gears in the Tri-Drive would be sufficient to resist this. However, as previously mentioned, the backdrive level was too low. Upon further reflection, it would have been difficult to characterize the stop and hold level without running vibration tests on the unit.
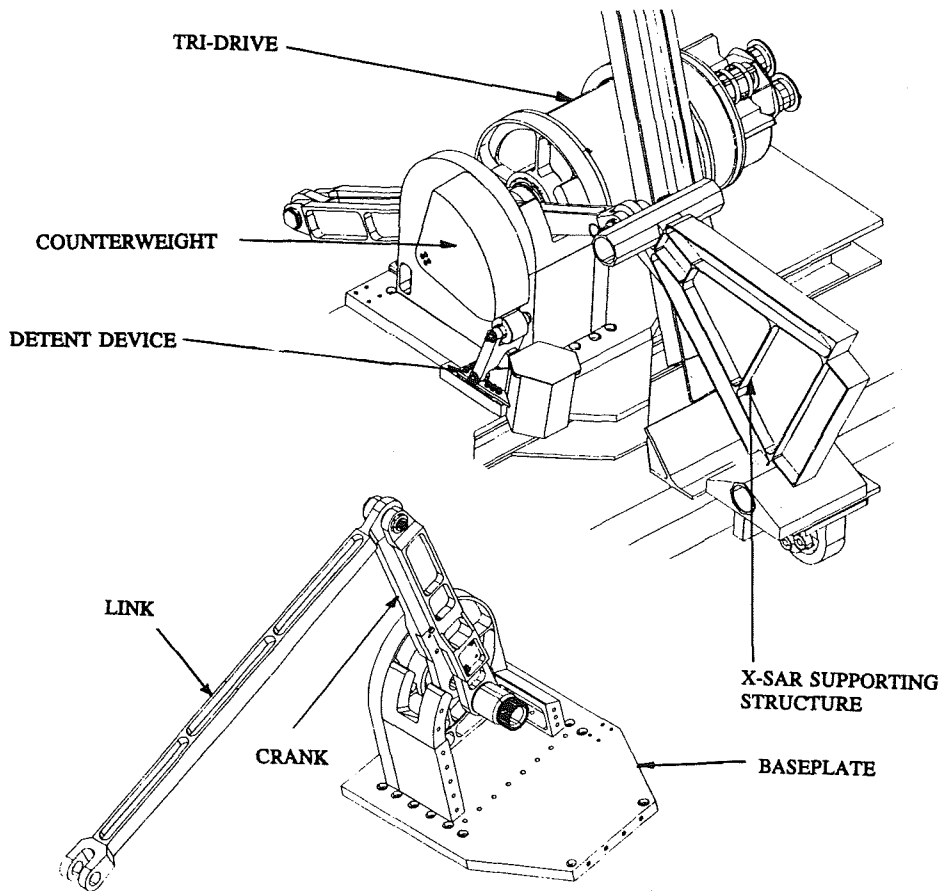
Figure 12. Crank and Linkage Assembly

159

Detent Device

Therefore, we developed the Detent Device (Figure 13), which automatically preloads the mechanism in the stow position with 268 N-m (2,400 in.-lb) of torque. The device consists of a cam, rollers, pivot, cable assembly, spring and housing. The critical spring is not guided. Instead, we kept the aspect ratio (free height to diameter) low (2:1) and minimized side loads to eliminate any possibility of buckling. A multi-strand cable with double fittings connected between the spring cup and a lever arm provides precise control of the virtual load points for compression of the spring. By minimizing the cable length and lowering the fitting points as much as possible, we gained additional margin for buckling resistance. Deflections as high as 12.7 mm (0.5 in) were detected at the top of the spring during transverse vibration tests, but the assembly was not damaged, compression was maintained and no buckling occurred.

The detent roller rides against a steep, 45° ramp while in the stow position to produce the 268 N-m (2,400 in.-lb) preload. The ramp slope then reverses, producing a torque of about 25 N-m (225 in.-lb) tending toward deployment. This ramp is an involute and gradually drops off until the roller is no longer in contact during mission data-take operations.

Caging Hinges

The X-SAR supporting structure does not have sufficient rigidity to be kinematically supported by only two hinges along the tilt axis during launch and landing. On the other hand, a kinematic support is desired for mission data collection to eliminate redundant load paths in the structure and higher bearing friction/stiction in the hinges. The Caging Hinges were specially designed to meet this requirement.

They are located in the positions described in Figure 6. The Caging Hinges are subjected to a maximum of 1090 N (4800 lb) radially and 860 N (3800 lb) axially in launch and landing. The two outer hinges are mounted to swiveling bipods attached to the X-SAR support structure. These hinges constrain the antenna in the Y-Z plane only. The center hinge is rigidly mounted to the XBS and provides a translational constraint in X-Y-Z. Each hinge is identical in all other respects.
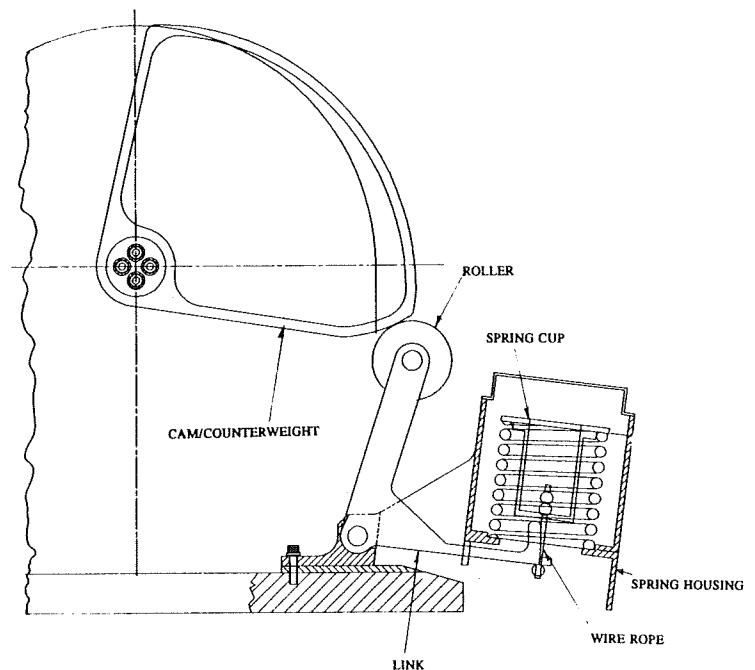

Figure 13. Detent Device

160

Figure 14 shows an exploded view of the hinge and a cross section in stowed and deployed positions. The rollers are in contact with the lobes of the cam when the X-SAR is stowed. Upon deployment, there is a gap of about 6.4 mm (0.25 in.) freeing up the interface in the STS Y-Z plane.
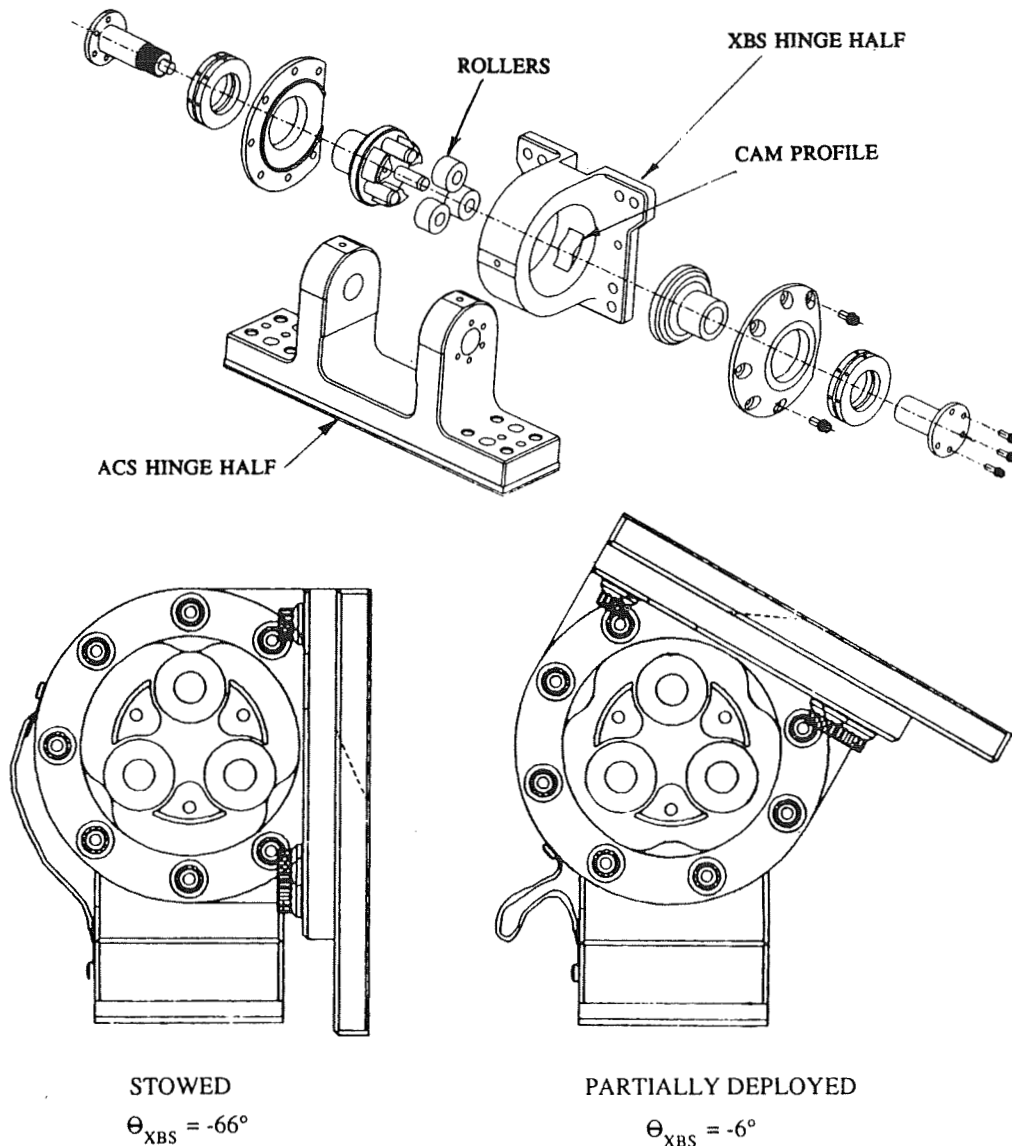

STOWED
$\Theta_{XBS} = -66°$

PARTIALLY DEPLOYED
$\Theta_{XBS} = -6°$

Figure 14. Caging Hinge

Since there is no contact with the cam rollers when the antenna is deployed, redundant bearing surfaces are not required. The thrust surfaces on either side, do, however, incorporate redundancy and verification spanner wrench holes.

Bipod Hinges

The Bipod Hinges are shown in Figure 15 and are located on the ACS as shown in

161

Figure 6. They are mounted on XBS bipods, much as the two Caging Hinges are, and thus carry only Y-Z plane forces, which have a maximum value of 500 N (2,200 lbs). Each hinge makes use of a spherical bearing to prevent any binding that might otherwise occur due to small local angular misalignments. The hinge encoders, used for X-SAR position telemetry, are mounted to these hinges using a flexible bellows coupling.
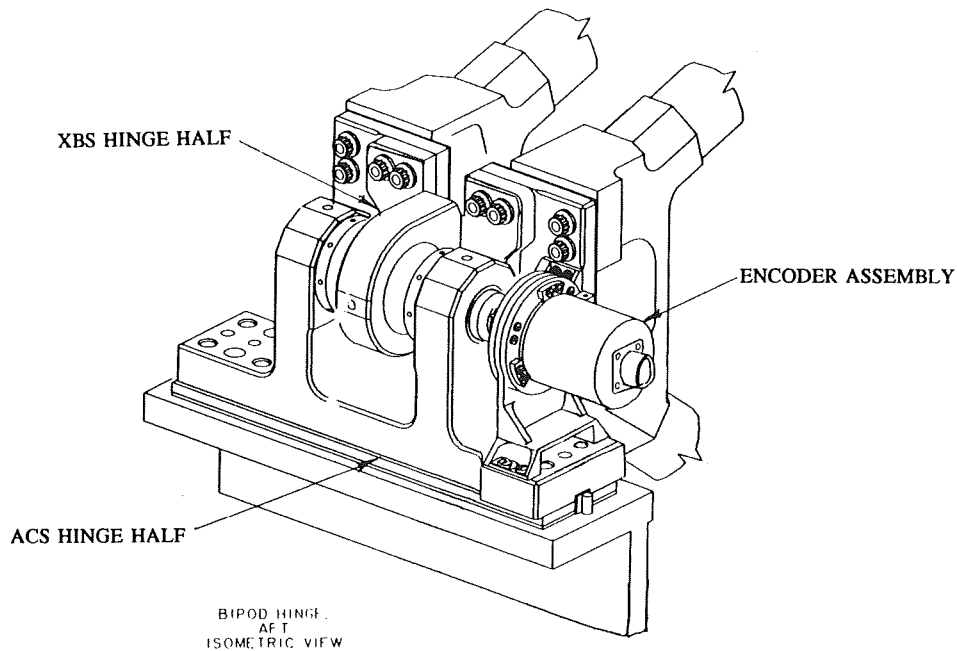

BIPOD HINGE
AFT
ISOMETRIC VIEW

Figure 15. Bipod Hinges

Backlash Eliminator

The Backlash Eliminator's purpose is to eliminate the lost motion or "play" in the tri-drive harmonic gears and the linkage joints (Figure 16). The device is a commercially manufactured mechanism procured from AMETEK Hunter Spring Products Company that has been mounted in a specially designed enclosure in order to meet STS mass containment requirements.

The major components of the device consist of a cable, spool, constant force spring and enclosure. One end of the cable is attached to the X-SAR antenna substructure and the other to the spool. The negator spring keeps the cable at a nearly constant 1.1 N (5 lb) tension regardless of the extension length. This produces approximately 5.58 N-m (50 in.-lb.) of torque about the tilt axis per unit. Should the cable somehow break and then snag and act against the tilt actuator torque, the Tri-Drive has adequate torque at 670 N-m (6,000 in.-lb.) (F.S. of 40) to break the cables and continue to operate. Some pointing control accuracy would be lost, however, due to the extra play.
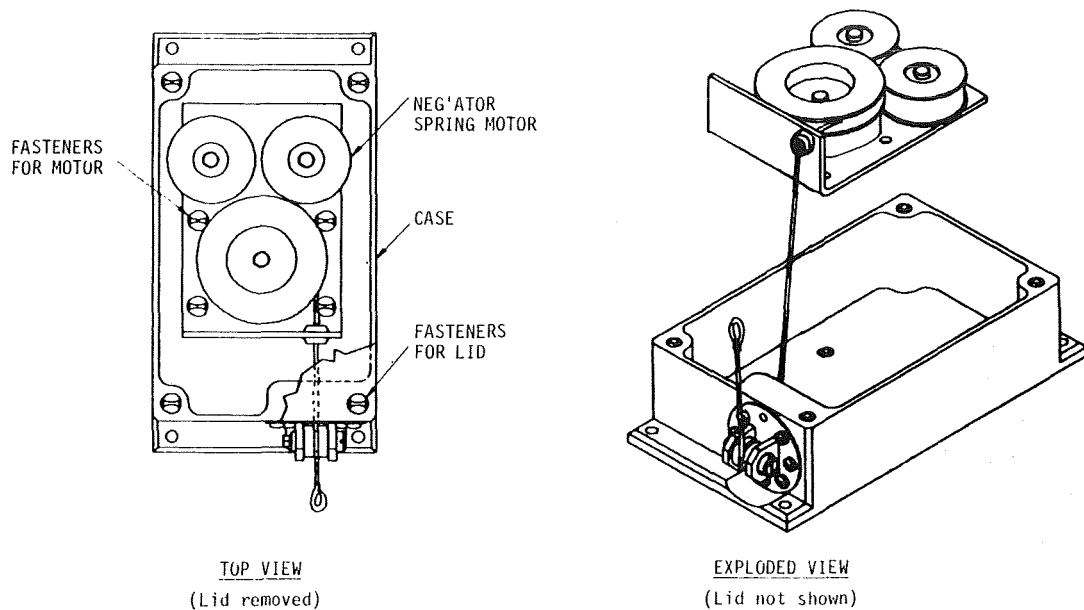
162

FASTENERS FOR MOTOR

NEG'ATOR SPRING MOTOR

CASE

FASTENERS FOR LID

TOP VIEW
(Lid removed)

EXPLODED VIEW
(Lid not shown)

Figure 16. Backlash Eliminator

CONCLUSIONS

All of the mechanisms described in this paper have been built, tested and integrated. The system has successfully passed the Johnson Space Center Shuttle Safety Review - Phase II. The phase III review is scheduled for Spring of 1993.

Some lessons learned include the following:

o   Designs cannot always be extrapolated into a larger scale. Early attention should be paid to dynamic analysis of deflections and stresses when doing so, before additional significant resources are expended in detailed design of mechanism subsystems.

o   As usual, friction is not there when you need it. Do not rely heavily upon the nonbackdriveability of gear trains.

o   Aircraft-quality AC motors can be qualified for use in spacecraft mechanisms.

o   It is possible to design and develop a truly dual fault tolerant actuator for use in a Space Shuttle safety critical application.

163

REFERENCES

[1]   Hornyak, S.: "Inherent Problems in Designing Two-Failure Tolerant Electromechanical Actuators," <u>Proceedings of the 18th Aerospace Mechanisms Symposium</u>, p. 155, May 1984.

[2]   Packard, D. T.: "Dual Drive Actuators," <u>Proceedings of the 16th Aerospace Mechanisms Symposium</u>, p. 123, May 1982.

[3]   Siebert, C. J.: "A Dual, Fault-Tolerant Aerospace Actuator," <u>Proceedings of the 19th Aerospace Mechanisms Symposium</u>, p. 293, May 1985.

[4]   Teske, D. R.: "Design of a Dual Fault Tolerant Space Shuttle Payload Deployment Actuator," <u>Proceedings of the 19th Aerospace Mechanisms Symposium</u>, p. 305, May 1985.

ACKNOWLEDGEMENTS

Reference herein to any specific commercial product, process, or service by trade name, trademark, manufacturer, or otherwise, does not constitute or imply its endorsement by the United States Government or the Jet Propulsion Laboratory, California Institute of Technology.

/ 9 9 4 0 2 5 7 1 3 4

4 3 4 6 6 8

Optical Chopper Assembly
for the Mars Observer

Terry Allen[*]

ABSTRACT

This paper describes the Honeywell-developed Optical Chopper Assembly (OCA), a component of Mars Observer spacecraft's Pressure Modulator Infrared Radiometer (PMIRR) science experiment, which will map the Martian atmosphere during 1993 to 1995. The OCA is unique because of its constant accurate rotational speed, low electrical power consumption, and long-life requirements. These strict and demanding requirements were achieved by use of a number of novel approaches.

INTRODUCTION

The Mars Observer is a cost-effective mission that will continue the exploration of the inner solar system, initiated in 1971 by the Mariner mission and carried on by the Viking mission. Mars Observer will further unravel the history of Mars, laying the foundation for further expeditions to the Red Planet.

One of the seven scientific experiments, called PMIRR, will perform continuous radiometric mapping of the planet's atmosphere and surface throughout its one-Martian-year (687 Earth days) mission. Daily maps of surface properties, temperature structure, dust loading, and water vapor distribution will be derived from these measurements.

MARS OBSERVER MISSION

Mars Observer and its Transfer Orbit Stage (TOS) were launched aboard a Titan III rocket on September 25, 1992. During ascent, the Titan's booster rockets were jettisoned and the spacecraft/TOS separated from the Titan III. After repositioning for the orbit transfer, a TOS burn accelerated the spacecraft to the Earth escape velocity and a rendezvous with Mars in August 1993. The average transfer speed will be 25 km/s (56,000 mph) relative to the Sun. As the Mars Observer approaches Mars, a rocket thrust will maneuver the spacecraft into a highly elliptical orbit around the planet. Numerous adjustments during the next four months will move the spacecraft into a near-circular polar orbit for mapping at an orbital speed of 3.35 km/s (7,500 mph) relative to Mars. The mapping orbit will be Sun-synchronous so that the spacecraft passes over Mars' equator at the same local time during each orbit, which is about 2 pm on the day side and 2 am on the night side. In its mapping orbit, the Mars Observer spacecraft will be rotated once

---

[*]Honeywell Inc., Satellite Systems Operation; Glendale, Arizona

per orbit by onboard reaction gyroscopes directed by horizon and star sensors to keep the instruments continuously and uniformly pointed at the planet during the entire Martian year. For about 40 min during each 118-min orbit, the spacecraft will be in the Mars shadow and will rely on battery power. The spacecraft's solar panel (which generates more than a kilowatt of power) and storage battery provide sufficient resources to supply the spacecraft and instruments. Figure 1 shows the launch and transfer orbit sequence.

SCIENCE PLATFORM EXPERIMENTS

The Mars Observer spacecraft, shown in Figure 2, has two basic parts: the main body (the bus) and the science instruments (the payload). The bus houses the computers and other equipment necessary for operations. Four of the seven science instruments are mounted on the outside of the bus, and three instruments are mounted on booms attached to the bus. The functions of the Mars Observer's seven principal science instruments are:

- Gamma Ray Spectrometer - characterizes surface chemical elements
- Mars Observer Camera - photographs the Martian surface
- Thermal Emissions Spectrometer - measures infrared thermal radiation to determine the surface composition of Mars
- Mars Observer Laser Altimeter - measures topography
- Magnetometer and the Electron Reflectometer - search for planetary magnetic fields
- Pressure Modulator Infrared Radiometer - maps the Martian atmosphere

PRESSURE MODULATOR INFRARED RADIOMETER

PMIRR has nine spectral channels covering the wavelength range 0.3 to 50 microns and employs pressure modulation and filter radiometry in both limb and nadir sounding modes to perform continuous radiometric mapping of the atmosphere and surface of Mars. Daily maps of the surface properties and high vertical resolution three-dimensional daily maps of temperature structure, dust loading, and water-vapor distribution will be derived from these measurements. As a PMIRR component, the OCA will use its optic disc to direct light from a telescope aimed at the Martian surface, and light from deep space, into the PMIRR optical system. A schematic diagram of the PMIRR optical system is shown in Figure 3. The optical chopper, a 12-toothed, double-sided mirror disc is dimensioned and optically finished to provide 100% signal modulation at 800 Hz over the life of the mission. The OCA has a chopper-blade synchronization circuit to generate a signal for use in timing and signal chain phase synchronization demodulation. The circuit consists of a light-emitting-diode source to switch a light-sensitive transistor at the leading edge of an aperture, which is machined into a skirt on the drive motor shaft. This occurs once per revolution. The sync-circuit configuration is shown in the OCA cross section in Figure 4.

OPTICAL CHOPPER DESIGN REQUIREMENTS

The chopper's outline requirements were specified by NASA's Jet Propulsion Laboratory (JPL), and photographs of OCA are shown in Figure 5. Although a weight limit of 1.5 pounds was allowed, the OCA was designed to weigh only 1.0 pound. Nominal shaft speed is 67 Hz and steady-state power consumption (for the OCA only) is not to exceed 1 W while operating in the 10-to-45 °C temperature range. OCA runup power limit is 3.0 W maximum, and tooth jitter is not to exceed 1.0 μs rms or 4.0 μs peak to peak.

Time and cost budgets did not allow for an engineering model OCA. The only OCA built is now aboard the Mars Observer.

MOTOR DESIGN

The OCA disc is directly coupled to an AC hysteresis-synchronous, 2-phase, 6-pole motor excited by a 28-V, 200-Hz supply. The motor performance data is presented in Figure 6.

Although not as weight- and power-efficient as equivalent synchronous or DC motors, the hysteresis motor was selected because of its smooth torque, drive circuit simplicity, and because no commutation is required. Hysteresis motors do not exhibit anomaly torques, such as cogging and torque ripple, and offer excellent speed stability when run open loop from an accurate frequency supply. This makes them ideal for systems requiring low jitter with minimal drive-circuit complexity.

The OCA motor was built by Honeywell's Durham, NC, facility and was based on an existing design to minimize cost and schedule. The motor shares the same materials and fabrication methods developed by Honeywell for high reliability and long life and has been proven in numerous space applications over the past 25 years. The motor was subjected to component performance and acceptance testing prior to integration to ensure specification compliance and provide a data base on unit performance.

Honeywell included a split-winding feature in the motor design, which provides operational flexibility by allowing the motor to be operated with its windings either series or parallel connected. The motor is designed to be operated series-connected while mapping Mars but, during system checkout on Earth in a one-atmosphere ambient, the higher torque output provided by parallel winding operation is needed for the motor to reach synchronous speed.

A characteristic of hysteresis motors that affects jitter is a lightly damped rotational mode with frequency dependent on rotor inertia and the effective stiffness of the motor's magnetic field. The OCA motor has a rotational mode measured at 9 Hz when operated series-connected, which, when excited by system disturbances, caused rate variations about the average speed. Jitter on the synchronous circuit output signal was measured and found to be 7.0 μs peak to peak per revolution.

167

Because there are 12 teeth, this is well below the 4.0 μs per tooth jitter tolerance. A Hewlett-Packard model 5371 Modulation Analyzer was used for jitter measurements.

OPTIC DISC

The optical disc was machined from Brushwellman I-2208, Type 2 structural grade beryllium alloy. After lapping and polishing, discs were coated with vacuum-deposited silver over nickel. A vacuum-deposited magnesium fluoride protective coating provided final disc covering. The disc's dimensional and optical requirements are given below:

REQUIREMENT	SPECIFICATION
Outside Diameter	84.07 mm (3.310 + 0.004 in.)
Thickness	1.52 mm (0.O60 + 0.002 in.)
Number of Teeth	12
Tooth Edge Registration	50 Arcseconds
Flatness, Over Teeth	0.0006 mm(24 μin.)
Flatness, Over Disc	0.008 mm (300 μin.)
Parallelism, Side to Side	0.005 mm(200 μin.)
Scratch And Dig Code	60-40 (MIL-O-13830)
Surface Roughness	40 Angstroms rms
Tooth Corner Radii	0.005 mm (200 μin.)
Surface Coating	Silver (MIL-M-3508)
Reflectance	0.45 to 54 microns, 95% to 98%

BEARINGS

Custom bearings are preferred for space-flight applications such as OCA, where designs favorable to the intended application and nonstandard tolerances can be used. Race curvature for example, the race radius to ball diameter ratio, can be chosen to favor load capacity rather than drag torque or manufacturing cost. Custom bearings, however, usually require one year for procurement. Because of the OCA's schedule, dictated by the Mars Observer's launch window, procurement of a custom bearing was not possible. To meet schedule, off-the-shelf size R-3H bearings were selected to suspend the OCA drive motor rotor, and all size R-3H bearings, available from Barden and MPB bearing companies, were purchased. These bearings were disassembled and screened for possible use on OCA. Barden Bearing Company of Danbury, CT, measured the radius of each race, and Honeywell bearing engineers reviewed these data to select races to match the diameters of separately procured Titanium-Carbide (TIC)-plated balls that would provide the required load capacity.

168

The R-3H bearing is the angular contact type and utilizes a dam machined onto its outer race. During assembly, the ball complement is snapped over the dam to make the bearing inseparable. A drawing of the bearings cross section is shown in Figure 7. The ball cage was designed by Honeywell to have conical shaped ball pockets and is machined from sintered nylon, or Nylasint. The cages were impregnated with Coray 55 lubricating oil. The Nylasint material, which can hold up to 25% of its weight in oil, acts as a lubricant reservoir.

The TIC plating, applied to 440C balls by Centre Suisse D'Electronique et de Microtechnique, S. A. of Switzerland, provides exceptional bearing life and is just now beginning to see usage in space-flight applications. Ball-and-race combinations with curvatures as low as 54% were found. Analyses show that these bearings would support the required pyrotechnic shock and launch vibration loads. Bearing drag torque was minimized to meet the 1.0-W steady-state running power requirement by selecting acceptable preload and lubricant quantities. Prototype R-3H bearings and cages were tested on a torque dynamometer. These tests showed that bearings with seven-ball complements developed less than 2 gm-cm drag torque, and require less drive power than bearings with eight-ball complements. Also, cages with conical pockets were more spin stable than cages with cylindrical pockets. To disassemble and reassemble the bearings for testing, a fixture was made that allowed the ball complement to clear the dam without damaging the balls or races. The fixture tied the outer race thermally to a heat source and the inner race to a liquid-nitrogen reservoir. The fixture also prevented the ball complement and cage from contacting either race during the temperature transfer, which further increased clearances. When thermal equilibrium was reached, the bearing could easily be assembled (or disassembled) by applying a light force (50 gm) to the races.

LUBRICATION

Analyses and experience show that OCA bearing life depends almost entirely on lubricant life. Sacrificial lubricant reservoirs were therefore designed for OCA to ensure meeting the OCA's three-year life requirement.

Honeywell's experience with size R-3H bearings, used on hundreds of instrument gyroscopes, shows that 30,000-to-40,000-hr Mean Time Between Failures (MTBF) are achievable. Optical Disc Assemblies with R-4H bearings, sintered-nylon cages, Coray 100 lubrication, and operated at 40 Hz in an evacuated housing have up to 50,000 hr MTBFs. Nearly all bearing failures are lubricant related.

As the mission progresses, the OCA bearing's lubricant will be lost through the molecular flow of vapors from the bearing to deep space or within the spacecraft where lubricant vaporized by the vacuum environment will be deposited as it contacts colder bearing surfaces.

The OCA design calls for 2.0 mg of Coray 55 lubricating oil to be applied to the race surfaces of each bearing. This oil is in addition to approximately 20.0 mg

of oil absorbed by each Nylasint cage. The lubricant vapor loss rate from the bearing is reduced by a traditional labyrinth seal, which is an annular 0.1 mm (0.004 in.) radial clearance between the fixed-bearing lock ring and the disc mount. The labyrinth seal is shown in Figure 4, cross-sectional view of the OCA.

Another sacrificial lubricant reservoir is mounted within the OCA housing cover. This reservoir stores 1.05 gm of Coray 55 oil and maintains a constant lubricant vapor partial pressure within the housing. This constant pressure extends lubricant life by replacing molecules that escaped through the labyrinth seal.

BEARING LIFE CRITERIA

Measurements showed that no change in bearing drag torque occurs with free oil within the bearing reduced by 30%. Additional lubricant loss may be possible without increasing torque or reducing bearing life. A 35% loss of lubricant, therefore, provides the basis for acceptable OCA bearing performance, although a 30% loss is used for most Honeywell lubricant-loss analyses.

BEARING PRELOAD SYSTEM

A preload system is provided to maintain a near-constant 0.9 kg (2.0 lb) axial load on the bearings for all expected temperatures. The preload system prevents damage should temperature gradients cause thermal expansions that load the bearing. A schematic diagram of the preload system is shown in Figure 8. Axial length changes caused by temperature variations are prevented from loading the bearing because the bearing mounting cartridge is free to slide relative to the housing.

The preload system also prevents unloading during launch vibrations. Without the 2-lb preload, random-vibration accelerations greater than 13 g's would cause the 67.7-gm (0.149 lb) shaft assembly to unload the bearing, thereby causing hammering between the balls and races, which could damage the bearings.

DYNAMIC BALANCING

Dynamic balancing of the OCA rotor assembly is required. Forces induced by imbalance and bearing race irregularities are to be less than 7.7 gm (0.017 lb) between 40 and 50 Hz and less than 10.9 gms (0.024 lb) between 120 and 150 Hz. The Schenk Dynamic 30 balance machine was used for the balancing operations. Balance adjustments are made by positioning size 2-56 UNC setscrews, which are located in threaded holes machined into the rotor and disc mount.

MECHANICAL STRUCTURE

The OCA housing assembly, shaft, and bearing cartridge were machined from Type 6Al4V titanium alloy. The housing's exterior surfaces were coated with Tiodize V-E17 to improve emissivity for radiation heat-transfer purposes. Other

titanium surfaces were coated with AMS 2488 Type 2 Anodic Treatment, used as an antigalling coating for screw thread and bearing cartridge protection.

The disc mount and disc clamp were machined from the same Brush-Wellman structural grade beryllium alloy used for the optic disc. Surfaces that mate with the optic disc are machined to have flatnesses and surface finishes comparable to those of the disc. Helicoil inserts were installed into beryllium parts to receive threaded fasteners.

Versamid 140/Epon 828 epoxy adhesive is used to fasten the optic disc to the disc mount. Disc alignment was performed as the adhesive cured, which was approximately 45 min.

PMIRR CHECKOUT AT JPL

After assembly and acceptance testing was completed at Honeywell, the OCA was shipped to JPL for integration with PMIRR and system testing on the optic bench. During these tests, JPL found that operating the motor parallel-connected significantly improved PMIRR's optical performance but increased the OCA motor's steady-state power from 0.8 to 1.8 W. The advantages of the improved performance are considerable and JPL requested analyses to find the effect on bearing life of the higher motor power.

Estimates show the higher power increased bearing temperature from 47 to 57 °C. This reduces bearing life from 150,000 to 26,000 hr, with zero margin for the three-year (26,208 hr) mission. A performance comparison is presented in Table 1.

The OCA drive motor was sized for a load torque of 6.0 gm-cm, but power measurements show actual drag torque to be 12.0 gm-cm. Because drive-motor efficiency was higher than expected, the 1.0 W steady-state power specification was met — in spite of the high bearing drag torque — and the high torque source was not identified. Dynamometer tests on the flight OCA motor show 0.5 W are required to turn a 6.0-gm-cm load, and 0.8 W for a 12.0-gm-cm load. With the motor parallel connected, it is estimated that 1.8 W are required to drive a 12.0-gm-cm load; bearing temperature will reach 57 °C; and bearing life will be 26,000 hr. Power measurements by JPL, with the OCA assembled into PMIRR, agree with the 1.8-W value.

The 12-gm-cm power measurement could be caused by excessive lubricant, bearing misalignment, or higher preload. If excessive lubricant causes high torque, then bearing life may be increased by the extra lubricant.

Although assembly records show no discrepancies on the machined parts, the high sensitivity of bearing torque to misalignment makes misalignment a possible cause for the high torque. For misalignment to cause the high torque, high points on the races, cartridge, and other components would have to be aligned at assembly to maximize misalignment. Determining the probable torque magnitude will require tolerance and statistical studies.

Dynamometer test results (Figure 9) show that bearing drag torque increases significantly with lubricant quantity and, to a lesser degree, with preload. Preload was probably adjusted to within 0.25 kg (0.5 lb) and is an unlikely cause of the high bearing torque.

An observation during checkout suggests that the bearings have excessive lubricant: after a several-month period of nonoperation, a chirping noise coming from the OCA was heard immediately following motor startup. The noise was intermittent and went away completely after several hours of operation. The chirping noise was believed caused by gravity-related puddles of lubricant formed in the bearing-race area. The puddles caused the ball cage to become unstable, which caused the noise. After several hours operation, the lubricant became redistributed throughout the bearing and the noise ceased.

Bearing-life studies and PMIRR temperatures measured in flight are being evaluated at the time of this paper's preparation. JPL will review this data and, if needed, will have the opportunity of reducing the time OCA is operated with windings parallel connected. For example, during the long periods of Martian dust storms, PMIRR observations will be impaired, and the OCA might be operated series connected to prolong bearing life.

SUMMARY AND CONCLUSIONS

1. The OCA was designed, built, tested, and shipped on schedule. Cost and performance objectives were met.

2. Subsequent PMIRR system tests on the JPL optical bench showed that optical performance could be improved by operating the motor with its windings parallel connected, rather than series connected, as originally intended. Parallel operation increased motor power and raised the bearing temperature. A study to show the effect on bearing life was requested by JPL.

3. In the study, a data review showed that OCA bearing drag torque exceeded the design limit, however, better-than-expected motor efficiency brought motor input power within tolerance. The high torque is assumably caused either by excessive lubricant or bearing misalignment/high preload. If extra lubricant is present, bearing life will exceed the prediction. If misalignment/preload causes the extra torque, the three-year life requirement can be met with parallel operation, but with zero safety margin.

4. Honeywell studies will be continued to determine the effect of bearing misalignment, lubricant quantity, and related factors on drag torque and bearing life. This data can be used by JPL as needed to modify the OCA operational regimen during mapping.

5. The positive effect of TIC-coated balls was not considered in the bearing life estimates and will be further evaluated by Honeywell.

172

ACKNOWLEDGEMENT

C-3

Table 1. Motor Operating Mode Comparison

Motor Operation Configuration	Units	Start Parallel Run Series	Start Parallel Run Parallel
Pull out torque	gm cm	24	34
Power; 6.0 gm cm load	W	0.5	1.5
Temperature	°C	38.0	47.0
Bearing life	hr	>200,000	150,000
Power; 12 gm cm load	W	0.8	1.8
Temperature	°C	47.0	57.0
Bearing life	hr	150,000	26,000

Spacecraft Trajectory

Aphelion
March 1995

Mars at Launch

Earth at Launch
September 1992

Earth Orbit

Arrival at Mars
Orbit Orientation
August 1993

Perihelion
April 1994

Earth at Mars Arrival

Transfer Orbit Stage –
Solid Rocket Motor
Ignition

Mars Orbit

Solar Conjunction
December 1993

Titan III Separation

Mapping Phase Begins
December 1993

Booster Rocket
Separation

Ignition

Figure 1. Launch and Transfer Orbit

175
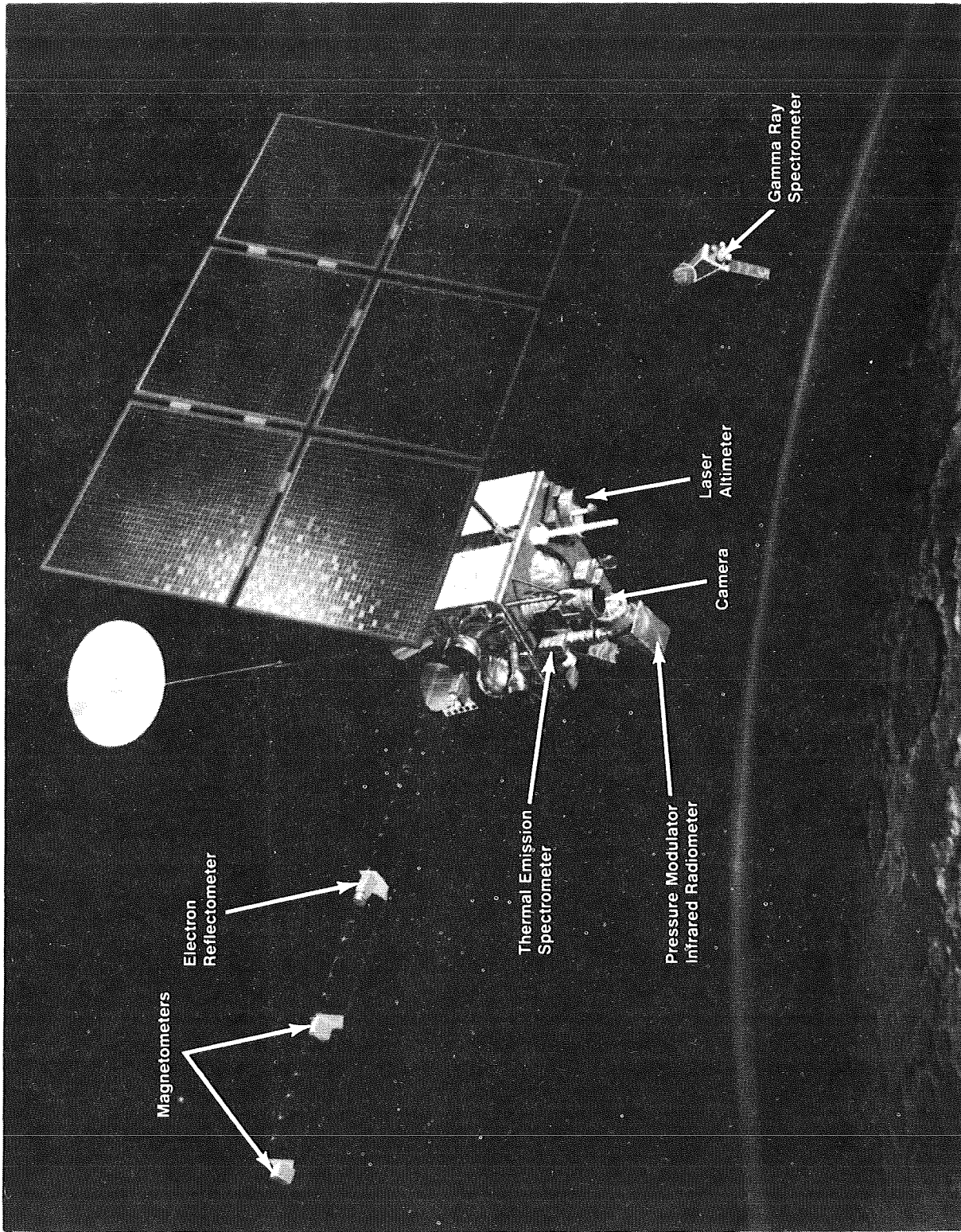
Figure 2. Mars Observer Spacecraft

176
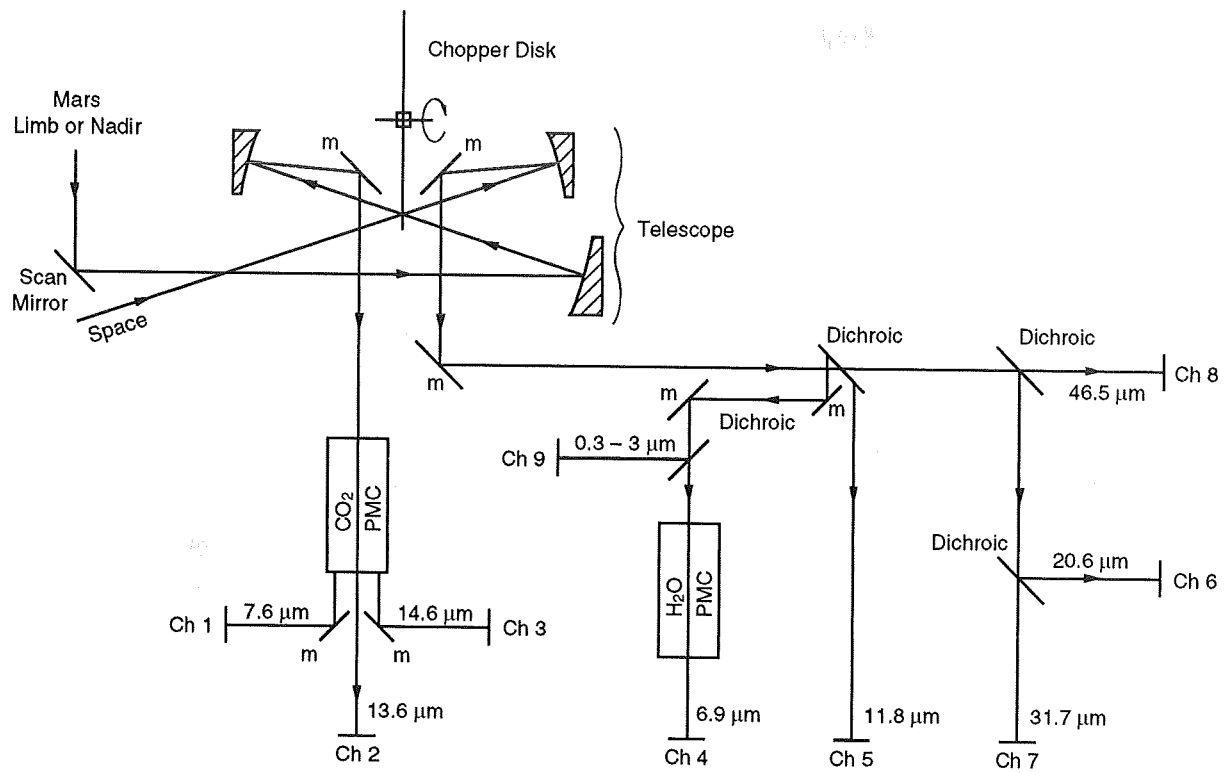
Figure 3. PMIRR Optical Schematic
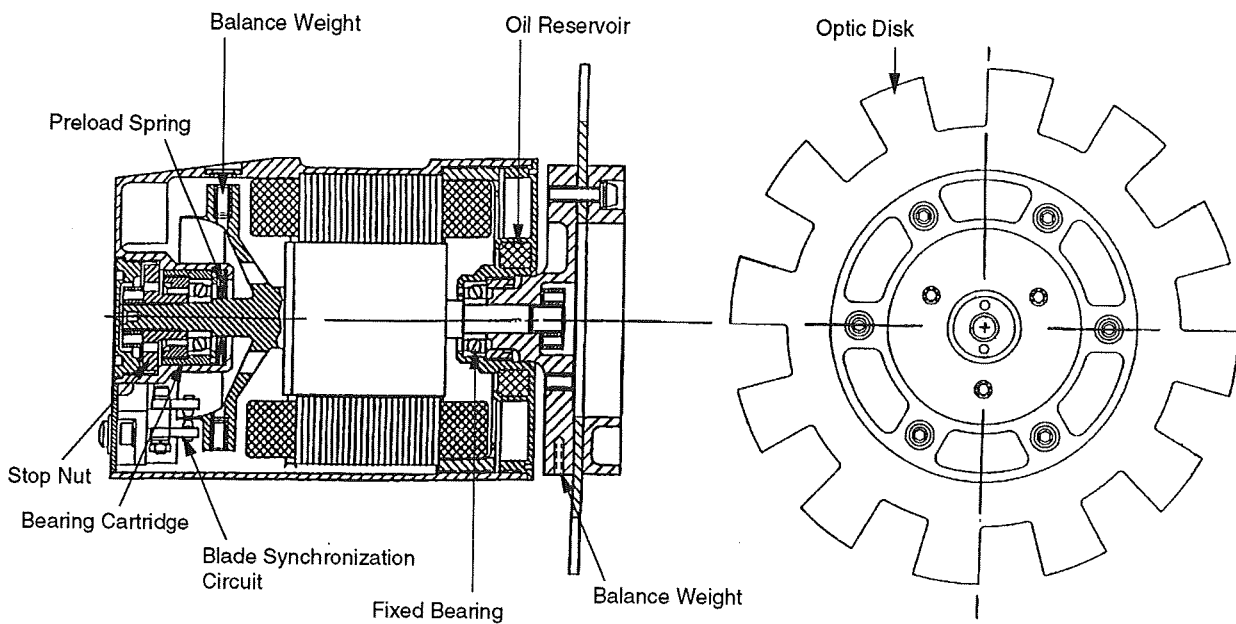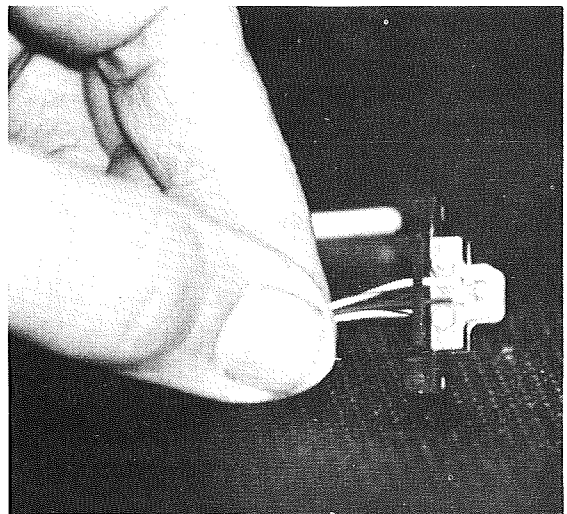

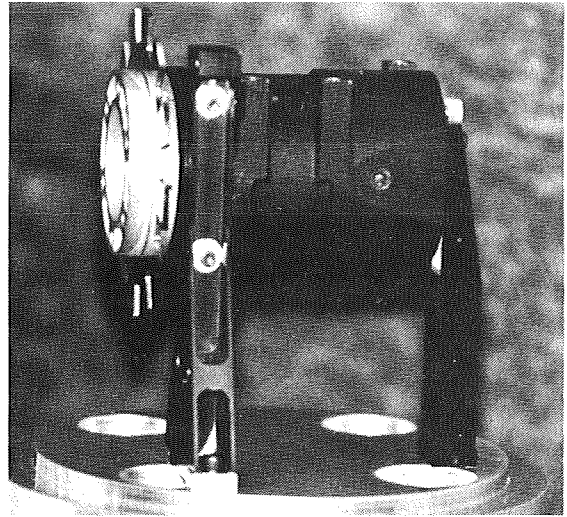Figure 4. Optical Chopper Assembly (OCA) Cross Section
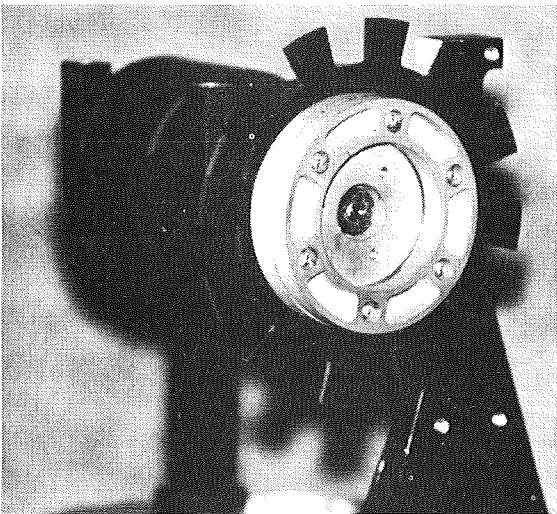
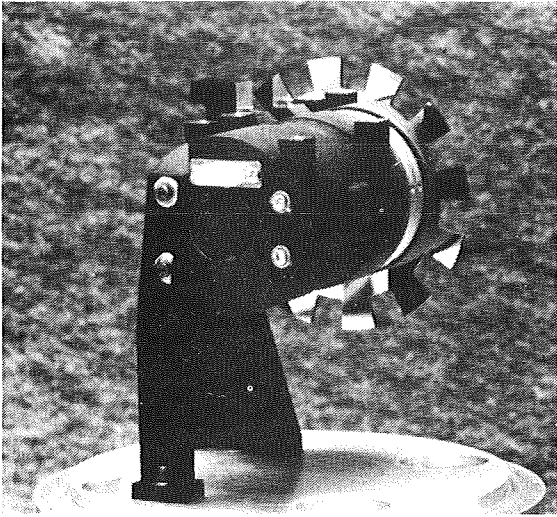Figure 5. Optical Chopper and Sync Circuits

Motor:	AC, Synchronous, Hysteresis
Phases:	2
Poles:	6
Weight:	10 oz
Rated Speed:	4000 rpm (67 Hz)

Torque:
  Running
  Runup
	
	4 gm-cm, minimum
	6 gm-cm, minimum

Power:
  Running
  Runup
	
	<1 W at 4000 rpm & 4 gm-cm
	<3 W
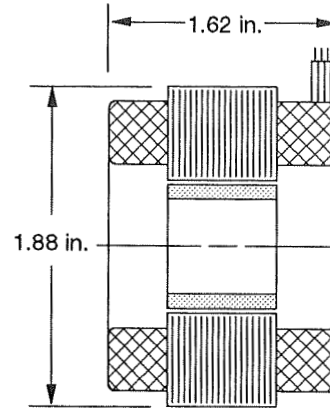
Excitation: 200 Hz, 27.5 ± 8% V rms

Split winding provides drive flexibility
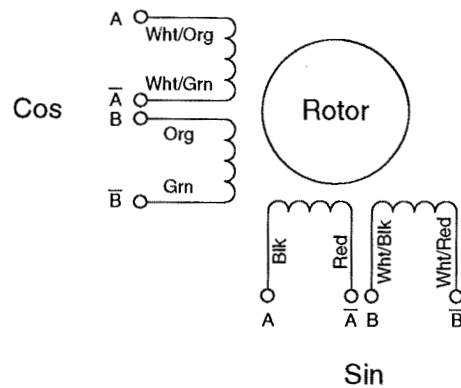
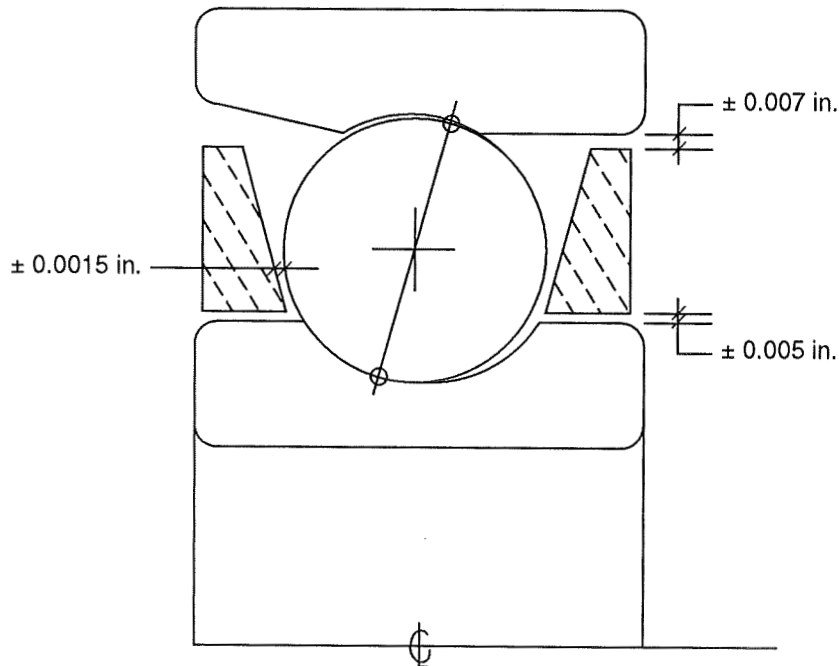Design satifies SOW paragraphs 5.2.2 and 6.2e

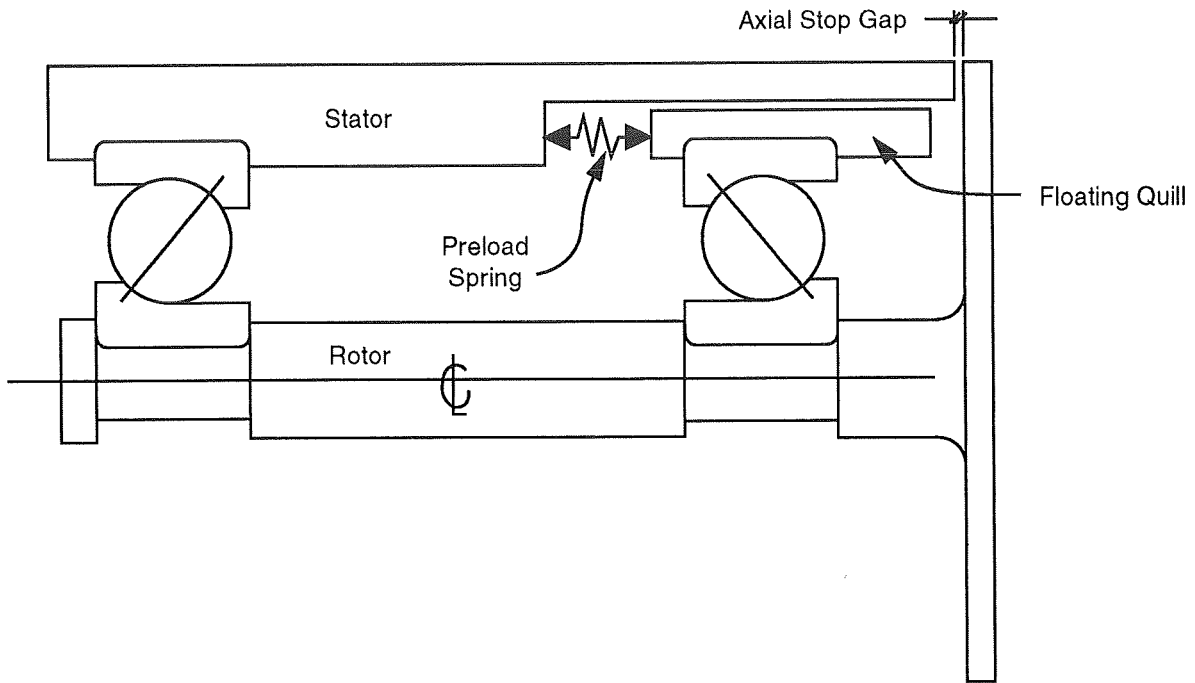Figure 6. Motor Performance Data

Figure 7. Bearing Cross Section
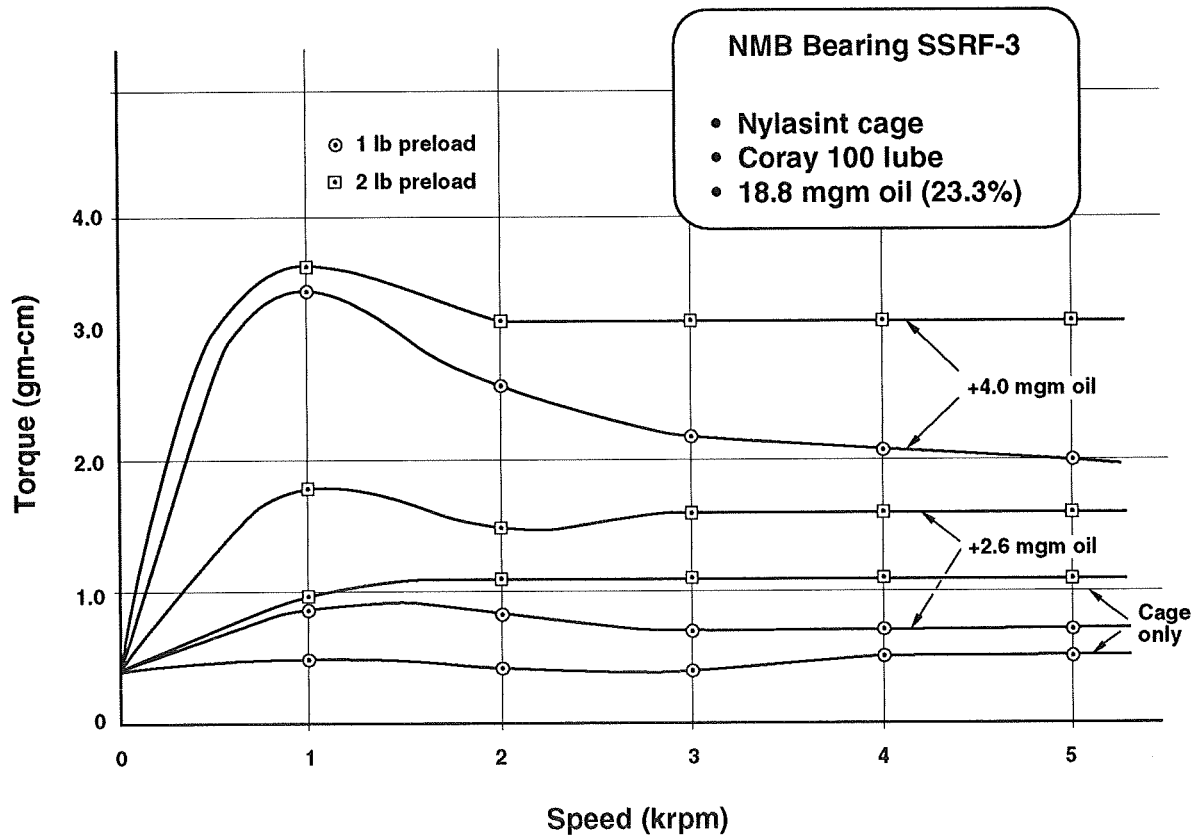
Figure 8. Bearing Preload System Schematic

Figure 9. Drag Torque Versus Lubricant Quantity

A GIMBALED LOW NOISE MOMENTUM WHEEL 434670

U. Bichler & T. Eckardt *

Abstract

The bus actuators are the heart and at the same time the Achilles' heel of accurate spacecraft stabilization systems, because both their performance and their perturbations can have a deciding influence on the achievable pointing accuracy of the mission.

The main task of the attitude actuators, which are mostly wheels, is the generation of useful torques with sufficiently high bandwidth, resolution and accuracy. This is because the bandwidth of the whole attitude control loop and its disturbance rejection capability is dependent upon these factors.These useful torques shall be provided, without - as far as possible, parasitic noise like unbalance forces and torques and harmonics. This is because such variable frequency perturbations excite structural resonances which in turn disturb the operation of sensors and scientific instruments.

High accuracy spacecraft will further require bus actuators for the three linear degrees of freedom (DOF) to damp structural oscillations excited by various sources. These actuators have to cover the dynamic range of these disturbances.Another interesting feature, which is not necessarily related to low noise performance, is a gimballing capability which enables, in a certain angular range, a three axis attitude control with only one wheel.

The herein presented *Teldix MWX*, a five degree of freedom Magnetic Bearing Momentum Wheel, incorporates all the above required features. It is ideally suited to support, as a gyroscopic actuator in the attitude control system, all High Pointing Accuracy and Vibration Sensitive space missions.

1. Introduction

Almost all spacecraft in orbit are equipped with ball bearing momentum or reaction wheels serving as actuators in the attitude control system. Among the various on-board system components, the wheels have been identified as one of the main source of vibration noise due to residual unbalances, bearing imperfections, etc.

Most approaches to overcome the vibration problem are either ineffective or cumbersome. A ball bearing wheel can be manufactured and balanced with higher and higher quality but this drives the cost to infinite while the relative improvements become asymptotically smaller and smaller. Putting a wheel on a passive isolator gives some improvements but such a device is bigger than the wheel itself. This introduces weakness and resonances and the direction of the

---

*Teldix GmbH, Space Department, Bosch Telecom. Grenzhofer Weg 36, 6900 Heidelberg, Germany.

momentum vector becomes uncertain. Moreover, the launch environment can degrade the mechanical quality of such systems. In the end, the vibration problem can only be avoided by the use of magnetic bearing wheels.

Magnetic bearing wheels have some general advantages such as higher speed, no mechanical contacts, no lubrication, no stiction etc. However, this alone is not such a significant reason to base a decision for the magnetic bearing, because the magnetic bearing's current disadvantage of more expensive electronics is at least counterbalancing.

The situation becomes entirely different with the MWX, where the following additional features are built in, which cannot be obtained with ball bearing wheels:

Low Noise

The magnetic bearing position control loops are equipped with a highly effective Active Vibration Suppression control law with isolates unbalance vibrations of the wheel from the spacecraft. This noise isolation is so effective that virtually every visible noise effect has been completely switched off when the isolation system has been invoked.
The wheel's internal actuators are of the electrodynamic force generation type, which enables a high bandwidth, bi-directional and linear response to attitude control system (ACS) commands. This high bandwidth is not affected by the Active Vibration Suppression (AVS).

Control Moment Gyro Mode

The momentum vector of the wheel can be tilted actively with respect to the spacecraft body ('vernier gimballing'), which allows to use the wheel in a control moment gyro mode. This means that in addition to the one rotational DOF which is implemented by the motor torque control, the other two attitude DOFs can be adjusted by the tilting of the wheel. Thus, it enables three axis attitude control of the spacecraft in a fine pointing range with only one wheel and eliminates, compared to a fixed momentum wheel system, the need for a separate nutation damping device.

The vernier gimballing is supported by a special gyro control law, which allows the wheel to be used just like three independent attitude actuators without suffering from disturbances caused by gyroscopic effects. The vernier gimballing maneuvers require very little power. The tilting of the rotor may also be used to store cross momentum in order to compensate for a varying momentum of other rotating members on the satellite, like antenna pointing mechanism.

Active Damping of Structural Oscillations

A magnetic bearing wheel has no mechanical contact between rotor and stator since there is a prescribed gap. Within this gap the rotor can be moved in all three translational directions (in addition to the above mentioned rotational directions) in order to generate reaction forces usable within an active damping system. This can be done with the full linearity, accuracy and high bandwidth of the electrodynamic force generation system. Moreover, in combination with

a side effect of the Low Noise control, it can even serve as a sensor for structural oscillations and can be extended to a stand alone damping device. Thus the wheel can be used further as a six DOF active damping device for flexible structures through fully controllable translational and rotational bearing forces - simultaneously with the main purpose of the wheel as three DOF attitude control actuator.

It shall not be forgotten to mention that the use of a magnetic bearing wheel permits the acceptance of a somewhat increased electronics complexity with inevitable impacts on mass, volume and reliability. A MWX is about 25% heavier than a ball bearing wheel of comparable size - however, this is an unfair comparison, since one MWX can substitute two or three ball bearing wheels.

Thus in the end the magnetic bearing solution can be very advantageous in an AOCS level trade-off and moreover due to the above mentioned unique features.

Possible applications are communication satellites, especially those with inclined orbit, satellites with optical communication links, micro-gravity missions, space telescopes and high resolution earth observation satellites. In long term manned space missions low noise wheels can reduce the effect of vibrations and the associated nerve-racking noise on the spacecraft environment and crew.

2. The Design of the MWX Wheel

A cross section of the MWX is shown in Fig. 1. The design goals were

>very low vibrational noise

>vernier gimballing capability

>pancake profile

>low weight, volume and power consumption

>high reliability

General design characteristics

The rotor is basically composed of a rim which is connected to a hub by a set of five spokes. Most of the mass is concentrated in the outer rim of the rotor contributing to the required moment of inertia.

The housing is devided into two compartments. The upper one contains the rotor and the signal processing electronics mainly consisting of sensors and controllers while in the lower one all the power electronics is accomodated.

Any deviation from the nominal rotor position is detected by a set of axial and radial position sensors and - using five control loops - balanced by forces generated in the actuators.

All five actively controlled degrees of freedom are of the electrodynamic (Lorentz) force generation type. This principle has many advantages with respect to controllability, low noise and the mass distribution between rotor and stator.

A brushless dc drive motor fits well to the magnetic bearing. An emergency bearing and a simple locking device complete the wheel.

Rotor rim

The electrodynamic force generation type led to a m-shape cross section of the rotor rim as shown in principle in Fig. 2.

Also the spoke design is very important for the noise behaviour of the wheel, because mechanical deformations of the rotor rim would lead to a dramatically increased tilt sensor noise and have thus to be avoided. The optimization lead to specially shaped spokes which are very weak due to the rotor stretching caused by centrifugal forces or heating, while in case of any movement of the rotor rim relative to the central part of the rotor these spokes are extremely stiff.

The detailed design of the rim as well as of the spokes was carefully optimized by FEM analysis in order to ensure that the stresses in the spokes and the rotor rim will not exceed the limit of half the tensile strength. The maximum possible rotational speed of this rotor is more than 12000 rpm with a safety factor of 2.

Force generation systems

The axial and tilt loop actuator elements are located in the outer slot of the rotor rim, see Fig. 2. The slot is equipped with permanent magnets which produce a circumferentially uniform magnetic field. Four epoxy embedded stator control coils, each of them covering nearly 90 ° of the circumference, are fitted into the slot. The current in each of these coils produces a force in axial direction. Applying equal currents to all 4 coils produces axial forces. Tilt torques are generated by exciting two opposite coils with opposite currents.

Since it is possible to generate the required forces and torques for the suspension by use of only three coils, sufficient redundancy is attained.

The radial bearings are located in the hub. A disk shaped coil system on the stator fits between two pole plates equipped with permanent magnets. Fig.3 shows the principal arrangement. Two opposite coils form the actuator for one radial DOF each.

The detailed design of the magnetic loops was optimized by three dimensional magnetic field computations with the goal, to get as much force as possible out of the system with the minimum thickness of the magnetic yokes.

Sensor System

The eddy current principle was chosen, because it is simple, of low weight and reliable, provides high bandwidth and is sufficiently linear if both mechanics and electronics are designed appropriately. All sensors are of the differential type in order to minimize drift effects.

The long term stability was calculated to about 0.5% gain and offset error for 10 years operation in space environment. This is in any case fully sufficient, since the position sensor of the magnetic bearing wheel is always in an inner loop superimposed by the AOCS.

Motor

The motor is of the brushless-dc type, which avoids magnetic cogging torque. The ironless three-phase, six-pulse design is featuring a high efficiency joined with an excellent torque controllability and assures minimum torque ripple. The wheel drive electronics incorporates a two quadrant converter and operates in either speed or torque control mode.

At low speed the wheel drive electronics receives the rotor position from a very simple eddy current sensor system and performs commutation switching. At higher speed (above 200 rpm) the commutation is derived from the electromotive force generated in the motor windings.

In case of a satellite power bus or main converter drop out, the motor is automatically switched into a generator mode to maintain the stable suspension down to about 1500 rpm when the electromotive force becomes too low to deliver enough power to supply the electronics.

Emergency bearing

The task of the emergency bearing is to provide a non-disturbing landing and a smooth run-down exhibiting minimum noise figures in case of a failure in the suspension electronics. It consists of two ball bearings, which are located inside the hub of the rotor. As a ball bearing lifetime of only 100 hours (about 200 run downs) is sufficient (only used in case of power drop outs at less than 1500 rpm or when a fatal failure occurs) there are only low demands to these bearings. Tests performed with gravity compensation have shown, that the emergency bearing operation is safe and uncritical. The rotor runs down with only little wobbling.

Locking mechanism

A locking mechanism with re-lock capability keeps the rotor in a safe mid-gap position during launch. The system, as shown in principle in Fig. 4, consists of two tubes of a special space prooven rubber. It is closed before launch by inflating the tubes with compressed gas and released in space by a redundant set of magnet valves.

The locking system is reusable, thus the wheel can be tested after transportation and assembly into the satellite and even in the rocket short before launch.

Technical Data (EM)

Diameter	343	mm
Height	105	mm
Total Mass (incl. electronics)	11.8	kg
Nominal Speed	± 6000...10000	rpm
Angular Momentum	63 ... 105	Nms
Gimballing Torque (around x and y axes)	± 3.9	Nm
Gimballing Angle	± 1.7	°
Slew Rate Capability	± 3.5	°/sec
Cross Angular Momentum (6000 rpm)	± 1.86	Nms
Motor Torque	± 0.15	Nm

185

Power Consumption (steady state, 6000 rpm)...	14	W
Force Noise	< 0.01	N
Torque Noise	< 0.01	Nm
Angular Rate Tolerance x,y axis	3.5	°/s
Acceleration Tolerance z-axis	9.8	m/s2
Acceleration Tolerance x,y-axis	2.2	m/s2
Limits without leaving AVS (1)		
Angular Rate Tolerance x,y axis	0.17	°/s
Acceleration Tolerance z-axis	0.5	m/s2
Acceleration Tolerance x,y-axis	0.1	m/s2
Reliability 10 years, non redundant	0.89	
Self Suspension Time at power drop out (2)	1200	s

(1) Limit can be overcome by active counterbalancing
(2) 0g condition.

3. Vernier Gimballing

The rotor and thus the momentum vector can be tilted actively within a range of about ±1.7°. A special tilt control law assures, that the tilt responses are not deteriorated by gyroscopic effects, i.e. a tilting in one direction is decoupled from the orthogonal direction. This is achieved by an overcompensated gyro-decoupling, which is essential to assure the tilt loop stability with large margins in view of parameter degradations.

The effect is demonstrated by the step responses shown in Fig. 5. Steps have been applied to one of the tilt axes and the responses of both have been measured at 6000 rpm. In the left column it can be seen, that with a simple uncoupled tilt control law the quality of the desired response is deteriorated and even the uninvolved axis becomes disturbed due to the gyroscopic effect. In the right column, the more sophisticated control law of the MWX has been applied which removes all these disturbing effects. It is easy imaginable, that such a behaviour is much better suited for spacecraft attitude control purposes.

It is a special feature of the MWX-X, that it is possible to exert gyro control torques for the attitude control of the S/C while the produced noise of the wheel is still low.

4. Isolation of Wheel Vibrations

Although there is no contact between rotor and stator, magnetic bearing wheels exhibit nearly the same magnitude of perturbations as ball bearing wheels unless special provisions are made to suppress this noise. The sources of the unwanted disturbing forces and torques are:

1. Imbalance, which means that the axis of the position sensors measurement surface is radially shifted (-> static imbalance) or/and tilted (-> dynamic imbalance) against the axis of inertia.

2. Mechanical imperfections of the rotating parts as irregularities in a sensor surface, a pole piece or a permanent magnetic field.

3. Poorly damped bearing control loops, for example due to passive nature, nonlinearities, structural modes or coupling effects between the different loops.

4. Poorly damped gyroscopic oscillations as nutational and precessional motions, which means a whirling motion of the spin axis around the angular momentum vector.

186

All this results in an unwanted movement of the rotor surface within the stator. If there is the typical force generating system which transforms gap variations into force and additionally a control system which tries to keep the gap constant then the same noise is produced as in a ball bearing wheel.

A simple suspension loop model, shown in Fig. 6, is used to introduce and discuss AVS, active vibration suppression.

The origin of all the noise is the gap variation, which can be found in the model as the center of gravity (CG)-position modified by the various gap disturbance sources mentioned above.

If there is a gap-force coupling in the bearing, the synchronous forces are produced in the bearing directly out of the gap variations before it is possible to filter them out. This is true for all electromagnetic force generation principles, where a change of the gap causes a change of the (bias or permanent) flux and thus of the force. Because of this the MWX is equipped with the electrodynamic bearing principle, where the generated force is independent of the relative position and the relative motion of rotor and stator.

The other noise path is the control loop itself and AVS means, that the sensor disturbances must be filtered out before reaching the power amplifier and becoming force or torque. The AVS method used in the MWX is the 'model following control'.

The principle idea of the model following control is to use the output of an observer for the control feedback instead of the disturbed position sensor signal. Fig. 7 shows the principle block diagram of the control loop with observer, which is fed with the force acting on the rotor.

To prevent the observer from long term drift effects, the low pass filtered difference between the real position signal and the model position is used to correct the observers state variables. Here the difference becomes evident: normally, the sensor output with it's noise is connected directly to the (differential!) controller, now there are a low pass filter and the observer in between. Thus from the real sensor signal only the lowest (near dc) frequency components are used. (Because of this, special care has to be taken with regard to control loop stability at these frequencies!) The noise contributors however are of the wheel's rotational frequency and harmonics thereof, thus of comparably high frequency. They are filtered out by a 4 1/2 order low pass filter. This is the reason why the noise suppression becomes effective at speeds say above 1000 rpm and is then further getting better and better.

The difference of the real position and the observer position is fed through a low pass filter to achieve the long term compensation of drift effects. To control faster externally impressed stator movements, for example when the satellite fires a thruster, this difference is additionally fed to a limit switch, which for example detects if the difference exceeds half of the gap. If so, it uses a second, stronger feedback to force the observer position immediately to the real position and, with this, the suspension loop can react and prevent a touch down of the rotor. During the activity of the limit switch, the low noise quality is of course reduced, but there is no low noise condition during an external disturbance anyway. When the external disturbance is over, the wheel automatically enters low noise condition again.

It can be further seen from Fig. 7, that the active spacecraft actuation is not influenced by the MFC, because the path from the position command to the (desired) force or torque remains unchanged.

Some results achieved with the real wheel equipped with MFC in all 5 magnetically suspended axes are shown in the next figures. In Fig. 8, the force Fx in radial x-direction, the force Fz in axial-direction and the torque Tx around the x-axis that are induced into the wheels mounting base, i.e. the satellite, are shown at a speed of 6000 rpm. (The forces and torques were measured with a six DOF dynamometer.) First, on the left hand side of the figure, the wheel is controlled by the conventional proportional-differential law of magnetic bearings, where there is practically no difference to a ball bearing wheel. On the right hand side, the wheel is controlled by the MFC low noise control system. It can be seen, that almost all the noise is removed.

In Fig. 9, the same is shown as Fourier plots, now for all five forces and torques (the sixth torque is that around the spin axis, i.e. the motor torque, which is not affected by AVS.) The synchronous component and the harmonics can be clearly seen at $n*100$ Hz ($n = 1..5$) in the conventionally controlled case (left), but hardly with the MFC (right).

Another view of the low noise behaviour is given in Fig. 10. The torque noise fundamental and the 1st and 2nd harmonics are plotted vs. speed. In the fundamental, the typical MWX noise suppression which increases with speed is clearly seen. The harmonics show a more undetermined behaviour, which is due to some parasitic resonances in the BB set-up. Theoretically, the harmonics should become suppressed almost like the fundamental, and with the EM wheel improvements are expected in this regard. However, the harmonics are already small and need not to be suppressed by the same factors like the fundamental.

The absolute noise values shown in the figures 8, 9 and 10 are not yet the achievable limit, since the wheel was a poorly balanced laboratory bread board model. The only goal was to demonstrate the relative attenuation of the produced noise - which is even now 100 .. 1000 times lower than with a ball bearing wheel of comparable or even smaller size. This was proven in a comparing investigation of the european space agency (ESTEC) /2/.

However, later, in space, it will be a high quality wheel, well balanced, with high circular uniformity of the magnetic field. Then the basic noise will be even more lower and the suppression will further attenuate it.

6. Active and Passive Damping Forces and Torques

The wheel can be moved freely within the mechanical gap of the emergency bearings, because all DOFs are actively controlled. Thus forces and torques can be generated by accelerating and decelerating the rotor.

These forces can be used to damp oscillations of antennas, solar arrays or large structures, i.e the wheel with it's translational or even tilt axes can perform on the side the task of an actuator within an active damping loop without any degradation of the wheels performance.

The left side of Fig. 11 shows a test measurement with the MWX with a movement of $\pm$ 0.1 mm of the rotor in axial direction ($\pm$ 0.6 are possible) that causes a force of $\pm$ 2 N at 10 Hz. The maximum forces that can be generated are functions of the frequency and the gap. These maximum forces are computed for the MWX and shown in the right sideof Fig. 11.

Another damping effect results passively from the bearing control loops. The wheel, in its low noise mode, is coupled to the stator only for very low frequencies up to about 4 Hz, but with a very good damping factor. This is illustrated by Fig. 12. Thus the wheel behaves like a passive damper below this corner frequency in addition to its active damping capability at all frequencies. There is no such coupling between the rotor and the satellite for higher frequencies.

Moreover, structural oscillations can be measured by the MWX, for all higher frequencies up to the wheel speed, since stator movements are not followed by the rotor and can therefore be seen in the signals of the 3 translational and 2 rotational position sensors. Thus the wheel, as is, without any increased complexity and without any degradation of its main purpose, can serve as both a sensor and damping actuator for structural oscillations up to some hundreds of Hz.

7. Applications of the MWX

The MWX in a Mechanical Double Gimbal System

If the MWX with it's low noise three axis attitude control capabilities is utilized, the small gimballing range (compared to mechanical gimbal systems) may be an unwanted limitation. A possible solution would be to mount the MWX into a mechanical double gimbal system. Then the large angular attitude maneuvers can be performed with the gimbals (the MWX with its tilt torque capability of some Nm has no problem with this). Thereafter, the gimbals can be locked in position and then the MWX resumes fine position control at low noise condition during the mission performance period.

The only disadvantage would be, that the spin axis will not necessarily point to the target any more and two axis pointing like with a telescope would additionally require reaction torques from the drive motor. However, in a low noise wheel there will always be a low noise motor present. Just the motor torque will be substantially lower than the gimbal torques and require more power.

Two MWX Substitute a Skewed Arrangement of Reaction Wheels

An interesting proposal is the use of two vernier gimballed wheels running in opposite direction to produce a net momentum in any desired direction by tilting one or both wheels and spinning them up and down, respectively. By doing this it is possible to align the satellite in every desired direction in space by tilting the overall momentum of the satellite, which is stored in the wheels. The principle idea is shown in Fig. 13.

The advantages are that very little power is required for the maneuvers, since the vernier gimballing needs in principle little power. Also the drive motors would be used only in differential mode, i.e. the braking energy of one wheel would supply the other accelerating

189

wheel. The main advantage over a reaction wheel system and thus the main purpose of such a system is, of course, still the low noise performance.

The MWX in a communication satellite with inclined orbit

The inclined geostationary orbit is said to be a solution towards extended satellite lifetime by fuel-savings through less station-keeping. The angle of this inclined orbit will be about 5°. This angle is also considered as the limit for a future extension of the vernier gimballing capability of the MWX. Thus, a MWX can serve as momentum wheel for such a satellite, providing not only a constant attitude stabilization and compensation of cyclic torques through cross momentum storage but,at the same time, the periodic attitude maneuver in order to point constantly at the same location on earth during all the orbit.

Summary

The MWX provides a free-of-mechanical-contact momentum vector inside the spacecraft and allows to exert forces and torques in all directions between this vector and the spacecraft such, that a vibrationless 3-axis attitude control in conjunction with 6-axis active damping of structural oscillations results.

The special features of the wheel are:

- Low vibrational noise, about a factor of some 100 or more lower than of a ball bearing wheel of comparable or even smaller size

- Vernier Gimballing up to $\pm$ 1.7 (later 3° ..5°) with a gyro-disturbance removing control law, practically 'without' additional power, enabling:

    1) Two- or three axis attitude control in a fine angular range at low noise conditions
    2) The inherently linear, high bandwidth and very strong gimbal torques are ideal for fast, high quality attitude control and disturbance rejection at the same time
    3) Cross momentum storage capability;
    4) Nutation damping

- Active damping of structural oscillations, passive damping of structural oscillations, sensing of of structural oscillations.

All these features have been tested at the real BB wheel and all results presented in this paper are real measurements, no simulations.

The gimballing range can be extended to about 3° .. 5° from our present point of view without principal problems. The size of the wheel is not limited at all, just smaller ones cannot accommodate all the electronics and would require a separate box.

Although the theory of the MWX looks comparably adventurous, the technical realization is very safe and reliable. The mechanical elements are rugged, thanks to the launch vibrations lock out device, without any degradation and have the unlimited life. The electronics are not critical and the reliability is proven predictable. Finally the control law has been designed to be very robust with respect to parameter variations over time.

Thus an AOCS, build around this wheel, can be considered as a real and interesting alternative since it offers and combines different features not obtainable with ball bearing wheels. It can even be advantageous in terms of weight, volume and reliability, when the comparison is not performed wheel by wheel but on AOCS level.
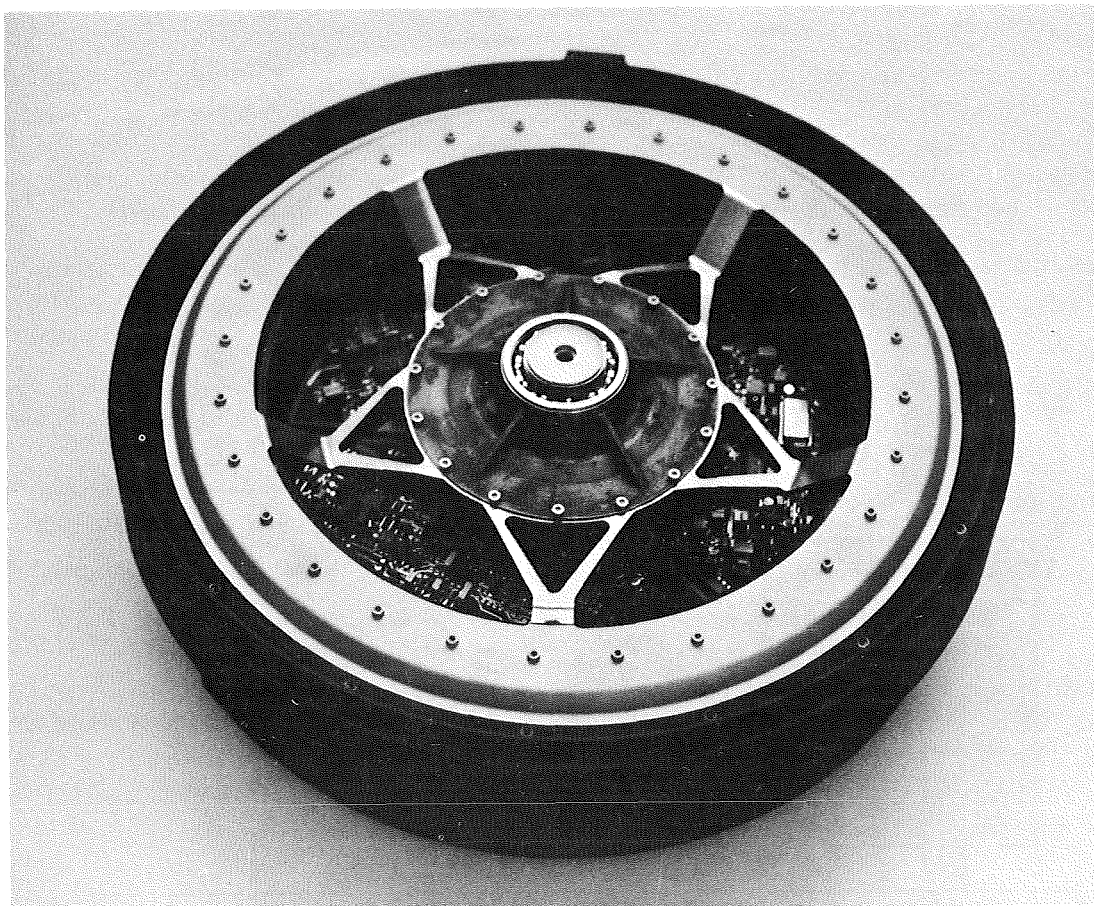
For high accuracy missions, it may be the only possible solution in the end.

Acknowledgements

References

1.   Auer, W., "Ball Bearing Versus Magnetic Bearing Reaction and Momentum Wheels as Momentum Actuators." *AIAA Global Technology 2000*, Baltimore 1980.

2.   ESTEC, BAe, Aerospatiale, Teldix, "Very High Pointing Accuracy AOCS Study". Study part 'Noise measurements of wheels'.

The MWX EM Wheel
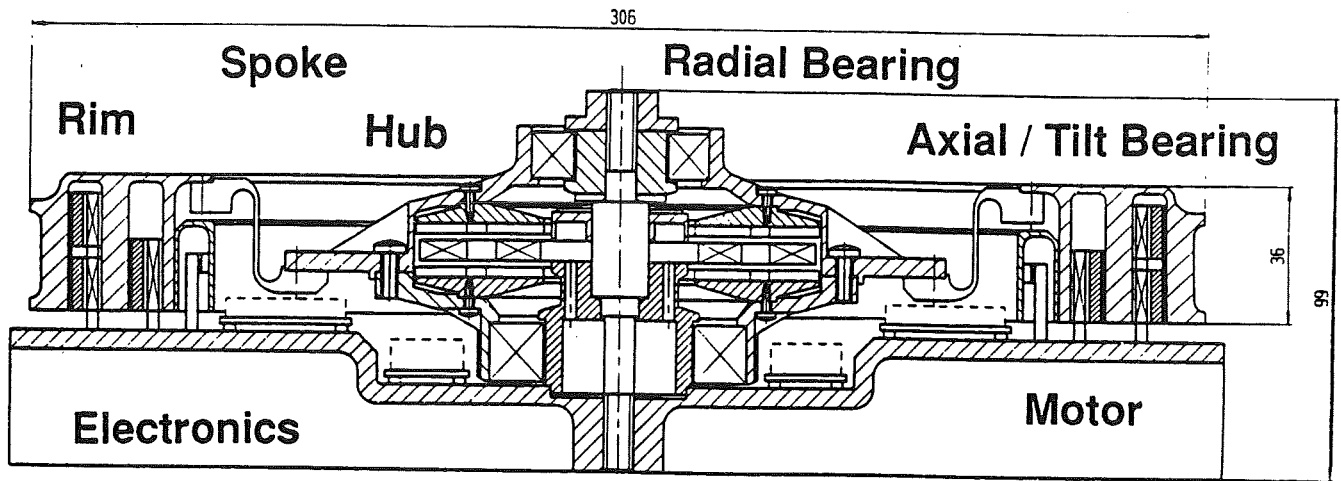
Fig. 1 Teldix 5–d.o.f. electrodynamic bearing wheel MW–X (EM)
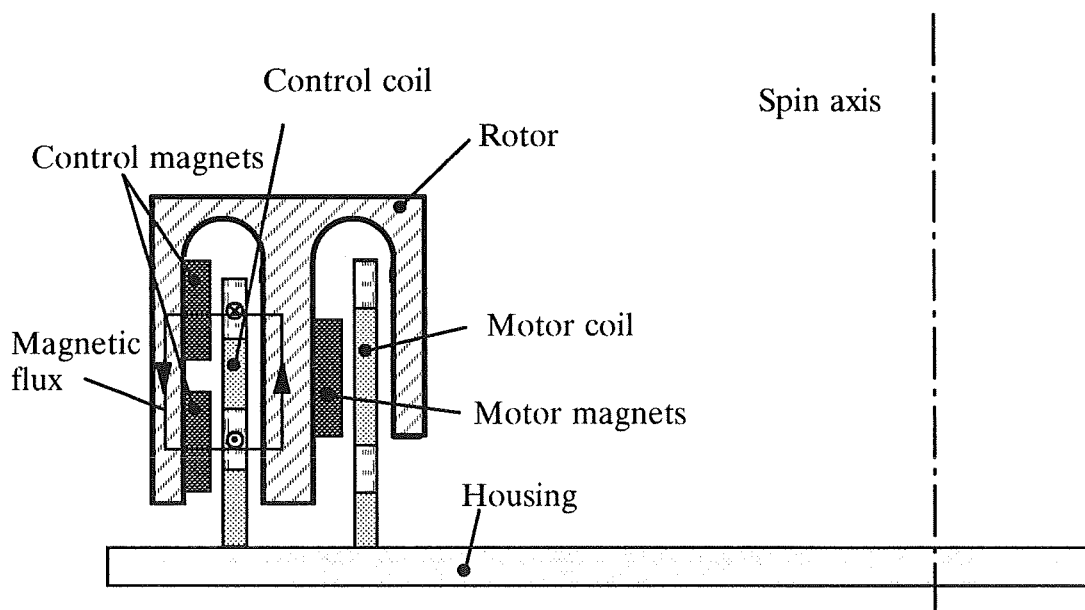
Fig. 2 Axial Force and Tilt Torque Generation

192
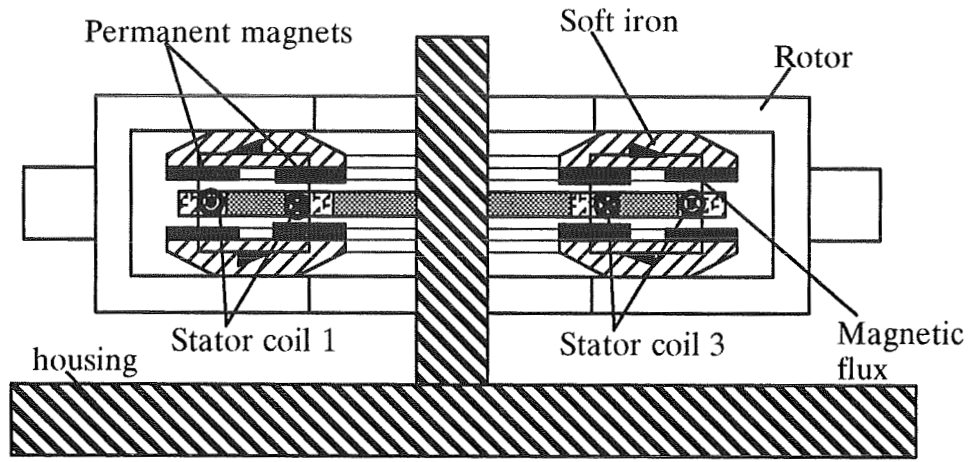
Fig. 3 Radial Force Generation
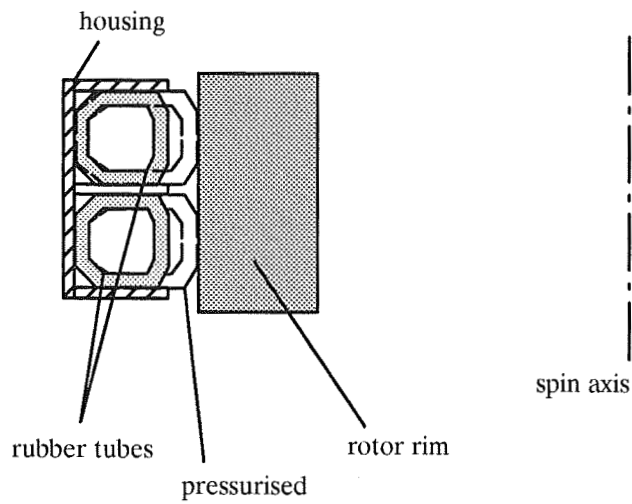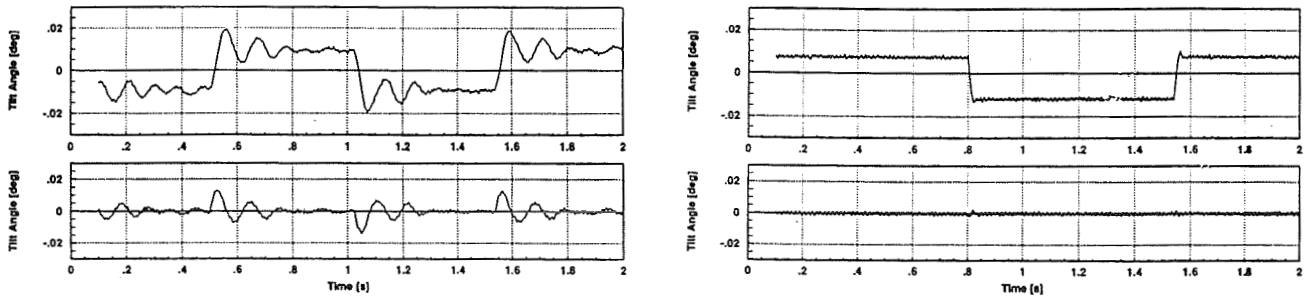

Fig. 4 Locking system

Fig. 5 Tilt Step Responses
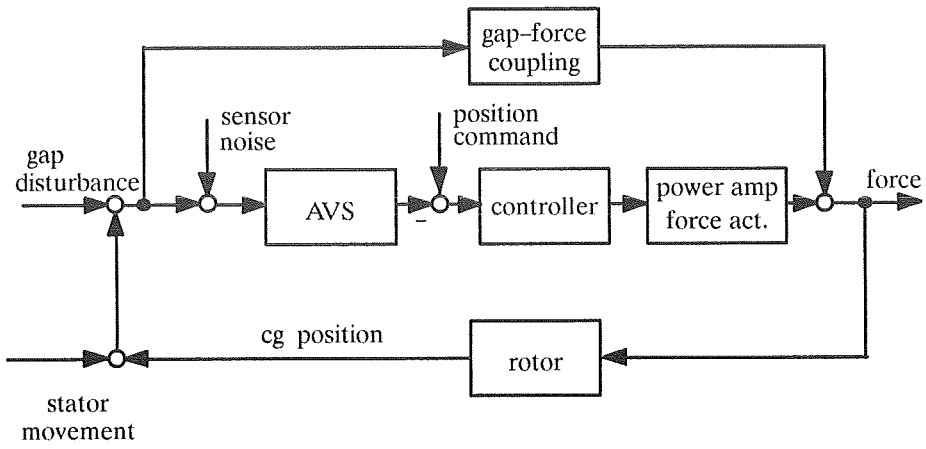*with and without Vernier Gimballing Control*
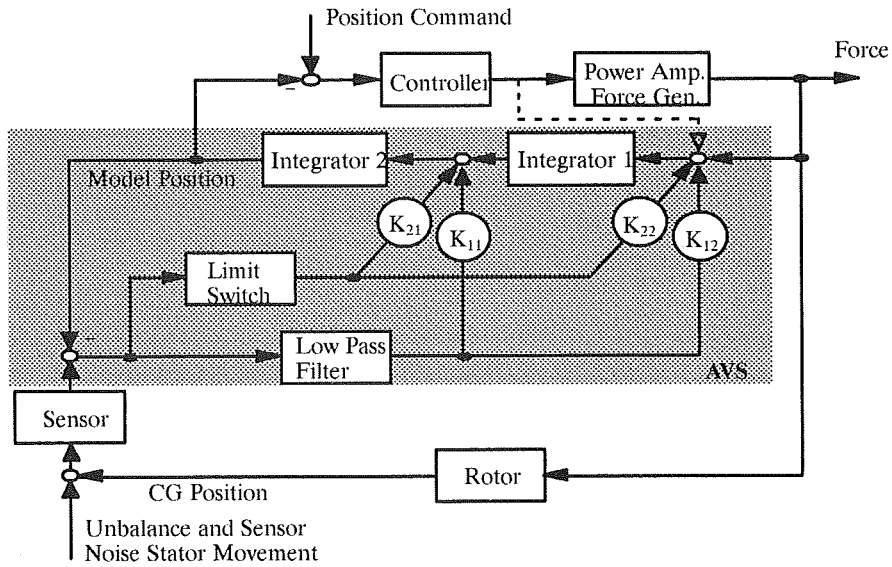
193

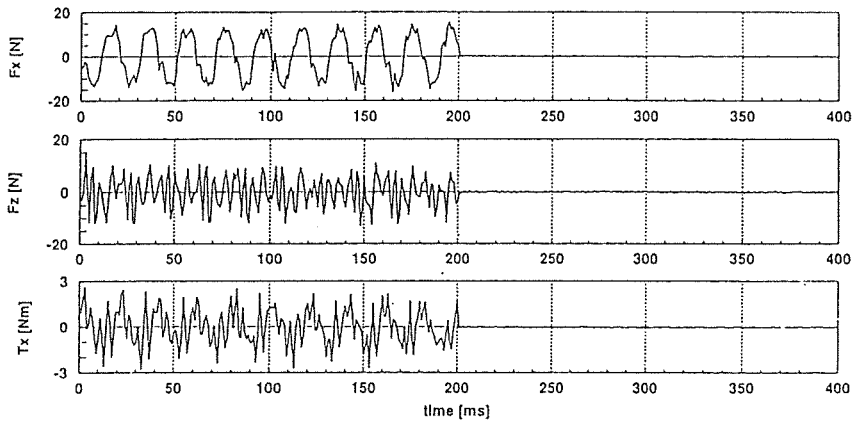*Fig. 6 Simple suspension loop model*

Fig. 7 Model Following Control

*Fig. 8 Wheel Force and Torque at 6000 rpm (time domain)
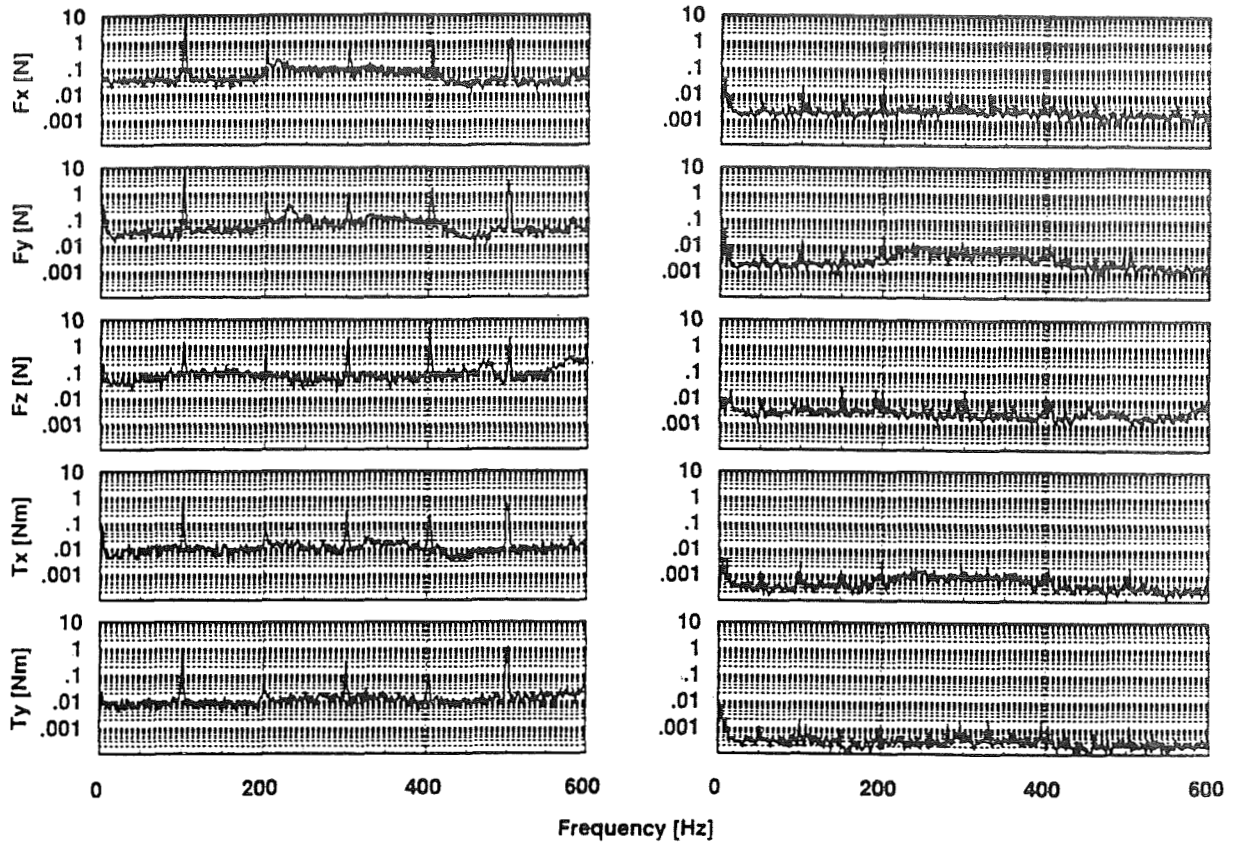with conventional (left) and MFC controllers (right).*

194

Fig. 9 Wheel Force and Torque at 6000 rpm (frequency domain)
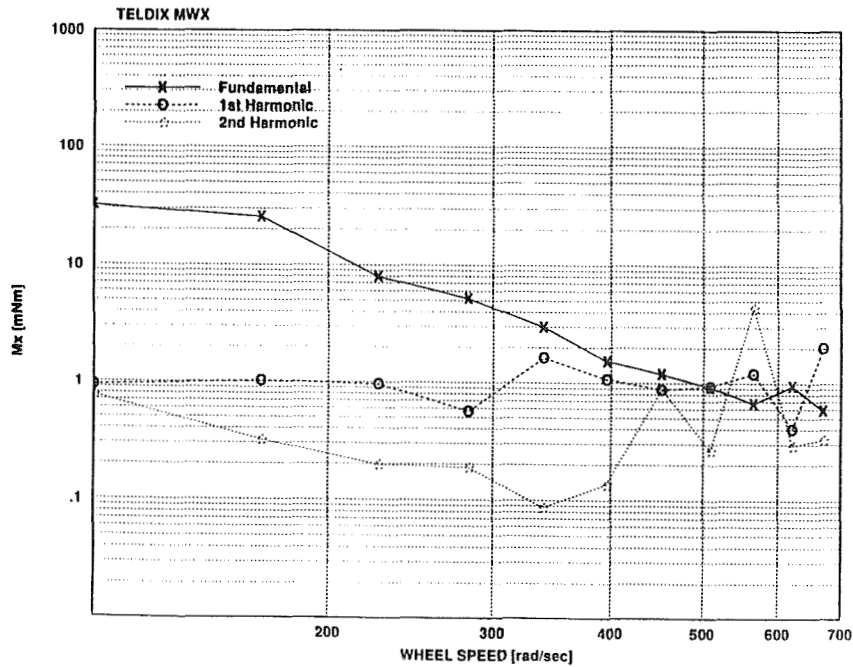*with conventional (left) and MFC controllers (right)*

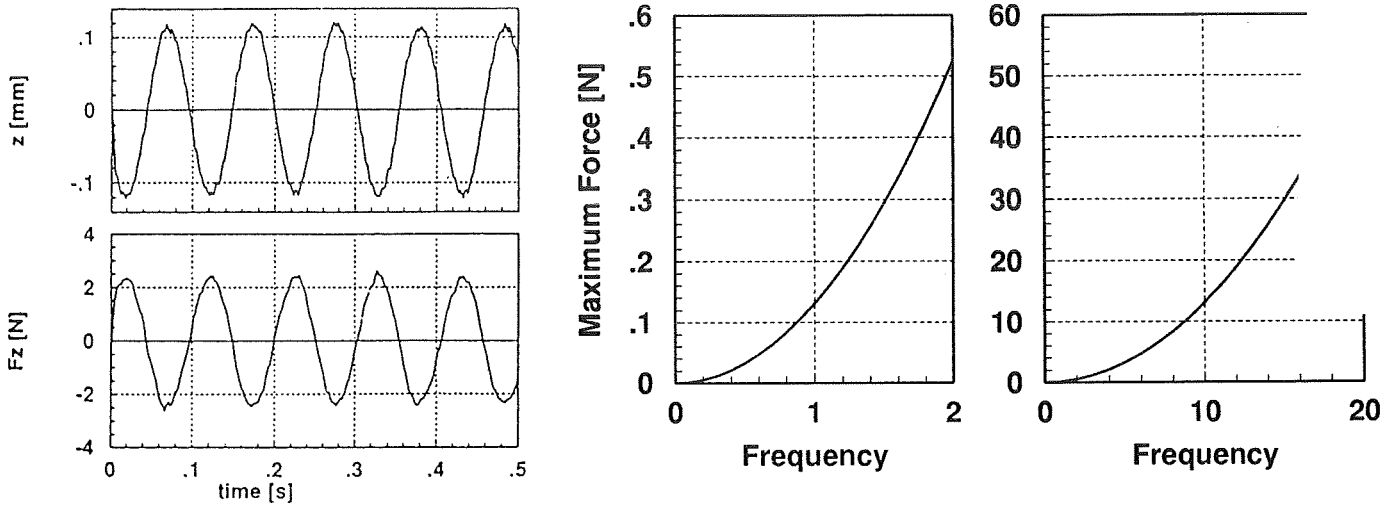*Fig. 10 Torque Noise Fundamental, 1ˢᵗ and 2ⁿᵈ Harmonics vs. Speed*

195

Fig. 11 Active Axial Force Generation and Maximum Possible Active Translational Force
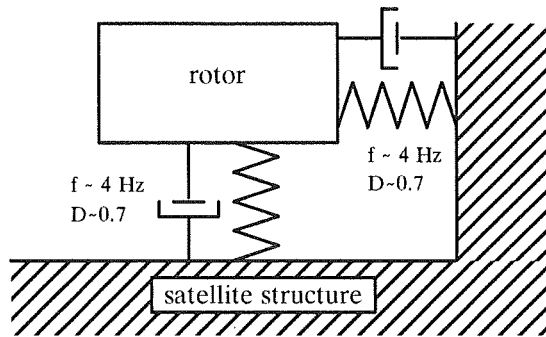

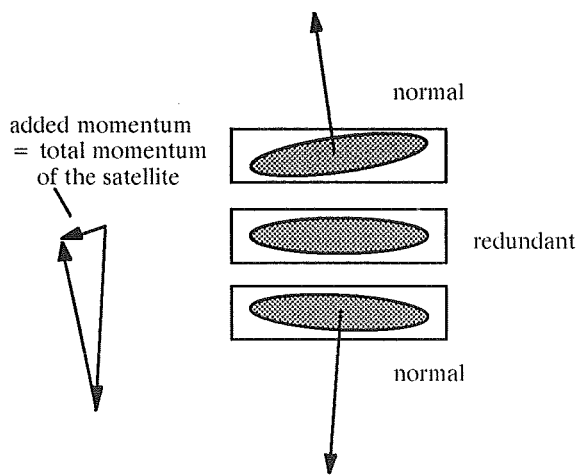*Fig. 12 Passive characteristic of the MW–X at low frequencies*

Fig. 13 Satellite with MW–X instead of a skewed arrangement of reaction wheels

The Use of Screening Tests in Spacecraft Lubricant Evaluation

Chris Kalogeras*, Mike Hilton*, David Carré*, Stephen Didziulis*, and Paul Fleischauer*

ABSTRACT

A lubricant screening test fixture has been devised in order to satisfy the need to obtain lubricant performance data in a timely manner. This fixture has been used to perform short-term tests on potential lubricants for several spacecraft applications. The results of these tests have saved time by producing qualitative performance rankings of lubricant selections prior to life testing. To date, this test fixture has been used to test lubricants for 3 particular applications. The qualitative results from these tests have been verified by life test results and have provided insight into the function of various anti-wear additives.

INTRODUCTION

Because of the stringent conditions placed on spacecraft lubricants and due to the lack of specific performance information, ground-based testing of lubricants is a major factor in the design of spacecraft mechanisms and in the process of selecting suitable lubricants. In most cases, the approach taken when testing lubricants for space qualification is to perform system level life-tests on actual flight hardware, or to perform simulation life-tests which attempt to duplicate the conditions of operation of the flight system. This approach usually produces useful results but is limited by the length of time necessary to obtain data and by the relatively high cost of testing. In most cases only one or two lubricant candidates can be tested, and their selection is usually based on past experience and not on reliable test information. There is a need for a test procedure which can rapidly screen potential lubricant candidates for applications before system-level life tests are performed.

In the course of our work, we have been confronted by this problem on several occasions. In response to this situation, we have developed a test fixture and a test procedure which can determine relative lubricant performances before lubricant candidates are committed to an application

---

* Mechanics and Materials Technology Center, The Aerospace Corporation, El Segundo, Ca

life test[1]. The test fixture utilizes low cost components and operates under accelerated conditions in order to reduce the time for lubricant evaluations. The test capability of this apparatus enables us to rank lubricants for suitability for application in life testing. In particular, we have used this test approach to select lubricants for the following application tests: an oscillating scanner mechanism, a harmonic drive actuator, and, recently, for a reaction wheel support bearing. With regard to the oscillating scanner and the harmonic drive, the results of the screening tests have been verified by life tests. In these situations, the results from the life tests have produced a relative lubricant ranking which is identical to the ranking determined by the lubricant screening test facility.

EXPERIMENTAL

The approach developed to evaluate spacecraft lubricants is centered around two different types of lubricant tests. The first step utilizes a lubricant screening test facility, to perform short term accelerated bearing tests on a number of lubricant selections. The results of these tests provide a generalized performance ranking of the selections and indicate the suitability of the lubricants with respect to the intended application. The next step is to perform life tests or simulated life tests in order to evaluate the suitable lubricants under realistic operating conditions. In both cases, post-test surface analyses are performed on the test specimens in order to understand the results of the tests.

SCREENING TEST BEARINGS

The bearings used for the screening tests are INA GT-1 thrust bearings. The primary reason for selecting these bearings was due to their low cost and availability. These bearings have a complement of 12 balls and a raceway diameter of 0.900 in. The balls, like the races, are made of 52100 steel and have a diameter of 0.187 in. For the purposes of our screening tests, the configuration in which the bearings were run during the tests was changed. Instead of using grooved raceways for both the top and bottom, the flat side of the bottom(rotating race) was polished to a 0.25 micron finish and used in place of the raceway. This change in configuration was done so the bearing could be run with a controlled amount of misalignment. The misalignment serves to accelerate the wear process, the implications of which will be described later. In addition, a flat contacting surface operates at higher Hertzian stress than the raceway, which guarantees that more severe tribological conditions will exist on the flat. This situation is crucial to the success of the test because the flat is far easier to analyze than the

grooved racetrack.

TEST FIXTURES

The mechanism that was developed to perform the screening tests is represented in Figure 1. This design was based on an earlier design[2], but was changed significantly in order to enhance its capabilities. Similar types of testers, based on the earlier design have been reported in literature[3]. In short, the apparatus consists of a bottom housing, which contains the support bearings for the drive shaft, and a upper housing which is designed to contain the test bearings. On the top of the test fixture is a plate which is used to load the test bearings. This plate is free to slide up and down along four studs which are threaded into the top of the upper housing. The test load is applied to this plate with a set of springs(one for each stud) which are compressed along the studs and against the load plate. This arrangement, in turn, pushes the bottom of the load plate against the stationary race of the test bearing. In order to determine the applied load, a load cell is placed between the load plate and the stationary race of the bearing. The load cell can measure loads from 0 to 100 lbs and has a resolution of 0.1 lbs.

The thrust bearings used for the screening tests are mounted in a housing located in the bottom of the load plate. During a test, these bearings are situated such that the stationary(top) race is mounted in the detachable housing and the rotating flat is on a shoulder of the drive shaft. The apparatus was designed to incorporate the detachable housing in order to vary the degree of ball skidding in the test bearing. As described earlier, the ball skidding is produced by mounting the upper race of the thrust bearing slightly off-center from the rotational center of the rotating flat. The resulting misalignment between the top and bottom races causes balls to skid as well as roll during operation. This type of motion imposes severe stress on the bearing and the lubricant because it forces the bearing to operate in a boundary lubrication regime. Consequently, test lives are greatly reduced in comparison to typical ball bearings. In addition, the eccentric operation of the bearing produces a relatively wide wear zone on the flat disk. This is beneficial because it provides a large area in which to conduct post-test surface analysis. The amount of eccentricity in the test bearing is variable and can be adjusted from dead center to 0.125 in.

In order to measure the reaction torque of the bearing, the upper housing is connected to the lower portion of the test fixture through a set of aluminum flexures. The flexures allow the upper portion of the test fixture to rotate slightly with respect to the bottom housing when a torque is applied to the test bearing housing. The reaction torque of the bearing is thus determined by measuring the amount of rotation of the upper housing with respect to the stationary, lower housing.

This is accomplished by mounting an inductive proximity sensor
to the latter and measuring the change in displacement between
it and a target plate mounted on the upper housing. The
proximity sensor is calibrated by applying known torques to
the upper housing and measuring its stiffness coefficient,
which is then used to convert measured displacements into
bearing reaction torques.

During the tests, the reaction torque of the test bearing
is monitored continuously with a data-acquisition computer. A
custom Fortran program is used to acquire the data and store
it to a disk file. The data are acquired at a relatively high
acquisition frequency(100 Hz) and are then time compressed by
a data averaging routine. The routine acquires 100 Hz data in
ten second intervals and computes a mean value for each
interval. The mean values are accumulated in a data array and
are stored to a data file on a periodic basis.   The averaging
routine allows the reaction torque of the test bearings to be
monitored continuously throughout the test without storing an
excessive amount of data.

In order to simulate the space environment, the test
apparatus operates in a vacuum chamber. The chamber is pumped
by a 360 l/s turbo-molecular pump and reaches a baseline
pressure of $1X10^{-8}$ torr. In addition, the chamber has the
capability of being sealed off completely and back-filled with
gases (e.g., He for certain reaction wheel bearings). Since
the drive motor is external to the vacuum chamber, a rotary
(Ferro-Fluidics) feed-through is used to transmit rotary
motion to the drive shaft of the apparatus.

In addition to testing thrust bearings, several different
sizes of angular contact bearings can be tested with only
minor changes in the upper bearing housing and load plate.
Recently, the test apparatus was modified to perform pin-on-
disk tests. This modification allows data to be obtained on
friction and wear of different materials and surfaces.

An accelerated life-simulation test fixture, referred to
as the Boundary Lubrication Test Fixture was used to verify
some of the results from the screening test. This fixture
utilizes modified bearing components as test specimens and
operates at speeds and pressures which are very close to those
experienced by the bearings in many low-speed oscillatory
mechanisms. This test fixture operates in an linear
oscillatory manner. The performances of the lubricants are
assessed by measuring the wear rate of the test specimens
during the testing. This is accomplished with capacitive
displacement probes which are mounted directly above the
specimens. Figure 2 shows the Boundary Lubrication Test
Fixture's bearing and sensor configuration in detail.

RESULTS AND DISCUSSION

CASE #1-OSCILLATING SCANNER BEARINGS

In this particular test program, the goal was to find a suitable replacement lubricant for a pair of R2 bearings which are used to support the shaft of an oscillating optical scanner. The original lubricant used in this application was G.E. Versilube F-50, a chloroarylalkylsiloxane(CAS) oil. This oil has a very low vapor pressure and excellent low temperature properties, but it does not function well under boundary lubrication conditions. In this application, the oil degraded very quickly which resulted in substantial bearing wear and reduced life. The goal of the screening tests was to find a replacement oil which had comparable vapor pressure characteristics and pour point as the CAS oil as well as enhanced boundary wear characteristics. Once identified, the oil was to be tested in a simulated life test in order to qualify it as a space lubricant.

After preliminary investigation, substitute oils were chosen for the tests. These oils, along with some of their physical properties, appear in Table 1. The CAS oil was included in the testing in order to obtain a performance baseline for comparison purposes. The PFPE oil, Brayco 815Z is a perfluoropolyalkylether oil and was selected on the basis of its low vapor pressure and viscosity properties. NYE 188B differs from the other oils because it is a synthetic hydrocarbon oil (poly-alpha-olefin, PAO). It was chosen because of its excellent physical properties and because it could be formulated with the anti-wear additive tricresylphosphate (TCP). The inclusion of an anti-wear additive in the oil was considered to be essential because the bearings operate in a boundary lubrication regime.

In this set of tests, the earlier configuration of the test fixture was used[1]. This version utilized a thrust bearing of the same dimensions as the INA GT1 but incorporated a custom 440C disk and 440C grade 10 balls. The test specimens were run in a vacuum environment at a speed of 1750 rpm and the load ranged between 20 and 50 lbs (229-310 ksi peak contact stress). The motor current of the test fixture was measured in order to get an estimate of the reaction torque of the bearing. Bearing failure was defined to occur when the motor current reached a level 1.5X the starting current.

The wear lives of the screening tests are shown in Figure 3. In this chart, the wear lives of the oils have been normalized with respect to the worst performer. As the chart indicates, the PAO oil had the longest life under these conditions. The primary reason for this result appears to be the superior boundary protection provided by antiwear additive (TCP) in the PAO oil. In the absence of antiwear additives, the CAS and PFPE oils could not protect adequately against direct metal-to-metal contact in the bearing. In addition,

both the CAS and the PFPE oils decomposed under use. The CAS oil was the most reactive, forming a hard "sand" like grit which caused significant wear and subsequent failure after only a short period of operation.

After these tests were concluded, the same three oils were tested in a simulated life test of flight grade bearings under conditions which mimicked the operational conditions on orbit. The results of the life testing appear in Figure 4. It is obvious that the PAO oil outperformed the other oils by a wide margin. Both the CAS and PFPE oils exhibited the same failure mechanism in this test as they had in the screening tests. The absence of an anti-wear additive, coupled with lubricant decomposition, was the most likely cause of the early bearing failures. By contrast, the PAO lubricated bearings operated over 3.5 years and did not display abnormal wear upon removal. The bearings still contained an adequate amount of lubricant, and the lubricant did not show any signs of degradation. More details on these test results can be obtained from the literature[4].

CASE #2-HARMONIC DRIVE SUPPORT BEARINGS

Another lubricant evaluation involved testing lubricants for a harmonic drive actuator mechanism. The goal of this study was to obtain comparative performance data between a frequently used neopentylester spacecraft oil(NPT-4), and a new synthetic hydrocarbon oil (Pennzane SHF-2000), a multiply-alkylated cyclopentane (MAC) which has some outstanding physical properties. Additionally, it was desired to gain a better understanding of the role of wear additives in oils and the mechanisms by which they provide protection. The additives of interest are TCP and lead naphthenate (PbNp).

In order to conduct this study, the Boundary Lubrication Test Fixture was used in combination with the Lubricant Screening Test Fixture. The Lubricant Screening Test Fixture was first used to determine the relative performance of the different oils and additives. While the relative ranking of the lubricants was being established, some of the oils were then tested in the accelerated life test fixture to see if the performance trends established by the screening tests were repeated in longer term tests.

The newer version of the Lubricant Screening Test Fixture along with INA GT1 bearings, described earlier, were used to perform the screening tests. These tests were run at a speed of 1800 rpm and were conducted in vacuum at a base pressure of 1×10^{-7} torr. The reaction torque of the test bearing was monitored continuously; failure was defined to occur when the reaction torque of the test bearing exceeded a level 3x the initial run-in torque. For these tests, a 4lb/ball load(288 ksi peak contact stress) was used in the test bearings, and each test bearing was lubricated with 60 μL of oil. This amount was somewhat excessive, but it was used

202

to eliminate lubricant starvation as a failure mechanism.
Table 2 lists the oils and oil/additive combinations that were
tested in the Lubricant Screening Test Fixture.

While the screening tests were proceeding, the Boundary
Lubrication test Fixture was used to conduct longer term wear
tests using the same oils and additives. The specimens in
these tests were loaded to a stress level of 113 ksi and were
run in an oscillatory manner with amplitude of 0.10" and a
frequency of 1 Hz. The tests were conducted in a vacuum
environment and had durations which ranged from 1000 to 1500
hrs. This time range was chosen because its length was
considered sufficient for wear processes to occur.

The test results of the screening tests appear in Figure
5, from which it is clear that oils formulated with wear
additives outperformed the base stock oils. The poor
performance of the unformulated Pennzane underscores the
necessity of using boundary layer additives under these
conditions. Of the combinations tested in the screening
tests, Pennzane with TCP had the longest life. The addition
of Pbnp in Pennzane also improved the life of the oil but not
to the extent that TCP did(see later for information on
failure modes for the two additives). NPT-4 was not
formulated with any of the wear additives because its chemical
structure and reactivity causes resulted in the formation of a
protective boundary layer. However, the boundary layer
produced by NPT-4 is not as effective as those produced by the
oil additives. Furthermore, the method by which NPT-4 forms
its boundary layer (chemical reaction with the steel surface)
may result in damage to the bearing surfaces.

Following these tests, the surfaces of the test specimens
were analyzed with energy dispersive x-ray (EDX) and/or Auger
electron (AES) spectroscopy. The profiles of the surfaces
were also measured using a DecTak 3030 profilometer. These
analyses were performed in order to determine the failure
mechanisms of the test specimens and to assess the performance
of the boundary wear additives.

The post-test analyses revealed that the test bearings
lubricated with TCP and PbNp containing oils failed by
different mechanisms. The bearings lubricated with
Pennzane+TCP appear to have failed by a wear process that
involves surface distress and metal removal from the wear
track. Figure 6 contains two surface profile scans across the
wear track of a Pennzane+TCP lubricated bearing. The graphs
in this chart indicate that a significant wear trough, along
with increased surface roughness, occurred in this test
bearing. The bearing appears to have failed at the point when
the additive could no longer provide satisfactory boundary
layer protection. The bearings lubricated with Pennzane+PbNp,
on the other hand, do not appear to have failed as a result of
metallic wear. Instead their increased friction appears to
have been caused by the formation of a tough, lead-containing
carbon film on the wear surface of the disk. The evidence for

the existence of the carbon-lead film was first detected by
EDX spectroscopy and later confirmed by profilometry
measurements. Figure 7 contains several EDX scans of a test
sample containing a carbon-lead film. As the plots show, only
the scan of the regions within the wear-zone contain elemental
carbon and lead in any quantity. Outside of this area, there
is little evidence of these elements on the surface. Figure 8
shows profilometry traces taken across the wear track of the
same raceway. The graphs confirm the existence of a film
build-up across the wear track and indicate that the film is
between 0.1 and 0.5 microns in thickness.

The apparent differences in the performances of TCP and
PbNp in Pennzane have suggested that the two additives cannot
be directly compared to each other. The test results suggest
that TCP and PbNp have different boundary protection modes.
Lead naphthenate appears to function by generating a
relatively thick film between the contacting surfaces. This
characteristic makes PbNp ideally suited to high stress
applications where maximum protection against wear is desired
and increased friction is not a factor. TCP, on the other
hand, seems to function by reacting with the steel and forming
a thin, friction reducing film on the contacting surfaces.
These characteristics make TCP well suited to light or
intermediate loads, where low friction and long life are
desired. However, as shown by Figure 6, TCP does not provide
the same degree of protection against wear as does PbNp. This
is an important consideration, especially in situations where
bearing stiffness is crucial to the success of the
application.

These results illustrated some of the difficulties of
performing comparative screening tests on different lubricants
and the need for careful consideration of the end application
in making final selections. Many factors, such as load,
speed, temperature and material compatibility must be
evaluated when determining the test conditions. Post-test
analyses of the test components are essential to proper
interpretation of the test results. Post test analysis was
extremely useful in our case, because it allowed us to
reevaluate the ranking established solely by the screening
test wear lives. Based on the screening test wear lives,
Pennzane with TCP appeared to be the best choice. However,
for the purpose of the harmonic drive application, the low
friction produced by TCP is not as important as the improved
wear protection which PbNp provides. Based on bearing wear as
the ranking factor, Pennzane with PbNp is the best combination
of those tested.

Due to the length of time necessary to perform the
accelerated life tests, not all of the lubricant combinations
tested in the screening tests were tested in the Boundary
Lubrication Test Fixture. Nevertheless, the results obtained
from this test fixture have confirmed most of the findings of
the screening tests. Post test analyses, similar to those

performed on the screening test samples have given us sufficient data to make this conclusion. Table 3 is a compilation of all of the test results from the screening tests and the low speed oscillatory tests. From these data, it is evident that the lubricant behavior in the screening tests has been replicated in the accelerated life tests. In addition to our findings, life testing performed on actual harmonic drive mechanisms with NPT-4 and Pennzane+PbNp has confirmed these results. Additional tests with Pennzane and PbNp have been planned. These tests will investigate the effects of varying additive concentrations on wear performance and will look for an optimum additive concentration.

CASE #3-REACTION WHEEL SUPPORT BEARINGS

The Lubricant Screening Test Fixture was also used to evaluate lubricants which have been considered for use in reaction wheel support bearings. In this study, the apparatus was used to test a well known spacecraft lubricant SRG-40, a highly refined mineral oil, and two synthetic oils which were considered as replacements for SRG-40. The synthetic oils consist of NYE 179, a PAO oil, and NYE UC-7, a poly-ol-ester oil (POE). All of the oils tested were formulated with TCP. Table 4 lists some of the properties of the oils tested.

Reaction wheel assemblies (RWAs) and gyroscopes often operate in atmospheres of helium or hydrogen gases. The particular RWA of interest uses a He-O_2 mixture (P_{tot} = 0.5 atm with 2% O_2), so it was decided to perform lubricant screening tests in several different environments. These environments consisted of: 1×10^{-7} torr vacuum simulating a worst case scenario of an on orbit leak; 1/2 atmosphere of 98% He 2% O_2, the operating environment used on orbit; and 1/2 atmosphere of pure He. The last environment was chosen because it was desired to see if the inclusion of oxygen was really necessary for the anti-wear additive TCP to function. Many spacecraft designers have included oxygen in the fill gases of reaction wheels based on intuition rather than experimentation. The premise for this has been that TCP will only bond to an oxide surface. Hence the addition of oxygen to the helium fill gas will ensure that all metal surfaces will be covered with an iron oxide film, which can be replenished if worn off. In our experience, however, we have never observed that oxygen is necessary for TCP to function correctly. In fact, our concern here was that the inclusion of oxygen in the fill gas may actually be detrimental to life of the bearing because it could degrade the lubricant. Therefore, several additional tests were run in a 7 torr atmosphere of O_2. This amount represents the equivalent of the 2% O_2 added to the helium, and it was felt that this condition would accentuate both the reactive effect of oxygen on the lubricant and any potential effect of oxygen on TCP.

The test conditions and procedures for the screening

tests performed in this study were virtually identical to those performed for the harmonic drive actuator. The only difference, aside from the different environments, was that some of the tests were run with a lighter applied load (3lb/ball).

The wear lives of the screening tests performed in vacuum and 7 torr O_2 appear in Figure 9. In this chart, the wear lives represent the mean values of several tests per oil. As the graph indicates, the synthetic oils outlasted SRG-40 by a wide margin in vacuum. The main factor that accounts for this result seems to be the high vapor pressure of SRG-40. It is felt that this high vapor pressure, combined with the extreme operating environment, led to rapid lubricant loss from the bearings and subsequent failure. The synthetic oils, with their lower vapor pressures, appear to have remained in the bearings for a greater duration which resulted in their longer wear lives. Gas chromatography was later performed on the oil residues of all the test specimens which confirmed that significant lubricant evaporation occurred in the SRG-40 test bearings, while there was much less evaporation in those lubricated with the synthetic oils.

Although not all of the oils were tested in 7 torr of oxygen, the results from those that were tested indicate that the presence of oxygen in the operating environment did not improve the test lives, and, in the case of UC-7, the wear life was significantly decreased. Figure 10 is a plot which compares the bearing reaction torques for UC-7 in vacuum and in the oxygen environment. From this figure it is obvious that the addition of oxygen to the operating environment results in higher torque, more torque noise, and greatly reduced wear life. Visual inspection of the bearings after the tests also revealed extensive lubricant degradation in the case of the oxygen tests and little or no lubricant breakdown in the vacuum tests. This finding was later supported by findings from the 1/2 atmosphere tests.

The wear lives from the tests performed in the 1/2 atmosphere environments appear in Figure 11. In general, these tests ran for a much greater period because the presence of the fill-gas reduced lubricant evaporation and allowed the bearings to operate at a lower temperature, providing a more direct comparison of the respective boundary layer performances of the oils. The tests that were performed with the helium-oxygen mixture (SGR-40 only) confirmed the results obtained from the 7 torr oxygen tests. The test lives in this case were significantly shorter than any of those performed under a helium only atmosphere. In the helium only test condition, UC-7 was the only oil that failed consistently, according to our torque failure criteria. In contrast, the tests performed with the other oils were either terminated before failure, due to time constraints, or were run for a great length of time in order to fail(179). Consequently, post test analyses, similar to those performed

in the harmonic drive study were carried out on test specimens from all of the test environments in order to clarify the results

The most notable finding, from the surface analyses(AES and profilometry) is that TCP does not appear to function as an anti-wear additive in UC-7. The Auger spectroscopy performed on the UC-7 wear disks never detected any trace of phosphorus on the steel surfaces. The absence of phosphorus in this case, combined with the detection of a carbon residue on these surfaces, suggests that the reactive nature of ester oils interferes with the normal protective mechanism of TCP. By contrast, all of the samples run with 179 and SRG-40 contained phosphorus in the wear track, indicating that TCP was active in this region and indicating that oxygen is not required for TCP to function.

The profilometry measurements revealed large wear troughs in the wear tracks of the UC-7 test specimens. Measurements made of the other wear disks indicate that SRG-40 operates with less wear than UC-7, and 179 appears to have the lowest wear rate of all the oils tested under these conditions. The presence of this type of wear and its relative absence for the other oils suggest that the reactive boundary layer film, that UC-7 generates under use, is not as effective as TCP in preventing wear. In fact, this method of boundary layer protection may actually damage the steel surfaces of the bearings and cause increased "chemical" wear.

The wear lives of the screening tests and the post test analyses performed on the test specimens, indicate that Nye 179 was the best overall choice for this application. Its performance in vacuum was far better than that of SRG-40, and its performance in helium was considered to be the best of all the oils tested. Furthermore, the use of oxygen as a component in the fill gas of reaction wheels was determined to be unnecessary and generally harmful to the life of the bearing lubricant. These findings have been conveyed to the manufacturer and have been used to determine the configuration of a reaction wheel lubricant validation test which is currently underway.

SUMMARY

The Lubricant Screening Test Fixture and the procedure developed for its use have proven to be quite useful for acquiring performance information for spacecraft lubricants. The chief advantage of this approach is the ability to obtain qualitative rankings of different lubricants through the use of low cost, short duration bearing tests. This is significant, when considering the lengthy test times and high costs associated with most spacecraft lubricant tests. The test fixture and test procedure also can be used to perform more fundamental studies on the interactions of lubricants and

additives with bearing surfaces. The case studies described in this paper have demonstrated that this test fixture, in conjunction with the appropriate post-test analyses, can be used to identify different wear protection mechanisms as well as to determine bearing/lubricant chemistry.

The results from the case studies, however, have also demonstrated some of the limitations of this approach. The results have shown that screening tests alone are not sufficient for most lubricant studies. The fact that the test bearings used in these tests are significantly different from the configuration of most satellite bearings makes it almost impossible to predict accurately an application's life based solely on screening test lives. The test results from the case studies have also highlighted the necessity of choosing the appropriate test conditions. The effects of test parameters, such as load, speed, temperature, atmosphere and lubricant quantity, on the test life need to be understood if a valid lubricant ranking is to be established. Even more important is the selection of appropriate post-test analyses. These analyses are often necessary in order to identify performance traits, such as additive surface effects, which may not be discernable in a torque trace or a wear life. This need was most evident in the harmonic drive study, where post-test analysis rearranged the initial lubricant ranking based on wear lives.

If these limitations are understood, however, the proper use of lubricant screening tests can play a major role in the process of qualifying a spacecraft lubricant. They can save considerable time and expense by identifying unsuitable lubricants, thus eliminating unnecessary life tests. In addition, they can often be used to troubleshoot lubricant problems with existing mechanisms, as was most noticeable in the case study involving the reaction wheel lubricants. In this case, with the screening tests, we were able to identify almost all of the lubrication problems associated with the actual flight bearings. Considering their strong points, it seems reasonable to integrate lubricant screening tests into the overall process of lubricant flight qualification.

ACKNOWLEDGEMENTS

REFERENCES

1. D. J. Carré, 1988, "The Performance of Perfluoropolyalkylether Oils under Boundary Lubrication Conditions", Tribology Trans., Vol. 31, pp. 437-441.

2. D. J. Carré, 1986, "Pefluoropolyalkylether Oil Degradation: Inference of FeF_3 Formation on Steel Surfaces under Boundary Conditions", ASLE Trans., Vol. 29, pp. 121-125.

3. S. Gill, M. K. Vine, R. A. Rowntree, 1991, "BLAST, A New Lubricant Screening Tester for Space Oils & Greases", 5th European Space Mechanism and Tribology Symposium, Noordwijk, The Netherlands, (28-30 Oct 1992), ESA Proceedings, in press.

4. D. J. Carré, P. D. Fleischauer, C. G. Kalogeras, H. D. Marten, 1990, "Comparison of Lubricant Performance in an Oscillating Spacecraft Mechanism", ASME Journal of Tribology, Vol. 113, pp. 308-312

TABLES

Table 1. - Oils Tested in Scanner Bearing Case Study

Property	CAS	PFPE	PAO
Viscosity, cS −40 °C 40 °C 100 °C	640 52 16	2600 129 40	--- 107 14.5
Viscosity index	--	350	145
Pour point (°C)	−73	−73	−55
Specific gravity	1.045	1.866	--

Table 2. - Oils Tested in Harmonic Drive Case Study

Oil	Additive
NPT-4	None
Pennzane SHF-2000	None
Pennzane SHF-2000	PbNP (5%)
Pennzane SHF-2000	TCP (1%)

Table 3. Test Results of Harmonic Drive Case Study

OIL	EDX/AES		PROFILOMETRY	
	SCREENING TESTS	ACCELERATED LIFE TESTS	SCREENING TESTS	ACCELERATED LIFE TESTS
NPT-4	carbon film	carbon film	N.A.	wear patch
PENNZANE	no film	no film	wear trough	wear patch
PENNZANE + PbNp (5%)	carbon + lead film	carbon + lead film	film buildup	film buildup
PENNZANE + TCP (1%)	thin carbon	N.A.	wear trough	N.A.

Table 4. - Oils Tested in RWA Case Study

Oil	VISCOSITY (300K)	POUR POINT	VAPOR PRESSURE (300K)
SRG-40	30.3 cs	-26 °C	~ 1×10^{-4} Torr
NYE 179 (PAO)	40.8 cs	<-60 °C	~ 1×10^{-7} Torr
NYE UC-7 (POE)	45.8 cs	-57 °C	~ 1×10^{-7} torr
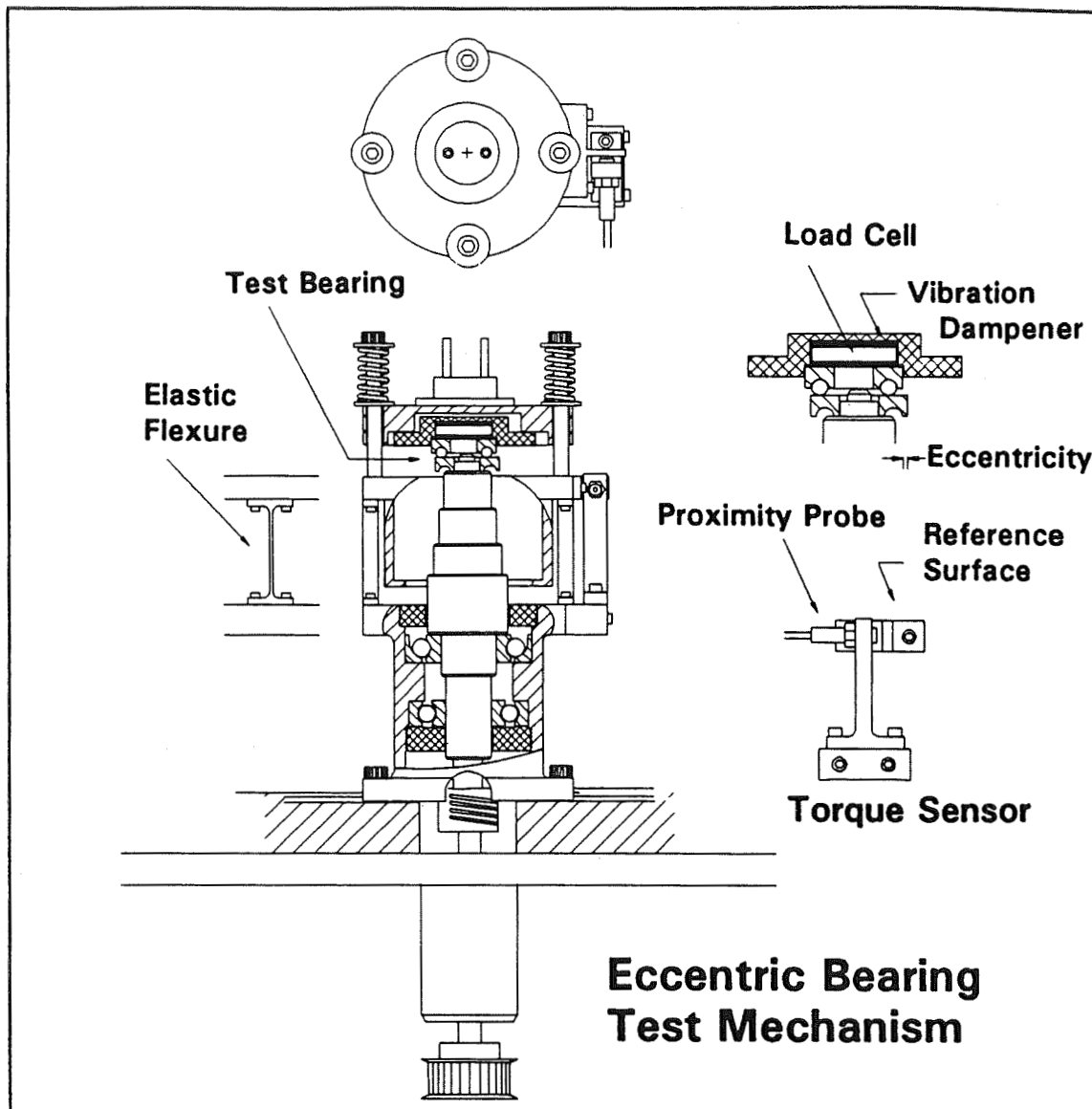
Fig. 1 - Lubricant Screening Test Apparatus

211
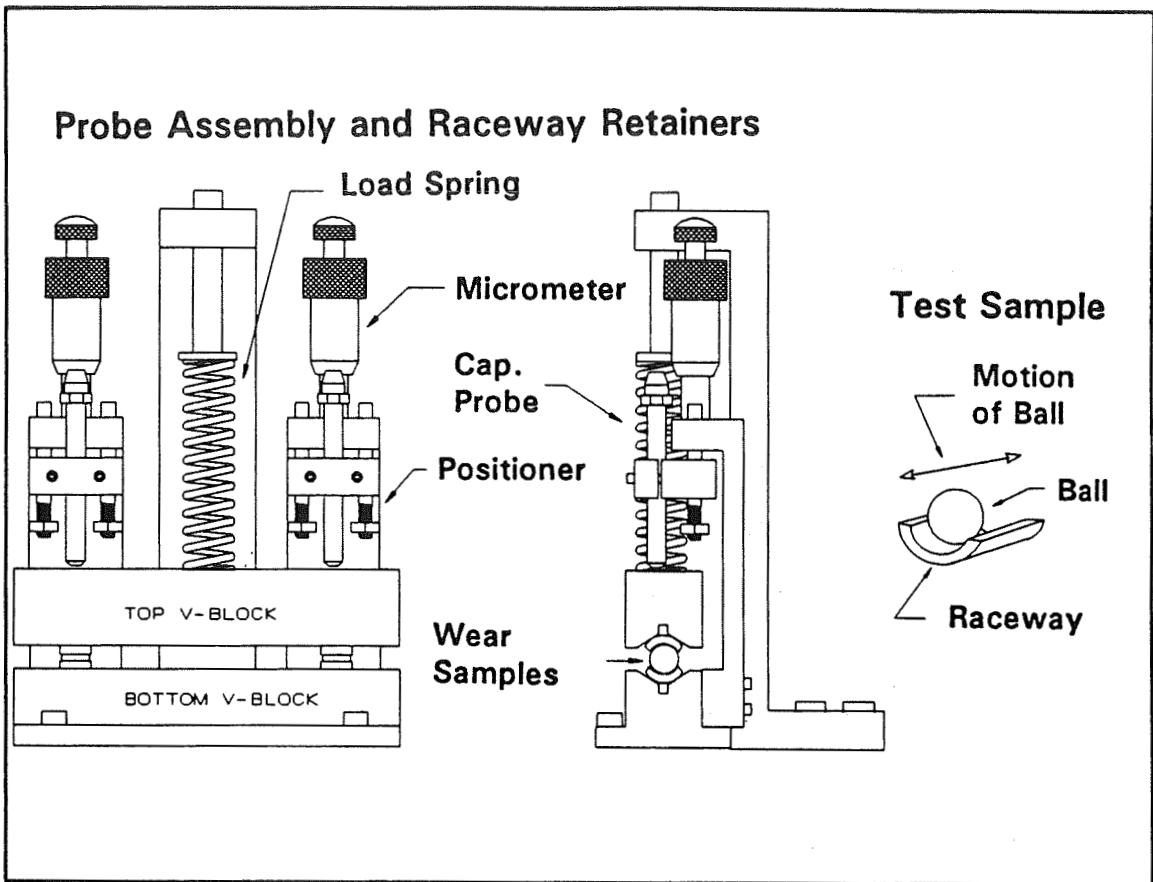
Fig. 2 - Boundary Lubrication Test Fixture, Bearing and
Sensor Assembly
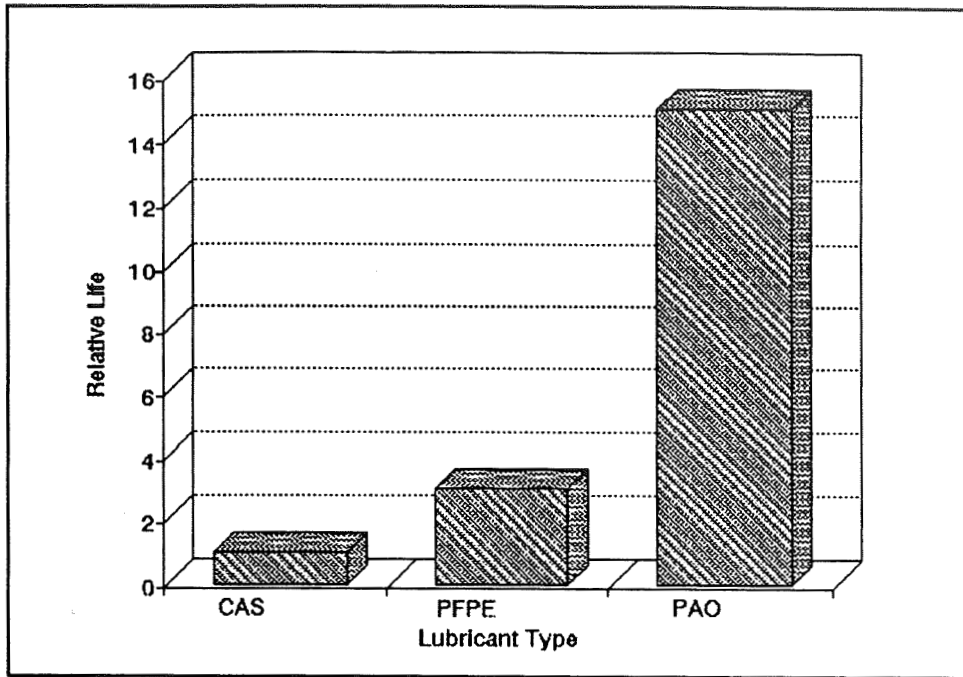
Fig. 3 - Screening Test Results (Scanner Mechanism)
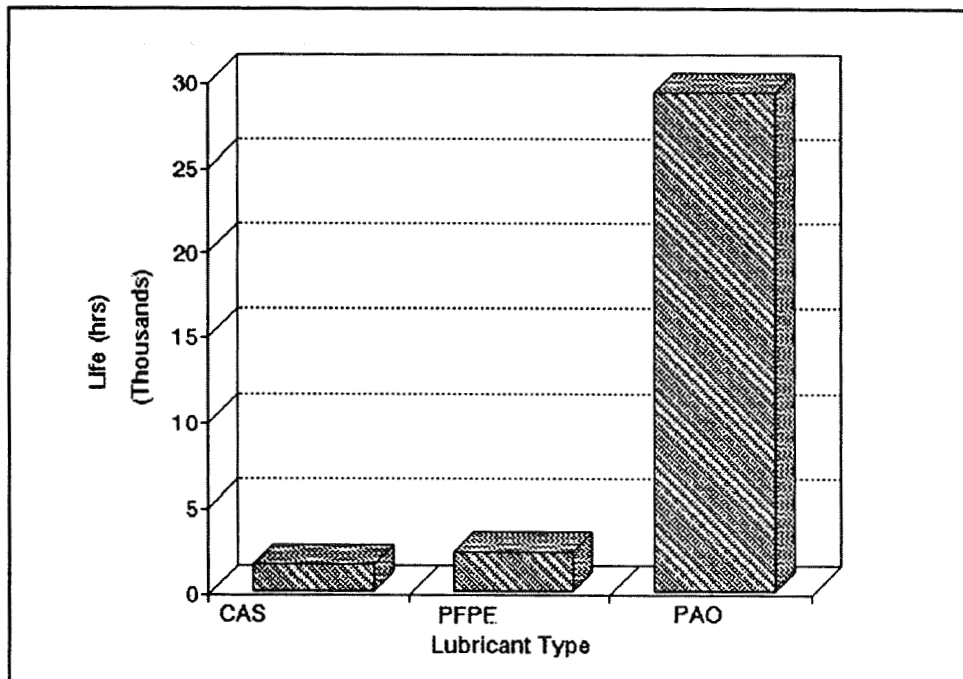
Fig. 4 - Life Test Results (Scanner Mechanism)

213
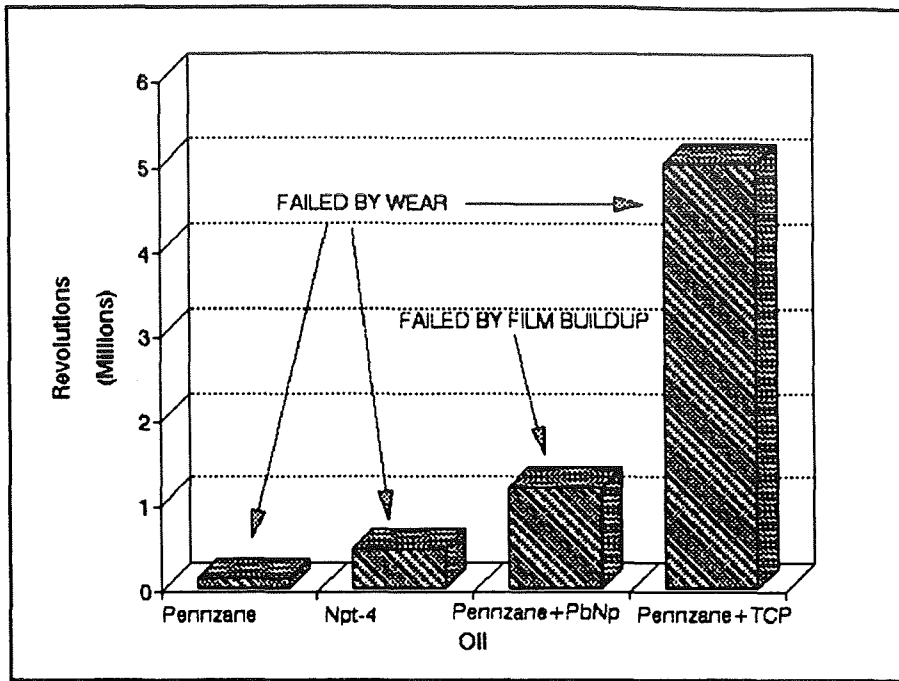
Fig. 5 - Screening Test Results (Harmonic Drive)
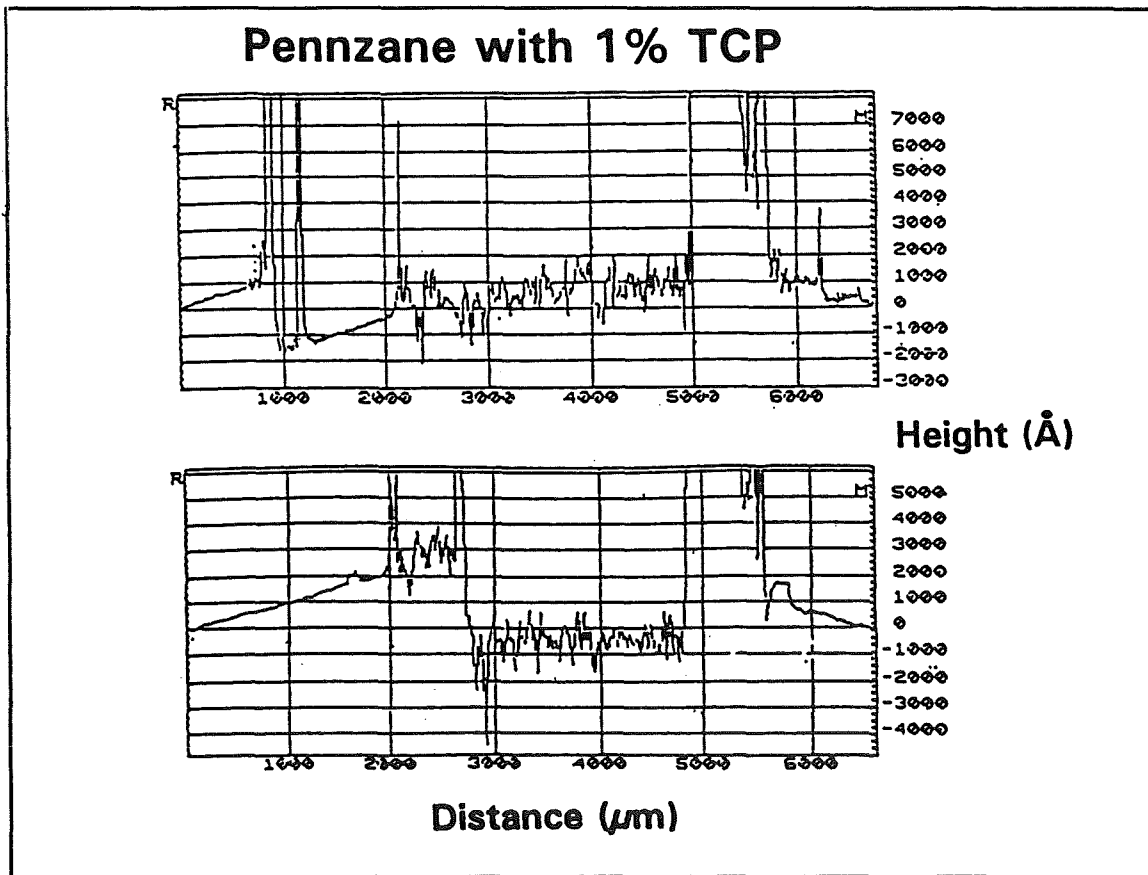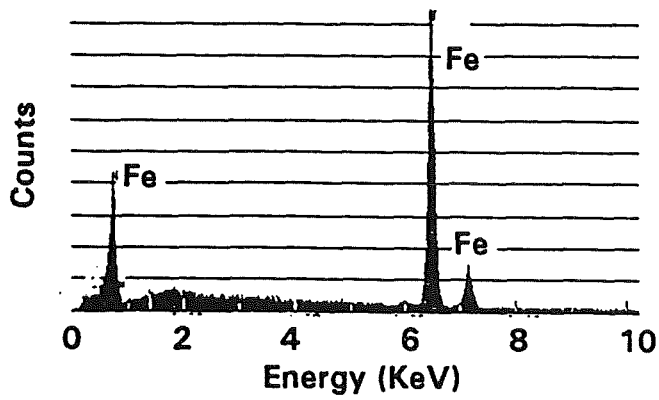

Fig. 6 - Profiles of Pennzane+TCP Wear Disk

214
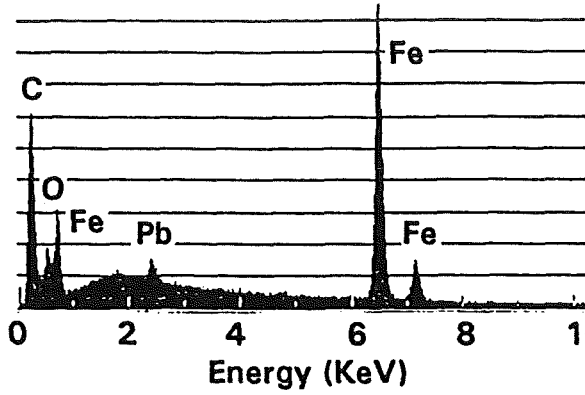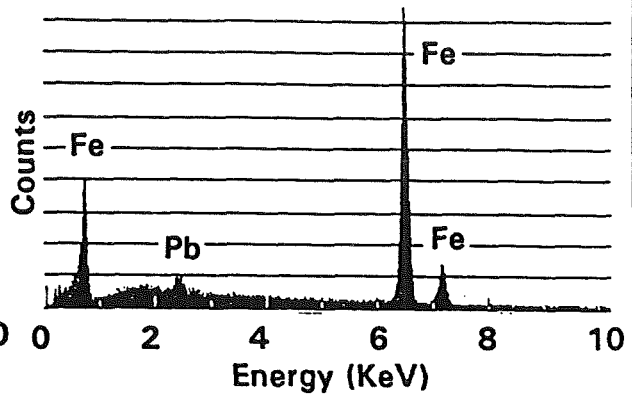
Fig. 7 - EDX Spectra of Pennzane+PbNp Wear Disk
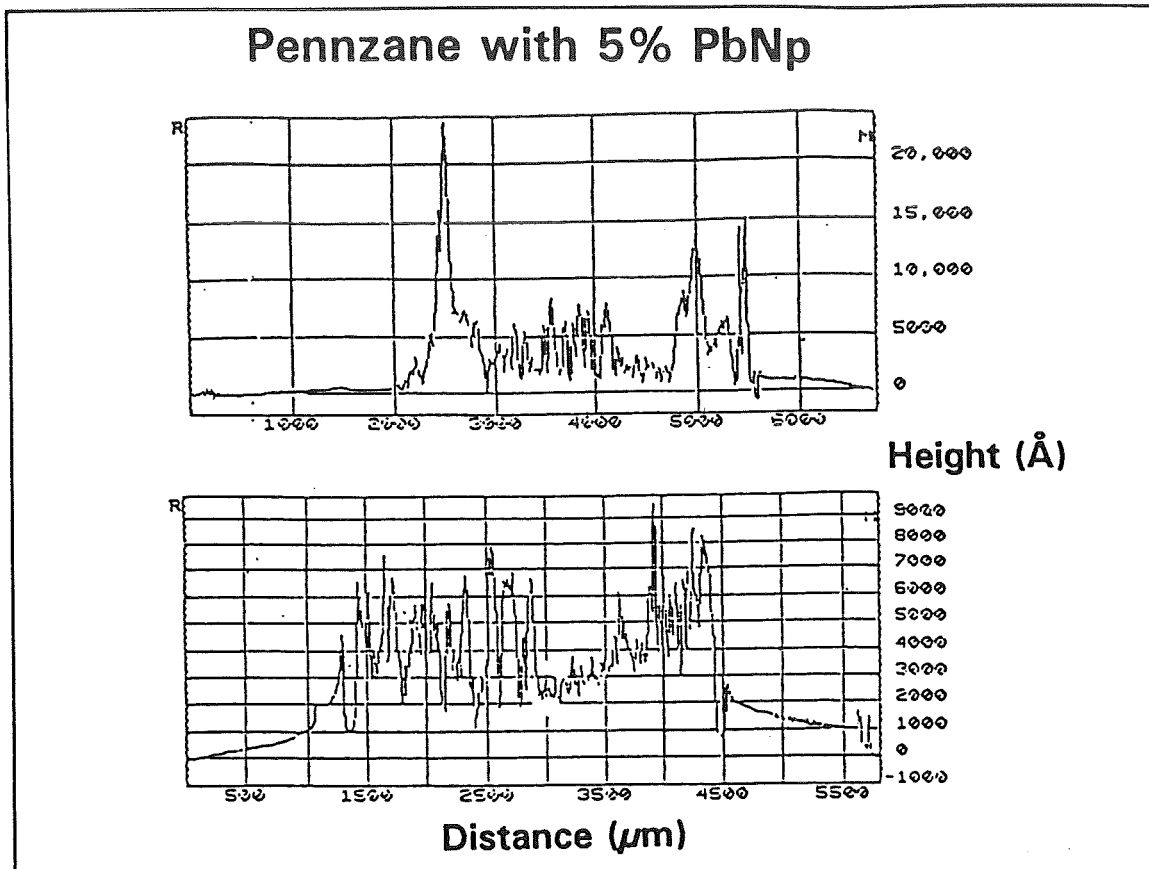
Fig. 8 - Profiles of Pennzane+PbNp Wear Disk
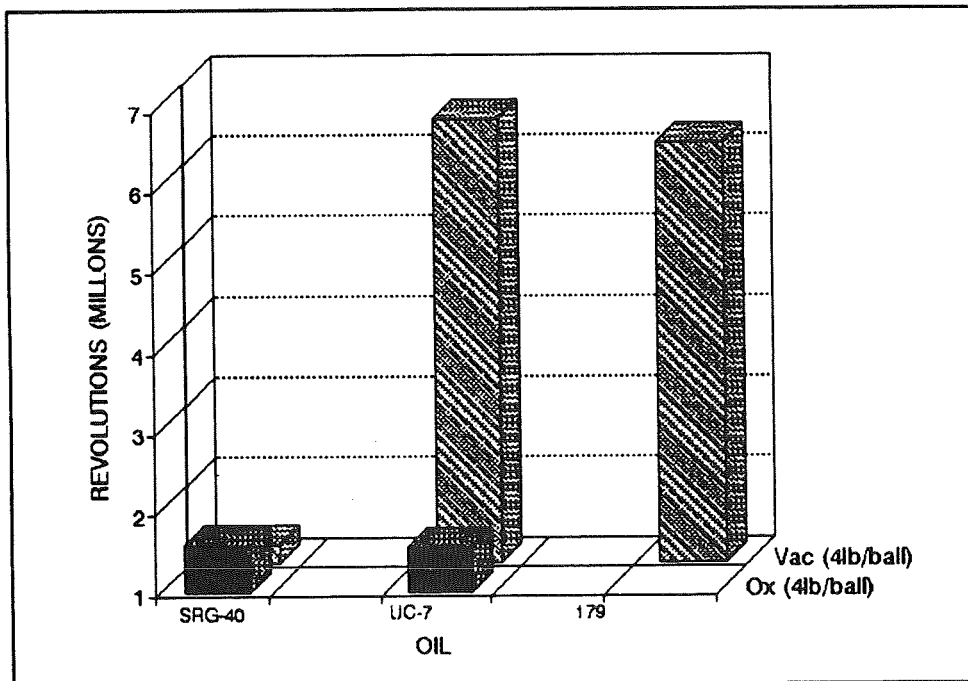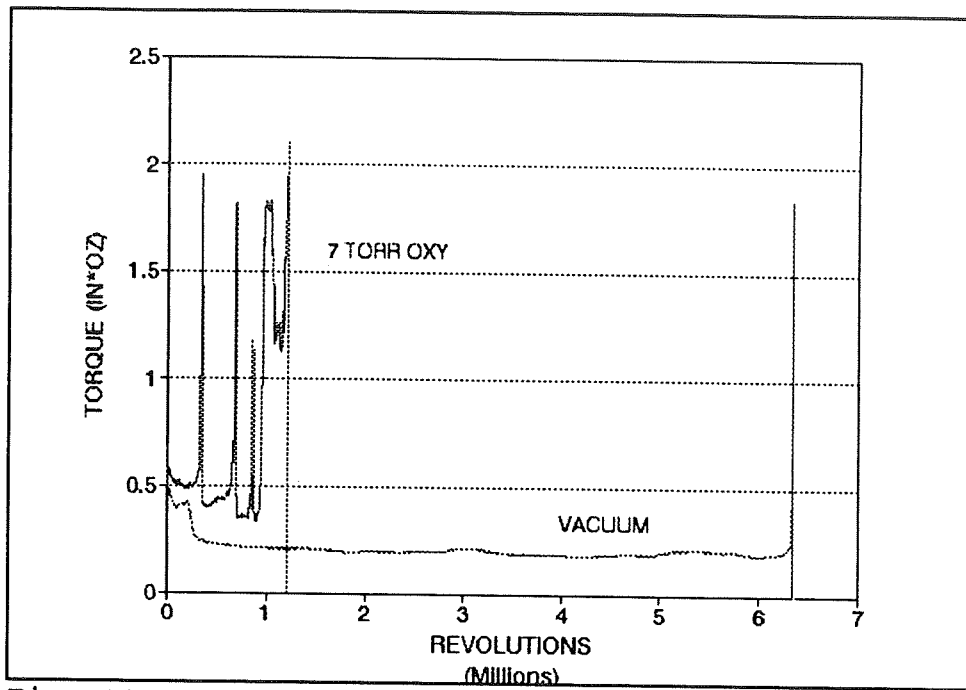

Fig. 9 - Vacuum and O_2 Screening Test Results (RWA)
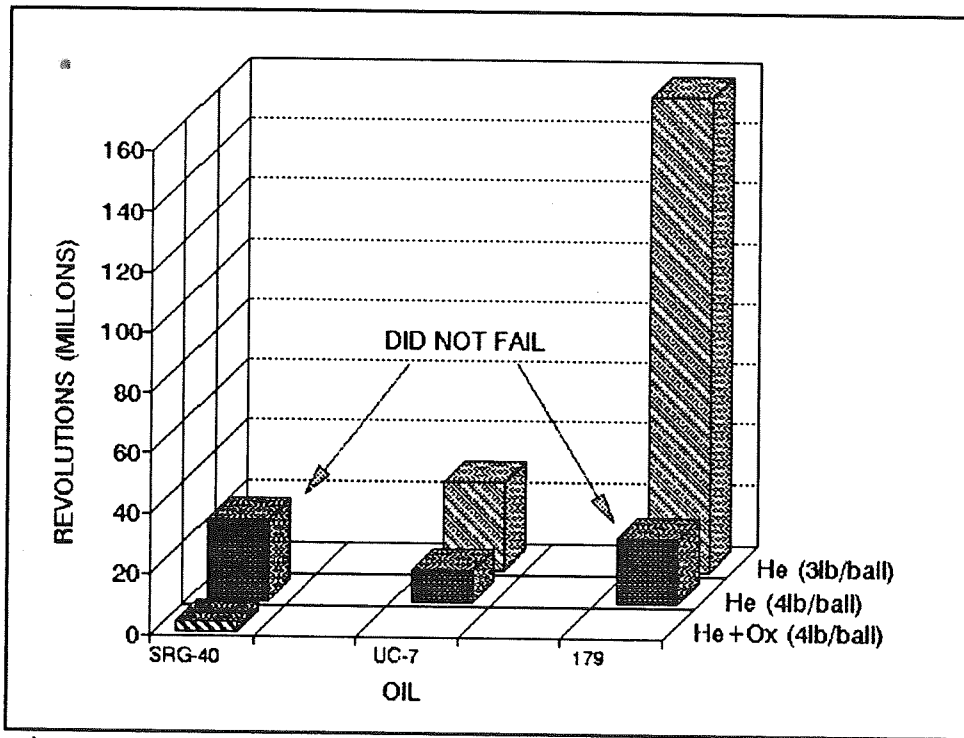
Fig. 10 - Torque Traces of UC-7 in Vac. and O_2 (RWA)

Fig. 11 - 1/2 Atm Screening Test Results (RWA)

217

Three High Duty Cycle, Space-Qualified Mechanisms

/ 3 4 6 7 3

David Akin, Lockheed Palo Alto Research Laboratory
Ralph Horber, H.Magnetics Corporation
Jake Wolfson, Lockheed Palo Alto Research Laboratory

INTRODUCTION

The Michelson Doppler Imager (MDI) is a scientific instrument aboard the Solar and Heliospheric Observatory (SOHO) spacecraft. In 1995 the spacecraft will be put into a halo orbit about the L1 Lagrangian point (equal sun and earth gravity). The MDI looks at the sun continuously and takes a picture with a large format CCD camera every 3 seconds. The design goal of the mission is 6 years, so over 60 million pictures will be taken. The sun, being a high intensity source, provides a signal with a single pixel noise level of 0.2%. Many images are combined to measure the oscillatory motion of the sun so very high performance is required of the mechanisms in order that they not add noise to the data. The MDI instrument is made up of two parts, the electronics package and the optics package. Figure 1 shows the layout of the optics package. This paper describes the design and testing of three mechanisms on the MDI which are required to operate large numbers of times.

SHUTTER

The shutter precisely controls the exposure time of the CCD camera, and additionally selects either a magnified or an unmagnified beam path. Its design uses a brushless DC motor with an integral, optical, shaft angle encoder (figure 2). The motor is an Inland Motor RB-00502 unhoused brushless DC motor. The rotor is supported by a wave spring preloaded pair of ball bearings. The bearings are MPB part number SR3FCHH lubricated with BRAYCO 815Z. The motor drives a thin aluminum disk that contains a pie shaped opening of 80 degrees. The encoder provides the position feedback for commutating the motor, as well as the information required for measurement of the realized exposure at 9 locations across the image. Figure 3a shows exposures, measured by the encoder, as the shutter motor was being life tested. Each point represents a single 100 millisecond exposure taken after 20,000, 50 millisecond exposures. Figure 3b shows 500 consecutive exposures, and 3c is a histogram of 3b.

Shutter Characteristics:

Exposure	40 ms to 65 sec.
Uniformity	50 microseconds p-p.
Repeatability	80 microseconds p-p.
Absolute Exposure Accuracy	250 microseconds
Design Life	60 M Exposures
Power	15 V @ 150 mA peak
	5 V @ 80 mA peak
Weight	125 grams (motor and blade)

A single exposure requires the shutter motor to make 3 moves. First the motor moves to start the exposure. After waiting in the open position for the desired exposure period the motor then closes the shutter. Because of the way the shutter is used to select the 1X or 3X path (see figure 1) a third move is needed. After the CCD camera reads out the image (this requires darkness and takes about 2 seconds) the shutter moves to where it can begin another exposure. Figure 4 shows a computer simulation of a 100 millisecond exposure. At time = 0 and position 200 degrees the motor is started in order to open the shutter. The motor operates open loop (BEMF limits the motor speed) until position 260 degrees (label B). At this time the windings are shorted and the motor comes to a stop at the 280 degree position. At time = 100 milliseconds (the desired exposure) the motor is started in order to close the shutter. The windings are shorted at 340 degrees and the motor comes to a final stop at the 360 degree position.

We compensate for the opening edge of the shutter moving through the field of view (A to B in the figures) by having the closing edge (C to D) move in exactly the same way with respect to the field of view. The non-uniformity resulting from the opening edge of the shutter moving across the field is thus canceled by the closing edge. Since the motor is a brushless DC motor there is some inherent torque ripple (one ripple per commutation step) that causes some speed variation even after the motor has reached its no-load speed. By placing the opening edge of the blade an integral number of commutation steps from the closing edge, the exposure non-uniformities caused by torque ripple during the opening move are canceled by the same torque ripple on the closing move.

The MDI shutter is very similar in design to the shutter used on the Soft X-ray Telescope (SXT) on the Yohkoh space mission. On the SXT shutter we minimized the effect of the magnetic detent on the exposures by selecting a motor with an odd number of stator teeth. The SXT shutter motor has 8 rotor magnets and 27 stator teeth, or 216 potential magnetic detent positions. The result of the small spacing of the detents is that under certain conditions small changes in voltage or bearing friction can cause the motor to stop in a different detent. Another difference between the MDI and SXT shutter is the SXT shutter has a single beam path and two openings in the blade, a 3 degree opening for 1 millisecond exposures, and a 60 degree opening for 20 milliseconds and longer.

For the MDI shutter we took a different approach. We selected a motor with 6 rotor magnets and 18 stator teeth. This causes a total of 18 magnetic detents, 1 detent for each commutation step. Since the motor is designed to stop in the center of a magnetic detent it can be off by as much as +/- 10 degrees without falling into the next detent. We take advantage of the even spacing of the magnetic detents to insure that the opening and closing edges of the shutter blade always start from the same position.

MICHELSON TUNING MOTORS

The Michelson tuning motor assembly (figure 5) is used to tune the passband of the Michelson interferometers by rotating 1/2 wave retarders. The assembly consists of 2 brushless DC motors in a single housing. The motors were designed and built for MDI by H.Magnetics. The motors have hollow rotors to which the waveplates are directly attached, and incremental encoders for position feedback.

Tuning Motor Characteristics:

Repeatability	+/- 1 arc min.
Design Life	60 M moves
Step Size	2 degrees
Power Dissipation	50 mJ / 24 deg move (dissipated at the motors)
Power	15 V @ 100 mA peak
	5 V @ 80 mA peak
Weight	590 grams (2 motors)

An unusual feature of the tuning motors is that each motor contains a single thin-section ball bearing. The bearing is an MPB part number S2936 thin section ball bearing. A preload force is applied by offsetting the rotor axially from the stator. This preloads the bearing because the magnets try to pull the rotor into the stator. The preload force was measured to be approximately 18 N (4 lbs). In order to verify that the tuning motor met the positioning requirements of MDI a test was done where a small mirror was glued to the center of the waveplate. By observing the mirror through a theodolite we verified that the motor could be positioned repeatably to well within the specification over a wide range of motor voltages.

FILTERWHEELS

The MDI contains three wheels, each of whose purpose is to place one of four optical elements into the beam path. The polarization analyzer wheel selects the polarization of light which enters the MDI in order to measure the magnetic field of the sun. The other two wheels comprise the calibration/focus system, which has two purposes. First they provide calibration of the MDI optical system by placing a pair of lenses into the optical path. In addition they enable one to adjust focus on-orbit by inserting flat glass elements of different thicknesses into the beam path. Each wheel consists of a brushless DC motor with an integral, optical, incremental encoder. The motors have hollow rotors within which reside the optical elements. The rotors are supported by wave spring preloaded pairs of ball bearings. The bearings are MPB part number SR4FCHH lubricated with BRAYCO 815Z. The motors were also designed and built by H.Magnetics for MDI. Figure 6 shows the filterwheel assembly.

Filterwheel Characteristics:

Repeatability	+/- 1 arc min.
Design Life	2 M moves
Step Size	2.5 degrees
Power	15 V @ 100 mA peak
	5 V @ 80 mA peak
Weight	420 grams

COMPUTER SIMULATIONS

Prior to building the motors, computer simulations were run for each of these mechanisms. These simulations were very helpful in the proper sizing of the motors and in the selection of their windings. In addition they provided disturbance torque data to the spacecraft designers.

The simulations were done in IDL (Interactive Data Language). The technique is to take a large number of small time steps. The motor windings are modeled as a series resistor and inductor. The motor current is calculated by subtracting the BEMF from the motor supply voltage, and applying it to the resistor and inductor. Torque ripple is modeled with the BEMF "constant" actually being a function of rotor position. Magnetic detent is assumed to be a sinusoidal function of rotor position. To initiate the simulation the motor is stopped, voltage is applied, current increases through the resistor and inductor, current causes torque, and torque causes speed and position to change. Speed causes BEMF which is subtracted from the applied voltage for the next time step. Figure 7 shows the output of this program as well as an actual oscilloscope measurement of the motor current. Figure 8 shows the IDL program which was used to model the tuning motors.

CONTROL SYSTEMS

The control systems for all three types of mechanisms are very similar. The Michelson tuning motors and the wheel mechanisms use identical electronics, a block diagram of which is shown in figure 9. The control system of the shutter is similar except that it incorporates a programmable timer to control the exposure, and does not have the ability to stop the motor at an arbitrary position.

To move a filterwheel or tuning motor, the Dedicated Experiment Processor (DEP) first loads the desired stopping position into a latch in the motor drive electronics. Then the DEP tells the motor to run in either the clockwise or counterclockwise direction. The motor runs until the programmed stopping position is reached, plus a small time delay. The windings are then shorted together and the motor's energy is dissipated in the windings as the motor brakes to a stop. After another delay, the encoder is shut off to conserve power while the motors are not being used. Very little power is therefore consumed by these mechanisms when they are not moving. The first delay is adjusted so that the motor comes to a stop exactly in the center of the

next detent. The second delay insures that the motor is completely stopped before the encoder is shut off.

The method of operating the motors open-loop and making use of the magnetic detent for position accuracy allowed for a simple control system. This method of controlling the motors has proved itself to be robust, as the motors continued to function acceptabaly throughout their life tests even though in some cases the bearings had deteriorated considerably. This can be attributed to selecting (or designing) motors with adequate torque margins.

LIFE-TESTING

These mechanisms have all undergone extensive life-testing in a vacuum chamber. Prior to placing the mechanisms in the vacuum chamber they were subjected to a vibration test. Pressure in the vacuum chamber during the life tests varied from about 10^{-6} to 10^{-7} Torr. The shutter and wheel mechanisms were at room temperature, and the tuning motors were in a temperature controlled oven at 35 C. This simulates the environment in which the mechanisms will actually be used. A PC clone controlled the mechanisms through prototype versions of their flight control electronics. The PC also controlled test equipment over an IEEE-488 bus, enabling the life-test to be automated. Each mechanism was alternately cycled through 20,000 operations, and then characterized by running at 5 different voltages while recording the current and speed at each voltage.

The design goal of the shutter and tuning motor mechanisms is 60 million operations each since these mechanisms will be used once every 3 seconds for 6 years. In order that the life tests of these mechanisms be completed in a reasonable time it was necessary to accelerate the tests. This was done by running the motors at their design speeds, and on the same voltage they will run on in flight, but spending very little time between moves. The shutter test was done with a 50 millisecond exposure time, long enough to insure that the motor comes to a complete stop but much shorter than the planned exposures. The tuning motor tests were made with one motor making 30 degree moves and the other 60 degrees. This is how they will be used in the instrument. The test acceleration was done by reducing the time the motors spent stopped between moves. In this way we were able to make approximately 4 moves per second on each motor, rather than a move every 3 seconds.

The shutter and wheel mechanisms both used ball bearings lubricated with BRAYCO 815Z. The shutter life test put the equivalant of 67 million exposures on the motor. The friction during the test (figure 10) was essentially constant. Examination of the bearings after the test showed them to be in perfect condition.

The filterwheel test showed a gradual trend of increasing friction and of increasing variation of friction (figure 11). The test was considered a success because the design life of the filterwheel is 2 million operations. The filterwheel continued to function perfectly throughout the test. Examination of the bearings after this very excessive over test showed them to be in poor condition.

The Michelson tuning motor has had three sets of bearings installed for three different life tests. The first tuning motor test used Teflon toroids and was lubricated with BRAYCO 815Z oil. Figures 12a and 12d show the friction vs. time for the two motors. Each point represents a motor characterization done after 20,000 moves. After 34 million moves the friction of one of the motors was increasing at an unsatisfactory rate and the test was stopped. The Teflon separators showed considerable wear.

This first tuning motor test used a constant power heater to attempt to keep the temperature at 35 C. Closed loop heater control was added for the second and third tests. An improved method of measuring current was also included in the second and third tests. The reduction of the scatter in the calculated friction for the second and third tests can be attributed to these improvements in the test setup.

The second tuning motor test (figures 12b and 12e) used separators made of SALOX-M, a mixture of Teflon and bronze, and was also lubricated with BRAYCO 815Z. This second test was stopped when one of the motors again exhibited rapidly increasing friction. Examination of the bearings showed a lack of lubrication and a considerable amount of wear particles, especially in the bearing whose motor showed increasing friction.

The third test (figures 12c and 12f) used bearings with SALOX-M separators lubricated with BRAYCOTE 600 grease. This test lasted 7 months, put 66 million moves on one motor and 102 million on the other, and was stopped after a 6 year equivalent mission life was

reached. Visual examination of the bearings showed them to be in fine condition. BRAYCOTE 600 grease lubricated bearings are being used in the flight tuning motors.

CONCLUSION

The requirements on these flight mechanisms (tens of millions of cycles, performance stability, minimal disturbance torque, and low power consumption) led to custom designed, high pole-count, permanent magnet motors in conjunction with a unique control approach. The filterwheel and tuning motors designs were a cooperative and iterative effort by Lockheed Palo Alto Research Laboratories (LPARL) and H.Magnetics. LPARL designed the housings, encoders, and control electronics, while H.Magnetics designed the rotors and stators in accordance with LPARL requirements. An extensive, in-vacuum test program was conducted and in the case of the tuning motors design changes (lubrication) were required, as was retesting. At this time the mechanisms described in this paper have been fully qualified and are about to be installed into the flight MDI. They are also planned for use in a new solar payload.
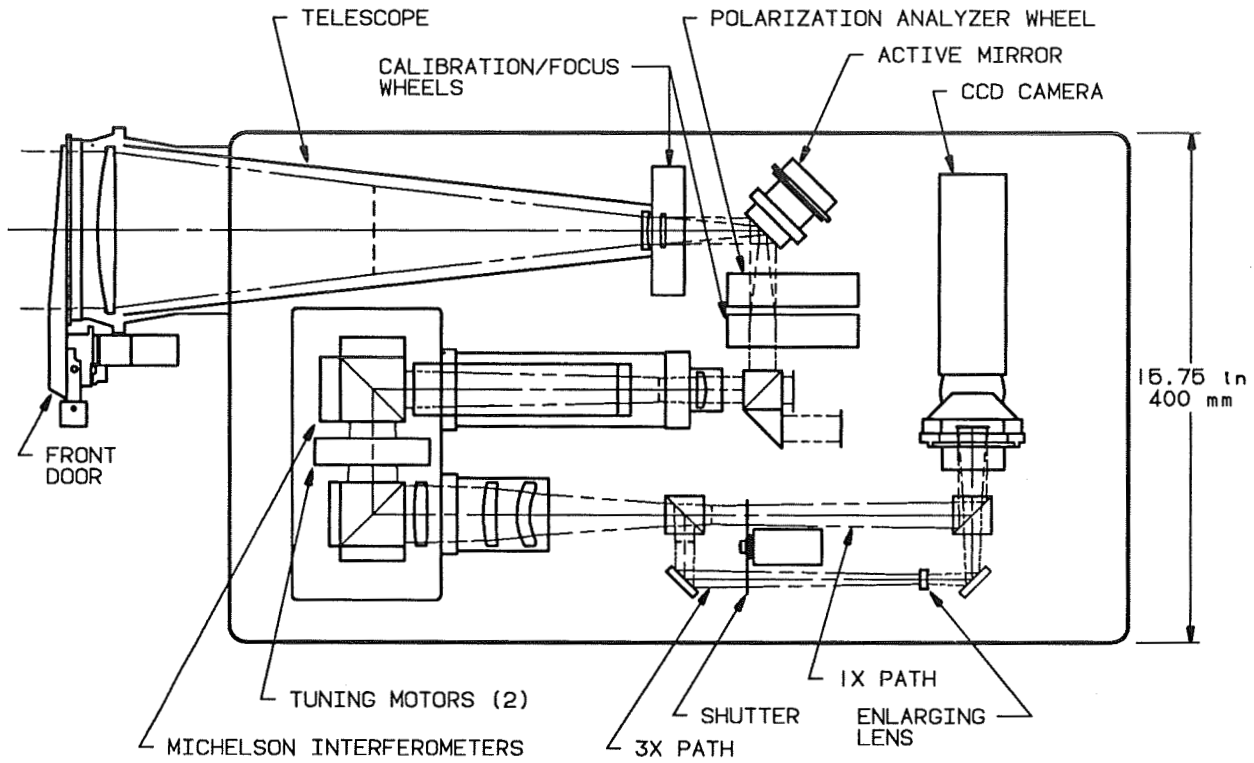
ACKNOWLEDGMENTS

Figure 1. MDI Optics Package Layout
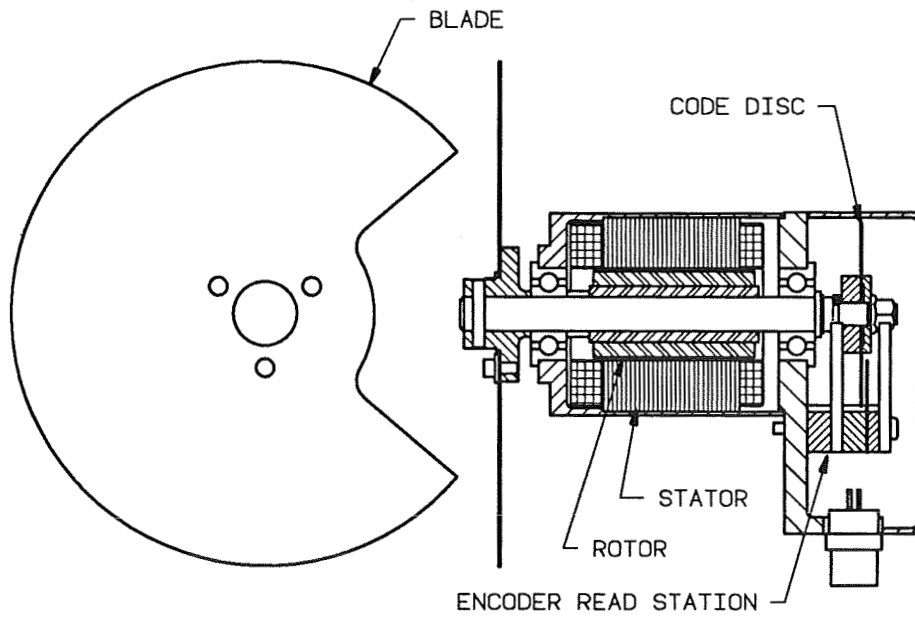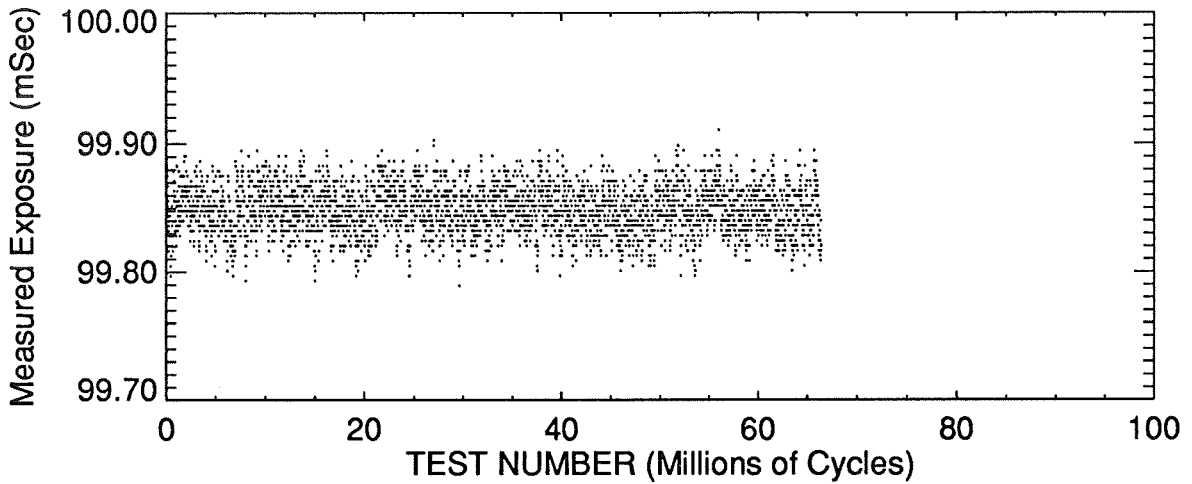

Figure 2. Shutter

227

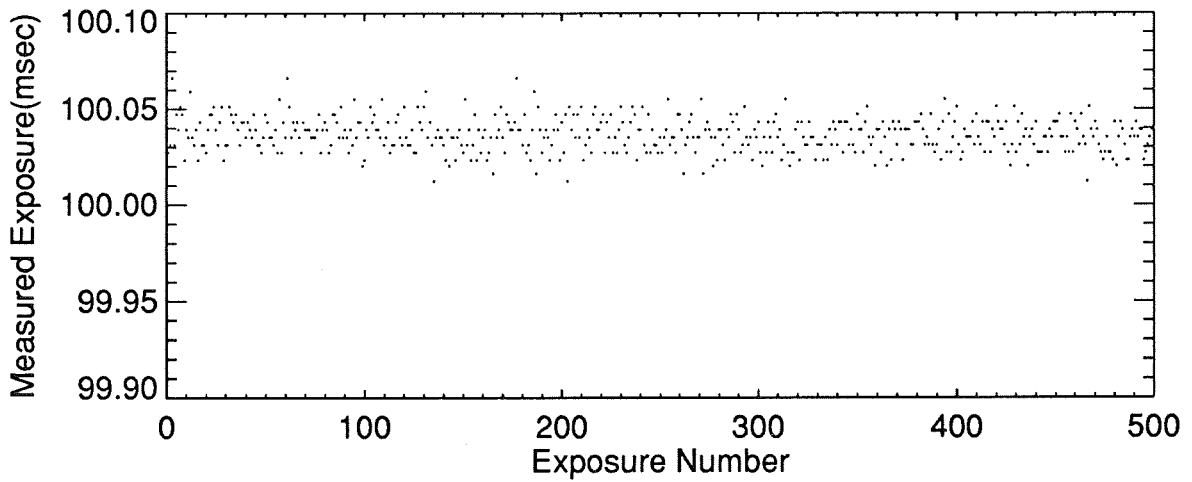**Figure 3a.** MDI Life Test Shutter (each point is after 20,000 exposures)

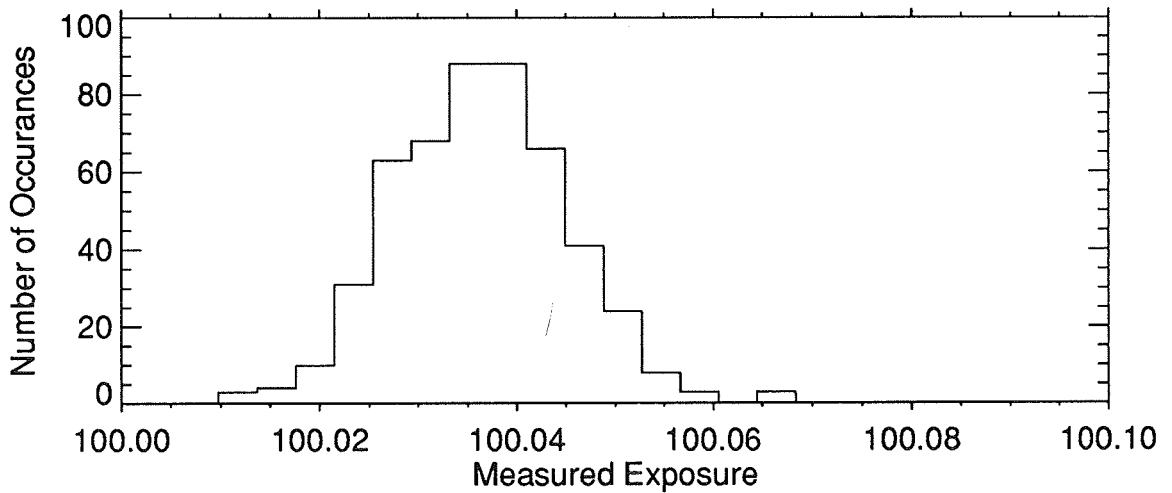**Figure 3b.** 500 Consecutive Exposures, MDI Flight Shutter
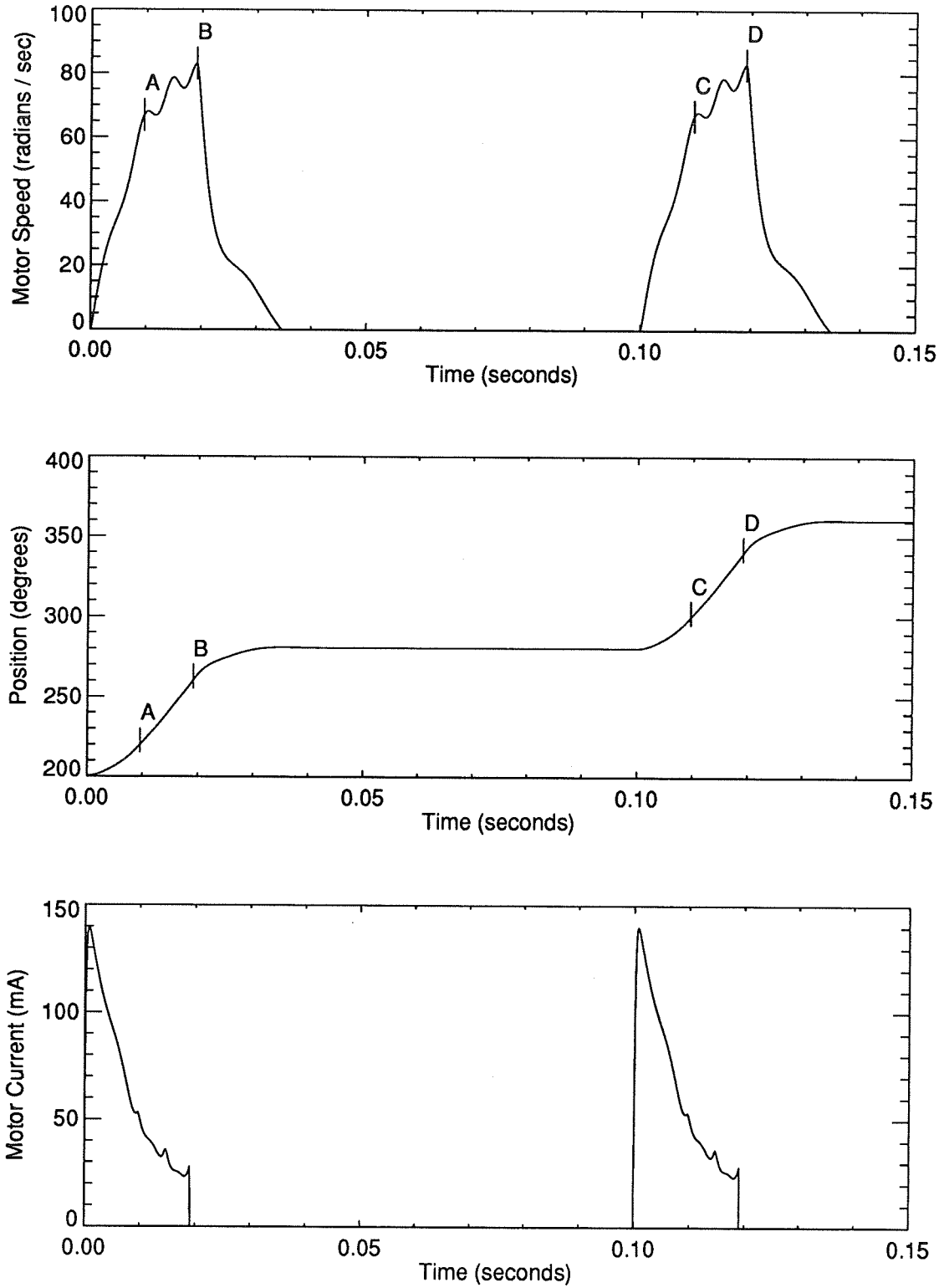

Figure 3c. Histogram of Figure 3b

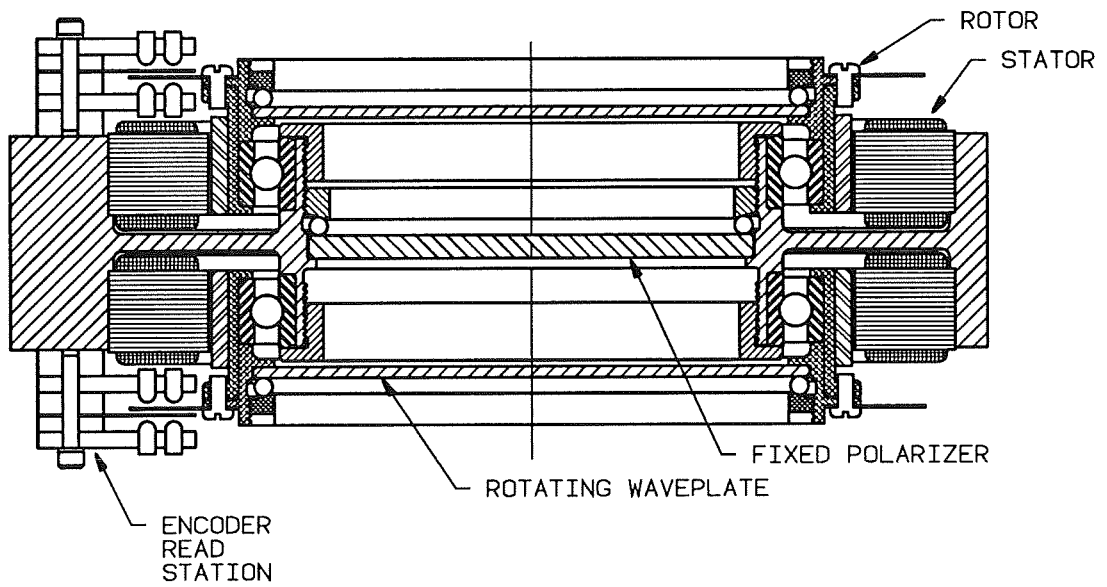**Figure 4.** Computer Simulation of 100 millisecond Exposure

ROTOR

STATOR

FIXED POLARIZER

ROTATING WAVEPLATE

ENCODER
READ
STATION
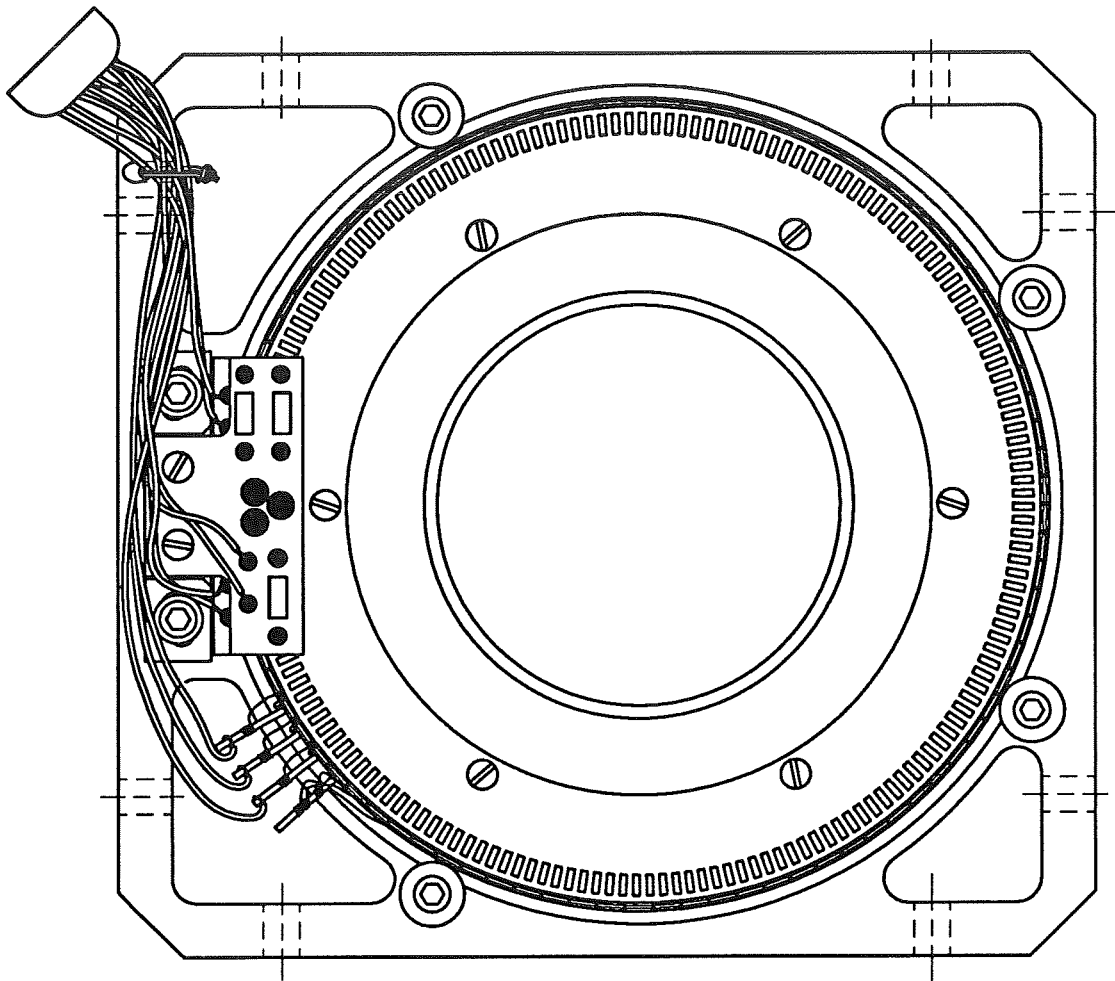
Figure 5.   Michelson Tuning Motor Assembly

CODE DISK

STATOR   WAVE-SPRING WASHER

4.00 in sq
101.6 mm

1.00 in
25.4 mm

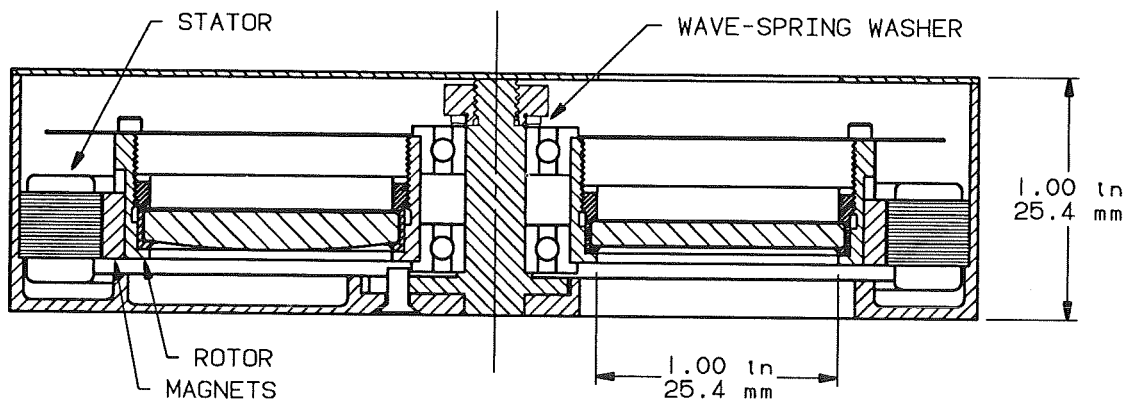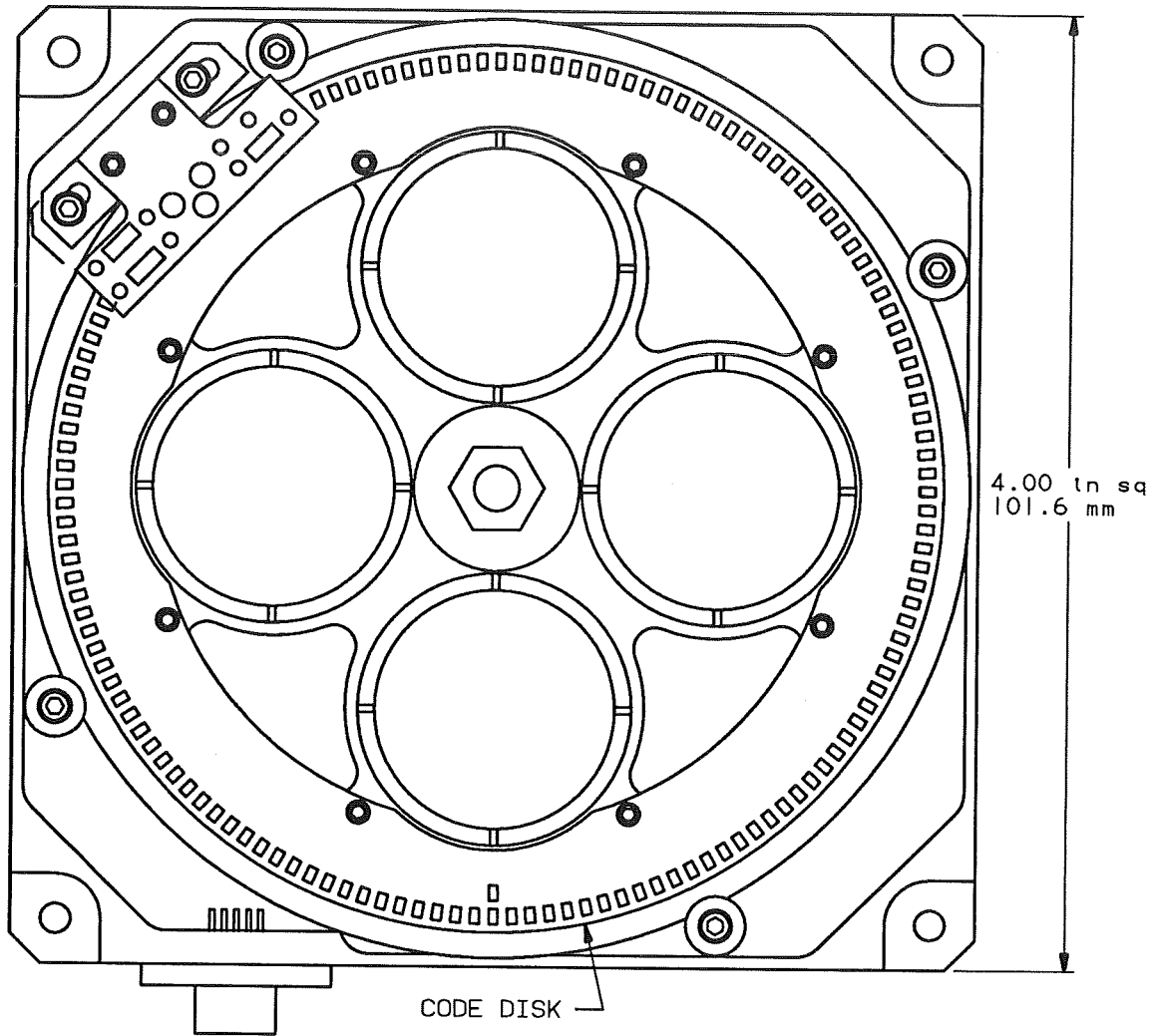1.00 in
25.4 mm

ROTOR
MAGNETS
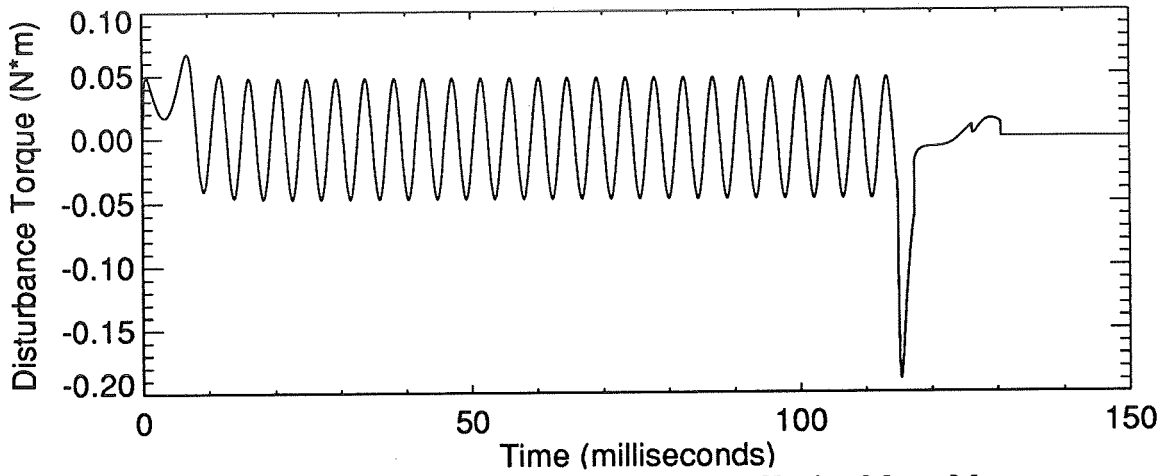
Figure 6.   Filterwheel Assembly

231

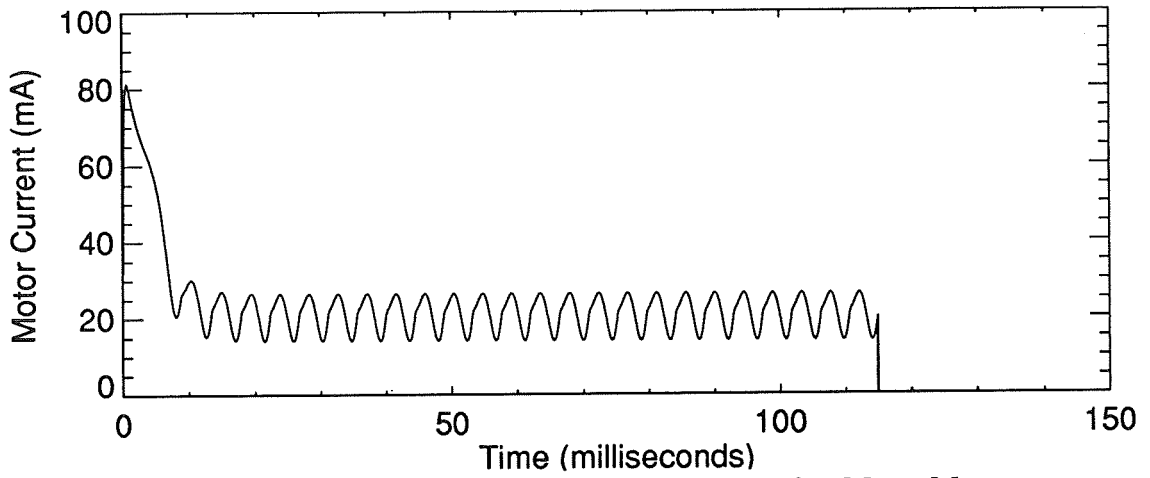**Figure 7a.** Computer Simulation of 50 Degree Tuning Motor Move

Figure 7b. Computer Simulation of 50 Degree Tuning Motor Move

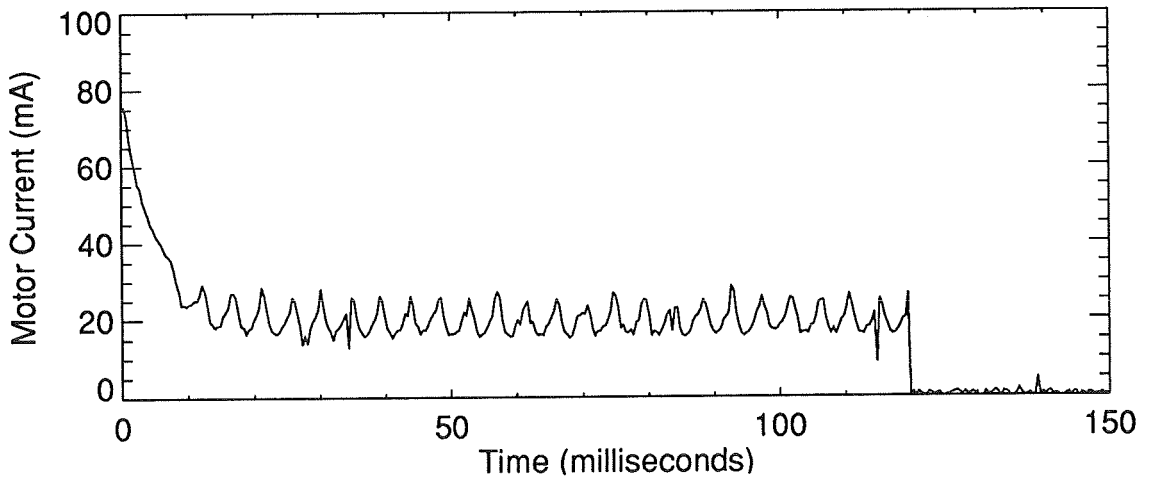**Figure 7c.** Oscilloscope Measurement of 50 Degree Tuning Motor Move

```
RANGE = .10                                              ; plot range
DT = .00002                                              ;time step
NUM = RANGE/DT                                           ;number of time steps
KP = 1.48                                                ;V / rad/sec
J = .0052                                                ;inertia (oz-in sec**2)
R = 172                                                  ;resistance
VO = 15.4                                                ;motor voltage
L = .032                                                 ;inductance (Henries)
NPP = 30                                                 ;number of pole pairs
DF = .17                                                 ;viscous damping (oz-in / rad/sec)
TD = 5.0                                                 ;detent torque (oz-in)
STOPD = 50                                               ;stopping position (degrees)
STOP = STOPD/57.2958                                     ;stopping position (radians)
HDRAG = 2.8                                              ;drag torque (oz-in)
A=FLTARR(NUM,6)


FOR I=1,NUM-1 DO BEGIN
A(I,0) = A(I-1,0) + DT                                   ;ime
A(I,1) = A(I-1,1) + DT*A(I-1,5) / J                      ;omega (rad/sec)
IF (A(I,1)GE 0.) AND (A(I-1,1)LE 0.) AND (ABS(TORK)LE HDRAG) THEN A(I,1)=0.
IF (A(I,1)LE 0.) AND (A(I-1,1)GE 0.) AND (ABS(TORK)LE HDRAG) THEN A(I,1)=0.
A(I,2) = A(I-1,2) + DT*A(I,1)                            ;theta (rad)
IF A(I,2) GT STOP THEN VO=0.
THETAE = A(I,2)*NPP                                      ;theta-electrical
K = KP*SIN((THETAE MOD 1.0472) + 1.0472)                 ;torque ripple
IF A(I,2) GT STOP THEN K=KP*1.155                        ;stopping K
A(I,3) = (VO - A(I-1,4)*R - K*A(I,1)) / L                ;dI/dt
A(I,4) = A(I-1,4) + DT*A(I,3)                            ;current
IF A(I,1) GT 0. THEN DRAG = HDRAG ELSE DRAG = -HDRAG
TORK = K*141.6*A(I,4) - DF*A(I,1) - TD*SIN(6*THETAE+.75)
A(I,5) = TORK - DRAG                                     ;torque
IF (A(I,1)GE 0.) AND (A(I-1,1)LE 0.) AND (ABS(TORK)LE HDRAG) THEN A(I,5)=0.
IF (A(I,1)LE 0.) AND (A(I-1,1)GE 0.) AND (ABS(TORK)LE HDRAG) THEN A(I,5)=0.
ENDFOR
Z=0                                                      ;I=0 after stop
FOR I=1,NUM-1 DO BEGIN
IF A(I,2) GT STOP THEN Z=1
IF Z EQ 1 THEN A(I,4)=0
ENDFOR


SET_PLOT,'PS'
DEVICE,/PORTRAIT,/INCHES,YOFFSET=.5,YSIZE=10.,XSIZE=7.
!P.FONT=0
!P.POSITION=[.12,.8,.85,1]
!Y.TITLE="Motor Current (mA)"
!X.TITLE="Time (milliseconds)"
PLOT,A(*,0)*1000,A(*,4)*1000
!Y.TITLE="Disturbance Torque (N*m)"
PLOT,A(*,0)*1000,A(*,5)/141.6                            ;convert torque from oz in. to Nm


END
```

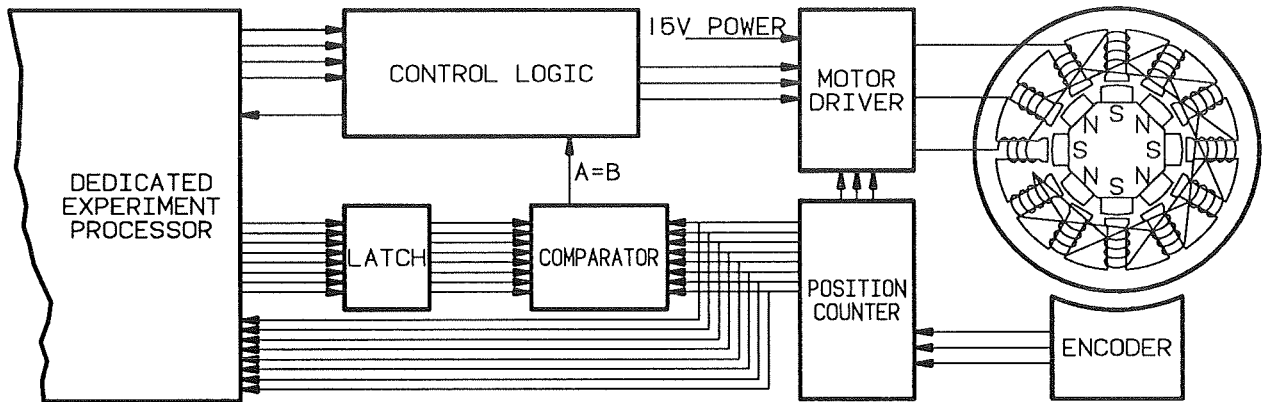**Figure 8.** IDL Program for Brushless DC Motor Simulation

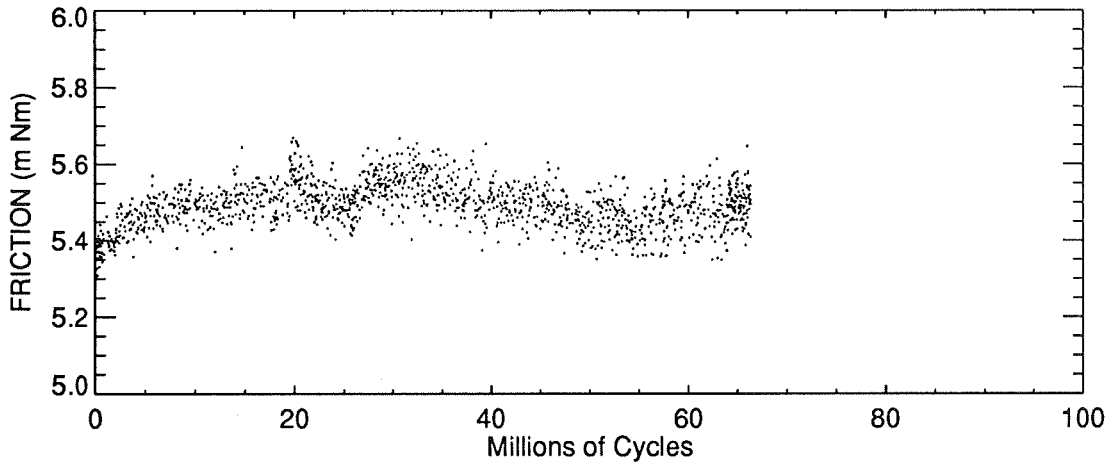**Figure 9.** Filterwheel and Tuning Motor Control System Block Diagram
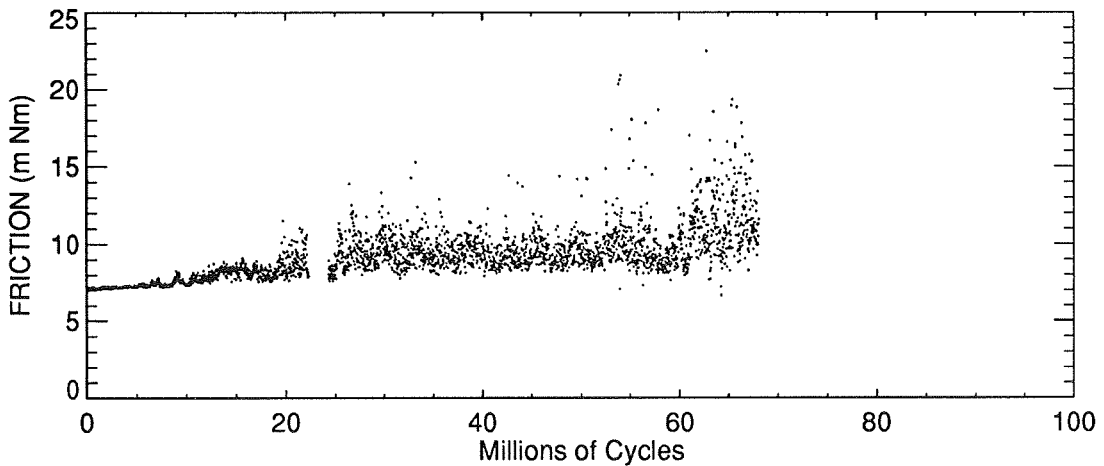

Figure 10. Shutter Life Test

Figure 11. Filterwheel Life Test

234

Figure 12a. Tuning Motor Test #1
Teflon toroid separators, 60 degree move, BRAY 815Z lubrication

Figure 12b. Tuning Motor Test #2
SALOX separators, 60 degree move, BRAY 815Z lubrication

Figure 12c. Tuning Motor Test #2
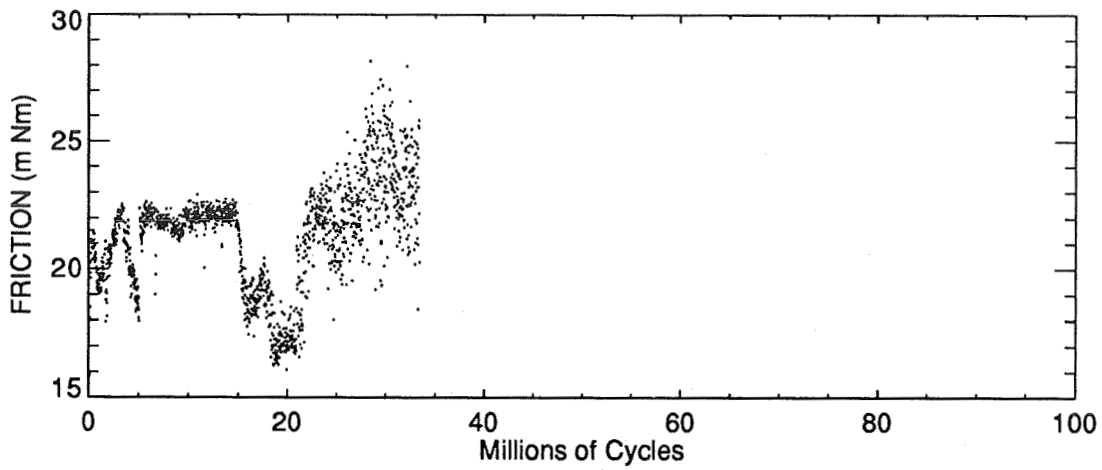SALOX separators, 60 degree move, BRAYCOTE 600 lubrication

235

Figure 12d. Tuning Motor Test #1
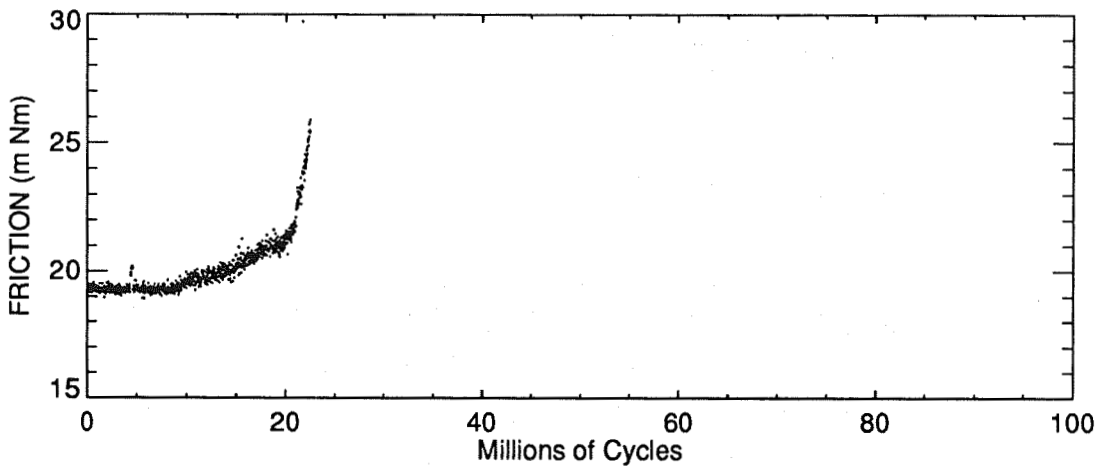Teflon toroid separators, 30 degree move, BRAY 815Z lubrication

Figure 12e. Tuning Motor Test #2
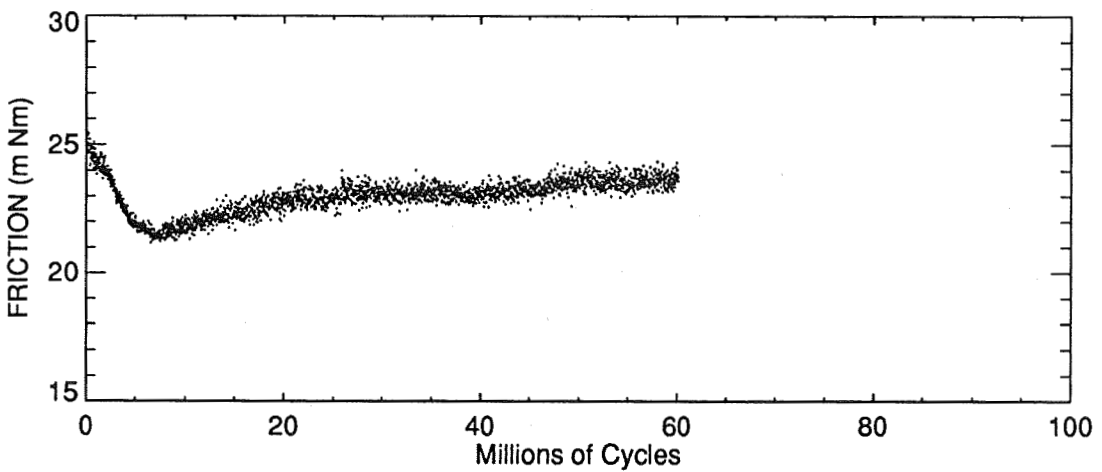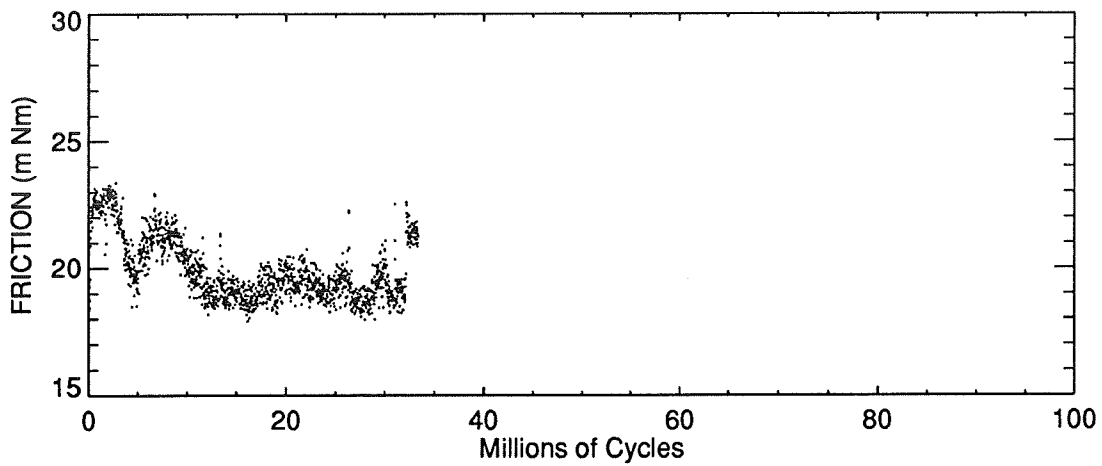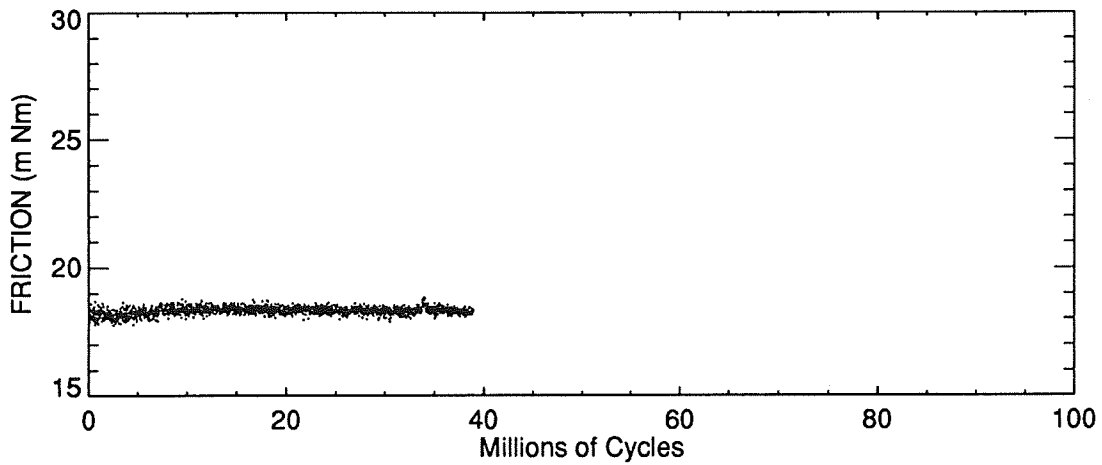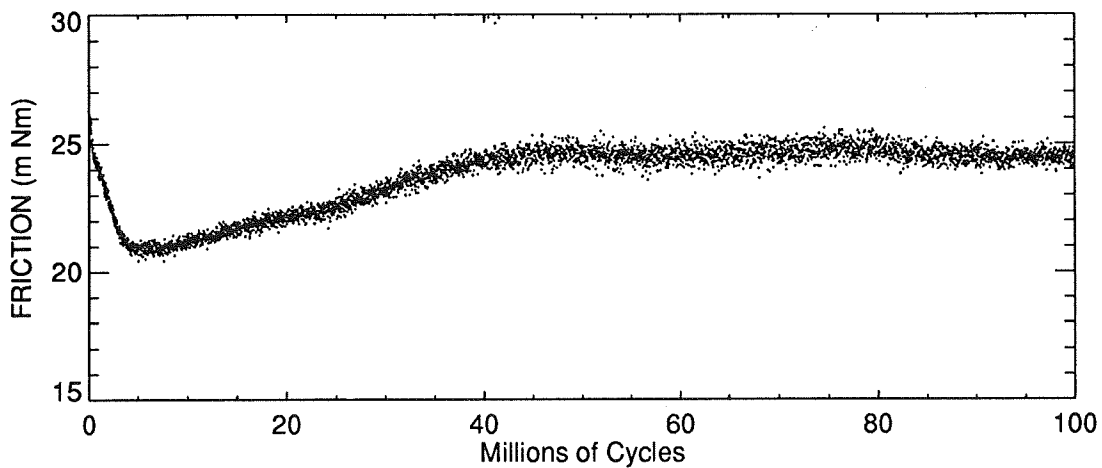SALOX separators, 30 degree move, BRAY 815Z lubrication

Figure 12f. Tuning Motor Test #3
SALOX separators, 30 degree move, BRAYCOTE 600 lubrication

Parachute Swivel Mechanism for Planetary Entry 434675

R. Birner, J. Kaese[*] , F. Koller, E. Mühlner [**] , H.-J. Luhmann [***]

ABSTRACT

A parachute swivel mechanism (PSM) for planetary entry missions such as a Mars probe (MARSNET) or return of cometary material samples (ROSETTA mission) has been developed. The purpose of the PSM is to decouple the spin of the probe from the parachute, with low friction torque, during both the deployment and descent phases.

Critical requirements are high shock loads, low friction, low temperatures, and several years of storage in the deep space environment (during the cruise phase of the probe, prior to operation).

The design uses a main thrust ball bearing to cope with the load requirement and a smaller thrust ball bearing for guiding of the shaft. Except for use on the Viking and Galileo swivels, it appears that this type of bearing has very rarely been employed in space mechanisms, so that little is known of its friction behavior with dry lubrication. A slip ring assembly allows the transfer of electrical power for post-reefing of the parachute.

A test program has been conducted covering the environmental conditions of Mars entry and earth re-entry.

This paper describes requirement constraints, model missions of planetary entries, a bearing trade-off, analyses performed, design details, the lubrication system, and test results (friction torque versus load / spin rate). In addition the design of the test rig is addressed.

---

[*]   Deutsche Aerospace AG, Munich, Germany
[**]   ORS, (Österreichische Raumfahrt- und Systemtechnik GmbH) Vienna, Austria
[***] ESTEC, Noordwijk, The Netherlands

1. INTRODUCTION

The PSM for decoupling the parachute rotation from spinning probes during descent is a critical device which must operate after long storage time under severe environmental conditions. Very low friction torque is required and knowledge of its characteristics is essential for managing the spin of the probe by means of vanes for stabilization and scanning onboard instruments. The operational conditions and requirements have been identified and analyzed. A PSM has been designed, manufactured and tested. The basic PSM design will be used on swivels of the HUYGENS probe parachutes for Titan entry.

1.1 Model Missions

According to Reference [1], probes for parachute-borne descent in the atmospheres of Earth and Mars, with mass in the range between 45 kg and 300 kg, are considered typical applications for the PSM. The corresponding descent profiles are defined in Table 1.

The baseline data, i.e., total probe mass, altitude at start of parachute deployment, etc. were taken from available references, see e.g. [2], [3]. The number of parachutes (drogue, pilot, main) were defined using a trajectory calculation for vertical descent so as to meet the requirements as far as velocities and altitudes were concerned.

2. DESIGN APPROACH AND ANALYSES

2.1 Trade-offs

A review of existing technology revealed that swivels with the required load capacity predominately utilize a pair of axial ball bearings.

The baseline concept was selected as a result of trade-off studies. First, a bearing trade-off study was focused on the selection of promising bearing types (see Fig. 1). These types were then entered into a trade-off to find suitable bearing arrangements optimized for high and low loads. A third trade-off study was made to

select the baseline for the test model and considered load bypass, preload and lubrication techniques

Baseline Design Selection Criteria   The design was directed toward the following functional tasks of the PSM, to be accomplished with a minimum-mass requirement:
- decoupling of the probe and parachute with lowest possible friction torque
- reliable functioning after long-term storage on the ground and in deep-space vacuum
- assurance of mechanical and electrical connection (bonding)
- provision for load transfer
- withstanding deployment shock
- provision for power transfer

The crucial elements of the swivel are its bearings; for this reason a detailed bearing trade-off study was performed. The main tasks for the bearings are:
- high shock load capability
- resistance to extreme environmental conditions
- lowest friction torque
- no contamination risk due to the lubrication

The evaluation of all bearing candidates revealed that the most advantageous design in terms of mass, size, lowest friction level and load capability utilizes a thrust ball bearing.

A design with load by-pass was also taken into account. The load by-pass design is shown in Fig. 2a. The needle bearing of high load capacity is normally off-floaded (by an axial clearance of ≈ 0.15 mm). Under parachute-inflation shock loading, the Belleville spring allows an axial motion of the shaft to load the needle bearing and to off-load the main axial ball bearing. This approach is of special interest for a parachute system having a very high opening shock (i.e. greater than 25 kN), in relation to the post-opening drag force level.

Preload Technique   To ensure smooth running of the bearings, which means no sliding between balls and race, and to ensure a correct geometrical point of contact, a specified axial preload must be applied.

This force may be applied in two ways:
- **Rigid preloading**: created by an exact dimensioning of the housing and shaft and a predetermined elastic deformation
- **Compliant preloading**: induced by spring force (Belleville springs) on the bearings

The rigid preload is very sensitive to thermal changes (gradients) whereas the compliant (spring force) preload can be designed to cover a large temperature range, so that only small changes in preload and friction torque occur. Another advantage of the compliant preload is that the bearings can better tolerate debris in the race ways without high risk of blocking or seizing, via the inherent high degree of flexibility. Therefore compliant preloading was selected.

Lubrication System   Since the swivel is required to tolerate cryogenic temperatures and to fulfil stringent cleanliness requirements, only dry lubrication was feasible. Candidate lubrication systems considered in a trade off study were:

- Races: Sputtered or ion plated lead films
                 CVD [4] or sputtered MoS_2 [5] Coating
                 Tungsten Stabilized Carbon Coating [6]

- Balls: Sputtered lead films
                 CVD or sputtered MoS_2 Coatings
                 TiC coating only or
                 TiC + MoS_2 coating

- Retainers: PTFE/MoS2/Glass fibre composite [7](Duroid, Rulon A, Klueberplast LD)
                 Steel with CVD or sputtered MOS_2 coatings or tungsten
                 Stabilized carbon coating or leaded bronze

The trade-off resulted in an initial selection of lubrication systems for thrust ball bearings as follows:
- Races: MoS_2 thin film coating (PVD)
- Balls: TiC Coating (CVD), and MOS_2 thin film coating (PVD)
- Retainers: MoS_2 thin-film-coated steel

240

The rationale for selection was:
- MoS$_2$:   Provides lowest friction coefficients
- TiC: Assures very low wear, provides best cold welding protection

After the first tests of this system, in an attempt to minimize the friction torque the following changes were successfully introduced:
- On the main bearing, TiC balls were used without MoS$_2$ thin film coating
- The standard retainers made from steel were replaced by special retainers (washer type, raceway guided) made from Rulon A
- Bearing radial runout was measured and taken into account at assembly for compensation.

2.2 Analyses

Load Analyses   A two degree-of-freedom analytical model of the Probe-PSM-Parachute System (PPPS) was developed for calculation of the loads on the PSM due to parachute inflation. The Mass-Time Method, as described in [4], was applied. A typical force-time history of these calculations is shown in Fig. 3. As a result, the maximum loading on the PSM can be limited to 7000 N by proper design of the drogue, pilot and main parachutes.

A more sophisticated model of the PPPS, characterized by four degrees of freedom, was developed for determining the loads acting on the PSM when the probe with fully inflated parachute is subjected to vertical or horizontal gusts or wind shear. The dynamic model utilized for this analysis is depicted in Fig. 4. Wind shear can readily be converted into an equivalent horizontal gust. Even a sudden gust, which represents a conservative assumption, leads to negligible radial loads on the PSM and causes axial loads of the same order of magnitude as parachute inflation (see Fig. 5).

Thermal Analysis   The thermal analysis considered heat transfer by conduction, radiation, and on the outside surface, forced convection. The assumed inital temperature was -20°C for the function-critical, cold case. The results were low temperature extremes of -44 °C for Earth reentry and -37°C for Mars entry missions. A maximum gradient analysis revealed 12°C between housing and shaft for Earth

reentry. The maximum temperature difference for the Mars mission was predicted to be 5°C.

Structural Analysis Analytical and numerical methods were used for stress and strength analysis. The chosen design load capacity of the PSM of 16000 N was found to be suitable to withstand the loads, as derived from the mission requirements, with sufficient margin.

Thermal Effects The PSM design is insensitive to expansion. Its compliant preloading by two Belleville springs compensates the expansion. The temperature-induced preload change is in the range of 20 N, which has minor impact on the friction level. The nominal preload was initially set to 160 N but was reduced to 100 N after the first tests in an attempt to minimize the friction torque.

3. DESIGN DESCRIPTION

The baseline design (see Fig. 2b) employs axial ball bearings for the main and guiding bearing (FAG types 51203/51100). This combination was found to be optimum with respect to the restricting demands of very low torque and mass, under the applicable load conditions. The maximum static load capacity of the PSM main bearing is 27 kN.

The housing is made of aluminum 7075. The housing and shaft include lugs for the interface to the parachute and to the probe. Low friction between the parachute clevis and PSM is attained by use of a bonded MoS_2 film in order to minimize radial loads on the swivel bearings. The same treatment was applied on the lug of the shaft. The shaft is made from titanium which matches the thermal expansion coefficient of the bearing races.

Power transfer through the swivel for the post-reefing system of the parachute (pyro cutter or release device) is accomplished with a MECANEX slip ring assembly. The slip ring has 5 lines of 2 amps capacity. One of the slip rings serves as electrical bonding between shaft and housing. The 4 remaining lines allow power transfer to a redundant post-reefing actuator, if required. The slip rings are of an alloy composed of gold, silver and copper, while the brushes are made from an alloy composed of

gold, silver and palladium. Each brush contact is redundant. The brushes are embedded in a block of epoxy resin.

The PSM size and mass is:

	Outer diameter:	46 mm
	Length:	120 mm
	Mass:	38 grams

The applied tribological system is as follows: The balls, made from AISI 440C stainless steel, are coated with titanium carbide (TiC). The nominal thickness of the coating is 3-4 μm, with a fine grained microstructure (0.1 μm typically) and high hardness (3500 HV). High accuracy balls (Grade 3) and a very smooth surface finish (0.006 μm Ra) are obtained. The race washers of 1.3505 steel are coated with 3-5 μm of thin dense chromium for corrosion protection and are lubricated with 0.4 μm MOS_2 (PVD process). The bearing cage is machined from Rulon A. The cage has been designed to achieve low friction by low surface roughness and to ensure a positive clearance for the balls under temperature extremes.

The total friction torque comprises the contributions of friction in the main bearing, the guiding bearing and slip rings. The main bearing is loaded with the descent load and the preload, whereas the guiding bearing is loaded with the low preload of 100 N only.

Torque predictions were performed by ESTL using a sliding friction coefficient for MoS_2 and steel in vacuum of 0.07 (worst case). A comparison of prediction and test results is shown in Fig. 7.

4. TESTING

4.1 Test Program

The test sequence comprised electrical tests of slip rings, followed by a torque characterization test at room temperature with loads from 100 N to 8800 N at rates between 1.5 and 60 rpm. A shock load test at no rotation consisted of 10 load cycles up to 8800 N (7000 N parachute-inflation load times an uncertainty factor of 1.25). A life test in a simulated Mars environment (CO_2) required 4 hrs operation at 500 N load at - 55°C and at a pressure of 1 mbar.

An Earth environment life test in humid air of 70% RH required 10 minutes of operation at 3000 N at 15 rpm. A static load test of 20 kN completed the test program.

4.2 Test Results

The test results of the torque characterization test are shown in Table 2. A typical torque test record in the simulated Mars environment is shown in Fig. 6. Plots of the test results are depicted in Figures 7 and 8. The mean torque is determined by the difference of torque at rate reversals. The PSM survived the test program without detrimental degradation in performance.

The influence of rate on the torque which was experienced had not been predicted. The measured torque was lower than the predicted torque at high loads and vice versa at low loads. For low load cases one has to consider that the predictions by ESTL did not cover the friction of the cages. The slip ring friction (not directly measured) is considerably below the predicted value of 0.4 Ncm.

Operating Life Test

Earth Environment: The mean friction torque at room temperature, 70% RH, was 12 Ncm under a 3kN Load at 15 rpm. The torque was found to be higher by a factor of 3 than the values at vacuum or dry GN2. The predicted factor was a minimum of 3. The post life test at 100 N load showed an increase about 0.2 Ncm in torque (slight degradation) compared to the test value at 100 N load at the beginning.

Mars Environment: The mean friction torque at -55 °C , 1 mbar CO_2, was about the same as measured at room temperature at 1 bar GN_2. The mean and ripple torque both showed considerable variation. No residual degradation occurred. These variations may be caused by traces of humidity in the test atmosphere. It is possible that the vapor entered the test chamber via the O-ring seal of the mechanical drive feedthrough of the test rig.

4.3 Test Rig   A special Test Rig (see Fig.9) was designed and manufactured to allow simulation of PSM operation under the loads and environmental conditions to be expected during parachute-borne descent through a planetary atmosphere.

The PSM to be tested is suspended by means of brackets inside of the sealed test chamber. Arbitrarily composed atmospheres from very low pressure to ambient pressure can be established in this test chamber. A "cold wall" envelopes the PSM to perform radiative heat transfer. This wall consists of a sheet metal surface with an attached tube coil for circulation of a cooling or heating fluid, such as liquid or gaseous nitrogen A test at a temperature of -55°C was successful. Temperatures to -180°C are considered to be feasible.

The brackets are attached to fiber glass rods used to minimize conductive heat transport to the PSM from the exterior of the chamber. Axial load and torque are transferred to the PSM through these brackets and the fiber glass rods. The axial load can be applied either statically or as a transient starting from a specific value and increasing to a preset force.

The Test Rig can be used for performing tests in atmospheres of arbitrary composition and for pressures between 100 Pa and 100 kPa as follows:
(i) Measurement of PSM friction torque in the range from 1 Nmm to 3 Nm for specified static axial loads up to 16 kN at rotational speeds from 1 to 20 rpm and different temperatures,
(ii) Application additionally of transient load to the (rotating) PSM and measurement of the same friction torques as in (i).

5. CONCLUSION AND SUMMARY

A low-torque parachute swivel mechanism for planetary entry missions has been developed. Analysis of the loads acting on the probe-parachute system during parachute inflation and parachute-borne descent showed that radial loads are negligible. A test model was built and subjected to torque measurement. Descents in the low-temperature Mars atmosphere and the Earth atmosphere were simulated. The tests were successful. The mean friction torque at -55°C , 1 mbar CO_2, was about the same as measured at room temperature at 1 bar GN_2. The friction torque of thrust ball bearings exhibited an unexpected increase in friction at rates above 1.5 rpm on both unlubricated and lubricated bearings. The thin, dense chromium plating survived all tests.

ACKNOWLEDGMENT

REFERENCES

1. Luhmann, H.J.   "Parachute Swivel for Planetary Entry"   Statement of Work YMM/DWR/481, ESA/ESTeC, Noordwijk (1990).

2. ----------------   "Rosetta/Comet Nucleus Sample"   Return System Definition Study. Final Report, 1991.

3. Chicarro, A.F., et. al   "Marsnet Assessment Study"   ESA Report.,Publication SCI(91)6, Jan. 1991.

4. H.J. Boving and H.E. Hintermann   "Properties and Performance of Chemical-Vapor-Deposited TiC-Coated Ball-Bearing Components"   *Solid Films*, 153 (1987) pp 253-266.

5. E.W. Roberts   "Thin Solid Lubricants in Space",   *Tribology International*, April 1990, Vol. 23, No.2.

6. J.P. Bosch, G. Farges, E. Bergann   "Wear Resistant Thin Films"   Presented at the 14th International Conference on Metallurgical Coatings, San Diego, CA, March 1987

7. M.J. Kubitchek   "SRTF/IRS Cryogenic Grating Drive Mechanism" *Proceedings of the 25th Aerospace Mechanism Symposium*, (8-10 May 1991), NASA CP 3113, pp 107-124.

celestial body	m [kg]	para-chutes	v_0 [m/s]	ρ_e [kg/m³]	h_0 [m]	v_e [m/s]
Earth	300	drogue	457.0	0.0184	30000	61.4
		pilot	61.4	0.4663	9000	30.6
		main	30.6	0.9091	3000	6.0
	250[1]	no	457.0	0.0184	30000	105.0
		pilot	105.0	0.4663	9000	27.9
		main	27.9	0.9091	3000	6.0
	45		457.0	0.0184	30000	26.3
		main	26.2	0.9091	3000	6.0
Mars	300	pilot	336.0	0.004	18000	86.7
		main	86.7	0.0106	6400	25.0
	84[2]	main	270.0	0.0074	11000	25.0
	66[3]	main	270.0	0.0074	11000	80.0

[1] ROSETTA (Land)

[2] MARSNET Semi Hard Lander

[3] MARSNET Hard Lander

m   total mass, i.e., mass of probe, PSM and parachute

v_0 velocity of probe at start of parachute inflation

ρ_0 atmospheric density at start of parachute inflation

h_0 altitude of probe at start of parachute inflation

v_e velocity of probe at touch-down or at start of inflation of next parachute

Table 1 Probe Masses and Descent Profiles Representing Typical Applications for the PSM.

LOAD [N]	RATE [RPM]	MEAN TORQUE [NCM]	RIPPLE TORQUE [NCM] 0-peak
100	1.5	0.4	0.2
300	1.5	0.6	0.3
300	60	1.2	0.2
500	1.5	0.4	0.4
500	15	1.5	0.3
500	60	1.5	0.25
1000	1.5	0.6	0.35
1000	15	2.2	0.45
1000	60	2.1	0.6
3000	1.5	2.8	1
3000	15	4.3	0.5
3000	60	4.2	0.9
8800	1.5	11.5	2
100	1.5	0.2	0.2

Table 2   Summary of Torque Characterization Test Results
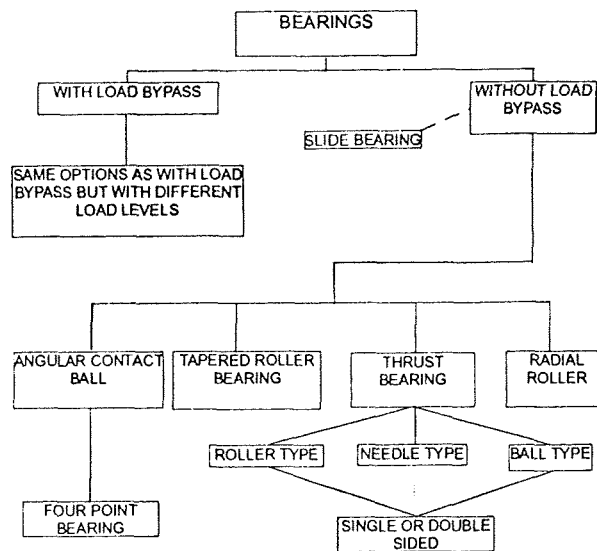
Figure 1   Bearing Trade Off Tree

248

HIGH LOAD PATH

LOW LOAD PATH

BELLEVILLE SPRING

MAIN BEARING

GUIDE BEARING

SLIP RING ASSEMBLY

Figure 2a   High Load PSM Design with Load By-Pass
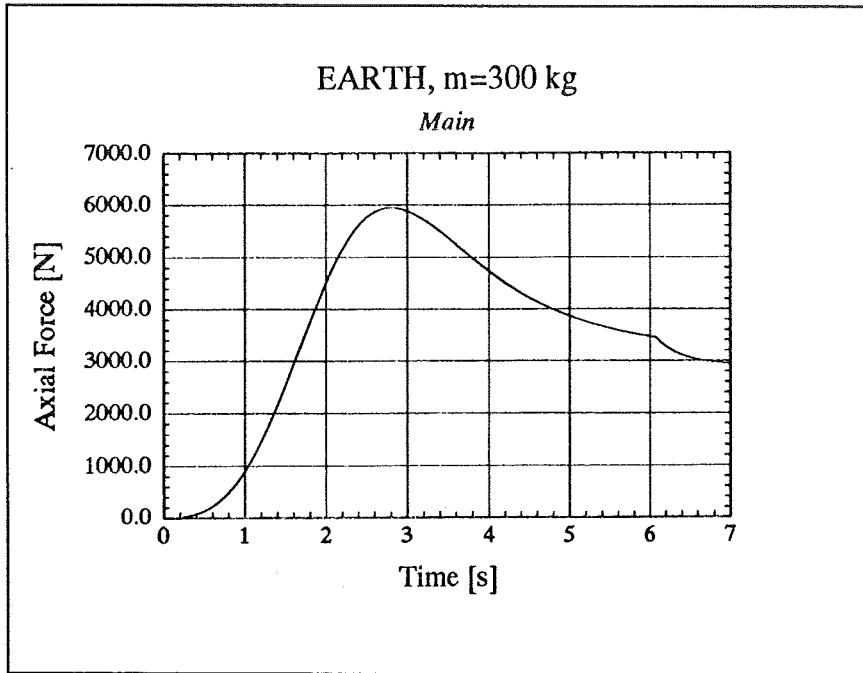
Ø46

NEEDLE BEARING
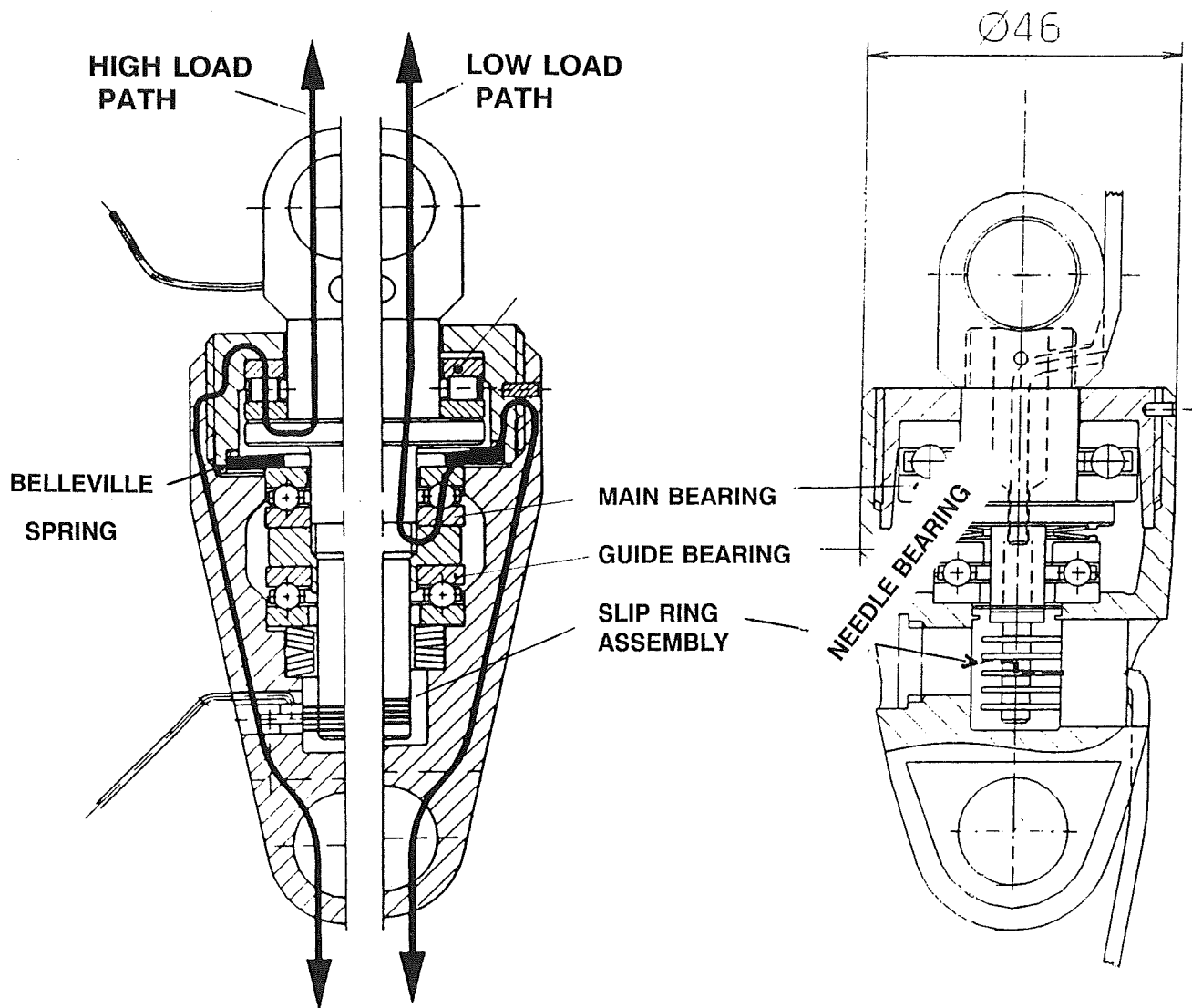
Figure 2b   PSM Baseline Design

249

Figure 3   Force vs. time during inflation of the main parachute for earth descent, probe mass m = 300 kg, see Table 1 for reference.
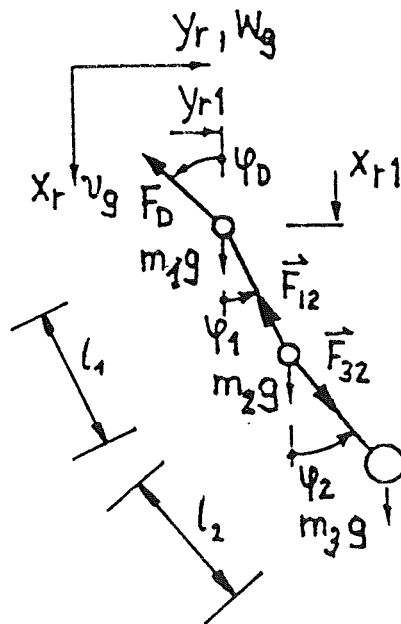

Figure 4   Dynamical model of the Probe-PSM-Parachute System represented by three point masses (four degree of freedom model).
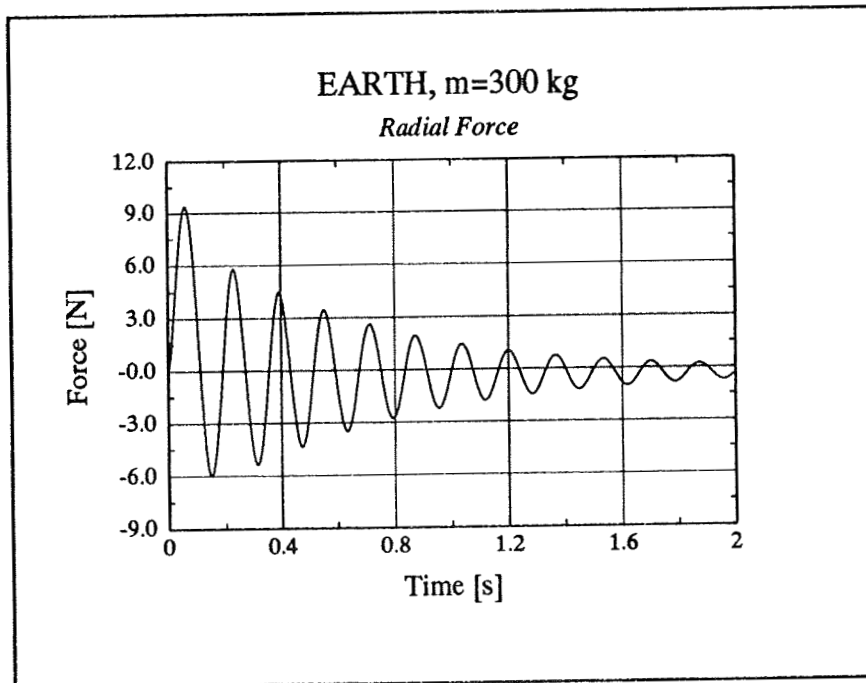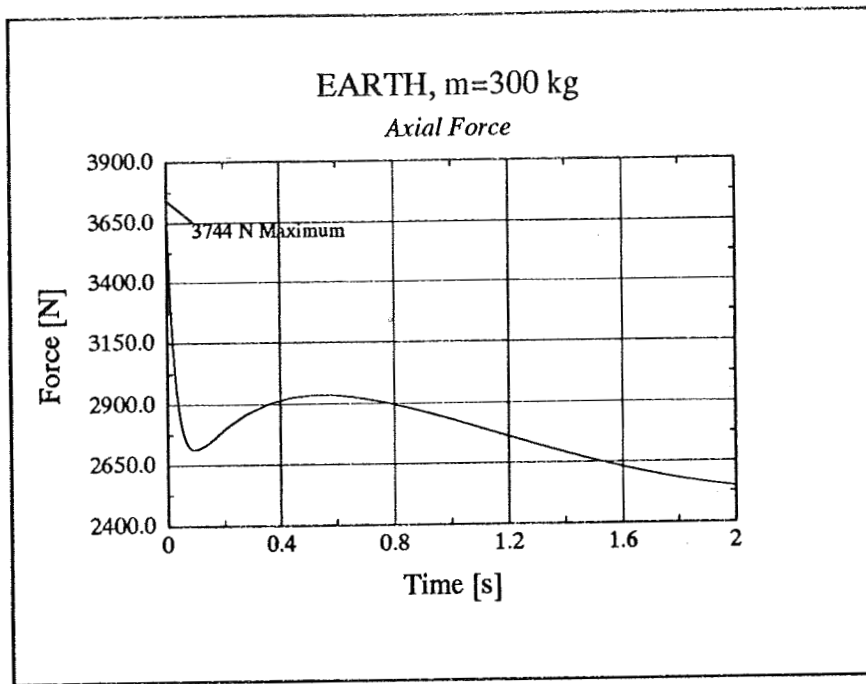
250

EARTH, m=300 kg
Axial Force

EARTH, m=300 kg
Radial Force

Figure 5a Response of the Probe-PSM-Parachute System (PPPS) represented by three point masses (four degree of freedom model) to a sudden horizontal gust. The PPPS is initially in steady state vertical descent with 6m/s (parachute fully inflated). See Figure 5b for further data of Probe-PSM-Parachute System.
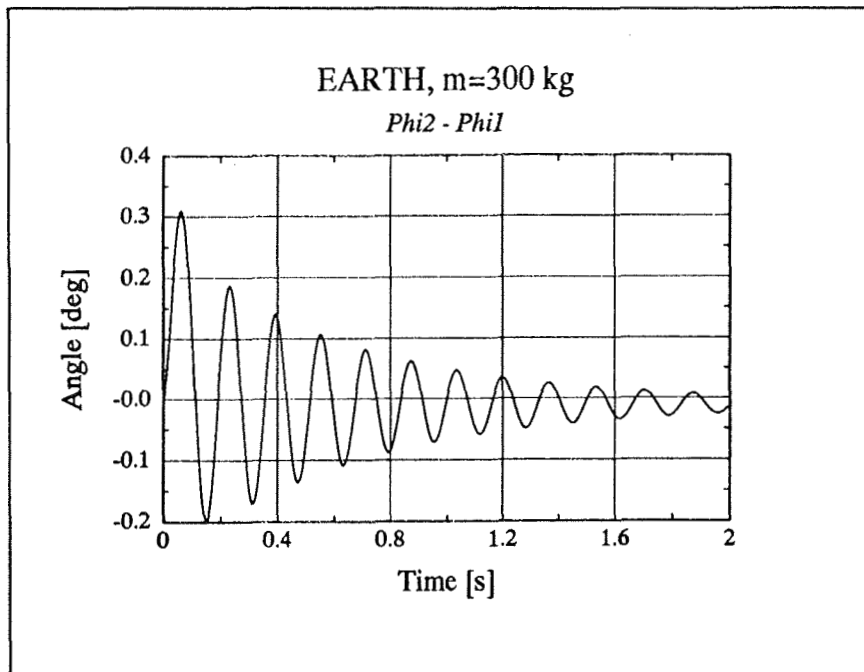
EARTH, m=300 kg

Phi2 - Phi1

Figure 5b Difference between the angles φ_1 and φ_2 as a function of time. Masses: m_1 = 30 kg, m_2 = 0.6 kg, m_3 = 269.4 kg; parachute: area = 190.6 m^2, drag coefficient c_D = 0.7; atmospheric density = 1.225 kg/m^3; gust: 6 m/s, suddenly in horizontal direction.
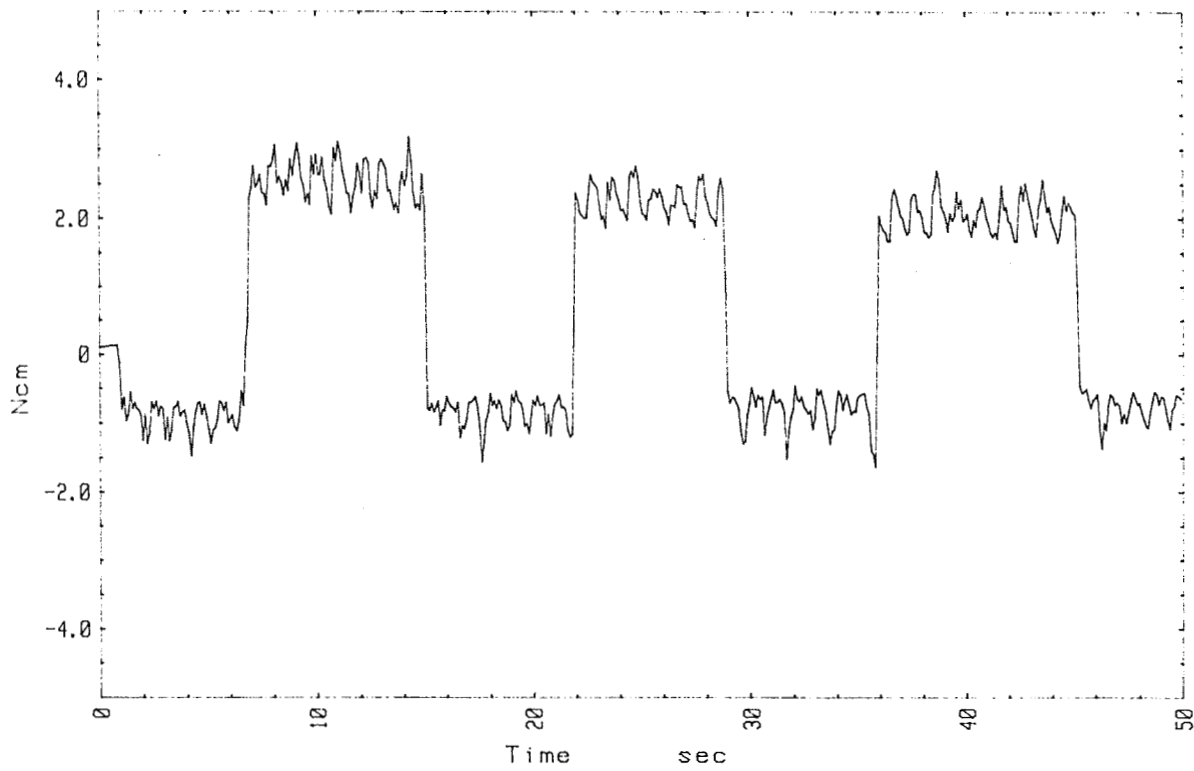
252

Figure 6 Torque versus Time at 500 N Load, 60 rpm, -55°C, 1mbar CO_2
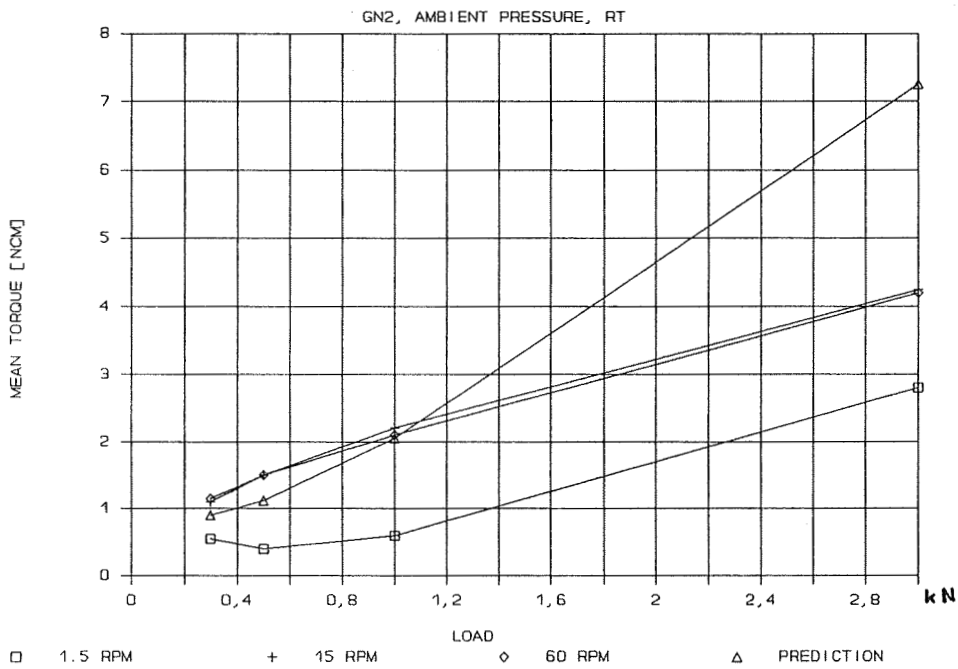

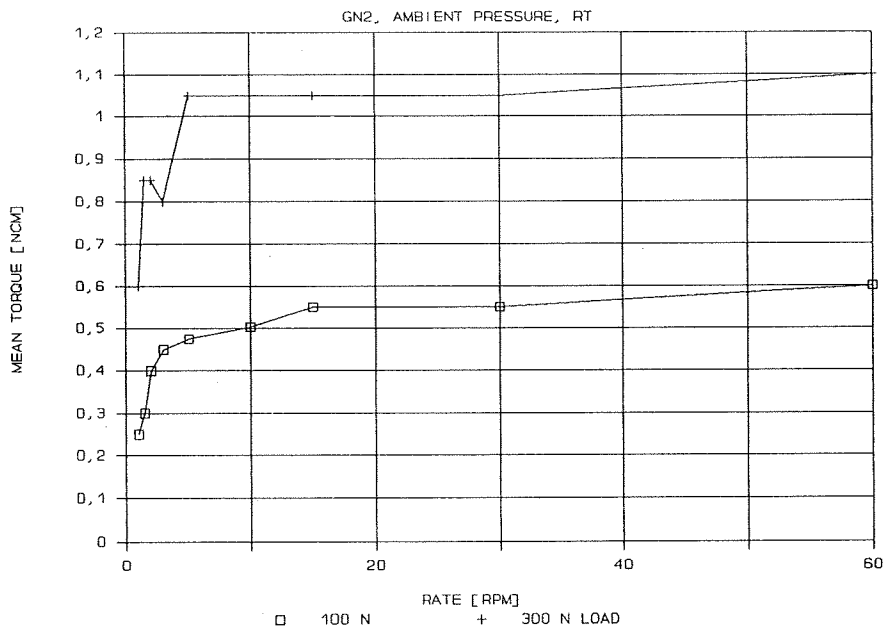Figure 7 Torque versus Load up to 3 kN

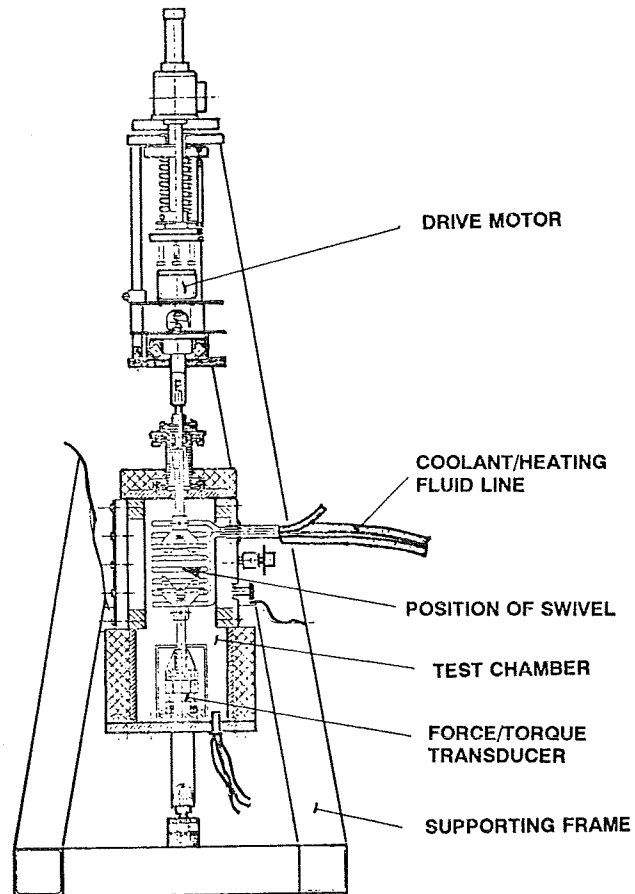Figure 8   Torque versus Rate at 300 N Load, 1.5 rpm

Figure 9   Test Rig for Simulation of PSM Operation under Loads and Environmental Conditions to be expected during Parachute-borne Descent through a Planetary Atmosphere.

254

Low Melting Temperature Alloy Deployment Mechanism and Recent Experiments

434676

M. J. Madden[*]

ABSTRACT

This paper describes the concept of a low melting temperature alloy deployment mechanism, U.S. Patent 4,842,106. It begins with a brief history of conventional dimethyl-silicone fluid damped mechanisms. Design fundamentals of the new melting alloy mechanism are then introduced. Benefits of the new over the old are compared and contrasted. Recent experiments and lessons learned complete this paper. We find this mechanism to be particularly promising, and may soon be recommending its use. A demonstration unit is powered-up to visually illustrate the deployment.

INTRODUCTION

Spacecraft are launched with a variety of large payloads which are folded or stowed to minimize envelope and to withstand launch loads. In general, these structures are weight optimized and delicate. It is necessary to limit their rate of deployment during the mission to prevent damage. Deployment rate can be rigidly controlled by using a motor drive or simply limited by providing a damping feature on a spring or centrifugally driven deployment. This is generally provided by coulomb, viscous, or eddy current damping. While these methods have all been employed with varying degrees of success, all have significant drawbacks. Motor drives are complex mechanical assemblies which require special drive electronics. Coulomb damping or friction typically leads to a very small torque or force margin which jeopardizes the success of the deployment. Eddy current dampers can be as complex as motorized drives. Viscous dampers are moderately complex and create a potential source of contamination if leakage were to occur. All methods have narrow performance ranges, require some sort of launch lock to restrain the payload during launch, and are typically faced with backlash, latching and stiffness problems.

Hughes Space and Communications has been a leader in spacecraft production for more than 25 years. A family of over fifteen different spring driven, rotary, viscous damped deployment mechanisms has evolved over the years. Over 100 units have been built and more than 60 have provided successful mission

----

[*] Hughes Space and Communications, El Segundo, California

deployments. These mechanisms have a perfect track record - no mission failures! Despite this impressive record, a low melting temperature alloy deployment mechanism is an attractive and exciting development which offers many advantages.

DESIGN PHILOSOPHY

First, consider our traditional dimethyl-silicone fluid filled damper found in Figure 1. The cylindrical housing contains a pair of internal opposing teeth. The shaft boasts a pair of associated opposing paddles. Caps complete with o-rings and bearings seal off the ends. All gaps around the moving paddle are very closely controlled. The main radial gap determines the damping rate, as all other parasitic gaps are held as small as possible. Constant force springs (not shown) supply the driving torque for the mechanism. When the driving torque is applied, the fluid is forced to flow from the high pressure side of the paddles to the low pressure side. The viscous shear resistance developed in the process results in a slow, damped movement. Deployment continues until stops are reached. During the mission, thermal expansion and contraction of the fluid is accommodated by a spring-loaded o-ring sealed piston reservoir arrangement.

Now, take this traditional unit and alter it into the low melting temperature alloy damper, shown in Figure 1A. Remove one paddle from the shaft, and the related tooth from the housing. Discard the temperature compensation assembly. Keep the same bearings, o-rings, and end caps. Open all the gaps to be very generous. Fit a heater to the paddle. Replace the fluid with the alloy. In this arrangement, when a driving torque is applied, nothing happens until heat is selectively put to the paddle. When deployment is desired, heaters are powered-up, warming the shaft paddle and it slowly sweeps its way through the melting alloy like a hot knife through butter. Melt rate is controlled by heater power compared to the energy required to melt the alloy. Deployment continues until hard structural stops are reached. Once heater power is terminated, the alloy solidifies and the rigid joint configuration is recovered.

BENEFITS

This is a logical development of the existing viscous damping technology used extensively at Hughes, and the benefits of this device are overwhelming.

- Stiffness improvements are remarkable, since the alloy freezes whenever power is off.
  - zero backlash is achieved
  - no latches are required

- Complexity is reduced, since there are fewer parts.
  - tolerances open up

- design, assembly, and fill are easy
- bearings may not be needed
- clean room assembly is obsolete
- no need for highly-filtered fluid
- cost savings are dramatic

- Low shock situation is achieved, since explosive launch locks are unnecessary.

Other significant advantages are:
- larger deployment angles are available
- temperature compensation is unnecessary
- phased, sequential deployments are possible
- less dependency on bulk unit temperature
- single design provides a range of deployment rates
- modeling of complex non-Newtonian fluid not required

A summary comparison chart of new vs old and its benefits can be seen in Table 1.

DEVELOPMENTS

The engineering model of the first Hughes viscous damped actuator was built in 1976 and provided rate control for the deployment of the omni-directional antenna on the HS-376 satellite. In 1986 this unit was disassembled, fitted with a conventional heater, and filled with a low melting temperature alloy. The mechanism has been repeatedly cycled at presentations to demonstrate the concept and has shown no signs of degraded performance. No performance testing has been conducted with this mechanism. A patent application was filed in 1987 based on this device, and a United States patent was awarded in 1989; patent number 4,842,106, Rate Controllable Damping Mechanism.

Hughes is now in the process of testing a second generation engineering model unit, patterned after the new family of HS-601 deployment mechanisms.

The fluid-filled HS-601 Solar Wing Actuator is shown in Figure 2, and the as-tested melting alloy version of that unit is shown in Figure 2A, Figure 3 and Figure 4. The modified unit is of simplified design for ease of test. The following items were test plan performance objectives:

- foil heaters vs. cartridge heater at similar power levels
- different power levels
- same power level, but different allocation
- eutectic vs. non-eutectic alloy

257

- resistive torque vs. angle
- stiffness

RESULTS

Figure 5 illustrates that for the shaft, a cartridge heater arrangement is slightly more efficient than foil heaters. This efficiency increased the deployment rate near the end of deployment. Figure 6 results are obvious; namely that higher power level produces a faster deployment. Figure 7 power allocation curves show that if a steady deployment rate is desired, then power should be biased to the housing heaters. Some efficiency is lost, and deployment time increases. Figure 8 shows that there is no deployment rate distinction between the use of eutectic vs. non-eutectic alloys. Resistive torque tests were performed at various speeds, and consistent resistance readings indicate that there are no viscous effects in this unit. The melting of the alloy itself is key. Stiffness tests were inconclusive, since soft non-metallic sleeve bearings were used. All tests were run in air at room ambient temperature.

OBSERVATIONS

Foil heaters applied to the wall of the housing bore with RTV worked well, but ones applied to the radius and leading edge of the shaft paddle delaminated. In an attempt to prevent delamination, a top layer of RTV was applied to the foil heaters. They held, but blew-out when powered-up due to the reduction of heat transfer rate. A cartridge heater in the shaft centerline is definitely the way to go. The approach is much cleaner, as there are no heater wire feed-throughs, RTV mess, delamination, or burn-out issues. For best efficiencies of the cartridge heater, intimate contact area must be preserved. Housing heater wires were passed through a hole in the housing adjacent to the fill plug and RTV'ed without incident.

The melting alloy was very easily poured into the warmed mechanism. The unit was assembled and disassembled many times. The only time-consuming task was to scrape off a thin residual film of the alloy from wetted surfaces. No signs of wear or scoring have been noticed on the housing, shaft, sleeve bearings, or o-rings. An automotive type paper gasket was tried at the housing-to-end-fitting interface and performed very well.

LESSONS LEARNED

Given the findings mentioned above, our next test unit will do the following:

- use a cartridge-type shaft heater for simplicity
- use precision ball bearings for increased stiffness
- minimize the amount of alloy used for weight and heat-up time benefits
- start with a clean sheet of paper in design

We made use of a spare housing, and what we thought was convenient became a trap. It put unnecessary constraints and compromises into our test design.

ACKNOWLEDGEMENTS

Those who assisted in generating this patent have encouraged me to spread this new idea to like industries in America and overseas.

REFERENCES

"Rate Controllable Damping Mechanism" U.S. Patent 4,842,106

NEW	OLD	BENEFIT
solid rigid joint	adequately rigid joint	improved stiffness
zero backlash	some backlash	simplified attitude controls
no latch mechanism	latches required	improved torque margin
leaky alloy goes solid	leaky fluid migrates	near zero risk of contamination
low complexity	very complex	ease of assembly
wide tolerances	tight tolerances	ease of machining
a few simple drawings	many precision drawings	simplicity of design
fill on a workbench	fill in a vacuum	air bubbles permitted
bearings are optional	bearings are required	lower cost
assemble on a workbench	clean room assembly	insensitive to contamination
no fluid filtering	highly filtered fluid	tolerant to particulates
no launch locks	launch locks required	low shock
narrow paddle	wide paddle	larger deployment angle
no temperature compensator	compensator required	weight savings
phased deployments	single deployment	more applications
independent of bulk temperatures	bulk temperature sensitive	no thermal analysis
range of deployment rates	unit has one rate	greater versatility
simple "melting ice cube" analysis	complex non-Newtonian fluid	less modeling
heat dependent performance	torque dependent performance	load independence

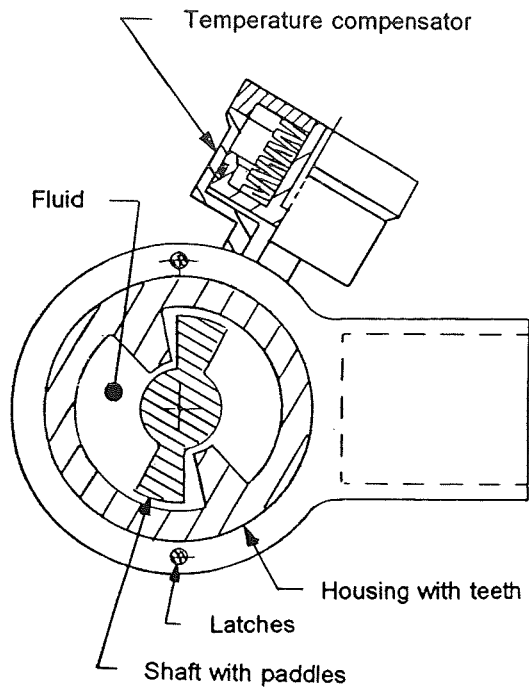Table 1. Summary Comparison Chart of New vs. Old

260

Figure 1. Conventional Fluid Filled Damper
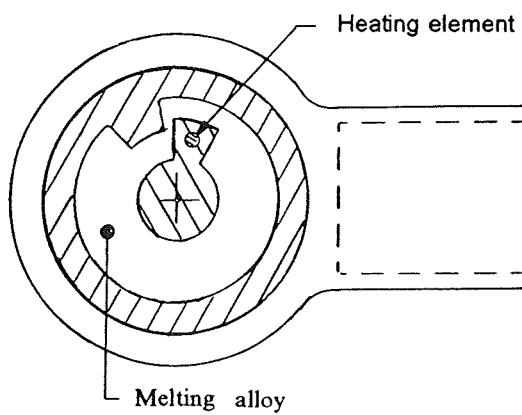(HS-376 Omni Actuator)

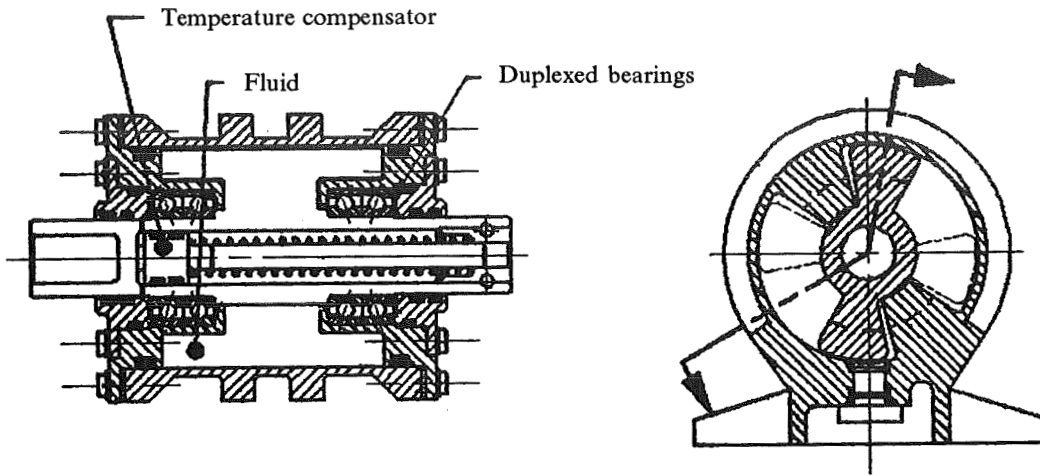Figure 1A. Low Melting Temperature Alloy Damper

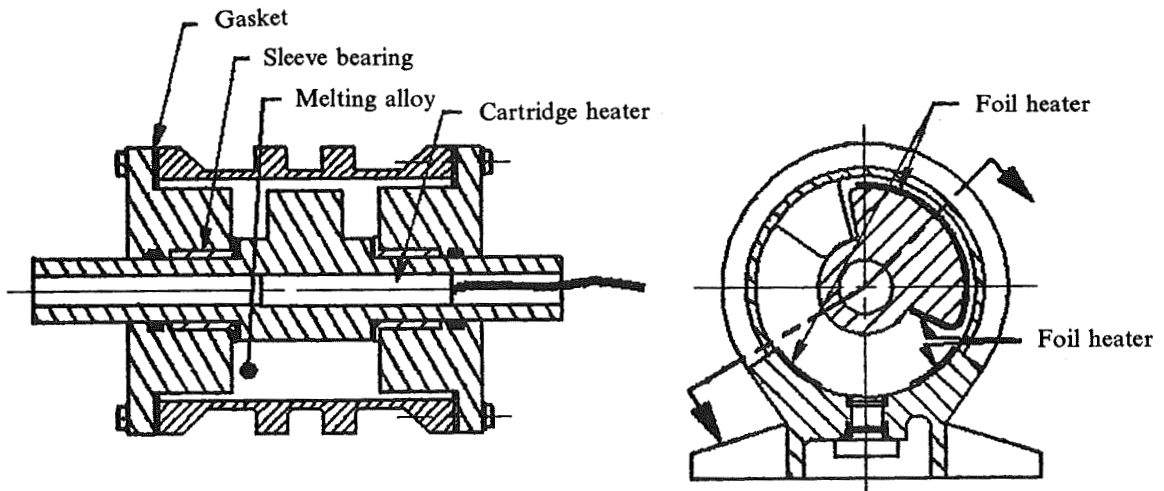Figure 2. Conventional Fluid Filled Damper
(HS-601 Solar Wing Actuator)

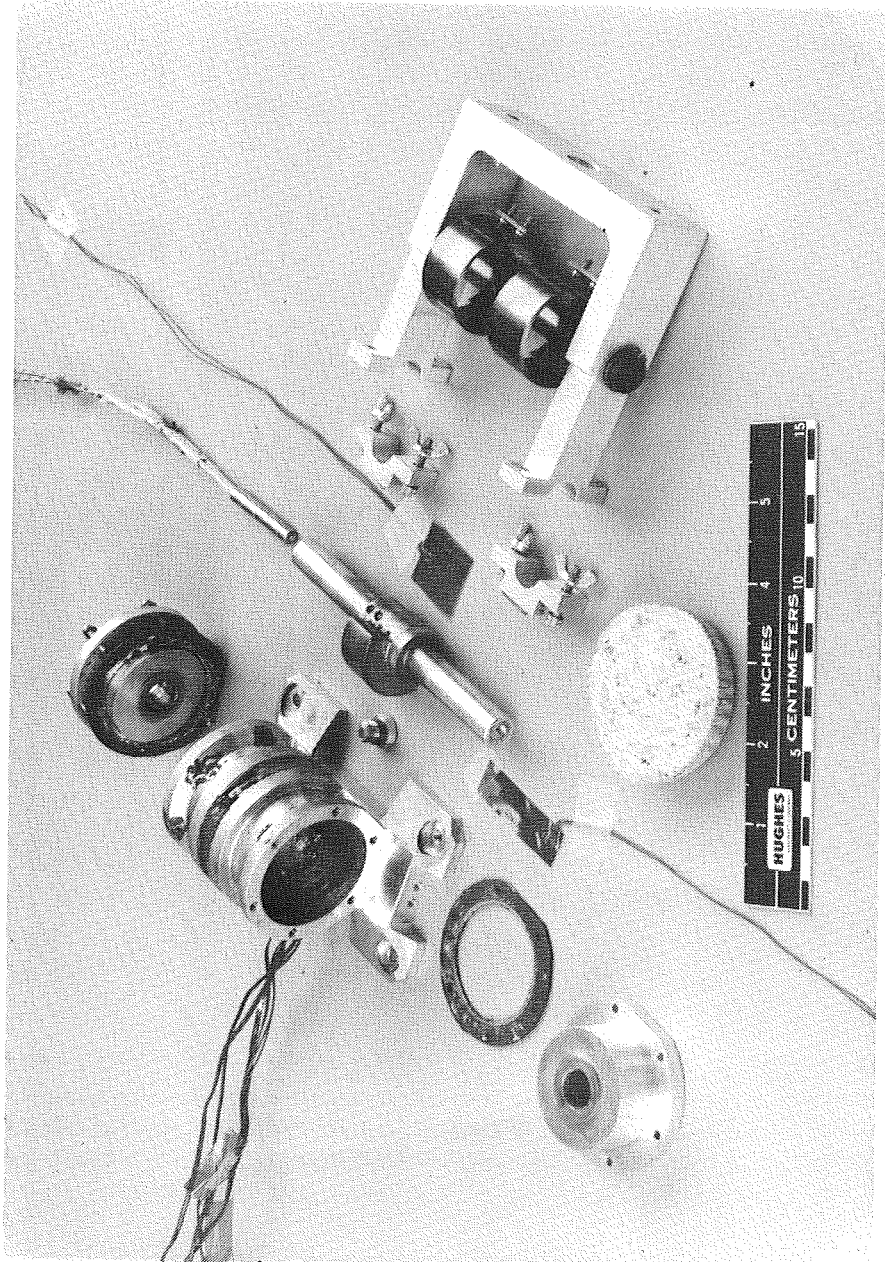Figure 2A. As-Tested Low Melting Alloy Damper
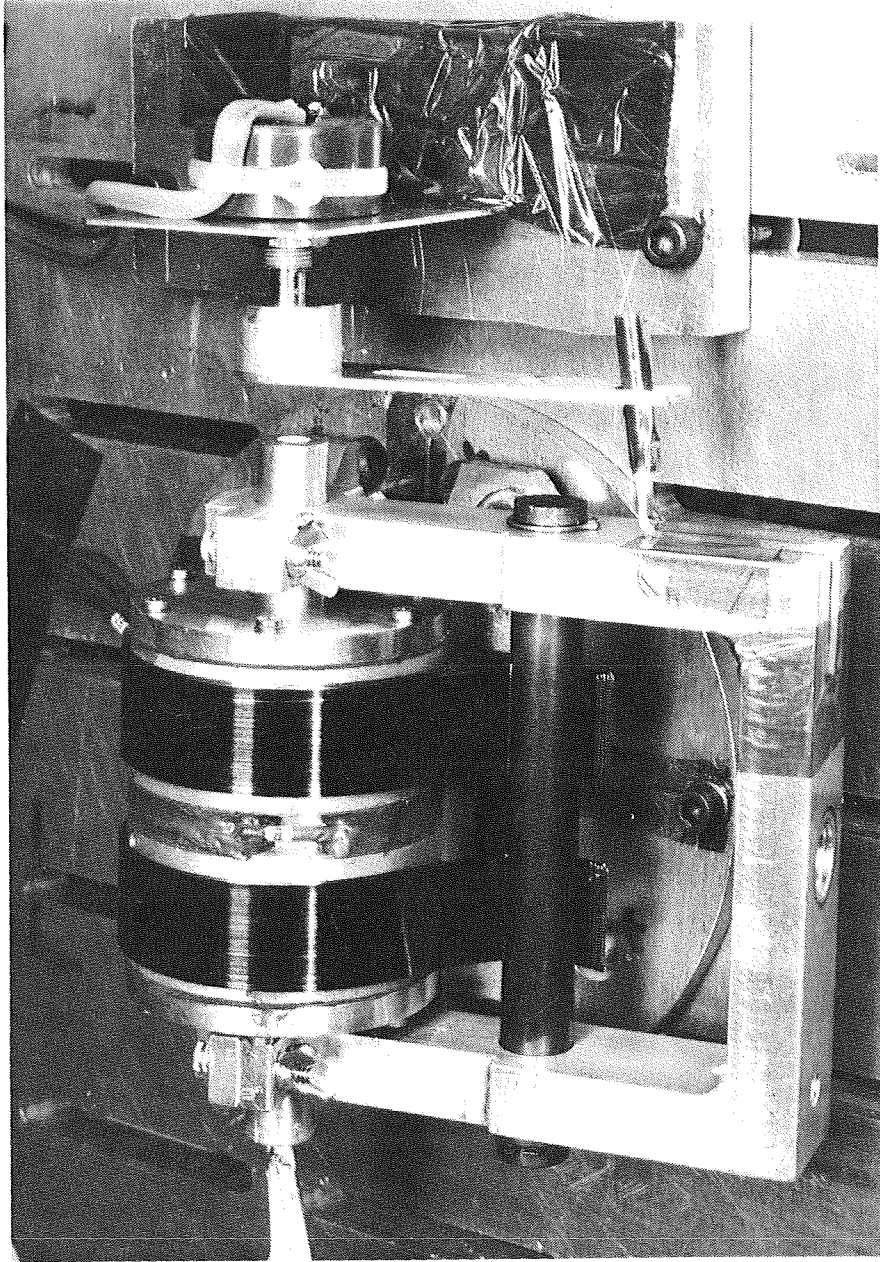
Figure 3. Exploded View Photograph
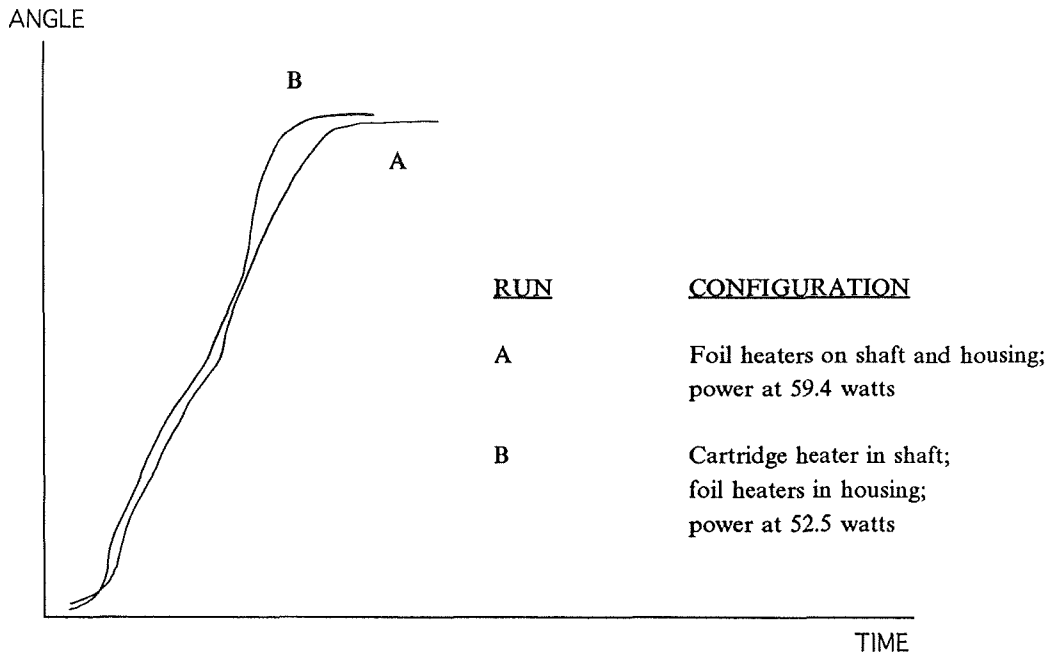
Figure 4. Photograph of Deployment Test Configuration

264

ANGLE

RUN	CONFIGURATION
A	Foil heaters on shaft and housing; power at 59.4 watts
B	Cartridge heater in shaft; foil heaters in housing; power at 52.5 watts

TIME

Figure 5. Comparison of Foil Heaters vs. Cartridge Heaters
at Similar Power Levels

ANGLE

RUN	CONFIGURATION
B	Cartridge heater in shaft; foil heaters on housing; power at 52.5 watts
C	Same as Run B except power at 32.5 watts

TIME
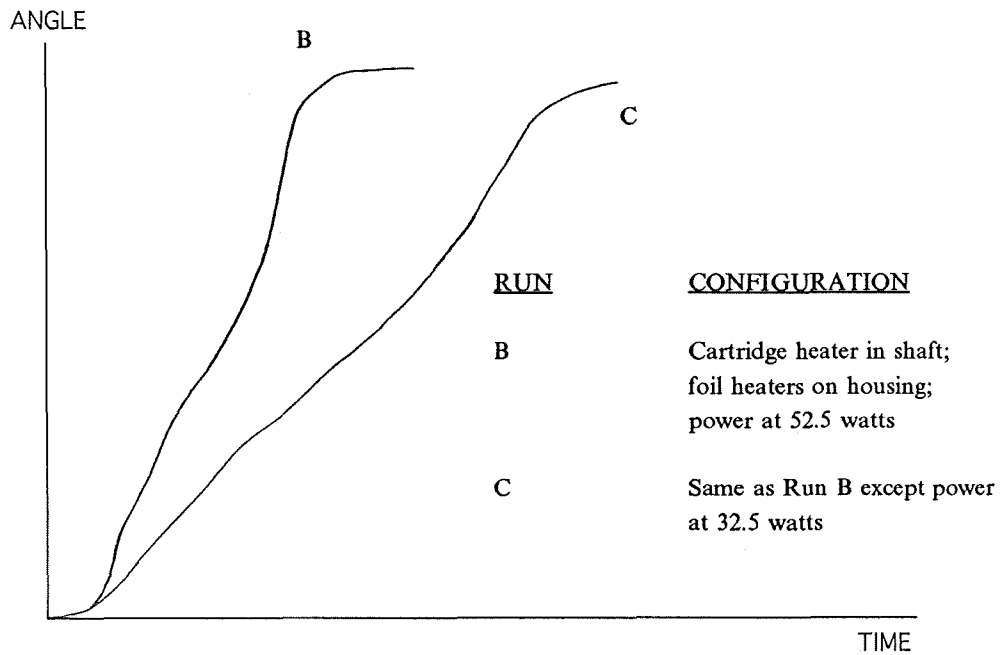
Figure 6. Comparison of Different Power Levels

265

ANGLE

C

D

RUN	CONFIGURATION
C	Cartridge heater in shaft at 18.5 watts; foil heaters on housing at 14 watts
D	Cartridge heater in shaft at 12.5 watts; foil heaters on housing at 20 watts

TIME
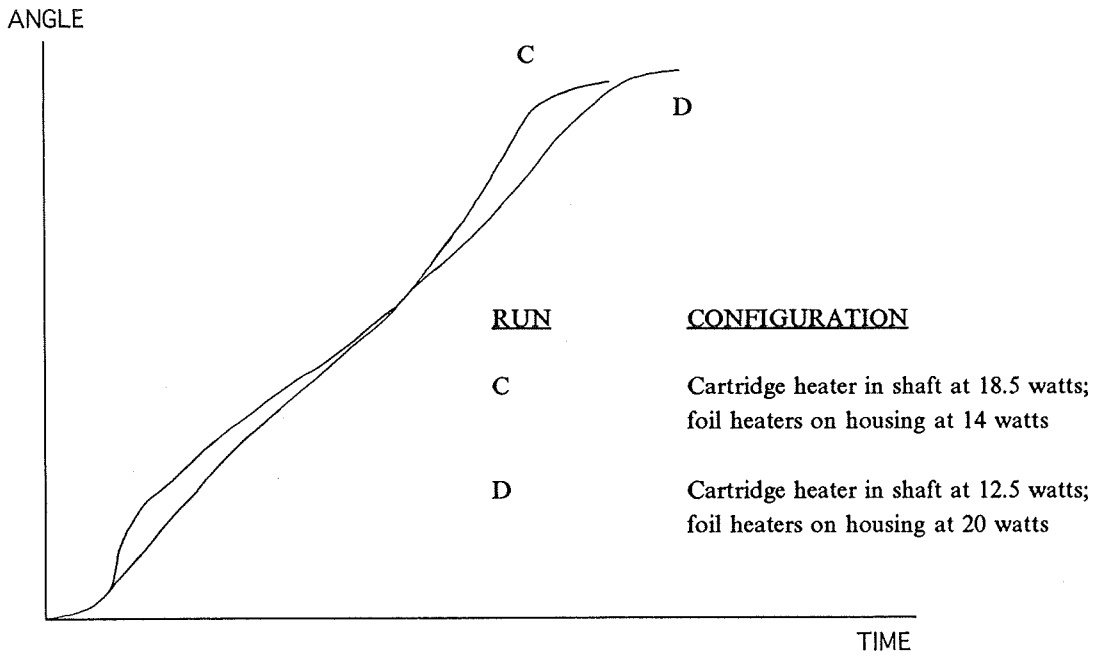
Figure 7. Comparison of Same Power Level, but Different Allocation

ANGLE

D

E

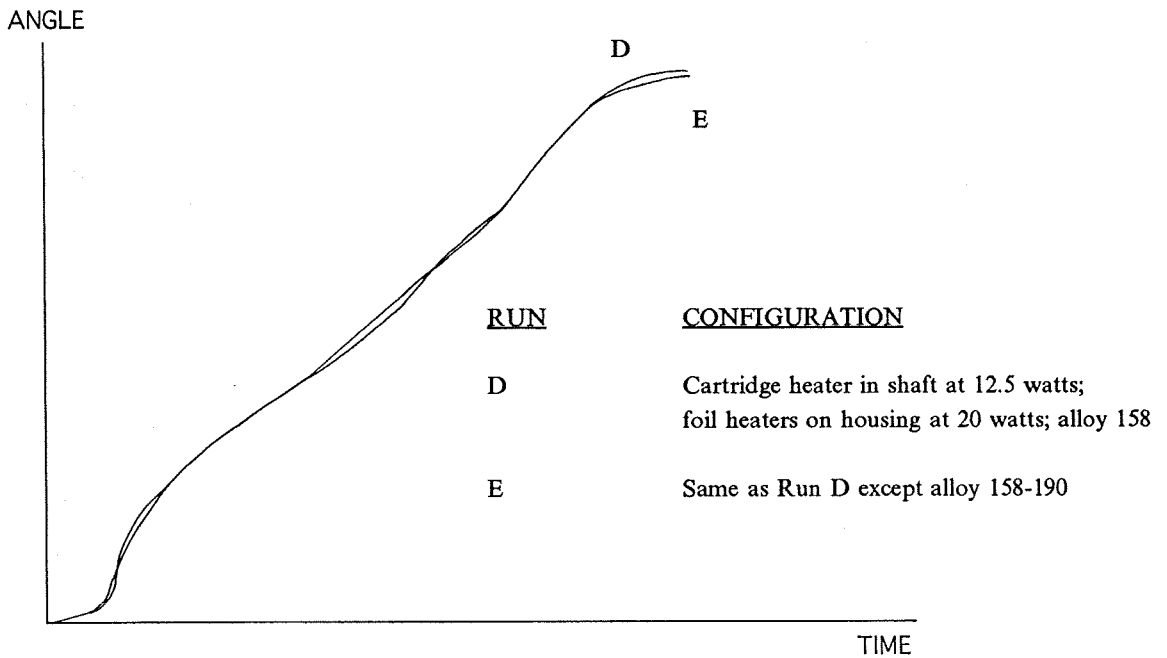| RUN	CONFIGURATION
D	Cartridge heater in shaft at 12.5 watts; foil heaters on housing at 20 watts; alloy 158
E	Same as Run D except alloy 158-190

TIME

Figure 8. Comparison of Eutectic vs. Non-Eutectic Alloy

266

C-4

434677

THE SOLAR ANOMALOUS AND MAGNETOSPHERIC

PARTICLE EXPLORER (SAMPEX)

YO-YO DESPIN AND SOLAR ARRAY DEPLOYMENT MECHANISM

James W. Kellogg[*]

ABSTRACT

The SAMPEX spacecraft, successfully launched in July of 1992, carried a yo-yo despin system and deployable solar arrays. The despin and solar array mechanisms formed an integral system as the yo-yo cables held the solar array release mechanism in place. The SAMPEX design philosophy was to minimize size and weight through the use of a predominantly single string system. The design challenge was to build a system in a limited space, which was reliable with minimal redundancy. This paper will cover the design and development of the SAMPEX yo-yo despin and solar array deployment mechanisms. The problems encountered during development and testing will also be discussed.

INTRODUCTION

The Solar, Anomalous and Magnetospheric Particle Explorer (SAMPEX) was the first in a series of Small Explorer class satellites (see photos, figures 1 and 2). SAMPEX, with its cluster of particle detectors, was launched into a near polar orbit aboard a Scout launch vehicle from Vandenberg Air Force Base on July 3, 1992. The SAMPEX spacecraft carried a yo-yo despin system and deployable solar arrays. The launch of SAMPEX and the successful operation of the yo-yo despin and solar array deployment culminated about two and a half years of development effort at NASA's Goddard Space Flight Center.

The SAMPEX yo-yo despin and solar array deployment mechanisms formed an integral system as the yo-yo cables held the solar array release mechanism in place. Tying the yo-yo and solar array operation together allowed one spacecraft command to both despin the spacecraft and deploy the solar arrays, thereby reducing the number of actuators, relays and wiring. Once the yo-yo cables unwrapped, the release mechanism was free to unlatch and deploy the solar arrays.

SAMPEX is a small spacecraft weighing 157 Kg (347 lb) with a launch size of .74 meters in diameter by 1.4 meters in height. The width after solar array deployment grew to over 2 meters with the arrays providing about 1.6 square meters of solar cell area. The solar arrays consist of two mirror image wings, each wing comprised of two hinged honeycomb panels. The array deployment was spring driven with viscous fluid damping.

The SAMPEX design philosophy was to minimize size and weight through the use of a predominantly single string system. The design challenge was to build a reliable system in a limited space with minimal redundancy that would function under extreme conditions. A major hurdle was to have the system operate at the worst case test temperature of -75°C.

This paper will discuss the design of the SAMPEX yo-yo despin and solar array deployment mechanisms. The problems encountered during testing and their resolutions will also be covered.

---
*NASA Goddard Space Flight Center, Greenbelt, MD

DESIGN REQUIREMENTS

Yo-yo Despin Mechanism

The SAMPEX spacecraft was launched atop a Scout launch vehicle which has a spin stabilized 4th stage. A system was needed to despin the spacecraft to a rate at which the attitude control system could operate. The Scout vehicle offers a standard yo-yo despin system but we chose to provide our own for two reasons: first, in the early design stages we were very weight critical and could save weight by designing our own despin system; second, because our solar arrays and lower antenna extend below the vehicle separation plane, a spinning separation was desired to minimize any tip-off that might occur during separation from the 4th stage. The design requirements of the yo-yo despin mechanism were:

> Despin the spacecraft after 4th stage separation to an absolute spin rate of less than 3 rpm from an initial spin rate of 141 ± 10 rpm.

> Yo-yo despin operation must initiate the Solar Array deployment.

> The total despin system mass must be less than 2.27 Kg (5 lb), the mass of the Scout provided despin system.

Solar Array Deployment Mechanism

The solar array design requirements were determined by a number of factors. Most important of these were; spacecraft power requirements, attitude control system constraints, instrument pointing requirements, launch vehicle interface, spacecraft dynamic and thermal environment, and spacecraft testing requirements.

The instrument pointing scheme and attitude control plan allowed the use of fixed solar arrays. The arrays were sized based on the spacecraft power requirement of approximately 100 watts, using fixed arrays with gallium arsenide cells. The design requirements, both given and derived, of the solar array deployment mechanism were:

> Provide 1.67 square meters (18 ft^2) of fixed solar array area.

> Withstand launch and spin loads while in the stowed position. For this launch the thrust loads were 10g, lateral loads were 4.5g with spin loading of 12g. There were also significant shock and random loads.

> Fit within .735 meter (30 inch) diameter envelope of the Scout .86 meter (34 inch) diameter heatshield in the stowed position.

> The fundamental mode of the solar array panels in the stowed position must be greater than 30Hz. This prevented coupling between the spacecraft and the solar arrays (the spacecraft had a requirement for first bending mode between 15Hz and 30Hz).

> The minimum natural frequency of deployed array must be greater than 2Hz to prevent coupling with the attitude control system.

> Withstand spacecraft spin rate up to 3 rpm during deployment.

> System must withstand its own induced dynamic loading during deployment.

> Deployment must be possible in a 1g environment for ease of testing.

> System must operate at temperatures from +30°C to −75°C.

SYSTEM DESIGN

The solar array system consists of 2 symmetric wings, each comprised of 2 solar array panels as shown in figure 3. The panels are attached to the spacecraft primary structure and to each other by spring loaded hinges with dampers to control the rate of deployment. Each wing was held in the stowed position by a primary release mechanism restrained by the yo-yo despin cables. The cables were wrapped twice around the spacecraft circumference and the despin weights at the end of the cables were held captive by electro-explosive pin pullers.

Firing the pin pullers released the yo-yo weights, allowing the cables to unwind and fly free, thereby despinning the spacecraft. The release levers, unrestrained by the yo-yo cables, slowly rotated out releasing the arrays. Upon release the panels were pushed out about a centimeter by kickoff springs and then slowly deployed to their operating position where they locked in place.

Yo-yo Despin System

The yo-yo despin mechanism consisted of a pair of weights and cables wrapped around the spacecraft and was required to despin the spacecraft to an absolute spin rate of less than 3 rpm after 4th stage separation. A cable guide (top view, figure 3) consisting of nine separate sections, formed a circular path on which the cables were wrapped. The total mass of the despin system including cables, weights, pin pullers, cable guides and other hardware was 1.8 Kg (3.9 lb).

The yo-yo weights were held in place by electro-explosive pin pullers. When the pin pullers fired the weights came free and the cables unwrapped. At the point where the cables completely unwrapped and reached a point radial to the spacecraft they flew free. Due to the conservation of angular momentum and kinetic energy the spacecraft was despun. Through the use of well defined equations, the system components were sized to despin to the desired rate.[1,2] The variables needed to size the yo-yo system and the values for the SAMPEX spacecraft were:

Spacecraft Moment of Inertia, I = 9.79 Kg-m^2 (7.23 sl-ft^2)
Spacecraft Radius, a = .38 m (1.24 ft)
Total Mass of Tip Weight, m = 154.15 grams
Length of Yo-yo Cable, l = 4.7 m (15.443 ft)
Lineal Density of Cable, p = 21.9 gm/m (.0147 lb/ft)
Spacecraft Initial Spin Rate, W_o = 141 RPM
Spacecraft Desired Final Spin Rate, W_f = 0 RPM
Release Angle of Cable Relative to Radial, Θ = 0°

Yo-yo despin systems have been used on many spacecraft and sounding rockets with great success and the basic design is quite straightforward. The SAMPEX design though, had several unique features. One, the spacecraft has a tank containing 8 Kg of isobutane fluid. There was great concern that this fluid would affect the ability to balance and despin the spacecraft accurately. Next, the yo-yo cables held the solar array deployment mechanism in place. Finally, due to the criticality of meeting the ±3 rpm final spin rate, a sensitivity analysis was performed to assure normal variations in the input variables would not significantly affect the despin accuracy.

The isobutane tank on the SAMPEX spacecraft is unbaffled and mounted directly on the spin axis. We had two main concerns about the tank: the first was that the fluid would affect the accuracy of the spacecraft moment of inertia measurement, a value needed for the despin analysis; the second was that the fluid would affect the accuracy of the despin itself. To deal

with the inertia measurement concern the fluid inertia was calculated as if it were a solid and found to be about .6% of the total spacecraft inertia. This number was added to the inertia tolerance numbers used in the sensitivity analysis. To determine the effect of the fluid on the despin itself two extreme cases were analyzed. The first case assumed the fluid would act as a solid and therefore not affect the despin at all. The second case assumed the fluid was completely decoupled from the spacecraft and after despin would slowly dissipate its momentum into the spacecraft. Fortunately, the difference between these two cases was only about half an rpm, well within the 3 rpm limit.

The fact that the yo-yo cables held in the solar array release also posed two main concerns; one, that the spring loaded release levers would push out during despin, altering the spacecraft radius; and two, that the arrays may begin deploying before despin was complete, possibly damaging the arrays or affecting the despin. As it turned out, once despin had begun, the tension in the cables was sufficient to hold the release levers in place. To prevent the arrays from deploying prematurely, dampers were added to the release mechanism to slow down the release time to several seconds, whereas the despin time was less than one second.

A sensitivity analysis was performed because it was very critical to meet the ±3 rpm despin target. This was mainly due to power limitations, as the solar arrays needed to be pointed at the sun before the spacecraft battery was depleted. At spin rates higher than 3 rpm this could not be guaranteed. At even higher rates the attitude control system would become unstable, unable to stabilize the spacecraft, and the mission would be lost. This analysis varied all input variables simultaneously to obtain worst case positive and negative final spin rate. The tolerances applied to all the input variables were:

Spacecraft Moment of Inertia, I: ±1%
Spacecraft Radius, a: ± 6.3 mm (.25 in)
Total Mass of Tip Weight, m: ± .1 gm
Effective Length of Cable, l: ± 12.7 mm (.5 in)
Lineal Density of Cable, p: ± .06 gm/m
Spacecraft Initial Spin Rate, W_o: ± 10 rpm
Release Angle of Cable Relative to Radial, Θ: ± 5°

The worst case spin rate using these conservative tolerances with no fluid effect came to 1.98 rpm. The worst case rate including the fluid correction (vary I ± 1.6%, decouple fluid during despin) came to 2.42 rpm, within the 3 rpm target.

Solar Array Panels

The 4 SAMPEX solar array panels are aluminum honeycomb, 1.15 meters tall by .37 meters wide (45.2 by 14.5 in.). The core is 9.5 mm (3/8 inch) thick with face sheets of .2 mm (.008 inch) 7075-T73 aluminum alloy. Hardpoints for hinge and component mounting are integrally bonded into the panels. The bare panels weigh about 1.4 Kg (3 lb) each. The panels with the gallium arsenide cells installed weigh just over 2.3 Kg (5 lb) each. The minimum mode of a panel, simply supported at the hinge locations is about 45 Hz.

Panel Hinges

The panel hinges (figure 4) act in pairs, upper and lower, to form a hinge line. All hinges use spherical bearings with a 6.35 mm (1/4 in) stainless steel shaft. The upper hinge bearings are fixed to the shaft to carry the thrust loading of the array. The lower hinge bearings are free to slide along the shaft to allow for misalignment and thermal expansion.

270

Each upper hinge has a potentiometer to provide position data while a fluid damper is incorporated into each lower hinge. The dampers dissipate the deployment energy and minimize impact loads at panel lock in. The stainless steel torsional springs are adjustable in 45° increments.

The main difference between the inboard and outboard hinges is the inboard hinges travel 90° while the outboard hinges travel 180° (see figure 5). This required a slightly different configuration and different torsional springs but otherwise the designs are identical.

To enable the deployed array to meet the 2 Hz minimum frequency requirement, each hinge includes a locking feature. This locking feature consists of a simple pin/detent design as shown in figure 6. Each hinge contains a spring loaded stainless steel pin. When the hinge reaches its fully deployed position, the pin slides into a detent, locking the array in the open position. The surface where the pin slides on the hinge is finished with teflon impregnated, hard anodize. The deployed panel frequency is over 2.6 Hz.

Rotary Viscous Damper

There are a total of 6 dampers on the solar array deployment mechanism, one on each solar array hinge line and one on each primary release mechanism. These dampers are D.E.B Manufacturing, Sesco Model 1080 Sub-Miniature Rotary Viscous Damper. The dampers are very small, 3.5 cm diameter by 5 cm long, and have the following properties:

    Damping Rate: 2.8 N-m/rad/sec (25 in-lb/rad/sec)
    Friction Torque: .03 N-m (4 oz-in)
    Maximum Torque Capacity: 11.3 N-m (100 in-lb)
    Weight: 85 grams
    Damping Fluid: McGhan Nusil CV-7300 silicone fluid

Primary Release Mechanism

There are two symmetric primary release mechanisms, one for each solar array wing. The primary release mechanisms held the arrays in the stowed position and were released by the deployment of the yo-yo cable. When the yo-yo cable unwrapped, the spring loaded release levers were free to move. Each release lever turns out thereby rotating a deployment shaft which is linked to an upper and lower release plunger. The rotary motion of the shaft is converted to linear motion at the release plungers. The plungers pull clear from their mating slots in the outboard hinge bodies and the arrays are free to deploy. The deployment shaft is tied by means of a linkage to a rotary damper to slow down the deployment and prevent any possibility of the arrays deploying before despin is complete. A primary release mechanism is shown in figure 8.

The entire arrangement is set up to prevent backdriving the system. The loads carried by the release plungers are not taken by the release mechanism drivetrain. The upper plunger carries only thrust direction loads and panel out of plane loads. The lower plunger carries only panel out of plane loads. These loads are reacted by the plunger housing which is mounted directly to the spacecraft primary structure. Loads in the direction of the plunger are taken by the opposing inboard hinge.

All of the release mechanism parts, except pins, bushings and fasteners, are made from 7075-T73 aluminum alloy. This alloy has high strength and low susceptibility to stress corrosion cracking. All areas of sliding friction are finished with teflon impregnated hard anodize. A light coating of Braycote 601 grease was also applied to these surfaces. The deployment shaft is mounted using teflon bushings.

Outboard Panel Release Mechanism

The outer panel release mechanism consists of a passive ball/detent arrangement as shown in figure 7. A hook with a steel ball is mounted to the outer panel opposite each hinge location. When the arrays are stowed, the ball fits into a detent in the fixed half of the inboard hinge assembly. Upon primary release, the inboard and outboard panels rotate together for about 30 degrees. At this point, due to the geometry of the system, the ball is clear of the detent and the outer panel is free to deploy, driven by its damped spring system.

Kick-Off Plungers

There are two spring loaded kick-off plungers on each inboard solar array panel. The plungers are located at each edge of the panel directly under the yo-yo cable location. The plungers serve a dual purpose. First, upon release of the primary release mechanism, the kick-off plungers provide an initial impetus to the arrays to help overcome any static friction. Second, the plungers act as standoffs between the outer solar array panel and the spacecraft structure to prevent the tensioned yo-yo cable from deflecting or damaging the panel.

Thermal Concerns

Our main thermal concern during design was that thermal expansion or contraction would causing binding and lockup the mechanism. This was accounted for in the hinge and release mechanism design. The upper hinges and upper panel release mechanisms carried the panel loads in the thrust direction. The lower hinges and release mechanisms were free to slide in the thrust direction allowing for thermal expansion. Similarly the hinged side of the panel (inboard hinge for the inboard panel) carried the lateral loads in the plane of the panel where the release mechanisms allow expansion and contraction in that direction.

We had two other thermal concerns. One was damper freezing at cold temperatures and the other was heat from the arrays conducting into the spacecraft through the inboard hinge. The solar arrays get very hot due to the solar flux and the power system shunts mounted to the back of the arrays. This heat could flow into the spacecraft and cause overheating under certain conditions. To solve this problem the hinge piece mounted to the inboard solar array was made from titanium; thus reducing heat flow from the arrays but allowing heat to reach the inboard dampers, preventing them from freezing. In the event of a cold deployment, heat flow from the spacecraft would protect the inboard dampers; however, the outboard dampers were at risk of freezing. A heater was applied to the outboard damper to prevent possible freezing.

SYSTEM TESTING

The testing of the SAMPEX spacecraft consisted of a combination of environmental, functional and measurement tests. Since the SAMPEX spacecraft was a completely new design, vigorous testing was required to qualify it for flight. To accomplish much of the testing, a mechanical Engineering Test Unit (ETU) of the spacecraft was built. The ETU was structurally and mechanically identical to the SAMPEX flight unit. All instruments, electronics and other components were represented by mass

models. The tests performed on the SAMPEX ETU were:

Yo-yo despin mechanism deployment test, ambient and vacuum
Deployment testing of the solar array, ambient and thermal vacuum
Vibration testing
Spin balance
Mass properties measurement (Spin axis moment of inertia only)

The tests performed on the SAMPEX flight unit were:

Deployment testing of the solar array, ambient and thermal vacuum
Vibration testing
Spin balance
Mass properties measurement
Acoustics testing

Other "non-mechanical" tests are not enumerated here. Despin testing was not performed on the flight unit as it was deemed too risky.

Despin Testing

Our first set of despin tests was performed at NASA's Wallops Flight Facility in October 1991. The tests were performed outdoors since the test required an area 10.5 meters in diameter and we could not find a suitable indoor facility. At that time our predicted initial spin rate was 162 rpm, it was later revised to 141 rpm when the true spacecraft mass properties were known. We initially wanted to run 3 tests, one nominal spin rate, one high spin rate, and one low spin rate. Due to an anomaly the first test was repeated. Each test was recorded on video tape and high speed film. We were initially wary of allowing the arrays to deploy after despin because they could be damaged if the despin did not function properly. After several runs, the system appeared to be functioning properly and the arrays were released on the final test. The result of each deployment test were as follows:

Test 1: 162 RPM, Arrays Locked (not deployable)
Result: Spin table failed to declutch, and one cable failed to release due to out of spec ball end on cable.

Test 2: 162 RPM, Arrays Locked
Result: Test appeared successful but only despun to about 4.6 RPM

Test 3: 192 RPM, Arrays Locked
Result: Test appeared successful but only despun to about 8 RPM

Test 4: 142 RPM, Arrays Unlocked
Result: Test successful, despun to about 2.3 RPM, arrays deployed successfully

An anomaly occurred in Test 1 where the swaged ball on one cable failed to release from the cable retainer. The spin table also failed to declutch on this test. We originally thought that the table malfunction caused the failure by not allowing the cable to reach the radial (release) position. Upon review of the high speed film however, it was apparent that the cable did reach the radial position and should have released. Inspection of the hardware found that the cable ball was caught in its release slot because the ball was .1 mm oversize and the slot was .08 mm too small. Due to the small nominal clearance (.15 mm), these out of specification conditions caused interference and the ball wedged in the slot. To resolve this problem the slots were opened up to provide 1.7 mm

of nominal clearance, all hardware was reinspected to assure compliance with the drawings, and an analysis was performed to assure no interference could occur due to thermal contraction or expansion. Only one of the despin tests performed met the ± 3 rpm despin requirement. We attributed this to air resistance since the lower the initial rate, the closer the despin was to zero. To assure the accuracy of the system and checkout the fixes made to correct the release problem, we decided to run another despin test in vacuum.

The final despin test was performed in a 16 meter diameter vacuum chamber at NASA's Langley Research Center in April 1992. This test was performed using the spacecraft ETU with the flight cable retainers and an improved spin table. This time the spacecraft despun to exactly zero rpm with no detectable residual rate.

Solar Array Testing

The solar array deployment mechanism was tested in ambient conditions and in thermal vacuum at hot, nominal and cold conditions. The system functioned flawlessly in all cases except extreme cold.

During our initial ETU solar array testing the system functioned properly at hot and nominal temperatures but the outboard panels failed to deploy at cold temperature (-65°C). Upon warming of the thermal vacuum chamber, the arrays deployed. In this test the outboard arrays failed to deploy. Upon investigation, it was discovered that the damper fluid freezes between -41°C and -42°C.

To alleviate the freezing problem, 1 watt heaters were applied to the outboard dampers. This modification incorporated a limit switch to turn off the heaters when the arrays started to deploy. The inboard dampers being thermally coupled to the spacecraft did not have a freezing problem.

The system was tested a second time with the heaters installed and again functioned properly at nominal temperatures. At cold temperature (-75°C) however, the outboard arrays deployed to over 90% of their full open position then stalled. The dampers, even with heaters, were running about -33°C before deployment and the temperature dropped rapidly (below -40°C before movement stopped) when heater power was cut off at initial deployment. The arrays deploy very slowly at these temperatures, due to the high viscosity of the damping fluid. It was assumed (incorrectly) that the failure was due to the damper fluid freezing before the deployment was complete. Upon warming the chamber, the arrays fully deployed when the damper temperature read -38°C. The arrays deploying when warmed made trouble shooting difficult because the arrays could not be inspected in the failed configuration.

To solve the problems of the second test, three fixes were employed. Thermal isolation of the damper was increased by adding a non-conductive coupling to prevent heat loss through the damper shaft. The spring torsion in the hinge was increased to provide a faster deployment rate, thereby minimizing the effect of the temperature drop. The heater power was increased to 2 watts to provide a higher initial temperature in the damper. The increase in heater power was employed on only one solar array damper to determine if the other fixes would be sufficient to solve the problem.

After these fixes were employed a third ETU test was run at cold temperature (-75°C). The damper with the 2 watt heater was running about -19°C, the damper with the 1 watt heater was running about -41°C. We predicted that the 2 watt side would open because we had successful deployments below -19°C and that the 1 watt side would fail because it had failed the previous test at a warmer temperature.

274

To our surprise the 1 watt side opened, while the 2 watt side opened about 90% then stalled. After verifying that the 2 watt heater was on the correct side the chamber was brought to ambient. Again the array deployed fully upon warming.

Upon inspection of the mechanisms we discovered a problem with the 2 watt side that was not evident on the 1 watt side. On the upper outboard hinge, the rotating leg of the torsion spring was rubbing on the fixed hinge, causing a noticeable amount of drag that was not evident on the 1 watt side. This occurred because the torsion spring was catching in a gap between the spring mandrel and the hinge (see figure 9). The condition also put the torsion spring under a bending force which caused some galling between the coils of the spring. Apparently the spring would catch in the gap intermittently. The drag that occurred was not severe enough to prevent deployment at warmer temperatures. Apparently the aluminum hinge would contract at colder temperatures, aggravating the problem and preventing deployment. To fix this problem the spring mandrel was modified to eliminate the gap.

Based on our testing to this point we selected a flight unit configuration to minimize changes from the latest ETU test. This configuration consisted of 2 watt heaters on both outboard dampers, the outboard hinge spring torsion was increased, the dampers were thermally isolated, and the mandrels were modified to eliminate any gap.

The flight unit was tested at -50°C and deployed successfully. Unfortunately the cold temperature was limited by the cold limit on the SAMPEX instruments and the mechanism was not technically qualified to the worst case temperature of -75°C. A fourth ETU solar array test was then run at -75°C with the configuration identical to the flight unit. The arrays deployed very slowly at this temperature, but after sufficient hand wringing they finally deployed to the full open position and locked in place.

CONCLUSION

The SAMPEX launch took place on July 3, 1992 at 7:19 AM Pacific time. About ten minutes after liftoff the spacecraft separated from the Scout 4th stage with the despin command set to occur 12 seconds later. Although we had to wait four and half agonizing hours before the first ground contact confirmed the successful operation of our system.

ACKNOWLEDGEMENTS

REFERENCES

1. Fedor, J. V., Theory and Design Curves for a Yo-yo De-spin Mechanism for Satellites (NASA TN D-708, August 1961).

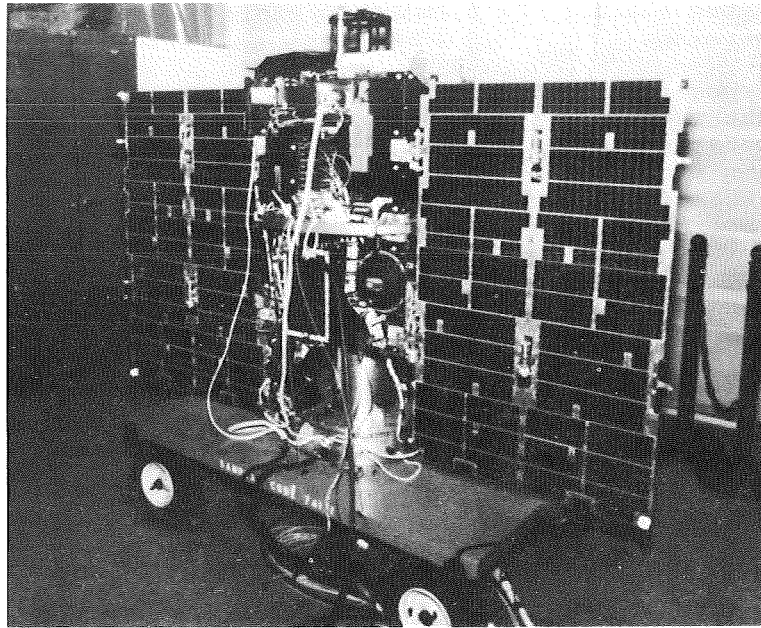2. Flatley, Tom, A Yo-yo Despin Analysis (NASA GSFC X-732-70-476, October 1970).

Figure 1:   SAMPEX During Integration at Goddard
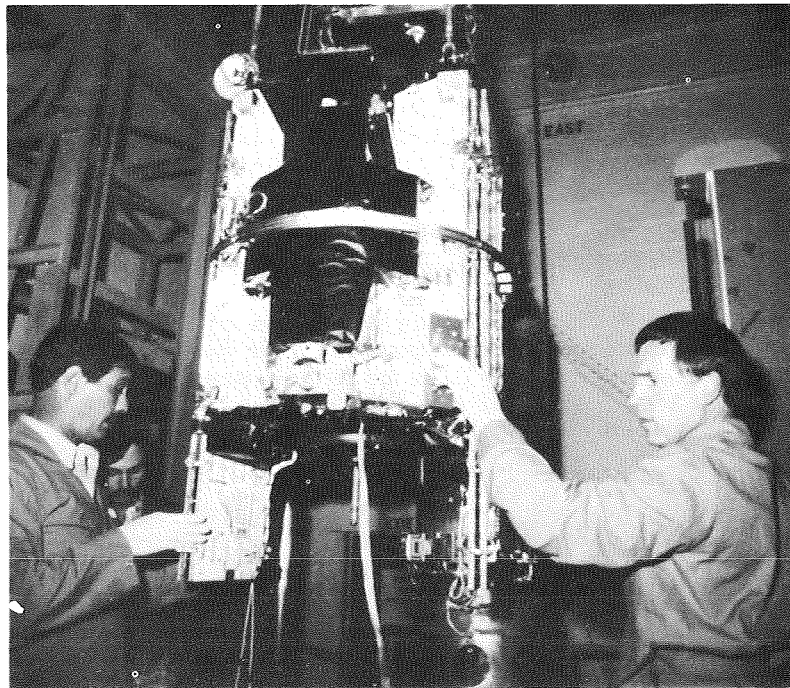   Space Flight Center, Greenbelt, MD

Figure 2:   SAMPEX Prior to Fourth Stage Mating in
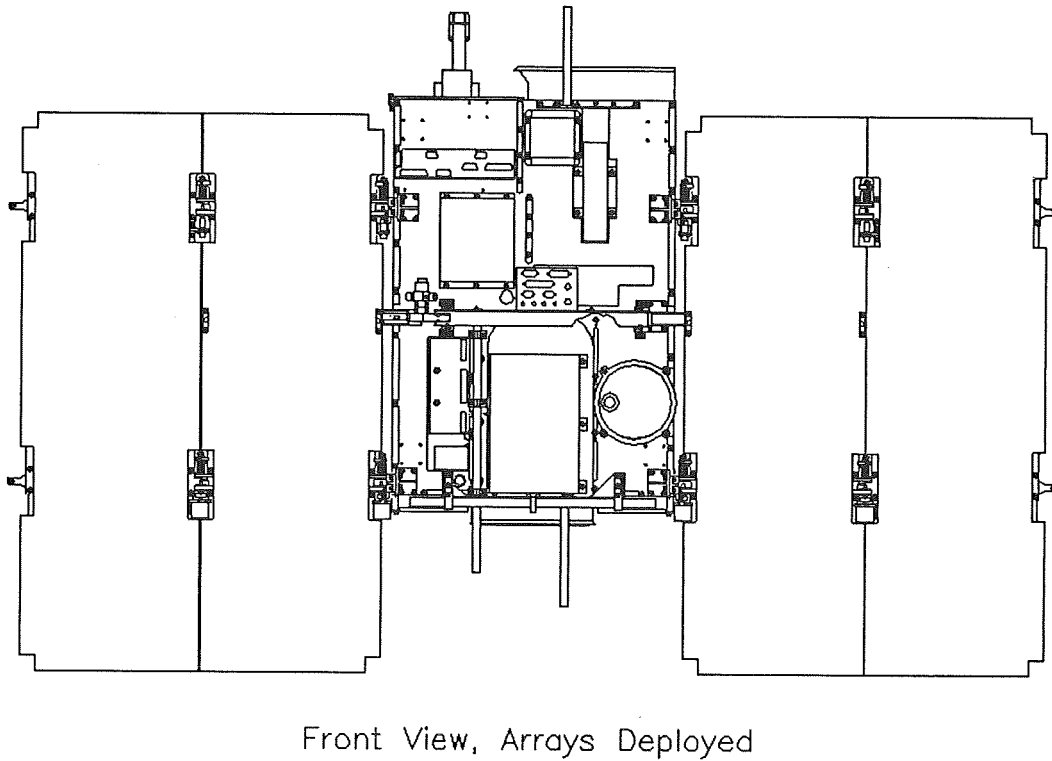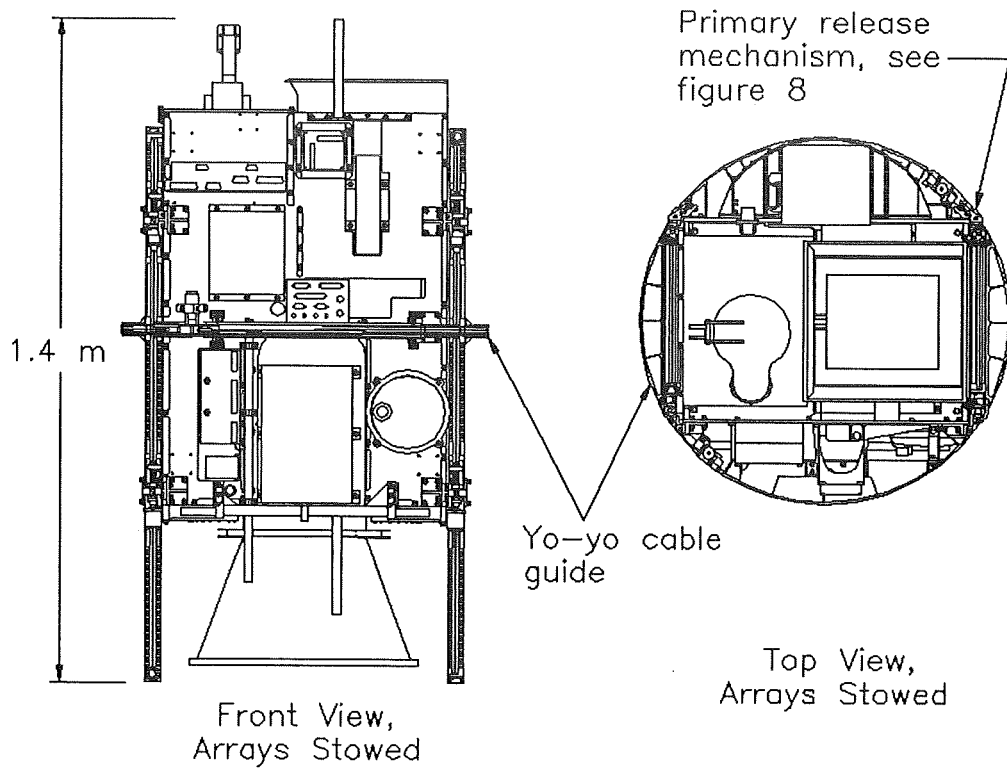   Scout DBF, Vandenburg Air Force Base

Primary release
mechanism, see
figure 8

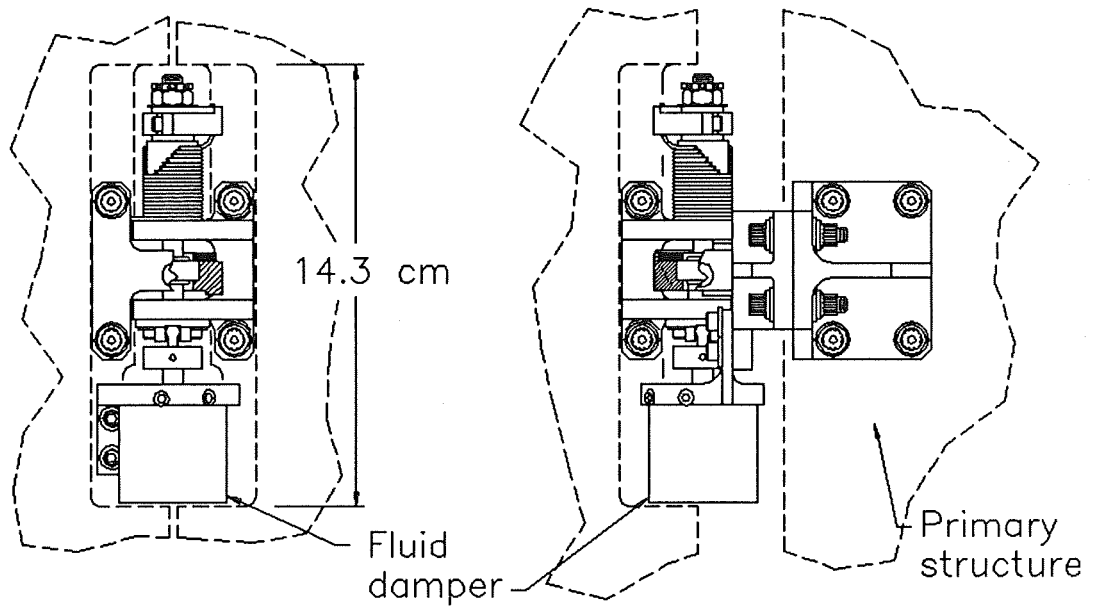1.4 m

Yo-yo cable
guide

Front View,
Arrays Stowed

Top View,
Arrays Stowed

Front View, Arrays Deployed

Figure 3: SAMPEX Spacecraft
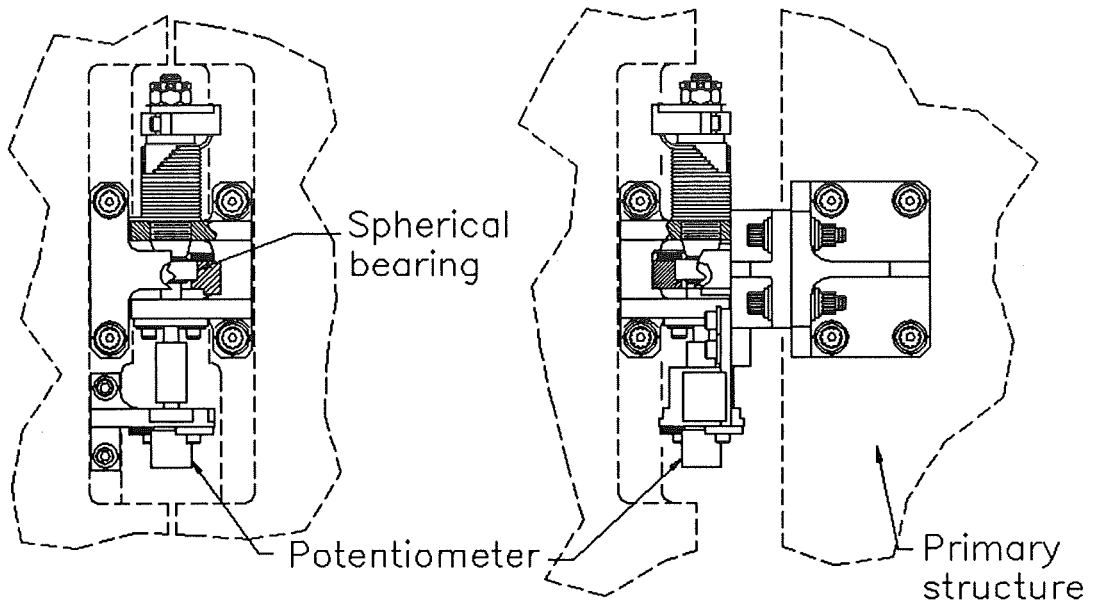
Figure 4: Solar Array Hinges

(a)

See detail,
figure 7

(b)

(c)

See detail,
figure 7

(d)

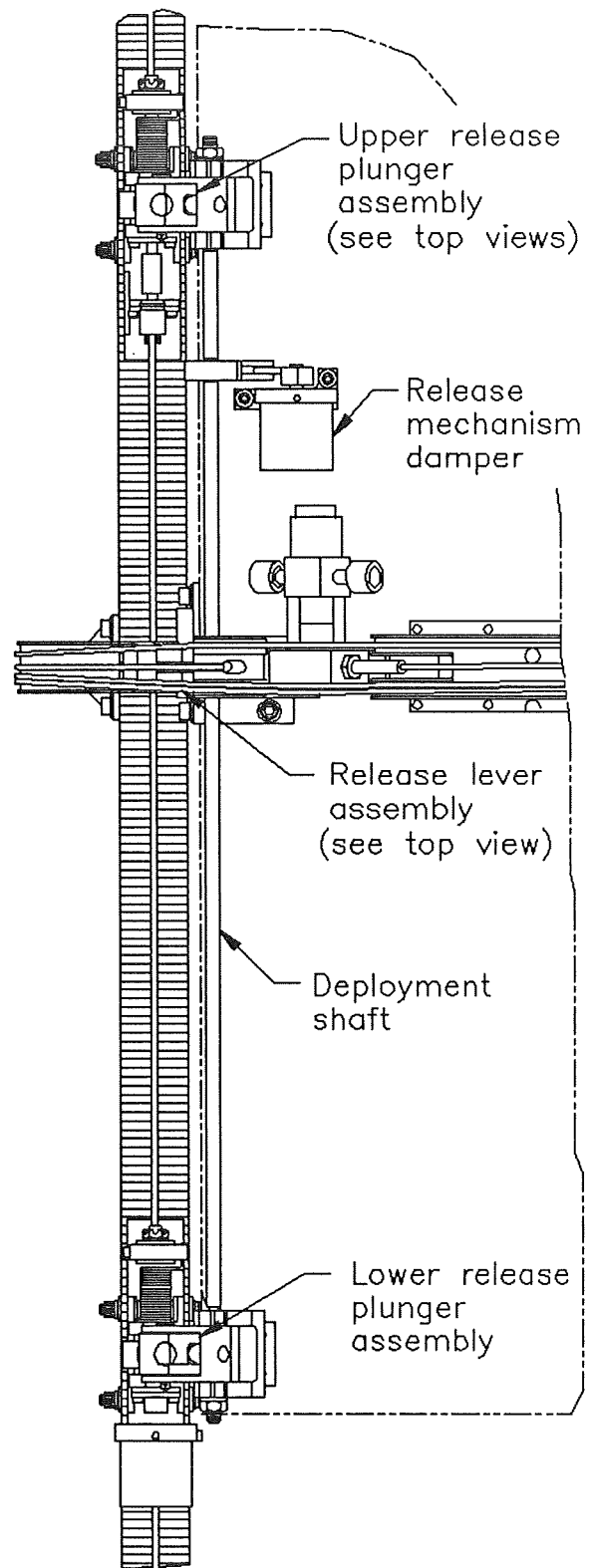(e)

(f)

See detail,
figure 6
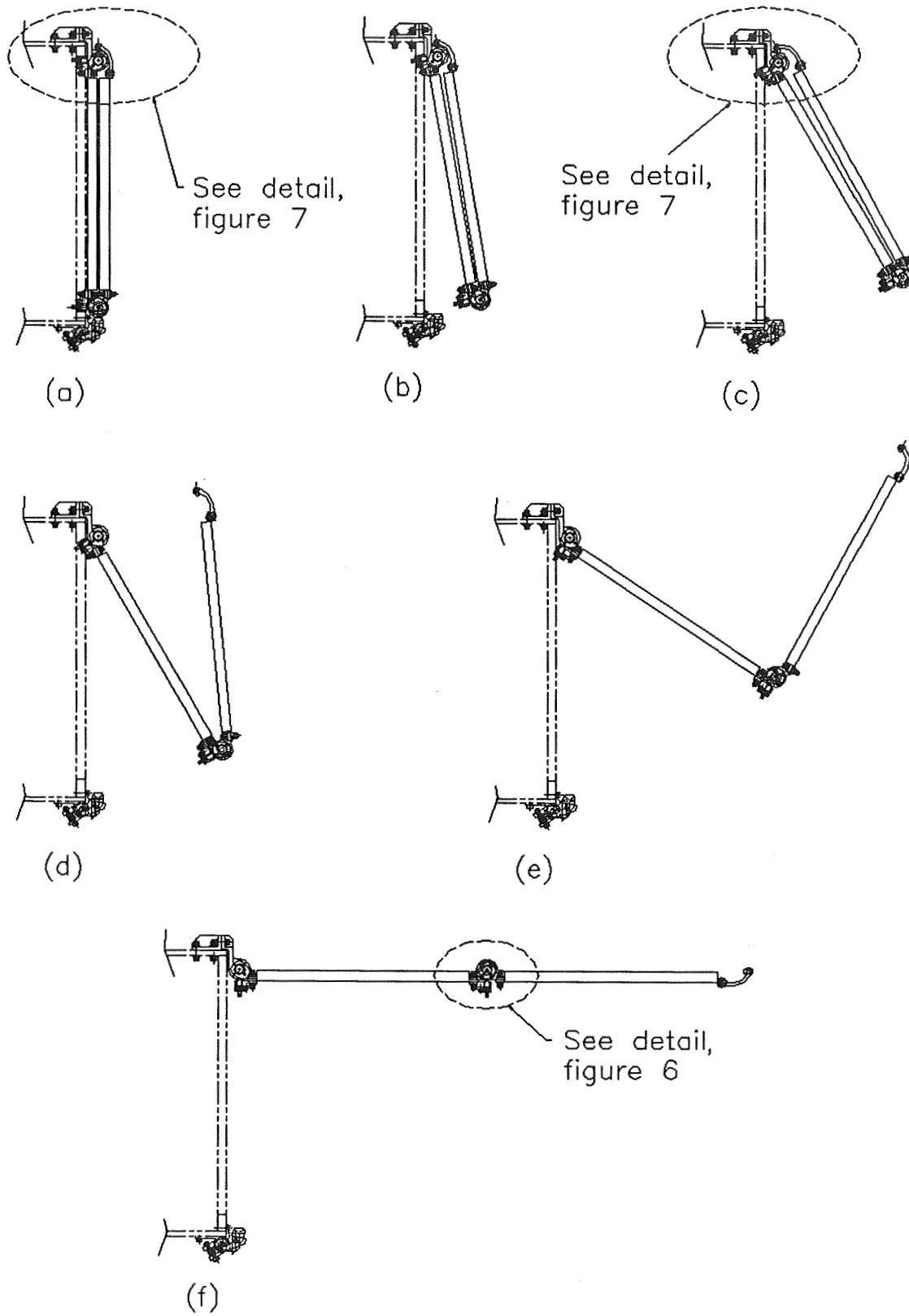
Figure 5: Solar Array Deployment Sequence

279

Locking pin
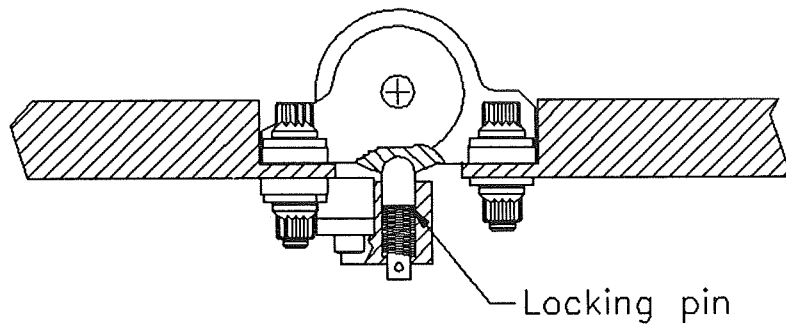
Figure 6: Outboard Hinge Locking Mechanism

Ball in detent

Ball clear of detent

Inboard hinge lock

Stowed Position

Free Position
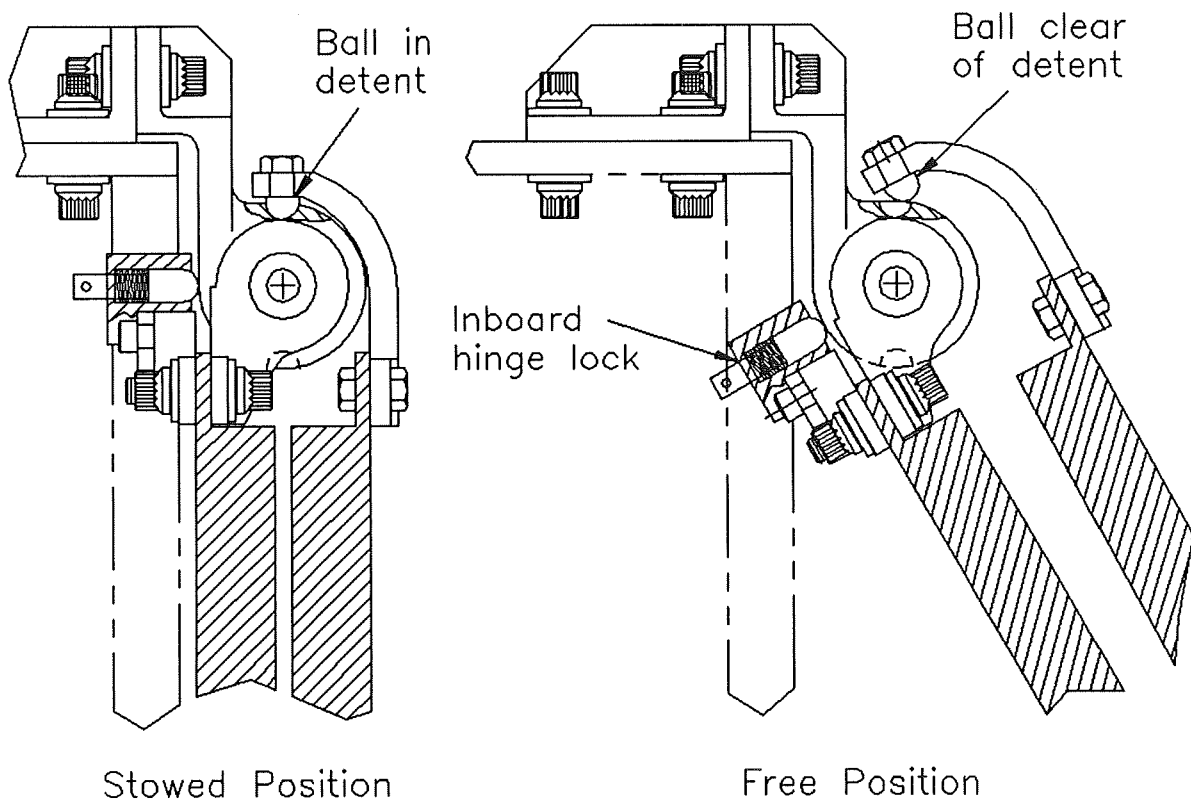
Figure 7: Outboard Panel Release Mechanism

Release
plunger

Plunger Assembly, Stowed
Top View

Release
plunger

Plunger Assembly, Released
Top View

Release lever

Deployment
shaft

Released
position

Yo—yo cable

Release Lever Assembly
Top View

Upper release
plunger
assembly
(see top views)

Release
mechanism
damper

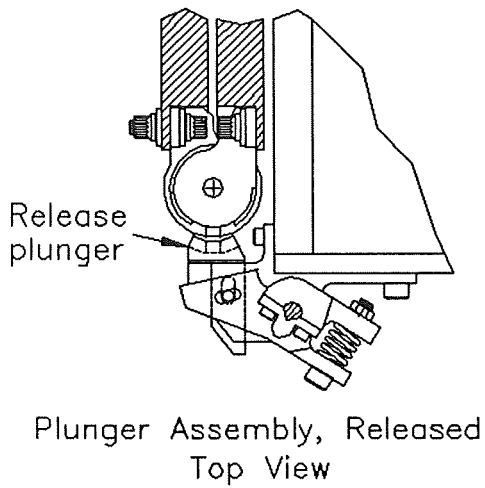Release lever
assembly
(see top view)

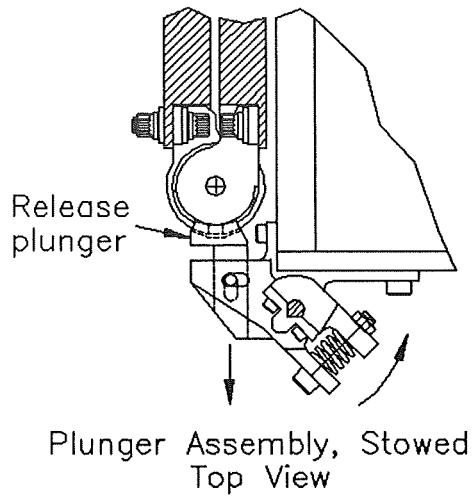Deployment
shaft

Lower release
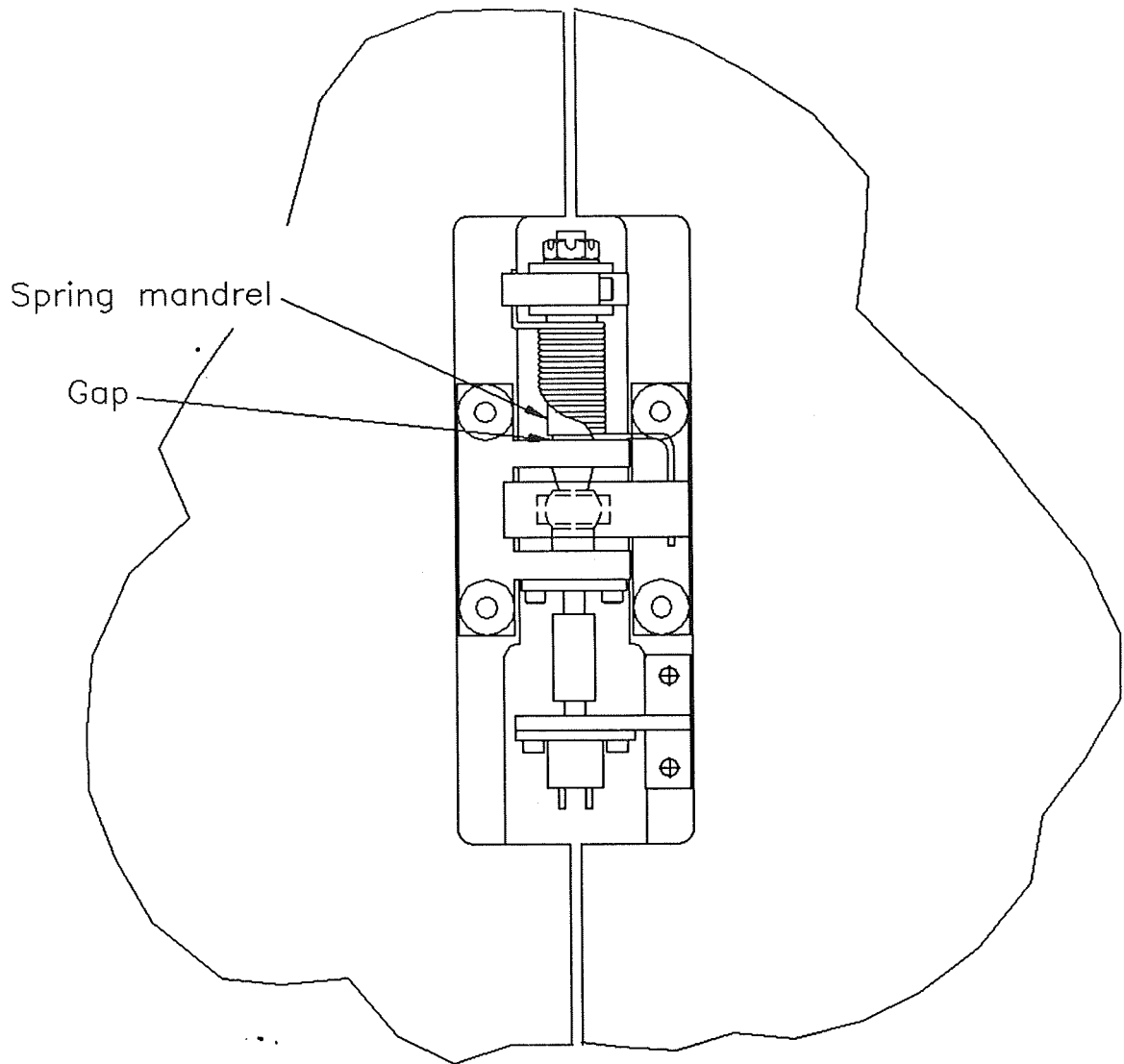plunger
assembly
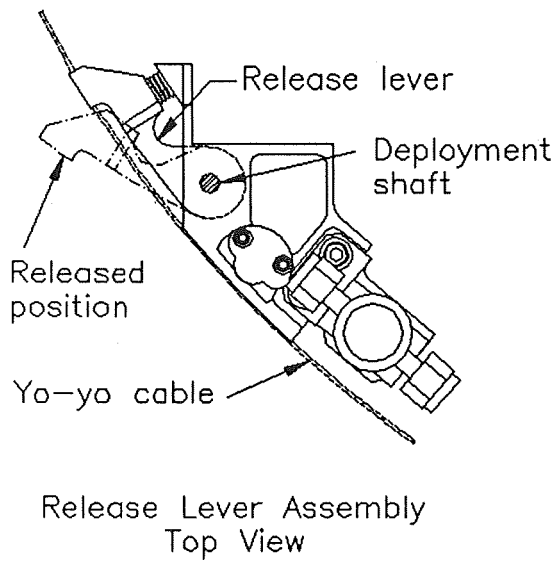
Figure 8: Primary Release Mechanism

Figure 9: Upper Hinge Problem

LOCK-UP FAILURE OF A FOUR-BAR LINKAGE DEPLOYMENT MECHANISM

43468/

Michael Zinn*

ABSTRACT

A successful failure investigation of a four-bar linkage deployment mechanism has been performed. Possible failure causes such as the mismatch of material coefficient of thermal expansion (CTE), excessive hinge friction, limit switch interference, and thermal-gradient-induced resistive preload were investigated and are discussed. The final conclusions and corrective actions taken are described. Finally, valuable lessons learned during the investigation are discussed.

INTRODUCTION

Four-bar linkages have been used extensively in aerospace mechanisms to transmit torque, motion, and power, and/or to transform one type of motion or force to another (e.g. linear to rotary). The popularity of four-bar mechanisms among aerospace mechanism designers is due to their unique characteristics including (1) the rapid increase in their effective gear ratio (mechanical advantage) as the linkage approaches the top-dead-center toggle position and (2) the ability of a four-bar linkage to provide positive lock-up at the end of travel without the increased resistive torque associated with latching mechanisms.

The work described in this paper was performed in response to a functional failure of a panel deployment system which employs a set of eight four-bar linkages to transmit torque and to provide positive lock-up at the end-of-travel (Figures 1 and 2). During a gravity off-loaded cold thermal-vacuum deployment test, three of the four outboard hinge four-bar linkages failed to lock-up into their over-center position after the panel had fully deployed. Review of high-speed film showed that the input (drive) links of the three outboard four-bar linkages that had failed had come within approximately 5 to 10 degrees of their top-dead-center positions (see Figure 3). After the test, as the chamber

---

* Lockheed Missiles and Space Company, Inc., Sunnyvale, CA

temperature was increased, each of the four-bar mechanisms that had failed to lock-up at -100°C moved into their over-center positions by the time the chamber temperature had reached 0°C - 5°C. The four inboard hinge four-bar linkages, which had functioned properly during the cold thermal-vacuum deployment test and are of a different design than the outboard linkages, are not discussed in this paper.

MECHANISM DESCRIPTION

The panel deployment system is made up of a set of four spring-driven four-bar linkages that were designed to provide a redundant deployment system for a two-panel configuration (see Figure 1). There are two inboard and two outboard hinges. Each hinge has two four-bar linkage mechanisms which provide redundant drive torque sources. The individual spring-driven four-bar mechanism of the outboard hinge consists of a helical torsion spring, a monoball main hinge bearing, and a four-bar linkage. The outboard four-bar linkage is formed by a drive (input) link, a turnbuckle link, and the structural frame of the inboard and outboard panels (see Figure 2). The driving or input torque of the torsion spring is applied to the input link and is transmitted through the linkage to the main (output) hinge. The output torque about the main hinge causes the outboard panel to rotate 180° with respect to the inboard panel, from its stowed position to its deployed position.

The four-bar linkage is designed so that it reaches its top-dead-center position when the outboard panel has fully rotated (deployed) from the inboard panel. As the linkage moves beyond it top-dead-center position the input link hits the input link stop which arrests the deployment. The high mechanical advantage of the input link just beyond the top-dead-center position prevents any back-driving of the input link. In addition, there is a hard stop between the inboard and outboard panels that (1) helps absorb the lock-up load forces and (2) provides a bearing surface between the inboard and outboard panels through which a "locking" preload is applied to eliminate any backlash in the joint after deployment (see Figure 2).

During assembly, the inboard and outboard panels are aligned to each other (coplanar in their deployed configuration) by adjusting the hard stop between the inboard and outboard panels. The next adjustment involves setting the over-center distance of the four-bar linkage (see Figure 4). This adjustment is performed by adjusting the input link stop. The over-center distance is set nominally to 0.762 mm

(0.030 inch). Finally, the four-bar linkage turnbuckle is adjusted such that the mechanism preloads the outboard panel into the inboard panel in order to eliminate hinge backlash while still being able to travel over-center and lock-up.

INITIAL FAILURE INVESTIGATION

Initially, the failure investigation focused on the most probable causes which included (1) possible mismatch of the linkage material's coefficient of thermal expansion which could cause binding in the mechanism pivots, (2) possible excessive hinge friction torque of a monoball bearing which had caused a deployment failure in a previous cold deployment test, or (3) excessive actuation force produced from mechanically actuated limit switches which are used to verify four-bar over-center motion.

CTE Mismatch

An initial review of the linkage design revealed that the material of the linkage pins was different than that of the linkage itself. Because of the difference in their CTEs, suspicion arose that interference between the linkage and the pivot pins had caused the mechanism to seize. However, the possible mismatch of the linkage material's CTE was eliminated as a failure cause after a review of the design showed that the clearance between the linkage pins and links was more than sufficient for the temperature range of the test. The analysis included the differential expansion of the pins and links due to their different material CTE, worst-case cold bulk temperature change and temperature gradients between the pin and link. In addition, analysis of the friction torque that would be present if the pin-link interference did occur, showed that the maximum possible level of linkage hinge friction (0.2 N-m) was well below the drive capabilities of the input torsion spring after having been transmitted through the four-bar linkage (>5 N-m).

285

Excessive Hinge Friction

In an earlier deployment test of the panel, the main hinge monoball bearing had caused a deployment failure of the panel. Very high monoball friction, caused by the differential growth of the steel monoball and its aluminum housing, had caused the deployment motion of the panel to stop (at approximately 120°) before it reached its deployed position (180°) during cold temperature deployment. As a result, the monoball bearing was immediately suspected as the cause of the recent failure. However, after reviewing high-speed camera data of the deployment, the possibility that excessive monoball bearing torque had caused the failure was eliminated. The camera data clearly showed that the panel deployment motion proceeded in a normal fashion and within the expected deployment time, which proved that the hinge friction torque was no greater than in prior successful deployments. In addition, the monoball bearing design flaw[1] that had caused the previous deployment failure had since been corrected.

Limit Switch Resistive Force

To verify four-bar mechanism lock-up, a limit switch had been incorporated into the mechanism design. When the linkage moves over-center, the input link actuates the spring-loaded limit switch (see Figure 4). The resistive spring force applied to the input link from the limit switch is not insignificant and, as a result, during assembly, special care is taken to properly adjust the limit switch so that it does not interfere with the over-center motion of the linkage. Because the panel deployment failure involved the failure of the four-bar linkage to move over-center, a possible misadjustment of the limit switches was suspected as the cause of the failure. However, the limit switch actuation force was disproved as the cause of the failure when an additional cold vacuum deployment test, with the limit switches adjusted so as to minimize the limit switch resistive spring force, also failed. In addition, the limit switch resistive spring torque (<0.1 N), measured after the limit switches were readjusted, was much less than the measured deployment spring force[2] (>3.0 N) and, therefore, would

---

[1] Epoxy that was applied to the threads on the exterior surface of the bearing outer race acted as a shim when exposed to cold thermal vacuum testing and caused the bearing to bind.

[2] The limit switch resistive torque and the available spring torque were measured about the input link pivot axis.

not be large enough to prevent over-center motion of the four-bar linkage.

DETAILED FAILURE INVESTIGATION

With the most probable failure causes eliminated, the investigation focused on the conditions of this test that might make it different from previous successful cold thermal vacuum tests. The investigation focused on what mechanism assembly adjustments were performed and how the cold thermal vacuum environment could affect the mechanism's behavior.

Linkage Kinematics

During assembly, the linkage is adjusted such that the hinge line of the panel is preloaded against a hard stop in its deployed position to prevent relative motion of the inboard and outboard panels (see Figure 4). As the linkage approaches the top-dead-center position, the hard stop on the outboard panel is preloaded against the end of the inboard panel by the spring force. The preload reaches a maximum at the linkage top-dead-center position. As the four-bar continues past top-dead-center to its final over-center position, the outboard panel backs away from the inboard panel because of the rocker-crank kinematic property of the four-bar mechanism [1], and the preload in the hard stop is reduced (see Figures 5 and 6). It is the reduced preload in the over-center position that prevents relative motion between the inboard and outboard panels. The assembly adjustment instructions require that the preload be adjusted such the outboard panel is securely preloaded against the inboard panel while still allowing the input link to be driven over-center by the deployment spring. As a result, the level of the preload force is not measured and is set purely by feel.

Effect of Linkage Thermal Gradients

During the cold thermal-vacuum test, the orientation of the cold wall in the thermal vacuum chamber creates a non-uniform temperature distribution in the four-bar mechanism links and surrounding hardware. The total gradient across the mechanism was approximately 10°C which was measured during the cold deployment test. The change in the four-bar geometry, brought on by the differential thermal expansion of the mechanism, modified the kinematic properties of the linkage such that the outboard hard-stop

prematurely preloaded against the inboard panel (see Figure 7). As a result, an extremely high resistive torque develops as the four-bar mechanism approaches top-dead-center. The magnitude of this resistive torque is dependent upon the temperature gradient created as well as the stop stiffness of the four-bar mechanism. The stop stiffness depends on the instantaneous geometry of the linkage, the local stiffness of the mechanism links and pins, and the stiffness of the preload hard stop (see Figure 8). Note that the relative change in link lengths due to their differential thermal expansion is very small (0.011 mm for a 10° C gradient) while the corresponding change in resistive torque can be very high (> 30 N-m).

The resistive torque developed by the hard stop preload for various levels of linkage temperature gradient and the available input spring torque are shown in Figure 9. The torques in Figure 9 are measured about the main hinge of the panel and are plotted vs the input link angle as measured from the top-dead-center position. The torques are plotted vs the input link angle so as to increase the resolution of the torque calculations very close to the top-dead-center position. Note that the resistive torques developed are a direct result of the temperature gradient *across* the linkage, not as a result of a gross temperature change of the linkage which would not cause a change in the kinematic properties of the linkage. Figure 9 clearly shows that a temperature gradient of 10°C or greater could create a resistive torque which exceeds the available torque of the input spring.

Effect of Linkage Adjustments

During assembly, the linkage is adjusted such that the hinge line of the panel is preloaded against a hard stop in its deployed position to prevent relative motion of the inboard and outboard panels. The turnbuckle link is adjusted such that the spring force of the input link is capable of pushing the input link to its over-center position while maintaining the preload of the outboard to inboard panels. The preload developed is at a maximum at the top-dead-center position. As the linkage travels to its over-center position, the outboard hard stop backs away from the inboard panel and relaxes the preload. The amount of relaxation depends upon the over-center distance adjustment which is determined by the adjustment of the link stop (see Figure 2).

Because of the difficulty of taking measurements at the exact top-dead-center position of the linkage, the adjustments described below are performed as the linkage is in its over-center position. As a result,

the measurable adjustment parameters include the linkage over-center distance and the gap between the hard stop on the outboard panel and inboard panel while the linkage is in its over-center position (see Figure 4). Both parameters affect the maximum level of hard stop preload which occurs at the linkage top-dead-center position.

The resistive torque developed by the hard-stop preload for various levels of hard stop gap and linkage over-center distance are shown in Figures 10 and 11, respectively. Figure 10 shows that as the hard stop gap is decreased, as measured in the over-center position, the maximum resistive torque developed at the top-dead-center position increases. In addition, Figure 11 shows that as the over-center distance is increased, as measured in the over-center position, the maximum resistive torque developed at the top-dead-center position increases. In fact, for a measured hard stop gap of less than 0.0025 mm (0.0001 inch) or for a measured over-center distance of greater than 1.143 mm (0.045 inch) the resistive torque exceeds the available torque of the input spring.

Affect on Torque Margin and Mechanism Function

Additionally, factors such as linkage-to-pin backlash and pin friction torques significantly contribute to the resistive torque as the linkage approaches top-dead-center. The sum of these resistive torques, created by and/or significantly increased by the effects of differential thermal expansion, can exceed the available torque from the torsion input spring and cause a negative torque margin[3] condition which could prevent over-center lock-up of the four-bar linkage. Figure 12 shows the minimum torque margin for various levels of linkage temperature gradient and hard stop gap. The over-center distance was set at its nominal 0.76 mm (0.03 inch) distance for Figure 12. Torque margin calculations of less than 0% indicate that the linkage will fail to move over-center and lock-up.

During the panel deployment lock-up failure, the total gradient across the mechanism was measured at approximately 10°C. The hard stop gap distance, measured in the over-center position, ranged from 0.000 mm (0.000 inch) to 0.0254 mm (0.001 inch) while the over-center distance was set precisely at 0.760 mm (0.030 inch). Figure 12

---

[3] Torque margin is defined as the quotient of the quasi-static available torque to resistive torque minus 1.0.

clearly shows that the conditions described above would cause the panel deployment mechanism to fail.

CORRECTIVE ACTIONS AND SUBSEQUENT TESTING

In order to eliminate the cause of the failure, the preload requirement between the inboard and outboard panels had to be relaxed. In fact, discussions with experienced technicians revealed that during previous testing the linkage was adjusted with some hinge line backlash. The technicians had observed that the mechanism performed correctly when some backlash in the hinge was allowed. These previous units had all successfully passed their thermal vacuum deployment tests. This would explain why previous cold thermal vacuum tests of an identical mechanism were successful. However, relaxing or eliminating this requirement created additional concerns about backlash along the hinge line of the panel and how this might possibly interact with other system elements. The final solution involved modifying the four-bar mechanism adjustment and preload procedure such as to minimize the panel hinge line backlash while guaranteeing positive over-center lock-up for the worst-case thermal environment.

The new procedure specified that the turnbuckle linkage would be adjusted such that a 0.254 mm (0.01 inch) gap would exist between the hard stop of the outboard and inboard panels. In addition, the over-center distance of the linkage is to be adjusted to 0.760 mm (0.030 inch) or less. These adjustments would guarantee positive over-center lock-up for a worst-case temperature gradient of 55°C (100°F). Following the implementation of the modifications discussed above, there were three subsequent deployment tests, two in a cold vacuum and one at ambient. All three tests were 100% successful.

CONCLUSION

A successful failure investigation of a four-bar linkage deployment mechanism was performed. Possible failure causes such as the mismatch of material CTEs, excessive hinge friction, or limit switch interference were investigated and discarded. Further investigation revealed that thermal gradients across the linkage caused the outboard panel hard stop to prematurely preload against the inboard panel, which caused the resistive torques to exceed the available torque. Corrective adjustment procedures were implemented to minimize the

panel hinge line backlash while guaranteeing positive over-center lock-up for worst-case thermal environment.   Three subsequent deployment tests, two in a cold vacuum and one at ambient, have been successful.

Finally, the important "lessons learned" during our experience in this failure investigation include:

(1) Do not ignore resistive torque contributions close to the top-dead-center position: Mechanism designers often do not engage in a thorough analysis of the potential resistive torques that occur near the top-dead-center position because the analysis of a four-bar linkage is difficult and because of the presumption of near-infinite torque transmission.   In fact, the large increase in resistive torque (>30 N-m), due to very small change in the four-bar linkage geometry (~0.01 mm relative length change), occurred as a result of the same kinematic properties that make a four-bar linkage attractive to mechanism designers.   The major system-level thermal-vacuum test failure described in this report might have been avoided if a complete analysis had been performed beforehand.

(2) Importance of thermal gradient and direction of gradient: Thermal design considerations usually take into consideration only bulk temperature changes, which are important in the case of material CTE differences.   However, because the kinematic properties of a four-bar linkage are dependent upon the ratio of link lengths and not on the absolute link lengths, the relative link temperatures are the determining factor.   Mechanism designers should note that serious problems can arise in the presence of relatively small temperature gradients, as was the case in the test failure described in this report.

REFERENCES

1.   Gans, Roger F. *Analytical Kinematics: Analysis and Synthesis of Planar Mechanisms.* Butterworth-Heinemannm: Stoneham, MA, ©1991
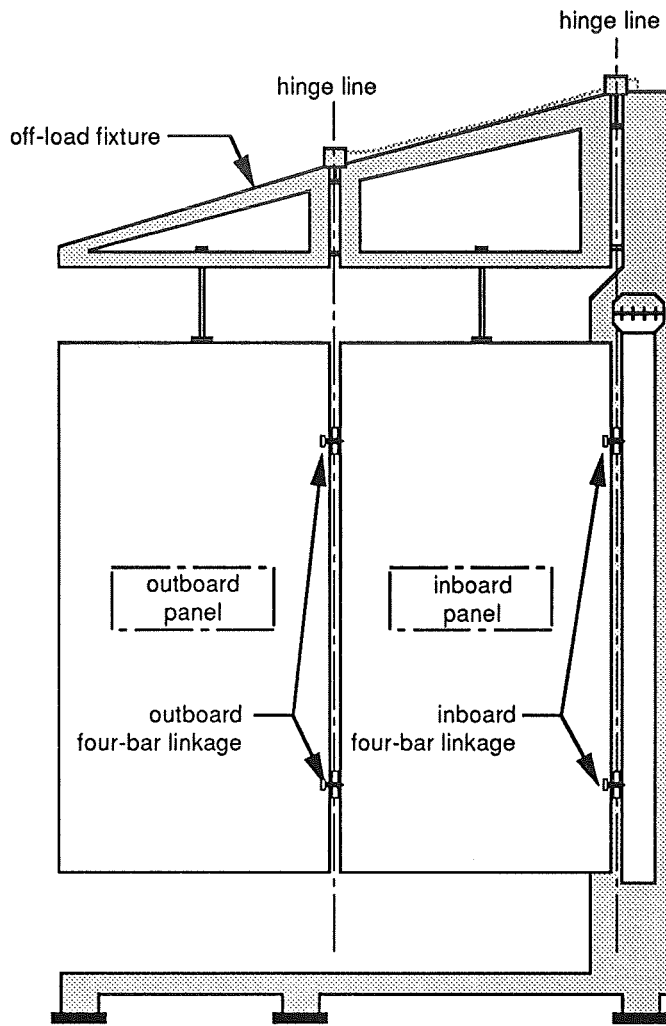
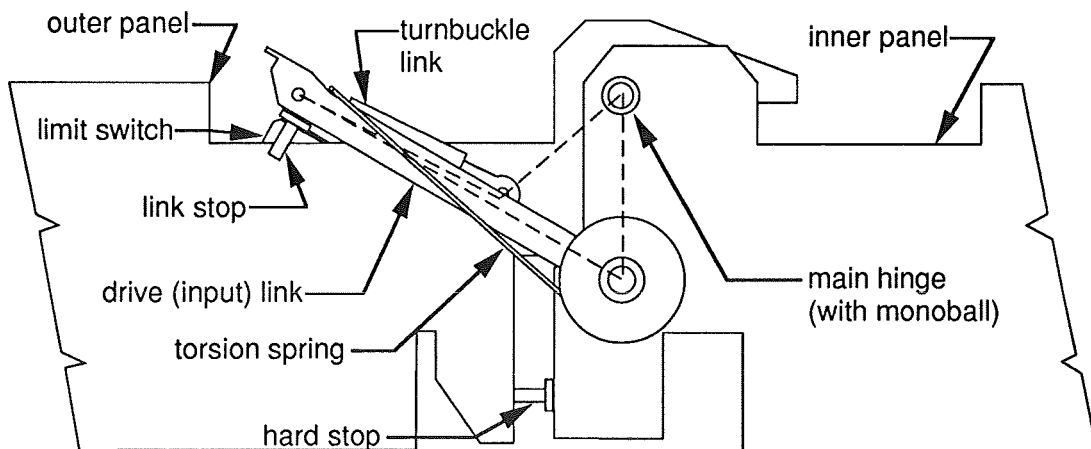**Figure 1. Panels Installed In Their Off-Load Special Test Equipment**
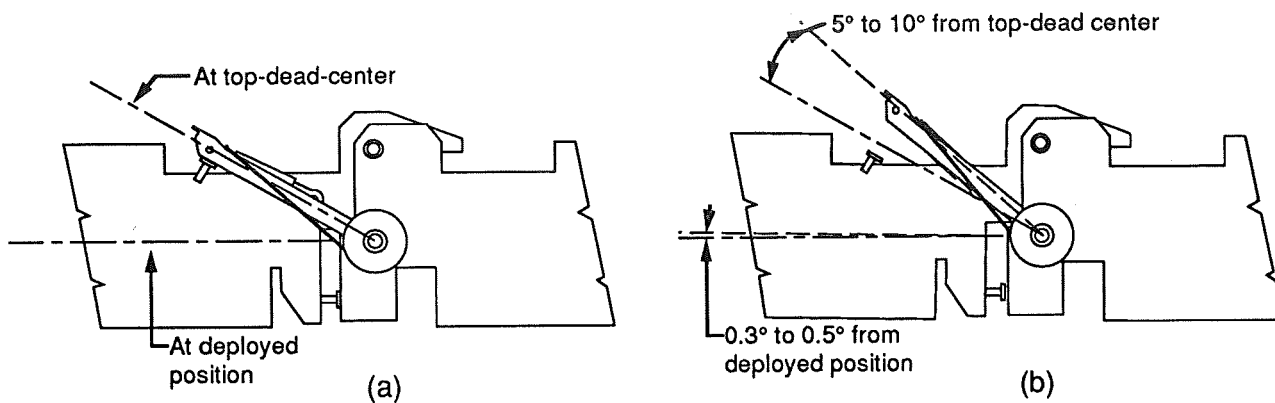

Figure 2. Linkage Schematic (Deployed Position)

Figure 3. Linkage Deployed Configuration: (a) Sucessful Lockup (b) Failed Lockup

detail A: linkage over-center distance

detail B: linkage limit switch (link stop not shown for clarity)
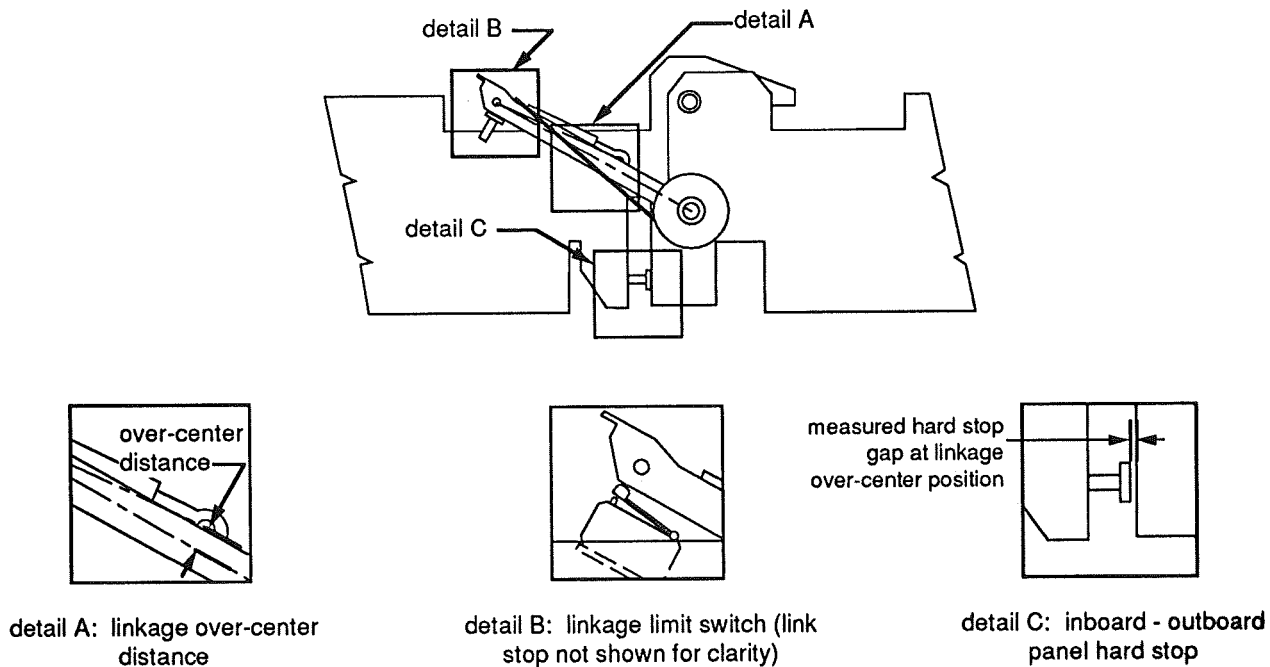
detail C: inboard - outboard panel hard stop

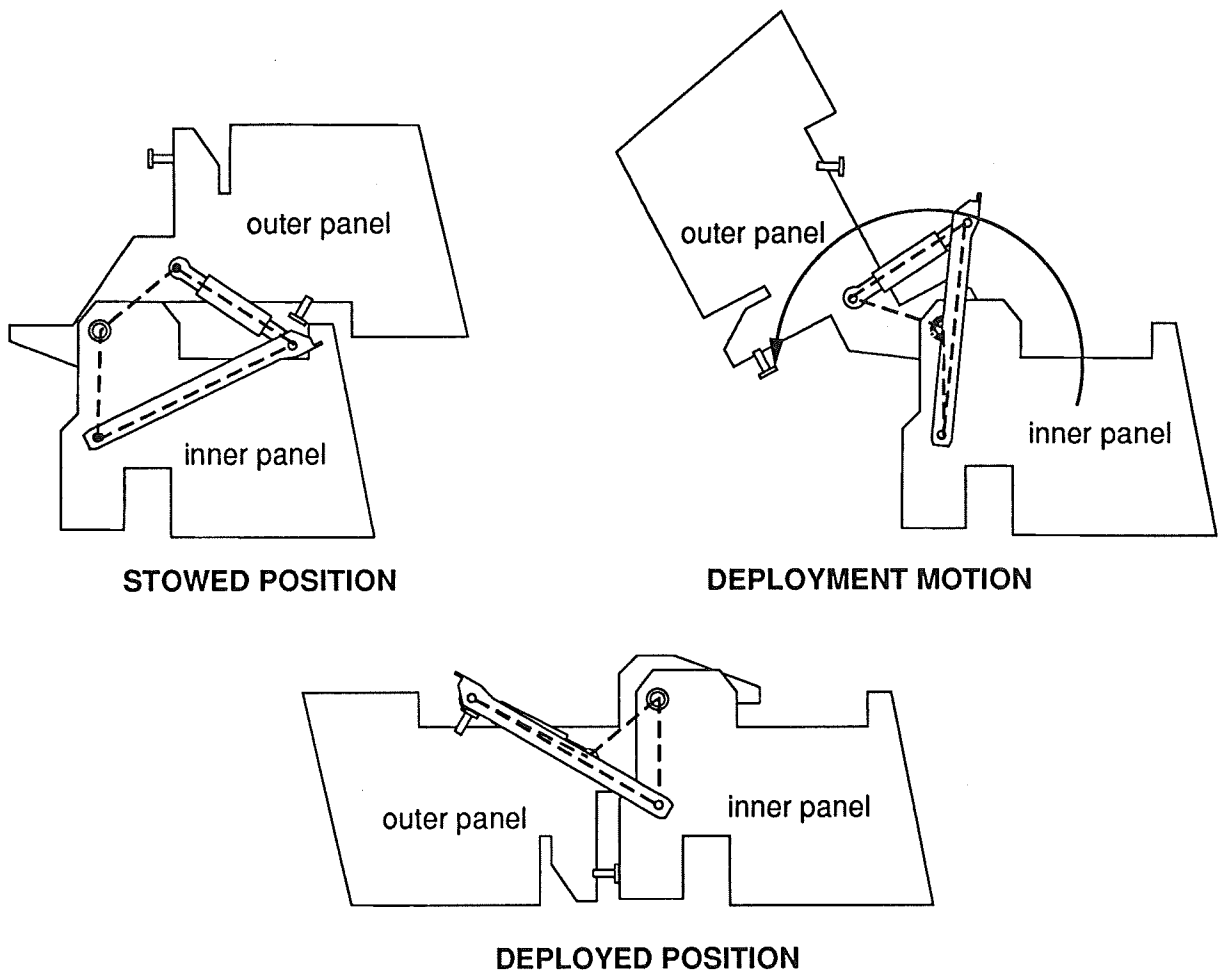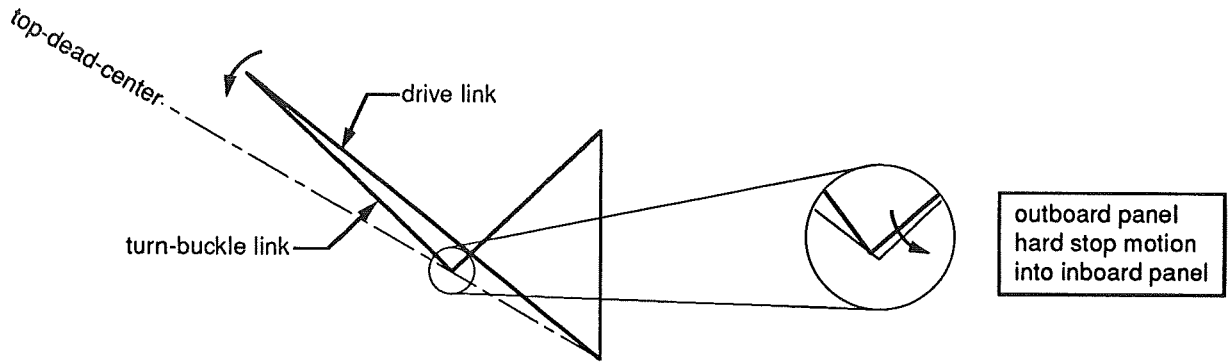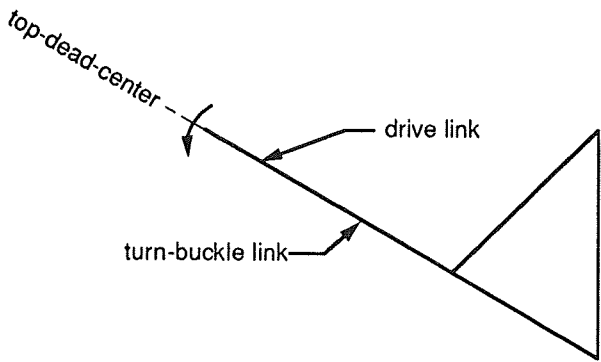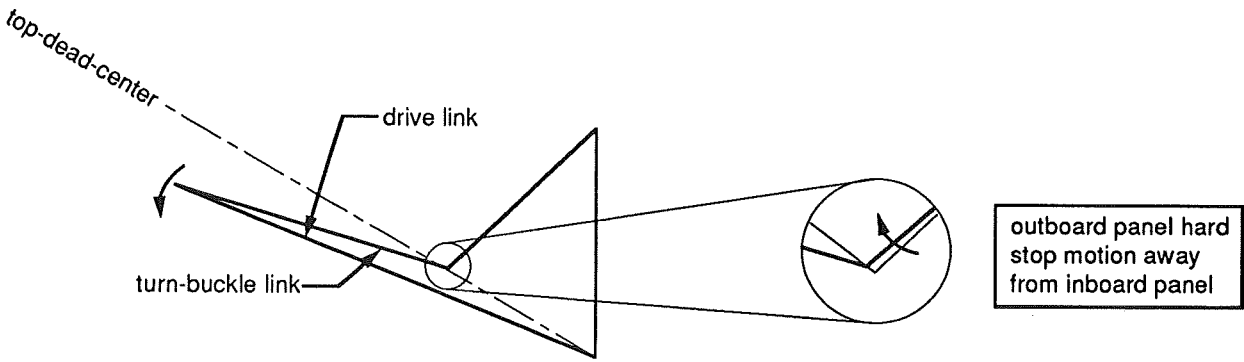**Figure 4. Linkage Details: (A) Over-Center Distance, (B) Linkage Limit Switch, (C) Inboard-Outboard Panel Hard Stop**

293

STOWED POSITION

DEPLOYMENT MOTION

outer panel

inner panel

DEPLOYED POSITION

Figure 5. Linkage Deployment Sequence (Springs Not Shown For Clarity)

top-dead-center

drive link

turn-buckle link

outboard panel
hard stop motion
into inboard panel

BEFORE TOP-DEAD-CENTER POSITION

top-dead-center

drive link

turn-buckle link

TOP-DEAD-CENTER POSITION

top-dead-center

drive link

turn-buckle link

outboard panel hard
stop motion away
from inboard panel

OVER-CENTER POSITION
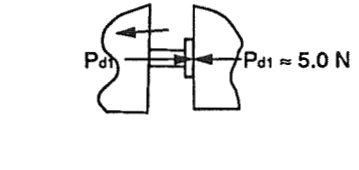
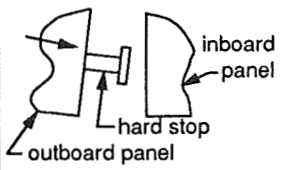Figure 6. Kinematic Behavior Of Panel Four-Bar Mechanism
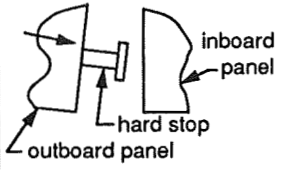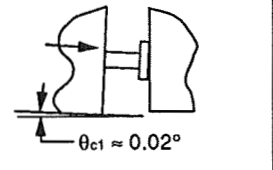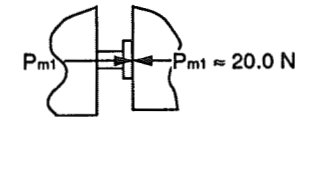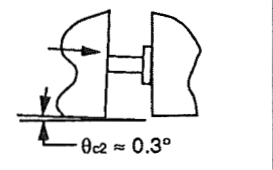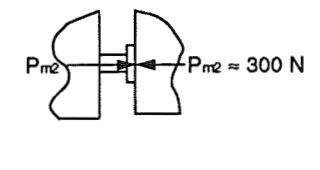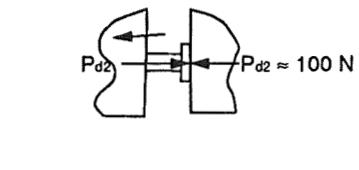
approaching deployed position	Initial stop contact	top-dead-center	over-center
four-bar linkage kinematics have changed due to gradient	outboard panel angle at time of contact (θ_c.)	max. hard stop preload (P_m)	final deployed configuration hard stop preload (P_d) note: $P_{d1} < P_m$
No gradient across linkage			
inboard panel / hard stop / outboard panel	$\theta_{c1} \approx 0.02°$	P_{m1} ← $P_{m1} \approx 20.0$ N	P_{d1} → $P_{d1} \approx 5.0$ N
10° C gradient across linkage			
inboard panel / hard stop / outboard panel	$\theta_{c2} \approx 0.3°$	P_{m2} ← $P_{m2} \approx 300$ N	P_{d2} → $P_{d2} \approx 100$ N

Figure 7. Inboard-Outboard Panel Hard Stop Kinematics (With and Without 10°C Gradient Across Linkage)

resultant hard stop stop-torque (or stiffness)

four-bar linkage stiffness derived from load path

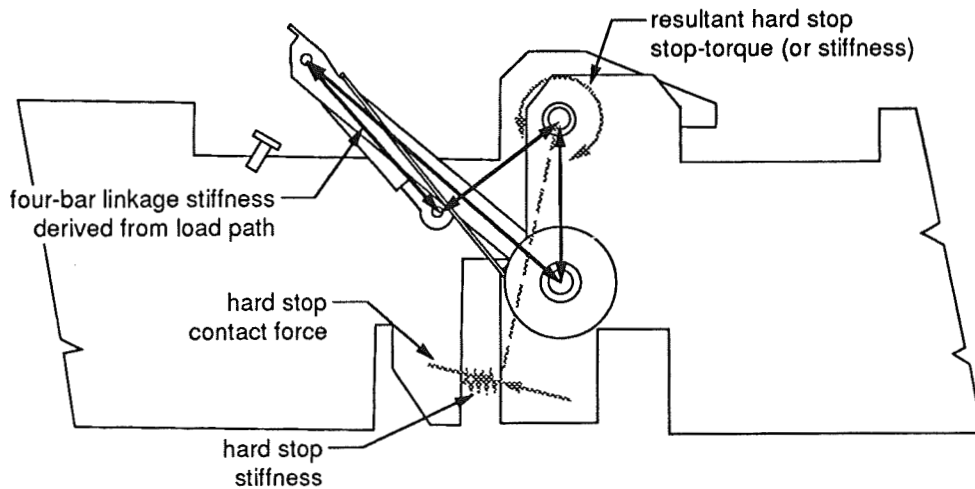hard stop contact force

hard stop stiffness

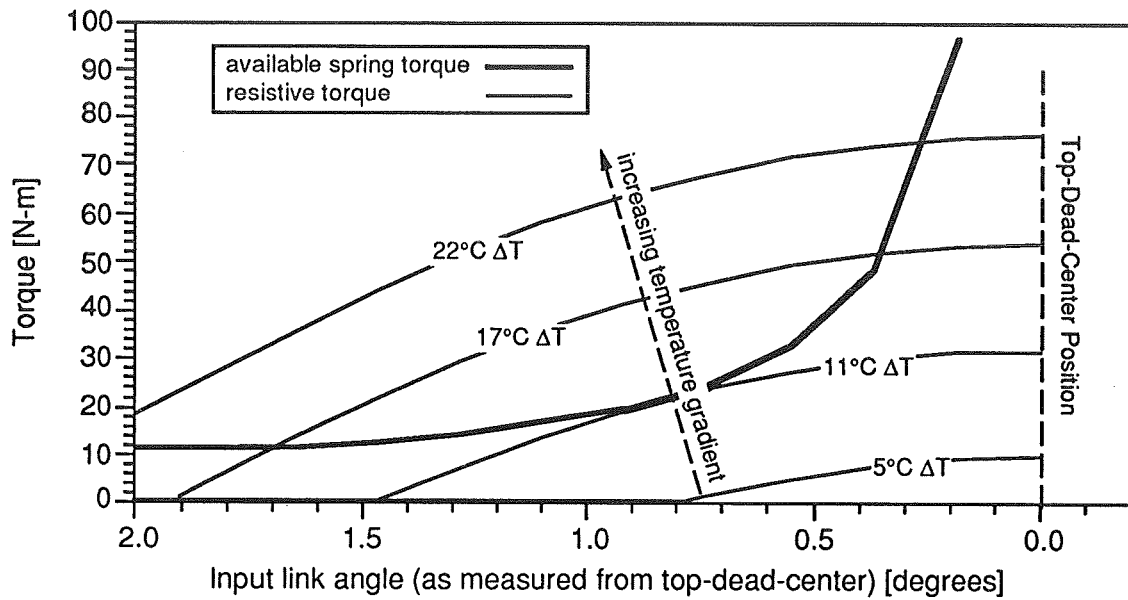**Figure 8. Schematic of Four-Bar Mechanism Stop Stiffness**

Figure 9. Effect of Temperature Gradient: Available Spring Torque and Resistive Hard Stop Torque
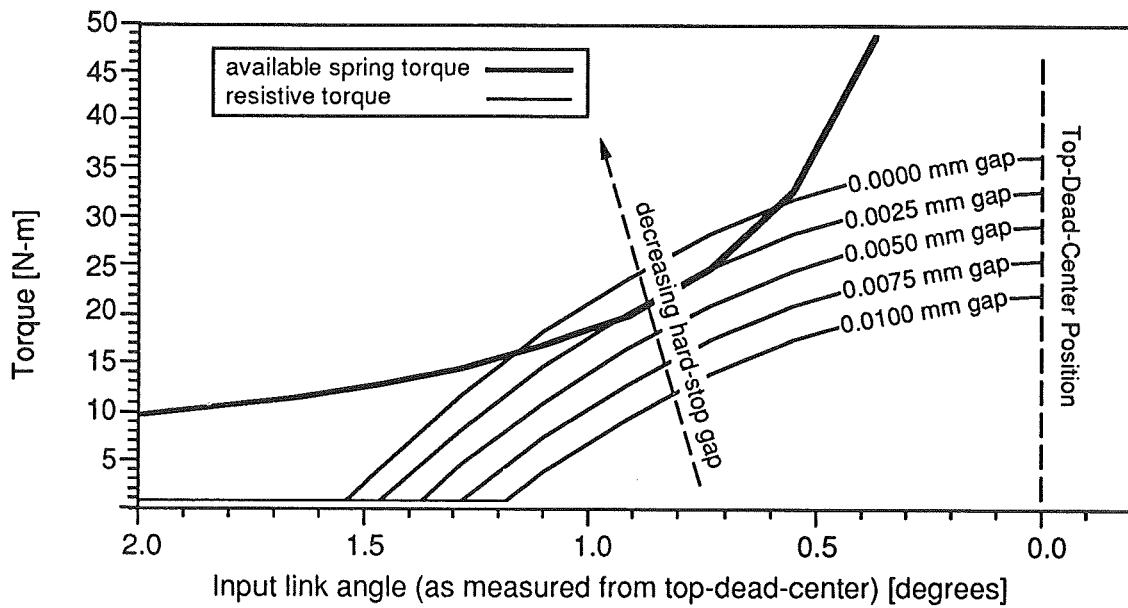

Figure 10. Effect of Hard Stop Gap Adjustment: Available Spring Torque and Resistive Hard Stop Torque
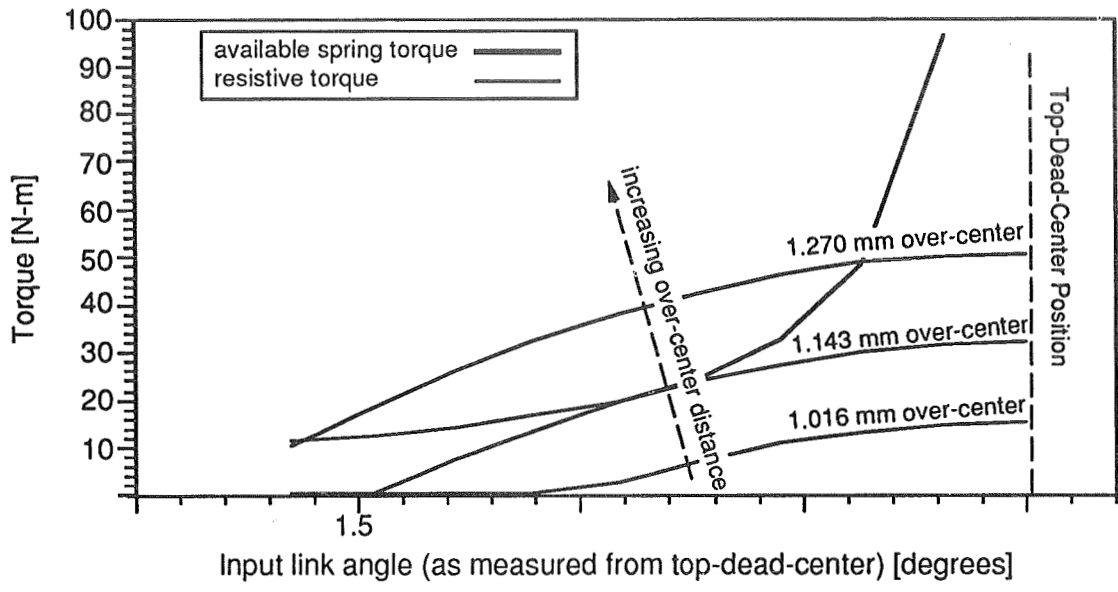
Figure 11. Effect of Over-Center Adjustment: Available Spring Torque and Resistive Hard Stop Torque
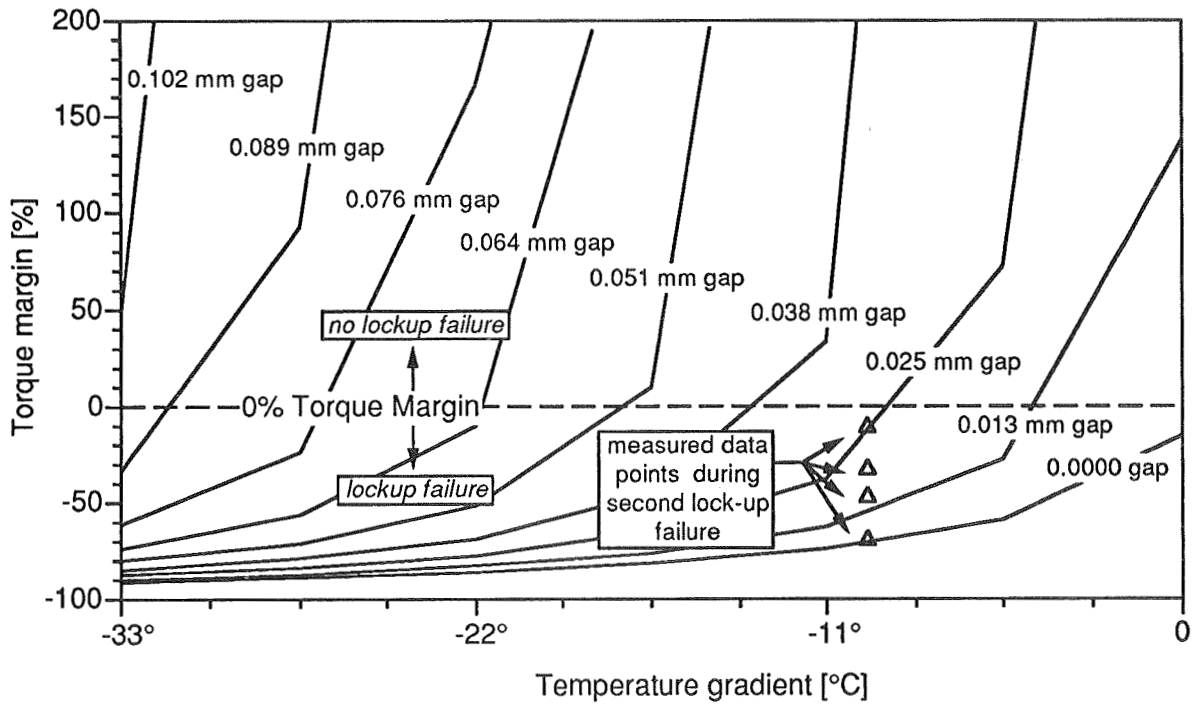

Figure 12. Minimum Torque Margin vs Temperature Gradient and Stop Gap Size

MINIATURE LINEAR-TO-ROTARY MOTION ACTUATOR

Michael R. Sorokach, Jr.*

ABSTRACT

A miniature hydraulic actuation system capable of converting linear actuator motion to control surface rotary motion has been designed for application to active controls on dynamic wind tunnel models. Due to space constraints and the torque requirements of an oscillating control surface at frequencies up to 50 Hertz, a new actuation system was developed to meet research objectives. This new actuation system was designed and developed to overcome the output torque limitations and fluid loss/sealing difficulties associated with an existing vane type actuator. Static control surface deflections and dynamic control surface oscillations through a given angle are provided by the actuation system. The actuator design has been incorporated into a transonic flutter model with an active trailing edge flap and two active spoilers. The model is scheduled for testing in the LaRC 16 Foot Transonic Dynamics Tunnel during Summer 1993. This paper will discuss the actuation system, its design, development difficulties, test results, and application to aerospace vehicles.

DESIGN CRITERIA

The actuation system had to meet the following requirements in order to accomplish research objectives:

- Actuation system operating range from 0-50 Hertz for control surface deflections of 0 to $\pm$ 15 degrees.

- A maximum of $\pm$ 0.3 degrees rotary motion play in the system over the frequency range.

- Mechanically efficient design.

- Compact design due to space restrictions.

- Maximum actuator operating pressure of 1000 psi.

- Reliable and simple to maintain.

---

* NASA Langley Research Center, Hampton, VA

♦ Conform to the design guidelines and safety requirements of the Wind Tunnel Model Systems Criteria (NASA Langley LHB 1710.15).

MECHANISM DESCRIPTION

The actuation system consists of a linear, piston driven, hydraulic actuator with direct load measurement instrumentation and a linear-to-rotary motion conversion insert. Figure 1 is a schematic of the actuator assembly identifying its components. The actuator consists of its body, piston, two end cap subassemblies (composed of the end cap, an air bleeding screw, fitting, and supply line) for enclosing the system, a drive link subassembly (consisting of the drive link, bearing, journal, and retaining ring), forward and aft drive link constraints which are used to restrict the drive link to linear motion, o-rings for sealing the system, and attachment screws. Two miniature pressure transducers capable of monitoring servo loads are incorporated into the end caps. Figure 2 shows the actuator, both assembled and disassembled, and its components. The actuator is a single-degree-of-freedom mechanism allowing drive link translation along the piston axis.

Figure 3 is a schematic showing the manner in which the linear motion of the piston/drive link arrangement is produced. The cutaway sections shown on the actuator assembly are located along its centerline. A servovalve is connected to the actuator by means of two supply lines, each of which is brazed to an end cap, and the necessary fittings. The end caps channel the flow of hydraulic fluid into the left and right side chambers of the actuator body. The chambers are round holes bored in-line through the actuator body to accommodate the piston. Piston length regulates the amount of linear travel for the drive link. The actuator body is relieved between the two chambers to allow for drive link translation. The amount of relief between the two chambers on the actuator body is larger than the combined chamber clearance between the end of the piston and end cap on both sides. As a result, the piston will bottom out on the end caps when full actuator throw is encountered. This prevents damage to the drive link from occurring since it cannot make hard contact with the sidewalls of the actuator body relief at maximum travel. An o-ring on both ends of the piston is used to seal each chamber at the actuator body relief/chamber interfaces.

To initiate drive link motion, the system is first pressurized to 1000 psi. The servovalve then pulsates a small volume of hydraulic fluid into each chamber at alternating time intervals. The alternating flow of fluid between the two chambers causes the piston to translate in a reciprocating manner. The drive link follows the same motion as the piston since it is attached to the piston. The desired frequency and displacement of drive link oscillation is controlled by a closed loop feedback system which adjusts the time interval and mass flow rate of fluid pulsation into each chamber.

The linear, reciprocating motion of the actuator is converted to rotary motion for control surface actuation through a linear-to-rotary motion conversion insert. This insert has a high precision, helical trough machined in it and the insert is incorporated into the actuated control surface as part of its leading edge. Figure 4 is a view showing the actuator assembly and the linear-to-rotary conversion insert attached to the model trailing edge control surface. The control surface is mounted to the wing on two needle roller bearings. Nylon shims, located at the flap/wing interface, are used as a bearing to restrict axial free play of the control surface. As the drive link assembly reciprocates linearly, the helical trough on the insert converts the actuator linear motion into rotary motion of the control surface about its hinge line. The frequency of drive link reciprocation is equal to the rate of control surface oscillation. This actuation system is kinematically equivalent to a reverse cam mechanism, i.e., linear motion is converted to rotary motion.

The bearing which is attached to the drive link rides inside the helical trough on the insert during actuation. The bearing is fabricated to a very close running fit (.0001-.0002 inch clearance) with the helical trough to reduce the free play between the two components. Any excessive free play between the bearing and helical trough will introduce undesirable rotary free play into the system. The bearing is fabricated from graphitic molybdenum-alloy tool steel (ASTM A681, Type 06) and is tempered to Rc 61-64. The linear-to-rotary conversion insert is fabricated from PH 13-8 Mo stainless steel, heat treated to Rc 43-45. As a result, any high points on the contacting surfaces of the helical trough will wear to form a continuous helix upon initial operation of the actuator. This "wearing-in" of the helical trough will reduce the rotary play and help to sustain the rotary play in the system to a constant value. The combination of high hardness and the inherent lubricating properties of the bearing help to reduce its wear.

Constraining the rotation of the drive link about the piston axis (see Figure 1) is another factor which reduces rotary play in the actuation system. Restricting the drive link to linear motion is accomplished by reducing the cumulative tolerance buildup between the drive link and the contacting surfaces which prohibit any drive link rotation (forward and aft drive link constraints and the upper surface of the actuator body relief). These mating surfaces actually make contact with the drive link. A nickel alloy plating (NEDOX*) is applied to all surfaces having relative motion to improve their surface hardness (Rc 63-67) and lubricity, thus decreasing galling and wear. The internal bore in the actuator body which houses the piston is also plated to help decrease o-ring wear, thus prolonging seal life. Since the piston o-rings exhibit inherent compressibility, they are the only components of the actuator assembly which introduce rotary play into the system. The other location where rotary play occurs in the system is at the interface between the bearing and helical trough. The

---

* General Magnaplate Corporation, Linden, New Jersey

301

cumulative rotary play in the actuation system was measured during testing and determined to be ± 0.3 degree.

Actuator loads are monitored by the means of two miniature pressure transducers. Each transducer is located on an end cap and monitors the pressure load on its respective chamber (see Figure 2). The hinge line torque output of the actuation system can be calculated from these pressure load measurements. Any pressure fluctuation in the chambers can be determined and compensated for by the servovalve during operation.

DESIGN OVERVIEW

The actuation system is designed to conform to the requirements of the Wind Tunnel Model Systems Criteria (NASA Langley LHB 1710.15). This document addresses various design guidelines and safety requirements for models and model systems which are to be tested at the Langley Research Center facilities.

The weakest link in the actuation system is the journal which supports the bearing on the drive link subassembly (see Figure 1). Journal failure during wind tunnel testing would result in no damage to the facility since the journal is not a structural attachment for the control surface. The control surface is hinged to the wing body and would remain attached to the wing in the event of journal failure. The journal is fabricated from 18 Ni 300 grade maraging steel. Under normal wind tunnel testing operating conditions (20 Hertz oscillation for control surface deflections of ± 5 degrees) the worst case stress, including stress concentration factors, results in a safety factor of 23 on the material ultimate strength. For the upper limit operating conditions (50 Hertz oscillation for control surface deflections of ± 15 degrees), the worst case stress results in a safety factor of 1.2 on material ultimate strength. The upper limit operating conditions of the actuation system will not be exercised during wind tunnel testing. However, the actuation system may be operated to obtain short throw, high frequency control surface deflections (± 5 degrees at 40-50 Hertz) during testing. The worst case stress for this scenario results in a safety factor of 3.7 on the material ultimate strength.

Figure 5 shows the results of a fatigue analysis performed on the journal for normal wind tunnel testing operating conditions and upper limit operating conditions. This analysis conforms to the requirements of NASA Langley LHB 1710.15 which assumes a strength reduction factor of 0.5 to account for surface finish, reliability, etc. The analysis is therefore conservative. As stated previously, the upper limit operating conditions will not be applied during wind tunnel testing. For short throw, high frequency control surface deflections (± 5 degrees at 40-50 Hertz), journal life is increased by a factor of 406 as compared with journal life at the upper limit operating conditions.

302

The actuator body, end caps, and forward and aft drive link constraints are fabricated from 15-5 PH stainless steel, heat treated to Rc 35-38. To eliminate any difficulties associated with galling, the piston and drive link are fabricated from PH 13-8 Mo stainless steel, heat treated to Rc 43-45. As discussed previously, all contacting surfaces with relative motion are nickel alloy plated to decrease wear. All fasteners are 180 ksi minimum tensile strength and are preloaded to manufacturer's specified torque.

The transonic flutter model for which the actuator design has been incorporated is shown in Figure 6. Cover plates and the upper spoiler are removed to show the access compartments which house the actuators and instrumentation. The model is equipped with an active trailing edge flap and two active spoilers. Fifty-eight pressure transducers are installed chord wise at 60 percent model span (mid-span on the control surfaces) for dynamic pressure distribution measurement. Additionally, 17 pressure transducers are installed at 40 percent model span, slightly inboard of the control surfaces, to measure any unsteady pressure distributions due to control surface actuation. Accelerometers are mounted on the wing panel and control surfaces to measure model displacements and control surface dynamic response during actuation. Rotary potentiometers are used to monitor control surface angular displacements.

Figure 7 is a detail of the actuators showing their locations and method of control surface actuation. As discussed previously, the flap actuator converts its linear motion to control surface rotary motion through the leading edge insert on the flap. The spoiler actuator consists of two servos incorporated into a common body and is similar in design to the flap actuator. The upper and lower spoilers are independently actuated and static deflections or dynamic control surface oscillations about a given angle are provided by the actuator. The chord wise, linear motion of the spoiler actuator is converted into upper and lower spoiler rotary motion through the control arm shown on section B-B in figure 7. Maximum spoiler deployment is 45 degrees from the undeflected position as shown in figure 7. Rotary play in the spoiler actuator is not a major concern due to geometry and since control surface deflections are parallel to the plane of actuation. The spoilers are fabricated from unidirectional graphite tape to increase stiffness and reduce their mass moment of inertia. The wing panel and trailing edge control surface are manufactured from 7075-T651 aluminum alloy. The wing panel and trailing edge control surface are also designed and fabricated to minimize their mass moment of inertia without sacrificing structural integrity.

TESTING AND EVALUATION

Prior to the fabrication of the production actuator (shown in figures 1-4), a prototype actuator, similar to the production configuration, was designed and fabricated for validation testing and evaluation. Figure 8 is a schematic of the

actuator bench test setup. The bench test setup consists of the testbed, actuator assembly, flap simulator, rotary potentiometer, bellows coupling, servovalve, supply lines, and the necessary mounting hardware. The production actuation configuration is shown with the bench test setup in figure 8. The setup also includes a differential pressure transducer for monitoring the difference in actuator chamber pressure and can be used if so desired. The rotary potentiometer is used to measure angular displacements and is connected to the generic control surface by a bellows coupling to compensate for any misalignment. The flap simulator is designed so its mass moment of inertia is equivalent to the mass moment of inertia for the trailing edge control surface on the model. The inertia of the flap simulator is easily modified by either adding or removing material as necessary. Figure 9 shows the bench test setup with the prototype actuator which is similar in design to the production configuration.

Testing and evaluation of the prototype actuator has revealed its capability of short throw, high frequency control surface oscillations (± 5 degrees at 40-50 Hertz) and long throw, low frequency oscillations (± 15 degrees at 5-10 Hertz). Control surface deflections were found to be accurate within 0.3 degree over the frequency range. As a result, the rotary play in the actuation system fell within the acceptable margin. It was determined that the actuation system was capable of meeting research objectives. Prior to wind tunnel testing, the production configuration will be tested and evaluated in the same manner as the prototype system.

LESSONS LEARNED

Four significant problems were resolved while the actuation system was undergoing testing and evaluation. A needle roller bearing was originally used to transfer the motion of the drive link to the helical trough on the insert for control surface actuation. Excessive rotary play was detected in the system and it was determined that the needle roller bearing was the primary source. This excessive rotary play was eliminated by replacing the roller bearing with the solid, precision ground bearing fabricated from graphitic molybdenum-alloy tool steel. In addition to eliminating a significant source of rotary play in the system, wear in the helical trough on the insert was reduced by the inherent lubricating capability of the bearing material.

Another origin of rotary play was introduced into the actuation system from the manner in which bearing and linear-to-rotary conversion insert manufacturing was carried out. Initially the insert was fabricated and then the bearing was hand fitted to the insert. It was determined that the curvature of the helical trough was not a perfect helix. As a result, the trough had some high and low spots on it (.002 inch maximum deviation). Since the bearing could only be manufactured to a specific diameter, the fit between the bearing and helical trough varied over the length of the trough. This varying fit between the two components resulted in a varying amount of rotary play in

the system. To meet research objectives, the rotary play in the system needs to be a constant value.

The method of bearing and insert fabrication was reversed to eliminate the variable amount of rotary play. A range of bearings in increments of .0001 inch above and below nominal helical trough height were manufactured. The helical trough will then be fitted to the bearing by progressively changing the bearing diameter until the trough is "worn-in" to fit a specific size bearing over its length. That bearing size will then be used on the actuator. This lapping operation will help to sustain the rotary play to a constant value and at the same time reduce the amount of rotary play due to the bearing/trough fit.

Wear between mating surfaces with relative motion due to rubbing contact was initially a problem. This wear was relieved by coating the components with the nickel alloy plating as previously discussed. The plating greatly improved surface lubricity and hardness, thus decreasing wear and prolonging component life.

Piston o-ring wear led to increased free play between components, decreased o-ring life, and fluid leakage. An o-ring material more appropriate for high frequency reciprocating motion was selected to remedy these problems. Coating the internal bore on the actuator body with the nickel alloy plating also helped to decrease o-ring wear. Rotary play was reduced since the new o-ring material was harder and therefore less compressible than the originally selected material.
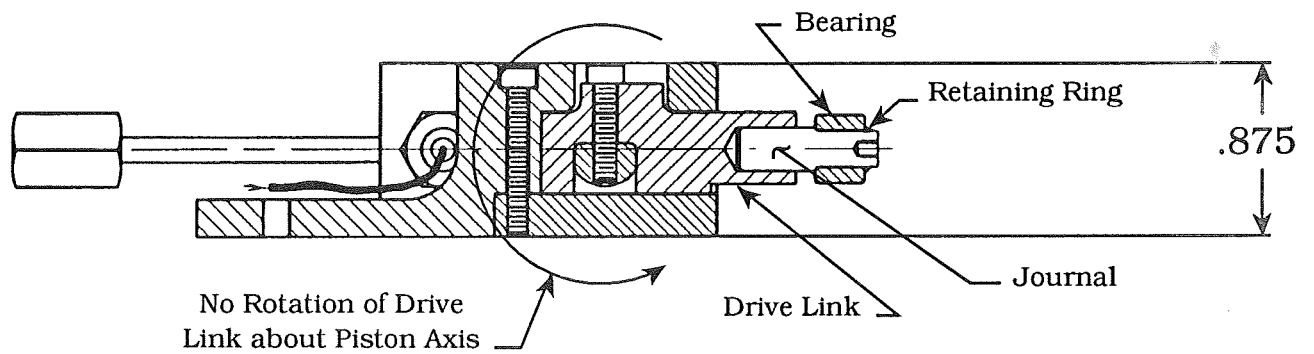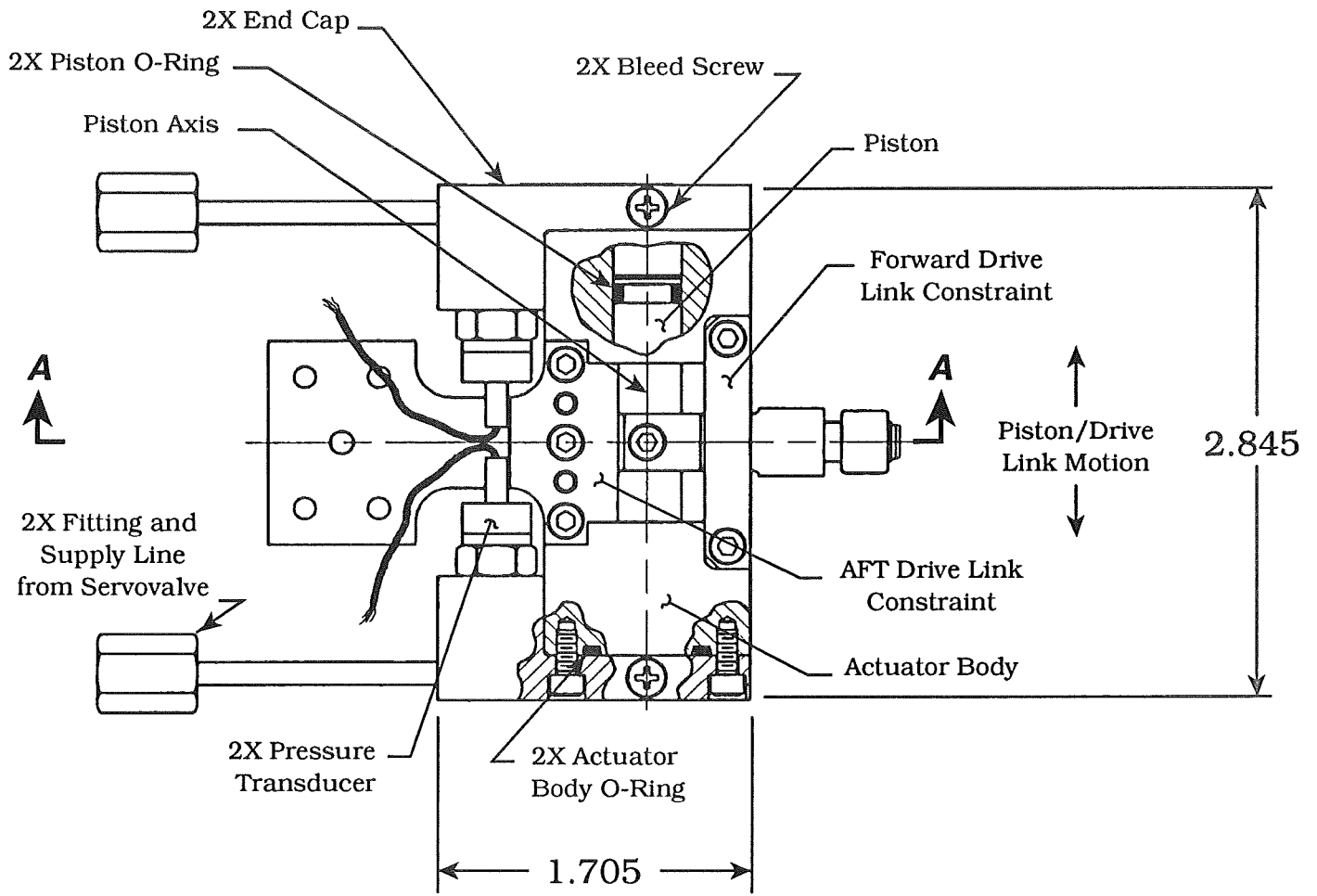
APPLICATION TO AEROSPACE VEHICLES

The primary function of this actuation system is provide flutter suppression capabilities for dynamic wind tunnel models. The system could be applied to military and commercial aircraft which require a flutter suppressing control surface actuation system. Compactness and mechanical efficiency are two merits of this actuation system when space constraints and torque requirements are design parameters which need to be addressed.

Another application of the system is it can be used as a rotary actuator in the traditional sense. Static control surface deflections for any aircraft configuration can be provided for by the actuation system. For applications where airfoil thickness is very thin, the compact design of this actuation system is advantageous. For example, the High Speed Civil Transport has airfoil thicknesses as low as two percent chord length and could be a possible candidate for the system because of its compact design. The quick response of the actuator to its input (the servovalve) is another trait of the system which could be applied to aerospace vehicles.

For applications where rotary play in the control surface is not a concern ($\geq \pm 1$ degree), manufacture of the actuation system is less difficult and less expensive. The reason is manufacturing tolerances do not have to be held as tight as those for applications requiring minimal rotary play ($\pm 0.2 - 0.3$ degree). The manufacturing

cost is inversely proportional to the amount of tolerable rotary play in the actuation system.

2X End Cap

2X Piston O-Ring

2X Bleed Screw
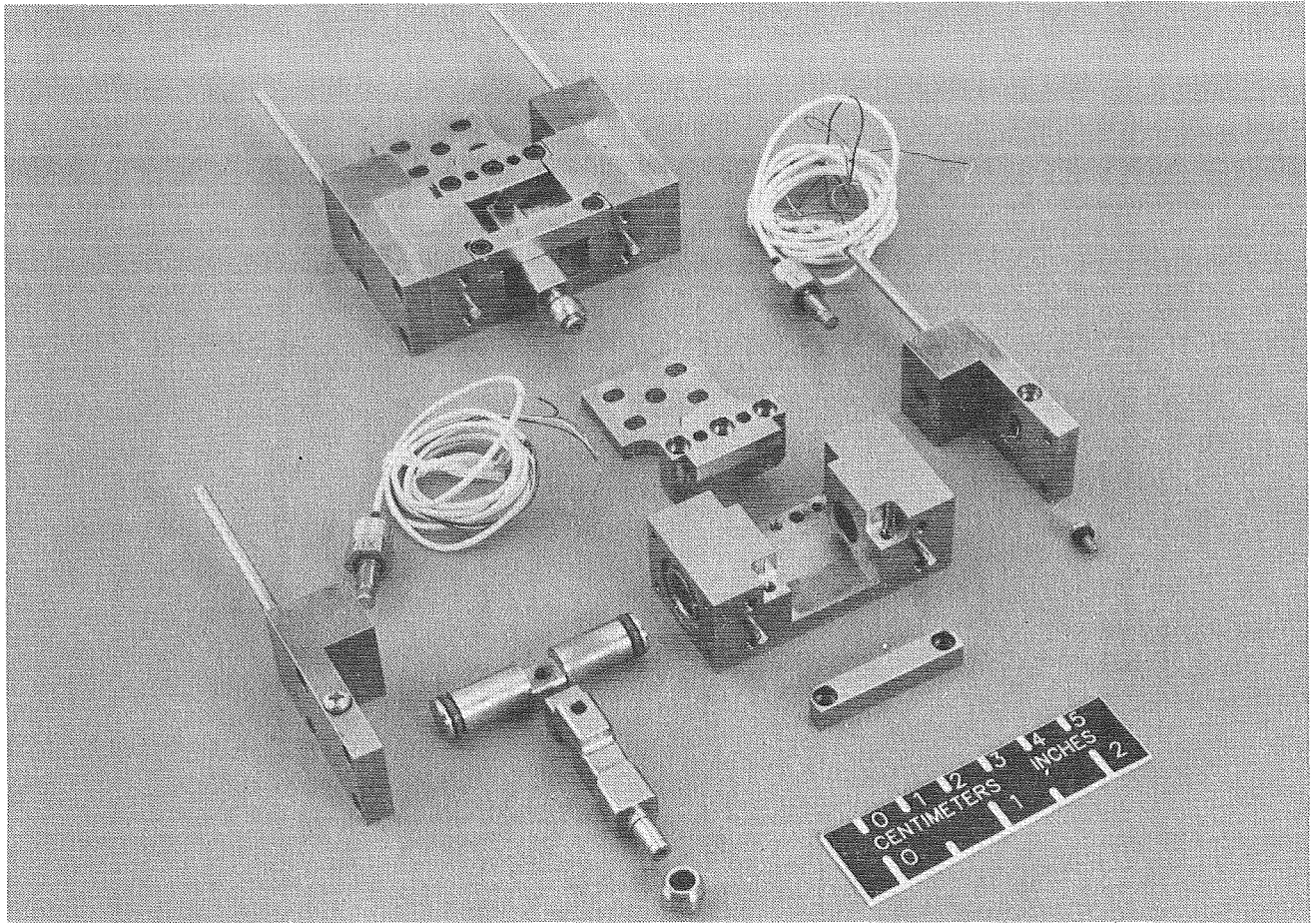
Piston Axis

Piston

Forward Drive
Link Constraint

A ◄ A ►

Piston/Drive
Link Motion

2.845

2X Fitting and
Supply Line
from Servovalve

AFT Drive Link
Constraint

Actuator Body

2X Pressure
Transducer

2X Actuator
Body O-Ring

1.705

Bearing

Retaining Ring

.875

No Rotation of Drive
Link about Piston Axis

Drive Link

Journal

Section A - A

Figure 1. Actuator Assembly

307

Figure 2. Actuator Assembly and Components
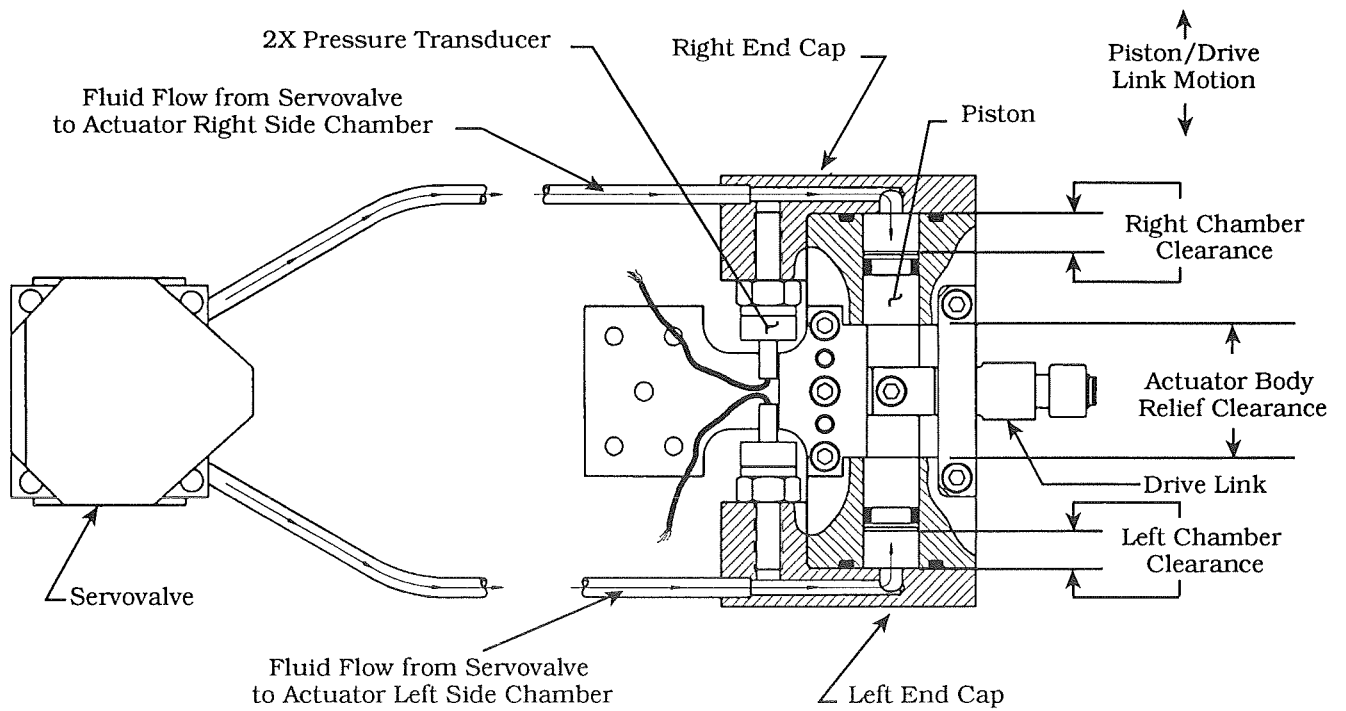

Figure 3. Servovalve/Actuator Operating Schematic
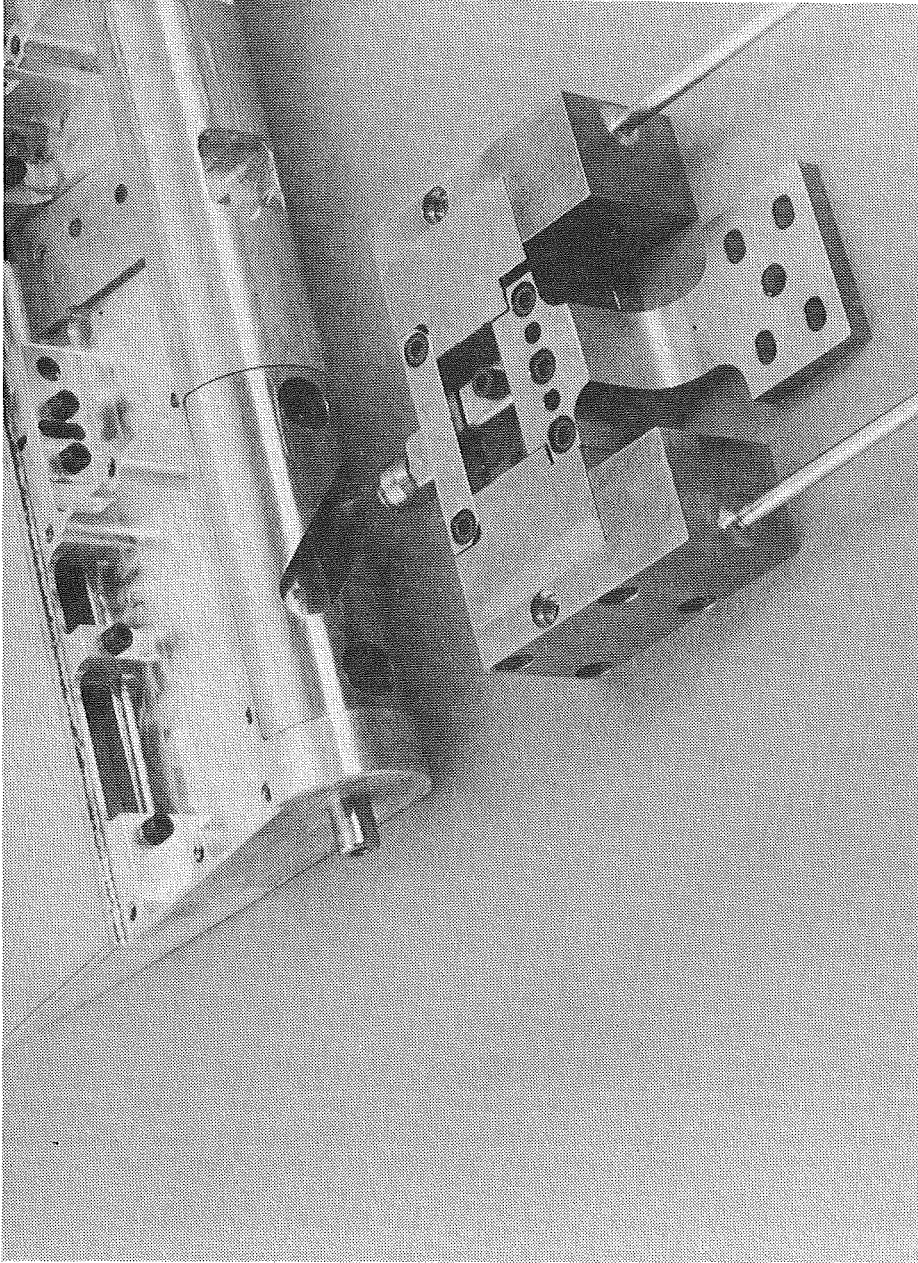
Figure 4. Actuator/Linear-To-Rotary Motion Conversion Insert Detail

Journal Fatigue Analysis for Normal Operating Conditions

|				
Yield Stress	psi	(Sy)	=	270000.
Ultimate Stress	psi	(Su)	=	280000.
Endurance Limit	psi	(Se)	=	140000.
Mean Stress	psi	(Sm)	=	3468.
Stress Amplitude	psi	(Sa)	=	3468.
Stress Concentration Factor			=	1.75
Adj. Endurance Limit		(Se')	=	40000.
Fatigue Limit	psi	(Sf)	=	3511.
Infinite Life	cycles	(Ne)	=	10000000.
Fatigue Life	cycles	(Nf)	=	376788474
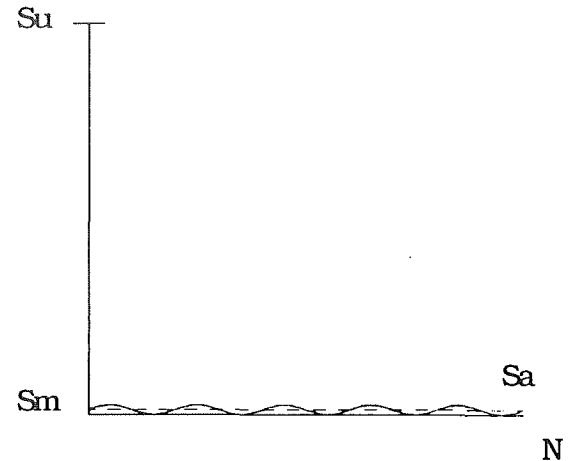
Operating Conditions: 20 Hertz for control surface deflections of ± 5°

T = Journal Life for 20 Hertz Operating Frequency @ ± 5°

$$T = Nf/w = \left[\frac{376788474 \text{ cycles}}{20 \text{ cycles per sec}} \right] \left[\frac{1 \text{ hr}}{3600 \text{ sec}} \right]$$

$$T = 5233 \text{ hrs}$$

Journal Fatigue Analysis for Upper Limit Operating Conditions

Yield Stress	psi	(Sy)	=	270000.
Ultimate Stress	psi	(Su)	=	280000.
Endurance Limit	psi	(Se)	=	140000.
Mean Stress	psi	(Sm)	=	64382.
Stress Amplitude	psi	(Sa)	=	64382.
Stress Concentration Factor			=	1.75
Adj. Endurance Limit		(Se')	=	40000.
Fatigue Limit	psi	(Sf)	=	83606.
Infinite Life	cycles	(Ne)	=	10000000.
Fatigue Life	cycles	(Nf)	=	11474.
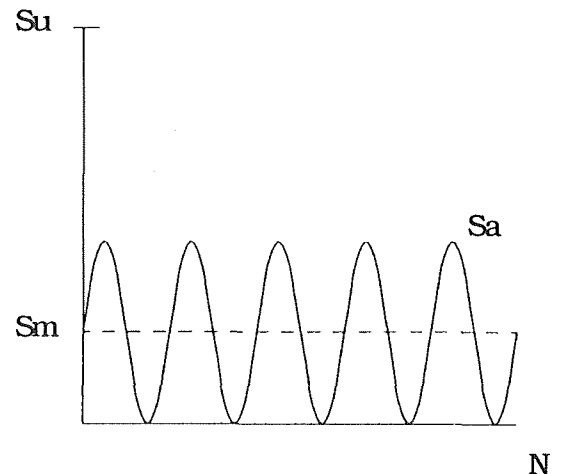
Operating Conditions: 50 Hertz for control surface deflections of ± 15°

T = Journal Life for 50 Hertz Operating Frequency @ ± 15°

$$T = Nf/w = \left[\frac{11474 \text{ cycles}}{50 \text{ cycles per sec}} \right] \left[\frac{1 \text{ min}}{60 \text{ sec}} \right]$$

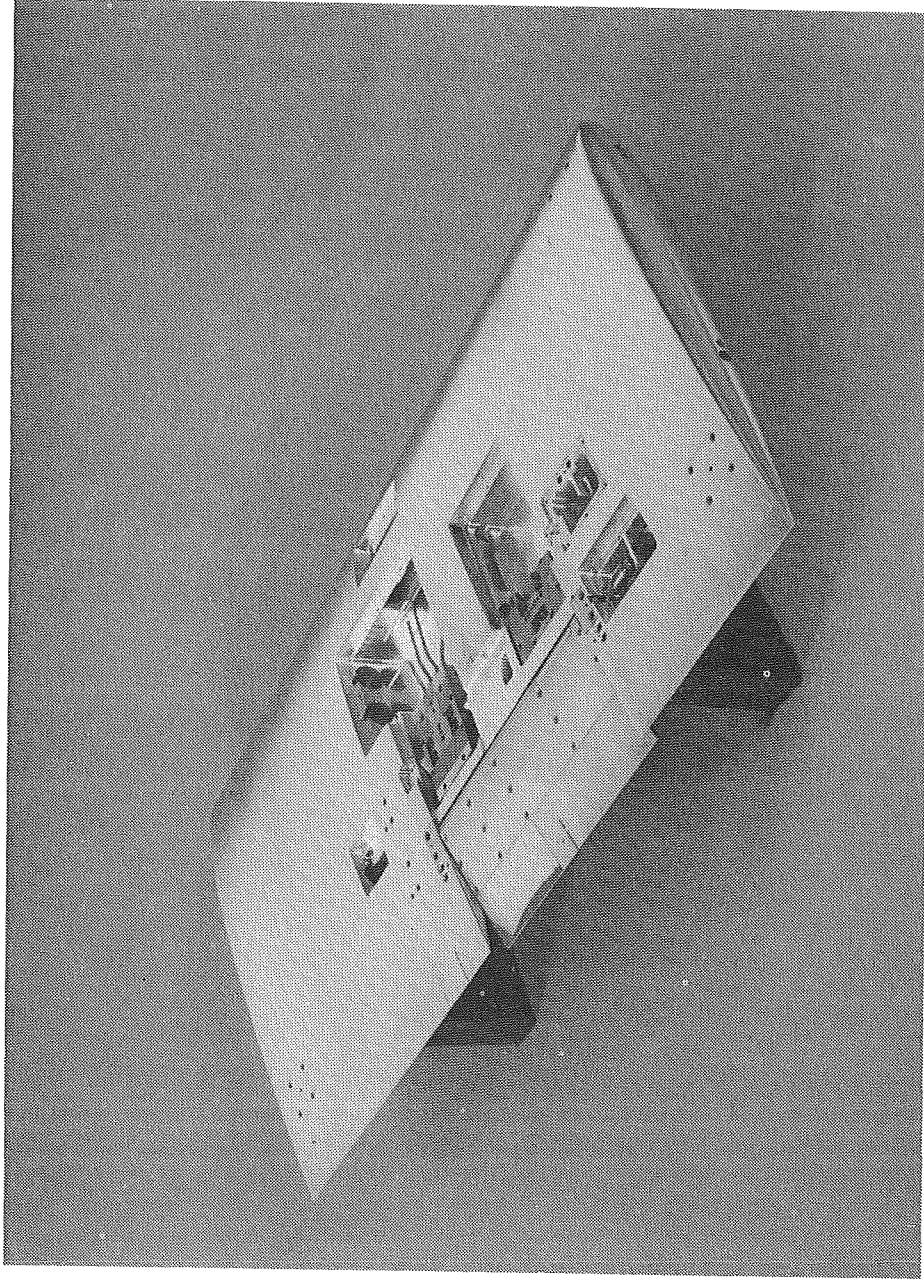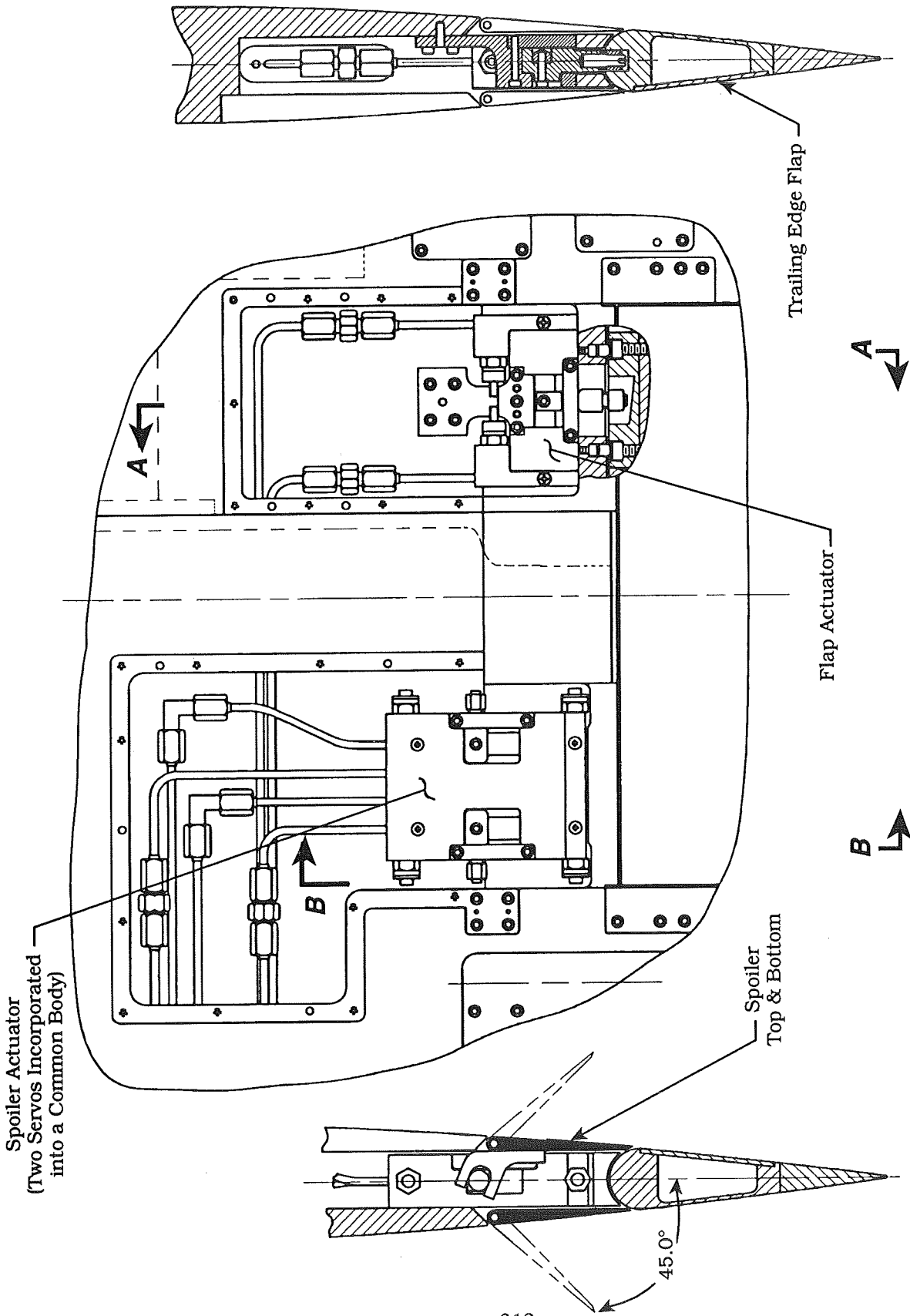$$T \cong 4 \text{ min}$$

Figure 5. Journal Fatigue Analysis

Figure 6. Model Assembly

Section A-A

Trailing Edge Flap

Flap Actuator

Spoiler Actuator
(Two Servos Incorporated
into a Common Body)

Spoiler
Top & Bottom

45.0°

312

Section B-B

Figure 7. Actuator/Wing Panel Detail

2X Bearing Block

Flap Drive (Linear-To-Rotary Conversion Insert)

Bellows Coupling

Rotary Potentiometer

Flap Simulator

A

A

Testbed

Actuator Assembly

Differential Pressure Transducer

Supply Lines

Servovalve

Manifold
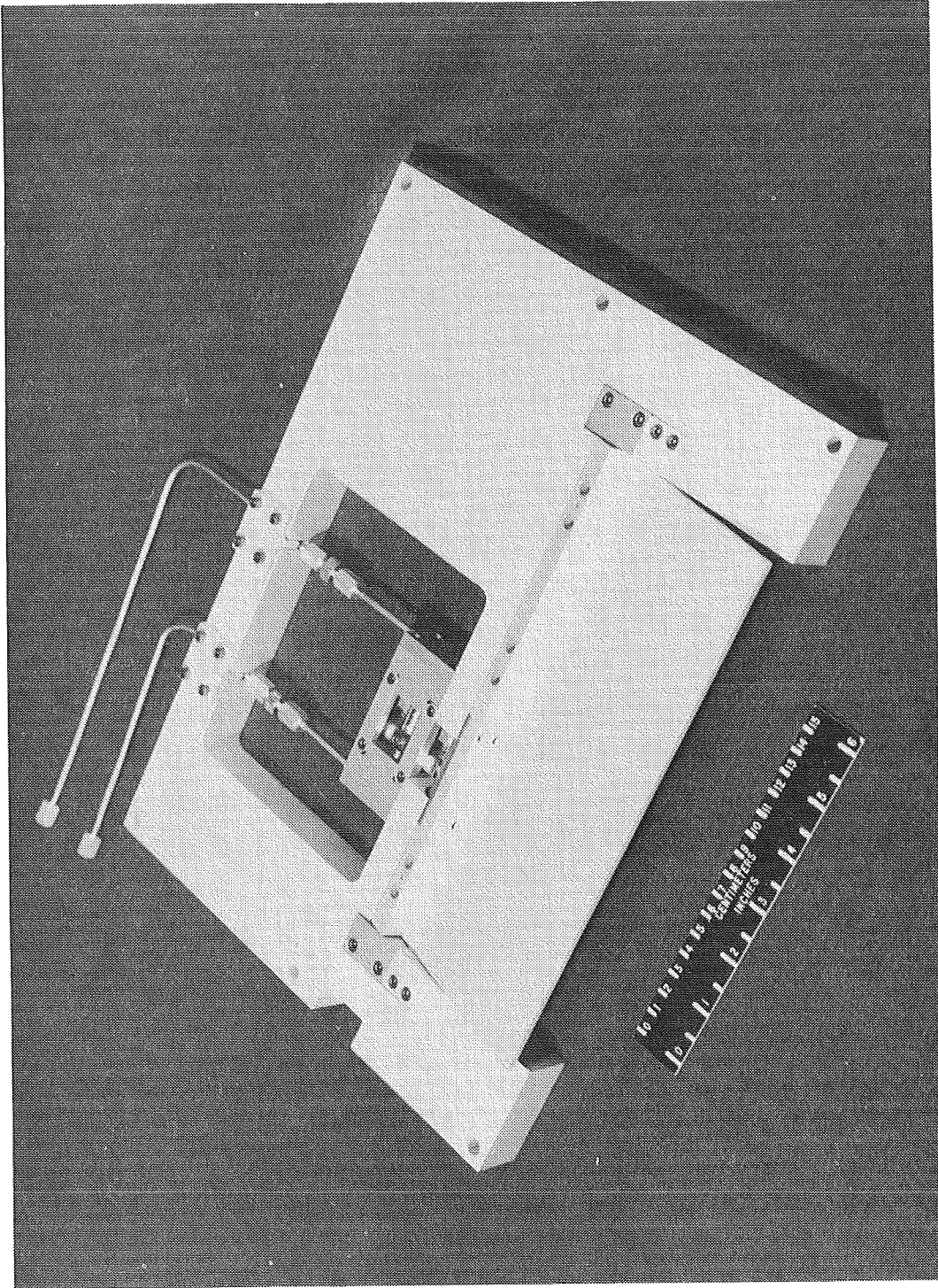
Section A-A
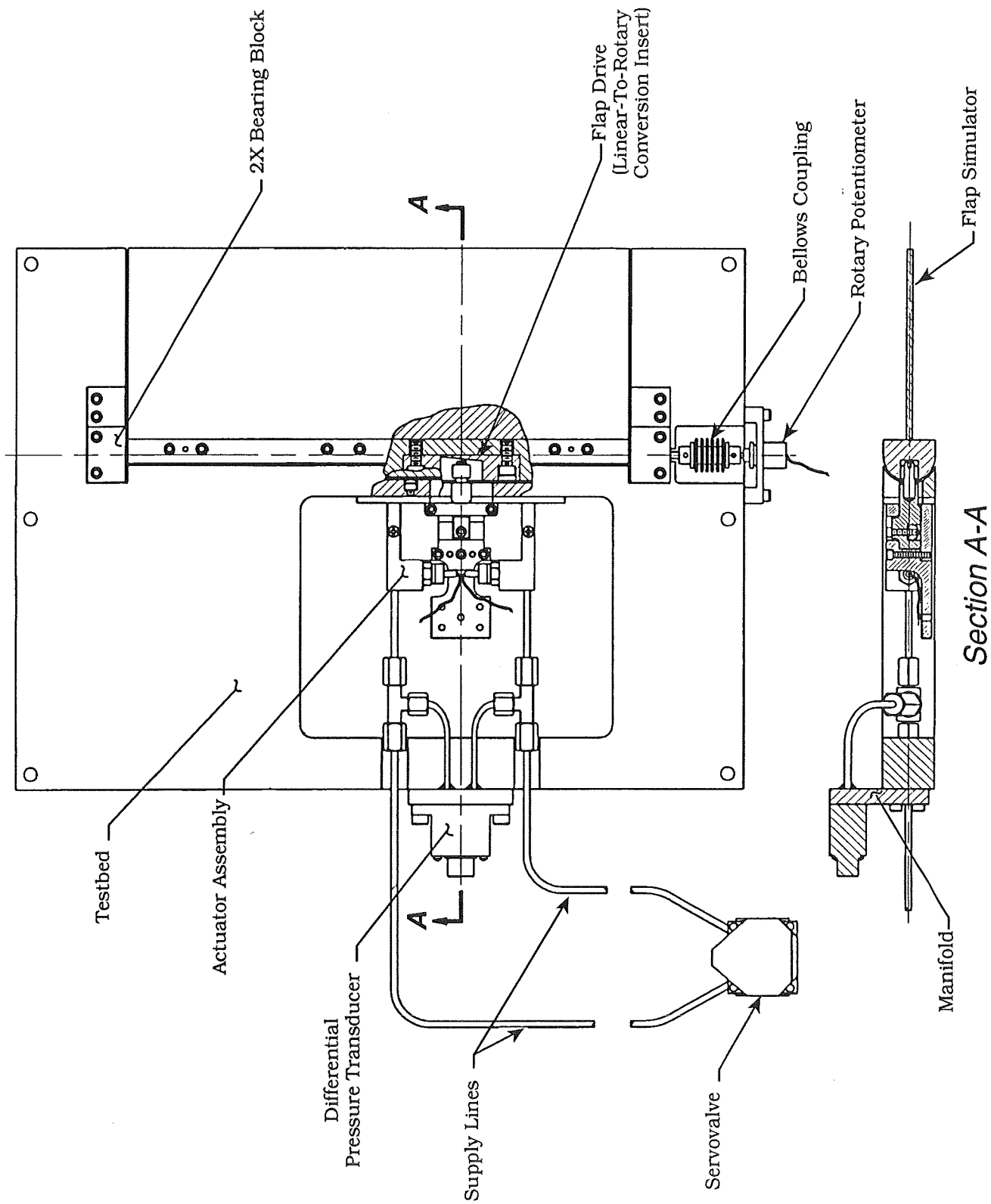
Figure 8. Actuator Bench Test Schematic

Figure 9. Actuator Bench Test Setup

Portable Linear Sled (PLS) for Biomedical Research

434684

Will Vallotton**, Dennis Matsuhiro*, Tom Wynn*, and John Temple**

ABSTRACT

The PLS is a portable linear motion generating device conceived by researchers at Ames Research Center's Vestibular Research Facility and designed by engineers at Ames for the study of motion sickness in space. It is an extremely smooth apparatus, powered by linear motors and suspended on air bearings which ride on precision ground ceramic ways. (FIGURE 1).

INTRODUCTION

Bioaccelerometers in the inner ear sense head motion and orientation relative to Earth gravity. These sensors automatically control eye position during head motion to ensure stable vision. An important objective of NASA's Biomedical Research Program is to understand how this system adapts to weightlessness and re-adapts to Earth gravity on return from space. To achieve this objective, responses must be recorded during well-defined, well-controlled, noise-free (<.001 g) linear oscillations. Linear sleds to provide such accelerations to human and animal subjects already exist at Ames. The purpose of the present report is to present a description of a new portable linear sled (PLS) designed to be transported to a pre-launch and post-landing test-site in Russia for pre- and post-flight testing of rhesus monkey responses. The paper will focus on the mechanical design of the PLS, as well as the problems and solutions found during design and system development and deployment.

PROJECT REQUIREMENTS AND PERFORMANCE SPECIFICATIONS

This project required the design of an exceptionally smooth linear motion sled capable of distortion free sinusoidal motion. Unlike current Ames models which ride on large granite blocks, it had to be portable allowing it to be transported to different locations and to be carried and set up by hand. In addition, there were only 22 months to take the project from initial concept to operational status in Russia.

*NASA-Ames Research Center, Moffett Field, CA
**Sverdrup Technology Inc., Ames Division, Moffett Field, CA

The performance specifications of the PLS were derived from the needs of the Principal Investigators to have a linear sled capable of smooth, distortion free sinusoidal motion to:

- Prevent "cueing the test subject that a change in direction had occurred or was about to occur.
- Allow the use of simple single frequency Fourier analysis vs. more rigorous analyses that would be required if distortion or non-linearities were present.

Distortion and noise levels were not to exceed .001g. This requirement was dictated by the science community as being just below the threshold of perception of human and animal subjects and therefore, necessary if the data was to be free of ambiguity. It encompassed all noise and vibration caused by the PLS structure, drive system and controls. Vibrations coming from the site locations or installation (external sources) are not included in the .001g noise limit requirement.

The drive system is designed to requirements for generating sinusoidal acceleration with a peak value of 1 g at frequencies ranging from 1 to 5 Hz. Maximum peak to peak travel of 20 inches occurs at 1 Hz and 1 g. Peak to peak travel at 5 Hz and 1 g is .8 inches. It was also required that the system be capable of either horizontal of vertical operation. (FIGURES 1 and 2).

DESCRIPTION OF THE PLS SYSTEM-MECHANICAL

The PLS consists of an air bearing supported, linear motor driven carriage. Trunnion mounted to the carriage is a capsule designed to accommodate a rhesus monkey. When operating vertically, the 650 lb. weight of the carriage and capsule are balanced by an air powered equilibration system. This system consists of 95 psi air applied to a 3" diameter piston. The piston and it's cylinder reside along the central axis of a 7" diameter by 84" long reservoir cylinder. Air is ported from the reservoir into the pressure side of the piston. A 1/2" diameter polished steel rod is connected to the piston. It passes through a seal and is, then, joined to a 1/4" diameter wire rope, routed over two sheaves and connected to the carriage. (FIGURE 2).

The reservoir in pressurized until the weight of the carriage and capsule are exactly balanced at the mid-travel position. The ratio of displaced volume to total system volume is such that the pressure balancing force variation (even for the 20 inch travel) is just over 2.5% at the travel extremes.

Similar air equilibration systems, which greatly ease motor control, have been used successfully for many years in aircraft motion simulators at Ames.

The capsule position on the carriage can be oriented about three independent axes. The monkey's behavior is monitored as it is taken through a

program consisting of many sinusoidal acceleration profiles with different capsule orientations in both the horizontal and vertical operating configurations.

The interior of the capsule can be completely blacked-out during motion generation or the cover over a large window directly in front of the subject's head can be removed. A point-light source is also used in the studies with the window covered.

Referring to FIGURE 3, the portion in the lower center of the figure is called the "backbone". It consists of two roughly 6"x12"x84" long, honeycomb structures bolted to the sides of the rectangular aluminum structure housing the equilibrator assembly. To the upper surface on each side of the backbone are bolted the hollow, ceramic rails (or ways) on which the air bearings ride. Also bolted to the backbone are the motor coil assembly, and the "foot" which supports the entire system when operating in the vertical mode. The carriage itself, which resembles a reclining capital "E" in cross section in the figure, is also a honeycomb structure. It is made in two, roughly "C" shaped sections for portability and joined along the centerline at assembly.

The ceramic rails were manufactures by Wilbank Division of Coors brewing company, at Portland, Oregon to specifications dictated by the PLS project engineers. Each rail consists of two, roughly 6" square by 1/2" wall by 84" long, aluminum oxide ceramic tubes. After firing, the sets of tubes were bonded together and all outside surfaces were ground to a 16-20 micro-inch finish. Once they are fired, the rails can only be machined using diamond tools. The very low "flying height" of the air bearings requires that the surfaces of the rails be extremely smooth and flat. Flatness, parallelism and perpendicularly were held to less than 0.001" over their entire length and the flatness, over any 6" length of the surfaces, was held to less than 30 millionths (0.000030) of an inch.

One half inch thick ceramic plates were bonded into place to close the tubes and a number of holes were bored through both the upper and lower surfaces so that tubular, ceramic inserts could be bonded into place for mounting the rails to the backbone.

The air bearings are state-of-the-art and operate with a flying height of only 0.0003". They are 5.6" in diameter and about 3" high. Two different configurations are used, ball joint mounted and rolling diaphragm mounted units (FIGURE 4). The two types of bearing assemblies are mounted in opposed sets. The ball joint mounted types establish the position of the carriage relative to the rails and the rolling diaphragm type permit tiny variations in the rail thickness. Both types allow for the minute variations in parallelism and perpendicularly. The minimum pressure required to float the carriage is about 25 psi. The optimum pressure, from the standpoint of system stiffness, is 56 psi.

Only the rail on the left side in FIGURE 3 is used to guide the carriage parallel to the motor axis (in the horizontal plane). Counterweights

approximately equal to the mass or these bearings are added to the carriage on the opposite side to maintain mass symmetry about the motor thrust axis.

Both rails are used to support the dead weight load in the horizontal operating mode and to react the overturning moment in both the vertical and horizontal modes.

A light weight gantry crane was designed, built and shipped to Russia with the rest of the equipment so that it could be used to unload equipment and to erect the 2000 pound PLS into the vertical operating position. The very tight schedule did not permit time even to try out this system at Ames. After a few bugs were ironed out, though, it worked very well at the Russian site. (FIGURE 5).

ELECTRICAL-ELECTRONIC

The drive system for the PLS consists of a brushless DC, 3-phase, linear motor, with a total stroke (displacement) greater than 20 inches; a 3-phrase, Pulse-Width-Modulate (PWM) power amplifier using an optical position encoder to generate the commutation switch-over commands; and an isolation transformer which could operate from 3-phrase 380 volt, 50 Hz supply or from a 3-phrase 480 volt, 60 Hz supply.

The motor is comprised of a configuration of eight coils and four permanent magnet assemblies (referred to as 'magnet tracks'). Two coils are aligned end-to-end in each magnet tract with four of these, two coil, assemblies arranged in parallel (FIGURE 6). The eight coils are each 5-pole, 3-phase units with a thrust coefficient of 20 pounds per amp.

The coil configuration was chosen to permit up to 640 pounds of sliding weight to be accommodates without causing over-heating problems. The 32 amps required to accelerate the 640 pound mass to one g requires only four amps per coil. With the heat load reduced it became possible to air cool the motors and to avoid water cooling and the operational problems that water would create.

The coil assemblies are constructed entirely of non-ferrous materials which permits operation without the 'cogging' effects which occur when a ferrous material enters or leaves the magnetic field surrounding a permanent magnet. This cogging effect can cause unwanted accelerations far in excess of the one milli-g smoothness required for the PLS's motion.

The coil assemblies are fixed and the magnet tracks are required to move as part of the carriage assembly payload. The coils weighed no more than a pound or so each and the magnet track assembly weighs over one hundred pounds, so from the standpoint of reducing payload weight it would have been better to reverse the situation. However, mounting the coils and moving the magnet tracks permitted hard wiring the stiff, heavy, power cables

and mounting the bulky air cooling lines rigidly to the backbone and this advantage was deemed far more important than the payload weight consideration.

The maximum displacement of the carriage is 20 inches peak-to-peak (at one g and one Hz, as mentioned earlier). The magnet tracks had to be long enough to permit this motion and still have the coils contained within a uniform magnetic field. The coil length is 12.4 inches and since there are two coils, end-to-end, in each magnet track, this requires a magnet track length of 48 inches. (FIGURE 6).

The control system for the PLS is a Digital Signal Processor (DSP) based, digital controller card located on the bus of an IBM compatible PC. The DSP controller card accepts position feedback from the carriage of the PLS, compares the coded position against the desired acceleration, and generates a command for the motor drive amplifier which will achieve the desired condition. The desired acceleration waveform is generated by the digital controller from the frequency and amplitude commands input by the operator to the control program for the particular test to be run. The actual waveform is obtained from the optical position encoder located on the carriage.

The controller operating software was successful in generating an operating scenario which allowed frequencies of 0.25 Hz to 10Hz to be generated at acceleration levels (g-levels) of 0.005 to 1.0 g, were run in Moscow to simulate space craft motions at the request of the Russian investigators. The PLS performed these loadings without any difficulty.

A separate, stand-alone safety system is used which continuously monitors the performance and operating conditions of the PLS and ensures that unsafe conditions are not allowed to persist. The safety system monitors motor coil temperature, air-bearing supply pressure, carriage position limits, carriage over-speed, power amplifier conditions, motor current limits and motor set-up procedures. Movement is not permitted to begin if any of these parameters are in an unsafe condition. If unsafe conditions occur during operation, the safety system will initiate a programmed shutdown while maintaining safe deceleration characteristics.

DESIGN PROBLEMS AND SOLUTIONS

The motor that was finally selected (manufactured by Trilogy Motor Company of Webster, Texas) was the third in a series of candidates for the job.

All linear motors have extremely high attractive forces between magnet and coil elements. In the standard, single interface configuration, used by the other motor candidates, it would have been required that these forces be reacted by the air bearings. At maximum motor thrust the attractive force can reach 3000#. This is approximately three times the design capacity of the bearings. An attempt was made to design around the problem using a second

319

motor candidate which promised slightly lower attractive forces, but without much success.

In the Trilogy motor design, the magnets are arranged on either side of the coil in a strong "U" shaped frame so that the attractive forces are balanced and there is no net reaction which must be carried by the air bearings. Needless to say, the introduction of this motor design was a real high water mark in the design process.

Like the motors, the rails are the third in a series of candidates designed to fill their function. The first set of rails was designed around the capabilities of an exclusive manufacturer of furnace brazed, aluminum foam composites. Each rail was to be made in three sections (because of the size limitation of the brazing furnace) and joined end-to-end. The air bearings were to operate on either side of the splice between two sections. Each section was to be ground and lapped to the final dimensions and finish. Unfortunately, the manufacturer of this system was unable to guarantee delivery of the finished product in a time frame which was compatible with the schedule for developing the PLS.

The second set of rails was based on an aluminum honeycomb composite structure. Finishing was to be done in the same manner as the first system, except that, without the constraint imposed by a brazing furnace, it was decided that they could be made in single, 84" long units. However, when the air bearing designer-fabricator was made aware of the change from three short sections to one long one, he strongly advised against it on the grounds that the grinding and lapping would be prohibitively time consuming and expensive. He recommended the ceramic rail approach which was finally developed for the PLS.

The extremely tight schedule for developing and checking out the PLS required that the motors and control system be tested in a parallel effort with the manufacture of the air bearings, rails and carriage structure. In order to do this a system (shown in FIGURE 7) was devised to simulate the configuration and mass of the PLS. This relatively inexpensive rail and ball bushing system was very stiff in the drive plane. Obviously, it couldn't be made nearly as smooth and friction free as the air bearing system, but it was adequate for motor check out and for control system and software de-bugging and refinement. The upside-down arrangement shown in the figure eased mounting problems and did not effect the performance.

IMPORTANT CONSIDERATIONS IN AIR BEARING DESIGN

The most important reasons for choosing air bearings over more conventional rolling or sliding bearings are as follows:

- To reduce friction
- To increase life
- To reduce mechanical noise

- To increase accuracy
- To provide the ability to dampen mechanical resonances

The first three items are guaranteed by the non-contacting nature of air bearings. With regard to the fourth item, air bearing systems have been designed for dimensional control down to the micron range. The last item was especially important to the development of the PLS because the requirement for light weight structures severely limited the amount of stiffness that could be built into the system. Air bearings can be designed with tuned internal cavities and restrictors such that particular frequencies can be selected or avoided. Space does not permit a detailed discussion of exactly how this is accomplished. A number of factors such as bearing gap and diameter, rail smoothness and flatness, laminar flow quality, flow restrictor type, etc., must be taken into account in this process.

In a system with near perfectly parallel rail surfaces, all bearings could be of the fixed gap (ball and socket) type. These systems are approximately 40% stiffer than the one used in the PLS. However, the requirement for relatively inexpensive, light weight rails demanded that they be less accurately made and, therefore, that a pre-loading device be used in half of the units as discussed earlier. The rolling diaphragm units are much easier to install and adjust than fixed spring type pre-loaders and have a much lower risk or resonance.

OPERATING RESULTS AT NASA-AMES

The PLS system was assembled at Ames and checked out completely for horizontal operation in July '92; two test subjects were run at 0.1, 0.3, 0.35 and 0.5 g-levels at all integer frequencies from 1 to 10 Hz. The PLS system was judged to perform satisfactorily and to meet the system test objectives even with a few deficiencies present.

The most obvious deficiency was the acoustic noise present when operating at high amplitude displacements and frequencies. However, since this acoustic noise was several hundred Hz's higher frequency than the data bandwidth, it was concluded it would not affect the test results and no further effort was made to eliminate it.

OPERATING RESULTS IN RUSSIA

The location of the operating lab in Russia was changed from the second floor room previously designated; it is on the ground floor and, fortunately, slightly larger than anticipated. The floor is not as rigid as the one at Ames. It is, however, much more rigid than the floor of any room on the second floor would have been. The larger room, (particularly the higher ceiling) reduced the acoustic coupling into the accelerometer used to measure the PLS's performance. The acoustic noise is approximately 10dB greater than that

321

achieve at Ames. A 15-20 dB increase in harmonic distortion was due two factors:

- The floor in Russia is much more compliant than the floor at Ames.
- The AC power line frequency of 50 Hz is less well conditioned and regulated than that at Ames.

The increase in harmonic content is more noticeable at 0.5 g level and higher; therefore 0.5 was selected as the maximum g- loading to be used. However, since the Russians did not want to expose the test subjects to g-levels higher than 0.5 g anyway, for fear of instrument failures, this limitation did not represent an additional constraint.

As mentioned earlier, the Russian investigators requested that the PLS be used to simulate the motion environment of the spacecraft in orbit. This required that it operated at frequencies as low as 0.25 Hz and at acceleration levels as low as 0.005 g. The PLS was not designed for, and was never operated (at Ames) at these, ultra-low g-levels and frequencies. However, the system performed without problems except that the accelerometer used to measure and display sled performance (but not used for control purposes) does not have sufficient dynamic range to measure accurately these ultra-low levels. The low frequencies did not degrade the performance of the accelerometer as did the low amplitude of acceleration. The accelerometer incorporates a nul-balance servo system which has DC (or zero Hz) frequency response. A different signal conditioner will have to be used if these ultra-low loading are to be repeated in an effort to obtain higher signal amplitude outputs to improve the signal-to-noise ratio.

RUSSIAN PROBLEMS IN RUSSIA

The machine and its support equipment were shipped to Russia in a total 16 large, heavy crates. Three weeks of intensive labor for three to five people was required in order to set up and check out the sled at the site. The change of location of the lab from the second to the ground floor helped, but certainly did not eliminate, the serious, hand-powered logistic problems. A method of lifting and transporting the heavy elements of the machine and the electronic racks and other heavy, bulky equipment had to be built and checked out in advance and shipped over with the machine (FIGURE 8). At the site, a method of providing about 40 feet of rolling surface from the nearest paved road to a door in the side of the building had to be devised so that equipment could be moved from the parking lot, staging area into the room which became the operating lab. (FIGURE 9).

Virtually everything that was required to set up and operate the equipment in Russia had to be shipped over. All tools, fasteners, adhesives, power cables, grout and mortar, even paper towels and toilet paper had to be sent over because these things are simply not available there. Even the

compressor to supply air to cool the motors and to float the air bearings had to be sent over because "shop air" was practically unheard of. Bottled air was available but in short supply and it was determined, in tests at Ames, that operating the PLS required one bottle of compressed air about every twenty minutes.

The compressor is powered by a 23 horsepower, gasoline engine. The noise and exhaust problems required that it be located outside the main building. The Russian winters and the possibility of losing the precious battery and fuel tanks required that the compressor be in its own, securable building. An assemble-in-place metal building had to be sent over with all the rest and a foundation had to be devised to set it up on. (FIGURES 10 and 11).

The lab at Ames was near clean-room quality. The room at the Institute for Biomedical problems in Moscow left a great deal to be desired from the cleanliness standpoint. The floor consists of terra cotta tile which had been applied directly to an earthen floor with mortar which varies from 1/2 to 1" thick. As a result, about 10% of the tiles are loose in their sockets and produce a constant stream of gritty dust as they are walked on. Repairs were made to the worst areas of the floor at the time the pads for mounting the machine were poured. However, the room remains dirty and dusty despite repeated wiping and vacuuming. This situation probably caused the air bearing "crash" experienced mid-way through the pre-flight test program. Replacement of the air bearing and repair of the ceramic rail was very expensive and difficult to accomplish without serious interference with the test schedule.

SUMMARY AND CONCLUSIONS

In spite of all the hazards and difficulties, the operation has been very smooth and, for the most part, trouble free. As of the present writing, all pre-flight testing has been completed.

The concern on the part of the Russian staff over the possibility of test subject instrumentation failure precluded testing in the vertical configuration. However, the machine was operated in that mode for the first time at the Moscow site and it performed extremely well. There is still a possibility that vertical testing will be performed after all other, post-flight tests are completed, since instrumentation failure at that point would not have disastrous consequences. Vertical operating capability will, no doubt, prove invaluable in future tests, both here at Ames and at other, more remote sites.
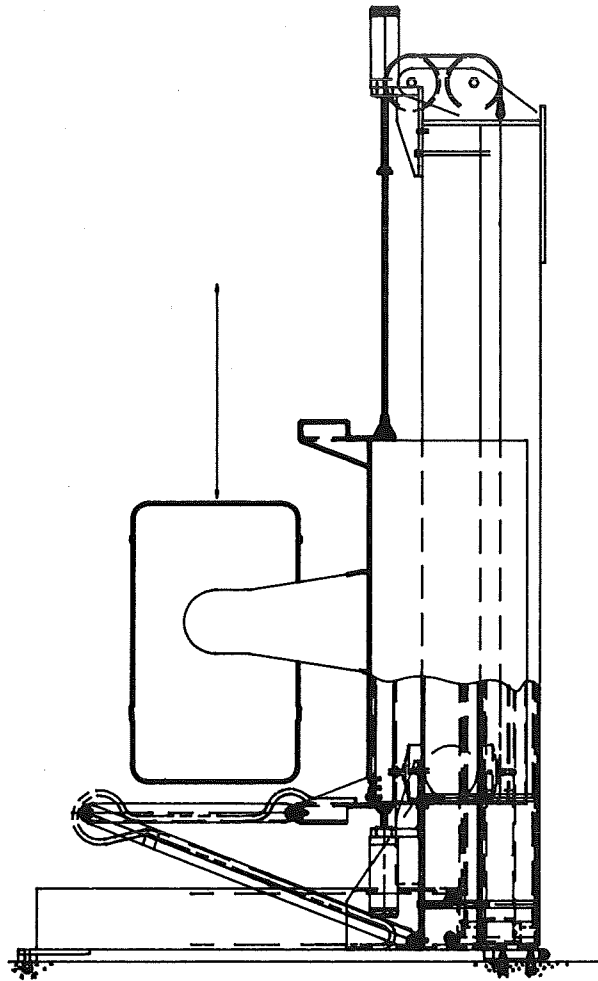
The space flight is currently scheduled to begin on December 29, 1992. And post-flight testing will begin immediately after the landing 10 to 14 days later.
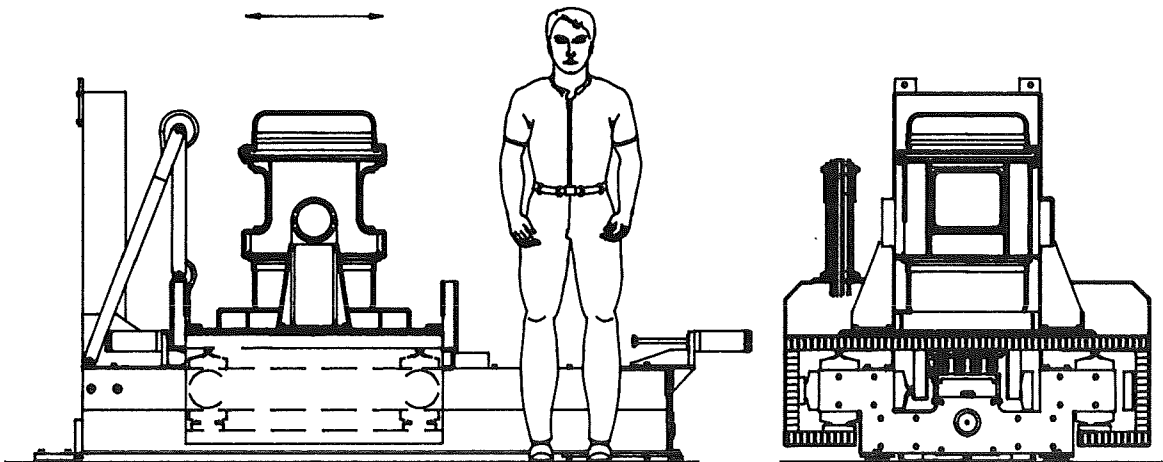
ACKNOWLEDGMENTS

VERTICAL

HORIZONTAL

FIGURE I   OPERATING CONFIGURATIONS

325

CARRIAGE TRAVEL ELEMENTS
(SIDE)

FIGURE 3   CARRIAGE TRAVEL ELEMENTS
(FRONT)

FIGURE 2   EQUILLIBRATION SYSTEM
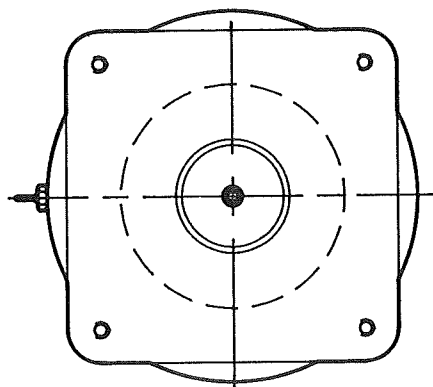
BELLOPHRAM TYPE
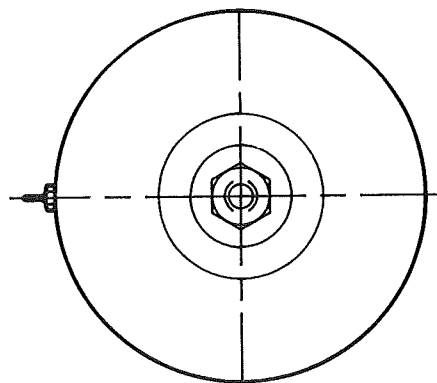
BALL-SOCKET TYPE
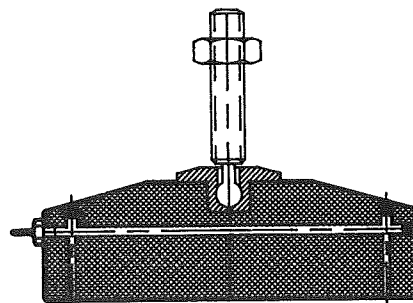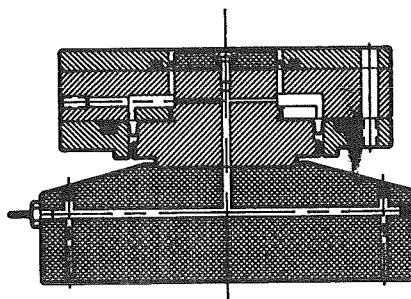
FIGURE 4   AIR BEARING CONFIGURATIONS

326

TABLE I
PLS MOTION

FREQ Hz	ACCEL g	DISPL IN-PK	VEL IN-PK/SE	
0.25	0.005	0.783	1.230	
0.3	0.01	1.088	2.050	
0.3	0.02	2.175	4.100	
0.5	0.005	0.196	0.615	ULTRA-LOW
0.5	0.01	0.392	1.230	RESPONSE
0.5	0.02	0.783	2.460	
0.5	0.04	1.566	4.920	
0.6	0.01	0.272	1.025	
0.6	0.02	0.544	2.050	
1	0.1	0.979	6.150	
1.5	0.1	0.435	4.100	
1.5	0.35	1.523	14.349	NORMAL
1.5	0.5	2.175	20.499	RESPONSE
5	0.1	0.039	1.230	
5	0.35	0.137	4.305	
5	0.5	0.196	6.150	
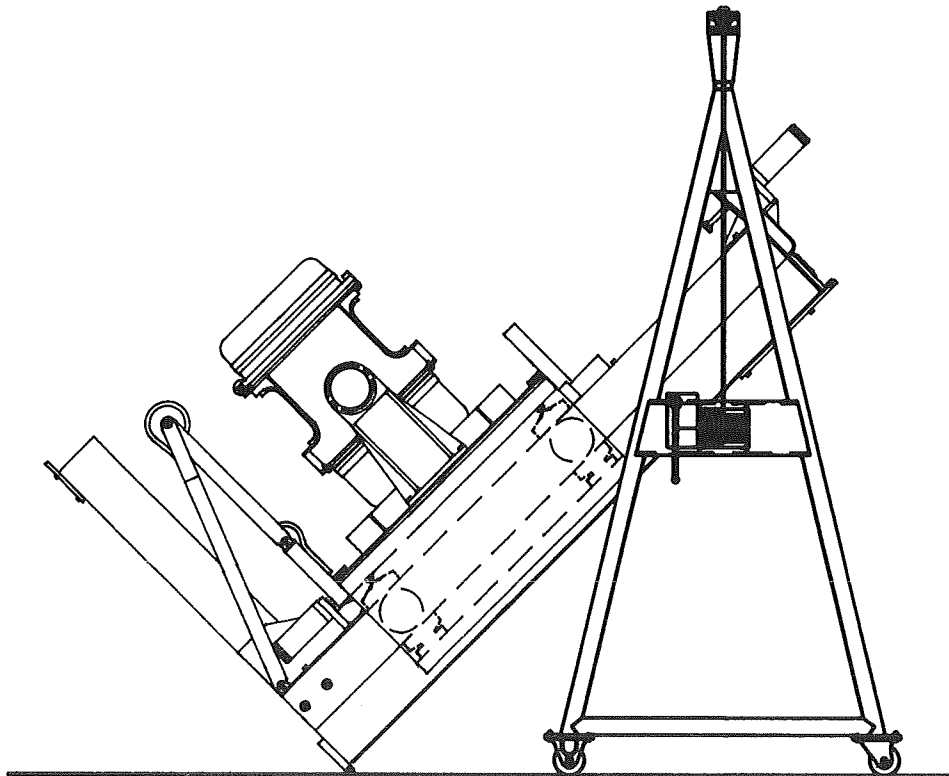
FIGURE 5   ERECTING FOR VERTICAL OPERATION

327

48" MAGNET TRACK LENGTH

SIDE VIEW   12.4"

(INDIVIDUAL COIL LENGTH)

FRONT VIEW OF SLED

FRONT VIEW OF MOTOR

COIL ASSEMBLY-ENCODER
SCANNER (FIXED TO BACKBONE)

MAGNET TRACK ASSEMBLY-
ENCODER BAR (MOUNTED
TO CARRIAGE)

STATIONARY ELEMENTS

MOVING ELEMENTS
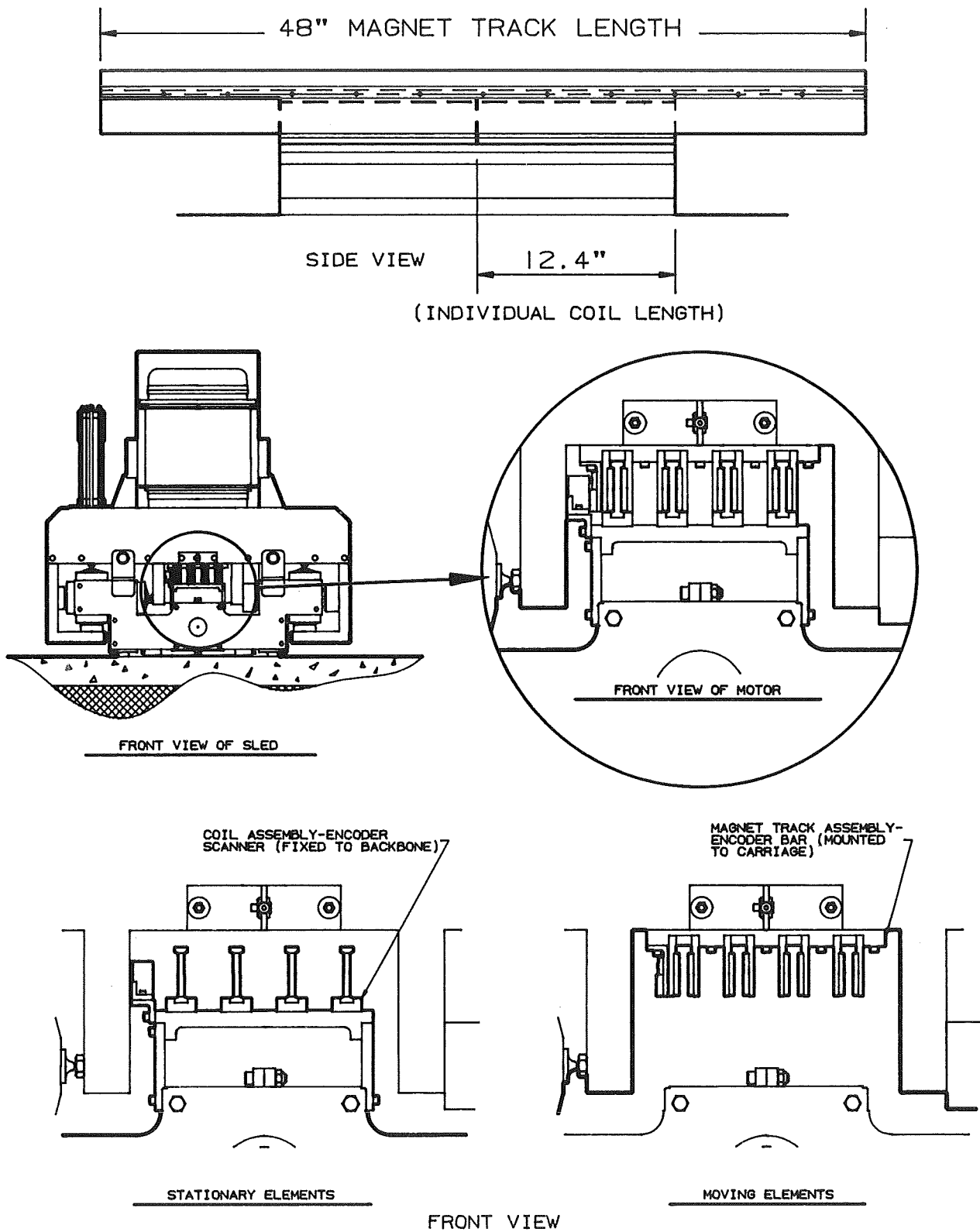
FRONT VIEW

FIGURE 6   MOTOR CONFIGURATION

328
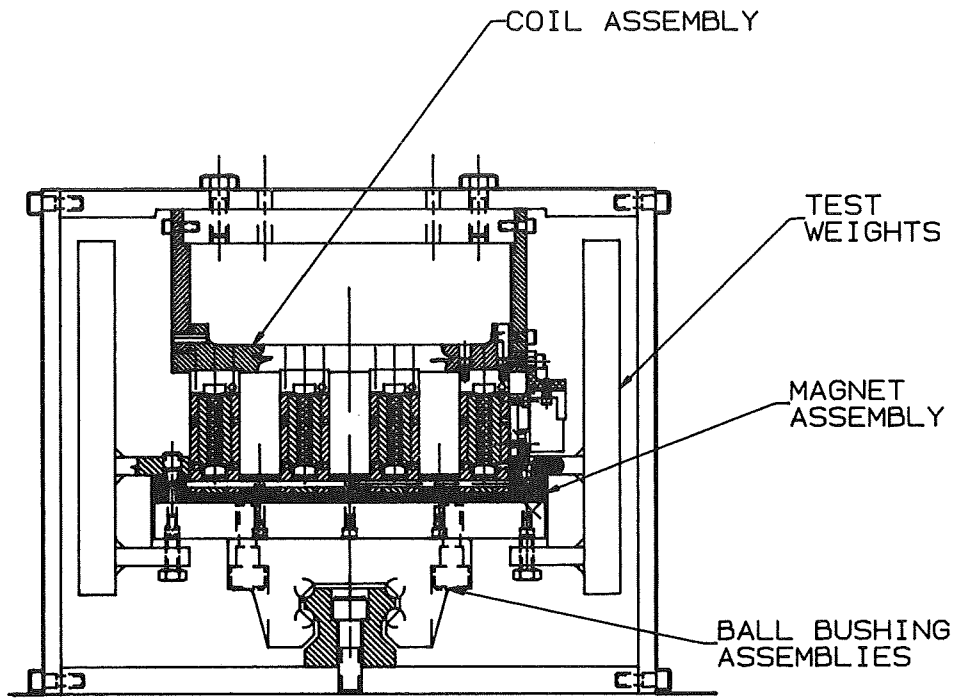
FIGURE 7   MOTOR CHECK-OUT CONFIGURATION

FIGURE 8   HANDLING EQUIPMENT

329

FIGURE 9   RUNWAY FROM PAVED ROAD TO BUILDING

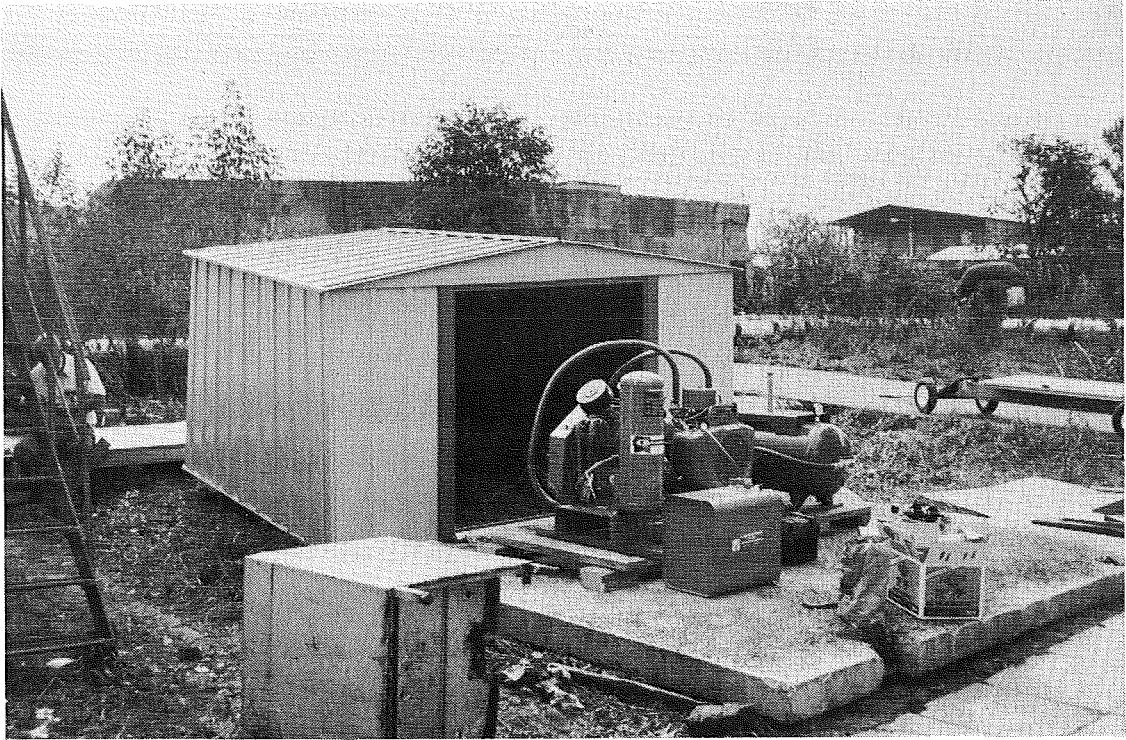FIGURE 10   TRANSPORTING SLABS TO RUNWAY AND COMPRESSOR SITES

FIGURE 11   COMPRESSOR IN PLACE ON SLAB

Laminar Flow Supersonic Wind Tunnel Primary Air Injector

Brooke Edward Smith [*]

Abstract

This paper describes the requirements, design, and prototype testing of the Flex-Section and Hinge Seals for the Laminar Flow Supersonic Wind Tunnel Primary Injector. The supersonic atmospheric Primary Injector operates between Mach 1.8 and Mach 2.2 with mass-flow rates of 62 to 128 lbm/s providing the necessary pressure reduction to operate the tunnel in the desired Reynolds number (Re) range.

Introduction

Research in supersonic flow has been reawakened with the recent interest in the commercial supersonic transports such as the High Speed Civil Transport (HSCT). Creating low-disturbance, laminar flow at supersonic speeds inside a wind tunnel has been elusive. The Laminar Flow Supersonic Wind Tunnel (LFSWT) at NASA-Ames Research Center will support supersonic laminar flow control research using a radically new design approach. Most wind tunnels, regardless of speed have either a blow-down or recirculating configuration. Blow-down tunnels are normally limited by the supply volume of compressed air. Recirculating supersonic wind tunnels are usually pressurized and require heat exchangers to remove the adiabatic-compression-temperature rise during each circuit. In addition, temporal and spatial turbulence is also a problem.

The LFSWT at NASA-Ames Research Center is a radical departure from existing wind tunnel designs. The LFSWT is a continuously operating, quiet flow, supersonic wind tunnel utilizing a nonspecific centrifugal compressor, settling chamber, nozzle, test section, two atmospheric air injectors, and the Center's existing 207 bar (3000 psi) air system (Figure 1). Most supersonic wind tunnels operate at higher than atmospheric

---

[*] NASA/Ames Research Center, Moffett Field, CA

333

pressure and all are "noisy" or high disturbance wind tunnels. Quiet supersonic wind tunnels are defined as tunnels with pressure fluctuations of 0.05% or less in the test core.[1] Wind tunnels are described by the size of the test section. The LFSWT is 20.32 cm (8 in.) high by 40.64 cm (16 in) wide. Mass-flow rates for the test section range up to 9.52 kg/s (20 lbm/s) with speeds ranging from Mach 1.6 to Mach 2.5. Reynolds numbers (Re) will range from one million to five million. To achieve the low end of the desired Re, the tunnel stagnation or total pressure (P_O) must be below the minimum exit pressure (P_E) at the throat. The stagnation pressure is the pressure created by bringing the flow to rest isentropically. This means the LFSWT must operate with a compression ratio uniquely less than unity (P_O/P_E down to 0.6251 with Re=1 million per foot at $P_O = 0.34$ bar (5 psia)).[1] To achieve a lower stagnation pressure than the capability of the compressor, two supersonic air injectors were utilized down stream of the test section. Taking advantage of extremely high mass-flow capability of the compressor (much higher than the 20 lbm/s required from the test section), two full-scale, supersonic ambient air injectors, Primary and Secondary, are used in the LFSWT. Supersonic air injectors create jets of low pressure, high energy air downstream of the test section. Air injectors are designed in pairs, opposite of one another. The low pressure created downstream reduces the Reynolds number and test section exit pressure into the desired range. Thus, by using two air injectors, the tunnel operates at lower pressure than the downstream indraft air compressor is capable of achieving. The first injector has a variable mass-flow and mach number. The second injector has a fixed geometry, a constant mass-flow of 95.2 kg/s (200 lbm/s), and an exit of Mach 2.0.

This paper will address the unique design requirements, full scale prototype development, and consequent design solutions for the Primary Injector (Figure 2).

The Primary injector is composed of two pairs of four moving component sub-assemblies; the Slider Assembly, the Flex-Section, the Contoured Throat Plate, and the Hinge Plate. The Contoured Throat Plate is actuated

by two sets of ball screws. One set of hand-operated ball screws controls the injector nozzle throat and the other set actuates the nozzle exit. Each ball screw set can be moved independently of the other. Moving the throat ball screw set varies the mass-flow rate through the nozzle. Moving the nozzle exit ball-screw set varies the exit velocity. The system was designed to be infinitely adjustable and to be repeatable within the design criteria described below. Infinite adjustment required that only one end of the mechanism assembly be fixed. The exit end of the Hinge Plate is attached to the tunnel side walls via an 88,960 N (20,000 lbf) radial capacity hinge. As the Contoured Throat Plate is positioned from maximum mass-flow rate and Mach number to the minimum mass-flow rate and Mach number, the Hinge Plate oscillates through ± 20 °. The Flex-Section is fixed to both the Contour Throat Plate and the Slider Assembly. The Slider Assembly allows only longitudinal motion and has a low pressure, sliding seal. When changing the nozzle and exit positions of the Primary Injector, the Contour Throat Plate moves longitudinally and rotates simultaneously. The Flex-Section and Slider Assembly combine to form a flexible, continuous duct through out all design parameters.

Overall Design Parameters

Speeds in the Primary Injector nozzle range from Mach 1.8 to Mach 2.2 while the injected mass-flow range changes from 30.46 kg/s to 60.92 kg/s (64 lbm/s to 128 lbm/s). Inside the injector and mixing region, the flow is unstable and, consequently, structural vibrations are high. Nozzle and exit geometries must be repeatable to within 0.136 mm (0.005 in). To insure accurate and repeatable measurements of the throat and exit geometries, optical encoders coupled to eight (four each side) zero-backlash ball screws are used for positioning. External pressure loads range from 0.136 bar (2 psia) at the two inlets to 0.92 bar (13.5 psia) in the mixing region. Due to the low internal pressure, all hinge and flex joints and sliding plates must be leak-tight and maintenance free in all positions. Slight leaks perpendicular to the flow will severely decrease injector performance. Pressure loads created during operation deflect the 50.8 mm (2 in.) thick Side-Walls so that moving the Contour Throat Plate is

335

not possible. The structure required for throat and exit adjustment during operation was not feasible.

Sealing Requirements

To seal the sides of the Slider Assembly, Flex-Section, Contour Throat Section and Hinge Plate a continuous, longitudinal, 1/4 nominal, buna-N O-ring was used on each side. A simple sliding motion study determined that the O-ring would not fail by twisting longitudinally inside the O-ring gland during repositioning (Figure 3).

Design/Prototype Development

Development and prototype testing concentrated on the Flex-Section and the Hinge Joints. The Flex-Section is between the Slider Assembly and the Contour Throat Plate. The hinge joints are between the Contour Throat Plate and the Hinge Plate and between the Hinge Plate and Bridge Plate.

Flex-Section Development

The Flex-Section Prototype was made from 0.81 mm (0.032 in) thick C1095 spring steel and a medium viscosity, adjustable durometer polyurethane (Figure 4). The urethane was cast to the spring steel to form a O-ring gland for the longitudinal O-ring seal. Speeds in the Flex-Section begin at Mach 0.3 and terminate at Mach 0.8 just before critical flow in the Contour Throat Plate. Bend testing of the prototype far beyond the operating range of motion yielded no problems. Two changes were made to the final design. First, the O-ring gland was moved downward until the bottom of the O-ring gland was formed by the spring steel. Urethane formed the other two sides. For the second modification, a 6.3 mm (0.25 in.) layer of polyurethane was bonded to the back side of the spring steel to dampen and lowered the spring steel's natural frequency (Figure 5).

336

Hinge Seal Development

Two zero-leak hinge joints are required. Each hinge joint must seal across the axis of hinge motion and seal longitudinally, using the linear O-ring seal. The range of motion for the hinge is $\pm 20°$ past center.

Three hinge concepts were tested and two failed. As with many great ideas, the translation from the concept/design phase to the testing phase was not always satisfactory.

Hinge Concept No. 1

The initial series of three prototypes only used the polyurethane rubber to form the flexible hinge section (Figure 6). (This idea is similar to the living hinges on plastic cases). If this concept had worked an O-ring gland for the longitudinal O-ring would have been cast into the hinge. Two of the prototypes had a triangular hinge joint design. The angle was determined by the maximum combined stress from the shear and tensile properties of the polyurethane material. Spacing between the metal parts was varied to determine the joint shear strength versus bending resistance. The third prototype had two straight joints perpendicular to the flow surface.

Test Results

Bending tests were performed using the Material Test System MTS 810 and Graphtec X Y Recorder. Force verses deflection graphs were plotted. The joint deflection was limited to 20 degrees. The first and second prototypes delaminated around the tip of the radiused triangle. Delamination and tears in the material were caused by strain over too little material. The third prototypes did not fail visibly, however the material continued to relax with sustained loading. Internally, the molecular bonds were breaking and would eventually fail, similar to an old rubber band. Shear tests on the joints were not performed.

Hinge Concept No 2.

The second series of prototypes was a combination of two ideas. A mechanical hinge on the top of the joint would eliminate the shear and some tensile loading from the polyurethane hinge seal. Since seal strength, other than pressure loading, was not important, three more hinge prototypes were fabricated with 60 durometer (softer) polyurethane instead of the 80 durometer polyurethane used in the first series (Figure 7). Installing the hinge on the top of the joint forced the seal to stretch outside the neutral axis of the seal. The trapezoidal seal shape was defined by a line from the center point of hinge action to the sealing edge. Calculations based on the allowable strain for the polyurethane determined the joint angle. To reduce the tensile forces required to open the hinge and compression forces required to close the hinge, two composite hinge seals were fabricated. The third seal was solid polyurethane. The Contoured Throat Plate and Hinge Plate material was changed from A-36 steel to 6061-T6 aluminum to reduce part machining time. The first prototype contained trapezoidal foam cores, each 3 inches long. Between the soft foam cores, a solid 12.7 mm (0.5 in.) rib of urethane material remained. The trapezoidal foam cores were smaller than the joint and surrounded by a 9.5 mm (0.375 in) thick urethane layer. The ribs helped restrain the thin seal membrane from folding into the air flow when the hinge joint was closed. The foam also helped reduce the actuation forces during operation. The second prototype contained seven, 9.5 mm (0.375 in.) diameter, 30 durometer, closed cell, neoprene cords strung laterally along the joint in a trapezoidal formation. Again the softer material reduced the actuation forces and stress on the joint during fabrication. The last prototype was solid, 60 durometer polyurethane. Each sample was oven cured to full strength before testing.

Test Results

The most promising design, the trapezoidal foam core prototype was tested first. Again the MTS 810 and graphic recorder test apparatus was used and the same parameters of force versus deflection were plotted. The

prototype delaminated along the outer flow side. However, the foam core concept seemed to restrain the flow-side membrane from popping out into the air flow when the joint was compressed during closing. The second, neoprene cored prototype did not delaminate. Actuation forces were not excessive. However it was the second prototype that called to our attention another design flaw. Because of the off-center hinge point, the strain in the bottom fibers was the highest. This caused the bottom corners of the seal to draw inward, away from the longitudinal O-ring seal on the side walls. This effect was created by a volumetric, (Poisson's) contraction due to the strain in the bottom fibers. The third, solid prototype failed at both the joint and in the middle of the seal. In all three cases, the stresses and strains were well within the manufacturer's recommendations. If the polyurethane hinge seal was to be used, the maximum strain had to be no more than 25 percent of the strains we tested.

More Design Concepts

Three more design concepts were considered. In each we tried to overcome the limitations of the material and meet the design criteria of 20° in each direction. The design concepts became more and more complicated requiring more prototype testing.

Final Design

The final design was a radical departure from the previously described hinge seals. Prototype testing of the Flex Plate inspired a similar design approach for the hinge seals (Figure 8). Two U-shaped pieces of stainless steel sheet with cast O-ring glands provided the sealing around both hinges. The hinge design was mechanically limited by the amount of travel in the downward position. The upward rotation was not directly limited, however, the seal sheet could only withstand so much rotation without permanent deformation. The sheet thickness was a compromise between buckling strength and bending stress. To eliminate the large bending stresses, the sheets were rolled to the average bend radius, thus dividing the required deflection. This modification did, however,

complicate the mold required to cast the polyurethane O-ring gland onto the sheet. To confirm the seal design and the influence of the polyurethane on buckling strength, a Patran/Nastran computer analysis was performed. The bucking strength was only increased by 2 psi with the polyurethane added.

Conclusion

The final design of the key sealing areas in the Primary Injector included three flexible composite seals. Each seal had an O-ring gland cast into each side to provide longitudinal sealing of moving parts. All parts are in fabrication at this time. The first test will be an F-16XL Aircraft wing in support of the Supersonic Laminar Flow Control (SLFC) studies.

Lessons Learned
1) Keep the design simple.
2) If you have a novel solution to a unique problem, test it first.
3) Simple models can be made to test and confirm ideas.
4) If your solution doesn't work the first time, don't take it too seriously. (Don't give up!!)
5) Keep the project in perspective.

Acknowledgments

The author wishes to thank each member of the LFSWT design team; Owen Greulich, Gary French, Victoria Matheny, Bob Meneely, Robert Press all members of the NASA-Ames Research Center Facilities Engineering Group. I also want to thank Jon Eastlund and his drafting team at Bentley Engineering Company.

References

1   Wolf, Stephen W.D. , Laub, James A., King, Lyndell S., Reda Daniel C. "Design Features of a Low-Disturbance Supersonic Wind Tunnel for Transition Research at Low Supersonic Mach Numbers." Paper 2B, European Forum on Wind Tunnels and Wind Tunnel Test Techniques. September 14-17, 1992.
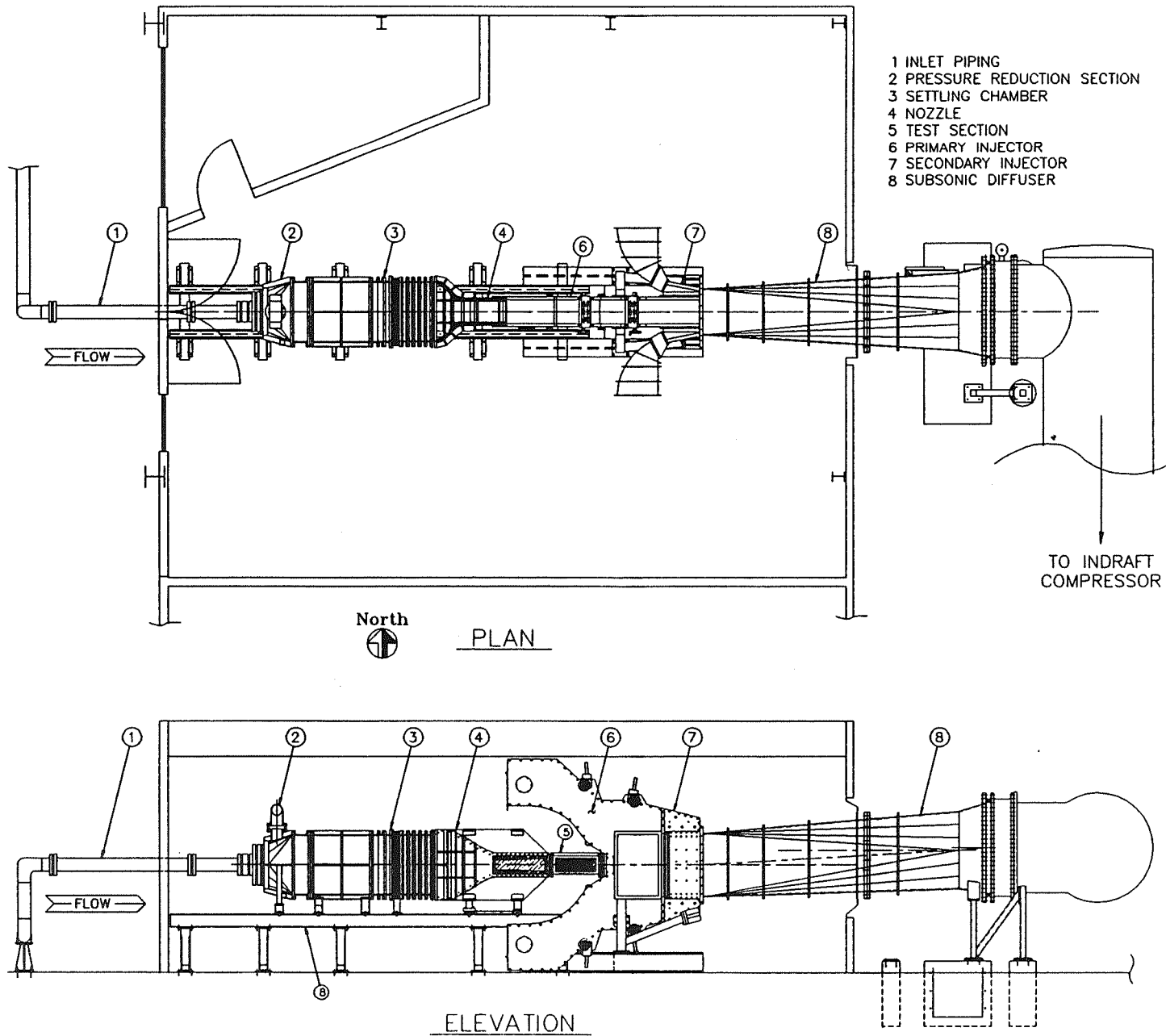
1 INLET PIPING
2 PRESSURE REDUCTION SECTION
3 SETTLING CHAMBER
4 NOZZLE
5 TEST SECTION
6 PRIMARY INJECTOR
7 SECONDARY INJECTOR
8 SUBSONIC DIFFUSER

FLOW

TO INDRAFT
COMPRESSOR

North

PLAN

FLOW

ELEVATION

Figure 1. Laminar Flow Supersonic Wind Tunnel (LFSWT)
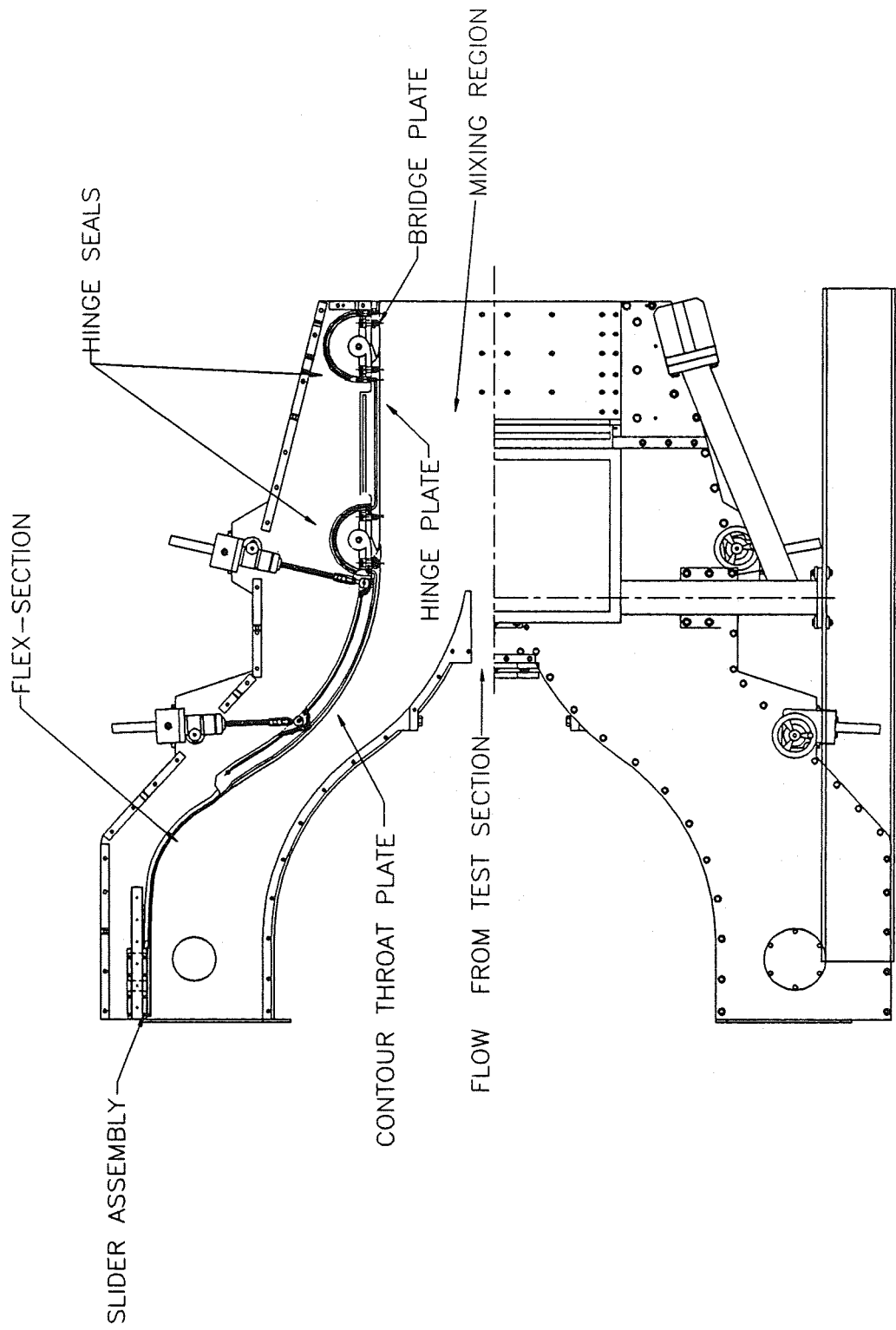
Figure 2. Primary Injector

HINGE SEALS

BRIDGE PLATE

MIXING REGION

FLEX-SECTION

HINGE PLATE

CONTOUR THROAT PLATE

FLOW FROM TEST SECTION

SLIDER ASSEMBLY

LONGITUDINAL O-RING SEAL
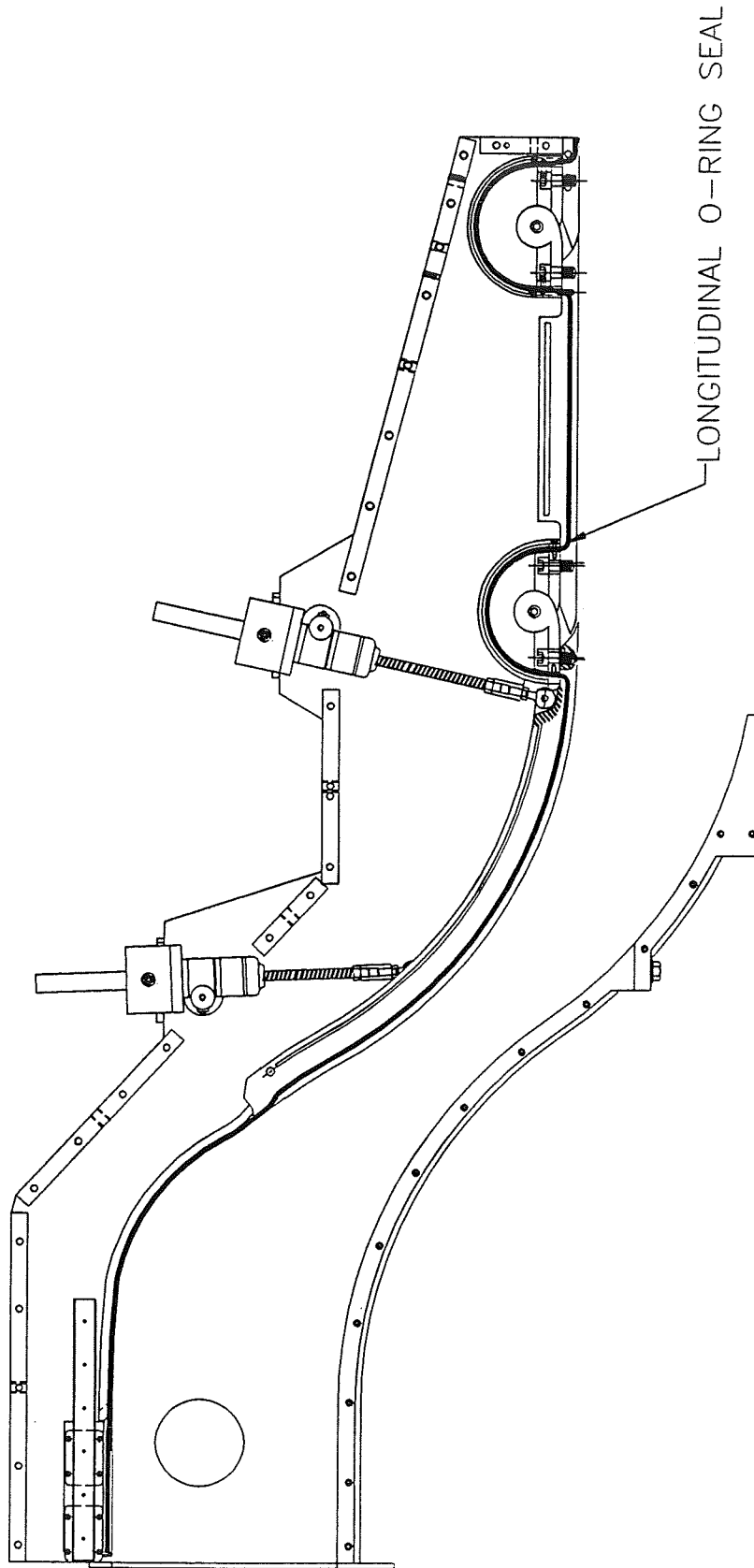
Figure 3. Longitudinal O-Ring Seal
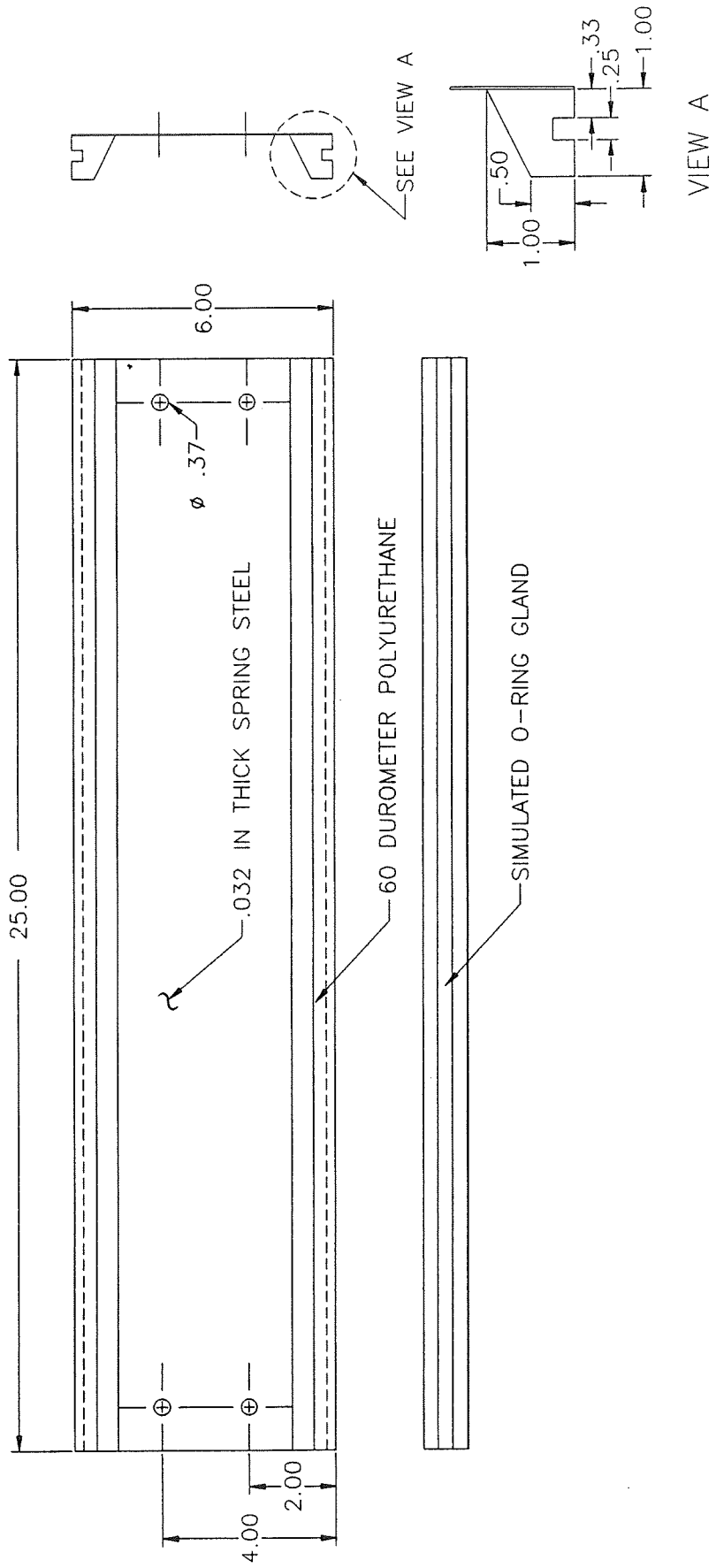
Figure 4. Flex-Section Prototype

SEE VIEW A

VIEW A

.33
.25
1.00
.50
1.00

6.00

Ø .37

.032 IN THICK SPRING STEEL

60 DUROMETER POLYURETHANE

SIMULATED O-RING GLAND

25.00

2.00
4.00

VIEW B

SECTION A-A

SEE VEIW B

CONTOURED
THROAT PLATE

SLIDER PLATE

¼" NOMINAL
O-RING GLAND

FLOW

345
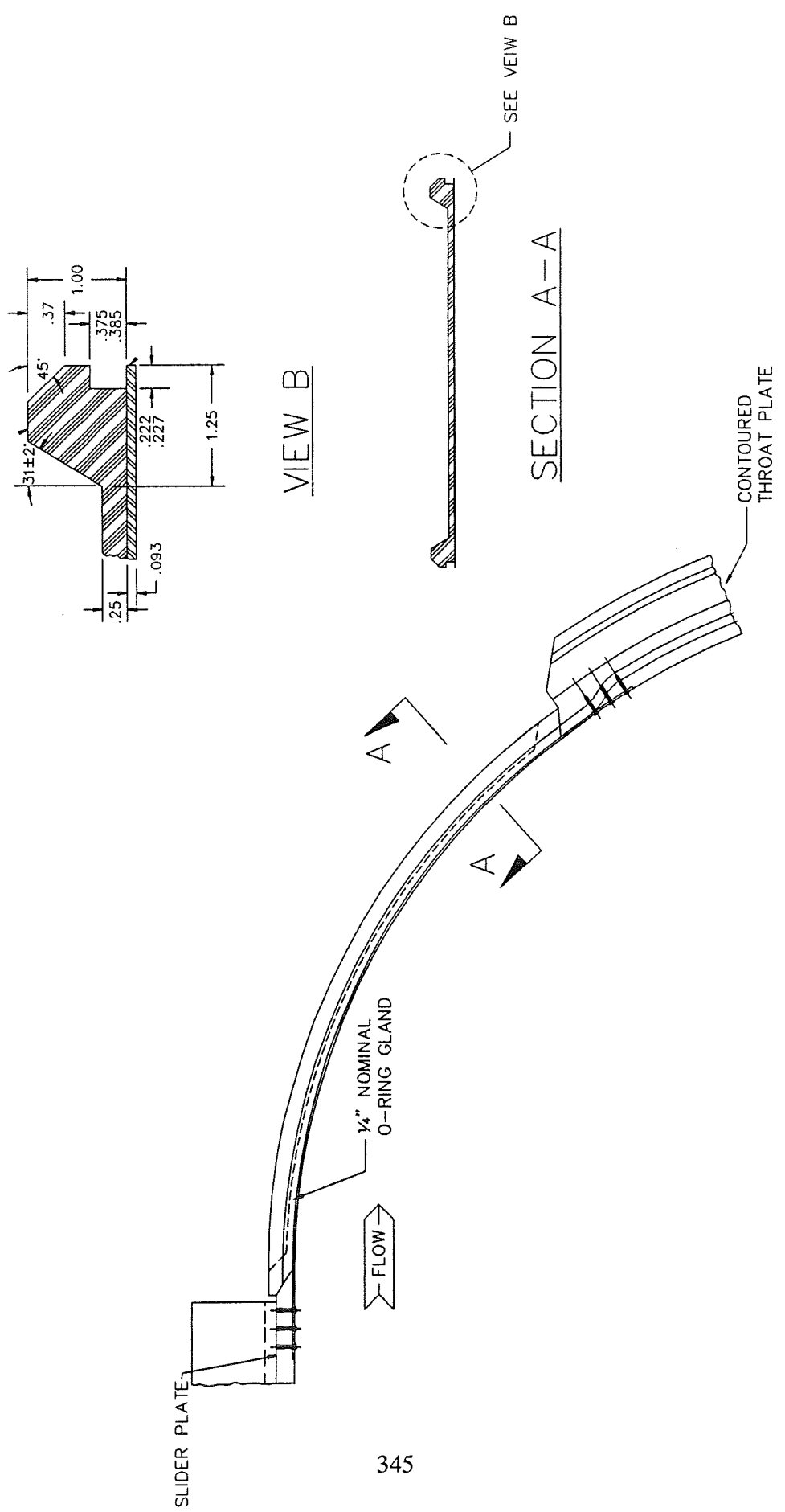
Figure 5. Flex-Section Final Design

POLYURETHANE

A-36 STEEL

4.0

1.5

.12 RADIUS TYP.

71.0°
TYP.

4.0

2.0

4.0

SEE VIEW B

PROTOTYPE NO. 2

POLYURETHANE

A-36 STEEL

4.0

1.5

.12 RADIUS TYP.

4.0

2.0

4.0

SEE VIEW A

PROTOTYPE NO. 3

AREA OF DELAMINATION
AND TEARS

VIEW B

POLYURETHANE

A-36 STEEL

4.0

AREA OF DELAMINATION

1.5

.12 RADIUS TYP.

71.0°
TYP.

4.0

3.0

4.0

PROTOTYPE NO. 1

VIEW A
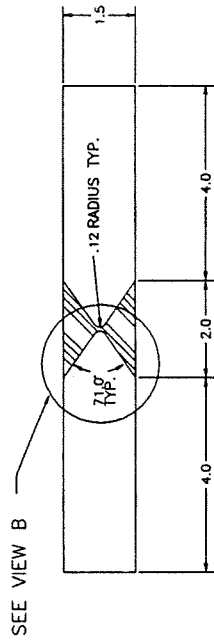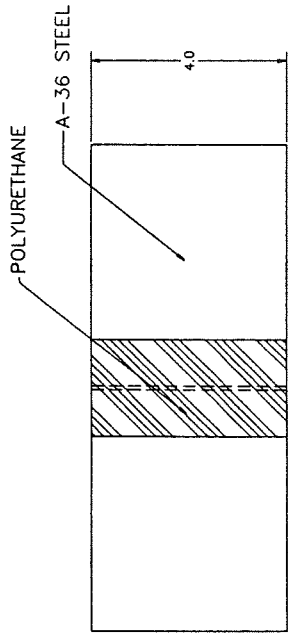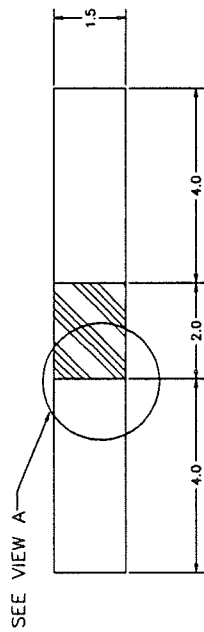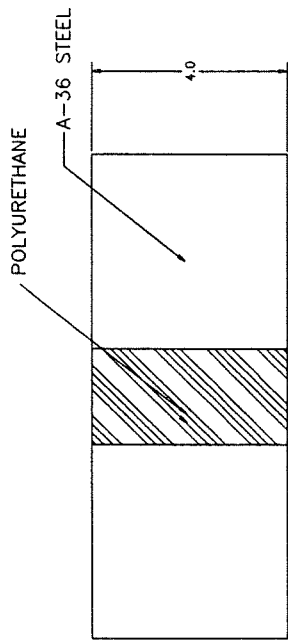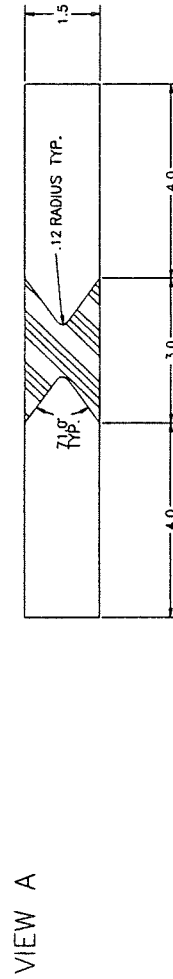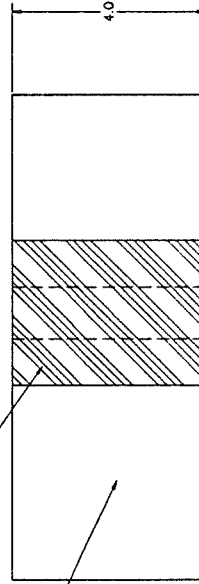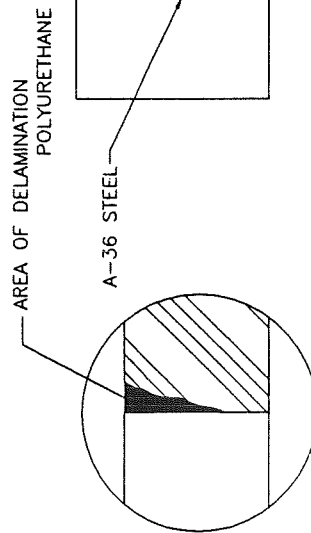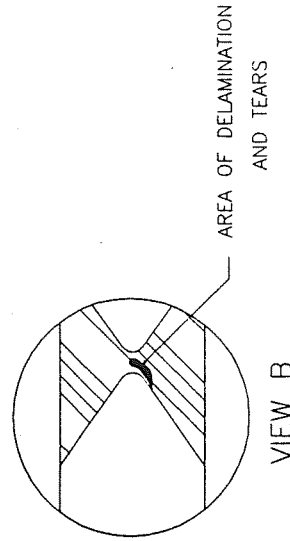
Figure 6. Hinge Concept No. 1

346
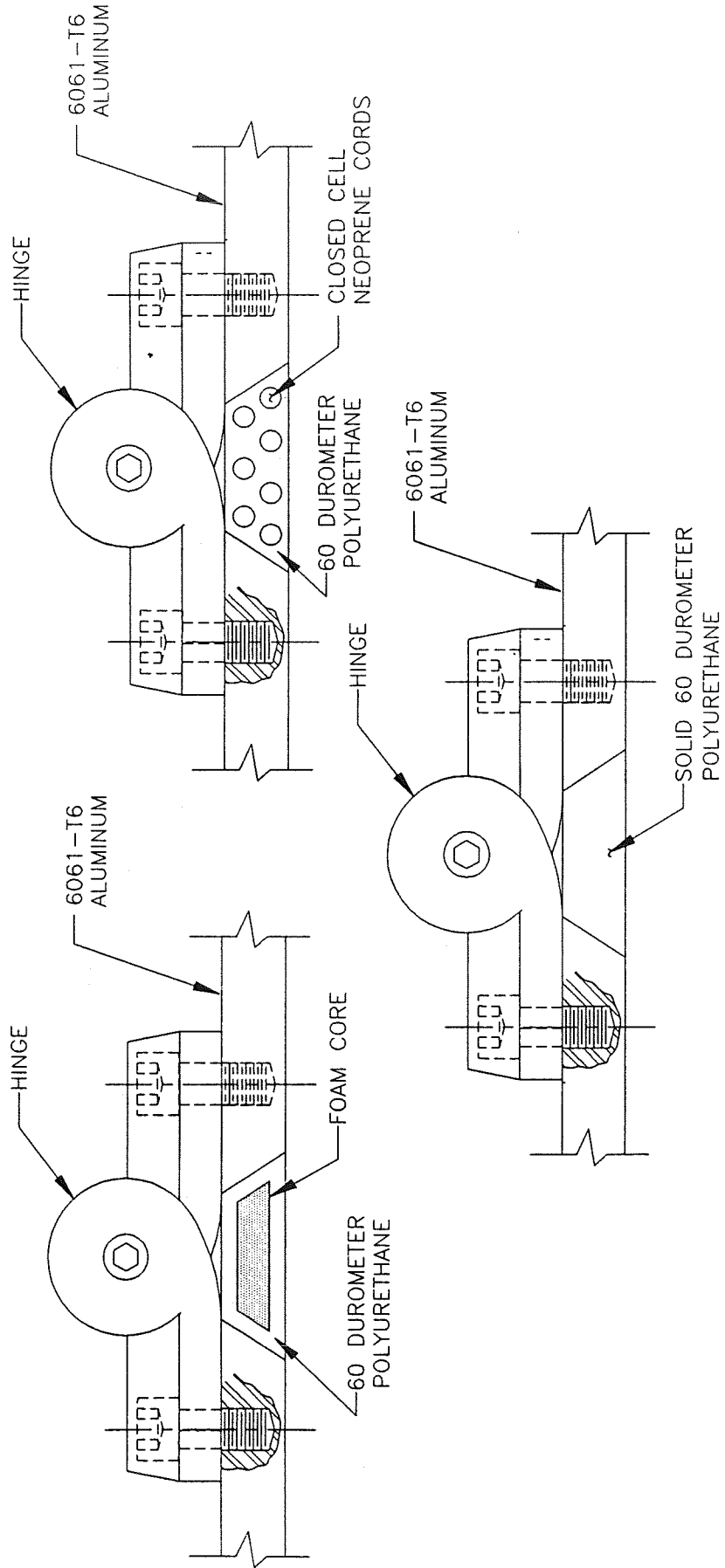
Figure 7. HINGE CONCEPT NO. 2

Labels in figure:
- 6061-T6 ALUMINUM
- HINGE
- CLOSED CELL NEOPRENE CORDS
- 60 DUROMETER POLYURETHANE
- 6061-T6 ALUMINUM
- SOLID 60 DUROMETER POLYURETHANE
- HINGE
- 6061-T6 ALUMINUM
- HINGE
- FOAM CORE
- 60 DUROMETER POLYURETHANE

347

FLEX SEAL WITH
URETHANE O-RING GLAND

LONGITUDINAL
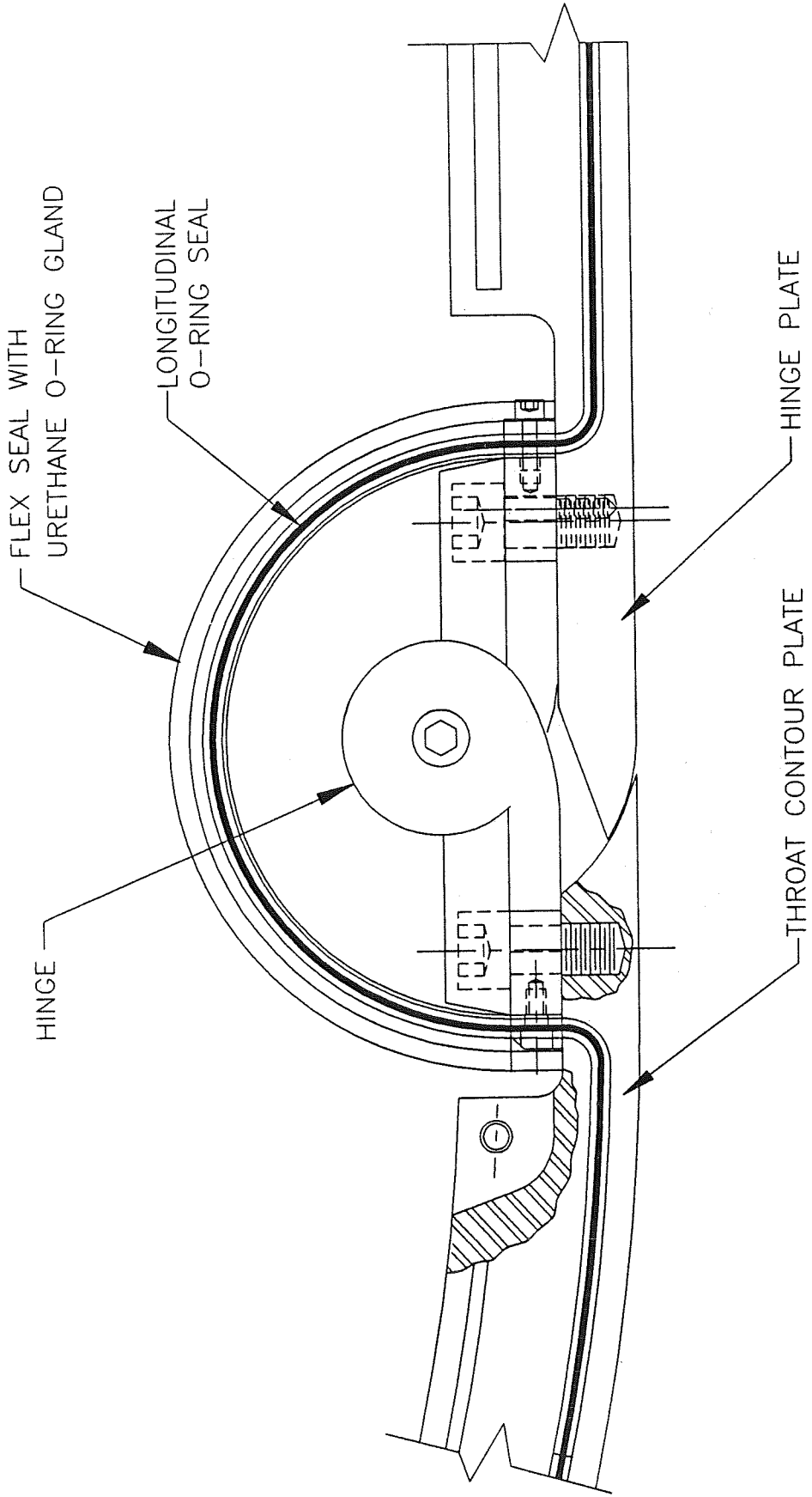O-RING SEAL

HINGE PLATE

HINGE

THROAT CONTOUR PLATE

Figure 8. FINAL HINGE SEAL DESIGN

348

Design and Test of Electromechanical Actuators for Thrust Vector Control

4/34687

J. R. Cowan* and Rae Ann Weir*
National Aeronautics and Space Administration
Marshall Space Flight Center

ABSTRACT

New control mechanisms technologies are currently being explored to provide alternatives to hydraulic thrust vector control (TVC) actuation systems. For many years engineers have been encouraging the investigation of electromechanical actuators (EMA) to take the place of hydraulics for spacecraft control/gimballing systems. The rationale is to deliver a lighter, cleaner, safer, more easily maintained, as well as energy efficient space vehicle. In light of this continued concern to improve the TVC system, the Propulsion Laboratory at the NASA George C. Marshall Space Flight Center (MSFC) is involved in a program to develop electromechanical actuators for the purpose of testing and TVC system implementation. Through this effort, an electromechanical thrust vector control actuator has been designed and assembled. The design consists of the following major components: Two three-phase brushless dc motors, a two pass gear reduction system, and a roller screw, which converts rotational input into linear output. System control is provided by a solid-state electronic controller and power supply. A pair of resolvers and associated electronics deliver position feedback to the controller such that precise positioning is achieved. Testing and evaluation is currently in progress. Goals focus on performance comparisons between EMAs and similar hydraulic systems.

INTRODUCTION

Recent studies have shown that hydraulic actuation systems cost the space program many valuable hours for tests, maintenance, and repairs. During the typical turnaround cycle for a space shuttle orbiter and its integrated systems, many maintenance personnel inspect the entire vehicle, repairing hydraulic leaks and examining lines, while at the same time qualifying each hydraulic unit for its next flight. Qualification alone necessitates extensive hours, or about 10 per cent of the total inspection time. Estimates submit that fully electric orbiters could possibly be readied for flight ten days earlier than

349

hydraulic ones. These problems affecting mission readiness have prompted investigations by NASA into alternate actuation systems for use in existing space applications, as well as new programs soliciting heavy lift TVC technology. Some reservations of implementing electric TVC systems into these very new programs overshadow the fact that EMAs have been in service for more than thirty years. A good example of an early EMA technology application is the Redstone Missile in the 1950's. In this system, an electrical chain drive actuated air fins for aerodynamic steering. As early as 1972, NASA engineers expressed concern over the space shuttle's hydraulic system due to difficult maintainability and some minor inefficiencies. In the last few years, many advances in the fields of power electronics and motor technology have renewed interest in the use of EMAs for both low and high power actuation in space applications. In 1987, the Control Mechanisms and Propellant Delivery Branch at MSFC designed and tested an electromechanical propellant valve actuator applicable to the space shuttle main engine. It performed as well as, and in some areas better than its hydraulic counterpart. Therefore, realizing the potential what this new science can provide for space vehicle actuation systems, MSFC has undertaken this project to explore the full potential of EMAs. After fine tuning of the hardware and system, implementation of a family of EMAs designed for use in multiple applications will follow.

DESIGN

The electromechanical thrust vector control (EMTVC) actuator was designed to meet basic loading requirements necessary to support future heavy lift space vehicles. These requirements are given in Table 1. The primary mechanical components of an EMTVC actuator can be seen in Figure 1. These components are, 1) some type of electric motor, 2) if needed, a gear train, and 3) a linear screw. Figure 2 shows an assembly drawing of the EMTVC.

Table 1. Basic Design Requirements

Dynamic Load Capacity: 35,000 lb
Linear Velocity: 5 in/sec
Maximum Stroke: +/- 6 in
Control: Two Channel Redundant
Bandwidth: >3.0 Hz
Linearity: < 2%
Accuracy: < 0.050 inch

350

I. Motors

Several types of motors were considered for this application. Through careful deliberation and various trade studies, three-phase, permanent magnet (PM), brushless, direct current (DC) motors containing a large number of poles were chosen. A fundamentally sound design and combined overall characteristics helped finalize this choice. PM, brushless motors have high torque-to-weight ratios and high torque capability at low speeds. They are able to operate at high speeds with moderately linear output (torque versus speed) curves. The most significant feature of the brushless PM motor that proves most beneficial to the actuator is its ability to integrate into a redundant single shaft system. In this arrangement, a shorted winding proves to be less of a problem than would be expected. A shorted winding in a redundant electric motor system forces the fully operational motor to overcome drag torque produced by the failed motor. To overcome this drag torque, or generator effect, requires extreme overdesign in motor sizing unless a type of clutching device is used to separate the systems. Figure 3 shows important data necessary to the design of the entire motor scheme. As can be seen by the curve, at higher speeds drag torque decreases sharply. This decrease in drag torque occurs due to the multiplicative property that signal frequency has upon the inductive element in an electric motor. More poles in the motor make available a larger reactive component of the impedance, which increases the total impedance. Thus, a smaller current through the motor winding is created and, therefore, less power to cause drag on the system. Others have done work using this theory and have proven it with credible results.

Characteristics of the motor used are:
- Type: Three-phase brushless dc
- No Load Speed: 9300 RPM @ 270 volts
- Torque Constant: 34.6 oz-in/amp
- Back EMF Constant: 25.6 v/1000 rpm
- Dimensions: 5.50 inch O.D.
  x 5.045 inch length
- Weight: 17 lb

II. Gear System

To satisfy linear velocity requirements, a speed reduction is needed to the output shaft of approximately 9:1. The two pass gear system utilizes a design such that backlash is nearly eliminated (Figure 4). Spur gears transmit high torques necessary to drive the system in either direction. A two piece idler shaft/gear allows for on assembly adjustment to aid in minimizing rotational play. Characteristics of the gear system are shown below:

- Type of Gearing: Spur
- Teeth: Involute, 20 deg
- Face Width: 0.50 in. (1st pass)
            0.75 in. (2nd pass)
- Material: Steel alloy 8620
- Lubricant: Molybdenum disulfide Grease

Internal gear stresses and tooth contact stresses were calculated, which directly affected structural sizing of the gears.

III. Linear Screw

Rotational motion is converted to linear motion using a roller screw. Roller screws are high efficiency linear devices which provide a robust means of transmitting very high loads with considerable accuracy. They consist of a threaded screw shaft and a nut which houses contacting rolling elements (Figure 5). Triangular threads, with an included angle of 90 degrees, are machined onto the main screw shaft. Thread pitch may range from 0.015 inch to as much as 1.250 inches with 4, 5, or 6 starts. The rollers housed in the nut are machined with a single start triangular thread. Contact is made between the nut and shaft by the rollers. A barrelled thread form provides a large contact radius for high load carrying capacity and rigidity.

Two critical areas of highest concern were:
1) Dynamic load capacity for the given geometric envelope
2) Shock load capability

The Dynamic load rating in an application depends on the type and magnitude of the load applied, and the life of the screw in millions of revolutions. In a TVC system, the maximum dynamic load is only

experienced at very short intervals during a flight. This characteristic duty cycle aids in compacting the actuators' geometry which, of course, is much to the advantage of the overall system design. Extreme shock loads and adverse environments may also be encountered on a mission. Transient shocks much larger than those loads experienced under normal continuous operation may be experienced by a TVC actuator at engine start up. Documentation shows that roller screws are best suited for these conditions. Data for the roller screw used are as follows:

- Material: Shaft - 4140, Nut - 52100
- Lead: 0.40 inches/rev
- Shaft Dia: 1.89 inches
- Lubrication: Molybdenum disulfide Grease

Other linear actuation devices were considered for this application, although none proved as worthy, based on all literature and performance data, as the roller screw.

IV. Electronic Controller

The Control Electronics Branch of the Information and Electronics Systems Laboratory was responsible for the design and fabrication of the analog controller (270V, 100A, 27kW) for the TVC actuator system. A switching regulator in the controller pulse width modulates (PWM) the 270 volt power source (currently provided by a battery bank). The modulated source is then passed through a coupling inductor to provide current for a three-phase, six transistor, six step, bridge network. The six transistors in this network aided by two additional transistors used in the PWM process, as well as the regenerative circuitry are insulated gate bipolar transistors (IGBT) rated at 500V, 200A. This bridge assembly provides the correct commutation of current to the motor windings. Synchronization is achieved by utilizing output applied to the commutation logic from motor Hall Effect devices. This logic also protects the circuit by ensuring that both transistors of a phase are not turned on simultaneously. Current is sensed out of the inductor by a separate Hall Effect device for current feedback to the controller. Position feedback is provided by the resolver at the output of the gear train. This signal is then compensated for the difference between measured position and the actuator position (at the output of the roller screw) before it is used for feedback to the controller. For redundancy purposes, a controller for each motor will be built.

353

TESTING

I. Facility

A rigorous testing program is currently under way in a full scale hydraulic test facility at MSFC. Component and subsystem development from concept through flight qualification can be performed. This facility, originally constructed for Apollo and Space Shuttle TVC systems, contains operational test facilities such as fluid pumping systems, flow test benches, static load application test fixtures, and dynamic inertia simulators which are fully supported by instrumentation, data acquisition, and analysis equipment. Data acquisition equipment used for all tests consisted of a 200 Hz, 12 bit, 8 channel computer operated system. Data analysis was performed using MATLAB based program.

This facility will allow comparisons to be made of the EMA to similar hydraulic provisions. A broad spectrum of capabilities are available.

Fluid power requirements for the entire facility are provided by several pumping systems. Two large units, when combined, have a flow capability of 800 gal/min at 5000 psig. Four small pumps provide fluid power to the smaller test fixtures. These units, rated 30 gal/min at 3500 psig, may be combined to supply 120 gal/min total capacity. A separate pumping network rated 15 gal/min at an operating pressure of 8000 psig supports a high pressure prototype system.

Hydraulic flow benches deliver directional flow and operational control to various test panels. Fluid manifolds and test blocks are available to interface with all standard servovalve and high flow deflector jet types. Pressure can be regulated from start-up to full system capacity. Flow and pressure instrumentation is available in real-time.

A dynamic load simulator (Figure 6), originally configured to simulate structural compliance, inertia, and mounting provisions for the TVC system on the Solid Rocket Booster (SRB) of the Space Shuttle facilitates testing of the EMA. Tests such as frequency response, stability, and step response are discussed in more detail in the next section.

Load stand characteristics are:
Pendulum mass: 5000 lbm
Moment arm: 65 in
Dynamic spring rate: 140 Klb/in
Power: 27 kw

II.   Testing   Scheme/Results

The first phase of testing has been completed. Data analysis for this series of tests was performed and documented and will be used to update mathematical models of the system. Tests include step response, discrete sine dwells, frequency sweep response, and linearity. In addition, actual flight duty cycles were performed by the EMA and hydraulic systems. These tests determined the performance parameters of the actuator for comparison against design parameters. All design parameters were verified with the exception of piston rate under maximum load. Rate-vs-Load tests were omitted due to inadequacies encountered with the load fixtures. These tests will be performed during the second phase of the testing program.

All tests were executed at full power (270V, 100A) and are summarized below. Peak power reached 33.75 kW when the current spiked to 125 amps. Five channels of data were acquired relating the following: command signal, actuator position, load position, motor current, and supply current.

Figure 7 shows a plot of the frequency response of the actuator. The envelope around the data exhibits the current SSME requirement. The bandwidth is 4 Hz with 20-25 degrees of phase lag at 1 Hz (an SSME requirement). Resonance with the load structure occurs between 8 and 9 Hz. The peak in response magnitude corresponds to a critical damping ratio between 0.5 and 0.6. Figure 8 shows both a small and large excursion step response. The small step (0.25 inches) falls within the requirement envelope of SSME specifications. A 15 percent overshoot is seen. Data from the large step (5.0 inches) demonstrates that the actuator exceeds the design requirement velocity of 5 in/sec, and is actually capable of 6.8 in/sec under inertia load. The overshoot corresponding to the large step is approximately 14 percent. Overshoot associated with these step responses relate to the damping ratio determined by the frequency response. During the next phase of testing, a piston velocity of 5 in/sec will be verified with the actuator under rated load. Linearity tests on the actuator produced excellent results. Position data for a large excursion (5.0 inches) resulted in an error less than 0.030 inch which exceeds the 0.050 inch requirement.

Both linearity and position error data may be seen in Figure 9. The position error for the small excursion was below the noise level of the data. For an initial comparison between the hydraulic and EMA systems, an actual STS flight profile was commanded to the actuator. Response to the STS-44 SRB command profile may be seen in Figure 10. Actuator position response error in relation to the command signal is shown in the bottom plot. Note though, that while the EMA showed less error than the hydraulic unit, the test was run on the inertia simulator only and lacked the flight loads the hydraulic unit experienced. The capability to apply flight type loads for testing purposes is included in future plans for the test facility.

Since this testing was performed, a new single pass gear system has been designed for the actuator. A rate loop has also been added and is now undergoing tuning such that all design parameters are accomodated. Following the completion of this task, an additional test series will be run. Testing the actuator in a redundant configuration will be the next milestone. These tests will prove helpful in future redundancy studies as well as the introduction of Vehicle Health Management (VHM) to these systems.

SECOND GENERATION EMA

A second generation high power EMTVC actuator has been designed and is currently being assembled at NASA, MSFC. This actuator incorporates features that will increase performance, reduce weight, and provide a more compact package than that of the first generation discussed earlier. The primary mechanical scheme of both actuators are relatively the same, yet the second generation EMA utilizes features that enhance the entire component design. This actuator also incorporates length, stroke, and power capabilities required to support TVC system testing for heavy lift vehicles. Basic Design Requirements:

o   Dynamic Load Capacity: 45,000 lb
o   Null Length: 47.330 inches
o   Maximum Stroke: +/- 6 in
o   Control: Four Channel Redundant
o   Linear Velocity: 5 in/sec
o   Bandwidth: > 4.2 Hz

Four high speed low inertia motors configured in a torque summing arrangement power the system. Since inertia is a major concern due to the EMA's nature of operation, optimization of horsepower, RPM, and motor rotor diameter is imperative. The

amount of inertia seen by the controller governs the power required for each cycle of the actuator. Calculations show that the amount of inertia created by the rest of the system is essentially negligible when compared to the inertia created by the cyclic action of each rotor inertia.

The motors deliver torque to a single pass gear reduction system. The gear system transmits the necessary torque to a roller screw shaft which has been hollowed to decrease inertia. Torque to the roller screw shaft is converted to linear movements by the roller screw nut. As the nut moves, precise gimbal outputs are translated to the output piston.

A small harmonic drive (Figure 11) has been added to aid in position control. It provides a reduction mechanism such that the moving resolver race will not rotate greater than 360 degrees.

High strength aluminum (7075) is used in more parts to reduce overall weight. Figure 12 shows the second generation EMA conception. Component specifications are shown in Table 2.

Table 2.   Component specifications

Motors:
- Type: Three phase DC brushless permanent magnet
- No load speed: 20,000 RPM @ 230 volts
- Torque constant: 16.8 oz-in/amp
- Back EMF constant: 13.8v/1000 RPM
- Dimensions: length-9.875 in
  dia-2.380 in
- Weight: Approx. 6 lb

Gearing:
- Type of gears: spur
- Teeth: Involute, 20 deg
- Face width: .625 in
- Material: Steel alloy 8620
- Lubricant: Dry film

Linear Screw: (same specifications as 1st generation EMA discussed earlier)

CONCLUSION

Conclusive system data concerning the EMA is forthcoming. Final testing goals will soon be fulfilled for this phase of MSFC's EMA program. These results are expected to supply greater confidence in the capabilities of EMTVC systems for future comparisons to hydraulic equivalents.

Following the final phase of testing, the 25 hp EM actuator will be shipped to Kennedy Space Center, Florida, where it will be used to familiarize personnel with operational issues associated with EM TVC systems. Design changes are being incorporated into the gear train and motors to better suit data criteria and EMA performance. Problem issues arising from the operations area may then be taken into account and incorporated into future actuator requirements and designs. Using information gained from experience with the first generation prototype EMA, MSFC will utilize the second generation, 4-motor, 45 hp EMA to further provide insight into topics such as load sharing (between channels), full redundancy implementation, and start transient load capabilities. MSFC test facilities will undergo upgrading to support this effort with additions of flight programmable loads to the inertia simulators, a possible VHM test platform, and other modifications to existing facilities to better handle specific requirements associated with the EMA. After the completion of extensive component testing, the actuator will undergo Technology Test Bed (TTB) qualification . TTB data will include vibration analysis, EMI/EMC, as well as thermal, shock, and acoustic information. The TTB hot fire tests will support the NASA Electrical Actuation Technology Bridging program.

NASA, MSFC plans to investigate all avenues of this technology such that optimization is accomplished. Upcoming EMA designs will aid in establishing a continued learning process to integrate test data and hardware for development of a proven EMTVC system.

REFERENCES

Shigley, Joseph Edward, and Charles R. Mischke. *Standard Handbook of Machine Design*, McGraw-Hill Book Company, 1986

Shigley, Joseph Edward, and Larry D. Mitchell. *Mechanical Engineering Design*, McGraw-Hill Book Company, 1983

Weir, R. A., and W. N. Myers. "Electromechanical Propellant Control System Actuator." AIAA 90-1946

Catalogs

Harmonic Drive, <u>Cup and Pancake Component Gear Sets</u>, 1989.
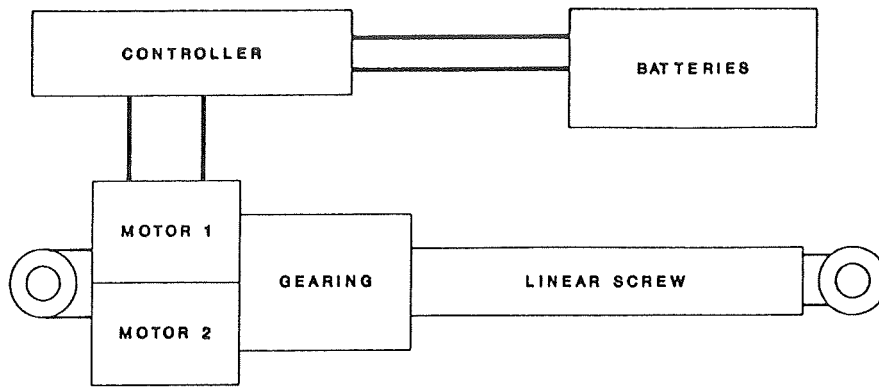
SKF, <u>SKF Planetary and Recirculating Roller Screws</u>, 1990.

Figure 1. Basic EMA Schematic
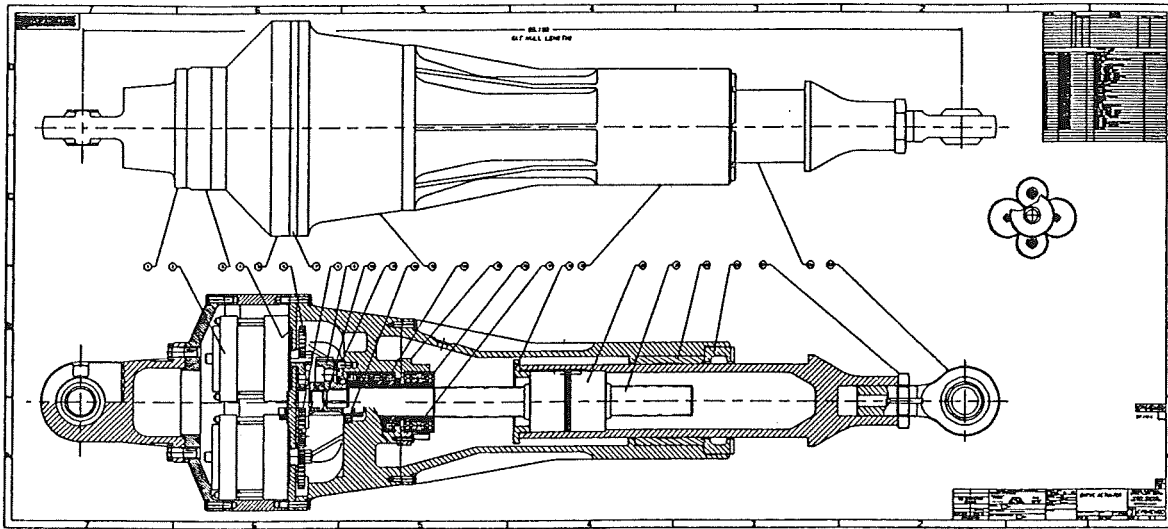
Figure 2. EMA Assembly Drawing
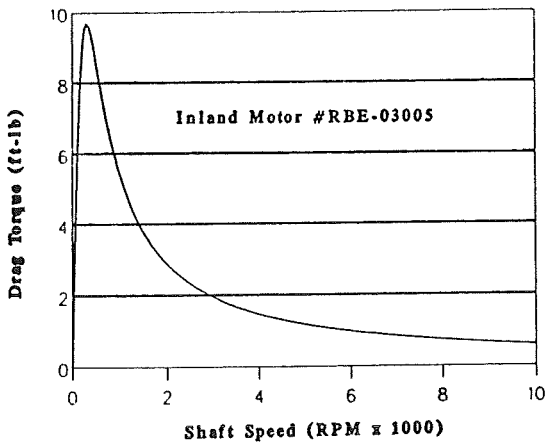
Figure 3. Motor Drag Torque-vs-RPM
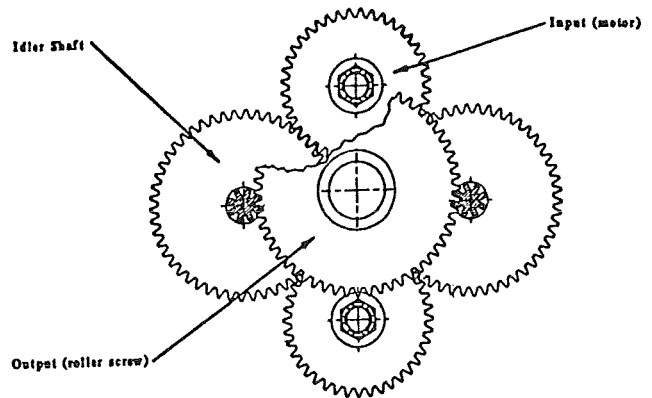
Figure 4. View of Gear Arrangement

360
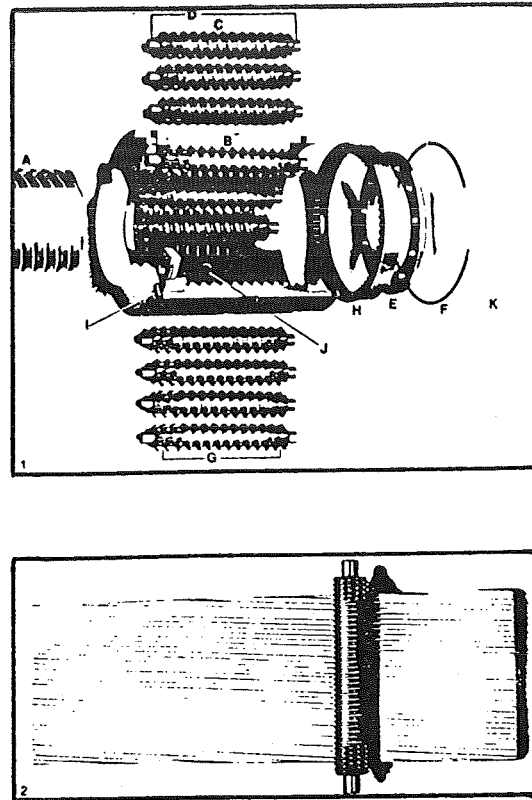
Figure 5. SKF Linear Roller Screw

ACTUATOR

5,000 lb
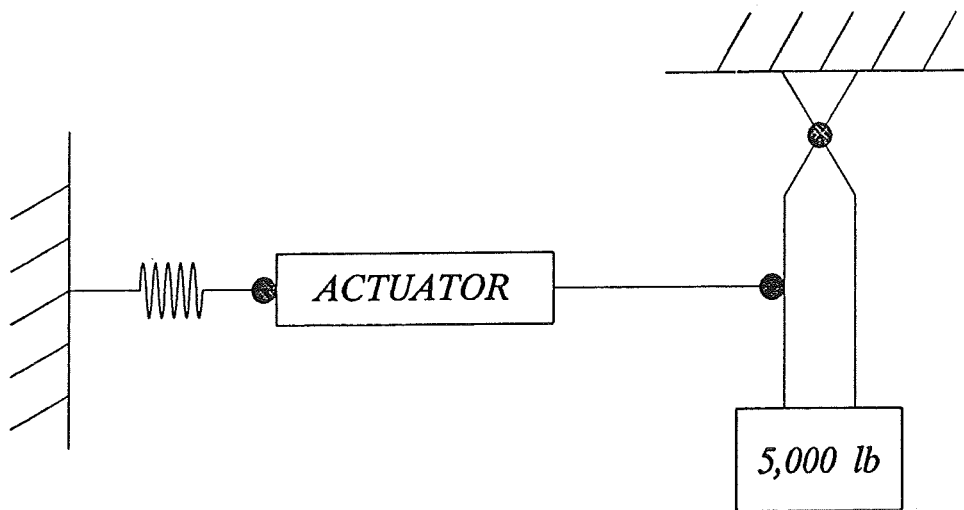
Figure 6. Dynamic Load Simulator (schematic)

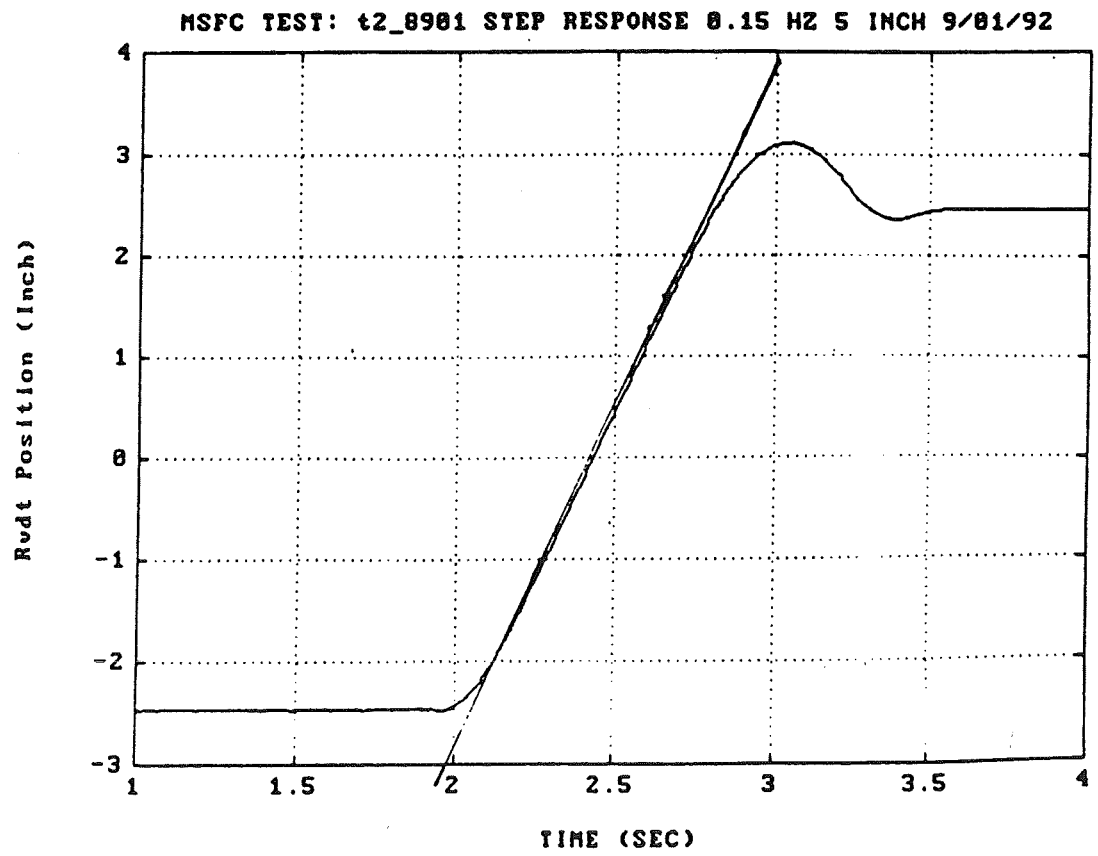361
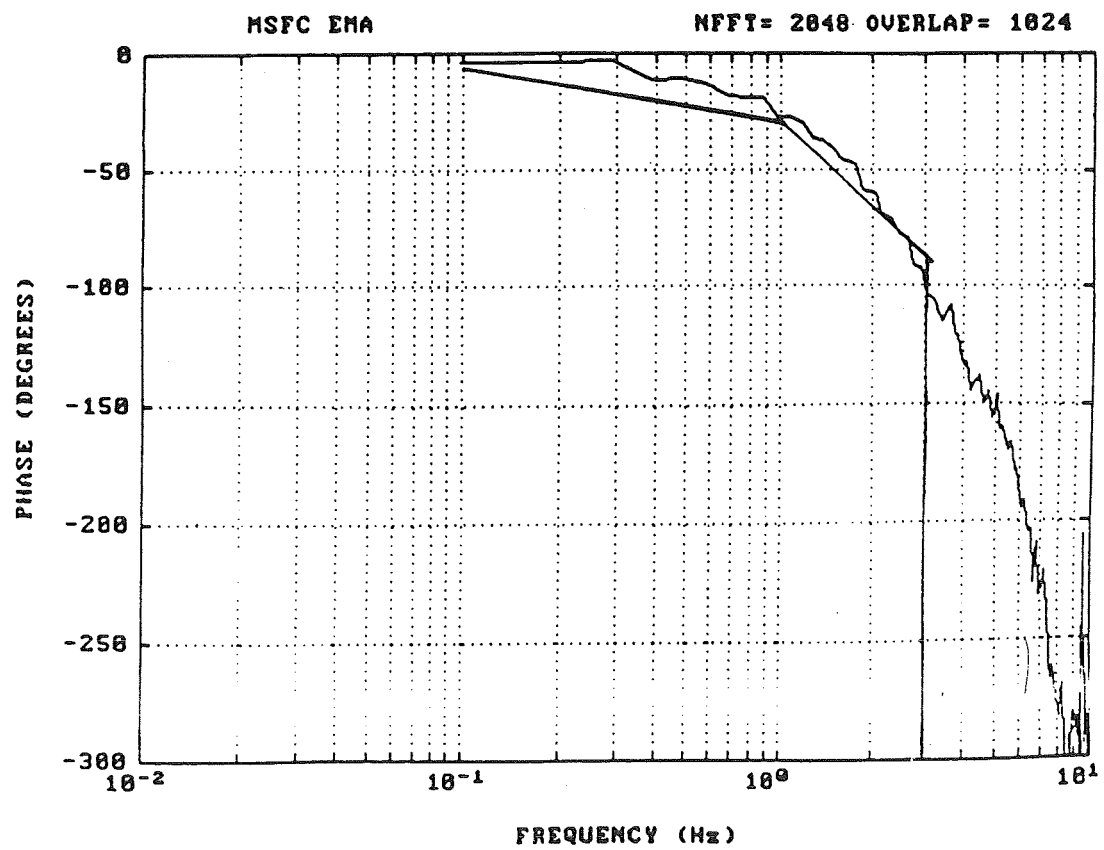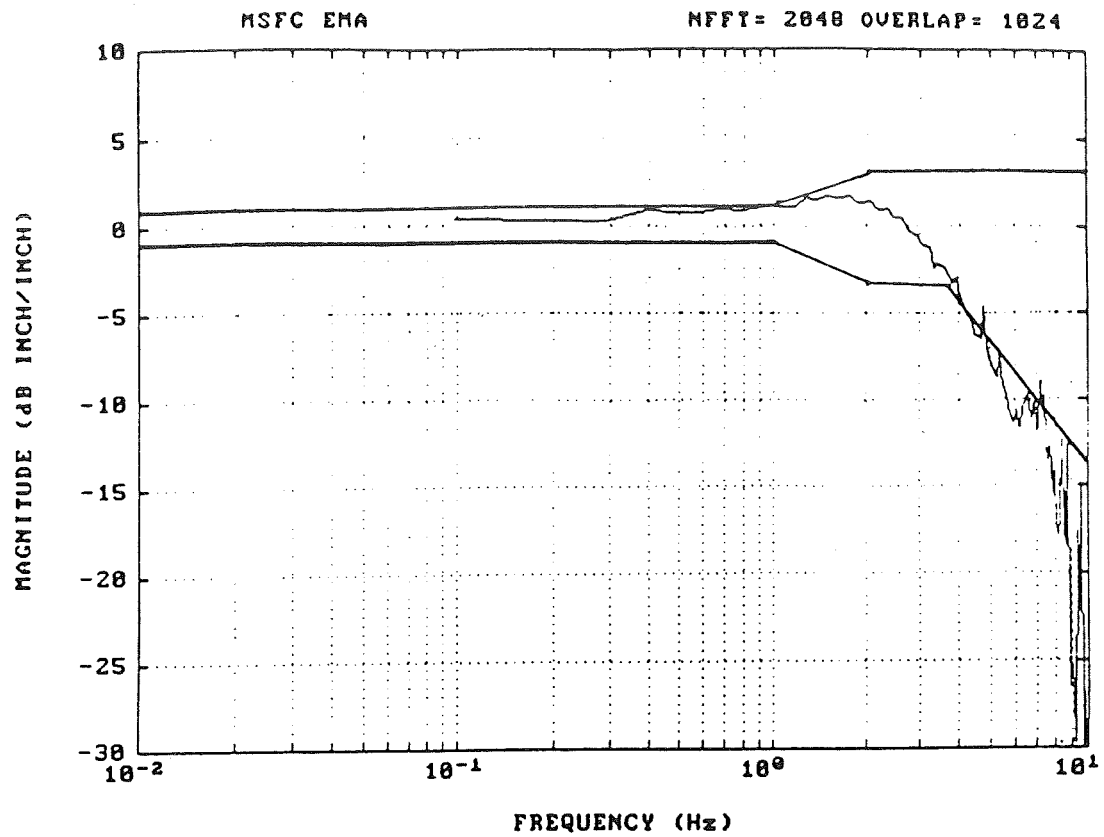
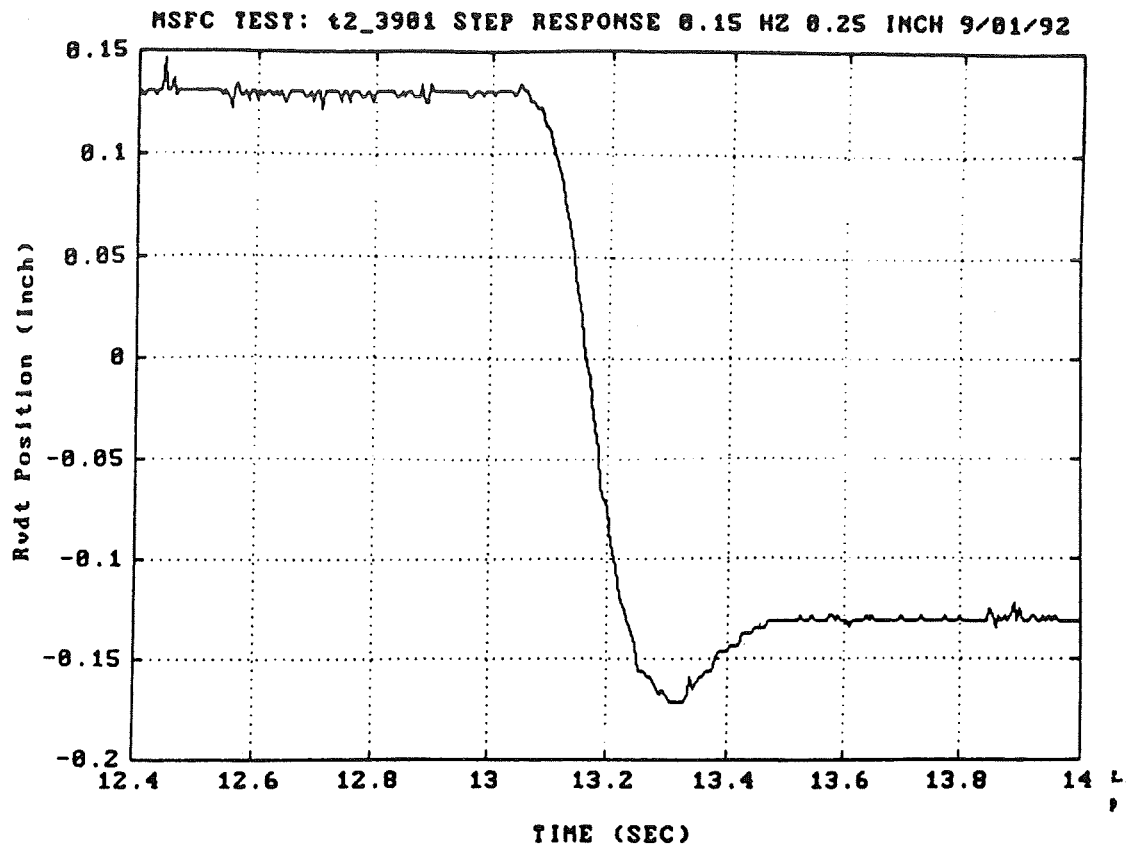Figure 7. Frequency Response With SSME Envelope Requirements
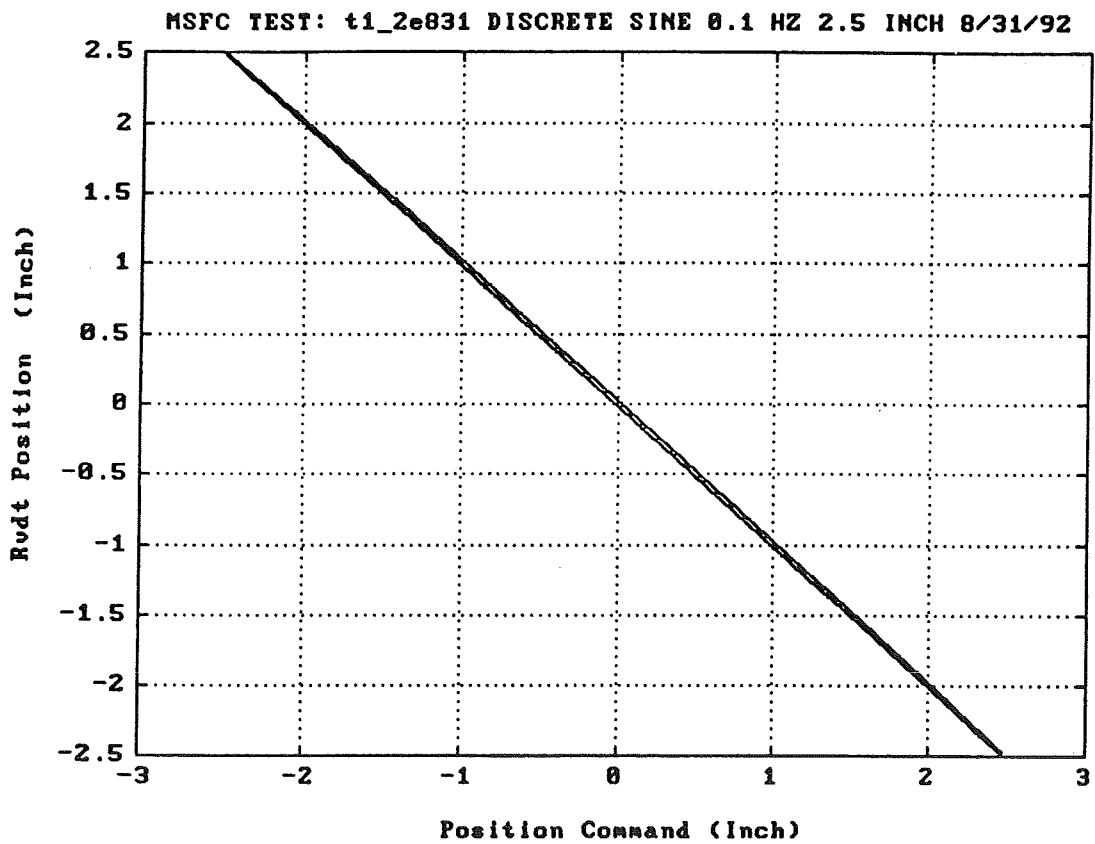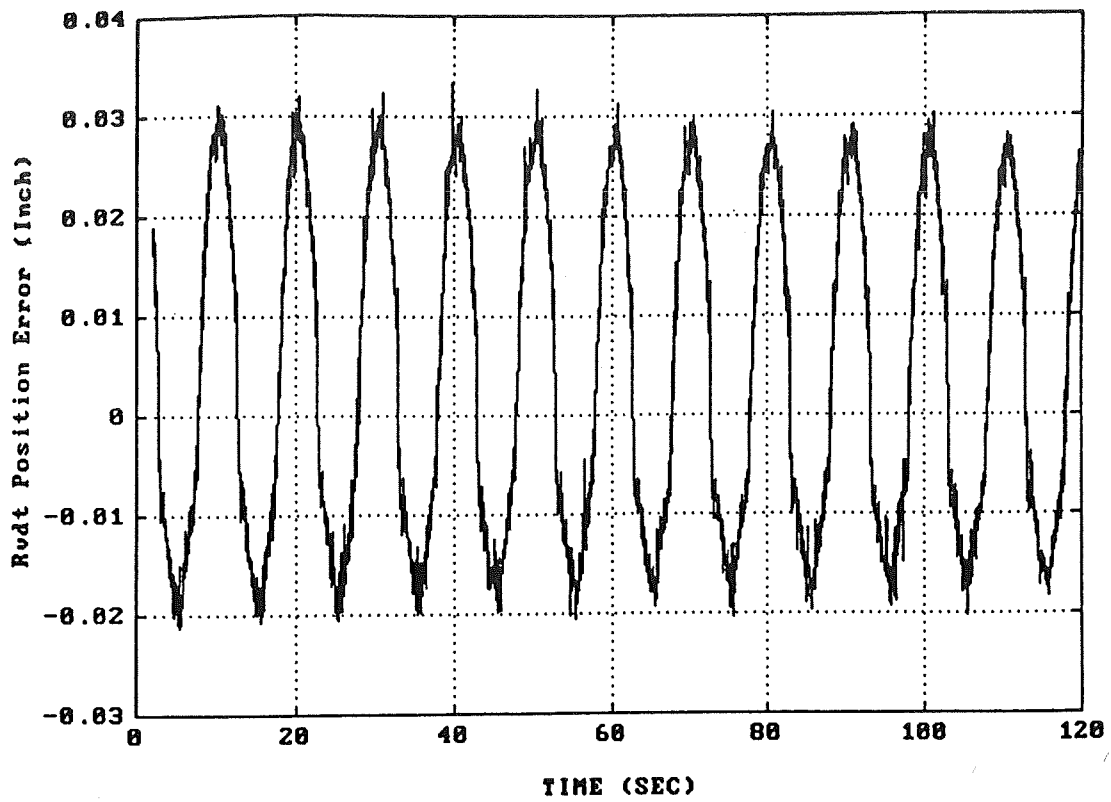
362

Figure 8. Small and Large Step Response

363

Figure 9. Large Excursion Linearity and Position Error

UNFILTERED RESOLVER DATA
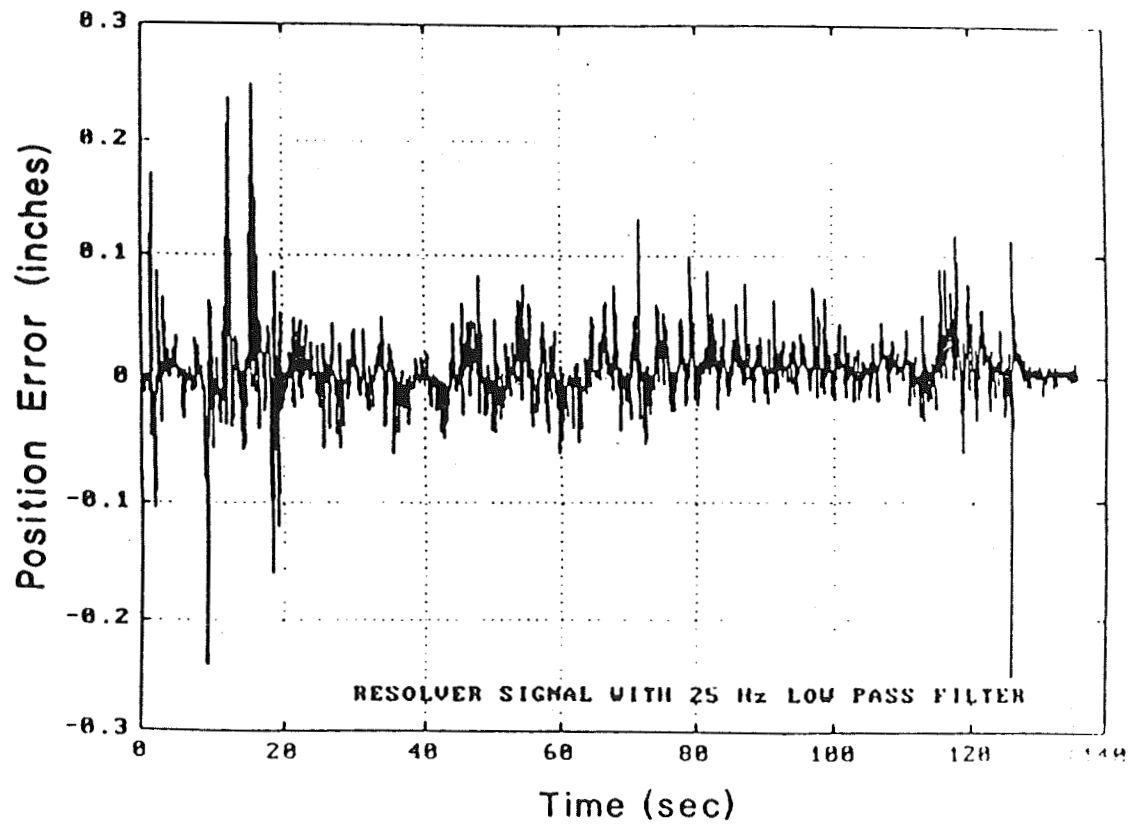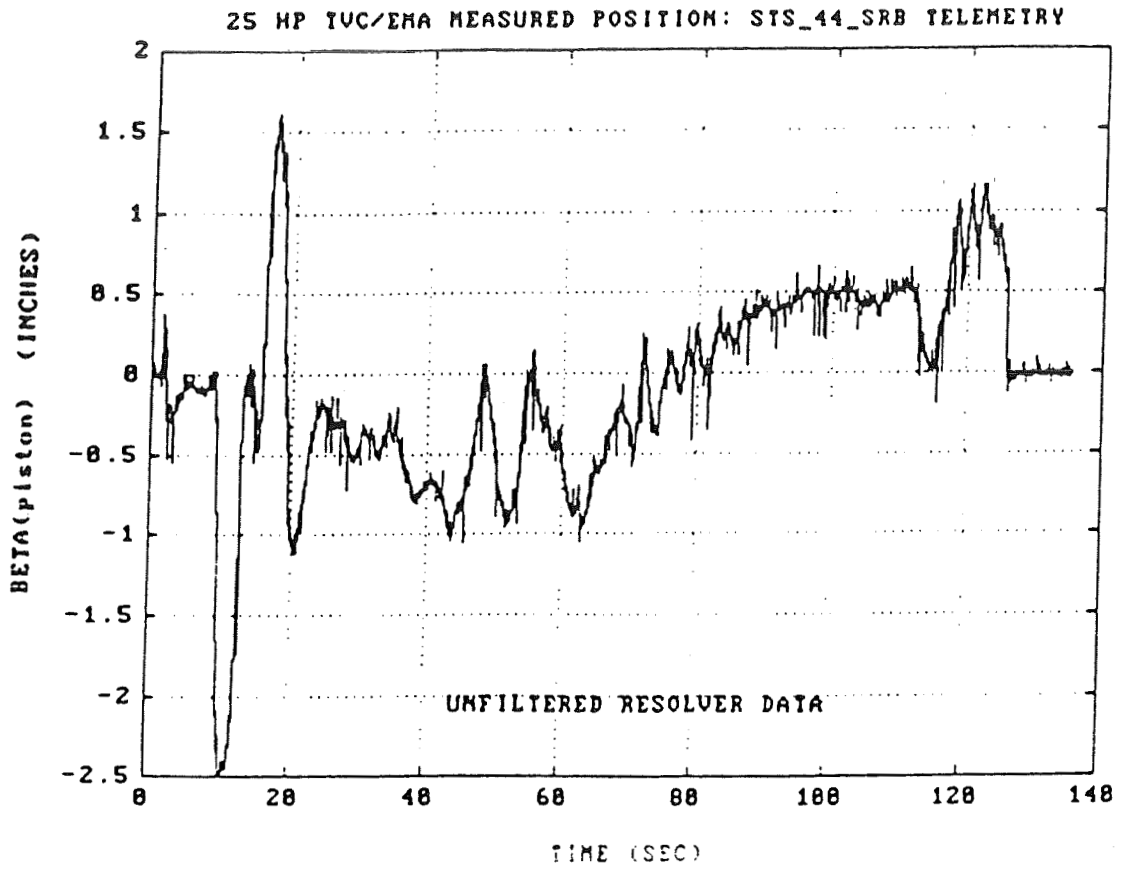
TIME (SEC)

RESOLVER SIGNAL WITH 25 Hz LOW PASS FILTER

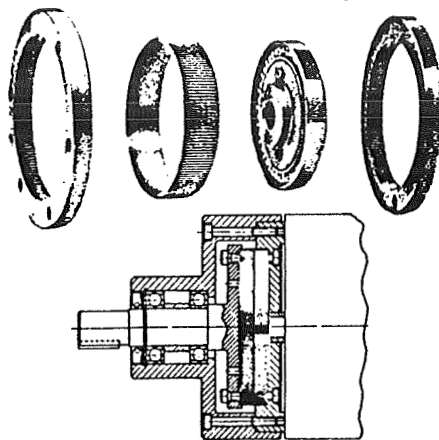Time (sec)

Figure 10. STS-44 Flight Profile Comparison
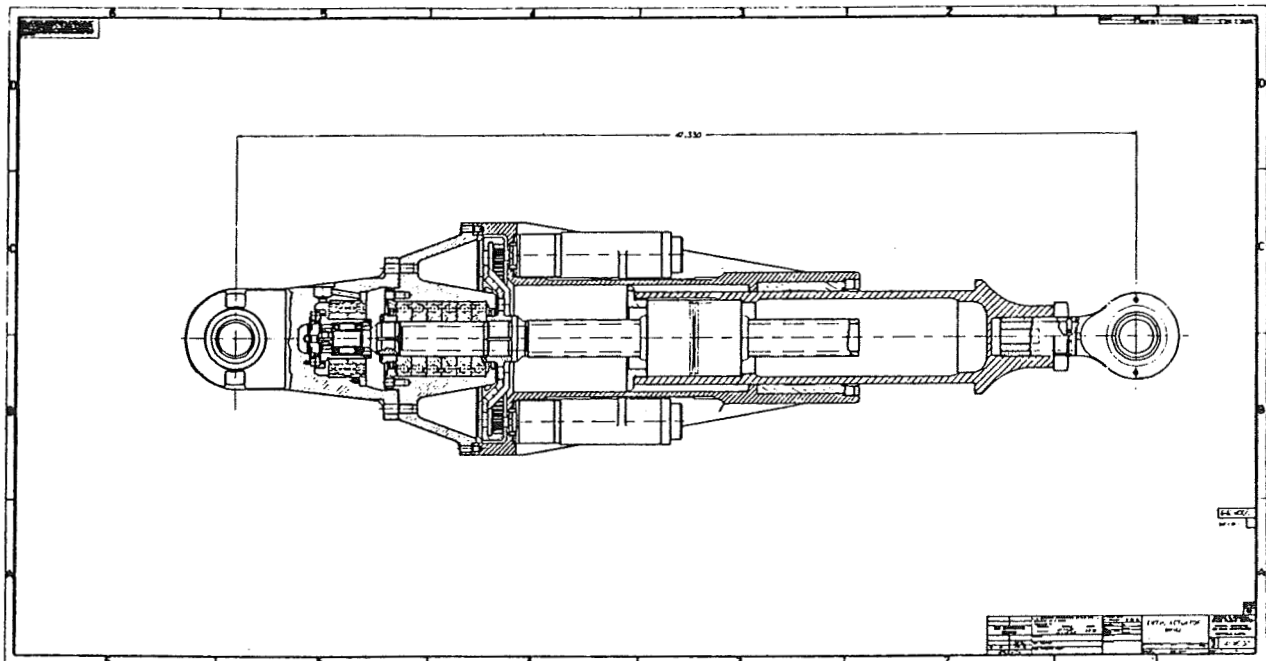
Figure 11. Harmonic Drive

Figure 12. Second Generation EMA Assembly

366

SP-100 Control Drive Assembly Development

Thomas Gleason*, A. Richard Gilchrist*, Gary Schuster*

ABSTRACT

The SP-100 is an electrical generating nuclear power system for space operation. This paper describes the nuclear reactor control systems and the methods used to assure reliable performance for the 10-year design life. Reliable performance is achieved by redundancy and by selecting highly reliable components and design features. Reliability is quantified by analysis using established reliability data. Areas lacking reliability data are identified for development testing. A specific development test description is provided as an example to demonstrate how this process is meeting the system reliability goals.

INTRODUCTION

The nuclear system control and shutdown functions are provided by the moving reflector segments surrounding the reactor core and by the in-core safety rods. The moving reflector drive system is capable of precise reactor control as well as reactor shutdown while the safety rod drive system provides fail-safe reactor shutdown capabilities. Figure 1 shows the overall reactor system arrangement and the relative locations of the two reactor control systems. Figures 2 and 3 show components tested and typical results obtained. Table 1 gives the nominal design environments of the control systems.

DESIGN DESCRIPTION

Reflector Control System

Reactor power control is achieved by moving neutron reflecting material axially relative to the reactor core. Electromechanical drive units located aft of the radiation shielding provide the power to move the reflector sections. A ball nut and screw assembly converts the rotary motion of the drive motor to linear motion needed to move the reflectors. A brake assembly locks the reflector in position when it is not being driven. Figure 1 includes a figure of the single reflector drive assembly. The drive system is capable of moving the reflector segments in small increments and has precise positioning capabilities. Figure 2 shows some of the test results for the reflector components tested.

---

*General Electric Company, San Jose, CA

Safety Rod

Reactor shutdown capabilities are provided by the incore safety rods for launch and for severe accidents. Figure 1 includes a schematic of a safety rod and its drive system. Figure 3 shows some of the test results and key features for the safety rod components. Each rod contains sufficient neutron poison to prevent operation. When the poison is located within the core region, the safety rod is mechanically locked in position to prevent inadvertent withdrawal. Electromechanical drive assemblies located aft of the reactor shielding provide the unlock and the drive functions needed to move the poison out of the reactor core region. Electromagnetic clutches and brakes connected to the drive motor are used to select the desired drive and/or unlock function. A spring motor device stores energy to move the safety rod to the shutdown position on command or automatically at predetermined reactor conditions.

Design Challenges

The mechanical designs of the two systems share many common features all of which share the challenge of reliable operation in the harsh environment of high temperature, vacuum and radiation. Both include stepper motors, clutches, brakes, bearings, sliding surfaces, and springs, all of which must remain functional and maintenance free for 10 years. Material selections are limited for this extreme environment. Changes in material properties and strength characteristics, dimensional stability, self-welding, diffusion and evaporation must be considered for each material selected and for each material couple.

Moving and sliding elements near the reactor core region are challenged by the extremely high temperatures. Refractory metals are needed for the structural materials with carbide coatings on the critical contacting surfaces. Radiation induced material swelling is a major concern for items located near the reactor core.

RELIABILITY CONSIDERATIONS

Overview

Reliability of the reflector control and safety rod drive assemblies for the overall 10-year mission depends upon the presence of initial operational reliability, operational reliability throughout the mission, and an end-of-life significantly beyond the mission time.

Initially, the reflectors and safety rods must be capable of moving to the

operational positions and remaining there with high reliability. This depends on the drive assemblies 1) being capable of performing their functions subsequent to fabrication and assembly--confirmed by acceptance testing, 2) surviving the launch--assured by design and structural analysis according to prescribed NASA methodology, validated by component and subassembly testing, and 3) reliably deploying and going into initial operation, given that they survived launch--assured by qualification testing, low component failure rates and the short time lapse before initial operation.

For the duration of the mission between start-up and end-of-mission, redundancy and low component failure rates assure the reliability of the reflector and safety rod functions to hold, scram, and shutdown. For most functions, the loss of a reflector or a safety rod can be tolerated.

Satisfactory margins between the mission time and the mean lifetime of the reflector control and safety rod drive assembly critical components assures that wear will not be a source of mission failure. Identification of failure modes and associated failure mechanisms in Failure Modes and Effects Analysis provides the basis for failure mechanism analysis, a process whereby identified failure mechanisms are examined for adequacy of data to support lifetime validation. If sufficient data are available, design margin studies are performed to provide an assessment of the margin of lifetime beyond the mission time. If sufficient data are lacking, specific needs are identified and factored into development programs planned or underway.

Assurance of Initial Operation Reliability

Prior to the SP-100 System Design Review held in 1988, structural analyses were done for the reflector control and safety rod drive assemblies. As part of these analyses, the structural response of the drive assemblies to the dynamic loading and vibration of launch were evaluated. Satisfactory margins were demonstrated for both types of drive assemblies. Since the System Design Review, the designs of both drives have changed; the changes to the safety rod drive assembly are small enough that the analysis results still hold true. The reflector control drive assembly changes are significant and, therefore, the structural analysis will be repeated. In the interim, preliminary analysis indicates satisfactory margin is available.

Mission Reliability Enhancement Through Redundancy

In the reflector control drive assemblies, redundancy has been built into the coils of the motor, brake, and position sensors, allowing reflector failures to be tolerated while meeting mission requirements.

In the safety rod drive assemblies, redundancy has been built into the safety rod drive motors, clutches, and brakes, supporting particularly the withdrawal function necessary for initial operation. To enhance the operational reliability throughout the mission, dual coils are built into the scram clutches so that inadvertent scram is less likely due to coil wire failure or a controller false signal. Multiple safety rod drive assemblies assure that the scram function will be reliable over the mission time, since, for most anticipated events requiring safety rod action, insertion of one safety rod is sufficient to safely shutdown the reactor.

Lifetime Reliability Through Failure Mechanism Control and Design Margins

Understanding of life limiting failure mechanisms through failure mechanism analysis (FMA) and the validation that lifetime margins exist through design margin studies (DMS), provide assurance that component end-of-life is sufficiently beyond the mission time. To date, 23 FMA's and four DMS's have been completed for the reflector control and safety rod drive assemblies.

Of the completed DMS's, one addressed the reflector and safety rod cladding failure due to embrittlement from oxygen released from the beryllium oxide (BeO) during irradiation. The conclusion of this study was that over the mission time the oxygen released in the lattice by the beryllium transmutation can be easily accommodated within the BeO lattice itself. As such, no oxygen release by diffusion from the BeO will occur. The potential failure mechanism identified and evaluated is not operative over the 10-year mission and cannot lead to safety rod or reflector element cladding failure.

Another completed DMS addressed the reflector and safety rod cladding failure due to BeO volumetric bulk expansion from irradiation induced swelling or microcracking. End-of-life was defined to correspond with take-up of the gap that exists at beginning-of-life between the BeO and the cladding. This is a conservative limit in that actual failure would correspond to considerable expansion beyond take-up of the gap, producing cladding distortion and, ultimately, jamming of the safety rod or reflector. Detailed designs will provide gaps that assure the desired lifetime goal are met.

A third DMS addressed the crack/ship/spalling/wear failure mechanisms of the alumina coating used to protect reflector drive assembly tantalum-tungsten alloy components within self-aligning bearings. The conclusion was that the coating, on the basis of tests performed in the early 1970's in connection with the advanced zirconium hydride reactor control system drives, had a reasonable margin on lifetime. This result will be reviewed for consistency with the modified application of the self-aligning bearing as we change the design from the hinged to the sliding reflector concept.

The fourth DMS addressed one of several failure mechanisms that could lead to self-welding of the safety rod to the molybdenum alloy thimble liner - specifically, the liner material fusing to itself in the event of liner material pickup onto the hardfaced safety rod slider bearing. Three generic material transport processes were identified as applicable to this failure mechanism.

Sufficient data were available to show that two of these processes had very large margins to failure over the mission lifetime; data to close out the third will come from experiments planned in the development program.
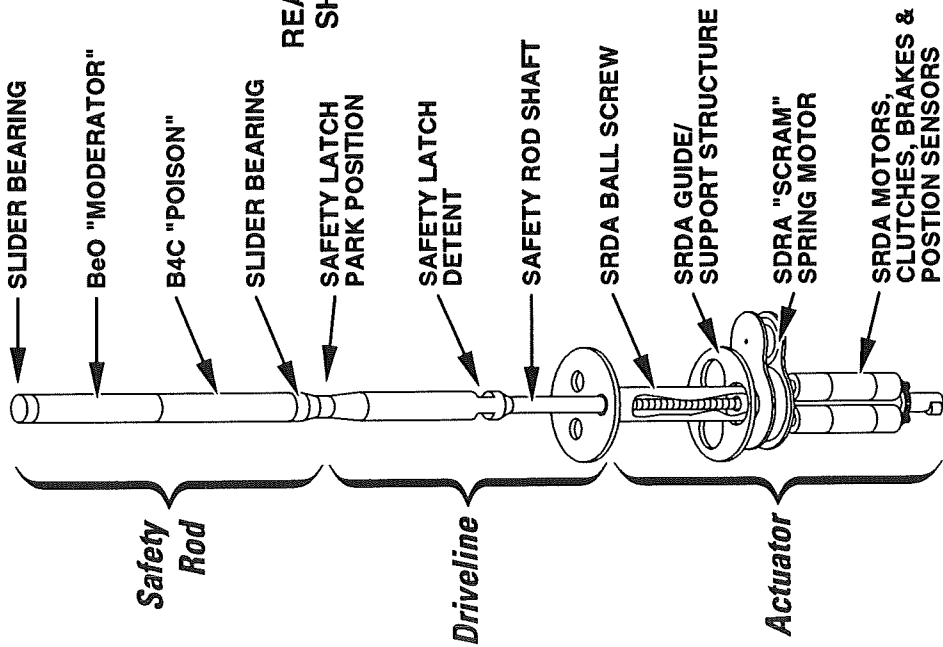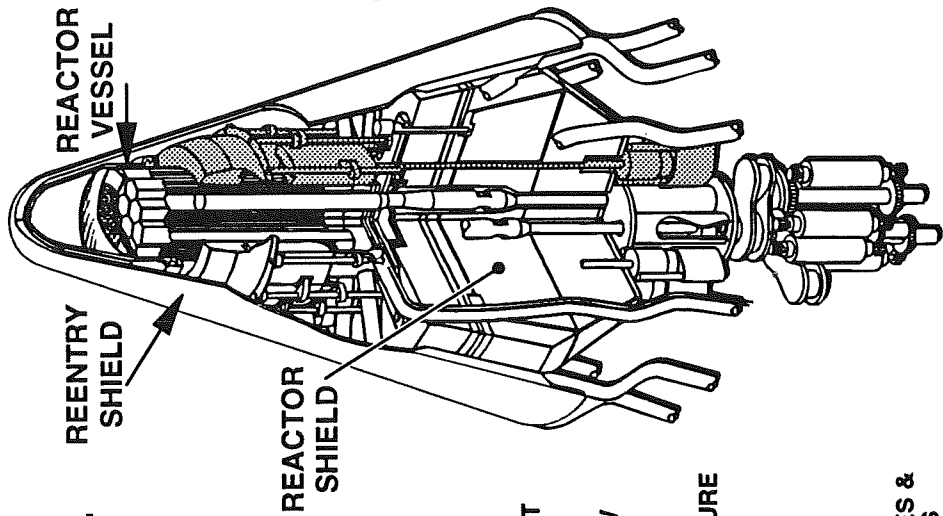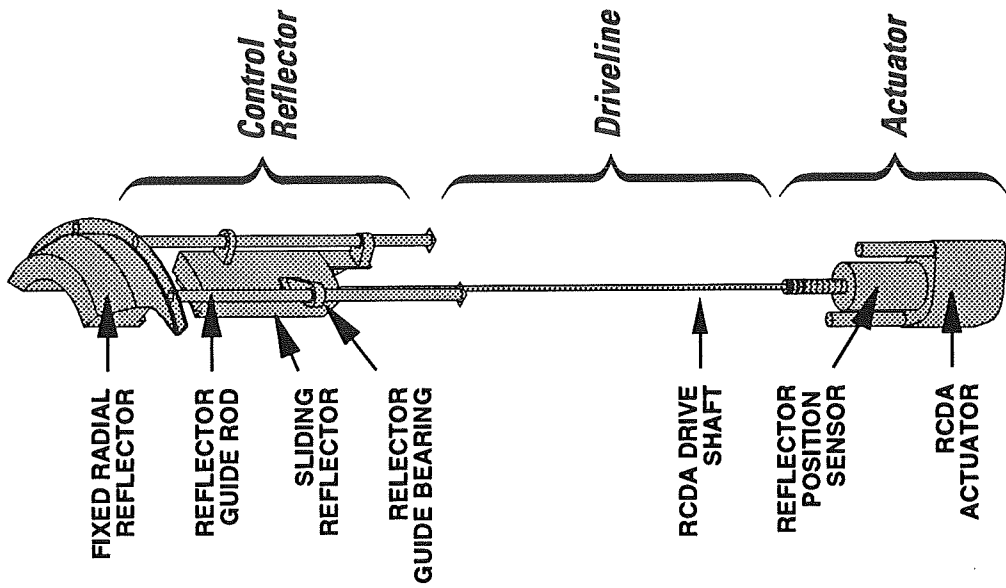
Twelve planned DMS's will address life-limiting failure mechanisms affecting coils, insulation and mechanical components. Included are several DMS's which explore other failure mechanisms that could lead to self-welding of the safety rod to the thimble liner. One of these is self-welding of the actual safety rod slider bearing carbide coating to the molybdenum alloy liner of the thimble. Another is the loss of the carbide coating in that, should loss of coating occur, the PWC-11 substrate material of the slider bearing would then be exposed to the molybdenum alloy, resulting in a couple more prone to self-welding. The causes that drive or enable these mechanisms to process have been identified as thermal aging, thermal cycling, and radiation. The need to adequately understand these failure mechanisms and the respective lifetime margins are the basis for the development programs described below. This program is a typical example of the ongoing process development and material evaluation resulting from the failure mechanism analysis.

SAFETY ROD MATERIAL SELECTION AND TESTING

Theoretical considerations and practical experience suggest a refractory metal carbide paired with Mo-41Re alloy is a promising material couple for use in the control rod/thimble system. This combination should not self-weld. Furthermore, the chemical stability of these carbides and their refractory nature make them likely to withstand the reactor core environment. Testing is required under prototypic conditions to validate material selections and applications.
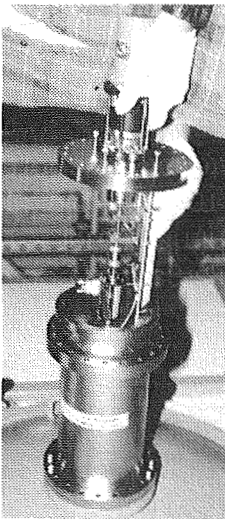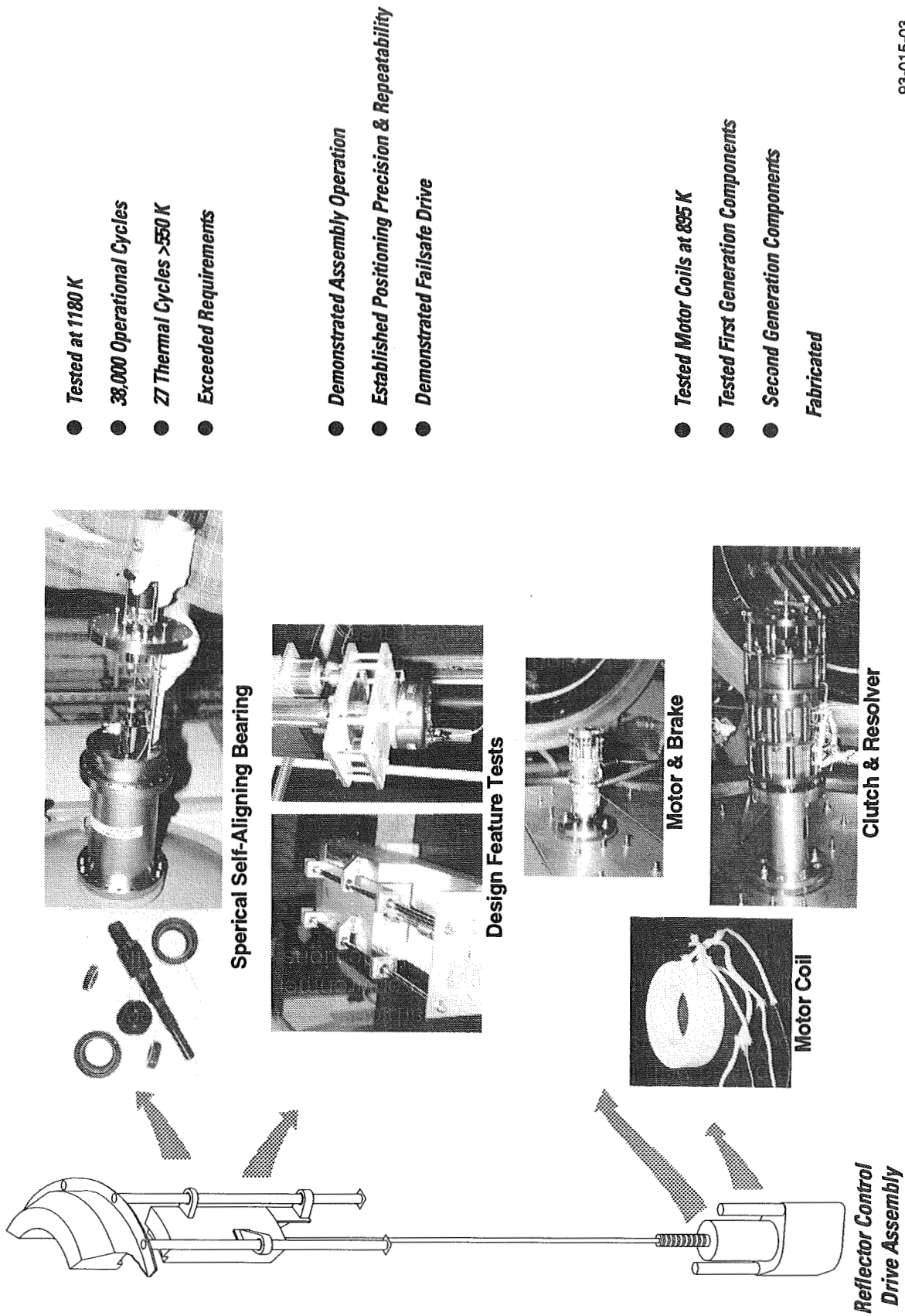
Table 1. Design Environment

	NOMINAL TEMPERATURE, K	NOMINAL PRESSURE, TORR
Reflector	1320	10^{-9}
Reflector Drive	811	10^{-9}
Safety Rod	1600	10^{-9}
Safety Rod Drive	811	10^{-9}

FIXED RADIAL REFLECTOR
REFLECTOR GUIDE ROD
SLIDING REFLECTOR
RELECTOR GUIDE BEARING
RCDA DRIVE SHAFT
REFLECTOR POSITION SENSOR
RCDA ACTUATOR

Control Reflector
Driveline
Actuator

93-015-01

REACTOR VESSEL
REENTRY SHIELD
REACTOR SHIELD

SLIDER BEARING
BeO "MODERATOR"
B4C "POISON"
SLIDER BEARING
SAFETY LATCH PARK POSITION
SAFETY LATCH DETENT
SAFETY ROD SHAFT
SRDA BALL SCREW
SRDA GUIDE/ SUPPORT STRUCTURE
SDRA "SCRAM" SPRING MOTOR
SRDA MOTORS, CLUTCHES, BRAKES & POSTION SENSORS

Safety Rod
Driveline
Actuator

Figure 1.   Control Drive Assemblies

373

- Tested at 1180 K
- 38,000 Operational Cycles
- 27 Thermal Cycles >550 K
- Exceeded Requirements

- Demonstrated Assembly Operation
- Established Positioning Precision & Repeatability
- Demonstrated Failsafe Drive

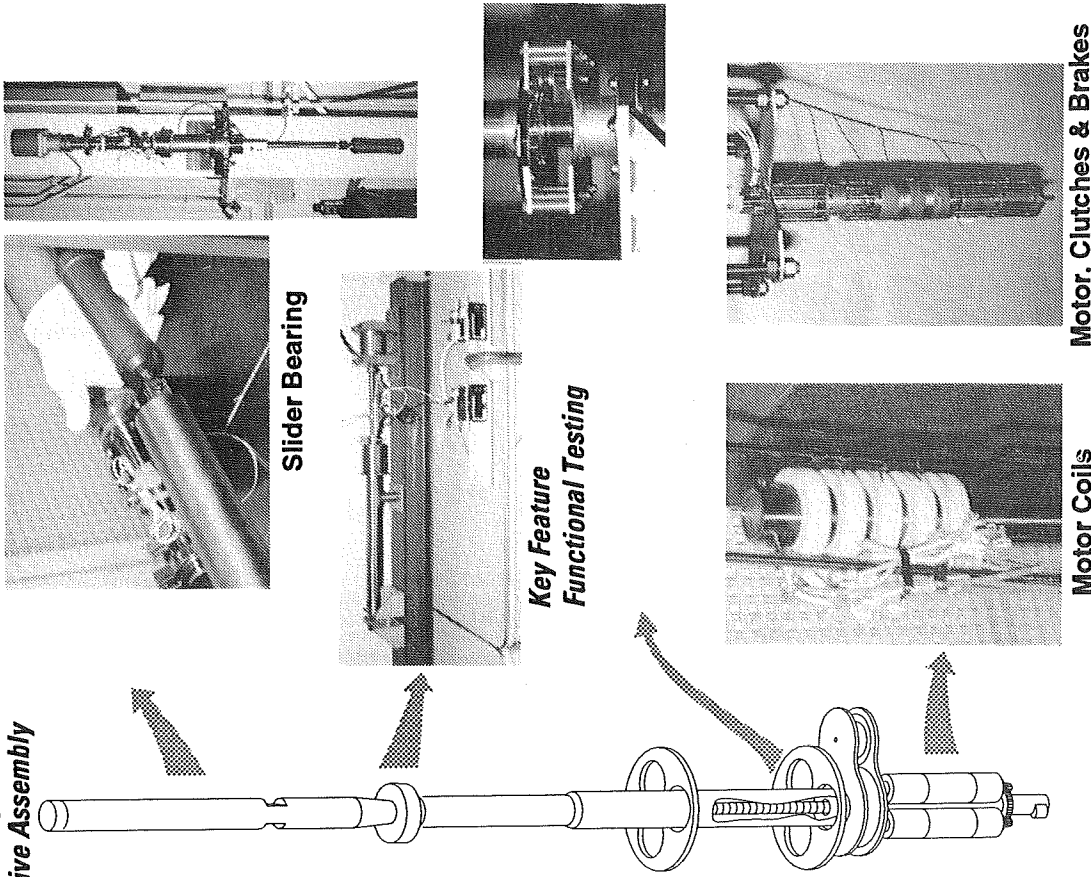- Tested Motor Coils at 895 K
- Tested First Generation Components
- Second Generation Components

- Fabricated

93-015-03

Sperical Self-Aligning Bearing
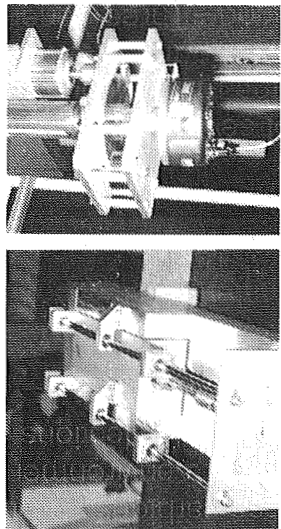
Design Feature Tests

Motor & Brake

Clutch & Resolver

Motor Coil

Reflector Control Drive Assembly

Figure 2. Reflector Drive Development

- *Carbide Coating Process*
- *HfC Irradiation Test*
- *Carbide Thermal Aging Test*
  Success at 1700 K
- *Coating Met Requirements*
  - *Initiated Component Testing*

- *Key Safety Design Features Tested*
  - *Failsafe Shutdown Spring Motor*
  - *Safety Latch*
  - *Safety Rod Separation Joint*

- *Motor Coils Tested at 895 K*
- *Tested First Generation Components*
- *Second Generation Test Components Fabricated*

93-015-02

Safety Rod Drive Assembly

Slider Bearing

Key Feature Functional Testing

Motor Coils

Motor, Clutches & Brakes

Figure 3. Safety Rod Drive Development

REPORT DOCUMENTATION PAGE

Public reporting burden for this collection of information is estimated to average 1 hour per response, including the time for reviewing instructions, searching existing data sources, gathering and maintaining the data needed, and completing and reviewing the collection of information. Send comments regarding this burden estimate or any other aspect of this collection of information, including suggestions for reducing this burden, to Washington Headquarters Services, Directorate for information Operations and Reports, 1215 Jefferson Davis Highway, Suite 1204, Arlington, VA 22202-4302, and to the Office of Management and Budget, Paperwork Reduction Project (0704-0188), Washington, DC 20503.

1. AGENCY USE ONLY (Leave blank)	2. REPORT DATE May 1993	3. REPORT TYPE AND DATES COVERED Conference Publication

4. TITLE AND SUBTITLE

27th Aerospace Mechanisms Symposium

5. FUNDING NUMBERS

6. AUTHOR(S)

Ron Mancini, Compiler

7. PERFORMING ORGANIZATION NAME(S) AND ADDRESS(ES)

Ames Research Center
Moffett Field, CA 94035-1000

8. PERFORMING ORGANIZATION REPORT NUMBER

A-93053

9. SPONSORING/MONITORING AGENCY NAME(S) AND ADDRESS(ES)

National Aeronautics and Space Administration,
Washington, DC 20546-0001; California Institute of Technology,
Pasadena, CA 91109; and Lockheed Missiles and Space Company, Inc.,
Sunnyvale, CA 94088

10. SPONSORING/MONITORING AGENCY REPORT NUMBER

NASA CP-3205

11. SUPPLEMENTARY NOTES

Point of Contact: Ron Mancini, Ames Research Center, MS 213-1, Moffett Field, CA 94035-1000;
(415) 604-6319

12a. DISTRIBUTION/AVAILABILITY STATEMENT

Unclassified — Unlimited
Subject Category 15

12b. DISTRIBUTION CODE

13. ABSTRACT (Maximum 200 words)

The proceedings of the 27th Aerospace Mechanisms Symposium, which was held at the Ames Research Center, Moffett Field, California, on May 12, 13, and 14, 1993, are reported. Technological areas covered include actuators, aerospace mechanism applications for ground support equipment, lubricants, latches, connectors, robotic mechanisms, and other mechanisms for large space structures.

14. SUBJECT TERMS

Pyrotechnics, End effector, Band drives, Tribology, Array deployment, Actuators, Latches, Linkages, Antennas, Pointing mechanisms, Sampling

15. NUMBER OF PAGES

393

16. PRICE CODE

A17

17. SECURITY CLASSIFICATION OF REPORT Unclassified	18. SECURITY CLASSIFICATION OF THIS PAGE Unclassified	19. SECURITY CLASSIFICATION OF ABSTRACT	20. LIMITATION OF ABSTRACT

NSN 7540-01-280-5500